ICHSF2014

Daejeon, Korea

May 26–29, 2014

6th INTERNATIONAL CONFERENCE ON HIGH SPEED FORMING

KAIST Korea Advanced Institute of Science and Technology

tu technische universität dortmund

SMD

IUL

HIGH SPEED FORMING 2014

PROCEEDINGS
OF THE
6th INTERNATIONAL
CONFERENCE

MAY 26−29, 2014

DAEJEON, KOREA

Edited by:

H. Huh
A. E. Tekkaya

In cooperation with:

BK21+ posco Welmate

I²FG Bmax shaping your future LEASPI

Preface

Since the first ICHSF, which was held in 2004 at the Technische Universität Dortmund, Germany, this biannual conference has grown into one of the major events for high speed forming technologies and its applications. This meeting series is now being organized with the support of the International Impulse Forming Group (I^2FG) that was formed in October 2008 through the vision of Professor Erman Tekkaya. His goal was to model this in many ways after the International Cold Forging Research Group which has been instrumental in applying cold forging to wide manufacturing practice. The public face of this site can be found at http://www.i2fg.org with useful information as well as the proceedings of all the ICHSF meetings. This 6th conference is organized as a joint event of the Department of Mechanical Engineering of KAIST (Korea Advanced Institute of Science and Technology) and the Institute of Forming Technology and Lightweight Construction of Technische Universität Dortmund.

Like its five predecessors, the ICHSF 2014 shall provide an international forum for the exchange of experience and knowledge to scientists, engineers, manufacturers, industrial operators as well as other interested persons. Especially this conference is, for the first time, held in the Asia region, which provides a truly international forum to disseminate cutting-edge information on the high speed forming. The large number of international participants from 12 different countries emphasizes the demand for discussions in this niche technology. 38 high quality papers are presented over a range of topics including impulse forming and equipments, joining and welding, and their modeling. The papers are contributed by 25 academic institutions, 6 industries, and 10 research institutions. Accordingly, the conference will serve as a platform to present research results regarding the process technologies, tools and equipment, energy, materials and measurement techniques, modeling and simulation, and industrial applications.

We would like to take this opportunity to cordially thank the authors and co-authors, the scientific committee as well as all participants of the conference for their valuable contributions. Special thanks are due to Mr. Min Kuk Choi, Mr. Joern Lueg-Althoff and Mr. Christian Weddeling for compiling these materials. It is our pleasure to express deep gratitude for strong support from POSCO.

We are particularly honored to welcome you to Daejeon, Korea.

We hope to see you at the next meeting in Dortmund in 2016.

Daejeon, May 2014

Hoon Huh
KAIST

A. E. Tekkaya
Technische Universität Dortmund

Scientific Committee:

Chairmen

Hoon Huh	Korea
A. Erman Tekkaya	Germany

Members

Charlotte Beerwald	Germany
Glenn S. Daehn	USA
Prashant. P. Date	India
Yuanwen Gao	China
Sergey Golovashchenko	USA
Yeong-Maw Hwang	Taiwan
Mehrdad Kashani	Japan
Matthias Kleiner	Germany
Erhardt Lach	France
Paulo Martins	Portugal

Organizing Committee:

Chairmen

Hoon Huh	KAIST
A. Erman Tekkaya	TU Dortmund University

Members

Jaebok Nam	POSCO
Chang Gyun Jung	POSCO
Bong Yong Kang	KITECH
Jung Han Song	KITECH
Geun An Lee	KITECH
Daeyong Kim	KIMS
Ji Hoon Kim	Pusan National University
Heon Young Kim	KNU
Woo Jong Kang	Kyungil University
Seho Kim	Daegu University
Myoung-Gyu Lee	POSTECH
Jeong Kim	Pusan National University
Jong Bong Kim	Seoul National University of Science and Technology
Seok Bong Kim	ADD
Yong Moon Ryu	Korea Automotive Technology Institute
Moon-Yong Lee	Sungwoo Hitech

Computational Solid Mechanics and Design Lab
Korea Advanced Institute of Science and Technology
Prof. Hoon Huh

Institute of Forming Technology and Lightweight Construction
Technische Universität Dortmund
Prof. Dr.-Ing. M. Kleiner
Prof. Dr.-Ing. A. E. Tekkaya

Table of Contents

Session 3 Process Technologies (Welding & Joining)

Session 4 Modeling and Simulation (Forming)

Session 5 Process Technologies (Welding & Joining)

Session 6 Process Technologies (Forming)

Session 7 Modeling and Simulation (Forming)

Session 8 Process Technologies (Forming)

SESSION 1

MATERIALS AND MEASUREMENT TECHNIQUES

Avoiding Bending in Case of Uniaxial Tension with Electromagnetic Forming *

O. K. Demir, C. Weddeling, N. Ben Khalifa, A. E. Tekkaya

Institute of Forming Technology and Lightweight Construction, TU Dortmund, Germany

Abstract

During electromagnetic forming, excessive bending of the specimen takes place due to high velocities and inertia. We show that the excessive bending can be prevented by optimizing the coil geometry in case of uniaxial tension. The process is simulated with various coil geometries, and the resulting amount of bending is compared to the case of standard Nakajima Test. The comparison shows that the bending can be minimised to acceptable levels to be able to call the method a decent way of determining forming limits. The results should be verified experimentally.

Keywords

Forming limits, Electromagnetic forming, Nakajima Test

1 Introduction

To determine the quasi-static forming limits of a material there are standard tests like Nakajima Test and Marciniak Test. In these tests, the material should be formed monotonically on distinct strain paths until failure. There is not a standard test in case of electromagnetic forming. The main reason for this is the difficulty to let forming proceed on a certain strain path monotonically: The specimen bends and twists in several planes due to practical impossibilities, high velocities, and inertia.

* *This work is based on the results of the German Research Foundation (DFG) project Te 508/10-2 (PAK343); the authors would like to thank DFG for its financial support*

In this paper, we focus on the electromagnetic forming on the strain path of uniaxial tension, and propose a solution to the problem of bending.

To stretch material uniaxially, a narrow specimen is formed into a die cavity. If this is performed with a spiral coil, the centre of the specimen cannot be pushed with the electromagnetic forces. This leads to excessive bending in the centre. In order to avoid this, instead of a spiral one, a straight coil should be used. This improves the situation in the centre, however; without an optimization of the coil geometry, a flat coil leads to excessive bending at the rim of the specimen.

Only if we can avoid any excessive bending, we can be sure that the forming proceeds monotonically on the strain path of uniaxial tension. And only in this case, we can be sure that the maximum strain achieved is the forming limit for uniaxial tension.

We simulate the electromagnetic forming of a narrow specimen into a round die cavity. This is done with a straight coil, and the coil geometry is optimized to minimize any unwanted bending. The simulation results are compared with the results of a conventional Nakajima-Test. The comparison shows that the unwanted bending and wavy form of the specimen can be minimized by coil geometry optimization.

2 State of the Art

Several researchers observed the bending of the specimen during forming into a die cavity. The bending was seen both in cases of a spiral coil or a straight coil.

Kleiner et al. (2005) investigated forming into a conical die using a spiral coil [1]. Simulation showed a "*strongly inhomogeneous velocity distribution in the sheet metal*". They stated: "*In case of spiral coils, the pressure in the centre of the workpiece is always zero; therefore a homogenous distribution is not achievable*". This inhomogeneous velocity distribution leads to the bending of the specimen during forming (see Figure 1).

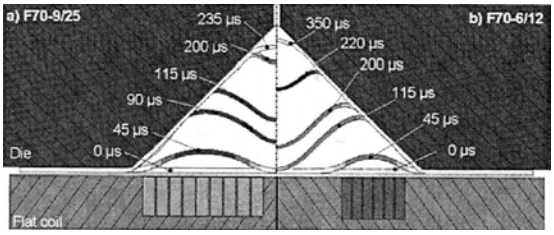

Figure 1 *The wavy forms the specimen takes in case of electromagnetic forming with spiral coils. A round specimen is formed into a v-shaped die cavity [1]*

Golovashchenko (2007) used a straight coil to form on the strain paths of plane strain and uniaxial tension (see Figure 2a) [2]. He reported a "*nonuniformly distributed electromagnetic field*" and a "*nonmonotonic character of deformation*". He observed a "*fold in the center of the sample*" (Figure 2b). By stating "*The shape is different from typical dome shape of samples after FLD testing*", he revealed that the method is not suitable to determine forming limits like in a decent "*FLD testing*" method.

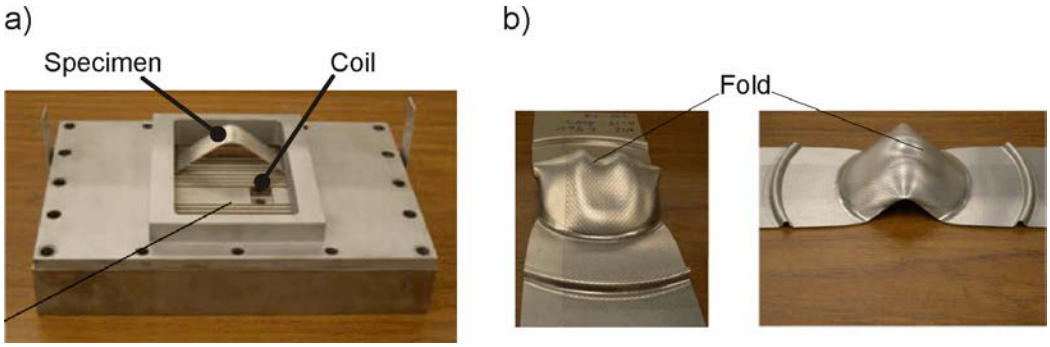

Figure 2 *a) Straight coil windings laying under the specimen b) The specimen after being formed with a straight coil [2]*

Kamal (2005) introduced a coil design, which is called Uniform Pressure Actuator, to be able to use straight coils more effectively [3]. In this design, a conductive part is added to the setup. This part is called the conductive outer channel. The channel and the workpiece form a closed circuit and the induced current flows through it. Imbert et al. (2006) used this design and compared the results with a spiral coil [4]. They reported drastic improvement in the uniformity of the velocity distribution, and thus less bending of the specimen.

They obtained this result by using a straight and a flat coil, and focused on the bending in the centre, not on the bending at the rim. Our simulation results show that a flat coil induces severe bending at the rim. In this paper we are going to change the flat shape of the coil, and optimize it to prevent bending.

3 Methods

3.1 The Finite Element Model

The specimen material is EN AW-5083 with temper designation H111. The quasi-static flow curve of the material was obtained by conventional tensile tests. The high strain rate flow curves until 1000 s^{-1} were determined by the company Nordmetall GmbH using a rotating wheel test, and published by Engelhardt et al. in 2010 [5]. These flow curves do not exhibit a significant strain rate dependency. That is why, the strain rate dependency of the workpiece material was neglected during the simulations.

The specimen is a scaled version of standard Nakajima Test specimen that is used to create uniaxial tension. Its dimensions can be seen in *Figure 3*. It is modelled with approximately 15000 nodes and 10000 3-dimenisonal brick elements with single integration points. The specimen thickness is divided into three elements. The element aspect ratio varies between 1 and 2.15.

The coil width was varied between 8.5 mm and 10 mm during the optimization. The thickness profile of the coil was also varied during the optimization. At the thickest point the coil is 14 mm thick (see *Figure 3*). The coil was modelled with 10000 nodes and 12000 3-dimensional brick elements with single integration points. The element aspect ratio varies between 1.3 and 2.

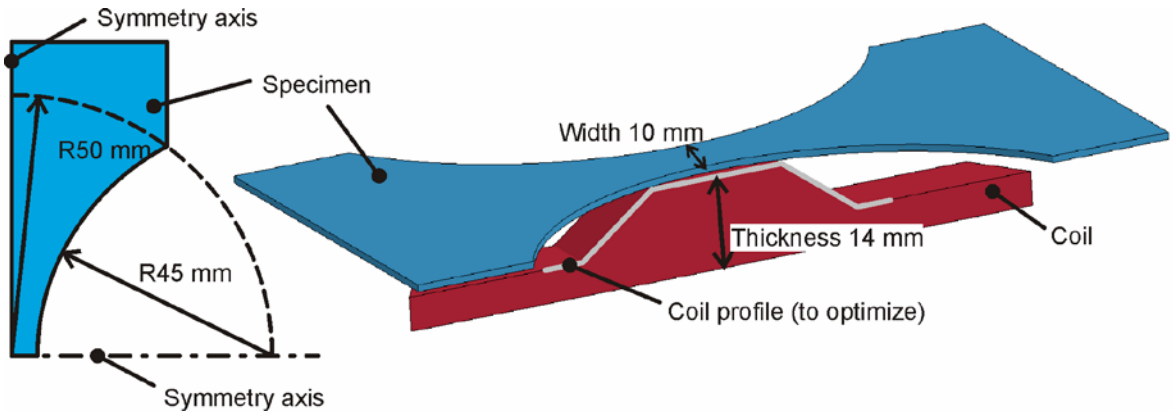

Figure 3 *The geometries of the specimen and the coil. The specimen has a thickness of 1 mm.*

The dimensions of the drawing ring are given in *Figure 4*. The edge radius of it is 5 mm. A 25 kN blank holder force and a draw bead at Ø150 mm was used in the model.

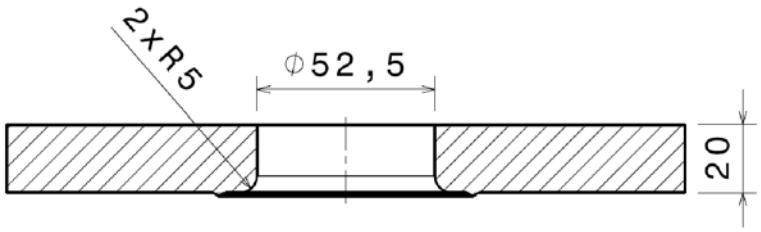

Figure 4 *The drawing ring has a round opening*

For the electromagnetic part of the simulation, the machine called SMU 0612 FS was modelled with its 80 μF capacitance, 4.2 mΩ internal resistance, 40 nH internal inductance, and 9 kJ maximum energy. This machine is used by the Institute of Forming Technology and Lightweight Construction (IUL) for electromagnetic forming, and was manufactured by the company Poynting GmbH.

The simulation was conducted with LS-DYNA v980. The electromagnetic, thermal and the mechanical parts of the problem were loosely coupled with each other. The electromagnetic matrices were updated every 5 microseconds. The electromagnetic and thermal solutions had a time step of 0.04 microseconds, while the mechanical solution had a time step of 0.02 microseconds.

In order to evaluate the simulation results, they were compared with a conventional quasi-static Nakajima Test. For that, Nakajima Test was simulated using the same specimen geometry with the electromagnetic simulation. A semi-spherical punch (Ø100 mm) was used in the Nakajima Test simulation. This simulation was performed by explicit finite element method using LS-DYNA v980.

3.2 Optimization

The optimization was performed manually, without using any special software. The width and the thickness profile of the coil were optimized. Three different widths were simulated: 8.5 mm, 9.25 mm, and 10 mm, which is equal to the specimen width. The various thickness profiles that were simulated can be seen in *Figure 5*.

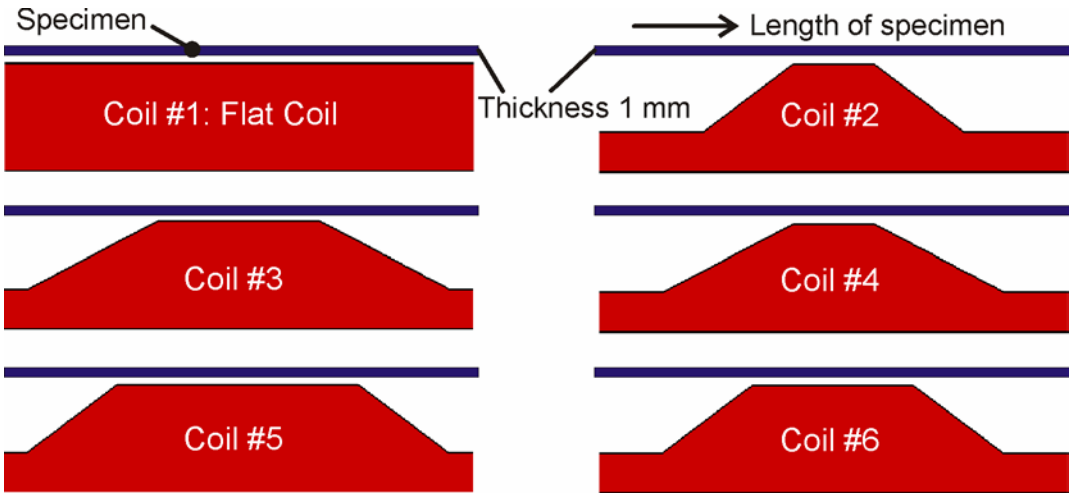

Figure 5 *Thickness profiles that were used in the simulations.*

The forms that the specimen takes during electromagnetic forming and Nakajima Test were compared with each other. This was done at two different forming depths: 2.8 mm (at the beginning of the process) and 12 mm (towards the end of the process). For that, the simulation was stopped at the desired forming depth, and a section cut along the length or width of the specimen was taken. In order to see the details of the cross-section geometry better and notice the nuances between them, the displacements were scaled up. The corresponding scaling ratios are given in the captions of the figures *Figure 6*, *Figure 7*, and *Figure 8*.

4 Results

4.1 Specimen profile along the length

To see the specimen profile along the specimen length, a section cut normal to the specimen width was taken. *Figure 6* and *Figure 7* show this section view. *Figure 6* reveals the comparison between three different coil designs at the beginning of the process (forming depth 2,8 mm). *Figure 7* shows the same comparison towards the end of the process (forming depth 12 mm).

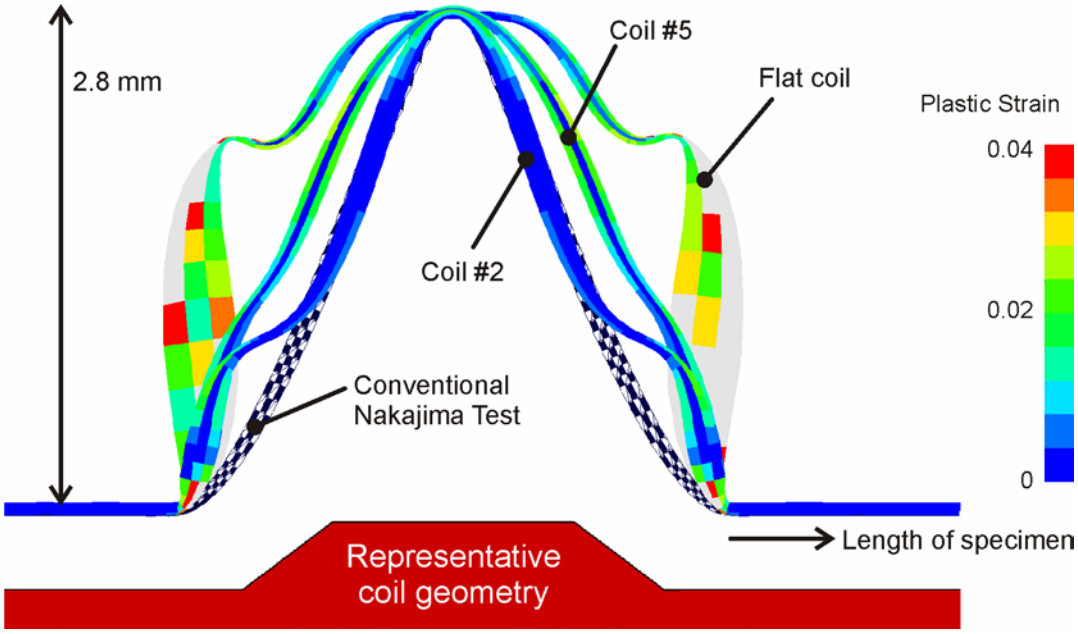

Figure 6 *Cross-sectional views of specimen in cases of different coil geometries given in* ***Figure 5****, and in case of conventional Nakajima Test. Displacement scale factor: 20*

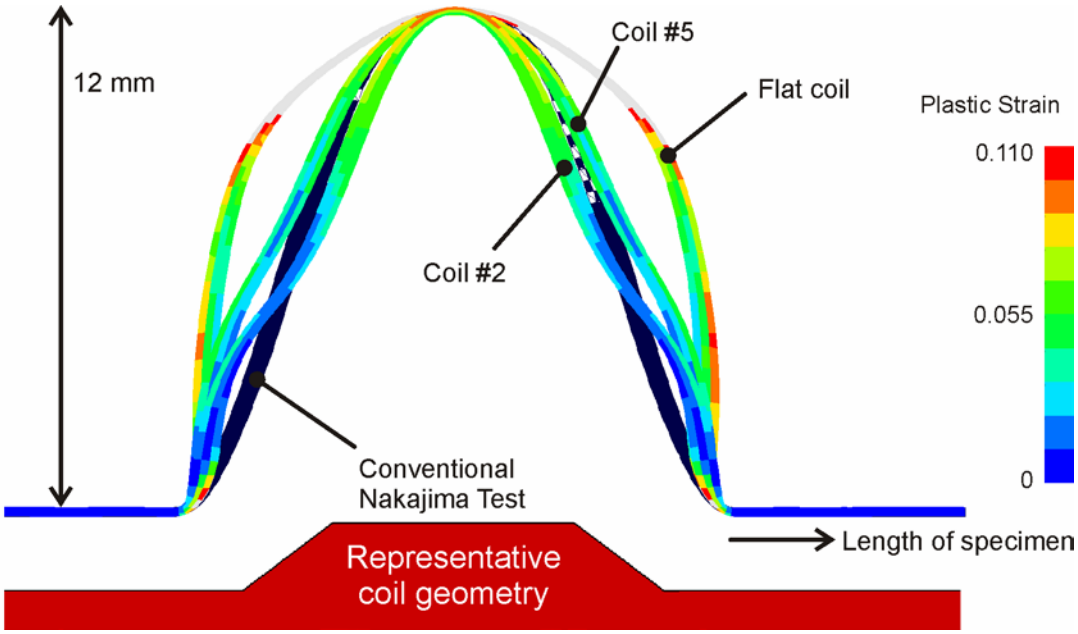

Figure 7 *Cross-sectional views of specimen in cases of different coil geometries given in* ***Figure 5****, and in case of conventional Nakajima Test. Displacement scale factor: 5*

4.2 Specimen profile along the width

To see the specimen profile along the specimen width, a section cut normal to the specimen length was taken. *Figure 8* shows this section view. *Figure 8* reveals the comparison between coils with three different widths: 8.5 mm, 9.25 mm, and 10 mm.

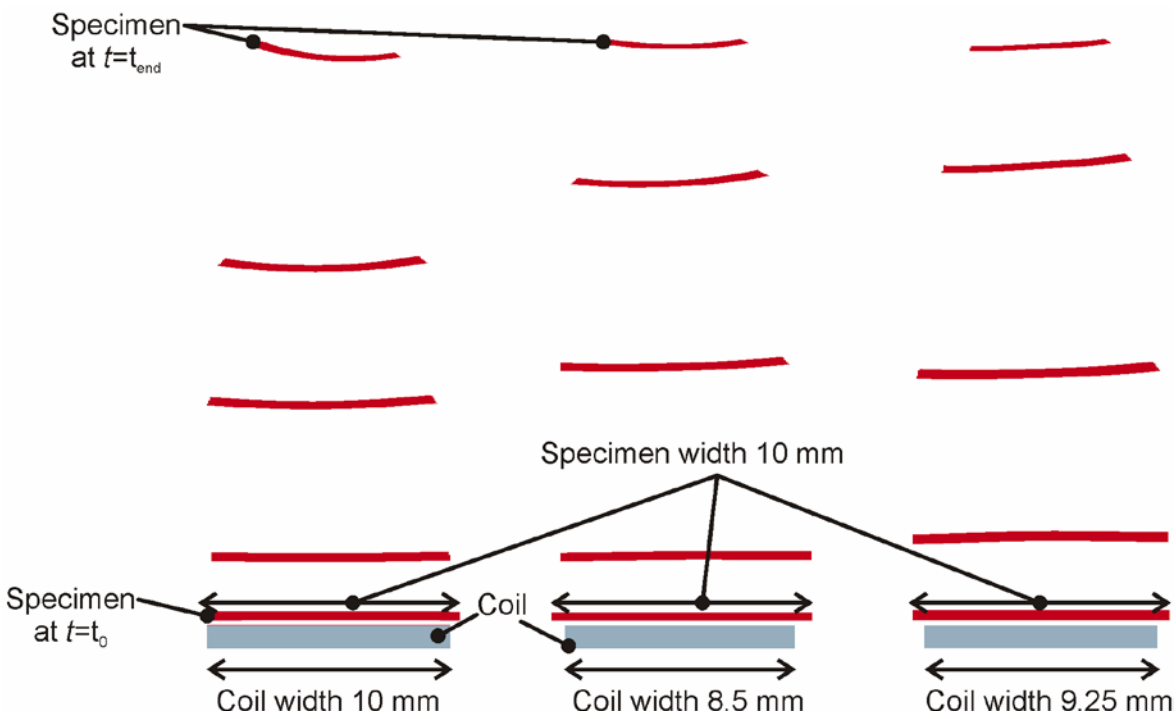

Figure 8 *Cross-sectional views of specimen during the test, in case of different coil widths. Figure not to scale. Displacement scale factor: 5*

5 Discussion

Figure 6 shows that the specimen experiences severe bending in case of a flat coil. The change of coil profile, in which it is thicker in the middle and thinner at the rim, improves the situation drastically.

At the beginning of the forming process (*Figure 6*), in case of Coil #2, the profiles of the quasi-static and electromagnetic cases overlap perfectly in the centre. Only the slight bending at the rim distinguishes the two results. In case of Coil #5, the profile does not overlap perfectly with the quasi-static case. The electromagnetic forming stretches the specimen more, compared to Nakajima Test. When we compare the results with Coil #2 and Coil #5, we see that Coil #2 leads to more bending in the specimen profile: The specimen profile with Coil #2 is wavier than the one with Coil #5.

Towards the end of the forming process (*Figure 7*), in case of Coil #5, the profiles of the quasi-static and electromagnetic cases overlap in the middle. Only the slight bending at the rim distinguishes the two results. When we compare the results with Coil #2 and Coil #5, we see that coil Coil #2 leads to more bending in the specimen profile: The specimen profile with Coil #2 is wavier than the one with Coil #5.

Coil #5 delivers at both the beginning and the end of the process the minimum amount of bending. This is an acceptable amount to call the test as a decent method of determining forming limits. This can be seen when the cross-sections delivered by Coil #5 and Nakajima Test are compared in figures *Figure 6* and *Figure 7*. The results show that it is logical to select Coil #5 as the optimized coil geometry.

Figure 6 and *Figure 7* show the bending in the plane normal to the width of the specimen. *Figure 8* shows that the specimen also experiences bending in the plane

normal to the length of the specimen. Such a bending does not occur when the forming is conducted quasi-statically with a punch. This bending is a severe disadvantage of using an electromagnetic coil instead of a punch, and must be minimized.

Figure 8 shows that the least bending occurs when the coil width equals 9.25 mm. So it is logical to select 9.25 mm as the optimized coil width.

6 Conclusion

In order to determine the electromagnetic forming limit of a material in case of uniaxial tension, a narrow specimen can be formed electromagnetically into a die cavity. However, during this process, the specimen experiences excessive bending in the planes normal to its length and width. Simulation results show that this bending can be minimized by optimizing the coil geometry. The optimized coil geometry delivers specimen geometries which are very similar to the specimen geometries encountered during the standard Nakajima Test.

To verify the conclusions drawn from the simulations, experiments should be conducted with the optimized coil geometry, and the results should be compared with the Nakajima Test.

References

[1] *Kleiner, M.; Risch, D.; Beerwald, C.; Brosius, A.:* Influence of the Velocity Distribution during the Process of Electromagnetic Sheet Metal Forming into Dies. Production Engineering Vol. XII/2, p. 95-98, 2005.

[2] *Golovashchenko S.F*: Material Formability and Coil Design in Electromagnetic Forming. Journal of Materials Engineering and Performance 16(3), p. 314-320, 2007.

[3] *Kamal, M.*: A Uniform Pressure Electromagnetic Actuator for Flat Sheet Forming. Ph.D. Dissertation, The Ohio State University, 2005.

[4] *Imbert, P.; Arroyo, A.; Eguia, I.; Fernandez, J.I.; Silveira, E.; Garuz, I.; Daehn, G.S.*: Efficiency Improvement and Analysis of Changes in Microstructure Associated to a Uniform Pressure Actuator. Proceedings of the 2nd International Conference on High Speed Forming - ICHSF 2006, p. 175 – 186.

[5] *Engelhardt, M.; von Senden genannt Haverkamp, H.; Kiliclar, Y.; Schwarze, M.; Vladimirow, I.; Bormann, D.; Bach, Fr.-W.; Reese, S.:* Characterization and Simulation of High Speed Deformation Processes. Proceedings of the 4th International Conference on High Speed Forming - ICHSF 2010, p. 229 – 238

Experimental investigations on forming limits for aluminium alloy sheet metal at various strain rates*

M. Engelhardt[1], C. Klose[1]

[1] Institut für Werkstoffkunde (Materials Science), Leibniz Universität Hannover, Germany

Abstract

The application of a pneumatic testing device for the high speed forming of aluminium alloy sheet metal is presented in this paper. Former publications of the authors showed the feasibility of a drop tower test rig for Nakajima testing of sheet metal (EN AW-6082 T6) at punch speeds of approximately 10 m/s or strain rates of approximately 100 s^{-1}. However, the pneumatic testing method allows for punch speeds of at least more than five times higher compared to the mechanical testing devices available. The modular design of the pneumatic-mechanical testing device enables the set up in a universal testing machine, as used for tensile testing, and thus, punch speeds in the range of 1 mm/s are also possible for testing at quasi-static strain rates.

The experimental set-up and the measuring system used for the trials will be described in detail. At first, experiments with a punch speed of 1 mm/s, according to DIN EN ISO 12004-2, were done using various specimen geometries in order to determine a forming limit curve for 1 mm thick aluminium alloy sheets (EN AW-5083) at quasi-static strain rates. Secondly, experiments with different air pressures were conducted to evaluate the speed capabilities and restrictions of the device. After verification of the desired speeds and possible quality, several specimens were tested at 21 m/s and the resulting strains were compared to those achieved at low forming speeds. Optical analysis was used to determine the resulting strains at fracture for all specimens tested.

Keywords

Aluminium Alloy, Forming Limit Test, Strain Rate Analysis

---

* *This work is based on the results of Paketantrag 343 "Methodenplanung für quasistatisch-dynamisch kombinierte Umformprozesse"; the authors would like to thank the German Research Foundation (DFG) for its financial support*

1 Introduction

Sheet metal forming is used for the mass production of parts with various geometries at high qualities for the automotive or aviation industries. Yet, the complexity of the sheet metal products is limited to the formability of the sheet metal material. These limitations can be overcome in different ways. For example, changing the strain path in a multi-step forming process is an effective way [1] without using high(er) temperatures as needed for superplastic forming (SPF) [2] or quick plastic forming (QPF) [3]. The need of multiple steps is a disadvantage when changing strain paths, since the changes are limited to geometrical and/or process restrictions. The temperatures required for SPF and QPF processes lead to the need of additional heating and/or processing equipment, combined with low to very low forming speeds and their corresponding processing times. Changes in microstructure and heat treatment conditions can lead to unbeneficial mechanical properties as well as additional costs for following heat treatments.

The use of high speed forming processes is an alternative method to increase forming limits. It has been researched intensely in the last years starting middle of the past century. The effect of increased formability at high forming speeds has later been named “hyperplasticity” by Balanethiram and Daehn (1994) [4]. The main phenomena causing this increase in formability are found to be due to inertia effects [5–7], changes in strain rate sensitivity [8–10], or a combination of both. An overview of the various processes and means to provide the energy required for the high speeds needed can be found in [11]. Commonly used methods are explosive, electro-hydraulic, or electromagnetic forming.

However, comparable experimental analysis of these processes, especially for the data generation and verification of simulations in high speed sheet metal forming, is still not established properly. The most common way to determine material data at high speeds is the use of tensile tests with a split Hopkinson Pressure bar, which lacks the flexibility to test at stress states different than that of uniaxial tension. Experiments using electro-hydraulic forming or electromagnetic punch stretching proved to be able to reach higher strain rates but miss the possibility of defined strain paths, reproducibility and, most importantly, their deformation cannot be standardized or directly compared to quasi-static results. The commonly used standardized tests for the evaluation of forming limits, as stated in DIN EN ISO 12004-2, are only valid at low forming speeds (punch speeds between 1 mm/s to 2 mm/s). Moreover, the available test equipment is not capable of reaching punch speeds needed for high speed forming. Recently published test setups in accordance to DIN EN ISO 12004-2 used a high-speed crash testing machine [12] and a drop tower testing device [13] to achieve punch speeds of around 10 m/s. Although the test setups showed suitable to predict the dynamic forming limit curves for the tested materials, the achieved deformation speeds were not sufficient to increase the formability of the tested sheet metals.

From the results and findings stated above, it is obvious that there is a need of a forming device capable of testing standardized sheet metal specimens at low to very high forming or punch speeds respectively. In this paper, a forming device capable to test at low punch speeds (<10 mm/s) and very high punch speeds (>10 m/s) is shown. In addition, the device is also capable of testing specimens at low and very high speeds in the same set-up.

2 Forming device

The general set-up of the device is shown in Figure 1. The selected air pressure is provided to the air inlet of the pressure valve. After the valve is open, the piston is accelerated inside the cylinder according to the set air pressure (up to 250 bar) until the connected punch hits the sheet metal specimen to be tested. A measuring set-up, made of a laser curtain, has been placed just above the specimen in order to measure the speed of the punch at the moment of impact.

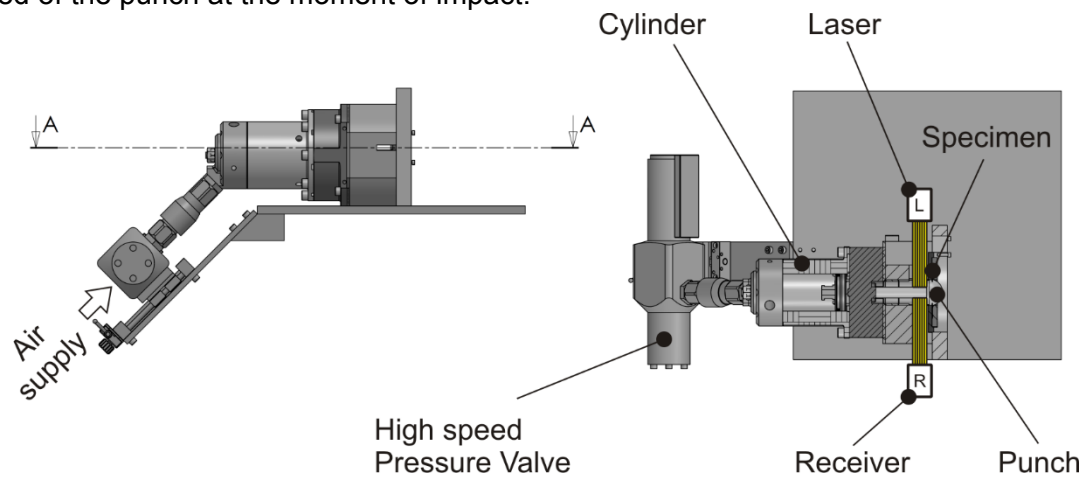

Figure 1: *Set-up of the pneumatic testing device in side (left) and section view (right)*

The forming device described above (Figure 1) can be roughly divided in three connected units, the energy supply, the forming device itself, and the speed measurement unit.

2.1 Energy supply

The energy supply (Figure 2) consists of a compressed air bottle, a pressure regulator, different valves, and an intermediate pressure storage. Compressed air bottles (volume of 50 litres) with a maximum pressure of 300 bar (standard) can be employed as air pressure supply used to fill the pressure storage. The interposed pressure regulator is used to set the air pressure between 20 bar to 300 bar as desired for the experiments, the adjacent check valve separates the compressed air bottle and the pressure storage during the experiments. Between the pressure storage and the high speed valve a manually operated 2/2-way valve is placed in order to detach the forming device from the air supply between experiments or when the device is not in use. The high speed pressure valve, type PCD-H 15 by müller co-ax AG, is an electronically controlled 2/2-way valve designed for pressures of up to 500 bar, powered with an additional pressure system operated at 10 bar, and a minimal switching time of 30 ms (opening and closing).

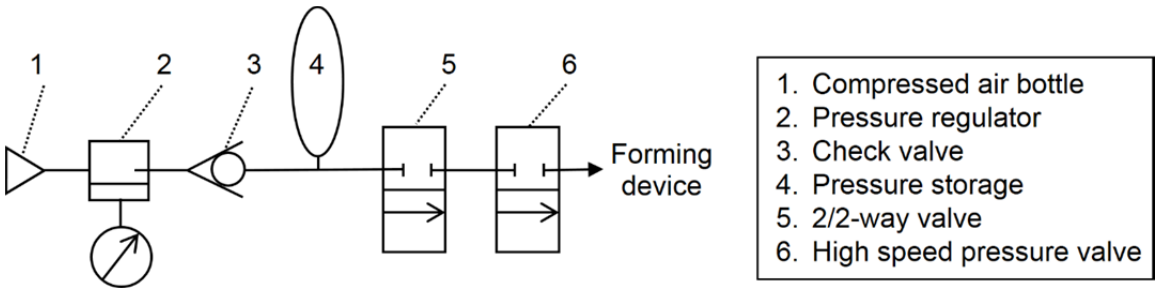

Figure 2: *Sketch of air supply system*

A pressure release valve attached to the pressure storage and a quick release coupling connecting the high speed valve and the forming device are not shown in Figure 2.

2.2 Forming device

A detailed CAD-drawing of the forming device is shown in Figure 3. The device works either pneumatic-mechanically (high speed mode) or manipulated externally with the help of a universal testing machine (low speed mode).

In both modes, the specimen (Figure 3, bottom right) is fixed between the blank holder and the draw ring. The width of the specimen is defined by the “X” dimension; in the case that a circular specimen “100” is used. Points of 1 mm diameter were laser engraved on the sheet specimens in a linear pattern with 1 mm distance in between and perpendicular to rolling direction. In order to evaluate the strains after fracture of the sheet specimens, the change in distance of the laser engraved dots was optically analysed using an ARGUS system by GOM mbH.

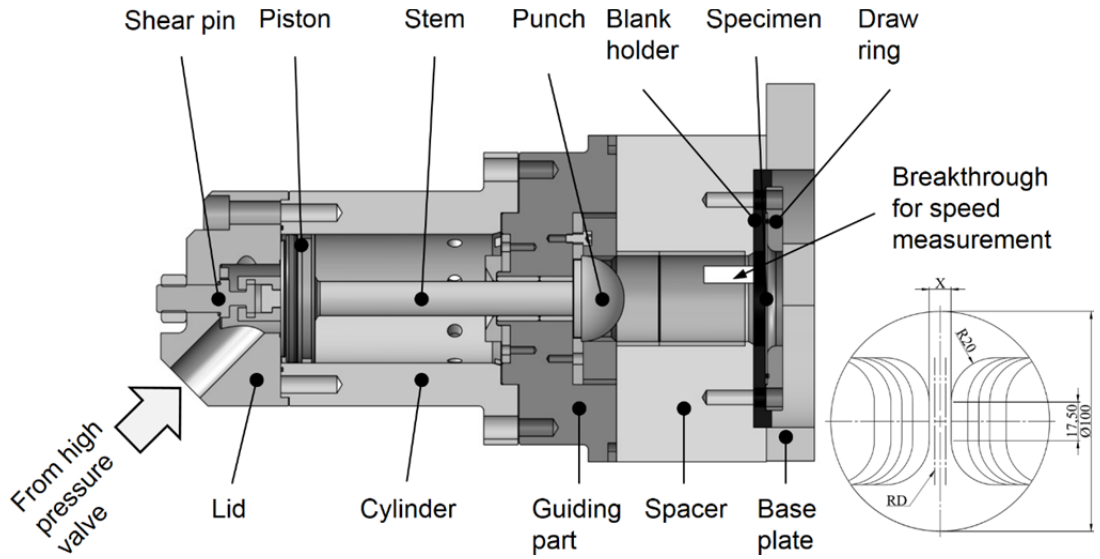

Figure 3: *Detailed drawing of the forming device and specimen shapes used for testing (bottom right)*

2.2.1 High speed mode

The initial state of the experiment is depicted in Figure 3. Here, the piston (Ø75 mm) is in contact with the lid. It can also be fixed using a shear pin. After the high speed pressure valve is activated (opening), the air flows in through the lid and enters the small pressure chamber (Ø40 mm). This small pressure chamber reduces the surface in which the air pressure is acting on, and thus, decreasing the force on the piston in the initial state. If a shear pin is used, the shear pin locks the piston in its position until the pressure/force working on the piston exceeds the yield strength of the shear pin. The reduced diameter of the small pressure chamber allows to reduce the required shear pin diameter for different working pressures. If no shear pin is used or if the shear pin fails, the piston-stem-punch unit (hemispherical punch Ø50 mm) is propelled towards the specimen, losing contact with the lid and instantaneously increasing the area on which the air pressure is working on, up to the full surface of the piston. The piston-stem-punch unit is then accelerated, hitting and deforming the specimen until it is stopped in the final position at the top of the guiding part. Here, the air pressure acting on the piston is released through the holes in the cylinder wall. The deformation depth can be adjusted using distance plates attached on top of the guiding part. After the high speed pressure valve is closed automatically, the system is pressureless and the deformed specimen can be removed.

2.2.2 Low speed mode

In the low speed testing mode, the cylinder, lid, and piston are dismounted, and the forming device is inserted vertically into a universal testing machine (not shown). In the initial state, the stem-punch unit is in contact with the specimen. The movement of the testing machine crosshead is then used to deform the specimen to a certain deformation depth or until rupture occurs.

2.3 Speed measurement

An ODC1201-20 Laser Beam Sensor by MICRO-EPSILON Eltrotec GmbH has been used for measuring the punch speed right before impact on the specimen. The sensor consists of a Laser, emitting a linear laser curtain with a height of 20 mm, with a cut-off frequency of 100 kHz and a dynamic resolution of 100 µm. The laser and receiver are placed just above the blank holder, in 10 mm distance to the specimen.

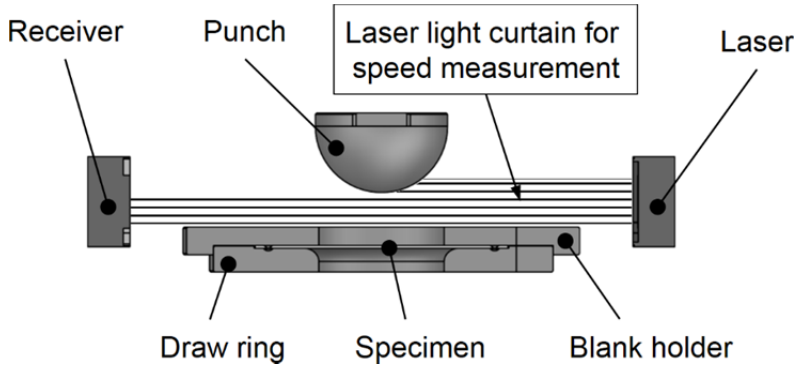

Figure 4: *Speed measurement set-up*

Figure 4 shows how the laser curtain is shadowed by the approaching punch. The sensor signal strength is between 12 V (when not shadowed) and 0 V (when shadowed completely). The sensor signal has been measured using a storage oscilloscope, which allows to manually evaluate the resulting speed as shown in Figure 5.

3 Results and Discussion

3.1 Punch speed adjustment

While the punch speed during testing in low speed mode equals that of the crosshead of the used universal testing device, to define the punch speed at high speed mode a speed adjustment is needed. For this, several trials at different air pressures, and with or without shear pins of different diameter, had to be performed. Examples for the resulting signals and the optical-manual evaluation of the punch speed (v_p) are shown in Figure 5.

First trials were performed using no shear pin with increasing air pressures, starting at 50 bar, increasing the pressure in several steps to a maximum pressure of 200 bar. Up to a pressure of 100 bar, the punch speed increases from around 12 m/s to 18 m/s. Nevertheless, the resulting deformation energy or mass of inertia of the punch is not sufficient to deform specimens with a width of more than 45 mm until rupture occurs. Above 100 bar the punch speed increases very slowly and with a high deviation of more than ±5 m/s. This is most probably due to changes in friction and pressure surges leading to premature movement of the piston-stem-punch unit. Only at pressures of 150 bar or higher, reproducible punch speeds with a standard deviation of about 1.5 m/s are possible, reaching 21 m/s at 150 bar and a maximum speed of around 23 m/s at 200 bar.

However, if a shear pin is used, much higher speeds are possible. Trials with different shear pin diameters at 200 bar air pressure were done. Punch speeds of 33.3 m/s and 52 m/s were possible with shear pin diameters of 5 mm and 7.5 mm respectively (Figure 5). Thus, exceeding the punch speed without a shear pin at 200 bar by a factor of 1.5 to 2.5.

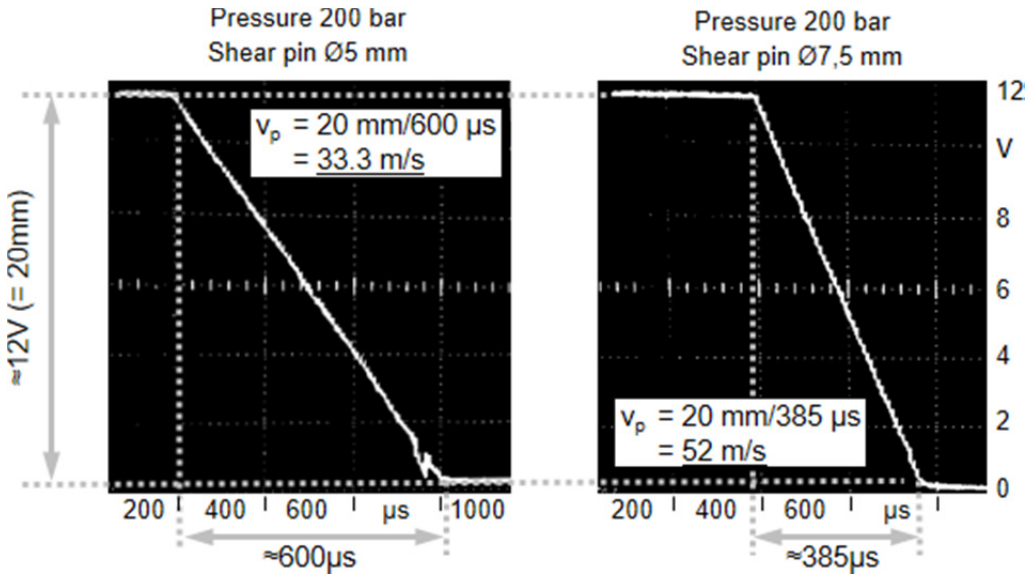

Figure 5: *Samples of speed measurement results*

3.2 Forming analysis at high speed

At first, low speed experiments were done with a punch speed of 1 mm/s in a universal testing machine. Several specimen geometries / widths were used to display the different stress states needed for defining the forming limit curve (FLC) shown in the forming limit diagram in Figure 6. Here, the horizontal axis shows the minor strain φ_2 and the vertical axis the major strain φ_1. The specimen widths of 7.5 mm, 10 mm, 15 mm, 35 mm and 55 mm as well as full circular specimens were chosen for these experiments.

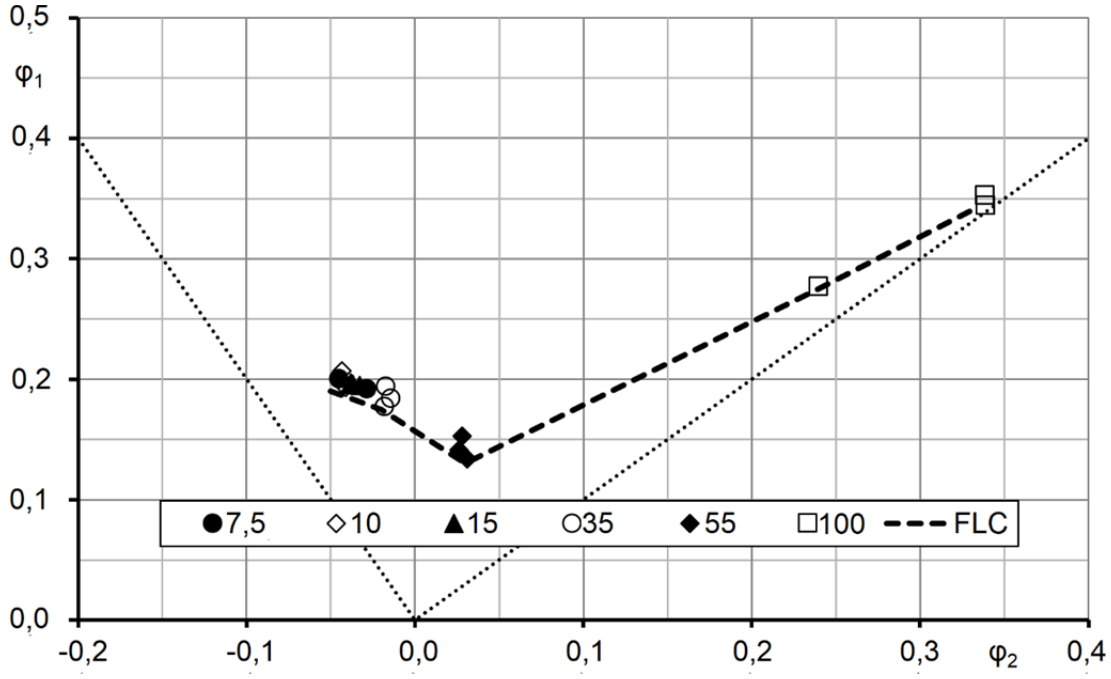

Figure 6: *Forming limit diagram, punch speed 1 mm/s*

The forming limit curve is in good accordance with forming limit diagrams presented by Naka et al. [14], although the forming limits presented here are approximately 10-20 % higher, especially for the full specimens. These differences could occur due to the different experiment settings, such as the punch geometry used (Naka et al.: flat/ Ø92 mm and here: hemispherical/ Ø50 mm), and specimens used (Naka: rectangular/ 170 mm to here: round/ Ø100 mm).

After the forming limit curve at quasi-static level or low punch speeds had been evaluated, high speed trials using 150 bar of air pressure and no shear pin with a resulting punch speed of approximately 21 m/s were done. This speed was chosen for the first high speed trials, since it depicts the lowest punch speed at which reproducible testing is possible, as stated before. As can be seen in the forming limit diagram for low speed testing, a specimen width between 7.5 mm and 15 mm results in almost the same values for minor and major strain. Therefore, different specimen widths, including 10 mm, 35 mm, 45 mm, 60 mm and full circular specimens (100), were chosen for the high speed testing.

Figure 7 shows the strains per dot and, for better visibility, the resulting strain paths (depicted by arrows) for the specimens tested at 21 m/s. It is obvious, that for all specimen geometries tested, the strains at fracture at a high punch speed of 21 m/s are much higher than those at the low punch speed of 1 mm/s. Furthermore, the chosen specimen widths allow for measuring more diversified strain states than those used for low speed testing.

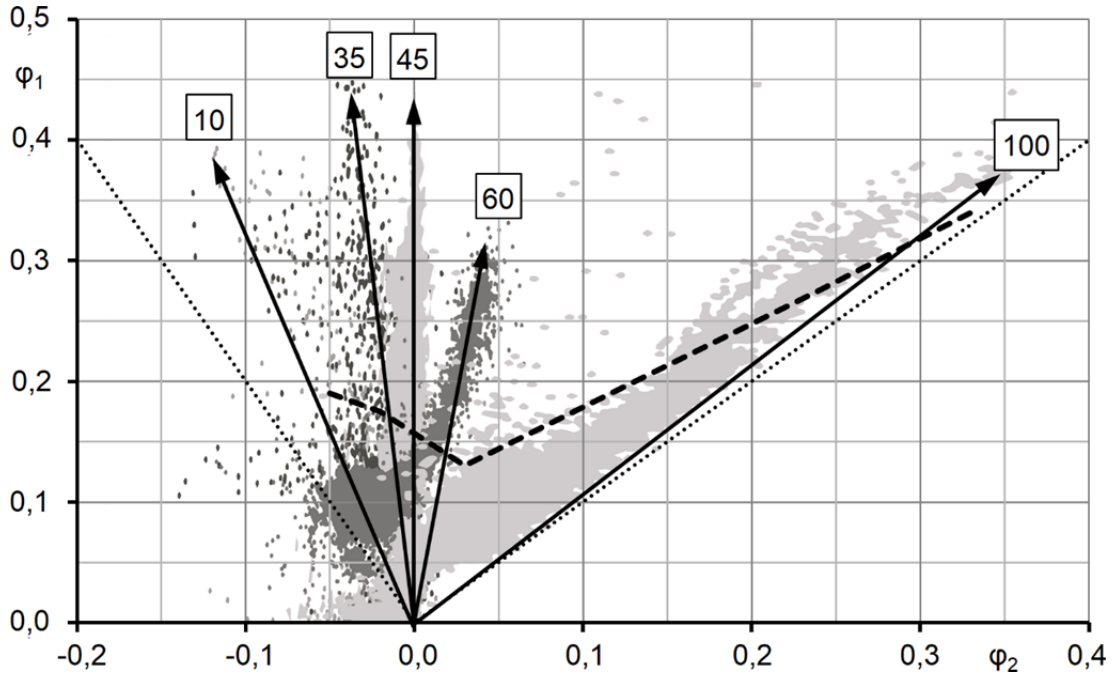

Figure 7: *Deformation of specimens of different widths tested at 21 m/s compared to the forming limit curve for 1 mm/s punch speed*

4 Summary

- The design of a pneumatic-mechanical forming device for testing of forming limits at low (<10 mm/s) and very high punch speeds (>10 m/s) for sheet metal has been presented.
- Experiments with different settings were done to define the limitations of the forming device. Here, the forming device has proven capable of punch speeds higher than 50 m/s.
- Further experiments are needed to evaluate the maximum capability of the forming device
- A forming limit curve for a 1 mm thick EN AW-5083 aluminium alloy sheet metal was determined at a low punch speed of 1 mm/s.
- High speed trials with a punch speed of 21 m/s stated that the achievable formability at this speed is higher than that at low speeds, such as the ones used for quasi-static testing according to DIN EN ISO 12004-2.

References

[1] J.V. Laukonis, A.K. Ghosh, Effects of strain path changes on the formability of sheet metals, MTA 9 (1978) 1849–1856.

[2] A.J. Barnes, Superplastic Forming of Aluminum Alloys, MSF 170-172 (1994) 701–714.

[3] M.S. Rashid, C. Kim, E.F. Ryntz, F.I. Saunders, R. Verma, S. Kim, Quick plastic forming of aluminium alloy sheet metal, 2000.

[4] V.S. Balanethiram, X. Hu, M. Altynova, G.S. Daehn, Hyperplasticity: Enhanced formability at high rates, Journal of Materials Processing Technology 45 (1994) 595–600.

[5] M. Altynova, X. Hu, G.S. Daehn, Increased ductility in high velocity electromagnetic ring expansion, MMTA 27 (1996) 1837–1844.

[6] V.B. Shenoy, L.B. Freund, Necking bifurcations during high strain rate extension, Journal of the Mechanics and Physics of Solids 47 (1999) 2209–2233.

[7] M. Gerdooei, B.M. Dariani, Strain-rate-dependent forming limit diagrams for sheet metals, Proceedings of the Institution of Mechanical Engineers, Part B: Journal of Engineering Manufacture 222 (2008) 1651–1659.

[8] A.H. Clausen, T. Børvik, O.S. Hopperstad, A. Benallal, Flow and fracture characteristics of aluminium alloy AA5083–H116 as function of strain rate, temperature and triaxiality, Materials Science and Engineering: A 364 (2004) 260–272.

[9] T. Mukai, K. Ishikawa, K. Higashi, Influence of strain rate on the mechanical properties in fine-grained aluminum alloys, Materials Science and Engineering: A 204 (1995) 12–18.

[10] E. El-Magd, M. Abouridouane, Characterization, modelling and simulation of deformation and fracture behaviour of the light-weight wrought alloys under high strain rate loading, International Journal of Impact Engineering 32 (2006) 741–758.

[11] M. Engelhardt, von Senden genannt Haverkamp, H., C. Klose, F.-W. Bach, Development of a Pneumatic High-Speed Nakajima Testing Device, in: A.E.

Tekkaya, G. Daehn, M. Kleiner (Eds.), High speed forming 2012: Proceedings of the 5th International Conference on High Speed Forming; April 24th - 26th 2012, Dortmund, Germany, IUL, Dortmund, 2012, pp. 155–164.

[12] S.B. Kim, H. Huh, H.H. Bok, M.B. Moon, Forming limit diagram of auto-body steel sheets for high-speed sheet metal forming, Journal of Materials Processing Technology 211 (2011) 851–862.

[13] Y. Kiliclar, M. Engelhardt, I.N. Vladimirov, M.P. Pietryga, von Senden genannt Haverkamp, Hermann, S. Reese, F.W. Bach, On the Improvement of Formability and the Prediction of Forming Limit Diagrams at Fracture by Means of Constitutive Modelling, KEM 504-506 (2012) 29–34.

[14] T. Naka, G. Torikai, R. Hino, F. Yoshida, The effects of temperature and forming speed on the forming limit diagram for type 5083 aluminum–magnesium alloy sheet, Journal of Materials Processing Technology 113 (2001) 648–653.

Extension of formability of the magnesium wrought alloy AZ31B-O at room temperature by pulse magnetic forming

E. Uhlmann[1], L. Prasol[1], R. Kawalla[2], C. Schmidt[3], T. Becker[3]

[1)] Institute of Machine Tools and Factory Management, TU Berlin, Germany
[2)] Institute of Metal Forming, TU Freiberg, Germany; NUST MISIS, Moscow, Russia
[3)] Institute of Metal Forming, TU Freiberg, Germany

Abstract

For having the lowest density of all metal construction materials of 1.75 kg/dm^3, magnesium wrought alloys are outstanding lightweight materials. The low formability at room temperature limits the industrial use of magnesium AZ31B-O. In this paper the influence of high strain rates was investigated with the aim to improve the formability of the alloy AZ31B-O at room temperature.

The negative strain rate sensitivity of quasi-static strain rates causes an early loss of material stability due to formation of local deformation zones on the work piece surface. This leads to a low formability in the forming state of plane strain, in which the forming limit (FLC) of magnesium alloy AZ31B-O has a critical minimum. For process illustration of multi-axial stress states - which appear in conventional forming processes - the pulse magnetic forming process is used. To create plane strain formability a flat coil is used. The applied die is used to control the free formability. Hereby, a change of the maximum loads on the power transfer zone to areas of plane strain formability occurs.

The results that have been achieved show that high strain rates at room temperature increase the permitted loads of the material with plane strain formability significantly. High speed forming is linked to a rising strain rate sensitivity which increases the flow resistance in critical forming areas, in favor of a rising material stability. This fact is represented by equally reduction of the sheet thickness on the power transfer area. The homogeneous work piece stress clearly increases the formability of AZ31B-O at room temperature compared to quasi-static forming process.

Keywords

Pulse magnetic forming, magnesium AZ31, plane strain formability

1 Introduction

National and international guidelines, e.g. reduction of CO_2 emission in automotives as well as the E-mobility sector due to previously limited energy density of batteries [1], require new lightweight components to reduce the whole weight of a vehicle and associated with these new production technologies. In comparison to steel components, lightweight components like magnesium alloys exhibit lower density and therefore lower mass.
The use of different materials – a so-called “multi-material design” – was investigated in the EU project “Super Light Car”. The mass of the front end structure of a vehicle was reduced up to 100 kilograms, thus the emission of CO_2 could be reduced to 8.4 gram per 100 kilometer. This value corresponds to a fuel economy from 0.3 to 0.5 liters [2]. Especially in the area of E-mobility the total weight of the vehicle structure exhibits a very important role. The average energy density of a lithium-ion battery is 0.10 kWh/kg. The average energy density of a gasoline engine, which was fuelled with premium gasoline, 12.0 kWh/kg. To achieve comparable distances with an electric motor in comparison to a combustion engine an accumulator with a huge energy density is required. The use of lightweight components at different areas in the car body is essential to reduce the weight. Therefore it is necessary to develop an efficient and environmentally sustainable process to form lightweight components like magnesium alloys.
Forming processes with optimal utilization of material and high productivity offer potential for excellent accuracy. Forming process of magnesium alloys is accomplished at high temperatures of 220°C currently. A general challenge in forming of magnesium alloys will be in the realization of forming processes at lower temperatures.
In the last years the pulse magnetic forming processes have gained an increasing attention from both manufacturing companies and research facilities [3, 4]. A considerable advance has been made in the field of process understanding. In this paper an approach for the extension of formability of the magnesium wrought alloy AZ31 by pulse magnetic forming at lower forming temperature is described.

2 State of the art

Formability of magnesium alloy AZ31

In the present work casting rolled and then hot-rolled sheets of the wrought magnesium alloy AZ31 in the condition O (O- temper AZ31B Mg sheet alloy) has been investigated. Magnesium crystallizes in the hexagonal densely packed unit cell (hcp) with an axial ratio c/a of 1.6236. As a consequence of its crystal structure, there are during the forming process at room temperature only two independent slip systems with ‹a›-Burgers vector on the ‹0001›-Basal plane [5]. The activation of the pyramidal slip system of second order which provides not only a deformation component with ‹c›-Burgers vector but also satisfies the ‘von Mises’ criterion of five independent slip systems takes place at temperatures above 225°C. Regardless the critical shear stress τ_{CRSS} possesses for dislocation motion on the ‹0001›-Basal plane the lowest values at all temperatures [6, 7]. Therefore, the ‹0001›‹10$\bar{2}$1›-sliding system is also at high temperatures the main sliding system of magnesium. Associated with this fact the expression of a sharp basal texture during sheet metal fabrication by rolling, in which the c-axis of the unit cell aligns parallel in the intensity

maximum of sheet plane normal [8]. Due to the lack of dislocation activity in the sheet thickness direction at room temperature - parallel uni-axial tensile stress to Basal plane - the material is not able to oppose the geometric softening with dislocation hardening. In addition, the logarithmic degree of deformation ranges in the sheet thickness direction not to mechanical pressure twins for an additional strain contribution along the c axis to form in the sheet thickness direction. This is associated with an early loss of material stability and also a low elongation [9]. After CONSIDÈRE criterion, the material is not stable when the increment of the reduction in cross section exceeds the increment of the stress (1), [10].

$$\frac{dY_f}{d\varepsilon} = Y_f \tag{1}$$

The connection between flow stress and deformation can be captured by using the „Ludwik“ equation in the power function by HOLLOMON (2), [11].

$$Y_f = C \cdot \varepsilon^n \tag{2}$$

The low hardening capacity of AZ31B-O alloy by Basal texture is associated with a hardening exponent less than 0.2. This is associated with an early diffuse constriction in the uni-axial state of stress in the tensile test which ends without strain localization in shear failure [12]. Despite declining hardening exponent formability of AZ31B-O alloy increases with increasing temperature [13, 14]. Macroscopic background is a rising strain rate sensitivity of AZ31B-O alloy [15]. In the extended approach of the HOLLOMON equation the strain rate is taken into account with the exponent *m* of the strain rate sensitivity (3), [16].

$$Y_f = C \cdot \varepsilon^n \cdot \dot{\varepsilon}^m \tag{3}$$

If a cross-section in the forming zone of the material occurs during the forming process an increase of the strain rate takes place. With a positive strain rate sensitivity in the forming zone the flow resistance increases in the relevant zone of the work piece and the forming zone differs in surrounding areas with low flow resistance. This is associated with an increase of the material stability in the form of uniform elongation [17]. At quasi-static strain rates at room temperature the AZ31B-O alloy has a low positive strain rate sensitivity of 0.05 which increases with increasing temperature at 0.7, [18]. Furthermore, the strain rate sensitivity can also assume negative values at pronounced tensile twinning. This reduces the achievable material stability significantly, [19].
The AZ31B-O alloy shows at high strain rates maximum CONSIDÈRE strain and maximum elongation at break at uni-axial stress state, see Figure 1. This circumstance is due to an increasing strain rate sensitivity m of AZ31B-O at high speed, [20].
In sheet metal forming, however, mainly multi-axial strain states are important. In particular, the plain strain constitutes for AZ31B-O alloy a critical state of deformation in deep-drawing processes and stretch forming processes. Due to the disabled minor strain the material flow mainly occurs from the sheet thickness. Therefore the forming limit curve (FLC) of AZ31 alloy has a critical minimum in the stress-strain state of deformation [21, 22, 23].

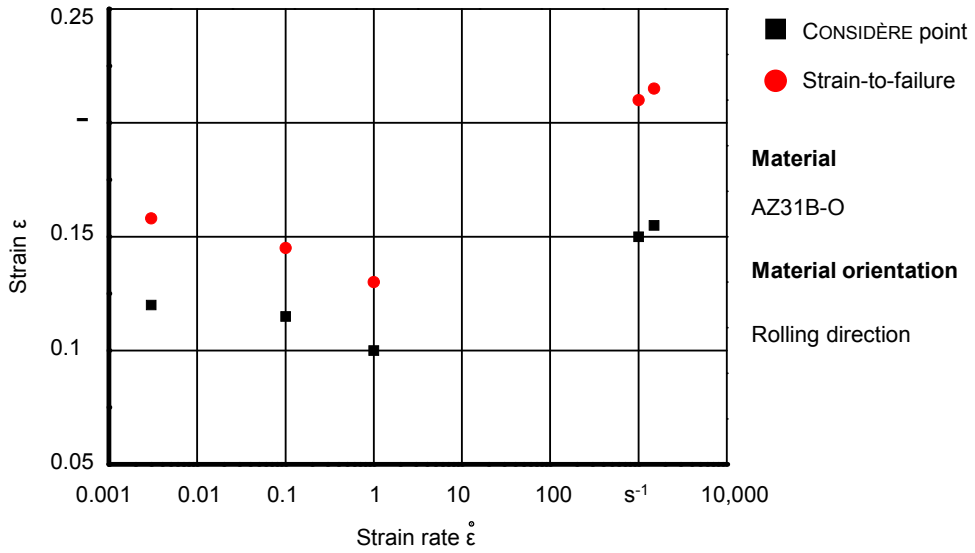

Figure 1: *Strain-to-failure strain and CONSIDÈRE strain of AZ31B-O at room temperature [20]*

ULACIA ET AL showed that an increase of strain rates up to $\dot{\varepsilon} = 1\ s^{-1}$ leads to a reduction of the deformability of the alloy AZ3 [24]. Increasing the strain rate $\dot{\varepsilon}$ comes along with an increase of the proportional elongation and breaking elongation [20]. Furthermore, it was shown that the magnesium alloy AZ31 shows a strong strain rate dependency. This results in an improved formability at high strain rates [25].

In the present study the behavior of the AZ31B-O is investigated in the state of plane strain. Pulse magnetic forming, which exhibit process-dependent high strain rates, is compared with a conventional quasi-static forming process at low strain rates.

3 Approach

Basically the forming behaviour of magnesium alloys at low forming temperatures is affected through process-dependent strain rates and the texture of the material [8]. By combining high strain rates which occur in processes like pulse magnetic forming as well as an optimized texture the formability of magnesium alloy AZ31B-O can be increased significantly.

Process principles

Pulse magnetic forming, which is an active-energy based process, is based on the physical effect of induction [26]. The required energy for the forming process is stored in capacitors by charging them to a high voltage U. By discharging the capacitors over a high-current switch, the arising large currents $I_{dis}(t)$ generate an intense magnetic field $H(t)$ outside the tool coil with the magnetic flux density $B = \mu H$ (see Figure 2). This magnetic field $H(t)$ induces eddy currents $I_{eddy}(t)$ in the workpiece which are running in the opposite direction compared to the primary currents $I_{dis}(t)$ in the tool coil (see Figure 2 A).

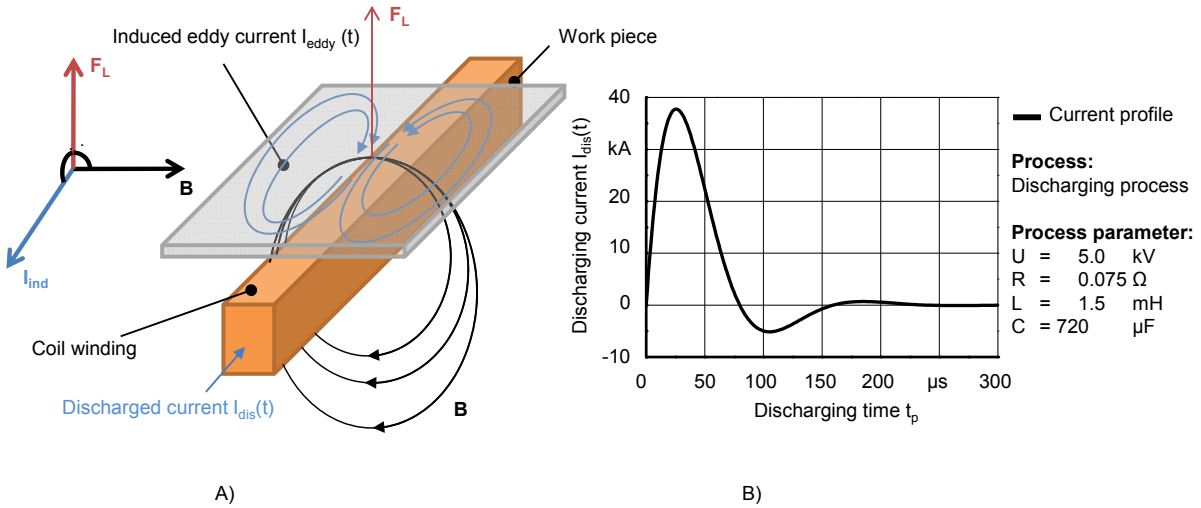

Figure 2: *Principle of discharging process and resulting Lorentz force F_L (A); characteristics of an damped sinusoidal discharged current $I_{dis}(t)$ (B)*

Due to the short process time t_p and high frequencies *f* of the discharging process (see Figure 2 B), the skin effect[1] causes that the induced eddy currents $I_{eddy}(t)$ are running near the surface of the sheet metal. Consequently the resulting Lorentz forces $F_L(t)$ which depend on the primary magnetic field *H(t)* are acting for a short time of 50 µs to 100 µs on the work piece. The acting Lorentz $F_L(t)$ forces are converted as a magnetic pressure on the work piece surface. As now work piece and tool coil repel each other, the work piece will be deformed. Here, the yield stress Y_f is exceeded and as a consequence plastic deformation of the work piece takes place within milliseconds.
Pulse magnetic processes are assigned to high speed forming processes due to the high strain rates occurring during the process. The whole forming process is realized without any mechanical contact between work piece and tool coil.

4 Experimental setup

For the experimental study of pulse magnetic forming of magnesium alloy AZ31 at room temperature an experimental setup was designed, see Figure 3. The design of the die makes it possible to create plane strain in the forming area.

[1]Skin effect is the tendency of an alternating current to become distributed within an electrical conductor such that the current density is largest near the surface of the conductor, and decreases with greater depths in the conductor.

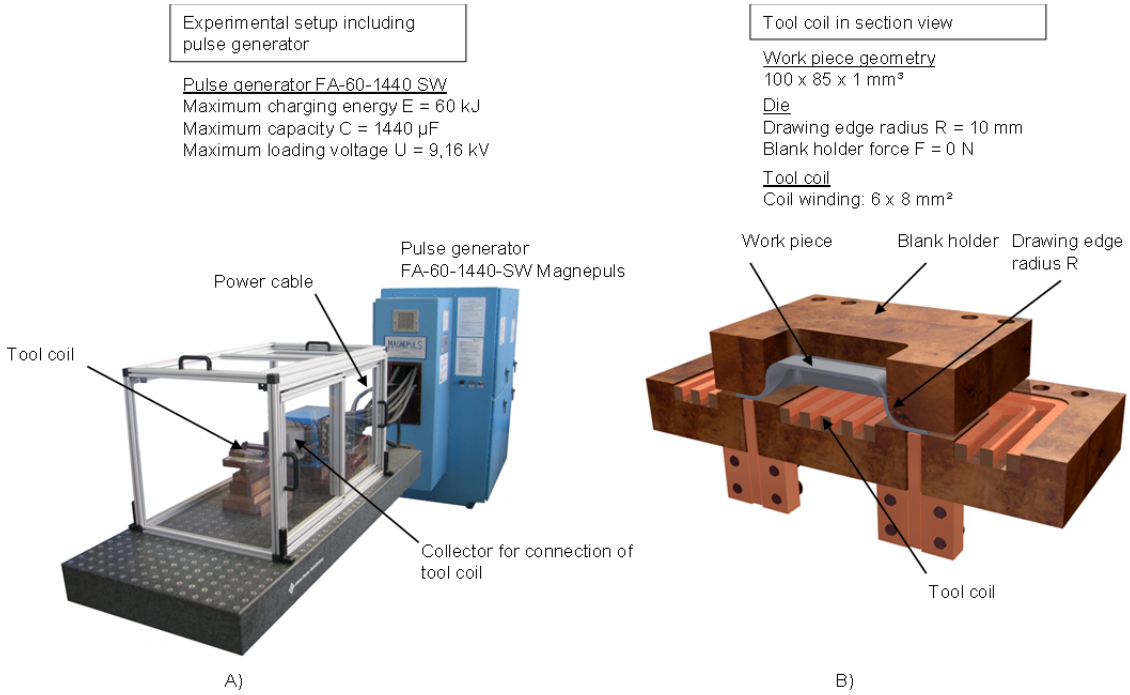

Figure 3: *Experimental setup including pulse generator A), tool coil in section view B)*

5 Results

Figure 4 shows a comparison of plain strain forming limit distributions between a deformation at a high strain rate applied during pulse magnetic forming and during conventional forming at a quasi-static[2] strain rate, both conducted at room temperature. The major axis strains achieved at failure during conventional forming with a quasi-static strain rate are comparable to [27]. During forming at high strain rates, however, an increase in major axis strain of 61 % could be reached without any evidence of macro or micro cracks. One reason for the non-failure of the work piece at high strain rates can be found in the investigated loading charging energy of the pulse generator of $E = 25$ kJ, which was not high enough to reach the forming limit of AZ31B-O. Five samples were investigated. Its shift in position on the axis of major strain compared to the quasi-static results is, according to [28], a result of increasing strain rate sensitivity. As has been the case for tensile tests, the increasing strain rate sensitivity m leads to an increase in strain and material stability, [17]. Hence, an increase in strain rate sensitivity combined with a constant strain hardening coefficient leads to a rising flow stress of AZ31B-O [29] expressed by an increase in cold work hardening.

[2]The sample shape was generated by deep drawing. For this purpose a mechanical punch was used.

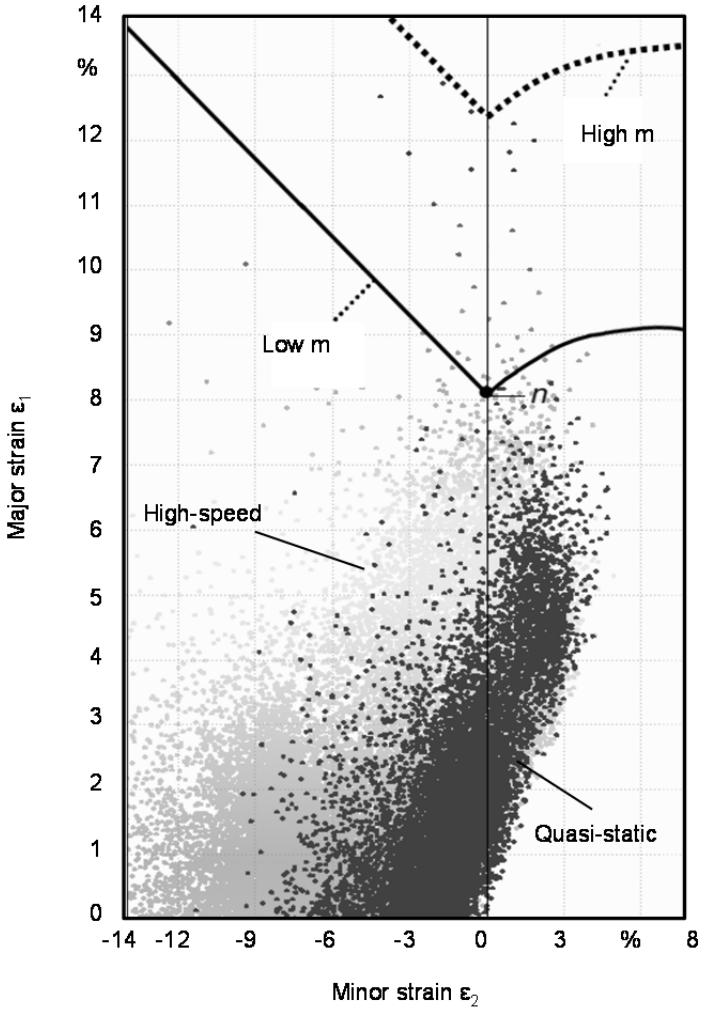

Figure 4: *Comparison of realized deformation in the field of plane strain of AZ31B-O with Basal texture; pulse magnetic forming (light gray) and quasi-static forming (dark grey) with the theoretical influence of strain rate sensitivity m on the location of the forming limit curve (FLC) [27]*

The quasi-static sample shows a significant gradient in terms of hardening which was obtained by determining the Vickers hardness *HV*. The hardness had been increased by 14.5 %, based on an initial hardness of 55 *HV* 4.9012/15, before cracks appeared on the upper surface. On the inner surface of the sheet, however, a hardly measurable increase in hardening of 3.6 % occurred. One possible reason for that behaviour can be found in the missing hardening mechanisms in sheet thickness direction due to the significant basal texture of AZ31B-O at room temperature. Consequently, the first cracks appeared on the outer surface of the sheet already after 8.1 % elongation.
The sample deformed by pulse magnetic forming also shows a significant gradient in hardening across the sheet thickness leading to a nonappearance of hardening on the inner side of the sheet just as it has been found for the quasi-static deformation. Despite this, the hardness of the upper surface increases by 27 % without the appearance of any

visible cracks, corresponding to a doubling in hardening compared to conventionally deformed samples. That increase is based on the strongly increasing flow stress of AZ31B-O during high speed deformation, [20]. Hence, the increasing ability for hardening during pulse magnetic deformation is tantamount to an increase in plain strain forming ability of AZ31B-O. According to the high material stability caused by an increase in strain rate sensitivity at high deformation speeds a consistent reduction in sheet thickness across the entire force transmission zone could be observed. On the other hand, during conventional deformation distinctive local deformation zones appear leading to a structural failure as a result of a strongly localized deformation. In conclusion, an increasing strain rate sensitivity at high speed deformations, reached e.g. in pulse magnetic forming processes, causes an increase in flow resistance at high strains which allows a better distribution of deformation on surrounding areas, leading to a consistent sheet thickness reduction. This results in an increasing forming ability of AZ31B-O at plain strain deformations.

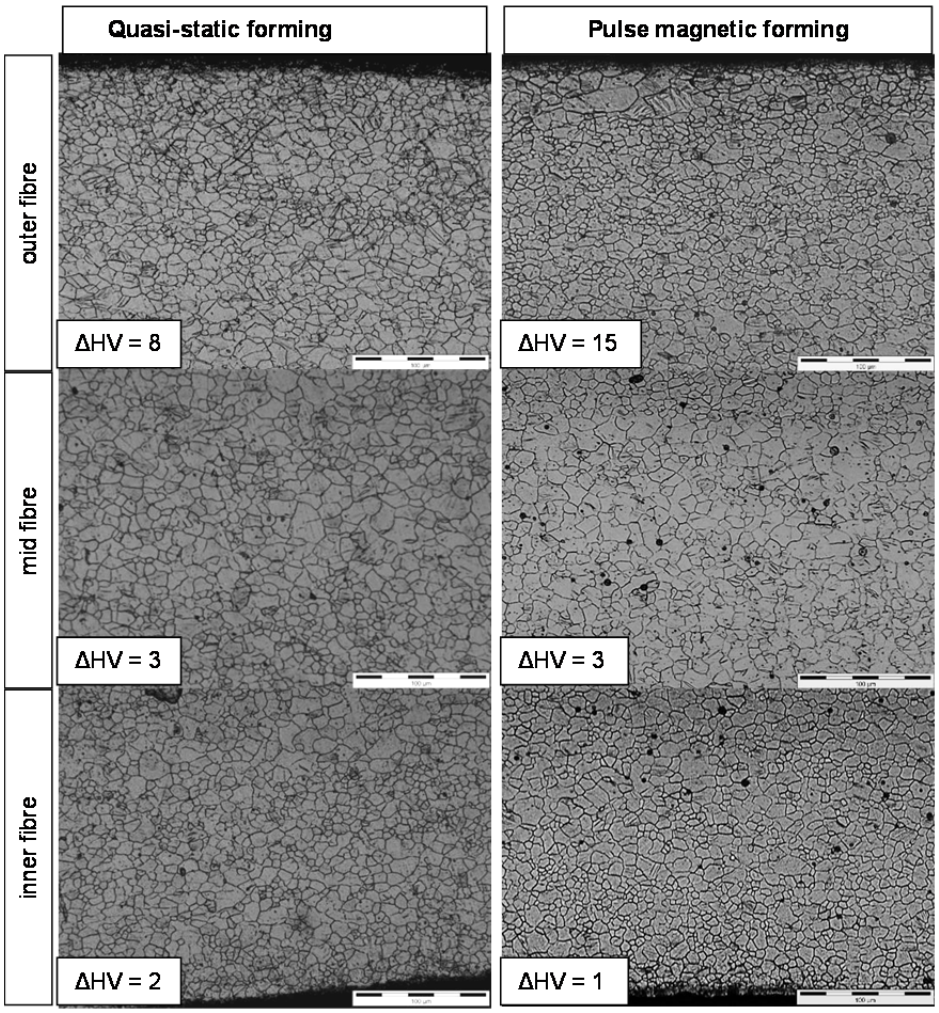

Figure 5: *Comparison of material hardening by measuring increase of hardness ΔHV of AZ31B-O (initial hardness: HV 4,902 55/15) at quasi-static rates and high strain rates (pulse magnetic forming)*

Conclusion

- The plain strain deformations achievable with pulse magnetic forming systems at least are higher than 61% compared to conventional deformation processes.
- During conventional deformation as well as during pulse magnetic deformation a significant gradient in hardness can be found across the sheet thickness at plain strain condition.
- High strain rates of pulse magnetic forming processes increase the hardening ability of AZ31B-O. This is caused by increased strain rate sensitivity at high speed deformations.
- The increasing strain rate sensitivity at high speed deformations enhances the material stability which is indicated by a consistent sheet thickness reduction across the entire load transmission zone.

References

[1] Pollet, B. G.; Staffell, I.; Shang, J. L.: Current status of hybrid, battery and fuel cell electric vehicles: From electrochemistry to market prospects. Electrochimica Acta 84, 2012, p. 235 – 249.

[2] Kopp, Gundolf; Beeh, Elmar: MAGNESIUM MACHT´S MÖGLICH - Super Light Car - Leichtbau durch Multi-Material-Design mit integrierten Funktionen. DLR - News, Edition121, 2008, p. 28 – 31.

[3] Zittel, R.: A Historical Review of High Speed Metal Forming. Proceedings of 4th ICHSF, 2010, Columbus, USA, p. 2 – 15

[4] Shribman, V.: Magnetic Pulse Welding for Dissimilar and Similar Materials. *Proceedings of 3rd ICHSF*, Dortmund, Germany, 2008, p. 13 – 22.

[5] Koike, J.; Ohyama, R.; Kobayashi, T.; Suzuki, M.; Maruyama, K.: Grain-Boundary Sliding in AZ31 Magnesium Alloys at Room Temperature to 523 K. Materials Transactions Vol. 44 No. 4, 2003, p. 445 – 451.

[6] *Barnett, M.:* A Taylor Model Based Description of the Proof Stress of Magnesium AZ31 during Hot Working. Metallurgical and Materials Transactions A Volume 34, Berlin Heidenheim, Springer Verlag, 2003, p.1799 – 1806.

[7] *Liu, X.; Jonas, J.J.; li, X.L.; Zhu, B.W.:* Flow softening, twinning and dynamic recrystallization in AZ31 magnesium. Materials Science & Engineering A 583, 2013, p. 242 – 253.

[8] *Schmidt, C.:* Textur- und Gefügeentwicklung bei der Umformung von Magnesium-Gießwalzband. Dissertation. TU Freiberg, 2012.

[9] *Kang, J.; Wilkinson, D.; Mishra, R. K.:* Inhomogeneous Deformation of AZ31 Magnesium Sheet in uniaxial Tension in Magnesium Technology 2011, 2011, p. 307 – 311.

[10] *Gottstein, G.:* Physikalische Grundlagen der Materialkunde. Springer Verlag, Berlin Heidelberg, 2007.

[11] *Reissner, J.; Schröder, G.:* Fließkurven, Fließortkurven und Formänderungsvermögen in Umformtechnik: Grundlagen Band 1, Springer Verlag, Berlin Heidelberg, 2002, p. 97 – 135.

[12] *Lou, X.Y.; Li, M.; Boger, R.K.; Agnew, S.R.; Wagoner, R.H.:* Hardening evoulution of AZ31B Mg sheet, International Journal of Plasticity 23, 2007, p. 44 – 86.

[13] *Johnson, C.F.; Chan, M.S.:* The Effect of Strain-Hardening and Process Paramters on the Forgeability of Wrought Magnesium Alloys, Magnesium: Proceedings of the

6th International Conference - Magnesium Alloys and Their Applications, Wiley-VCH, 2006, p. 294 – 299.

[14] Takuda, H.; Morishita, T.; Kinoshita, T.; Shirakawa, N.: Modelling of formula for flow stress of a magnesium alloy AZ31sheet at elevated temperatures. Journal of Materials Processing Technology 164–165, 2005, p. 1258 –1262.

[15] *Boissiere, R.; Vacher, P.; Blandin, J.J.; Khelil, A.:* Strain Capacities Limits of Wrought Magnesium Alloys: Tension vs. Expansion, Materials Sciences and Applications, 4, 2013, p. 768 – 772.

[16] *Ostermann, F.:* Anwendungstechnologie Aluminium 2. Auflage, Berlin Heidelberg, Springer-Verlag, 2007.

[17] *Kalpakjian, S.; Schmid, S.R., Ewald, W.:* Werkstofftechnik Herstellung, Verarbeitung, Fertigung, München, Pearson Education Deutschland GmbH, 2011.

[18] *Cheng-Wen, T.; Shan-Na, X.; Lu, W.; Zhi-Yong, C. Fu-Chi, W.; Hong-Nian, C.:* Effect of temperature on mechanical behaviour of AZ31 magnesium alloy. Transaction of Nonferrous Metals Society of China 17, Peking, 2007, p. 41 – 45.

[19] *Chun, Y.B.; Davies, C.H.J.:* Twinning-induced negative strain rate sensitivity in wrought Mg alloy AZ31, Materials Science and Engineering A 528, 2011, p. 5713 – 5722.

[20] *Hasenpouth, D.:* Tensile High Strain Rate Behavior of AZ31B Magnesium Alloy Sheet. Masterthesis: University of Waterloo, 2010.

[21] *Chen, F. K.; Huang, T. B.; Chang, C. K.:* Deep drawing of square cups with magnesium alloy AZ31 sheets. International Journal of Machine Tools & Manufacture 43, 2003, p. 1553 – 1559.

[22] *Bressan, J. D.:* Formability curves of AZ31 alloy sheet at high temperatures. International Journal of Material Forming Volume 2 Issue 1, 2009, p. 279 – 282.

[23] Chen, F. K.; Huang, T,B.: Formability of stamping magnesium-alloy AZ31 sheets. Journal of Materials Processing Technology 142, 2003, p. 643 – 647.

[24] Ulacia, I.; Imbert, J.; Salisbury, C. P.; Arroyo, A.; Hurtado, I.; Worswick, M. J.: “Electromagnetic Forming of AZ31B Magnesium Alloy Sheet: Experimental Work and Numerical Simulation”. *Proceedings of 3rd ICHSF*, Dortmund, Germany, 2008, p. 191 – 200.

[25] Ulacia, I.;. Salisbury, C. P.; Hurtado, I.; Worswick, M. J.: “Tensile characterization and constitutive modeling of AZ31B magnesium alloy sheet over wide range of strain rates and temperatures”. *Journals of Materials Processing Technology,* 2011, p. 830 – 839

[26] Daehn, G. S.; Altynova, M.; Balanethiram V. S.; Fenton, G.; Padmanabhan, M.; Tamhane, A.; Winnard, E.: High Velocity Metal Forming – An Old Technology Addresses New Problems. *JOM – Journal of the Minerals, Metals and Materials Society*, 1995, p. 42 – 45.

[27] *Stutz, L.; Bohlen, J.; Letzig, D.; Kainer, K.U.:* Formability of magnesium Sheet ZE10 and AZ31 with respect to initial texture. *Magnesium Technology 2011*, 2011, p. 373 – 378.

[28] *Hu, J.; Marciniak, Z.; Duncan, J.:* Mechanics of Sheet Metall Forming. Butterworth Heinemann, Oxford, 2002.

[29] Zhao, F.: Li, Y.L.; Suo, T.; Huang, W.D.; Liu, J.R.: Compressive deformation behavior of AZ31 magnesium alloy under quasi-static and dynamic loading. Trans. Nonferrous Met. Soc. China 20, 2010, p. 1316 – 1320.

Identification of material constitutive parameters for dynamic applications: Magnetic Pulse Forming (MPF) and electrohydraulic forming (EHF)

A-C Jeanson[1,3], G. Avrillaud[1], G. Mazars[1], G. Taber[2], G. Daehn[2], F. Bay[3], N. Jacques[4], M. Arrigoni[4]

[1] Bmax, 30 bd de Thibaud, ZI de Thibaud, 31100 Toulouse Cedex 9 – France
[2] Ohio State University, Materials Science and Engineering Department, Colombus, OH 43210 – USA
[3] Cemef MINES ParisTech, BP207, 06904 Sophia Antipolis Cedex – France
[4] LBMS, ENSTA Bretagne, 2 rue François Verny, 29806 Brest Cedex 9 – France

Abstract

Magnetic Pulse Forming (MPF) and electrohydraulic forming (EHF) are very promising high speed forming processes. During these kinds of processes, strain-rates are very high (typically between 100 and 10 000 /s), leading to some advantages: material behavior can change and provide a higher formability and a better accuracy due to the reduction of springback.
During the last decade, the industrialization of such processes has been strongly helped by the development of simulation codes, associated with growing computation facilities. To design accurately the forming process, numerical models require specific data such as dynamic constitutive laws for the workpieces.
The aim of the study presented here is to identify the parameters of a constitutive law (Johnson-Cook) by means of an electromagnetically-driven ring expansion test. Simulation conditions are optimized to enable an identification procedure, based on: LS-Dyna® electromagnetic/thermal/mechanical simulations, PDV measurement of the rings' expansion velocity, and the optimization tool LS-Opt®.

Keywords

Magnetic Pulse Forming (MPF), Material behavior, Identification

1 Introduction

Magnetic pulse forming and electrohydraulic forming are high potential processes for sheet forming [1], as they offer many advantages such as higher formability, fine engraving or reduced springback. They are also quite complex to design, as they are

multi-physical in dynamic conditions. Thus, they require numerical simulations, implying a coupled electromagnetic, mechanical and thermal resolution. The predictive quality of these simulations depends on the model representativeness and on the input data accuracy.

The present study describes a method to characterize the material behavior in conditions proper to magnetic pulse forming and electrohydraulic forming. These processes involve strain-rates between 100 and 10 000 s^{-1} [2]. In this range, the mechanical behavior of many metals is known to be possibly very sensitive to strain-rate [3]. Many constitutive models have been proposed to take into account dynamic effects in material behavior, and can be basically sorted in three classes: the phenomenological models such as the Cowper-Symonds or the Johnson-Cook's [4] models; the models derived from thermal activation analysis, some of them using microstructural internal variables in addition to the classical ones (i.e. strain, strain-rate and temperature); and the models that are more specific to shock regimes and viscous drag.

The test chosen to identify the model parameters is an electromagnetically-driven ring expansion. It has been used for material characterization in strain-hardening and fragmentation regimes [5]. The ring expansion test has been particularly studied and developed at the Ohio State University. One of the major developments is the instrumentation with a photon Doppler velocimetry (PDV) system, capable of measuring high speeds with a great accuracy [6]. Disposing of such data, the test can be used for material testing [7].

This study is based on copper ring expansions performed at the Ohio State University. The numerical studies and the material parameter identification have been done at Bmax.

2 Ring expansion experiments

The inducer is a five-turn coil made from C18150 (CrZrCu) alloy. It is connected to the high pulse circuit by two connection paths, one of them coming through the helix coil. The coil is electrically insulated, and the ring to be deformed is placed around. The ring material is C12200 (phosphorus-deoxidized, 0.04% P), and the ring dimensions are: thickness 0.81 mm; height 6.10 mm; outside diameter 50.8 mm.

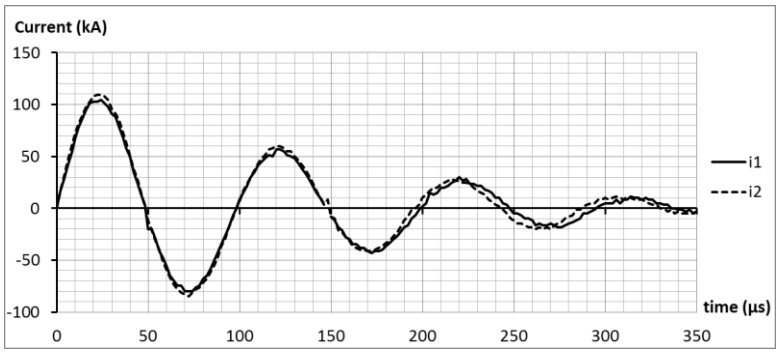

Figure 1: *Measured currents from Rogowski probes, for ring 1 (i1) and ring 2 (i2)*

The ring expansion system is instrumented with a Rogowski current probe to measure the high voltage and high intensity current discharged in the actuator. The ring radial expansion velocity is measured by means of a photon Doppler velocimetry system. The following material characterization is based on two rings expansions, whose input currents are presented on Fig.1. For each ring, two radial PDV probes were placed on opposite sides of the ring.

3 Numerical modeling

3.1 3D model

The numerical model for electromagnetic tube expansion is built in the code LS-Dyna®. The electromagnetic resolution is based on a coupling between finite elements for solids, and boundary elements for surrounding air. The input for loading is a time-dependent current curve applied through the actuator section.

A 3D model is built to serve as a reference for numerical validation of the 2D-axisymmetric model. The needed material parameters are summarized in Table 1. An arbitrary constitutive behavior is chosen for the ring material (taken from [4] for OFHC copper). A convergence study is done on the 3D mesh to define the required mesh size for valid calculation of the electromagnetic field, the induced current in the ring and its expansion velocity. The resulting reference mesh is presented on Fig.2.

Material	C18150 (coil)	C12200 (ring)
Mass density	8,890 kg/m^3	8,890 kg/m^3
Electrical conductivity	43.5 MS/m	58.0 MS/m
Thermal conductivity	320 W/m/K	320 W/m/K
Specific heat	385 J/kg/K	385 J/kg/K
Elastic coefficients	Young modulus 120 GPa Poisson's ratio 0.3	Shear modulus 45 GPa Bulk modulus 115 GPa
Plastic behavior		Johnson-Cook model A = 90 MPa; B = 292 MPa; n = 0.31; C = 0.025 ($\dot{\varepsilon}_0$ = 1 /s); m = 1.09
Fraction of mechanical work converted into heat : 1.0 Fraction of electrical work converted into heat (Joule effect) : 1.0		

Table 1: *Material parameters for LS-Dyna simulations*

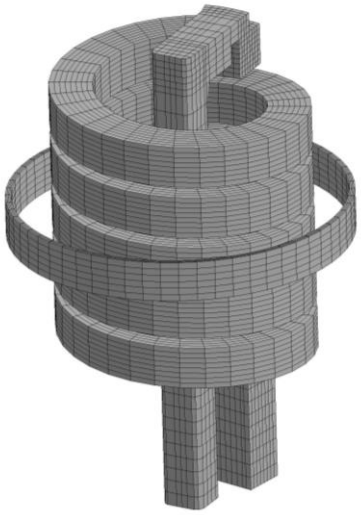

Figure 2: *3D mesh*

Thanks to the 3D simulations, it can be observed an influence of the helix shape on the ring deformation. In the radial direction, the calculated velocities show non-negligible differences and will be a point to be careful about in the test analysis. To take away the rigid body part of velocity, it can be necessary to deal with the mean of opposite velocity measurements.

3.2 2D-axisymmetric model

In an optimization perspective, 3D models are not suitable because of the needed computation time. A 2D-axisymmetric model is thus created (Fig.3). In this model, it is not possible to represent the return path inside the coil, as the current in this part flows in the axial direction.

The 2D model is run in the same conditions as the 3D reference model. It is observed that the radial velocity is about 10% higher in 2D than in 3D (Fig.4). This is the consequence of the absence of return path: it is confirmed by a 3D calculation without return path, which gives the same velocity as the 2D model. To take into account the return path in the 2D model, it has been chosen to apply a corrective factor on the input current. By multiplying it by 0.955, the radial velocity fits the 3D result.

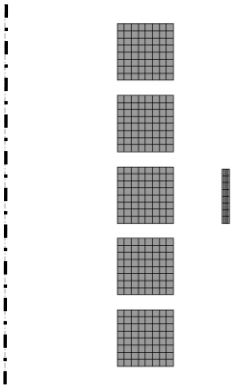

Figure 3: *2D mesh*

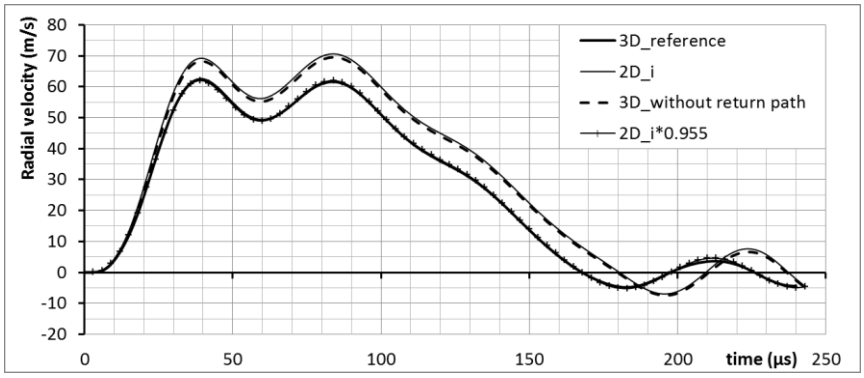

Figure 4: *Influence of the return path*

4 Material behavior identification

4.1 Material behavior modeling

The strain-hardening behavior of the ring is modeled by means of the Johnson-Cook's relationship [4] (eq.1).

$$\sigma = (A + B \cdot \varepsilon^n) \cdot \left(1 + C \cdot \ln\left(\frac{\dot{\varepsilon}}{\dot{\varepsilon}_0}\right)\right) \cdot \left(1 - \left(\frac{T - T_0}{T_{melt} - T_0}\right)^m\right) \quad (1)$$

where σ is the effective Von Mises stress, ε is the effective plastic strain, $\dot{\varepsilon}$ is the effective strain-rate, $\dot{\varepsilon}_0$ is a reference strain-rate (chosen to be 1 /s), T the material temperature, T_0 the room temperature (25 °C), T_{melt} the melt temperature (1083 °C). A, B, n and C are the material parameters to be identified. m is chosen to be equal to 1.09, as proposed by [4] for OFHC copper.

4.2 Identification procedure

The identification consists in searching material parameters, such that the computed velocity fits the measurement. To do so, the experimental current is used as an input for

the 2D model, and simulations are run iteratively with different sets of parameters [8]. For each set of parameters, the mean square error between experimental and computed velocity is evaluated, and the identification objective is to minimize this error.

Identifications are performed using the optimization tool LS-Opt®, whose role is to define the sets of parameters to be tested to reach the objective of minimal error. A hybrid algorithm is chosen, combining a gradient algorithm (Leapfrog optimizer for constrained minimization) to converge to a minimum, and a global algorithm (Adaptive Simulated Annealing) to avoid finding only a local minimum.

The identification is done simultaneously on both ring expansions, the function to minimize being the sum of each mean square error between the calculated and measured velocities. For ring 1, the opposite PDV signals C1_1 and C2_1 have given almost the same velocities; the identification is based arbitrarily on curve C1_1. For ring 2, the opposite signals have a peak difference of about 8 m/s, due to a rigid body displacement (effect shown on 3D simulations). In this case, the identification is thus based on the mean of curves C1_2 and C2_2.

4.3 Identification results

The identified parameters are: $A = 73.1\ MPa$, $B = 375\ MPa$, $n = 0.398$, $C = 0.0208$; and the velocity curves are well fitted (Fig. 5). The values found for the parameters, and in particular for the parameter C, are in the same order of magnitude than other parameters in the literature. For example, Johnson and Cook [4] have proposed for OFHC copper: $C = 0.025$. This gives some confidence in the present results.

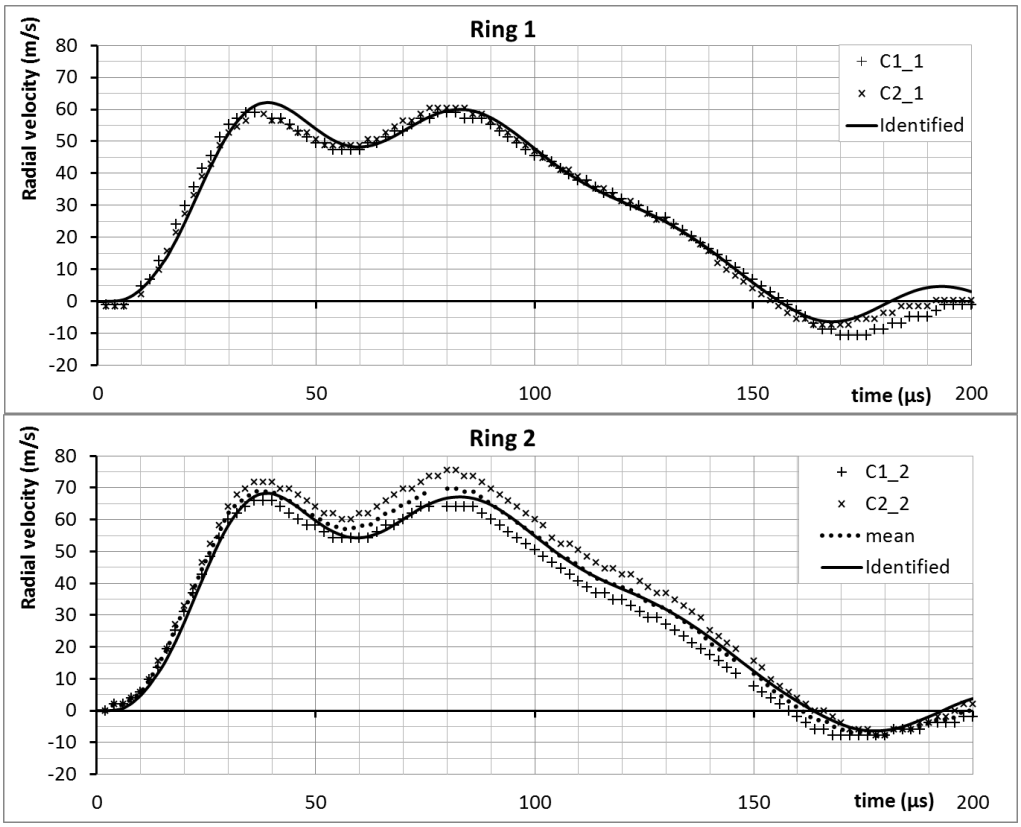

Figure 5: *Identification result on radial velocities for ring 1 (up) and ring 2 (down)*

5 Conclusion

The ring expansion test experiment is used to characterize the ring material mechanical behavior at strain-rates specific to magnetic pulse forming. The pulse current and the ring expansion velocity are measured. In parallel, a numerical study is led to define appropriate 2D-axisymmetric simulation conditions. From the experimental results and the numerical model, an optimization procedure is applied on the constitutive parameters. The constitutive parameter identification is performed simultaneously on two ring expansion tests. Parameter values are found for the Johnson-Cook's constitutive model.

The method shows its particular interest in dynamic material characterization, which is necessary in the development of high speed processes. A better knowledge in plasticity at high strain-rates is necessary to get accurate MPF or EHF models. The straining conditions can thus be studied more precisely, as well as the necking prediction.

References

[1] *www.bmax.com*

[2] *Psyk, V.; Risch, D.; Kinsey, B.; Tekkaya, A.; Kleiner, M.:* Electromagnetic forming - A review. Journal of Materials Processing Technology 211, p.787-829, 2011.

[3] *Follansbee, P.; Kocks, U.:* A constitutive description of the deformation of copper based on the use of the mechanical threshold stress as an internal state variable. Acta Metallurgica 36, p.81-93, 1988.

[4] *Johnson, G.; Cook, W.:* A constitutive model and data for metals subjected to large strains, high strain rates and high temperatures. Proceedings of the 7th international symposium on ballistics, Hague, Netherlands, p.541-547, 1983.

[5] *Gourdin, W.:* Analysis and assessment of electromagnetic ring expansion as a high-strain-rate test. Journal of Applied Physics 65(2), p.411-422, 1989.

[6] *Johnson, J. R.; Taber, G.; Vivek, A.; Zhang, Y.; Golowin, S.; Banik, K.; Fenton, G. K.; Daehn, G. S.:* Coupling Experiment and Simulation in Electromagnetic Forming Using Photon Doppler Velocimetry. Steel Research International, WILEY-VCH Verlag, 2009, 80, 359-365.

[7] *Johnson, J. R.; Taber, G. A. & Daehn, G. S.:* Constitutive relation development through the FIRE test. Proceedings of the 4th International Conference on High Speed Forming, 2010.

[8] *Henchi, I.; L'Eplattenier, P.; Daehn, G.: Zhang, Y.; Vivek, A.; Sander, N.:* Material constitutive parameter identification using an electromagnetic ring expansion experiment coupled with LS-DYNA and LS-OPT. Proceedings of the 10th International LS-DYNA Users' Conference, 2008.

SESSION 2

INDUSTRIAL APPLICATIONS

Design of Electromagnetic Pulse Crimp Torque Joints [*]

K. Faes [1], W. De Waele [2], M. Müller [3], H. Cramer [3]

[1] Belgian Welding Institute, Ghent, Belgium.
[2] Laboratory Soete, Ghent University, Ghent, Belgium
[3] GSI – SLV Munich - Gesellschaft für Schweißtechnik International

Abstract

Electromagnetic pulse crimping of form fit joints was investigated using tubes with a diameter of 50 mm and a wall thickness of 1,5 mm, in the aluminium alloy EN AW-6060. The tubes were crimped onto steel internal parts, which were designed to bear torsional loads. Grooved, knurl rolled and knurl cut internal workpieces were used. To assess the torque strength of the connections, a torque test set-up was designed and built.

In a first test series, grooved internal parts were used. The influence of the internal workpiece design and the energy level on the torque resistance was investigated. Related to the geometry of the internal workpiece, the following parameters were varied: the groove depth, the groove width, the edge radius and the number of grooves.

In a second test series, knurl rolled and knurl cut internal workpieces were used. For the joints with a knurl rolled internal part, the influence of the knurl pattern, defined by the pitch, was investigated. For the connections with a knurl cut internal part, the influence of the energy level was studied. The different joint failure mechanisms were determined.

Keywords

Electromagnetic pulse joining, Torque crimp joints, Failure mechanisms.

---

[*] *This work is based on the results of the CorNet collective research project "PulsCrimp"; the authors would like to thank IWT (Agency for Innovation by Science and Technology) for its financial support.*

1 Electromagnetic pulse joining

The electromagnetic pulse technology uses magnetic forces to deform and/or join work-pieces. The energy stored in a capacitor bank is discharged rapidly through a magnetic coil. Typically, a ring-shaped coil is placed over a tubular workpiece. When deforming tubular products, the magnetic field produced by the coil generates eddy currents in the tube. These currents, in turn, produce their own magnetic field. The forces generated by the two magnetic fields oppose each other and a repelling force between the coil and the tube is created. As a consequence, the tube is collapsed onto an internal workpiece, creating a crimp joint or a weld joint. In the electromagnetic pulse crimping process, no atomic bond is created; these joints obtain their strength from the combination of an interference and a form fit. A special profiled internal workpiece is therefore used, with for example grooves.

2 Literature survey

As in most mechanical assemblies, the performance of the manufactured joints is evaluated based on their mechanical strength. Figure 1 shows a torque joint made by the electromagnetic pulse crimping process, and with a torsional resistance higher than the tube base material. The feasibility and performance of such joints has been demonstrated, in for example [1,2,3]. However, a better understanding of the electromagnetic pulse crimping process has to be achieved to obtain large-scale industrial applicability.

Figure 1: *Magnetic pulse crimped torque joint used in the Boeing 737, 747 and 777 aircraft. Left: after torque testing [1]*

As discussed in [4], the transferrable torque of a joint is proportional with the circumferential forces and with the effective length of the joint zone, as long as this length has experienced the full influence of the electromagnetic field. When the joint length is larger than the work range of the coil or field concentrator, multiple pulses can be used. Furthermore, deeper grooves result in a higher transferrable torque, as long as the reduction of the tube wall at the groove edge is less detrimental to the joint strength than the additional interlocking surface is beneficial to the joint strength.
The transferrable torque is proportional to the number of grooves in circumferential direction. This last assumption is justified as long as the different grooves do not affect each other's strength. When using too many grooves, the width of the grooves is insufficient in comparison with the groove depth, leading to a weaker joint and eventually cutting of the tube during electromagnetic pulse crimping.

Guidelines for design values
In [4], experiments are described with tubes with a diameter and wall thickness of 46 mm and 1 mm resp., in the aluminium alloy EN AW-6063-T5. The following design rules are specified for joint strength optimisation:

- groove depth d: $t < d < 0{,}057 \times D$ [5]
- groove edge radius r: $(0{,}5t \text{ or } t)^* < r < \{0{,}5d \text{ or } \min(t; 0{,}5d)\}$

with: t: tube wall thickness (mm), and D: diameter of the specimens (mm)

*: The lower limit of the groove edge radius is significantly depending on the method of specimen testing. In [4], it was demonstrated that a smaller groove edge radius is allowed for torsion-loaded joints, due to the decreased dependency of the joint strength on the tube wall thickness reduction. A value of 0,5×t or t for the groove edge radius is a good guideline for respectively torque and axial joints.

The groove width should always be minimised because the smaller its value, the more grooves the internal workpiece can contain, leading to a higher torsional strength of the electromagnetic pulse crimped joint. Based on earlier work on axial joints [6], the lower limit for the groove width was determined as 3 to 4 times the groove depth, which results in reliable joints, exhibiting only limited tube wall thickness reduction.

For reasons of material cost, the groove length should be as short as possible without jeopardising the integrity of the torque joint or the load bearing capacity. Furthermore, the longer the internal workpiece, the longer the necessary axial length of the coil or field concentrator. For an increased work length, the required energy will also increase, together with the equipment cost.

3 Overview of the experiments

Electromagnetic pulse crimping of form fit joints was investigated, using tubes made of the aluminium alloy EN AW-6060 T6. The tubes had a diameter of 50 mm and a wall thickness of 1,5 mm. Solid internal workpieces were used, made of steel S355.
The experiments were performed using a Pulsar model 50/25 system with a maximum charging energy of 50 kJ (corresponding with a maximum capacitor charging voltage of 25 kV) and a discharge circuit frequency of 14 kHz. The total capacitance of the capacitor banks equals 160 µF. The pressure resulting from the magnetic flux induced by a 5-turn aluminium Bitter coil (length: 100 mm, internal diameter: 165 mm) is concentrated over the processing area using a conical field concentrator with a workzone width equal to 15 mm [7,8]. The crimp joints were produced using a single pulse.

In order to study the optimisation possibilities, knowledge concerning the occurring joining mechanisms is required. As the manifesting joining mechanisms are very dependent on the geometry of the internal workpiece, the relation between the occurring joint strength and the workpiece design was examined. In a first phase, crimp connections with internal parts containing longitudinal grooves were investigated. In a second phase, knurl rolled and knurl cut internal workpieces were used as an alternative concept.

To evaluate the performance of the crimp joints, the torsional strength of all specimens was determined using a torque testing set-up (Figure 2). With this device, the torsional resistance of the joints as a function of time and angular displacement was measured.

4 Design of torque joints using grooved internal workpieces

4.1 Design of torque joints with internal workpieces with 5 grooves

In a first test series, internal workpieces were used containing 5 longitudinal grooves, but no axial load bearing capacity (see Figure 3). By using this design of the internal part, it is possible to investigate the pure torque bearing capacity of the crimp connections.

In case of a 5 groove design, 5 parameters are of importance: the groove length, width and depth, the groove edge radius and the energy level. For obtaining an optimal design of the internal part in terms of torsional strength, experiments were performed in which the above mentioned parameters were varied. The groove length was assumed to be constant, and adapted to the internal field concentrator length (15 mm). The proportional influence of this factor on the torque strength justifies the choice to keep it constant in all experiments.
If 3 different parameter values for the 4 other parameters are considered, 3^4 or 81 experiments would be required to obtain a full understanding of the influence of all parameters. To reduce the amount of experiments, a statistical technique, called Response Surface Methodology (also called 'Box-Wilson' method) was used. This allowed a reduction of the number of experiments to 2^4 = 16 designs, and 2 additional experiments using an internal part with a so-called reference design (shown in Figure 4).

Figure 2: *Torque testing setup*

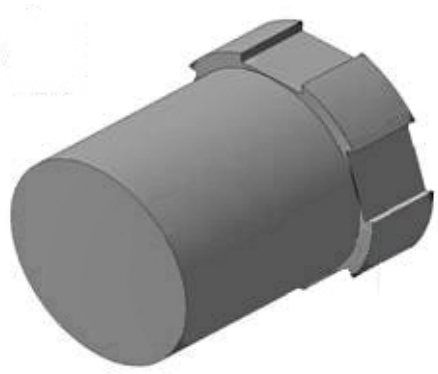

Figure 3: *Design of the internal part*

The parameters values of the reference design and the parameter range were determined as follows:

- Groove length. Since the used field concentrator has a work length of 15 mm, it was decided to keep the groove length constant at 12 mm.
- Energy (defined by the capacitor charging voltage). Based on preliminary experiments, the reference value was chosen equal to 3,9 kJ. The lower and upper value of this

parameter was equal to 3,4 and 4,5 kJ (corresponding with a charging voltage of 6,5 and 7,5 kV).

- Groove depth. Based on the design rules in [4], the following parameter range was found for the groove depth: 1,5 mm < d < 2,85 mm. As the influence of the tube wall reduction on the joint strength is not so big, it was decided to use larger values for the parameter range: 2,3 mm < d < 3,3 mm. The reference value was set equal to 2,5 mm.
- Groove width. As the ratio groove width/groove depth ≈ 3…4 provides a reliable form fit [6], the groove depth was varied at the values 8 and 12 mm. The reference value was equal to 10 mm. For aluminium tubes with a diameter of 50 mm and taking into account a sufficient width of the collar in between the grooves, the possible number of grooves can vary between 4 and 8. In this test series, the amount of grooves was equal to 5.
- Groove edge radius. In [4], the following range for the groove edge radius r is provided: 0,5×t < r < {0,5×d or min(t;0,d)}. This results in a range of 0,75 mm < r < 1,25 mm. A groove edge radius of 1 mm was chosen as the reference value. Since the range obtained by the design rule is very small, it was decided to widen this range, and the lower and upper limits were set at 0,5 and 1,5 mm respectively.

Figure 4 shows the drawing of the reference design. An example of a crimped connection is shown in figure 5.

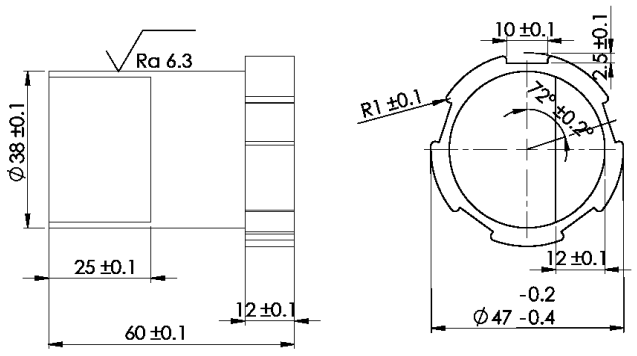

Figure 4: *Drawing of the reference design with the according parameter values*

Figure 5: *Example of a torque crimp connection (internal workpieces with 5 grooves)*

The crimp connections were mechanically tested in the torque test set-up to determine the torsional joint strength. For all connections, a torque versus angular displacement curve was obtained. The torque strength of the crimp connection with the reference design was equal to 215 Nm. In this test series, a maximum torque strength of 305 Nm was measured. The investigation of the influence of the parameters led to the following conclusions:

- The influence of the energy level is low in the investigated range. It can be expected that the influence of the energy is low as long as no severe tube wall reduction at the groove edges is observed after the crimping operation.
- Two failure mechanisms were observed; more specific bending of the tube out of the groove, with and without cracking of the tube wall. A higher joint strength is observed for the first failure mechanism (with tube cracking).
- A small groove edge radius is more beneficial. The large difference in joint strength proves the importance of this parameter. A similar conclusion was also found in [4].

- A significantly stronger joint is formed when using a groove width of 12 mm. A wider groove enables a better interlocking of the tube with the groove edge.
- The influence of the groove depth on the joint strength is not clear. Certainly, it is smaller than the influence of the groove width.

4.2 Design of torque joints with internal workpieces with 8 grooves

A test series was performed dedicated to the design of the internal workpieces with 8 grooves. Based on the results of the previous test series, it was decided that:

- A large groove width was used; this parameter was chosen equal to 12 mm.
- The groove length was again equal to 12 mm.
- A small groove edge radius was used; and chosen equal to 0,5 mm.
- The energy level was again varied between 3,4 and 4,5 kJ (corresponding with a charging voltage of 5,5 and 6,5 kV).
- In the previous test series, the influence of the groove depth was not completely clear; so 4 different groove depths were used for the internal parts: between 2,3 and 3,8 mm, in steps of 0,5 mm.

A drawing of the internal part with a groove depth of 2,3 mm is shown in Figure 5.

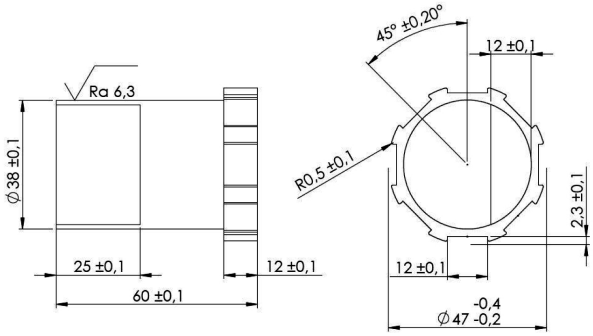

Figure 5: *Drawing of an internal workpiece with 8 grooves (groove depth 2,3 mm)*

The torque-angle curves obtained during torque testing of the 8 torque joints looked very similar to the ones obtained for the 5 groove design torque joints. Visual inspection of the workpieces after testing led to the conclusion that now only 1 failure mechanism was present. The failure mechanism consisted of bending of the tube out of the groove, together with cracking of the tube (see Figure 7). All tested specimens showed cracks at the groove edges. Since the design of the internal workpieces with 8 grooves was based on the best performing design with 5 grooves, which failed due to cracking of the tube wall, this was an expected observation.

An analysis of the influence of the parameters on the torque strength was carried out. Only the charging voltage and the groove depth were varied, as the influence of the other parameters was clear.

The influence of the energy level was again very small (<2% difference).

It was clear that a groove depth of 3,8 mm resulted in lower torque values (463 Nm). This is the consequence of a too big tube wall thickness reduction at the groove edges, as shown in Figure 8. A groove depth of 3,3 mm resulted in the highest torque value (526 Nm). A clear trend of the joint strength as a function of the groove depth remained however undetectable.

Figure 7: *Close-up of the groove zone of a test specimen before (left) and after (right) torque testing*

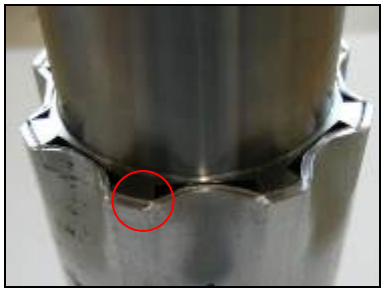

Figure 8: *Reduction of the tube wall at the groove edge*

All torque joints using internal workpieces with 5 or 8 grooves showed a joint strength lower than that of the tube base material. Figure 19 shows the relative joint strength of the connections, calculated as the absolute joint strength divided by the tube base material torsional strength. On average, a ratio of 1,617 was found between the torque strength of crimp joints with 5 and 8 grooves. This ratio is approximately equal to the groove ratio (8/5 = 1,6), which demonstrates the linear relation of the joint strength and the number of grooves, as expected from literature.

4.3 Conclusions concerning torque joints using grooved internal parts

- For both test series, the influence of the energy level is low for the investigated ranges. A limited amount of tube wall thickness reduction is allowed, as long as the beneficial effect of the additional interlocking capacity is not detrimental for the joint strength. This extra interlocking capacity forces the tube to fail by bending of the tube out of the groove, with cracking of the tube wall. A higher joint strength is observed for joints that fail by this failure mechanism. The maximum joint strength is observed at a lower angular displacement than for joints failing due to bending of the tube out of the grooves.
- A small groove edge radius (0,5 mm) and a large groove width (12 mm) are preferred.
- The groove depth has less influence on the joint strength than the groove width, but the optimal groove depth value remains undetermined.
- For similar grooves, a direct proportional relation exists between the joint strength and the amount of grooves, as was stated in literature. This conclusion applies to the range of 5 to 8 grooves. Experiments with designs with a larger amount of grooves should be performed to confirm further proportionality.

5 Design of torque joints using knurled internal workpieces

5.1 Design of torque joints using knurled rolled internal workpieces

In a first phase, preliminary experiments were performed with knurled rolled internal workpieces. The knurl zone had a length of 25 mm. With this size, a large region influenced by sufficient magnetic pressure to plastically deform the tube onto the inner workpiece is used and a maximum joint contact surface is generated. No clearance between the internal part and the tube was present, which means the tube internal surface and the knurl pattern made contact prior to the crimping operation. Three different knurl sizes were used, defined by the pitch: 1,2; 2 and 3 mm. All crimping experiments were done with an energy of 5,12 kJ. An example of an internal workpiece is shown in Figure 9.

The coarse knurl pattern provided the maximum torsional resistance (376 Nm), which is 2 times higher than for a fine knurl pattern (164 Nm).
The occurring failure mechanism was the same for all the test specimens. The internal workpiece started to slide in the tube and a wear mechanism developed. The steel knurl pattern made indentations in the internal surface of the aluminium tube. This wear mechanism could be observed in the torque curve as well (see Figure 10). A decrease of the torsional strength is detectable in the figure in the form of a decreasing amplitude of the load variation.

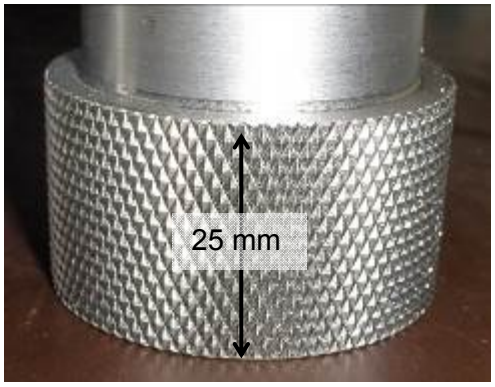

Figure 9: *Internal workpiece with a knurl zone of 25 mm*

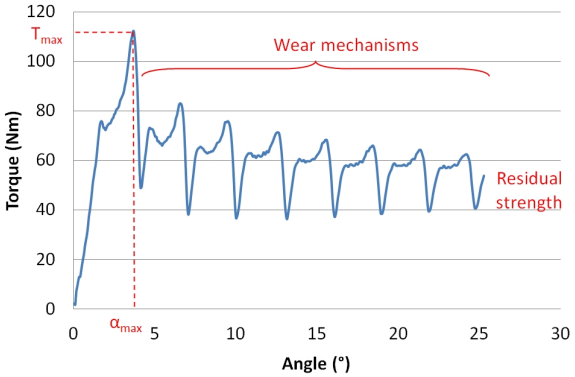

Figure 10: *Torque versus angular displacement of a knurled test specimen*

5.2 Design of torque joints using knurled cut internal workpieces

The length of the knurled cut internal surface was chosen equal to 25 mm (see Figure 11). This allowed to compare the results with the preliminary experiments using a knurl rolled internal part. The pitch size of the grooves was 2 mm, and a groove depth of 1 mm was created. The initial gap between the tube and the internal workpiece was equal to 1 mm. This allows the aluminium tube to impact with a higher velocity onto the internal workpiece. The influence of the energy level was investigated, which was varied between 5,12 and 20,48 kJ.

Since the grooves have dimensions comparable to the tube wall thickness, a limited amount of tube wall shearing into the grooves is possible, allowing interlocking to be achieved (see Figure 12).

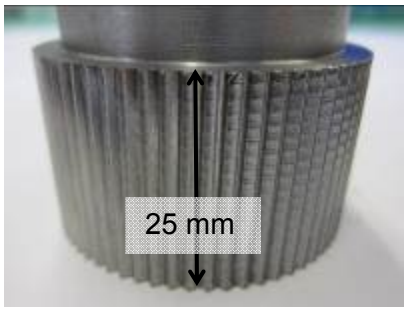

Figure 11: *Internal workpiece with a knurl groove geometry*

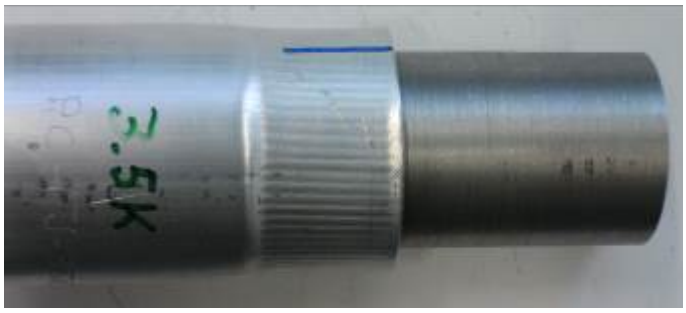

Figure 12: *Example of a torque joint with a cut-knurled pattern*

For every value of the charging energy, two experiments were performed. Every connection was mechanically tested. As can be seen in Figure 13, no influence of the energy level on the torque strength can be observed. Only for a charging energy of 5,12 kJ, somewhat lower torque values were measured. This implies that the energy level can be chosen in a broad range.

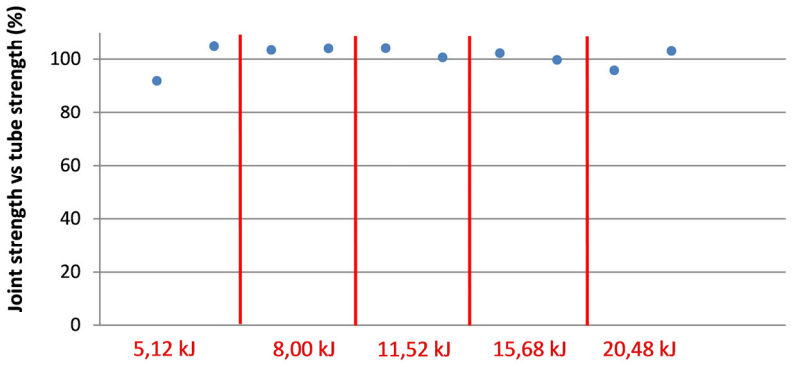

Figure 13: *Relative joint strength of the tested knurl groove joints.*

The following failure mechanisms were observed.
Failure mechanism 1: Sliding of the internal workpiece in the tube
The obtained torque-angle curve was similar to the curve obtained for the crimp connections with the knurled rolled internal parts (see Figure 10). A maximum torque value close to the theoretical tube strength was reached. Further angular displacement causes the internal workpiece to rotate inside the aluminium tube, causing wear at the internal surface.

Failure mechanism 2: Buckling of the tube, without cracking of the tube in the joint zone
The torque-angle curve of a specimen failing by this mechanism is shown in Figure 14. The repeating pattern observed in the previous case is no longer present. The decreasing torque value is no longer due to failure of the torque joint, but due to buckling of the aluminium tube (as shown in Figure 15).

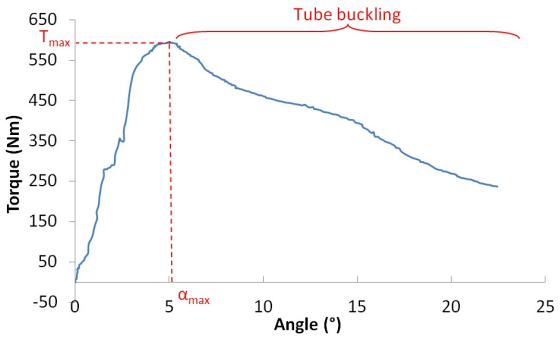

Figure 14: *Failure mechanism 2: torque versus angular displacement*

Figure 15: *Failure mode 2: tube buckling, without cracking*

Failure mechanism 3: Buckling of the tube, with cracking of the tube in the joint zone
The torque-angle curve of a specimen failing by this mechanism is shown in Figure 16. Although the load on the joint decreases due to buckling of the tube, this particular joint failed due to cracking of the tube shortly after the buckling initiated (Figure 17).

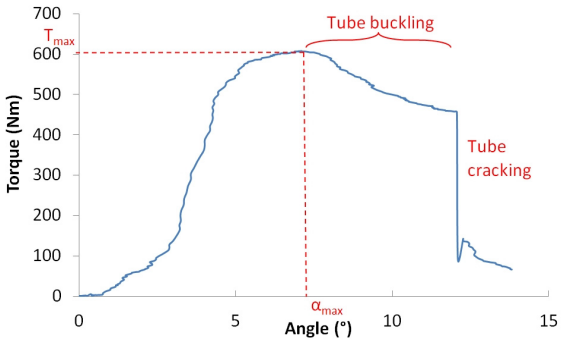

Figure 16: *Failure mechanism 3: torque versus angular displacement*

Figure 17: *Failure mode 3: tube buckling, with cracking*

Failure mechanism 4: Buckling of the tube, with cracking of the tube in the joint zone when using an internal support during torque testing
A steel support was placed inside the aluminium tube during torque testing. In the torque tests executed without the internal support, the maximum tube load is maintained for only a very short time, as the tube starts buckling from the moment the maximum load is reached. Placing a steel support inside the tube causes the tube to remain its strength, even for a higher angular displacement.
The torque-angle curve of a specimen crimped at 8 kJ is shown in Figure 18.

After a first maximum is reached, the tube starts buckling until the internal tube surface makes contact with the internal support. When sufficient contact between tube and support has been established, a reinforcement of the aluminium tube is noticed in the torque-angle curve. This reinforcement continues until cracking of the tube in the joint zone is observed.

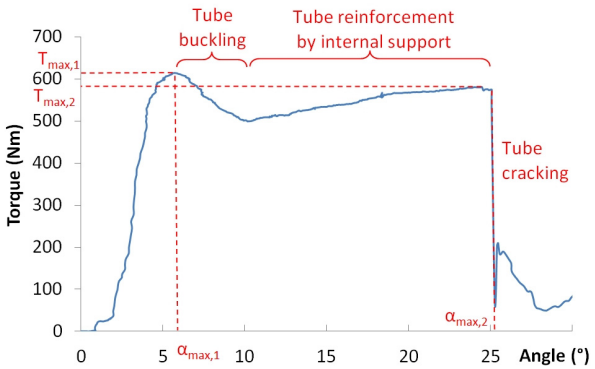

Figure 18: Failure mechanism 4: torque versus angular displacement

5.3 Conclusions

- The joint strength of crimp joint with a knurl cut internal workpiece is high, most of the crimped connections showed a strength equal to that of the tube base material.
- The influence of the energy level on the joint strength is low.
- Within the investigated range of the energy level (5,12 - 20,48 kJ), no detrimental effects of a tube wall reduction has been discovered. Still, the energy should not be set higher than required to obtain the full joint strength.

6 General conclusions

An overview of the relative strength of all tested torque joints is shown in Figure 19. The maximum measured torque strength of a connection using an internal part with 5 grooves was equal to 307 Nm. In case of a connection with 8 grooves, the maximum torque measured was equal to 527 Nm. Based on the average torque strength of all connections, a linear relationship between the torque strength and the number of grooves was observed.

The strength of the connections with a knurl rolled internal part significantly increased for a larger pitch of the knurl pattern. The coarse knurl pattern provided a maximum torque resistance which was 2 times higher than for a fine knurl pattern (376 Nm vs. 164 Nm).
The torque strength of the crimp connections with a knurled rolled internal part showed a large variation, dependent on the parameters used. Generally, the best performing connections had a strength approximately equal to that of the connections using an internal part with 5 grooves.

The crimp connections using a knurl cut internal part exhibit the highest joint strength, equal to the tube base material strength. Since the grooves of the knurl pattern have dimensions comparable to the tube wall thickness, shearing of the tube wall into the grooves was observed, creating a strong interlock of the tube with the internal part.

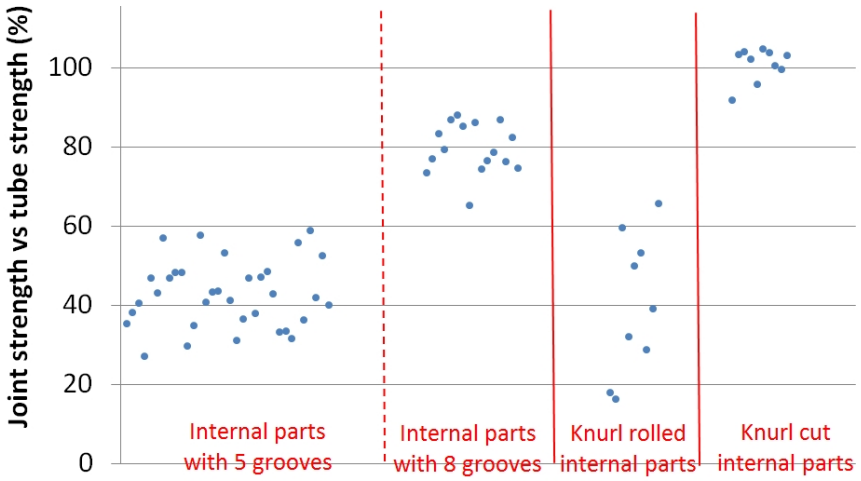

Figure 19: *Overview of the relative joint strength of all tested joints*

It was also concluded that for all designs, the influence of the energy level on the joint torque strength is low in the investigated range. For torque connections using longitudinal grooves, it is advisable to use a small groove edge radius and a large groove width. The groove depth has less influence on the joint strength.
Three types of failure mechanisms appeared during torque testing. In order of increasing joint strength, we can distinguish:

- The internal workpiece slides in the tube.
- The tube cracks at the joint.
- The tube buckles, and the joint does not fail. Instead, the tube base material fails.

References

[1] *Peihui, Z.:* Joining enabled by high velocity deformation., Dissertation presented in Partial Fulfillment of the Requirements for The Degree Doctor of Philosophy in the Graduate School of the Ohio State University, 2003.
[2] *ElMag:* http://www.elmaginc.com/index_files/history.htm (consulted Febr. 2014)
[3] *Magneform :* http://www.magneform.com (consulted Febr. 2014)
[4] *Park Y.; Kim H.; Oh S.:* Design of axial/torque joints made by electromagnetic forming., Thin-walled structures, 43 (2005), p. 826-844.
[5] *Min, D.K.:* A finite element analysis on the electromagnetic tube compression process., Journal of Materials Processing Technology, 38 (1993) p. 29-40.
[6] *Van Hulsel, P.; Van Wonterghem, M.:* Magnetic pulse crimping of mechanical joints., Master dissertation, Ghent University, 2011.
[7] *Faes, K.; Baaten, T.; De Waele, W.; Debroux, N.:* Joining of Copper to Brass Using Magnetic Pulse Welding. Proceedings of the International Conference of High Speed Forming, Columbus, Ohio, 9 - 10 March 2010.
[8] *Faes, K.; Zaitov, O.; De Waele, W.:* Electromagnetic pulse crimping of axial form fit joints. Proceedings of the International Conference of High Speed Forming, Dortmund, Germany, 24-26 April 2012, p. 229-242.

Influence of the Boundary Layer in Magnetic Pulse Sheet Welds of Aluminium to Steel

M. Geyer[1], A. Rebensdorf[1]*, S. Böhm[1]

[1)] Institute of Production Technology and Logistics, Department of Cutting and Joining Manufacturing Processes, University of Kassel, Germany

* Corresponding author: E-mail address: a.rebensdorf@uni-kassel.de;
Tel.: +49 5618043916

Abstract

In this paper, influential factors on the bonding strength of magnetic pulse welds between Aluminium (A1050) and Steel (S235JR) sheets are shown. First, a process window defined by varying charging energy and standoff distance for the welds. These welds will be characterised by the means of weld length and shear strength. Sound parameters are worked out at a standoff of 1.5 mm and a charging energy of 9 kJ. Nevertheless, no direct correlation between archived weld length and weld strength can be seen for the specific parameter set with a glass blasted, nearly polished surface. The achievable shear strength for this parameter set varies in the magnitude of 30 %.
The chosen parameters are used to investigate the effect of surface preparation on the weld. Surface preparation has an acceptable impact on the achievable weld length in the interface and on the maximum shear strength. Furthermore, a controlled surface appearance reduces the statistic deviation of the weld length. It is shown that machining, which cuts grooves perpendicular to the collision direction, enhances the joint performance as well as the achievable weld characteristics.
Furthermore, an acceptable impact of the rolling direction of the steel on the appearance of the joint interface will be shown. A rolling direction which lies perpendicular to the collision direction enhances the bulging of the steel into the aluminium.

Keywords

Welding, Aluminium, Surface

1 Introduction

1.1 Motivation

Lightweight design has been a permanent trend in various industrial areas in the last few years. Specifically for transportation applications it has gained an outstanding importance, due to its potential to reduce fuel consumptions and thus CO_2 emission. One of the main driving forces of light weight designs is the mixed material approach. Apart from the

occasional use of other alloys, the materials that are used mostly for lightweight designs are aluminium and steel. [11]
For this purpose, a joining operation for steel and aluminium alloys is necessary [11]. However, because of their properties, joining operations for the joining of aluminium to steel are limited. Basically, there are three approaches to this operation. The first is adhesive bonding, it ensures advantages in stiffness for the car body. Nevertheless, a sound surface preparation is needed to provide the aimed properties. Furthermore, an additional joining operation for the car body has to be considered until the curing of the adhesive is finished. The second approach to joining aluminium to steel are form fit joints, e.g. clinching. These joints have a good quality but are not suitable for crash relevant structures, because their behaviour is anisotropic and their strength is not as the results gained in other operations. The third approach is the welding of aluminium to steel through low heat input welding sources. In detail, this welding method equals the soldering of the aluminium to the steel partner; hence the wetting of the aluminium to the steel is dependent on the surface preparation. Furthermore, plenty of heat is generated and intermetallic phases are likely to be formed and have a disadvantageous impact on the joint performance.
A recent approach to joining aluminium to steel is the so called magnetic pulse welding technology (MPW). It is a promising process, which is also likely to solve various problems of other joining operations and enlarges the possibilities of multi-material designs with aluminium and steel. This paper aims to show the potential of this process for sheet metal welding and will discuss the impact factors of the boundary layer on the weld formation process.

1.2 State of the Art

The basic principle of magnetic pulse sheet welding is displayed in Figure 1. According to [1], an increasing coil current, which flows through the coil, induces eddy currents into the aluminium sheet. These eddy currents have the opposite direction to the current of the coil. Hence, a force between both currents occurs, which causes the aluminium to be deformed in certain positions. In order to form a bond between both materials, the aluminium impacts onto the steel parent mainly under an oblique collision angle and with a certain collision speed.

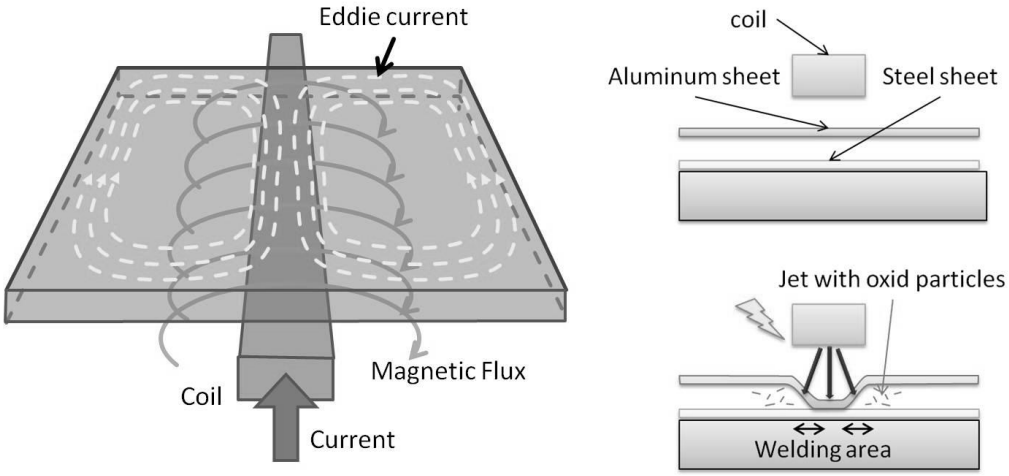

Figure 1: *Sheet metal welding, left according to Watanabe [1]*

All the papers, which are known to the authors and which deal with aluminium steel welds, are based on a small amount of specimens welded with the same parameters. They describe the weld formation phenomena in a qualitative way. *Lee* investigated the

interfacial microstructure of aluminium A6111 to SPCC steel weld [2]. With the help of optical micrographs, he showed that the aluminium seems to suffer a lot more deformation than the steel parent. Furthermore, the hardness distribution shows that a work hardening of the material near to the interface takes place and he assumes that the “work-hardened layer around the intermediate layer is considered to be the origin of high interfacial bonding strength“ [2].
The characteristics of a magnetic pulse weld of aluminium to steel are also discussed for tube welding by *Marya, et al.* in [3] and [4], [3] shows that the intermediate layer of an aluminium steel weld contains intermetallic phases which are likely to be formed due to non-equilibrium conditions. Furthermore, the work hardening is proved. The impact of the intermetallic layer on the tensile shear strength is investigated in [4]. The paper shows the impact of the minimum thickness of the interface layer on the tensile shear strength and states that a thickness of 5 µm delivers sound joints. However, only three different specimens were tested within the testing series for that paper.
A good sample for a process window research is [5], in which sheet metal welding of aluminium to stainless steel is described. A rather big amount of different process parameters were tested and plotted. The main focus of the investigation lay on the influence of different coil cross sections on the tensile shear strength. Hereby, the adjustable parameters charging energy and stand-off were varied, showing that a tapered cross section produces advantageous welds. The joined materials had a small thickness (steel: 0.25 mm; Al: 1 mm) and both joining partners were accelerated, hence the results are not directly transferable to a lot of applications, e.g. car body manufacturing. Overall, *Kore* achieved sound welds, but gave no information about the impact of the surface preparation on the weld formation as well as on the weld formation itself.

2 Aim of the Work

This paper aims to clarify the reliability of the MPW process for the welding of aluminium to steel. Research results from the University of Kassel, Germany, in [6], [7] and [8], as well as the results from [9], show that for the MPW of aluminium to steel a big variance in weld strength can be expected. Hence, this aspect will be examined for certain conditions during welding.
In context to past tests performed by the Department for Cutting and Joining Manufacturing Process at the University of Kassel, the hypothesis that weld length and tensile strength correlate was formed. This paper wants to show that the results of MPW can be treated as a Gaussian distribution and, in addition, shows the impact of the surface roughness on the process.

3 Experimental Setup

3.1 Specimen Material and Preparation

The specimen materials were AA 1050 as a flyer material with a thickness of 1.5 mm and a S235 JR as parent material with a thickness of 2 mm, Table 1.

	e-module [MPa]	$R_{p0,2}$ [N/mm²]	$R_{eH/eL}$ [N/mm²]	R_m [N/mm²]	$H_V0,1$	density [kg/cm²]
AA 1050	70	101,8		107,2	42	2,7
S235 JR	210	337,2/331,9		378,1	68	7,85

Table 1: *Mechanical properties of the flyer and base material*

For the evaluation of the reliability and the calculation of whether the process can be treated as a process under Gaussian distribution conditions, 50 specimens were glass blasted by a mikromat eco 50 machine, manufactured by joke Technology GmbH. The average size of the glass pearls was 110 µm – 70 µm.
To examine different surface preparations for the steel parent, a brown aluminium oxide (NKF 70) blasting with an average grain size of 180 µm – 250 µm was processed in the same machine. Furthermore, a grinding process with a band grinder, with corning number 80 and Al_2O_3 as corn material, was used for the surface preparation. Two directions of grinding were applied to the specimens, one parallel and one perpendicular to the collision velocity vector.
Finally, a cleaned laser system was used to form the surface with the help of the laser ablation technique. The laser was a Q-switch laser with a wavelength of 1064 nm and a maximum power of 50 W. The obstacles were machined perpendicularly to the welding velocity vector. All surfaces were documented, using a white-light interferometer, MicroProf manufactured by the company Fries Research & Technology GmbH. Before welding, the elements were cleaned by using ethanol and a paper towel. The aluminium flyer was simply cleaned with ethanol and a paper towel, because it will be deformed heavily and with regard to [10], no large impact of further surface preparations can be expected.

3.2 Testing

For testing, the specimens were machined using a wire eroding process with a Fanuc Robocut a-0 to keep the heat input and the mechanical load as low as possible. The preparation is shown in Figure 2. The round edges of the weld seam were cut out to ensure that only fully formed weld seams were tested. Hence, the weld seams have a uniform appearance. The micro section that was cut out is located nearer to the middle of the specimen. This ensures that the micro sections lie in the area of uniform welding parameters for the weld process.

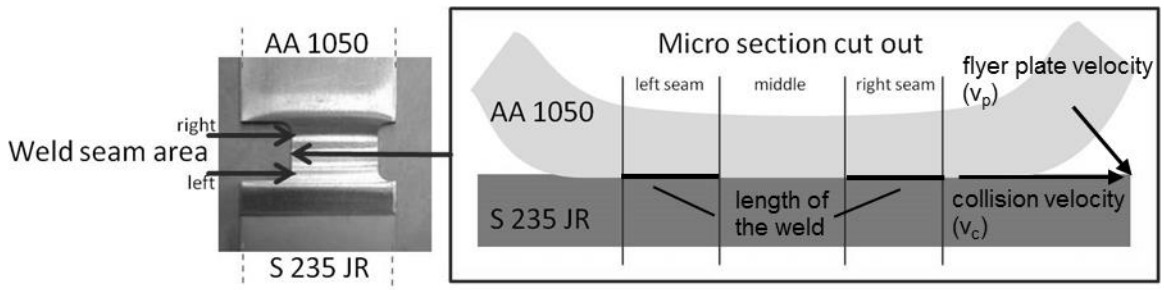

Figure 2: *Specimens' preparation and weld seam denomination*

Tensile tests of the specimens were carried out with a Zwick/Roell Z100 tensile testing machine. The micro sections were ground and polished to a 1 µm finish. Afterwards, a picture of the micro sections was taken with a microscope from Leitz and a CCD camera.

3.3 Magnetic Pulse Welding Process

For the welding process, a PS 48-16 magnetic pulse machine, manufactured by the company pstproducts GmbH, was used. The overall maximum charging energy is 52 kJ with a charging voltage of 16 kV as well as the coil has a web thickness of 5 mm.

The welding parameters were investigated by means of laser-polished surfaces. The charging energy of the machine was varied from 5 to 12 kJ as well as the standoff between flayer and target in 0.5 mm steps from 1.5 mm to 2.5 mm for specimens. The

process window was defined by comparison of the reached tensile strength and charging energy.

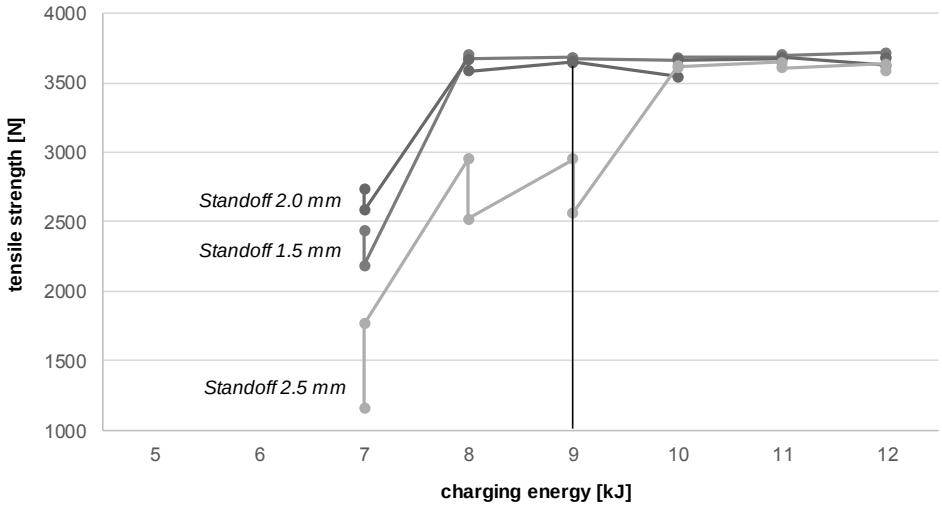

Figure 3: *Magnetic pulse welding process window*

Figure 3 shows the welding process window, which shows that an increasing standoff requires a higher charging energy. The lower standoff was taken, whereby low charging energy could be used for the process. This leads to low impact velocities and thus to small energy inputs into the base material. The charging energy of 9 kJ was selected to ensure welding within and not on the limit of the process window. In sum, the charging voltage was 6,642 kV and the overall circuit frequency of the process was 19.8 kHz. The standoff between flyer and target was 1.5 mm and the charging energy 9 kJ.

4 Experimental Work

4.1 Test of the Weld Properties for a Standard Deviation

First the reliability and reproducibility of the MPW process was investigated. Therefore, 50 specimens with a glass blasted and cleaned surface were welded. The results in Figure 4 show that no reproducible tensile strength and weld length for a carefully glass blasted and cleaned surface can be accomplished. The weld failure stands in no relation to the weld length, hence not only the weld length can be a criteria for the tensile shear strength of MPW bond.

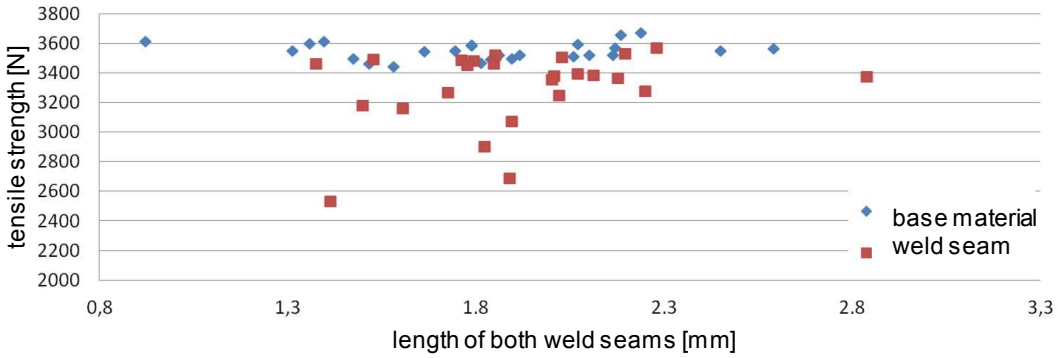

Figure 4: *Relationship between tensile strength, weld length and failure mode*

A Shapiro-Wilk-Test was carried out to test the weld properties for the hypothesis regarding the standard deviation using SPSS-Software by IBM [12]. First, a graphical evaluation of the specimens with histogram, boxplot and Q-Q-Plot was performed, Figure 5.

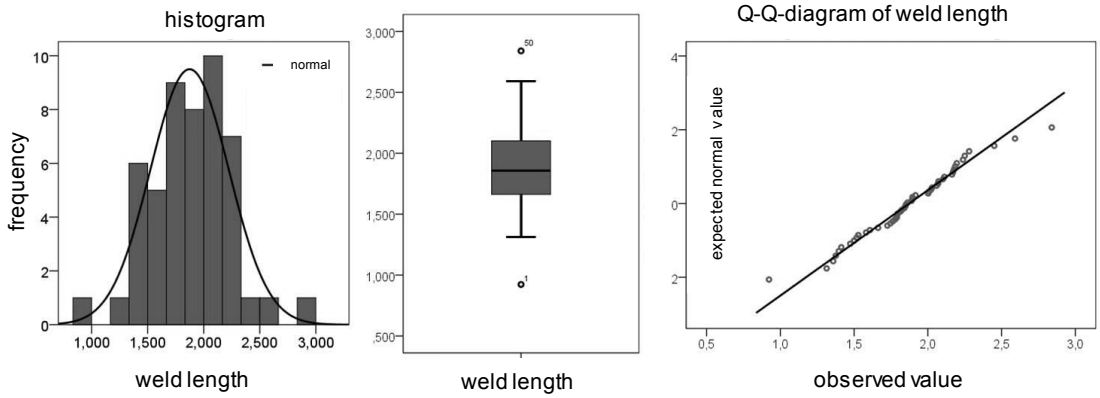

Figure 5: *Histogram, Boxplot and Q-Q-Plot of weld length*

The evaluation showed no signs for a deviation from a standard distribution. Therefore, the characteristics of the distribution can be compared with the characteristics of the standard distribution, Table 2. The comparison of the determined results displayed no significant deviation.

Parameter	Series of Measurements	Standard Deviation
(average value – median) / s	0,05	0
Quartile gap / s	1,30	1,34
Specimens in 1s interval	68 %	68 %
Specimens in 2s interval	96 %	95 %
Specimens in 3s interval	100 %	99,73 %

Table 2: *Analysis of weld length and standard distribution*

Based on the observed data, a null hypothesis is given as a result. Hence, the distribution of the weld length corresponds to that of the standard distribution. The significance of the standard distribution was determined with a high quality (low β-error) on the basics of tests for standard distribution and was compared with α-error, Table 3. As an option, a Kolmogorov-Smirnov-Test can be used additionally to the Shapiro-Wilk-Test. However, the Shapiro-Wilk-Test provides better quality for low sample sizes. Therefore the conclusions are based on results from this test. The assumed α-error is set at 5%, as the hypothesis is not true.

Testing procedure	Statistical significance value (α = 0,05)
Shapiro-Wilk	0,738
Kolmogorov-Smirnov	0,93

Table 3: *Tests for standard distribution*

The results of the statistical significance tests show that the values are clearly exceeded. Thus, the null hypothesis cannot be rejected. Furthermore, we can assume that the distribution of the lengths of the weld is a standard distribution and that statistical methods for the evaluation of the weld length can be used. The graphical analysis for standard distribution was also performed for the mid-width. Here, a standard distribution could not be demonstrated. The depiction of the distribution shows a right-skewed distribution, Figure 6.

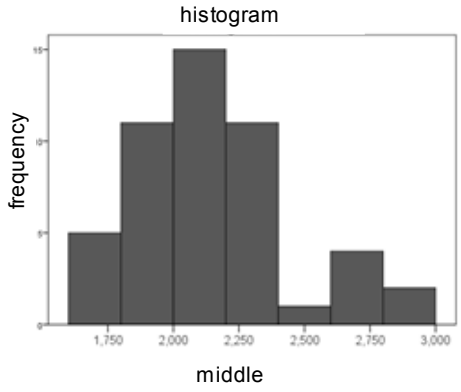

Statistic

middle

N	valid	49
	lacking	1
Average value		2,14693
Median		2,1222
Skewness		0,825
Standard error of skewness		0,34

Figure 6: *Graphic analysis for normal distribution of the middle width*

This distribution property is equally characterized for the whole length (right weld, middle and left weld). Therefore, median will be used for the evaluation of the middle and the whole length as a benchmark. The figure suggests that there is no linear dependence between weld length and tensile strength. This assumption is confirmed by a correlation calculation. Based on these results, we can assume that the length of weld is always normally distributed.

4.2 Influence of Different Roughness Characteristics

In addition, different surface preparations were applied to the steel parent and in each case 50 specimens were welded, as this was also the aim of the paper. The general appearance of the surface can be seen in Figure 7. The *glass blasted* specimens have the smallest value of average roughness of about 2 µm. The average roughness of both the grinded and Al_2O_3 *(NKF)* blasted profiles are quite similar as they are close to 3 µm. The laser machined surface has the highest average roughness of close to 5 µm.

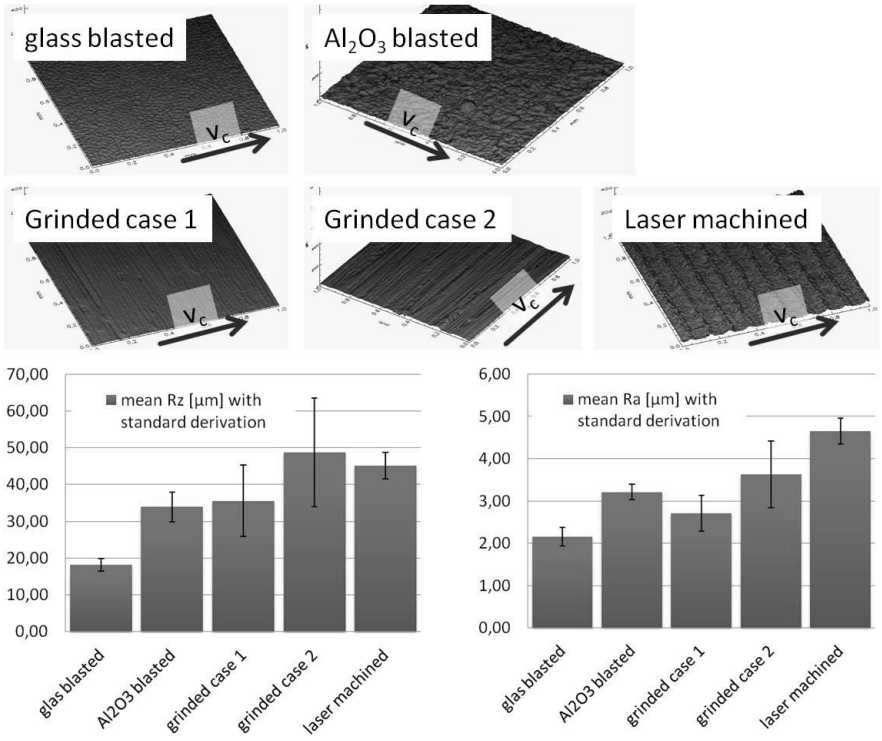

Figure 7: *Surface preparations*

A weld could be accomplished with all specimen preparations, except with the *Al_2O_3 (NKF) blasted* specimen. It was not possible to obtain a weld with this kind of surface. Hence, no metallurgical examination could be done for this specimen.
All other specimens were subjected to a metallurgical examination. The results of the measured weld length can be seen in Figure 8. For glass blasting and *grinding case 2,* the average weld length and the length of the middle section are nearly the same. For *grinding case 1,* the average weld length is approximately 30 % longer. For the laser machined specimen, the weld length is comparable to that of the glass blasted specimen but has a significantly wider middle section.

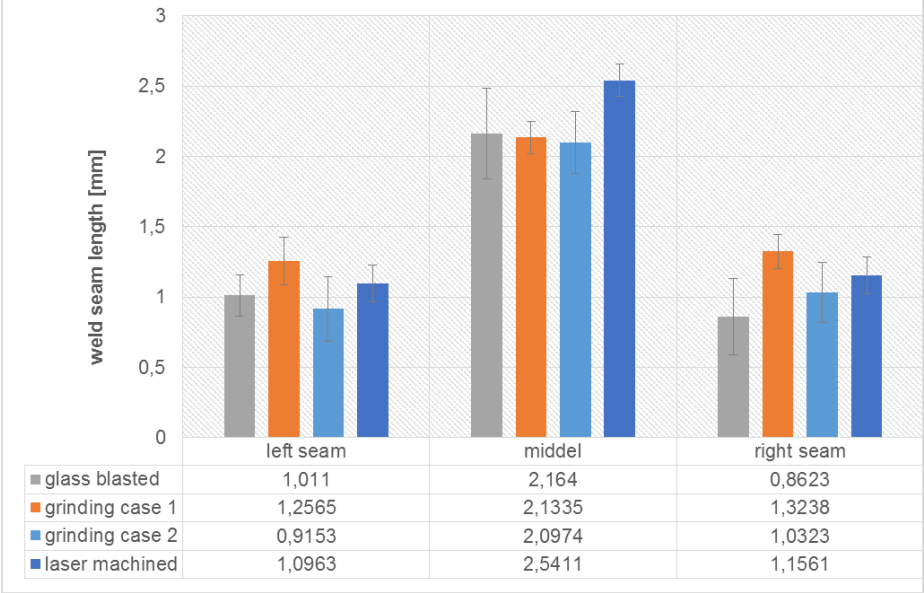

	left seam	middel	right seam
glass blasted	1,011	2,164	0,8623
grinding case 1	1,2565	2,1335	1,3238
grinding case 2	0,9153	2,0974	1,0323
laser machined	1,0963	2,5411	1,1561

Figure 8: *Interface weld length at different surface preparations*

The micro sections give a deeper understanding of the process behavior. When looking closely at the interface, intermetallic phases that occur after obstacles can be detected, especially in the *grinded case 1* and *laser machined* specimen, Figure 9. Furthermore, a wavy appearance, due to the preparation, occurs and hence a mechanical interlocking can be observed. The intermetallic phases are mainly located behind obstacles which were caused by the surface preparation.

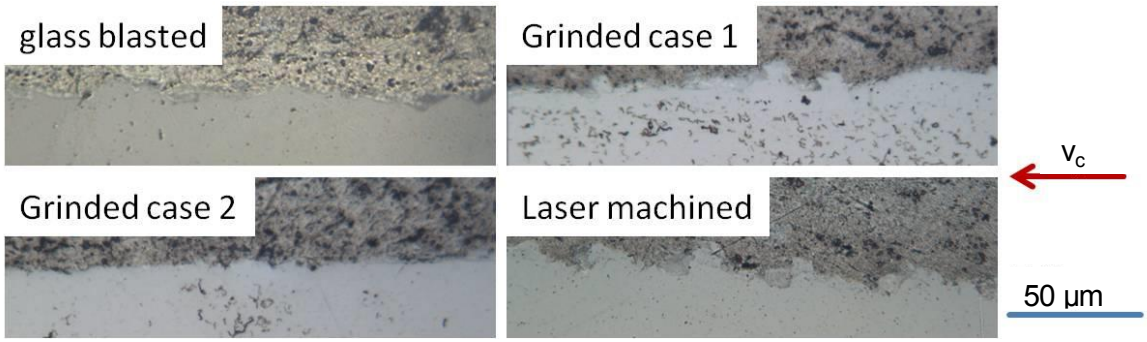

Figure 9: *Micro sections of the weld area for different surface preparations*

In terms of achieved tensile shear strength, both the *grinded case 1* and the *laser machined* surface preparation delivered sound welds with a failure only in the base material. Hence, the results have been very reliable. The glass blasted surface results

were shown previously in Figure 4. The same pattern was achieved for *grinded case 2* surfaces.
As regards the distribution, the macroscopic evaluation of the weld length shows no significant deviation from the theoretical basic value. Thus, we can assume that the average length of the welds in both directions is equal. However, the test showed one difference concerning the equality of variances.

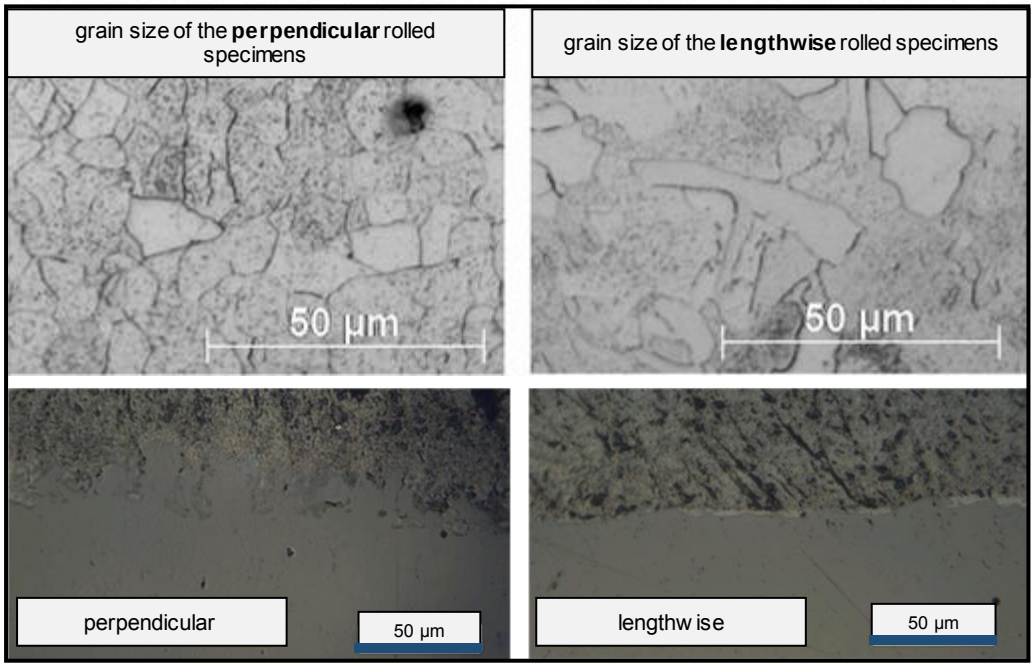

Figure 10: *Joint interface and grain size with perpendicular and lengthwise rolled steel*

The specimens with a perpendicular rolling direction to the collision vector showed a statistically significant lower variance. Thus, the formation of the weld with this specimens´ preparation is reproducible. Despite the equal length of the welds, the perpendicular rolled specimens have a significantly different interface than the lengthwise rolled specimens. For a comparison, two interface micrographs were taken 300 mm from the weld start. The two interfaces are displayed together with the receiving position in Figure 10.

5 Conclusion

As part of the investigation, the process window was defined by varying the parameters. The charging energy of the machine was set at 9 kJ for all specimens. This resulted in a charging voltage of 6.642 kV. The overall circuit frequency of the process was 19.8 kHz. The standoff between flyer and target material was 1.5 mm. In summary, we can state that no linear dependence between weld length and tensile strength is given.
In general, we could show that the surface treatment which is applied before welding with magnetic pulses influences the welding process of aluminium and steel significantly. In regard to the different surface preparations, we could demonstrate that a preparation, which forms uniform obstacles perpendicular to the weld seam, delivers sound welds with a reliable joint quality. The joint quality of these welds is produced by an interlocking of the boundary layer and a significantly longer weld length (up to 30% compared to other preparations, e.g. glass blasting, Figure 8, p.8) of the weld seams.

For the future the main questions that need to be answered are:

- Why do specimens that are prepared perpendicularly to the collision velocity vector have an advantageous behaviour?
- Why is the reliability of those specimens higher?
- Why is the middle sector for the laser machined surfaces bigger in comparison to the other preparation methods and why is this specimen still reliable?

To answer these questions we need to take a closer look at the formation of the weld, with regards to the time dependent behavior of the process.

References

[1] Watanabe, M. and Kumai, S. High-Speed Deformation and Collision Behavior of Pure Aluminum Plates in Magnetic Pulse Welding, 2035–2042.

[2] Lee, K.-J., Kumai, S., Arai, T., and Aizawa, T. Interfacial microstructure and strength of steel/aluminum alloy lap joint fabricated by magnetic pressure seam welding. Materials Science and Engineering: A 471, 1-2. 2007, 95–101.

[3] Marya, M., Marya, S., Priem, D., 2005. On the characteristics of electromagnetic welds between aluminium and other metals and alloys. Welding in the World 49 (5/6), 74–84.

[4] Marya, M., Rathod, M., Marya, S., Kutsuna, M., Priem, D., 2012. Steel-to-Aluminum Joining by Control of Interface Microstructures - Laser-Roll Bonding and Magnetic Pulse Welding -, in: Materials Science Forum, 539-543, pp. 4013–4018.

[5] Kore, S.D., Date, P.P., Kulkarni, S.V., 2008. Electromagnetic impact welding of aluminum to stainless steel sheets. Journal of Materials Processing Technology 208 (1-3), 486–493.

[6] Geyer, M. and Böhm, S. Prof. Dr.-Ing. Influence of contact surface on weldability with electromagnetic pulses. IIW Denver Annual Assembly 2012 – SC-Auto-52-12.

[7] Geyer, M., Böhm, S. Prof. Dr.-Ing., 2013b. Experiences in welding dissimilar Materials, especially aluminium-steel welds … with regard to macroscopic effects I2FG workshop, May 7th, Gent. I2FG, 13 May 2013.

[8] Geyer, M., Böhm, S. Prof. Dr.-Ing., 2013a. Welding of aluminium adapters to thin walled steel tubes with magnetic pulses. IIW International Congress. Accessed 18 July 2013.

[9] Aizawa, T., Kashani, M., Okagawa, K., 2007. Application of Magnetic Pulse Welding for Aluminum Alloys and SPCC Steel Sheet Joints, in: Welding Journal, vol. 86.

[10] Zlobin, B.S., 2002. Explosion Welding of Steel with Aluminum, in: Combustion Explosion and Shock Waves, vol. 38, pp. 374–377.

[11] Engelbrecht, L., Meier, O., Ostendorf, A., and Haferkamp, H. 2006. German: Einflüsse auf die mechanischen Eigenschaften lasergelöteter Mischverbindungen aus Stahl und Aluminium. http://onlinelibrary.wiley.com/store/10.1002/mawe.200500928/asset/272_ftp.pdf?v=1&t=h8cz8x9h&s=f0578ad7359a73b480960562b09cbbd36b5095c7. Accessed 16 October 2012.

[12] Toutenburg, H., (2000). German: Induktive Statistik - Eine Einführung mit SPSS für Windows. Berlin: Springer Verlag.

APPLICATIONS OF PULSED ELECTROMAGNETIC FIELDS IN POWDER MATERIALS HIGH SPEED FORMING

V. Mironovs[1], V. Lapkovskis[2] , M. Kolbe[3], V. Zemcenkovs[4], A. Shishkin[5]

[1,2,4,5]Riga Technical University, BF, LV-1048, Riga, Latvia, Viktors.Mironovs@gmail.com
[3]Westsächsische Hochschule Zwickau, Institut für Produktionstechnik, Zwickau, Germany. Matthias.Kolbe@fh-zwickau.de

Abstract

In current article, applications of electromagnetic pulsed fields for processing of powder materials are presented. The main attention is paid to the following applications of pulse electromagnetic fields in powder metallurgy and allied industries: pressing of powders, manufacturing of powder coatings, and conveying of ferromagnetic powders by means of pulsed electromagnetic field.

Keywords

Electromagnetic compaction, pressing, powder materials, coil, impulse currents, coatings, multilayer parts.

1. INTRODUCTION

Practical applications of pulsed electromagnetic fields in powder metallurgy are rather limited, yet it can be applied to a variety of technological processes such as, pressing of powders, processing of powder coatings, conveying of powders etc. A majority of research activities in this area was conducted in the USA, Germany, Russia, and Latvia. D. Sandstrom is pioneered the research of pulsed electromagnetic fields for consolidation of powder materials [1]. V. Mironov has investigated a method of magnetic-pulse pressing of powders on the basis of iron and hard alloys [2] [3] . N. Dorozhkin, A.Kot, etc. have studied influence and practical use of a method of magnetic-pulse processing of materials on powder metal coatings [4] . A comprehensive research in the field of consolidation of iron powders and hard alloys were carried out in Germany by H. Wolf and V. Mironovs [5] . The intensification

of processes of the expiration of powder materials from bunker devices under the influence of electromagnetic impulses was studied in work [6] . Application of pulse electromagnetic fields for joining of metallic materials obtaining a single-piece connections was investigated in works [7] [8] . Recently, applications of pulsed electromagnetic fields for conveying of ferromagnetic particles and metal powders have been studied [9] [10] .

A method of magnetic pulsed compaction of powders (MPCP) came from powder metallurgy and was reviewed in many papers, including [2] [3] [5] . Great technological capabilities of MPCP for manufacturing of complex configuration, multi-layered and high-density part were discovered. The current article overviews engineering and research activities of the Scientific Laboratory of Powder Materials of Riga Technical University (Riga, Latvia).

2. MAGNETIC PULSED COMPACTION OF POWDERS (MPCP)

In the past, the studies of MPCP process were conducted in the U.S. [11] [12] , Russia [13] , Israel [14] , Latvia [15] and other countries. The main aim of current research is in finding the ways for improving technological MPCP equipment, as well as a research of feasible applications for MPCP process. Preceding research [16] shows that MPCP process can be applied for laying and processing of anti-friction coatings.

Magnetic pulsed compaction of powders is a process which occurs under the action of electromagnetic pulsed loads. A principle of MPCP process is illustrated in Figure 1.

The MPCP is a very complex process with many influencing factors on the compaction results:

- work piece dimensions,
- properties of the powder,
- electrical parameters (current frequency),
- wall thickness,
- electromagnetic pressure,
- work-piece pre-treatments,
- form of particles,
- discharge energy (capacity, voltage),
- gap between coil and work piece,
- coil properties.

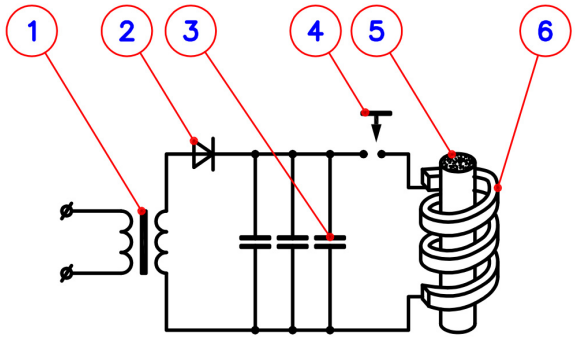

Figure 1: *Schematics of magnetic pulsed compaction of powders (MPCP).*

1 – transformer; 2 – rectifier; 3 – battery of capacitors; 4 – discharger; 5 – ferromagnetic powder in shell; 6 – coil

In this case the electromagnetic pressure can be determined by the following expression (1) [3]:

$$p(t) = \frac{1}{2} H_m^2 \mu e^{-2\beta t} \sin^2 \omega t \quad (1)$$

where, H_m - magnetic field strength in the gap between coil and details, μ - magnetic constant, β – damping of discharge current, ω – current angular frequency, t – time. Technical parameters of electrical current and pulse pressure obtained on equipment designed at Riga Technical University are shown in Figure 2.

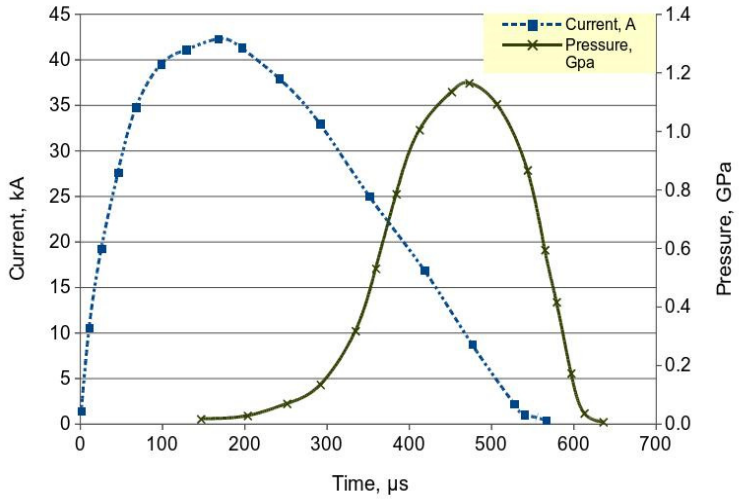

Figure 2: *Change of pulse current and produced electromagnetic pressure.*

Main advantages and disadvantages of MPCP process are outlined in Table 1.

Advantages of the MPCP process	Disadvantages of the MPCP process
✓ Obtaining PM parts made of different powder materials, including ferromagnetic, ceramic and amorphous powders. ✓ By means of MPCP process it is possible to achieve up to 75-85% of theoretical density for green PM parts. ✓ Manufacturing of multilayer parts.	× Need of liners (conductive plates) or shells used for pressing powders, × Low-precision product that requires subsequent machining, × A short lifespan of equipment.

Table 1: *Advantages and disadvantages of MPCP process.*

Another MPCP technique is a stepped radial compression of rod-shaped or tubular parts [15] with a length to diameter ratio greater than 2.5 Figure 3. This technique can be applied either along a whole length of tubular part or in certain points of a tubular shell.

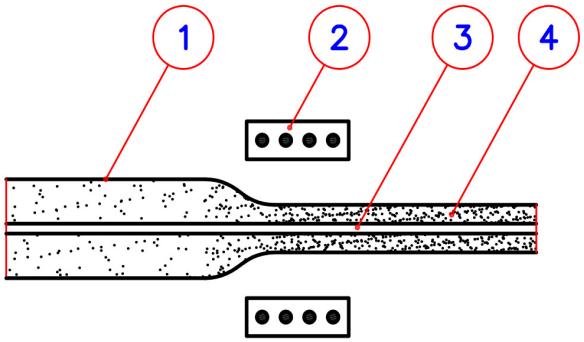

Figure 3: *Schematics of stepped radial compression of rod-shaped or tubular parts.*
1 – shell filled with powder; 2 – coil; 3 – mandrel (made of solid of powder material); 4 – compacted powder;

However, a stepped radial compression in shell technique is characterised by advantages and disadvantages shown in Table 2.

Advantages of stepped radial compression	**Disadvantages of stepped radial compression**
✓ Compaction of ceramic or granular materials, obtaining porous structures with variable porosity. ✓ Tight crimp of powder materials in shell. ✓ Obtaining compacted powder parts with variable density.	× Transverse cracking by axially acting tensile stresses during the compression process × Density drop in the radial direction, inhomogeneity of the density and strength. × Tubular parts can be manufactured with wall thickness up to 8 mm with sufficient density distribution in the radial direction by magnetic force compaction using a driver.

Table 2: *Advantages and disadvantages of stepped radial compression technique.*

The MPCP process opens an opportunity to manufacturing of metallic coatings, where material of coating have solid or porous structure. Here, a method of powder compaction in a conductive deformable shell (outer layer) by pulsed electromagnetic field [5] and the method of magnetic-pulse treatment of pre-stowed and then sintered powder layer [17] can

be applied. Methodology and recommendations on use of MPCP process in shells for anti-friction part manufacturing are described in [4] . These recommendations are based on the possibility of obtaining high anti-friction properties of parts by means of Fe-C-Cu materials. Experimental studies were carried out on the equipment described in [18] . In conducting the experiments the following sequence of operations was developed Figure 4.

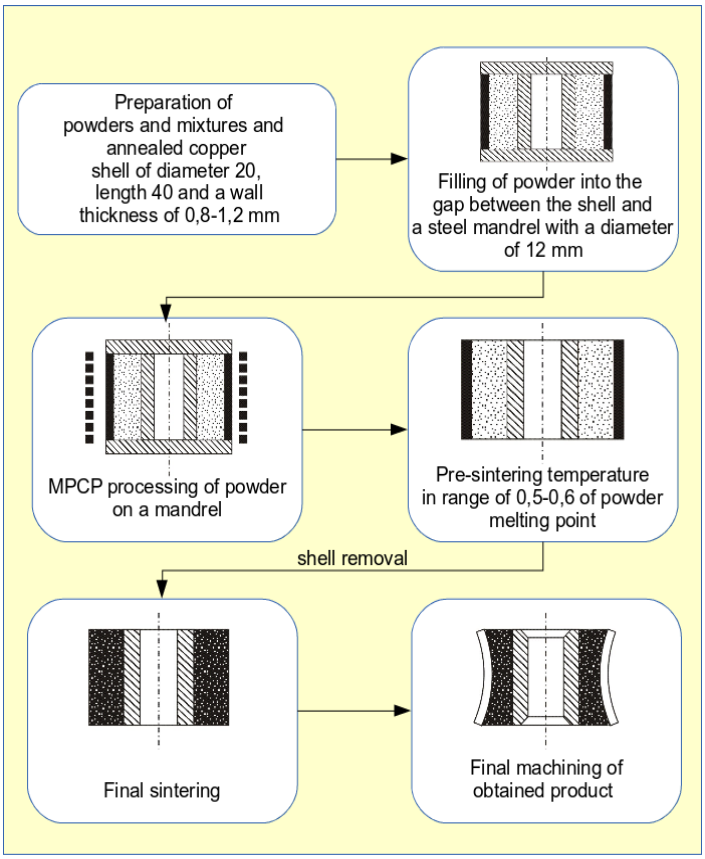

Figure 4: *A sequence of operations for powder coating manufacturing by means MPCP process.*

Advantages and disadvantages of powder coating manufacturing process are listed in Table 4.

Advantages of powder coating manufacturing	Disadvantages of powder coating manufacturing
✓ Obtaining compacted porous powder coating which can be impregnated by lubricants. ✓ Manufacturing of multilayer elements with variable properties for each layered material.	× The implementation of radial pressing of powder coating is related to the problem of ensuring the coating properties uniformity. × Adhesion strength of coating is determined by conditions of mandrel surface, powder material, and by discharge parameters.

Table 3: *Advantages and disadvantages of stepped radial compression technique.*

3. CONCLUSIONS

This article outlines scientific and engineering developments of the Scientific Laboratory of Powder Materials of Riga Technical University (Riga, Latvia) related to magnetic pulsed compaction of powders process. Applications of pulsed electromagnetic fields have a number of positive features, opening great prospects for improvement of technological processes in powder metallurgy:

- flexible opportunity for generation of pulsed pressure with variable amplitude and duration,
- concentration of pressure in certain locations of PM part,
- directed action of pulsed electromagnetic fields on a material with the aim of changing its properties.

At the same time a number of technical constraints are limiting the use of pulsed electromagnetic fields for mass production of PM parts. For example, a need for reliable and affordable high-performance equipment for industrial applications [19] and related manufacturing procedures in order to ensure a constant and high-quality final products.

4. BIBLIOGRAPHY

[1] D. J. Sandstrom, “Consolidating metal powders magnetically,” Met. Prog., vol. 86, no. 3, pp. 215–221, 1964.
[2] V. Mironov, “Pulververdichten mit Magnetimpulsen,” *Planseebericht fur Pulvermet.*, vol. 24, pp. 175–190, 1976.
[3] V. A. Mironov, *Magnitno-impulsnoe pressovaniye poroshkov /in Russian/*. Riga, Zinatne, 1980, p. 196.
[4] N. N. Dorozhkin, V. A. Mironov, and A. A. Kot, *Jelektrofizicheskie metody poluchenija pokrytij iz metallicheskih poroshkov*. Riga (Latvia): Zinatne, 1985, p. 131.
[5] V. Mironov and H. Wolf, “Pulververdichten durch elektromagnetische Kräfte Herstellunsmöglichkeit für Werkzeugaktivelements,” *Fertigungetechnik*, no. 9, pp. 558–590, 1980.
[6] V. Zemchenkov, V. Mironovs, and J. Viba, “Intensification of technological processes with electromagnetic impulses,” in *5th Int. DAAAM Conf*, 2006, pp. 307–310.
[7] V. Mironovs and I. Boyko, “Application of the electromagnetic impulses for joining of details and compacting of powders,” in *10th Int. Conf. TMT-2006*, 2006, pp. 205–208.
[8] M. Kolbe and V. Mironovs, “Gemeinsame Forschungsarbeiten zur Impulsstrombearbeitung mit Wissenschaftlern der TU Riga,” *IfPnews der Westsächsischen Hochschule Zwickau*, no. 12, 2011.
[9] V. Mironov and J. Viba, “Elevator for Powders,” in *EuroPM 2007 Conference (Vol. 2)*, 2007, pp. 39–44.
[10] V. Lapkovsky, V. Mironov, A. Shishkin, and V. Zemchenkov, “Conveying of Ferromagnetic Powder Materials by Pulsed Electromagnetic Field,” in *Euro PM2011 – Tools for Improving PM: Modelling & Process Control*, 2011, pp. 253–258.
[11] B. Chelluri and E. Knoth, “Powder Forming Using Dynamic Magnetic Compaction,” *4th Int. Conf. High Speed Form.*, pp. 26–34, 2010.
[12] A. G. Mamalis, D. E. Manolakos, A. G. Kladas, and A. K. Koumoutsos, “Electro-magnetic Tooling for Metal Forming and Powder Compaction : Numerical Simulation,” pp. 143–154.
[13] V. Banin and S. Paranin, “Processing of nanostructured oxide ceramics with magnetic pulsed compaction technique,” *Key Eng. …*, 2001.
[14] V. Shribman, “Take advantage of the new magnetic pulse welding process,” *Svetsaren, a Weld. Rev.*, no. 2–3, pp. 14–16, 2001.
[15] V. Mironov and V. Lapkovsky, “Tubular articles with the high permeability by uses of the MIOM technology,” in *Engineering materials and Tribology-2004*, 2004, pp. 201–205.
[16] V. Mironov, I. Boyko, and V. Lapkovsky, “Production of Fe-C-Cu powder coatings by pulse magnetic pressing and infiltration,” in *tmt.unze.ba*, 2011, pp. 137–140.
[17] I. Boyko, V. Mironov, and V. Lapkovsky, “Property and Structure Changes of Sintered Powder Materials by The Treatment in The Pulse Electromagnetic Field,” in *Proceedings of Euro PM 2007 (Vol. 3)*, 2007, pp. 439–444.
[18] V. Mironovs and I. Boyko, “Application of the electromagnetic impulses for joining of details and compacting of powders,” in *10th Int. Conf. TMT-2006*, 2010, pp. 205–208.
[19] C. Beerwald, “Anlage zur elektromagnetischen Umformung – SMU SSG 3020,” *Poynting GmbH Dortmund*, 2010.

The Present Situation of the Research and Development of the EMF in the China

Lu Xin

The general secretary of the China Society for the Technology of Plasticity
Address: 702 Room No 18 the Xueqing Road Haidian Distract Beijing China 100083
Email:13601322657@163.com; luxin0522cn@aliyun.com
Tel:0086-13601322657

Abstract

This article introduces the current research in China's electro-magnetic forming(EMF) technology, including research in the area of EMF theory, the production of EMF equipment, the EMF of pipe and plate parts, the application of punch and rivet etc, and also some new forming craft. Although China's research potential in the area of EMF is still rather low compared to more developed countries, but as market demand continues to increase, the level of research will also continue to rise.

Keywords: the electro-magnetic forming; electro-magnetic punch; electro-magnetic rivet

China's research into EMF techniques started from the 1960s, and was interrupted by the Cultural Revolution. Towards the end of 1970, the Harbin Institute of Technology started researching the basic theory and craft of EMF, and through experimental devices, successful made the first nationally produced EMF machine in 1986. Currently, there are many institutes of higher education and research that have started studying applications of EMF and also started production[1].

1 Progress in theoretical research.

Electromagnetic forming process involves the study of electricity, magnetism, electrodynamics, plastic dynamics as well as many other multidisciplinary subjects, making theoretical studies very different difficult. Electromagnetic forming theory includes two aspects: research on electromagnetic force and research on deformation of the workpiece by this force. The former is the theoretical basis of electromagnetic forming technology, the results of the analysis applied directly to the deformation of the workpiece. Theoretical research on analysis electromagnetic force is based on using spiral coil, plate coil and former etc. for the plate coil, it can be a layering many different radius single spiral coil, the former can be seen as two single spiral coil with through current in contrast. Therefore, analysis of spiral coil is the very foundation of electromagnetic forming theory,

and the plate coil and the former can be derived based on the foundational theory, collective known as column coil deformation [2-3].

Cylindrical electromagnetic coil tube bulging process has always been the main object of study, and researchers have conducted in-depth process of theoretical analysis and experimental study. Since the late 1980s, the Harbin Institute of Technology electromagnetic forming study groups have been carrying out systematic study of cylindrical coil electromagnetic forming process theory. Early work was primarily based on experimental research, and systematically started to develop analysis and experimental research on expand and contract deformation with column coil. In the late 1990s, we introduced finite element method into our study of EMF theory, and accelerated the search process, obtaining a number of research results[3]. Numerical simulation of electromagnetic forming has been increasingly viewed as important by researcher, and we are still at the exploratory research phase. However, reports of using research on complex part or simulating of complex part forming are still rare. Currently, mainland research mainly use three kinds of major theoretical research: the equivalent circuit method, finite element method and the analytical method.

Prof. Zhang Shou Bin[4] used the equivalent circuit method to analyze the process of discharge in the steel pipe part expanding, and on that basis, received the process of deformation of the steel pipe part under electromagnetic force, and research analysis results reveal phenomena that occur or may possibly occur during deformation. Experimental research was also conducted on the strength of magnetic sensibility of tool(coil) and blank. Research suggests that the strength of magnetic sensibility is connected to the length of the coil. When the coil is quite short, magnetic sensibility distribution is not even; when the coil is longer, magnetic sensibility tends to be more even. The distribution of magnetic sensibility is affected by the gap between the coil and blank, and is also related to distribute of strain after blank deformed.

Dr. Zhao Zhiheng [3] used the finite element method to study the magnetic field of the electromagnetic bulging, and some of his conclusions verify the distribution of magnetic sensibility as described above. He also discovered that the inside of the whole pipe has expand electromagnetic force, and it is decrease along the thickness from inside to outside. This is different from other bulging processes, and therefore helps deepen our understanding of electromagnetic forming deformation mechanism. Wang Shang Yu used the analytic method to research the distribution of magnetic fields of plate EMF, and calculated the EMF process using finite element method.

In order to better understand the magnetic fields of the workpiece while undergoing electromagnetic formation, some have used the finite element method to study the pipe contract, pipe forming with die, and the distribution pattern of magnetic fields of plate part forming. Research confirms that the energy discharged, the former can increase the magnetic field at the specially position in the pipe, and create large deformations. The die will absorb a small amount of magnetic field lines, producing a “magnetic cushion” effect. Therefore, we need to optimize the gap between die and the workpiece during molding. While the plate coil is expanding, the magnetic field is strongest at one half of the radius of the blank. The larger the radius, the smaller the magnetic field, and this conclusion is the same as that in the prevailing literature [2].

The literature[5] studied the magnetic field distribution and its impact on deformation of oval-shaped coil by using the analytical method. The magnetic sensitivity is 0 at centre of the oval-shaped coil, and starts to increase quickly starting from the start of wire , and

then following this increasing trend, and after it exceeds the area of the coil it reduces drastically. As the distance from the coil increases, magnetic sensitivity swiftly declines. The distribution of The magnetic sensitivity of radius direction also reflects the distribution pattern of magnetic fields felt by blank.

2 Advances in technological research

Electromagnetic forming can be widely used in the pipe part bulging, necking, punching, connecting ; the plate parts punching, coining, forming, assembling ; powder pressing; electromagnetic riveting [1]。

2.1 Pipe bulging

The pipe bulging is one of the areas of electromagnetic formation technology that has more applications. The main ones are free-tube bulging with mold forming, school-shaped tube, pipe flange, flaring and shaped tube forming etc. While undergoing electromagnetic formation, the deformation distribution is even in the tubing, hardening is not significant, and therefore the formability of the material is improved. When compared to static punching, electromagnetic formation methods can improve the bulging factor by 30% to 70%. The thinning and even rupture of the tube walls is the major problem. Current technology is already applied to narrowing and shaping some important parts and components.

2.2 Pipe necking

When positioning the external coil, it is easy to achieve a reduction in the diameter of the necking, localized necking and necking pipe section etc. The connection of the external coil can also deform the necking, and can make possible pipe connections and pipe rod connections etc. Electromagnetic forming is the same as conventional stamping in that its limiting factor is in the destabilizing wrinkling of the tube. Therefore, preventing wrinkling and diminishing wrinkling is the most crucial problem that tube necking technology must resolve. Axle necking technology is an effective method to prevent wrinkling. Using steel axle can dramatically increase the limit of shaping. The mechanism behind axle prevent wrinkling is the flat action, therefore the size of the axle cannot be too small, and it must be appropriately lubricated to make it easy for the metals to flow in the deformation process. Currently, China already has specialized tube necking technology applied to missile assembly. Furthermore, tube necking can be used for the metal foil packaging of beverages.

2.3 Plate blank forming

The plate blank forming can be divided into two kinds: free shaping or mould shaping. The former is mainly used for cone shaping that have low requirements for precision, and the latter is often used in embossing, indenting, and other surface parts forming and punching. Because tablet roughcast shaping creases uneven force distribution, therefore it affects the quality of the product. The shape of parts produced by free shaping is hard

to control, and there problem of the precision of forming. [1] the oval-shape coil forming is one form of table roughcast shaping machinery. According to the distribution principles of oval-shape coil magnetic fields, we should use oval-shape coil as opposed to circular coil in the long workpiece; and for core parts where shaping is more demanding, we should select circular coil. This is because oval-shape coil will not sufficiently shape the core parts, and this is more serious than for circular coil.

3 Electromagnetic equipment

China began to study the electromagnetic forming device in the early 1960s, after a standstill for some reason. 1986 Harbin Institute of Technology developed the first 7. 2 kJ electromagnetic forming machine. After the mid-1990s, those studying electromagnetic forming devices were the Shanghai Aerospace Bureau, Beijing Institute of Electrical and development and manufacturing with a 30 kJ electromagnetic forming machines, has gradually developed 1. 2 ~ 30 kJ of energy ranging from seven electromagnetic forming device. In addition, there are other institutions who produced and have made electromagnetic forming device. Harbin Institute of Technology now has three domestic and one imported from the former Soviet Union 56 kJ electromagnetic forming machine, is currently one of the units of a strong electromagnetic forming process and equipment research and development capabilities. Newly developed equipment with power protection, overvoltage protection, automatic unloading, security troubleshooting, simulation run other functions, equipment, operating flexibility has been greatly improved.

Although there has been gradual improvement of electromagnetic forming equipment, storage size, structure, control and security, it still suffers from the following disadvantages:

(1) Equipment Energy is not big enough, the largest of 50 kJ, the maximum foreign to 500 kJ;

(2) the energy efficiency is low, typically 10% to 20%, the maximum does not exceed 30%;

(3) the cost is still high and difficult to spread.

4 Test Technology

(1) measuring the resistance measurement of large currents: the use of measuring tools to measure DC current resistance is the method first used. We measure resistance with a standard resistor. It is characterized by its simple structure, its accuracy and reliability, but it can only be used to safely measure the resistance for electric currents under a few thousand DCs.

(2) Hall transducer measurement of large currents: the magnetic field and electric current are closely linked. Therefore, the Hall element for measuring the magnetic principles can also be used to measure the amount of current. Characteristics of the Hall transducer are its small size, its wide operating frequency range. Its disadvantages are that its linearity error is relatively large, and it is sensitive to temperature changes.

(3) measuring pulse current shunts: In order to measure the pulse current shunt, we must have inherent inductance as small as possible in order to meet the accuracy requirements. The use of pulse current shunt measurement test circuit is relatively simple, and it is also accurate and reliable.

(4)magnetic level gauge measuring pulse current : magnetic level gauge can be used to measure the pulse current , which is a measure commonly used . Its characteristics are its simple structure, and its does not have an inherent problem with stability of heat and electricity. Hundreds of more than a thousand real-time measurement of pulsed high current performance is still very stable. Its disadvantages are that its magnetic level gauge accuracy is not high, and its test circuit is complex, and that it only applies to large and rapid changes in the measured value of the pulse current . Measurements of the magnetic field is varied. From the measurement principle of view, there are two relatively simple method of magnetic field measurement method, which are the magnetic line and electromagnetic induce method.

5 Looking forward

Electromagnetic forming technology and other high-energy rate forming process have many advantages, such as its good production conditions, lack of pollution, its convenience of production, the ease of implementing machinery automation , and high production efficiency . Especially for some special and unique parts, electromagnetic forming is the only selectable method for forming. This accounts for the widespread use of electromagnetic forming compared to other high energy methods. Although the electromagnetic forming device has become stable products on the market, there is still continuous improvement. For example the use of multiple circuit technology in order to make devices safer and more reliable. Using the capacity with the high capacitance rate can make the device structure more compact, and can also improve the capacity of the equipment. We can also add heating and detection devices in the equipment, in order to facilitate the processing of large workpieces, collecting test data recording and processing. Electromagnetic forming process described above can also be used to position, assemble and form metal parts on glass, which is difficult to achieve using other processes . The use of high- speed electromagnetic forming characteristics can be successfully applied to the composite blanking and forming, too .

The current state of research suggests that if instead of using steel structures, we use aluminium structures, the quality of the car body will be reduced to half the original , and the extensive use of aluminum body structure for cars is driven by the trend. However, since the formation limit of aluminiumis less than that of steel, it can easily tear at high strain zones. Aluminium is not stiff, it is prone to rebound, and low stiffness can cause rather big deformation. Deformation of parts before assembly can greatly reduce the precision of its measurements. Although aluminum superplastic forming technology can solve this problem, it is very expensive Current research suggests that composite forming technology (ordinary stamping technology and electromagnetic forming technology combined) can be used to solve aluminum shaping problems in the car industry.

References

[1] 李春风.高能率成型技术[M] .北京:国防工业出版社. 2001.

[2] 黄尚宇,常志华.板坯电磁成形载荷计算方法及分布特性[J] . 中国有色金属学报. 1998, (8) : p.441- 445.

[3] 赵志衡.管坯电磁胀形磁场力的研究[D] .哈尔滨:哈尔滨工业大学, 2001, p.1- 100.
[4] 张守彬.电磁成形技术的现状与前景[D] .哈尔滨:哈尔滨工业大学, 1990, p.1- 39.
[5] 初红艳,费仁元,吴海波,等.椭圆线圈在平板电磁成形中的应用研究[J] .锻压技术, 2002, (5) : p.38- 41.

SESSION 3

PROCESS TECHNOLOGIES (WELDING & JOINING)

Electromagnetic Pulse Welding: Process Insights by High Speed Imaging and Numerical Simulation*

C. Pabst[1], P. Groche[1]

[1] Institute for Production Engineering and Forming Machines, TU Darmstadt, Germany

Abstract

Most researches on the mechanisms of impact welding in general base their results on the investigation of the joint area after the process, primarily by destructive testing. A detailed analysis of the joining process itself, especially concerning electromagnetic pulse welding, has not been performed yet and thus leads to a lack of understanding. As a consequence of this, the design of the joint area and the process parameters are almost exclusively found empirically.

With the help of a special image intensifier camera and a laser, which illuminates the joint area, a new attempt is made to visualize the impact in electromagnetic pulse welding. The results suggest that at least some mechanisms are currently not fully understood. Explanations are developed, mainly concerning jet formation (surface cleaning during the impact) and material behavior of the workpieces under the high strain rates of the process. Areas of large strain rates (liquid-like behavior of the metal) and areas of comparably small strain rates can be found within one workpiece. The question will be discussed whether process parameters can be gained with the help of a simulation that is sufficiently accurate at least in the macroscopic scale.

Keywords

Welding, impact, electromagnetic pulse welding, test rig

---

* *The investigations presented in this paper are gratefully funded by the German Research Foundation (DFG). The authors would also like to thank Baumüller for their support during the installation of the test rig's electric drives, PSTproducts for enabling the experimental investigations of electromagnetic pulse welding as well as PCO AG and Acal BFi for their support in high speed imaging.*

1 Introduction

Impact welding is a process which enables metallurgical bonds even between dissimilar metals. Explosion welding was the first practical implementation several decades ago. It uses the blast wave of powerful explosives and allows joining greater areas and thus is therefore mainly used for cladding. One important application is the production of vessels especially for the chemical industry, where high strength steels are combined with corrosion resistant metals, for example. A few decades later, electromagnetic pulse welding has been developed. It draws its energy from charged high voltage capacitors. The accelerating force on the workpiece is generated by a coil, through which the current is driven by discharging the capacitors. Compared to explosion welding, a much lower amount of energy is available and therefore only line-shaped joint areas can be achieved. However, it is safe and easy to conduct because no explosives are needed and the welds can be repeated in the range of seconds. Nowadays, the necessary coils and pulse generators meet the industrially requested lifetimes. The main applications of electromagnetic pulse welding are the construction of hybrid space frames, the gas-tight sealing of high pressure containers or low-ohmic joints between aluminum to copper for the electromobility. The joints produced with impact welding are very tough, because the joint area is not weakened by thermal influences but exhibits fine grains [1].

Despite all advantages of impact welding in general and of electromagnetic pulse welding in particular, the latter is still not widely spread. One reason is the comparably poor predictability of the weld, which requires an empirical design of the joint area and the machine setup. The investigation of the process principles is challenging: Explosion welding is a stationary process, but requires large amounts of explosives and is therefore hard to observe. Electromagnetic pulse welding can be easily observed, but the impact parameters constantly change during the collision [2].

The basic mechanisms are understood [3,4] and illustrated in Figure 1: One workpiece has to impact another at velocities (v_{imp}) in the range of roughly about 250 m/s and above. The impact has to occur under a certain impact angle (β_{imp}). This leads to a collision point (or line) travelling across the surface.

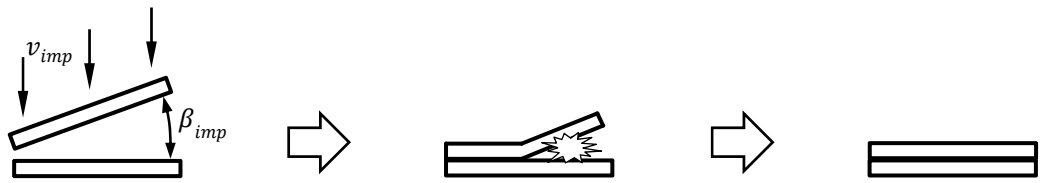

Figure 1: Schematic illustration of impact welding.

Due to the high strains and strain rates in this area, superficial oxides and impurities are removed and driven out of the closing gap. The impact is accompanied by a bright flash which is characteristic for this process. The metallically pure surfaces are then pressed together by the immense pressure of the impact, which finally evokes the metallurgical joint. [5]

2 Experimental Setup

For the basic investigations, a special test rig has been developed at the PtU. It avoids the drawbacks of explosion welding and electromagnetic pulse welding by colliding and welding flat sheets mechanically. The buildup consists of two rotors which are driven by one synchronous motor each. Each rotor holds an aluminum tube with a length of 500 mm. At one end of each rotor a welding specimen is mounted and a counterweight is attached to the opposite side. Figure 2 shows the test rig without housing.

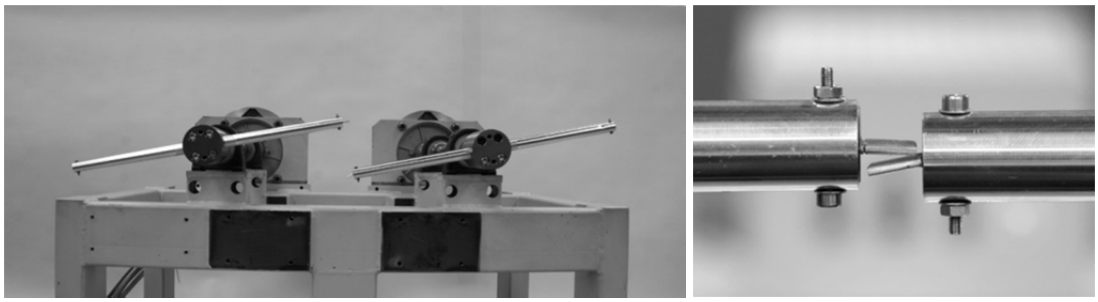

Figure 2: Left: Test rig without housing. Right: Rotors with specimens in collision position.

Both rotors have the same sense of rotation, so the specimens' velocity adds when they meet in the center. The maximum speed of 6000 rpm equals an impact speed of about 300 m/s. Further improvements are planned in order to increase the collision speed by greater lengths of the aluminum tubes. When the specimens are welded successfully, they rip off their clamped rest with the help of a predetermined breaking point. The welded specimens (EN-AW1050A) and the clamped parts are shown in Figure 3.

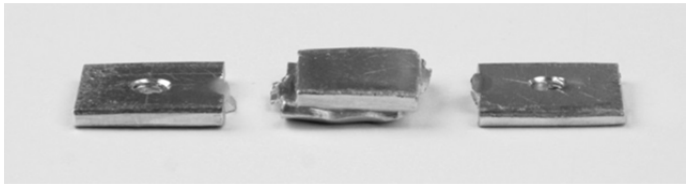

Figure 3: Welded specimens (center) with the clamped parts.

The test rig allows to set the initial impact angle (β_{imp}) and the initial impact velocity (v_{imp}) independently. The latter is independent of the specimens' mass in contrast to explosion welding or electromagnetic pulse welding. To adjust the desired impact angle, one specimen is bent correspondingly (right image in Figure 2). The test rig has proven its capabilities in first results, which are described in [2] in more detail.

3 Numerical Simulation

As motivated above, one aim is to be able to predict the necessary process parameters and, with the help of this knowledge, the extent of the actual metallurgically joined area. This allows to find the ideal design for the joint area and to achieve the best possible weld during the development of the products without costly experimental parameter studies. One of the greatest challenges here are the high strain rates of the impact welding processes: Directly at the bond area, strain rates are in the order of magnitude of 10^5-10^7 1/s. At these high strain rates, metals show a liquid-like behavior without being actually molten. A result of this is the wavy interface of the weld and the emission of superficial impurities as the so-called jet. If the small weld area is to be simulated, the material model has to be able to represent these properties. Material models like for example Steinberg-Lund or Zerilli-Armstrong are suitable for this task. In addition, the contact definition and the discretization have to be chosen correspondingly. In [6], for example, the Smooth Particle Hydrodynamics method (SPH) has been used to model the joint formation. Both the jet and the wavy interface have been simulated successfully by applying a hybrid mesh consisting of Lagrange elements for the base material and the SPH method for the actual impact area. This procedure provided good results but at the same time exhibits two disadvantages: It is quite complex and the necessary parameters for the material model at very high strain rates are required. The latter are difficult to obtain and therefore very expensive. Hence it would be very advantageous if the weld could be predicted without the need for a detailed simulation in a microscopic scale.

Therefore the aim of the numerical simulation in this paper is to investigate whether it can be sufficient to model the impact process in a macroscopic scale. Process windows are known from explosion welding, which depend on the angle β directly at the collision point and its velocity v_c. Figure 4 shows both quantities and a qualitative process window. It can be easily seen that impact velocity v_{imp} and impact angle β_{imp} are not equal to v_c and β, respectively. All angles and velocities are macroscopically visible and thus should be easy to observe and to simulate.

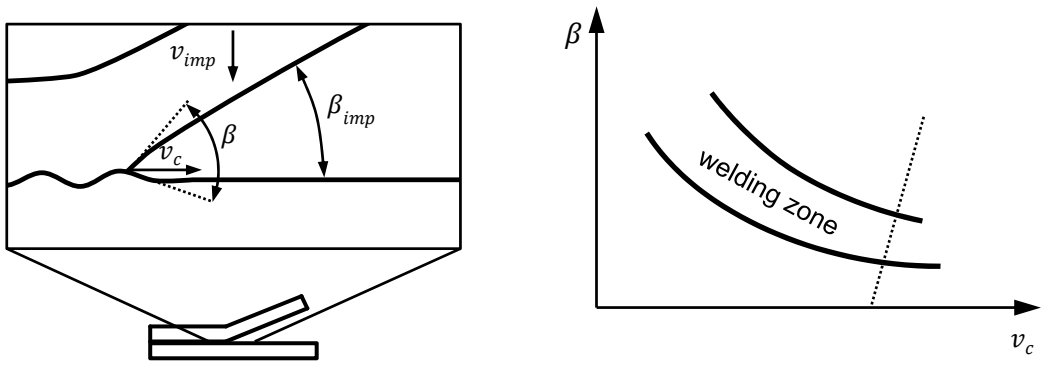

Figure 4: Left: Angles and velocities close to the collision point. Right: Qualitative process window derived from explosion welding.

The thickness of the jet and the amplitude of the wavy interface are small compared to the other dimensions. Consequently, it appears possible to neglect their influence on both angle and velocity. In doing so, element size can be increased and the maximum

strain rates are lower, because the areas of large strain rates (and strains) are just one small part of an element. Thus, computation time is reduced and the material definition can be simplified.

In this paper a simplified and two-dimensional geometry is used for the simulation which represents the collision in the test rig. It consists of two sheets with a thickness of 2 mm and a length of 10 mm approaching each other. The angle and the velocity are set independently. The simplified Johnson-Cook material model is used with the parameters for EN-AW1050A A = 140 N/mm², B = 75 N/mm², n = 0.65 and C = 0.0125. The calculation is carried out with a solver of LS-DYNA. Figure 5 shows the setup of the simulation and its evaluation. The coordinates of the superficial nodes on the opposing faces are analyzed and the angle β at and the velocity v_c of the collision point are calculated for each time step by an additional script in Matlab. A more detailed description of this procedure and the estimated process window can be found in [2].

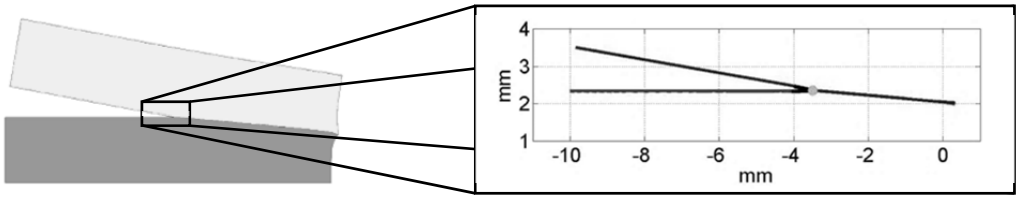

Figure 5: Left: Setup of the simulation. Right: Evaluation of angle β and velocity v_c as seen by the script running in Matlab.

Irrespective of the simplification, the question arises whether material properties have a great influence on the results. Due to the great dynamic of the impact process it could be expected that the material density has a significant effect on the deformation behavior. To check this assumption, each of the parameters of the Johnson-Cook material model (A, B, n and C) is varied by 40 % in positive and negative direction which equals the factors 0.6 and 1.4, respectively. For example Parameter A, which is 140 N/mm² by default, is set to 84 N/mm² and 196 N/mm². The result is a fictional material. The following Figure 6 shows the results for the collision point angle β versus the collision point velocity v_c for a variation of all four parameters. The impact angle β_{imp} is always set to 10° and the normal impact velocity v_{imp} of each sheet is always set to 125 m/s, which equals 5000 rpm of the test rig. Starting with A, it is quite obvious that it has a great influence on the impact angle β.The parameters B and n only have a minor effect on the result as well as the parameter C. An attempt can be made regarding the governing formula developed by Johnson and Cook [7]:

$$\sigma = \left(A + B\,\epsilon_p^n\right)(1 + C\,ln\dot{\epsilon}) \tag{1}$$

ϵ_p and $\dot{\epsilon}$ denote the effective plastic strain and the (normalized) strain rate, respectively. B and n determine the influence on the plastic strain which explains the negligible effect on the results: The maximum plastic strain at the impact area is even below 0.5. The low sensitivity to parameter C is surprising at first glance, because it is directly linked to the (plastic) strain rate. However, it can be easily explained by the logarithm which weakens the effect of even the high strain rates.

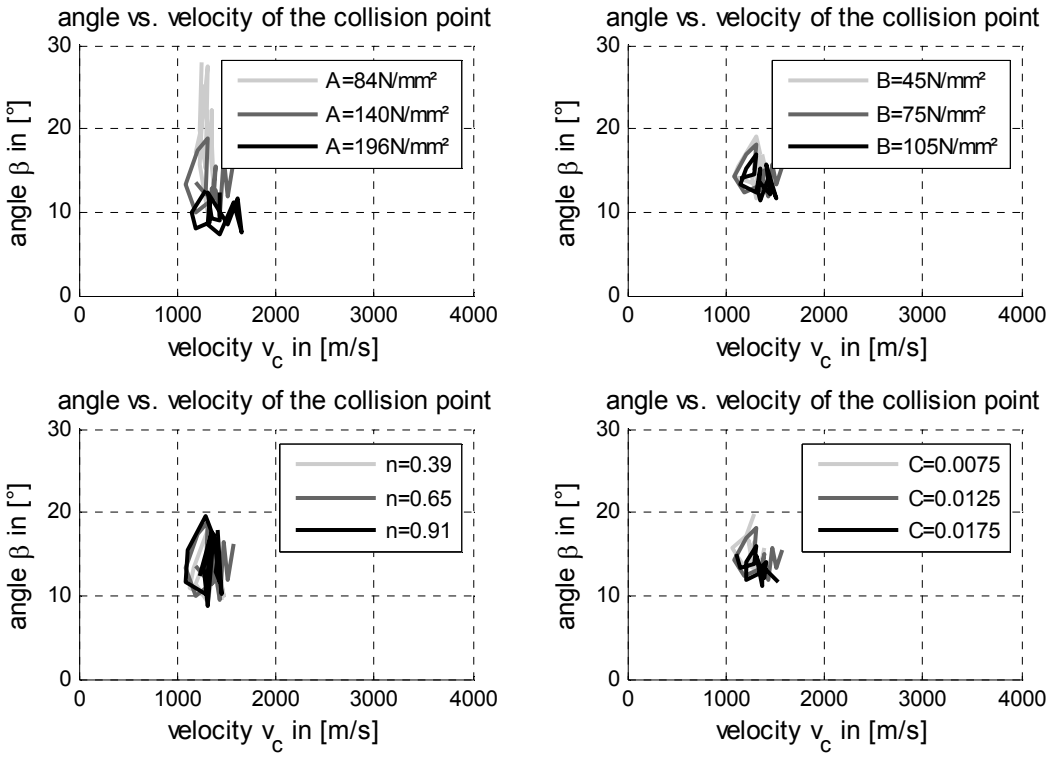

Figure 6: Collision angle versus collision point velocity for different sets of material model parameters (left to right, top to bottom : A, B, n, C).

The material density is varied next, again by adding and subtracting 40 %, respectively. The resultant plot is given in Figure 7 (left). As assumed above it is clearly visible that the density of the colliding joining partners has a great effect on the results, mainly on the impact angle. Preliminary to a detailed discussion, the calculation will be extended to the variation of the impact velocity of both parts. Although a much lower deviation of ± 20 % is chosen, both angle β and velocity v_c are significantly shifted to higher values. The resultant plot is shown in Figure 7 (right).

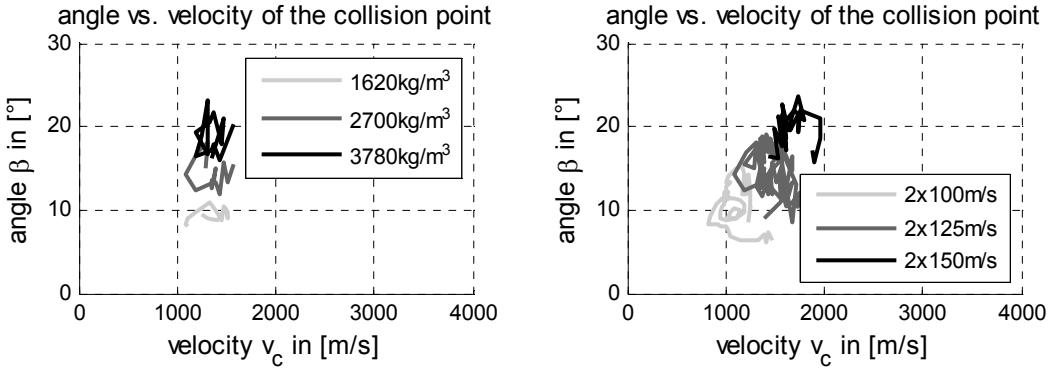

Figure 7: Collision angle versus collision point velocity for three different material densities (left) and three normal impact velocities (right).

Comparing the plots for different densities and for different velocities, a common trend becomes obvious: Higher velocities and higher densities lead to higher angles. This effect is plausible as an increase of the speed and/or the angle is equivalent to an increase in kinetic energy. This kinetic energy in turn depends on the impact velocity and the mass (density). The exact reason for the increasing angle might be some kind of a "whip effect" during the impact. The increasing collision point velocity, when increasing the impact velocity, may be caused by the geometric constraints: Ignoring the deformation of both joining partners and with regard to the geometric constellation depicted in Figure 4, the collision point velocity can be estimated by

$$v_c = \frac{\mathrm{v_{imp}}}{\tan \beta_{imp}}. \tag{2}$$

A similar behavior can be observed in simulations of electromagnetic pulse welding. The calculated setup involves two aluminum sheets with a thickness of 2 mm and an initial distance of 2 mm. The current is driven through a nearby coil at a frequency of 20 kHz. A more detailed description on this numerical setup and the electromagnetic simulation can be found in [2]. The evaluation of the results for different maximum currents (Figure 8) shows that higher currents and thus higher impact speeds lead to higher angles and velocities as well, especially at the end of the process (left half).

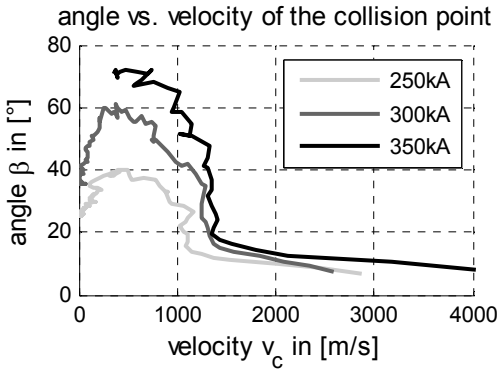

Figure 8: Collision angle versus collision point velocity for three different peak currents.

4 High Speed Imaging

As the actual impact and the joint formation take place in only few microseconds, the process is hard to capture with a conventional high speed camera. Hence for these research works, an image intensifier camera is used. It allows exposure times and frame delays in the range of nanoseconds at still remarkable spatial resolutions of up to more than 1000 pixels.

Filming the impact is accompanied by two more obstacles in addition to the high speeds: During the impact, a bright flash covers the actual joint area. Its formation will be discussed in the following chapter. Exact triggering is the second challenge, because the camera technique does not allow pre-triggering. Due to the fast turning rotors, the exact measurement of the momentary angle is hardly possible.

The bright process glare can be suppressed by a trick which is also used when conventional welding processes are investigated. As the glare is usually whitely, it can be concluded that its intensity is spread almost constantly across all (visible) wavelengths. The light source which is mandatory for the high speed images only emits light in a small wavelength range. Thus, its intensity is much greater than the process glare, even if the latter appears to be brighter to the human eye. Figure 9 illustrates this issue.

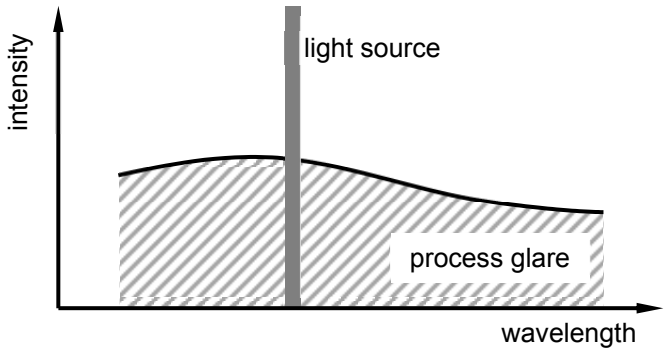

Figure 9: Emitted wavelength range of the light source and the wavelength distribution of the process light.

To suppress all other wavelengths, an optical bandpass filter is fitted to the camera in addition to the special light source. In the experiments, a laser with a nominal wavelength of 640 nm ± 10 nm is used together with a filter for 640 nm ± 5 nm. The laser is comparably easy to handle, because the light is visible and the emitted beam itself is neither coherent nor collimated. This avoids speckling and makes reflections harmless even despite the power of 400 W. The laser pulses are synchronized with the camera, because their length is limited to a few microseconds only due to the limited duty cycle which prevents a constant illumination.

Triggering is realized by using the two rotors as a kind of switch for the trigger circuit. A voltage is applied to one rotor whereas the other rotor is connected to ground. In addition, each rotor is mounted electrically insulated from the test rig's framework. When the specimens collide, the circuit is closed and a voltage signal is generated which can be directly used as trigger signal. This system is very robust and even works if the specimens do not collide exactly at the center.

The following Figure 10 shows the process in two independent experiments immediately after the finished impact with and without bandpass filter. It can be clearly seen that it is almost impossible to investigate the impact in detail without the filter.

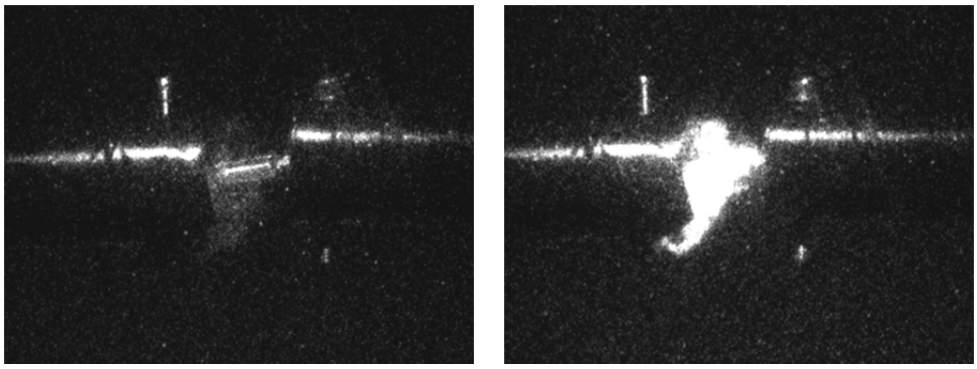

Figure 10: Propagation of the jet 20 µs after the impact with (left) and without (right) optical bandpass filter.

5 Jet Formation and Process Glare

A common explanation for the process glare is that it is caused by the jet. The jet does not only consist of oxides, but also of parent material [6]. The theory states that this parent material burns whilst being emitted and thus causes the intense light. However, it is generally accepted at the same time that high temperatures or even melting do not occur during the impact and welding process. Thus, a sufficient energy source which is capable of initiating the oxidation should actually not exist.

In order to examine jetting and glare in more detail, the electromagnetic pulse welding process is investigated under different atmospheres. It is more convenient than the test rig because only the small volume around the tool coil has to be filled with the respective gas. The complete housing of the test rig has a volume of approximately 1 m³ and is not gas-tight. For the experiments, the coil is covered by an acrylic glass box, which is filled with an inert welding gas. It consists of argon and about 8 % CO2 which makes the inert gas heavier than the surrounding air and therefore simplifies its displacement. When the enclosure is completely filled with the inert gas, the pulse generator is charged and the weld is established after only few seconds. The following images show the welding of two aluminum sheets (EN-AW1050A) with a thickness of 2 mm by a peak current of 300 kA at 20 kHz. Figure 11 shows the welding process with the inert gas atmosphere (left) and with the surrounding air (right). The inert gas does not only significantly decrease the emitted light, but also strongly weakens the emitted pressure wave during the impact.

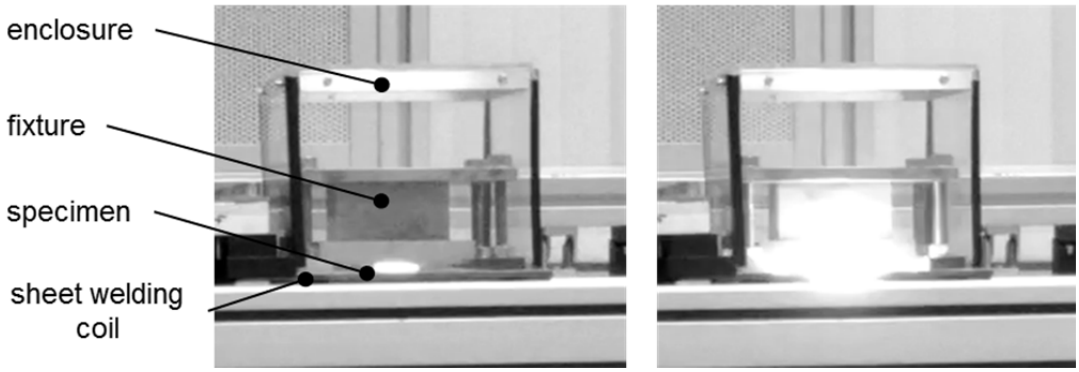

Figure 11: Electromagnetic pulse welding of two aluminum sheets with (left) and without (right) inert gas atmosphere.

Welds between two copper sheets (Cu-ETP, thickness 1 mm) show a different behavior: Neither the light emission nor the pressure wave is significantly influenced by the surrounding atmosphere. In both cases, it is comparable to aluminum welds with inert gas.

These experimental results suggest that an oxidation proceeds during the impact. Aluminum burns with a bright white flame and the oxidation is a highly exothermal reaction. As it can be seen in Figure 10, the emitted jet looks like a cloud of dust. If this dust does not only consist of superficial oxides but also of pure aluminum from the base material, which has been proven in past researches [6], a huge surface is created. Thus, if an appropriate energy source is available, a strong exothermal reaction can occur. This theory is supported by the experiments with the test rig: The extent of the glare and the extent of the jet are almost identical as highlighted in Figure 12. This indicates that jetting and glare are the same phenomenon or at least correlate closely.

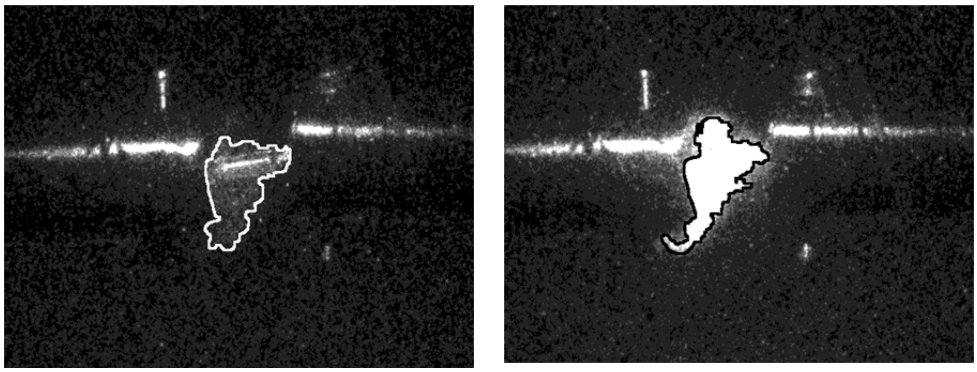

Figure 12: Highlighted propagation of the jet, with (left) and without (right) optical bandpass filter.

The auto ignition temperature of aluminum strongly depends on the particle size. The past research work in this field, which has been summarized in [8], shows that the auto ignition of aluminum powder with a particle size of under 10 µm can already happen at about 600 °C. As burning aluminum is even capable of splitting water molecules, a hydrogen explosion due to the atmospheric humidity might occur as well. Copper on the other hand does not burn, which explains why the surrounding atmosphere does not change the light emission.

Nevertheless, the question arises where the necessary temperature for the ignition is created. Two theories appear imaginable:

1. During the impact, temperatures reach higher values than generally assumed. Temperatures of several hundred degrees Celsius are possible and thus are capable of igniting the jet.
2. During the movement of the collision point, which travels at a multiple speed of sound, its supersonic pressure wave generates a plasma which in turn ignites the jet.

The first approach is supported by the welding trials with an inert gas atmosphere. A small luminous effect can be observed even though an oxidation can be excluded. This could imply that temperatures are reached which are even sufficient to heat up copper until it glows. This again might lead to molten areas, which actually should not occur in impact welding as a solid state welding process. However, studies have revealed that a thin intermetallic layer can be observed at least in dissimilar metal combinations [9]. Furthermore, the ultra-fine grains could be caused by a very fast melting and solidifying process. This appears possible as the molten area is very small and very rapidly cooled down by the surrounding material, because metals usually exhibit a good thermal conductivity.

The second approach relies on the minor radiance as well. Immediately after the first contact, the collision point travels at very high velocities along the surfaces (right half in Figure 8) and pushes the surrounding gas out of the closing gap. Due to the high velocity, which can reach more than ten times the speed of sound, a powerful shock wave is generated. The energy of this shock wave could be sufficient to create a plasma from the ambient gases. The plasma temperature is high enough to ignite the jet which can then be observed as a bright flash if oxygen is available.

6 Summary

The experimental setup which enables the investigation of the impact welding process in a secure way and under clearly defined conditions has been presented. The numerical approximation of the impact has been described and the results from a parameter study have been discussed. It has been shown that inertia seems to play an important role. A promising method to observe the actual welding process by high speed imaging has been presented and first images have been discussed. They enable the closer investigation of the welding zone. Experiments have been conducted to find out more about the jet formation and the process glare. Two theories have been developed and discussed. They will be closely investigated in the future.

7 Conclusion and Outlook on Future Works

The numerical simulation of the impact in a macroscopic scale provides plausible results, even though it is kept very simple. Even the influence of the breaking point of the specimens remains disregarded. Future experiments and high speed images will show whether this simplification is justified or not. It appears possible to give analytic explanations to the numerical results

The test rig will be steadily improved in order to achieve higher impact speeds under more exact impact conditions.

The high speed images will be helpful in investigating the formation of the jet the glare during the impact. By using a higher magnification and a higher frame rate, the identification of the origin of both the jet and the glare should be possible. This will prove whether one of the theories applies or not.

References

[1] *Zhang, Y.; Babu, S.; Daehn, S.:* Impact Welding in a Variety of Geometric Configurations. In: 4th International Conference on High Speed Forming, 2010, pp. 97-107

[2] *Groche, P.; Wagner, M. F.-X.; Pabst, C.; Sharafiev, S.:* Development of a novel test rig to investigate the fundamentals of impact welding. In: Journal of Materials Processing Technology. 2013. http://dx.doi.org/10.1016/j.jmatprotec.2013.10.008

[3] *Carpenter, S.H.; Wittman, R.H.:* Explosion Welding. In: Annual Review of Materials Science, pp. 177-199, 1975

[4] *Crossland, B.:* Explosive Welding of Metals and Its Applications. In: Oxford Series on Advanced Manufacturing, Clarendon Press, Oxford, 1982

[5] *Deribas, A.A.:* Treatment of Materials by explosive Energy. In: Combustion, Explosion and Shock Waves; September-October, 1987, Volume 23, Issue 5, pp. 639-648

[6] *Kakizaki, S.; Watanabe, M.; Kumai, S.:* Simulation and Experimental Analysis of Metal Jet Emission and Weld Interface Morphology in Impact Welding. In: Materials Transactions - Special Issue on Aluminum Alloys 2010, Vol. 52, No. 5, 2011, pp. 1003-1008

[7] *Johnson, G.R.; Cook, W.H.:* A constitutive model and data for metals subjected to large strains, high strain rates and high temperatures. In: Proceedings of the 7th International Symposium on Ballistics, 1983, pp. 541-547

[8] *Trunov, M. A.; Schoenitz, M.; Dreizin, E. L.:* Ignition of Aluminum Powders Under Different Experimental Conditions. In: Propellants, Explosives, Pyrotechnics, 30, 2005, No. 1, pp. 36-43

[9] *Göbel, G.; Kaspar, J.; Herrmannsdörfer, T.; Brenner, B.; Beyer E.:* Insights into intermetallic phases on pulse welded dissimilar metal joints. In: 4th International Conference on High Speed Forming (ICHSF), 2010

Magnetic Pulse Spot Welding: Application to Al/Fe Joining

A. P. Manogaran, P. Manoharan, D. Priem, S. Marya, G. Racineux

[1] Institut de recherche en génie civil et mécanique (UMR 6183) – GeM, Ecole Centrale Nantes, 1 rue de la noë, 44321 Nantes, France

Abstract

Magnetic pulse welding is a rapid process (takes place within few micro seconds) that joins both homogeneous and heterogeneous materials in the solid state. The process involves applying variable high current on an inductor to generate Lorentz forces on to the conductive primary part (flyer). To realize the weld it is necessary to accelerate the flyer to impact on to the secondary stationary part (base material) at a very high velocity attained over the distance, called air gap, between the parts. It is typically possible to perform welding of tubes and sheets provided there is an optimized air gap between the parts to be welded. As part of our work we have developed an innovative approach (Magnetic Pulse Spot Welding-MPSW) that eliminates the delicate task of maintaining the aforementioned air gap between the plates. The proposed method opens better viable perspectives for heterogeneous assembly of automotive structures or connecting batteries in a quasi-cold state. The developed approach has been validated on the heterogeneous assembly Al/Fe by tensile tests (quasi-static and dynamic) that attested the quality of welds.

Keywords

Welding, Magnetic pulse spot welding, Dissimilar Al/Fe joining

1 Introduction

Resistance spot welding is the most suitable method used for joining steel plates for motor vehicles. On average, it accounts to 4000 spot welds per car [1]. To reduce the fuel consumption of the vehicle, automotive manufacturers started to replace/join steel parts with parts made of aluminum or magnesium alloys [2,3,4]. This raises the problem of assembling these parts. Even though there are many methods to join steel with aluminum or magnesium alloys (magnetic pulse, laser, friction, etc.) [5], they are rarely compatible

with the constraints of automotive (cadence, positioning sheets, geometry, spot weld strength, etc.).

Among these methods we propose an evolution of the magnetic pulse welding process (MPW). Figure 1 shows the principle of MPW for joining two tubes together. The circuit is charged by accumulating a large amount of electrical energy in a capacitor bank. When the circuit is discharged, it liberates all the stored electrical energy to a high current solenoid (the inductor) in a very short time (within a few microseconds). If a conductive part (here an aluminum tube) is placed near the solenoid, it is subjected to a changing magnetic field which induces current at the skin of the aluminum tube (skin effect). This current is itself subjected to this magnetic field, resulting in generation of Lorentz forces on the surface of the tube and the tube starts to greatly accelerate away from the solenoid at very high velocity to impact on to the inner core (steel). The controlled impact of the aluminum tube on to the steel allows under certain conditions to produce a weld. This method is similar to explosive welding. Micrographic analysis of the weld in each case indicates a "corrugated/wavy" interface welding (Figure 2.a) [6].

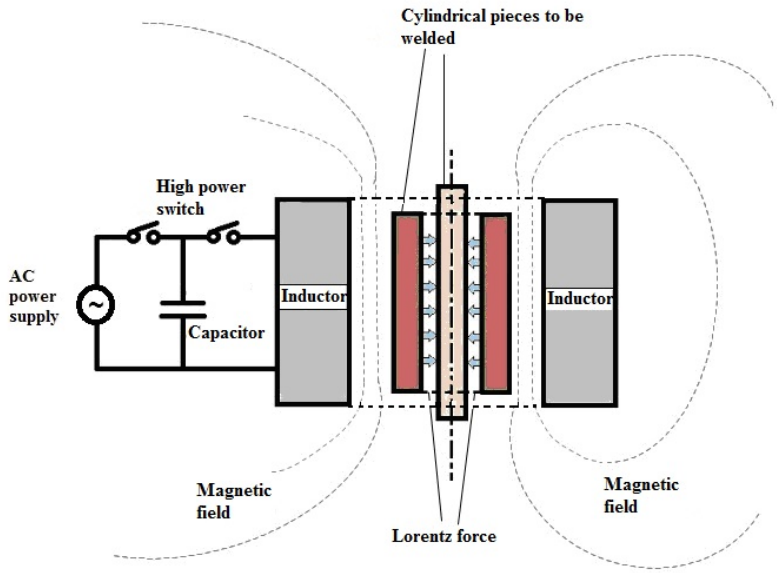

Figure 1: *Schematic diagram of the magnetic pulse welding.*

To achieve dynamic welding, be it explosive or magnetic pulse, it is necessary (Figure 2.b):

- To accelerate one of the parts sufficient enough to generate an impact on to the other to produce a very short but intense heat. This is achieved by means of an air gap between the two parts to be assembled with a generated impact velocity.
- To break away the oxides on the surface. This is ensured by the progressive collision of the flyer part on to the fixed part at a certain collision angle and collision velocity, so that the air jet formed expels the oxides away with it. By this way, the two contacting parts are provided with inter-atomically clean surfaces to form a metallurgical bonding.

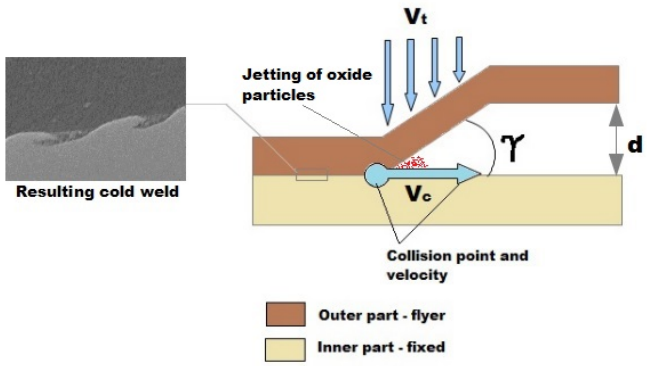

a. b.

Figure 2: *(a) Micrograph of the wavy interface, (b) Parameters of magnetic pulse welding.*

Almost 40 years after its invention, the only magnetic pulse welding configuration used commercially till the start of 2000s was tube/tube welding (Figure 3.a) [7,8]. Aizawa et. al. (2004) [9] developed a new method of magnetic pulse seam welding two flat plates by means of a double layer H shaped single-plane inductor coil (Figure 4.a). Here, the air gap was provided by means of an insulator placed between the two sheets. In 2007, the same team proposed a simple inductor: an E shaped one layer flat coil [10] (Figure 4.b) and more recently they have proposed a way of spot welding (single or multi spots) using an insulating mask between the two sheets (Figure 4.c and 4.d) [11]. In all the above cases, the requirement of ensuring an acceptable air gap of distance for each part to be welded makes it challenging to be implemented in automotive industry.

In our study we propose an evolution to the magnetic pulse welding process which produces spot welds between similar or dissimilar materials under conditions compatible with respect to the constraints in the automotive industry (cadence, robotics, resistance, etc.). The process is named as “Magnetic Pulse Spot Welding”.

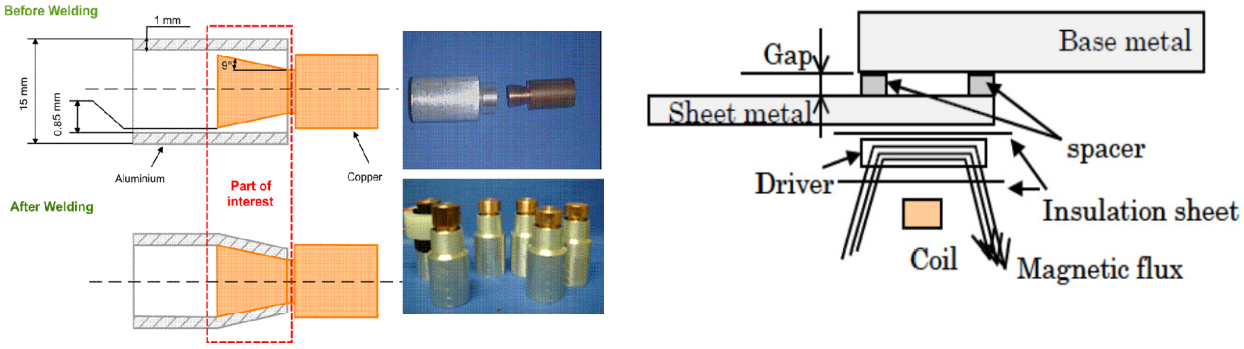

a. b. c.

Figure 3: *(a) MPW of two tubes, (b) Cu/Al parts before and after welding [8], (c) Schematic of the magnetic pulse seam welding process [9,10].*

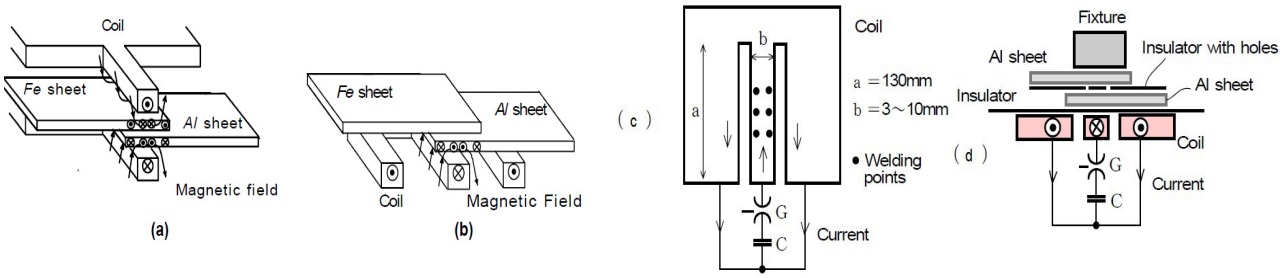

Figure 4: *(a) Double layer H shaped single-plane inductor coil [9], (b) Monolayer E shaped flat coil [10], (c) Spot welding with the help of insulating mask, (d) Welding system [11].*

2 Magnetic Pulse Spot Welding: Principle

Figure 5 shows the principle of Magnetic Pulse Spot Welding (MPSW) for spot welding two sheets together. As said earlier, the two plates are always in contact with each other before and after welding. So, in order to ensure that there is necessary gap between the plates for intended acceleration and impact of the flyer plate on to the parent plate (Figure 2); and also to ensure correct positioning of the sheets on each other before and after welding, we propose to carry out a prior local stamping, called "hump" (Figure 5). This hump geometry combined with the inductor geometry is critical in ensuring both the necessary collision rate and the removal of surface oxides. The inductor is designed in such a way that it is placed just above the hump. When the current is discharged, according to the MPW principle, the hump deforms and impacts on to the other material at a very high velocity to realize spot welding. Here, the geometry of the hump determines the size of the spot weld. Generally, the sheet with good electrical conductor is chosen as the flyer part, in our case, aluminum.

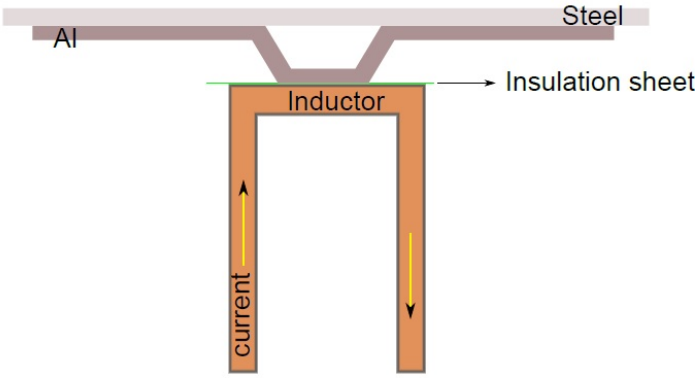

Figure 5: *Schematic of the magnetic pulse spot welding process (MPSW).*

3 Materials and Experimentation

To validate the principle of MPSW process we have chosen the heterogeneous assembly of Aluminum to Steel. The materials used are steel sheet (EN355) having a thickness of 1.5 mm, and aluminum sheet (AA1199) with a thickness of 0.5 mm. The MPSW process

utilizes a monolayer I shaped flat inductor that concentrates magnetic flux at the surface of the hump of the flyer sheet. Figure 6 shows the hump configuration and the intended spot welding location – hump on AA1199 aluminum sheet. The generator used for carrying out welding is developed at Ecole Centrale de Nantes which has a capacitance of 272 μF, 0.5 μH inductance and maximum energy of 30 kJ. Three different energies – 2.8 kJ, 3.4 kJ, 4.15 kJ are chosen to carry out spot welding and are compared.

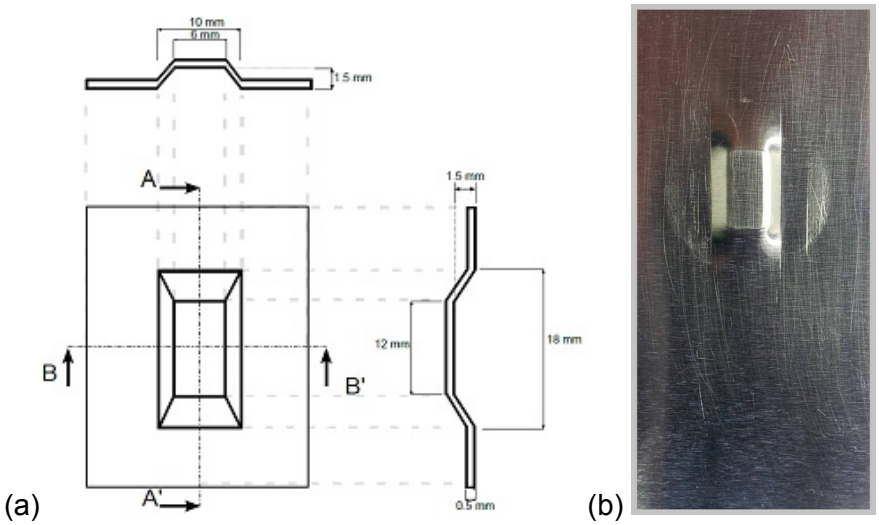

Figure 6: *(a) Hump configuration, (b) Intended spot welding location – "hump" in the AA1199 aluminum sheet.*

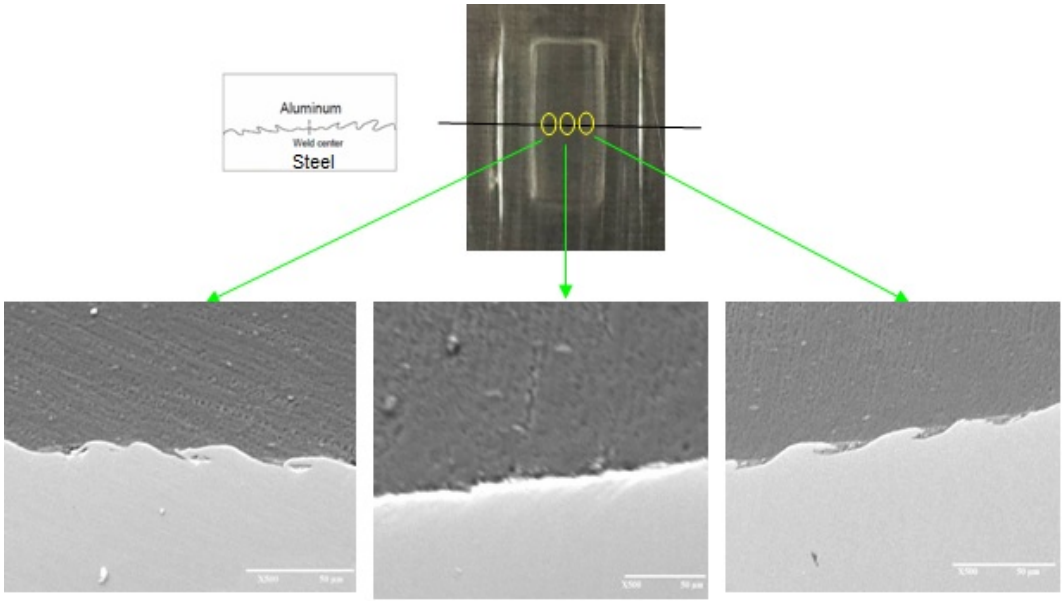

Figure 7: Micrographic analysis using SEM for Al/Fe magnetic pulse spot weld for 3.4 kJ energy.

4 Results and Discussion

Figure 7 shows the micrographic analysis of the welded area done using scanning electron microscope. We observe a characteristic corrugated/wavy interface typical to dynamic welding processes (explosive/magnetic pulse). However, unlike these processes, the waves on the interface are in opposite directions from the center. Moreover it can be verified that the center part of the part is not welded. The weld zone typically shows a rectangular region with no weld at the center as shown in Figure 7. A rectangular weld region is formed on the sheets which correspond to the side edges of the coil placed above it and no welding took place in the area between them i.e. at the center. Since, the process is rapid, only very thin intermetallic layers (2-5 μm) are formed and that too only around those wavy regions.

The size of the no-weld zone at the center was measured to be 1 x 6 mm^2 for all the weld specimen sets done by peel tests. Figure 8 shows the peel test results for different energies. In all the cases, the weld was good and only the aluminum sheet around the weld sheared off.

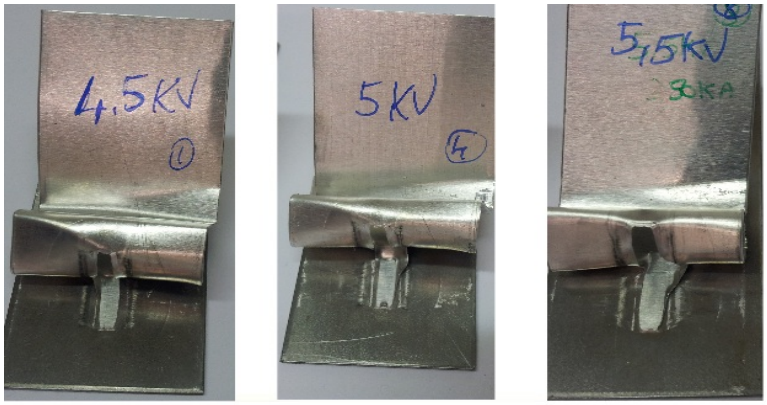

Figure 8: *Peel test carried out for different welding energies.*

Tensile tests were carried out on spot welded specimens for different discharge energies viz. 2.8 kJ, 3.4 kJ and 4.15 kJ. Figure 9 shows an example of tensile test results both quasi-static and dynamic tests. Quasi-static tests were carried out on a tensile/compression testing machine from Instron and dynamic tests are carried out on a machine developed by GeM, Ecole Centrale de Nantes. In all cases, the aluminum sheet were sheared off around the spot weld zone and the spot welds were in contact through out. We also see that, as we increase the discharge energy, the tensile failure load also increased indicating that the area of the spot weld has a great influence in the test results. This suggests that our welds are satisfactory and are stronger than the weaker base material (aluminum).

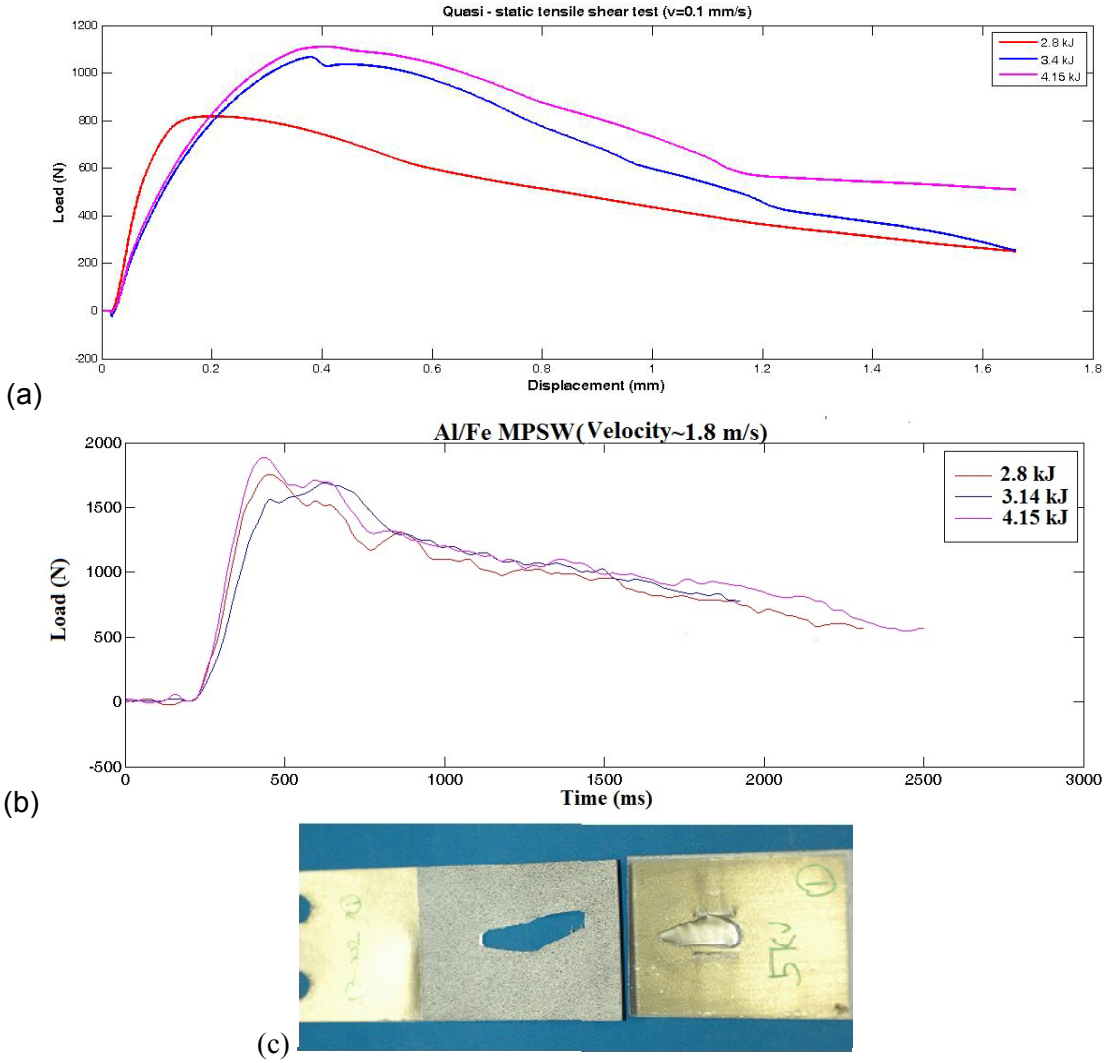

Figure 9: *(a) Quasi-static tensile test results, (b) Dynamic tensile test results, (c) Spot welded specimen after dynamic tensile test.*

5 Conclusion

In this study we developed a new method for spot welding two different sheets. The process is named as "Magnetic Pulse Spot Welding - (MPSW)". Like Magnetic Pulse Welding, it is a cold welding process which allows spot welding both homogeneous and heterogeneous materials. As the welding process is very rapid (takes place within few microseconds), the formation of thick intermetallic layers are avoided; for example, in case of Al/Fe joining, intermetallic formation cannot be avoided. From this process only very thin intermetallic layers (2-5 µm) are formed and that too only around those wavy interfaces. This makes it a very interesting process for spot welding heterogeneous materials especially, Al to steel for automotive applications.

In order to obtain spot welds, it is necessary to make a local stamping called “hump” on the flyer sheet where you intended to realize a spot weld. The welding operation (once the sheets are in place) lasts only a few microseconds. The sheets are always in contact

with each another before and after welding. This suggests the possibility of using this spot welding method in the automotive industry for joining light materials such as Al/Mg with steel.

References

[1] *M.A. Al-Jader, N. Wylie, J.D. Cullen and A.I. Al-Shamma*, Investigation into Spot Welding Process Sustainability for the Automotive Industry, 5th annual conference on BEAN (Built Environment & Natural Environment), Liverpool john Moores University, 2010.

[2] *D. Carle, G. Blount,* The suitability of aluminum as an alternative material for car bodies, Materials and Design, Volume 20, Issue 5, 267 – 272, 1999.

[3] The Aluminium Association, Inc.: Aluminium industry roadmap for the automotive market: enabling technologies and challenges for body structures and closures, May, 1999.

[4] R. Kawalla, G. Lehmann, M. Ullmann, Magnesium semi-finished products for vehicle construction, Archives of Civil and Mechanical Engineering, Vol. 8, No. 2, pp. 93–101, 2008.

[5] [Information on http://www.keytometals.com/page.aspx?ID=CheckArticle&site=ktn&NM=152, Welding of dissimilar materials, Key to metals, Aug 2006.

[6] *J. Verstraete, W. De Waele, K. Faes*, Magnetic pulse welding: lessons to be learned from explosive welding, Sustainable Construction and Design, 469 -475, 2011.

[7] *I. Masumoto, K. Tamaki, M. Kojima*, Electromagnetic welding of aluminum tube to aluminum or dissimilar metal cores, Transactions of the Japan welding society, Vol. 16, No. 2, Oct 1985.

[8] *S. Marya, G. Racineux, M. Marya, F. Gratecap*, Exploring magnetic pulse welding of dissimilar metals: Welding of axisymmetric aluminum -copper parts, 2nd International symposium on smart processing technology, Nov 2007

[9] *T. Aizawa*, Methods for electromagnetic pressure seam welding of Al/Fe sheets, Weld. Int. 18 (11), 868–872, 2004.

[10] *T. Aizawa, M. Kashani, K. Okagawa*, Application of Magnetic Pulse Welding for Aluminum Alloys and SPCC Steel Sheet Joints, Welding Journal, 86, 119 – 124, 2007.

[11] *T. Aizawa, K. Okagawa, M. kashani, Taizawa*, Multi-Spot Welding by Applying Magnetic Pressure, 2009.

High speed joining process by laser shock forming for the micro range

S. Veenaas[1], F. Vollertsen[1]

[1] Bremer Institut für angewandte Strahltechnik GmbH, Bremen, Germany

Abstract

The importance to implement more functionality on the same space pushes miniaturization and makes hybrid joints under various conditions, also in the micro range, necessary. Conventional joining processes, which are used in macro range, cannot be easily transferred to micro range dimensions. In this work a new high speed joining method for the micro range is presented, which is realized by a plastic forming process based on TEA-CO_2-Laser induced shockwaves. In a first step it is shown how sheet-sheet joints can be realized with this method. The experimental results illustrate the possibilities as well as the limits of the joining process by laser shock forming. Also the possible defects which can occur during the joining process are presented. Especially fracture of material at the edge. This is explained by the sharp edges in the joining area, which are caused by the production process of the specimen.

Keywords

High speed forming, Laser shock forming, Joining by forming

1 Introduction

Resource efficiency, reduction of production costs and function compaction are reasons of miniaturization. This makes also hybrid joints for micro range necessary. Conventional joining processes, which are used in macro range, cannot be easily transferred to smaller dimensions. With the ongoing trend of miniaturization so-called size effects appear [1], which inhibit sometimes the use of conventional manufacturing processes in total, or they can be used only with restrictions in micro range.

Typical joining processes for thin sheets of dissimilar materials are welding and brazing processes [2]. SHADOW® welding technique is a one of the processes which is used for joining of thin metal sheets with a material thickness <5 µm [3]. However, joining of dissimilar materials can result in formation of diffusion based intermetallic phases,

which are characterized by high hardness and high brittle behaviour. Furthermore these processes are thermal based, which can influence the geometry of the components through distortion. In case of micro engineering these problems by thermal influences are particularly significant, since there is a high density of technical elements to be carried out next to heat sensitive components.

Another solution for joining thin metal sheets of dissimilar materials is explosion welding [4]. The advantages of these processes are that they do not lead to typical heat affected zones or distortion and the occurrence of intermetallic phases is minimized [5]. One approach for manufacturing thin metallic hybrid joints by non-contact impact joining was done by Nd:YAG-laser induced shock waves [6]. A thin metal foil (thickness ≤ 200 µm) was placed on a solid joining partner tilted by a process specific angle. For the increase of the shockwave and for protecting the surface against thermal influence an ablation layer was applied. Finally the foil is accelerated by laser induced shock wave in direction of the solid body. Due to high pressure in the contact area the metallurgical bond was achieved. Thereby no intermetallic phases were observed and an increased micro hardness along the boundary layer after the joining could be measured [7].

How joining by laser shock forming using a TEA-CO_2 laser can be realized is presented in former publications [8]. Using a TEA-CO_2 laser enables a simple process handling and short process times without need of an ablation layer. This kind of shock wave formation is known since the 70s, e.g. [9]. Due to laser treatment free electrons are generated by thermo emission out of the surface [10]. The number of free electrons depends on focus size, laser pulse intensity and surface material [10]. These free electrons absorb energy by inverse bremsstrahlung absorption and can produce further ions and electrons by impact processes until an optical breakdown and thus a plasma formation is achieved [11]. The inverse bremsstrahlung increases with the square of the wavelength accomplishing a nearly complete absorption of the longer wavelength of CO_2-laser light by the plasma. If the energy density of the laser pulse exceeds a certain threshold, the fast expansion of the plasma forms a shock wave [12], which is initiated ~8 mm above surface [8]. This shock wave moves spherically [13]. The shock wave pressure, which is in the range of some MPa [14], leads to a forming of the surface [15]. The laser shock forming process first was used for deep drawing of copper and aluminium sheets [16] and later for joining process [8]. Thus this process is promising for hybrid joints in the micro range and the increasing need of micro joints i.e. in precision mechanics and electronic industry. In this work the process window of the joining process of aluminium and steel is presented.

2 Experimental setup

For the joining process a pulsed TEA-CO_2-laser (wavelength:10.6 µm) with a pulse duration of 100 ns, a spot size of 0.04 cm^2 and a laser pulse energy up to 6 J per pulse is used. The principle experimental setup is shown in Fig. 1. The setup consists out of 5 basic elements: the blank holder, Joining Partner I and Joining Partner II, a spacer and the bottom of the tool. The Joining Partner I and Joining Partner II are positioned upon each other. Joining Partner I is made out of aluminium with a thickness $t_{Partner\ I}$ of 20 µm or 50 µm. Joining Partner II is made out of stainless steel with a thickness of $t_{PartnerII}$ of 25 µm up to 300 µm and has a hole which is the diameter of with a diameter of 2 mm or 4 mm

and is specified as *d* the diameter of the joining area. Both parts are produced by a laser cutting process with a Nd:YAG short pulse laser, which ensures reproducible specimen geometries. Aiming to provide space for material flow of Joining Partner I to create an undercut, a spacer is located between Joining Partner II and the bottom of the tool. The spacer thickness (in the following t_{spacer}) is varied from 25 µm to 300 µm and the diameter of the spacer hole is 1 mm bigger than the hole of the used Joining Partner II. The blank holder is holding the partners in position during the process while the blank holder force is over the clamping force. This leads to a pure stretch drawing process. In the tools bottom ventilation holes are implemented, so that air below the specimens is not disturbing forming of the material. This tool ensures an exact positioning of the specimens and reproducible experimental conditions through alignment pins and bedstops.

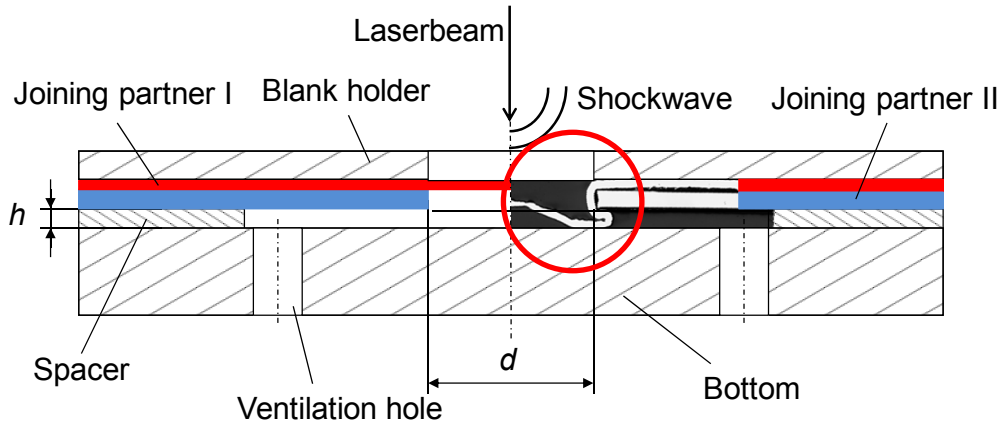

***Figure 1**: Experimental setup*

The laser irradiates on Joining Partner I with the focus lying on the surface. This leads to plasma formation about 8 mm above the surface [8]. The resulting shockwave forms the material in the joining area accomplishing an undercut which presents the joint itself, as shown in Fig. 1 inside the circle. The number of laser pulses is varied for different material thicknesses of Joining Partner I. For material thickness of 20 µm the pulses are varied from 10 up to 50 shots. For material thickness of 50 µm laser pulses between 50 and 200 are used. The repetition rate of the laser pulses is 20 Hz, and for each parameter set 5 experiments are carried out.

3 Results

3.1 Joining geometries and failure behavior

By varying the process parameters different joining results could be observed. These results are classified in three different main types, which are: joining could be achieved, no joining could be achieved because no undercut was created and material failure in the joining area. For the first main type: joining could be achieved, there are two possibilities, which are shown in Fig. 2.

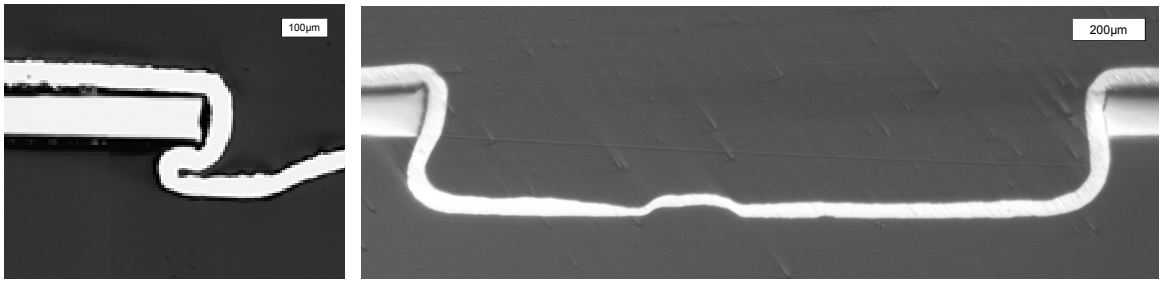

BIAS ID 140531

***Figure 2**: cross section of undercut bigger than double the material thickness (left) and small undercut (right)*

The first one is an undercut depth, which is more than double the material thickness and this undercut depth is constant over the whole joining area. The second one is a very small undercut depth which is smaller than the material thickness as shown in Fig. 2 on the right side. From the cross section of the joints it can be seen that the joint is achieved due to mechanical clamping of the upper sheet to the lower one. Material fracture during the process can occur in two different locations, in the bottom of the forming area or at the edge of Joining Partner II. These failure behaviors are shown in Fig. 3.

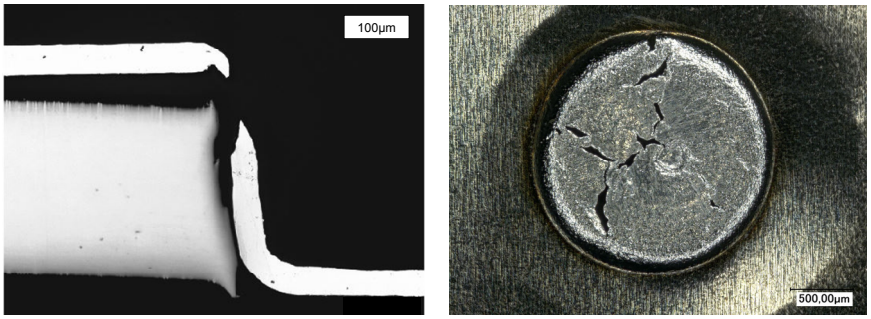

BIAS ID 140533

***Figure 3**: material failure, broken in the edge (left) and broken in the bottom (right)*

3.2 Process windows

For these experiments a joint is defined as a material fracture free joining area which is able to carry their proper weight. For each parameter set five experiments were carried out. As long as all five experiments result in a joint, this point is marked as “good joint”. For less than five joints the process is not reproducible and therefore not feasible for industrial applications. These points are marked as “not reproducible”. The points where no joint could be achieved, or a material failure appeared are marked as “no joint”.

Fig. 4 shows a schematic process window. For this process window the used laser pulses are varied above the different spacer thicknesses. The area marked as “A” shows the parameter, which leads to a good joining result. In area “B”, which is lying left and below the process window, no undercut could be observed. Area “C” and “D” are the areas where material failure occures. This kind of process window is made for different material thicknesses.

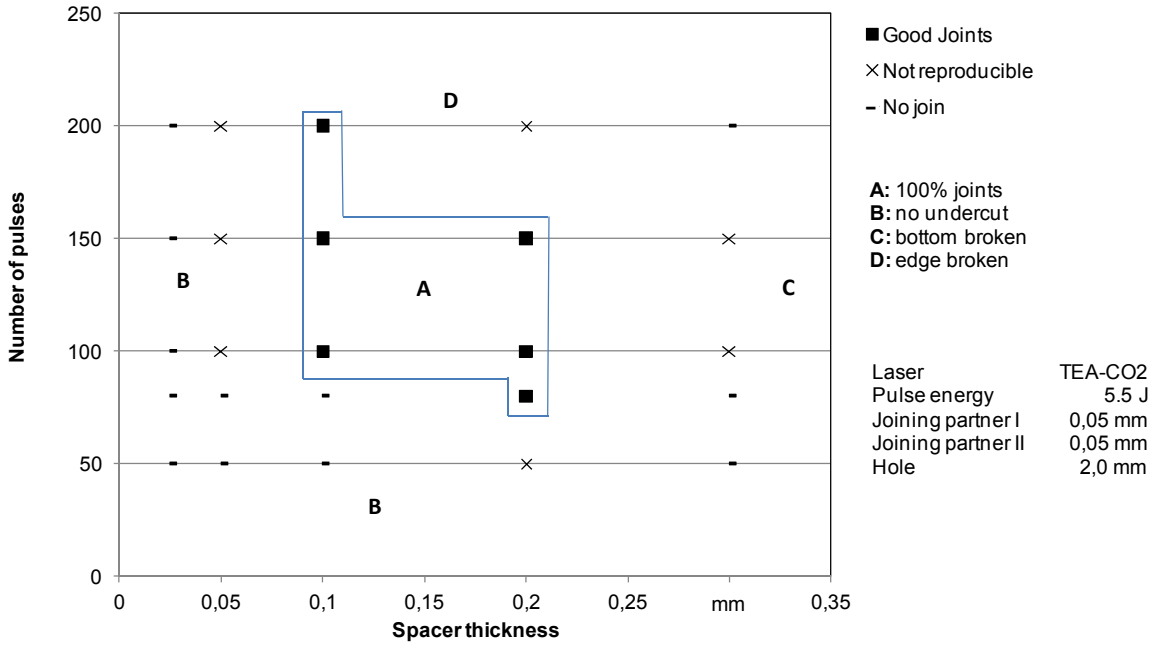

***Figure 4**: Exemplary process window*

In order to analyse the process behavior over different material thicknesses process windows are compared with each other. Therefore the limits of the process window needs to be described. One approach of describing the lower limit of the process window is shown in Fig. 5. For the illustration of this curve the lowest points of the process window are taken. These are for Fig. 4 the datapoints for 100 pulses with a spacer thickness of 0,1 mm and 80 pulses with a thickness of 0,2 mm. For comparing the other joining geometries, these parameters need to be scaled to a comparable value. Therefore the used laser pulses are divided through the material thickness of Joining Partner I. The same approach is used for the spacer thickness. With these two relative values a comparison of the different process windows to each other is possible, asshown in Fig. 5.

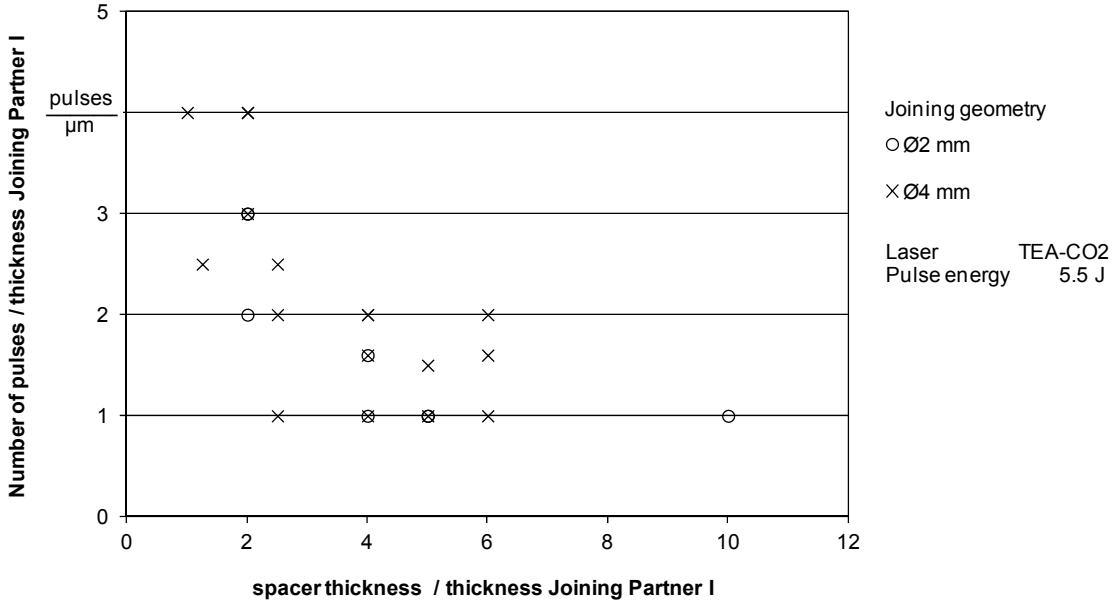

***Figure 5**: Needed laser pulses over spacer to Joining Partner I ratio*

It can be seen that for a bigger t_{spacer} / $t_{Partner\ I}$ ratio less energy is needed to create a joint. The amount of laser pulses which are needed, decreases exponentially to a value of 1 pulse / µm.

The ratio t_{spacer} / $t_{Partner\ I}$ has also an upper limit. When the total distance from Joining Partner I to the tool bottom reaches a certain distance, material fracture of Joining Partner I occurs. For the description the mean value for these limits are calculated and presented in Table 1.

Ø joining area	Thickness Joining Partner I	Mean height to material failure
2 mm	20 µm	187 µm
	50 µm	225 µm
4 mm	20 µm	137 µm
	50 µm	433 µm

***Table 1**:* Mean height as the sum of Joining Partner I and Spacer Thickness where material failure occurs

It can be seen that for a thickness of 20 µm the height for both geometries are in the same range, while for the thickness of 50 µm the height to material failure is nearly factor two bigger for a diameter of 4 mm.

4 Discussion

The results of this work illustrate the possibilities as well as the limits of the joining by laser shock forming. On one hand, the creation of joints is possible with all used joining geometries of 2 mm and 4 mm and on the other hand there are limits, especially with

thinner material, where more fractures occur. For the process window shown in Fig. 4 different limits of the process are presented.

The upper limit of the Process window is given by material failure. The joining process can be seen as a stretch drawing process. During a stretch drawing process the material, which is needed for increasing the surface, is taken from the material thickness. If the strain of the material is getting too high the material will crack. So the material failure is a result of too much induced strains. Especially material failure at the edge is a result of a sharp edge from the steel sheet, during the process. Beside this it results from a combination of applied laser pulses and a sharp edge which leads to stress concentration. Sharp edges at the hole are a result from the laser cutting process, where the material melts during the process and burr at the edge is created. Bottom tear in the material is occurring, when the distance between Joining Partner I and the bottom is too high. The mean values of these limits are shown in table 1. Differences in the limits for the different material thicknesses can be explained by the lower forming limit curve of thinner material [17]. When the material is touching the bottom of the tool before a bottom tear occur the material is supported by the bottom, which leads to lower induced tensile stresses in the bottom of the joining area trough the shockwave. This means that the induced stresses through a shockwave are higher in the groove and edge than in the bottom which leads to material fracture in the edge.

One influence of the difference in the maximum height to the bottom between the joining geometries is that the material failure material failure is not only occurring in the bottom. Material failures are also occurring in the edge of Joining Partner II, which is influencing the result of the maximum height to material failure.

In Fig. 5 it is shown that for a larger t_{spacer} / $t_{Partner\ I}$ ratio less energy or laser pulses are needed to create a joint. This fact can be explained by the geometry of the experimental setup and the joining geometry. For the creation of an undercut there should be enough space between Joining Partner II and the bottom of the tooling which should be more than double the thickness of Joining Partner I. This can be seen in the ratio of spacer to Joining Partner I. If the ratio is smaller than two there will be a resistance for the material flow into the space to create an undercut. This resistance can be overcome by using more laser pulses, but will only result in a small undercut depth. If the ratio from spacer to Joining Partner I is getting bigger the amount of necessary shockwaves is reduced. The contact surface, on which the pressure wave acts, is dimensioned by the die diameter and the spacer height. The effective force which is induced by the shockwave increases with the spacer height, which leads to less shockwaves needed to create an undercut.

5 Conclusion

By an experimental approach using different thicknesses of metal sheets and different size of joint geometries it was shown that joining of aluminium to stainless steel is possible by the means of laser induced shock waves. For nearly each combination of material thicknesses a process window could be detected. From the cross section of the joints it can be concluded that the joint strength is achieved due to mechanical clamping of the upper sheet to the lower one. Also could be concluded that for bigger spacer thickness to

thickness of Joining Partner I ratio less laser pulses are needed for the creation of an undercut and hence for the joining process.

Acknowledgments

This work has been funded by the Project VO530/65-1 ‘‘Fügen durch Hochgeschwindigkeitsumformen durch laserinduzierte Schockwellen’’. The authors would like to thank the Deutsche Forschungsgemeinschaft for their financial support within the project.

References

[1] Vollertsen, F., 2008. Categories of size effects. In: Production Engineering.-Research and Development, vol. 2, no. 4, pp. 377–383

[2] Smolka G, Gillner A, Bosse L, Lützeler R (2004) Micro electron beam welding and laser machining—potentials of beam welding methods in the micro-system technology. Microsyst Technol 10:187–192

[3] Wilden, J.; Bergmann, J.-P.; Holtz, R.; Richter, K.; Le Guin, A.: Einsatz von gepulsten Nd:YAG-Lasern für das Fügen von Werkstoffen und Werkstoffkombinationen mit anspruchsvollen Eigenschaften, DVS-Berichte Band 244 (Die Verbindungsspezialisten – Große Schweißtechnische Tagung, CD Band) (2007)13-18

[4] Neugebauer R, Bouzakis K-D, Denkena B, Klocke F, Sterzing A, Tekkaya AE, Wertheim R (2011) Velocity effects in metal forming and machining processes. CIRP Ann Manuf Technol 60(2):627–650

[5] Zhang Y, Babu S, Daehn GS (2010) Impact welding in a variety of geometric configurations. In: 4th international conference on high speed forming, pp 97–107

[6] Patent (USA) (2011) Low-Temperature Spot Impact Welding Driven Without Contact, Pub. Nr. US 2011/0000953 A1

[7] Zhang, Y., Suresh Babub, S., Prothec, C., Blakelyd, M., Kwasegroche, J., LaHae, M., Daehn, G.S. (2011) Application of high velocity impact welding at varied different length scales, Journal of Materials Processing Technology 211, pp. 944-952

[8] Veenaas, S., Wielage, H., Vollertsen, F. (2013) Joining by laser shock forming: realization and acting pressures, Production Engineering - Research and Development (WGP), DOI 10.1007/s11740-013-0521-z

[9] Barchukov, A. I., Bunkin, F. V., Konov, V. I., Lyubin, A. A. (1974) Investigation of low-threshold gas breakdown near solid targets by CO2 laser radiation, Sov. Phys.-JETP, 39-3, pp. 469-477

[10] Demtröder, W. (2010) Atoms, molecules and photons an introduction to atomic-, molecular-, and quantum-physics, Springer; 2nd ed., p. 37

[11] Miziolek, A. W., Palleschi, V., Schechter, I. (2006) Laser Induced Breakdown Spectroscopy, 1st ed., Cambridge University Press, Cambridge

[12] O'Keefe, J.D., Skeen, C.H., York, C.M. (1973) Laser-induced deformation modes in thin metal targets, J. of App. Phys., 44-10, p. 4622-4626
[13] Walter, D., Michalowski, A., Gauch, R., Dausinger, F. (2007) Monitoring of the micro-drilling process by means of laser-induced shock waves, Proceedings of the Fourth International WLT-Conference on Lasers in Manufacturing (LIM07), Hrsg.: F. Vollertsen, C. Emmelmann, M. Schmidt, A. Otto, AT-Fachverlag, Stuttgart, p. 557-562
[14] Vollertsen, F., Schulze Niehoff, H., Wielage, H. (2009) On the acting pressure in laser deep drawing, Production Engineering - Research and Development, 3/1, p.1-8
[15] Zhang, W., Yao, Y.L., Noyan, I.C. (2004) Microscale Laser Shock Peening of Thin Films, Part 1: Experiment, Modeling and Simulation, ASME, Vol. 126, p. 10-17
[16] Wielage, H., Schulze Niehoff, H., Vollertsen, F. (2008) Forming Behavior in Laser Shock Deep Drawing, International Conference on High Speed Forming 2008, ICHSF 2008, Proceedings, University of Dortmund, Institut für Umformtechnik und Leichtbau, Dortmund, Germany, March 11-12 2008, p. 213-222
[17] Vollertsen, F.: Effects on the deep drawing diagram in micro forming. Prod. Eng. Res. Dev. 6(1), 11–18 (2012)

Effect of Process Variables on the Al/Cu Weldment Using DOE for Magnetic Pulse Welding Process

J. Y. Shim[1], D. H. Park[2], I. S. Kim[3], B. Y. Kang[1]

[1] Environmentally Materials & Components Centre, KITECH, Korea
[2] Welmate Co.,Ltd., Korea
[3] Department of Mechanical Engineering, Mokpo National Univ., Korea

* Corresponding author: E-mail address: kanbo@kitech.re.kr; Tel.: +82 63 210 3710

Abstract

Magnetic Pulse Welding (MPW) process is one of the useful welding processes of the dissimilar metal joining, because this process has only employed the electromagnetic forces between the flowing currents in working coil and the induced-opposite direction currents in the specimen. For achieving the successful MPW, the selection of optimum process variables such as the charge voltage, the gap between specimen and the thickness of workpiece is most important. Therefore, the objective of this study is to investigate the effect of process variables on Al/Cu joint using DOE(Design of Experiment) and to develop the mathematical model for prediction for the leakage pressure. In order to carry out this, center composite design was employed to design of experiment. The MPW equipment manufactured by WELDMATE CO., LTD. has been employed and applied for the materials such as the A1070, C1221 for aluminium tube and copper rod respectively. After the sequent experiment, leakage test has been done to verify efficiency of the welding. The measured results have been shown the good agreement with the calculated results so that it means the developed mathematical model was suitable for expecting the leakage pressure. It is concluded that the charged voltage is major process variable for influence on quality of joint on Al/Cu in MPW process.

Keywords

Magnetic Pulse Welding, Electromagnetic Force, Design of Experiment, Process Variable, Mathematical Model

1 Introduction

Since aluminum is very low in price and lighter in comparison with that of copper and has thermal conductivity similar to that of copper so that it is advantageous to use aluminum in the aspects of product weight reduction and manufacturing cost. Accordingly, aluminum has been focused as a material to replace copper in refrigeration cycle, and its application is being expanded not only to home appliances, but also to automobiles. However, as two dissimilar materials such as aluminum and copper have been welded by an existing fusion welding such as brazing or resistance welding, a defect such as pore or crack occurs due to the difference in the material properties between the two materials during welding. Such a defect deteriorates the quality of the weld as well as generates environmental pollutants due to leakage of refrigerant gas caused by corrosion. Therefore, it is required to develop high quality welding technology for dissimilar materials that can save manufacturing cost, improve working environment and reduce the total emission of environmental pollutants.

Even if MPW is not a welding process recently developed, it has focusing as a welding technology for light weight materials and dissimilar materials in industry. Furthermore, MPW is an environment-friendly process that can be employed to manufacture high quality products without using gas, filler metal and lubricant which are sources of environmental pollution generated during welding. As no heat is applied to the material, no defect occurs due to the difference in the material properties, and high quality weld can be obtained as there is no part affected by heat. For such a reason, this process can be diversely applied across the whole industry including electric/electronic, automobile and aerospace industries, and is applied in actual production sites to obtain economic effect through high productivity and high quality. Recently, a study on optimization of MPW process is being carried out around IUL(Institute of forming technology and lightweight construction), IWS(Fraunhofer Institute for Material and Beam Technology) and OSU(Ohio state university) through establishment of systematic theory, joining experiment of dissimilar materials and numerical analysis. [1-4]

The process variables which affect the MPW process include device variables such as charged voltage, discharged time, and the shape of coil, as well as material variables such as material type, dimension of the materials, the gap between materials, electric conductivity, strength, elongation, and surface condition. Such process variables have been studied by some researchers in the basic aspect. In particular, To obtain high quality weld using the same apparatus and materials, it is very important to select optimal charged voltage as electromagnetic force, the gap between specimens and dimension of the materials.[5-6] Accordingly, prediction of leakage pressure related to the change in the main process variables during a MPW process is very important in commercializing this process and expanding its application field. For this, it is required to conduct experiments and systematically analyze the result data in conjunction with design which based on an effective experiment plan. The theory of main process variables in MPW process was studied by P. Zhang[4], and D. Dudkoet. et. al[7] reported the dynamic behavior of materials when high speed electromagnetic force is applied. Hokari et. al[5] reported on the optimal ranges of process variables for successful joining of aluminum and copper or aluminum and steel. V. Shribman[8] analyzed the effect of process variables on the joint in metallurgical aspect by observing the cross sections after welding aluminum and steel in different process conditions. Furthermore, Shim[9] studied the effect of process variables on the joint quality when welding aluminum and steel using the experiment design method and developed a regression

equation, there was a limit that it could only be utilized for dissimilar welding of a Al/Steel weldment. Kim[10] studied the effect of the gap between materials on welding strength. However, the study did not cover not only the effect of other process variables on the joint, but also the interrelation of the process variables. Therefore this study focused to the developed mathematical model for predicting the leakage pressure of Al/Cu tubular weldment depending on the change in the process variables. To achieve this goal, the charged voltage, gap between outer tube and inner rod and thickness of outer tube were selected as the process variables of MPW process on the bases of related researches [1-8]. And experiment design for Al/Cu magnetic pulse welding was established in accordance with CCD using MINITAB R14, a commercial software. Finally the sequent experiment in random welding condition was carried out to verify the developed mathematical model.

2 Experimental Works

2.1 Design of experiments

CCD generally is a most useful method of mathematical and statistical techniques that can be used for studying the effect of several factors at different level and their influence on each other. Furthermore, it helps us to obtain the surface contour that provides a good way for visualizing the parameter interaction.[11] The CCD included an imbedded factorial or fractional factorial matrix with center points and ‘‘star points’’ around the center point. If the distance from the center of the design space to a factorial point is ±1 unit for each factor, the distance from the center of the design space to a star point is ±α, where |α| > 1. A CCD always contains twice as many star points as factors in the design. The star points represent new extreme values (low and high) for each factor in this design. The factors included charged voltage, the gap between inner pipe and outer pipes and a thickness of an outer pipe at five coded levels, -α, -1, 0, +1, +α were shown in Table 1. For three factors (n=3) and two levels (low and high), the total number of experiments was 20 determined by the expression:2n(23=8: factor points)+2n(2×3=6: axial points)+6(center points: six replications), as shown in Table 2. The mathematical relationship of the response on the three significant independent factors such as the charged voltage(X_1), the gap between inner rod and outer pipe(X_2) and thickness of outer pipe(X_3) can be approximated by a quadratic polynomial model including 3 squared terms, 3 interaction terms, 3 linear terms and 1 intercept term as shown below;

$$\mathrm{Y} = b_0 + b_1X_1 + b_2X_2 + b_3X_3 + b_{11}X_1^2 + b_{22}X_2^2 + b_{33}X_3^2 + b_{12}X_1X_2 + b_{13}X_1X_3 + b_{23}X_2X_3 \quad (1)$$

Where Y is leakage pressure, b_0 is the average of the results of the replicated center point, b_1 , b_2 and b_3 are the main half-effects of the coded variables X_1 , X_2 and X_3 respectively b_{12}, b_{13} and $b_{23}$are two factor interaction half-effects.[11-12]

Table 1: Process variables and their levels

Factors	Code	-α	-1	0	+1	+α
Charged voltage (kV)	C(X_1)	5.4	6.0	7.0	8.0	8.6
Gap between inner rod and outer pipe (mm)	G(X_2)	0.5	0.6	0.8	1.0	1.1
Thickness of outer pipe (mm)	T(X_3)	0.5	0.6	0.8	1.0	1.1

Table 2: Experimental design and results based on the CCD

Trial No.	C(X_1)	G(X_2)	T(X_3)	Response variable Y
1	7.0	0.5	0.8	60
2	5.4	0.8	0.8	20
3	7.0	0.8	0.8	70
4	7.0	0.8	1.1	55
5	7.0	0.8	0.5	80
6	7.0	1.1	0.8	80
7	8.6	0.8	0.8	90
8	7.0	0.8	0.8	70
9	7.0	0.8	0.8	70
10	6.0	1.0	0.6	60
11	7.0	0.8	0.8	70
12	8.0	0.6	0.6	85
13	8.0	1.0	1.0	80
14	6.0	0.6	1.0	40
15	7.0	0.8	0.8	70
16	6.0	1.0	1.0	40
17	8.0	0.6	1.0	70
18	8.0	1.0	0.6	90
19	6.0	0.6	0.6	50
20	7.0	0.8	0.8	70

2.2 Experimental setup and procedure

To developed the mathematical model to predict the leakage pressure, as show in Figure. 1, the experimental employed in this study is a W-MPW manufactured by WELMATE CO., LTD.

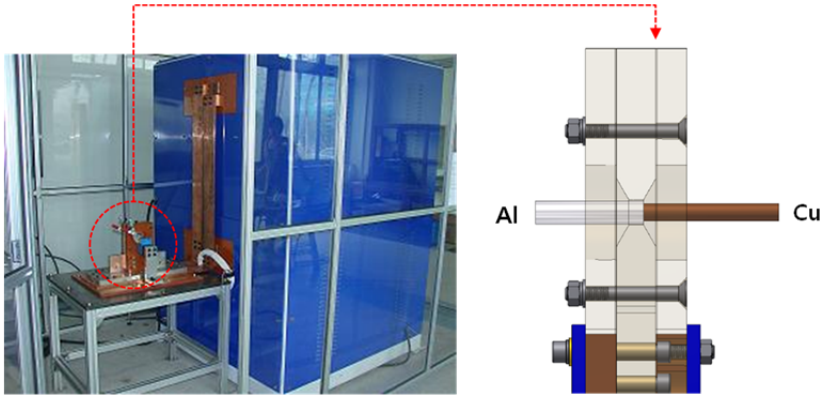

Figure 1: *Experimental setup for this study*

W-MPW has the maximum charging energy 60kJ. The A1070 tube of 10mm in diameter and C1221 rod were inserted within working coil as shown Figure 1. Also, the length of workpiece and overlap distance set up 110mm and 10mm respectively. The Al/Cu magnetic pulse welding was performed according to the designed experiment by CCD as shown in Table 2 and then leakage pressure was measured by leakage tester.

3 Results and Discussion

3.1 Development of the mathematical model

"Y" values from Tables 2 show the leakage pressure after Al/Cu weldment using MPW process. To analysis the effect of the process variables on the Al/Cu weldment and to develop the mathematical model were performed by Analysis of Variance (ANOVA) as shown Table 3. Since an exploratory tool to explain observations, ANOVA model has been widely used in the study of effects of multiple factors for designed experiments, ANOVA models with fixed effects has received a lot of attention in the past decades. The p value was employed to estimate whether F is large enough to indicate statistical significance. If p value is lower than 0.05, it indicates that the model is statistically significant.[12] As shown in Table 3, effect of linear terms and squared terms were statistically significant, but two factor interactions term were insignificant. These results show that there is no interaction between process variables.

Table 3: Analysis of variance for burst pressure

Source	Degree of freedom	Sum of square	Adj sum of square	Adj mean of square	F-value	p
Regression	9	6002.08	6002.08	666.9	49.72	0.000
Linear	3	5599.67	5599.67	1866.56	139.17	0.000
Square	3	393.03	393.03	131.01	9.77	0.005
Interaction	3	9.37	9.37	3.12	0.23	0.871
Residual error	8	107.30	107.30	13.41		
Lack-of-fit	5	107.30	107.60	21.46		
Pure error	3	0.00	0.00	0.00		
Total	19	6130				

Also a quadratic polynomial model which can predict the leakage pressure according to the process variables was developed using the regression analysis, which is as follow:

$$\mathrm{Y}_{\text{leakage pressure}} = -297.554 + 89.418\mathrm{X}_1 + 3.594\mathrm{X}_2 - 16.462\mathrm{X}_3 - 5.408\mathrm{X}_1^2 + 5.408\mathrm{X}_2^2 - 18.029\mathrm{X}_3^2 + 3.125\mathrm{X}_1\mathrm{X}_2 + 3.125\mathrm{X}_1\mathrm{X}_3 - 15.625\mathrm{X}_2\mathrm{X}_3$$

As the F-value of 49.72, developed model is significant with a highly satisfactory value of R^2 of 98.2%, which indicates that only 1.8% of the total variation is not explained by the model. Figure 2 shows the comparison between measured and calculated results from the developed mathematical model. As you can be seen, the calculated values was known good agreement with measured values.

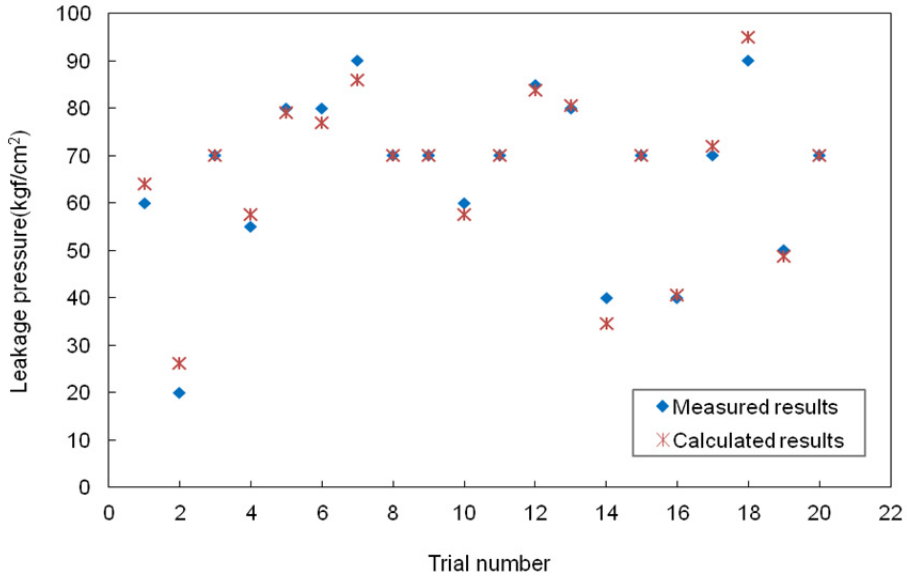

Figure 2: *Comparisons between measured and calculated results*

After developing the mathematical model in order to predict the leakage pressure according to the variation of process variables and analysis the effect of process variables, the plot of main effect was checked in Figure 3. As the charged voltage has been increased, leakage pressure has been increased sharply. However, the effect of gap between inner rod and outer pipe and thickness has been varied slightly.

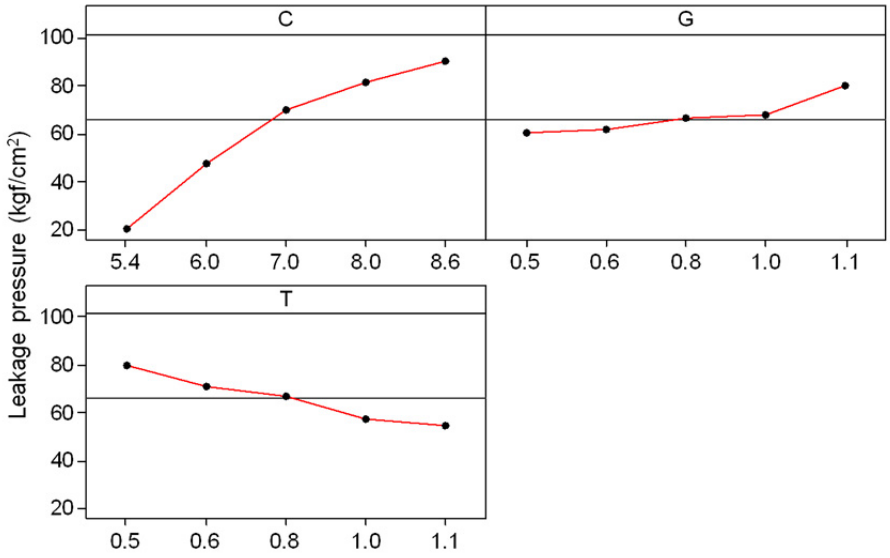

Figure 3: *Main effects on leakage pressure*

Actually, the charged voltage in MPW process means the kinetic energy without a small electrical loss for flying the outer pipe. Therefore, as the charged voltage has been increased,

sufficient energy for successful welding can be transferred to coil. As the thickness has however been increased, MPW process need the more electrical energy for flying the outer tube. Also, as the gap has been decreased, outer tube cannot obtain sufficient acceleration for a collision between two workpieces. Figure 4 shows the surface plot of leakage pressure with thickness of outer tube, the gap between workpeces. Although the effect of gap and thickness was slight, the lower thickness and the higher gap read to increase the leakage pressure. As a result, it is found that the charged voltage is the most effective process variable on the quality of joint.

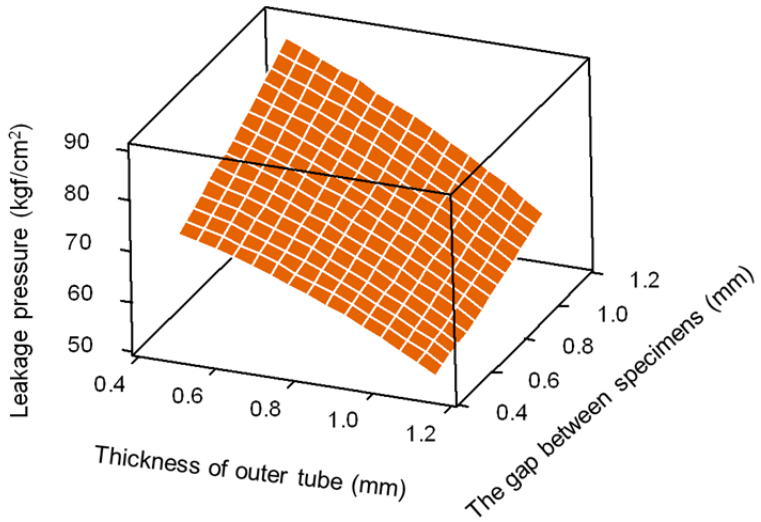

Figure 4: *Surface plot of leakage pressure with thickness and gap*

3.2 Verification Experiment

Verification for the developed mathematical model was performed as to test the accuracy of the developed mathematical model according to various welding condition. The experiment was carried out on 5 welding conditions as shown Table 4. After experiment, the measured and calculated results were compared as shown Table5. For getting exact results, additional experiment has been taken twice.

Table 4: Welding condition for addition experiments

Trial No.	C(X_1)	G(X_2)	T(X_3)
1	5.8	0.6	0.8
2	6.5	0.8	0.5
3	7.3	0.6	0.8
4	8.1	1.0	1.0
5	7.0	0.8	1.0

Figure 5 shows a graph that is the comparison between measured and the calculated results. The errors between the value of calculation and the value of experiment are showed in Table 5.

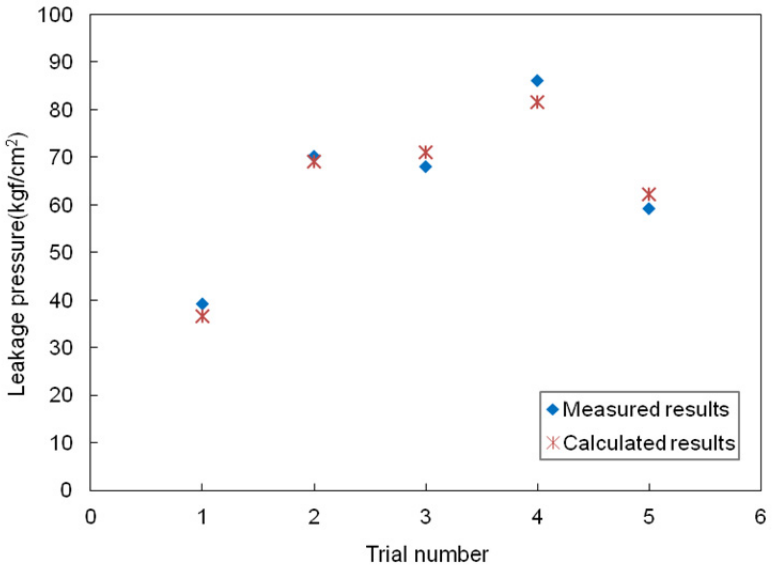

Figure 5: *Comparisons between measured and calculated results*

The errors between the calculated and measured results were less than 10% under the experimental numbers, so the developed mathematical model expected leakage pressure exactly.

Table 5: Results of verification of the developed model

Trial No.	Leakage pressure (kgf/cm^2)		Error (%)*
	Experiment	Calculation	
1	39	36.415	6.6
2	70	68.929	1.5
3	68	70.838	4.2
4	89	81.424	5.3
5	59	62.100	5.3

* Error(%)= (Exp.- Prediction)/Exp.×100

4 Conclusions

This research has been concentrated analysis of the effect of process variables of MPW process using DOE and reached with the following conclusion.

(1) Based on the related research, process variables were chosen such as charged voltage, the gap between outer tube and inner rod and thickness of outer tube. After selecting the process variables, the CCD was employed for design of experiment.

(2) The mathematical model was developed by experiment results using analysis of variance which is analyse code in MINITAB. The optimal process variables to achieve the high quality

joint through experiment result were 8.3kV charged voltage, 1.1mm gap between inner rod and outer pipe and 0.5mm thickness of outer pipe.

(3) The experiment results indicated the charged voltage is strongly effected process variable on the leakage pressure and the effect of the gap between outer tube, and inner rod and thickness of outer tube was slight.

(4) The developed mathematical model can also be employed to expect leakage pressure and tendency that is about effect of process variables of tube. It is expected that the developed mathematical could be used to choose the optimal process parameters in the Al/Cu tube welding of 10mm and less.

References

[1] *Gobel G.; Beyer E.; Kaspar J.; Brenner B.:* Dissimilar Metal Joing: Macro-and Microscopic Effects of MPW. Proc. Of the 5th International Conference on High Speed Forming, Dortmund, 2012, p. 179-188.

[2] *V. Psyk; G. Gerstein; B. Barlage; B. Albuja; S. Gies.; A. E. Tekkaya;, F.W. Bach: Process Model and Desigh for Magneitc Pulse Welding by Tube Expansion.* Proc. Of the 5th International Conference on High Speed Forming, Dortmund, 2012, p. 197-206.

[3] *R. Raoelison; M. Rachik; N. Buiron; D. Haye; M. Morel; B. Dos Sanstos; D. Jouaffre; G. Frantz: Assessment of Gap and Charging Voltage Influence on Mechanical Behaviour of Joints Obtained by Mangnetic Pulse Welding.* Proc. Of the 5th International Conference on High Speed Forming, Dortmund, 2012, p. 207-216.

[4] *P. Zhang:* Joining Enabled by High Velocity De-formation. Ph.D. Thesis, Ohio State University, USA, 2003.

[5] *H. Hokari; T. Sato; K. Kawauchi; A. Muto:* Magnetic Impulse Welding of Aluminium Tube and Copper Tube with Various Core Materials. Welding International, Vol.12, No. 8, p. 619-626, 1998

[6] *K. Okagawa; T. Aizawa:* Effect of gap on seam welding by applying magnetic pressure, Journal of the JSTP, Vol. 47, No. 7, p. 632-636, 2006

[7] *Dudko D.; Chudakov V.; Kistersky L.; Barber T.:* Magnetic pulse welding of tubing: Exploring the cold welding process. Fabricator, Vol. 26, No. 8, p. 62-66, 1996.

[8] *V. Shribman; Y. Livschitz; O.Gafri:* The Application of Magnetic Pulse welding in the automotive industry. Advanced Transmission Design & Performance, p. 21-27, 2005

[9] *J. Y. Shim; B. Y. Kang; I. S. Kim; M. J Kang; I. J. Kim; K. J. Lee:* Joining of Aluminium to Steel Pipe by Magnetic Pulse Welding. J. of Materials Transactions, Vol. 52, No. 5 p. 999-1002, 2011

[10] *S.W. Kim; C.K. Chun; S.H Kim:* Effects of the Stand-off Distance on the Weld Strength in Magnetic Pulse Welding, Journal of KWJS, Vol. 26, No. 6, p.48-53, 2008

[11] *I. Xiarchos; A. Jaworska; G. Z. Trznadel:* Response surface methodology for the modelling of copper removal from aqueous solutions using micelle-enhanced ultra filtration, Journal of Membrane Science Vol. 321, p. 222-231, 2008.

[12] *N. Sarlak; M. A. F. Nejad; S. Shakhesi; K. Shabani:* Effects of electrospinning parameters on titanium dioxide nanofibers diameter and morphology: An investigation

by Box–Wilson central composite design (CCD). J. Chemical Engineering Vol 210, p. 410-416, 2012.

[13] *V.Shiribman:* Take advantage of the new magnetic pulse welding process. Svetsaren, Vol. 2, No. 3, p. 14-16, 2003

[14] *M.Marya; D.Priem; S.Marya :* Microstructures at aluminum-copper magnetic pulse weld interfaces. Materials Science Forum, Vo. 426-432, p. 4001-4006, 2003

[15] *A.Stern; M.Aizenshtein:* Bonding zone formation in magnetic pulse welds. Science and Technology of Welding and Joining, Vol. 7-5, p. 339-342, 2002.

[16] *J.Y. Shim; I.S. Kim; K.J. Lee; B.Y. Kang:* Experimental and Numerical Analysis on Aluminium/Steel Pipe Using Magnetic Pulse Welding. Met. Mater. Int., Vol. 17, No. 6 p. 957-961, 2011

[17] *Zhang, Y.*; Babu, S,; Daehn, G, S.: Impact Welding in a variety of Geometric Configurations. Proc. Of the 4th International Conference on High Speed Forming, Columbus, 2010, p. 97-107.

[18] *Psyk, V.; Gershteyn, G.; Demir, O. K.; Brosius, A.; Tekkaya, A. E.; Schaper, M.; Bach, F.-W.:* Process Analysis and Physical Simulation of Electromagnetic Joining of Thin-Walled parts. In: Proceedings of the 3rd International Conference on High Speed Forming – ICHSF 2008, pp. 181-190, 2008.

[19] *Psyk, V.; Gershteyn, G.; Barlage, B.; Weddeling, C.; Albuja, B.; Brosius, A.; Tekkaya, A. E.; Bach, F.-W.:* Process Design for the Manufacturing of Magnetic Pulse Welded Joints. Key Engineering Materials Vol. 473, S. 243-250, 2011. DOI:

Magnetic Pulse Welding of dissimilar metals: Influence of process parameters

Inês Oliveira[1*], Pedro Teixeira[1], Ana Reis[1]

[1] INEGI, Institute of Mechanical Engineering and Industrial Management, University of Porto

Abstract

Magnetic pulse welding (MPW) is classified as a solid-state cold welding process, where the metallurgical bonding between materials is achieved by a high-velocity impact, derived from the dynamics of electromagnetic-mechanical phenomena. A current renewed interest is taken on this technique, promoted by its potential to join flat or tubular overlapped parts made of by different materials, with particular success in materials that present high electrical conductivity.

The major goal of this work is to define the weldability window for an aluminum-steel tubular application. A well-planned run of experiments was performed by using Taguchi's approach. Three process parameters were considered aiming to characterize welding conditions: the charging voltage, the air gap between the two parts to be welded and the tube distance inside the coil. The quality of the welded zone was assessed by means of destructive tests, such as compression tests as well as metallographic evaluations. The obtained experimental data was further analyzed in order to define the optimal values of process parameters.

Keywords

Impact Welding, Magnetic Pulse Welding, Joining Dissimilar Materials

1 Introduction

The most diverse industries, from consumer goods, sports to high technology applications in aerospace or automotive transportation are, at these days, more and more challenged to face the increasing requirements for better functional properties, reduction of overall energy consumption and minimization of carbon foot-print. These new concerns are often associated to material replacement, namely steel by aluminium, magnesium, titanium or other low density metals, and more recently by polymers or composites, resulting in lightweight structures. In fact, the increased use of these materials for engineering

applications is growing not only due to its high strength-to-weight ratio, but also due to its special performance in corrosion and erosion resistance or high-temperature strength. Accordingly, joining dissimilar materials is of paramount importance for the technical performance and success of these new hybrid structures [1-3].

Magnetic pulse welding (MPW) is a solid state welding process which uses a high velocity impact, driven by the dynamics of electromagnetic-mechanical phenomena, to create a bond. It is considered a cold welding process, capable to perform multi-material welding and crimping, with particular success in materials with high electrical conductivity [3-5].

A typical MPW system includes a power supply, composed by a capacitor bank and a high speed switching system, and a coil. Depending on the coil geometry, tubular or flat, overlapped parts can be welded. The energy required to the process is stored in the capacitor bank charged at an initial voltage. This energy is then discharged as current that flows through the coil (flat spiral, helical, etc.) using high speed switches. As result of this current discharge, which is a highly damped sinusoidal wave, a transient magnetic field is produced in the coil that penetrates into the workpiece, placed in its vicinity. This transient magnetic field induces Eddy currents in the workpiece, with opposite direction to the current that creates it. As two opposite magnetic fields repel each other, the repulsive forces, called Lorentz forces, lead to the workpiece movement and consequent impact against the inner part.

The weld takes place when two metals are compressed in such intensity that the atoms of the two materials start sharing electrons [6]. Since there is no heat or melting involved, dissimilar metals, with different melting points can be welded by this technique. In addition, several other advantages are associated to this process. In terms of quality of the welded zone, the good aesthetic and clean interface together with the absence of heat-affected zone, closely related with mechanical strength (typical joints are stronger than the parent material), absence of distortion and corrosion, are the most relevant advantages concerning the weld itself. Concerning the process, it is important to highlight benefits as the high-speed, the high repeatability and the nonexistence of filler materials.

The present work is dedicated to joining by tube compression. It is intended to study the phenomena behind the magnetic pulse welding process and its main parameters. For such purpose, the design of experiments method was used to experimentally evaluate the weldability of an AA 6063-T5- St37 application. Details of the experimental procedures and the main results are described in the next paragraphs.

2 Overview of the welding experiments

2.1 Process parameters

In order to ensure the quality of the weld as well as the efficacy of the MPW process, it is necessary to understand the effects of the process parameters. As shown in Figure 1, the bond is directly dependent on the angle and speed of impact [6]. The impact velocity is related to both pressure and kinetic energy necessary to accelerate the flyer and ensure the bonding between the two parts. This is one of the main process parameter and is dependent on the material's characteristics, geometry, properties of the setup, as well as the characteristics of the electromagnetic pulse machine. The angle between the parts to

be joined also plays a key role in the welding process and can be determined based on the geometry of the workpieces, as shown in Figure 2, where LWZ represents the length of the tube inside the coil and S the distance between the flyer tube and the rod. If collision angle and impact velocity are in the range of the weldability window (Figure 1), a jet will be created when the surfaces are collapsed against each other. The jet, often called backflow material, is a thin layer of metal that is disintegrated and ejected, as a result of the high-pressure impact at high-velocity (in the range of sound velocity) at the collision point. The emission of the jet results in cleaned surfaces, free of oxides or other contaminates, allowing that the impact at high velocity be able to overcome the forces between the atoms of the materials and approximate the atoms in such intensity that the electrons can be shared between the two materials, creating a bond. Depending on the application, it is mentioned in the literature that the optimum value of the impact angle is in the range of 6 º to18 º.

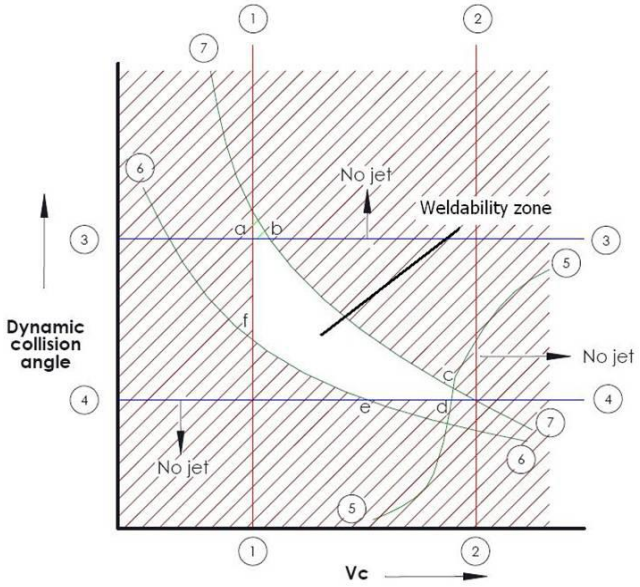

Figure 1: *The weldability window in explosive welding [7].*

It is important to refer that in terms of machine parameters, the charging voltage is the only factor that can be intentionally changed. Therefore, it is essential to ensure that the voltage imposed to the capacitor bank is sufficient to perform the weld. The amount of energy required essentially depends on the material properties and dimensions of the flyer. Also important to notice is that the success of the operation equally depends on frequency of the discharge current. However, this parameter will be invariable since it is inherent to the magnetic pulse welding setup. As a consequence, the electrical conductivity and thickness of the flyer should guaranty low penetration of the magnetic field in the workpiece, to avoid efficiency losses.

In short, numerous parameters will influence the impact velocity and impact angle and as consequence the quality of the welded zone. These parameters are inherent to the materials to be joined, to the geometry of the workpieces and to the electrical system. In the experiments that are presented in this work, three parameters were tested: LWZ, S, and the charging voltage in order to achieve the parameters that lead to the weldability zone, keeping constant the remaining parameters.

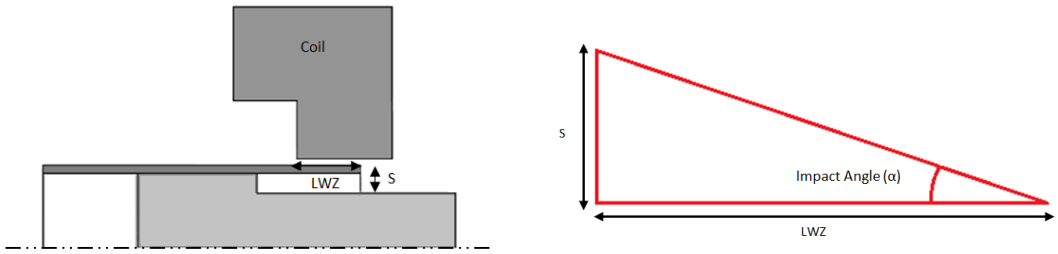

Figure 2: *Impact angle.*

2.2 Experimental aspects

Design of Experiments, or DoE, is an experimental or analytical method commonly used to statistically quantify the relationship between parameters (inputs of the process) and responses (measured outputs). DoE has several applications especially in the field of science and engineering. It is successfully applied in process development and optimization procedures, process management and validation tests [8]. The Taguchi's method, developed by Genichi Taguchi, is a fractional factorial design, commonly adopted in automotive, electronics and other processing industries. The objective of the Taguchi's method is, using a fraction of the total number of combinations of the input parameters; to determine the optimum input parameters, but neglecting the variation caused by uncontrollable factors or noises [9]. A three-level fractional factorial design was built. An analytical model was used to estimate the minimum values for the parameters, required to accelerate the flyer, ensuring the necessary plastic deformation and impact velocity to successfully obtain a weld. The properties of the materials to be joined, its geometrical characteristics as well as the machine properties were taken into consideration in this study. An overview of the experimental series of tests is presented in the following table.

Run	Stand-Off Distance [mm]	Field Shaper Overlap [mm]	Impact Angle [º]	Voltage [kV]
1	2.5	8	17.4	17
2	1.5	9	9.5	17
3	2.5	9	15.5	15
4	1.5	8	10.6	15

Table 1: *Overview of the DoE.*

The experiments were performed in a MPW 25 kJ-25 kV. The maximum energy storage is 25 kJ, being the maximum charging voltage and output current of 25 kV and 400 kA, respectively. The system is equipped with two capacitor modules, each one with a capacitance of 40 μF, having the machine a total capacitance of 80 μF. The total inductance is 0.1μH and an internal resistivity of 19 mΩ. The tool consists in a steel single turn coil which is suitable for welding cylindrical parts with an outer diameter of 20 mm. The welding samples and principal dimensions are presented in the Figure 3.

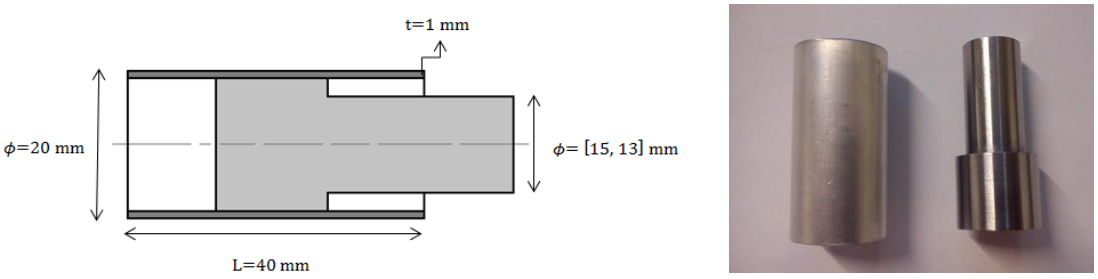

Figure 3: *Samples geometry and dimensions.*

3 Results and discussion

3.1 Weld characterization

The methods applied for the evaluation of the welded workpieces are presented in this section. Destructive tests were used to establish a measure for the weld quality, namely microscopic examination and compressive tests.

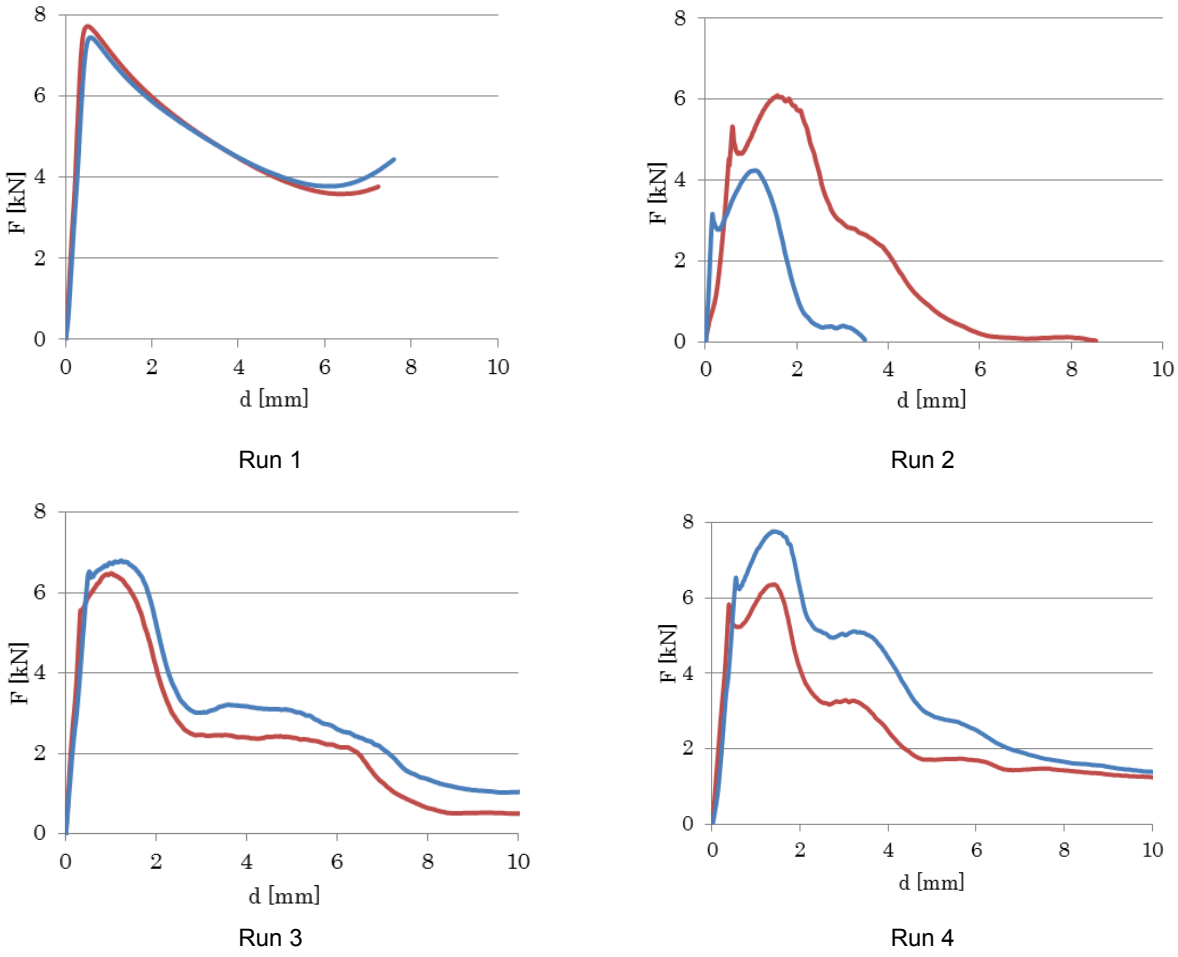

Figure 4: *Force-displacement curves resultant from compression tests.*

Two samples of each run were subjected to a compressive testing in order to ensure some reliability in the obtained results. Figure 4 shows the force-displacement graph acquired during the test and Figure 5 the final geometry of the samples. In the graph correspondent to run 1, it is possible to observe a linear relationship between force and displacement, indicating the development of elastic stresses. At a force of approximately 8 kN, the aluminum tube buckled, as shown in Figure 5. The failure of the aluminum tube before the weld indicates that the weld strength exceeds the compression resistance of the tube, meaning that the connection is stronger than the base material. This buckling phenomenon was only observed in this first run. In the remaining series of experiments, despite the similar values of maximum force, a relative movement between the rod and the tube during the compression test was verified, indicating that the resistance of the weld is lower than the resistance of the base materials.

Additionally, it is important to note that, in the first run, the curves are similar for the both specimens, and present a regular shape. In opposition, the remaining runs present an irregular evolution, probably due to the sliding phenomenon and consequent material dragging. In fact, the high value of force in the run 4 is probably associated to the dragging of material (in this case aluminum) by the edge of the inner rod.

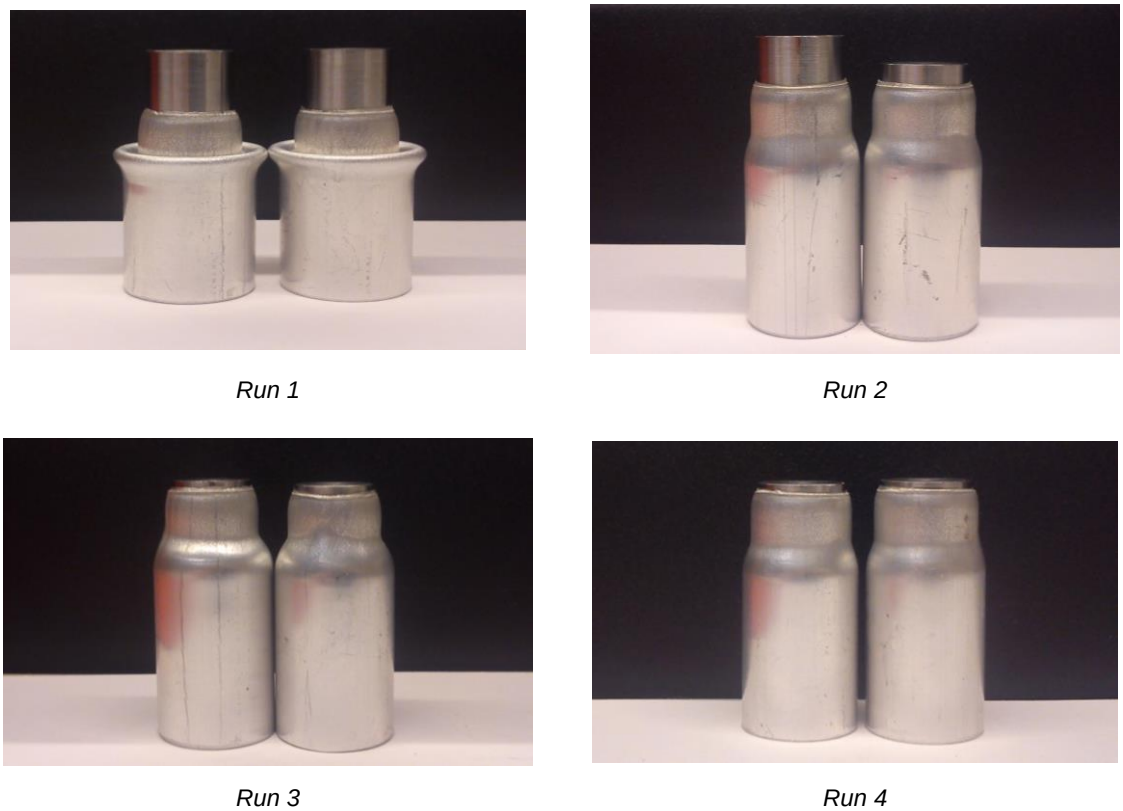

Run 1 *Run 2*

Run 3 *Run 4*

Figure 5: *Samples after compression tests.*

The samples were cut along the longitudinal direction, cleaned, embedded in epoxy resin and polished, as seen in Figure 6. As the aluminium is softer than the steel, several

polish steps were needed to obtain a surface without scratches or imperfections. The central cross-section of the weld region was observed by using an optical microscope.

Examination suggested that the parts of the first run were welded. As is stated in the literature, the welded zone can be divided in 3 regions, run-in zone, welded zone and run-out zone. The effective joining of the materials, typically, is verified in the middle, namely in the weld zone. These three zones are clearly identified in the run 1, as observed in the Figure 7. The image referent to zone 2 shows, as referred, that this interface has been welded since no voids are observed at a magnification of 300 times. In order to provide a more detailed study of the interface, the samples were etched by using nital 2%, during 15 seconds and examined by optical microscopy for a second time. It is possible to perceive that an amount of aluminium is incorporated inside the steel, and vice-versa. This fact can be associated to melting phenomenon that occurs during the impact. Therefore, and as preliminary remark, it is possible that the bonding mechanism is not only related to the dynamics of electromagnetic-mechanical phenomena but also with thermal effects, which results in a thin layer of melted material in the interface.

Figure 6: *Illustration of a sample prepared to microscopic evaluation.*

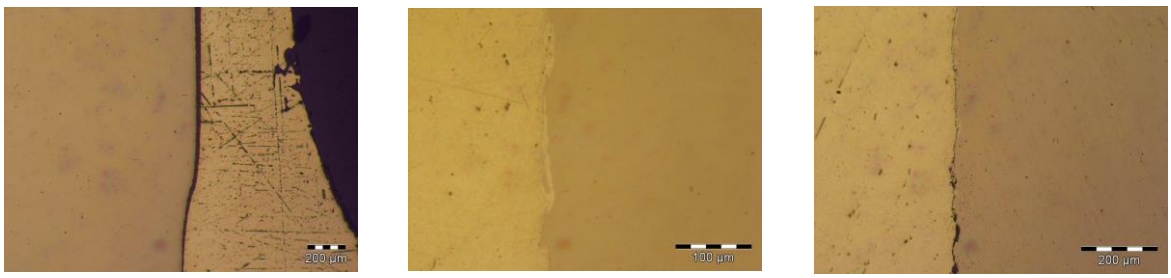

Zone 1(run-in zone)- 75x *Zone 2 (welded zone) - 300x* *Zone 3(run-out zone) - 150x*

Figure 7: *Illustration of the welded interface of run 1.*

The samples corresponding to run 2, 3 and 4 present a discontinuous interface with voids. However, it is important to note that, in the sample correspondent to run 3, adhesion of aluminum to steel can be punctually observed. As seen in Figure 8 a), the aluminum is coupled to the steel in several points. However a significant are of void is seen. Different phenomena can explain these results: the impact energy maybe was too high, causing a rebounding effect of the tube and consequent rupture of the connection or

was not enough to generate an effective bond. Moreover and most likely, the aluminum was melted and quickly solidified resulting in a low quality connection. Besides, a porous zone was found in the interface region of some samples, confirming the occurrence of melting phenomenon.

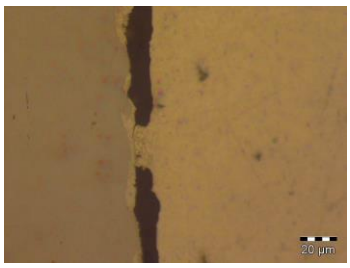

a) *Mixture of materials for the run 3, 750x.*

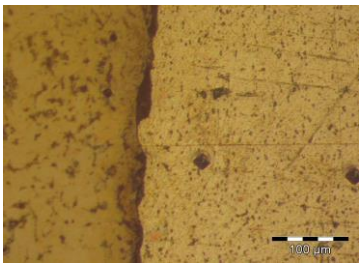

b) *Sample of run 1 etched,* 300x

Figure 8: *Illustration of the welded interface*

3.2 Micro-hardness measurements

The sample labeled as “welded” was subjected to micro-hardness measurements (HV0,2) in order to assess the hardness of the interface zone and to compare it with the hardness of the base materials, as shown in Figure 8 b). In Figure 9 it is presented the evolution of the micro-hardness as a function of their location, i.e. its distance from the interface. It is important to note that the distance scale was multiplied by a factor (10 x) for the AA allowing a more simply visualization.

A slight increase of hardness is visible in the vicinity of the interface. The values in the interface are clearly close to the hardness of the inner workpiece. Given these values, different possibilities are posed: the interface really presents hardness near to the steel, or, the hardness was not correctly measured in the zone of the interface, due to intrinsic difficulties in measuring micro-hardness in very small regions.

Concerning the flyer tube, a hardness increase is verified in comparison with the undeformed condition, probably as a consequence of the high strain-rate plastic deformation of the workpiece.

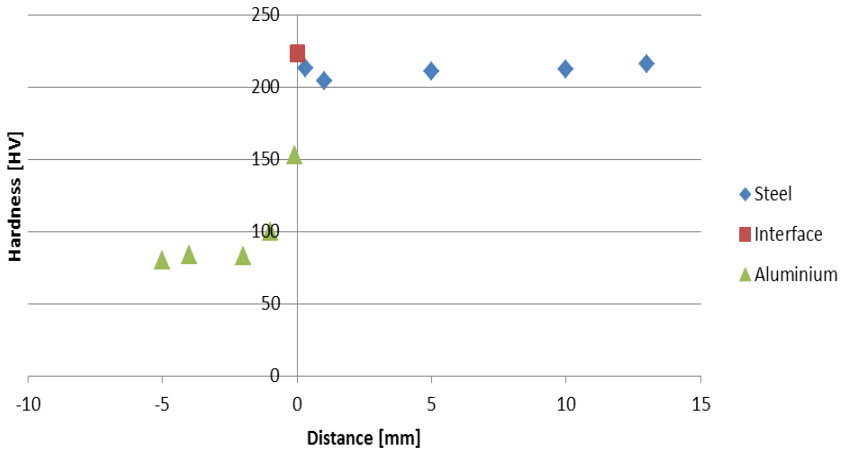

Figure 9: *Micro-hardness measurements*

3.3 Weldability conditions

In accordance with the analysis of results, only run 1 is considered as “welded”. Although the punctual linking between the aluminum and steel, verified in run 3, it has been qualified as no-quality weld, and, as for the remaining runs, is described as “not weld” in the weldability analysis.

In short terms, and as seen in Figure 10, the effective join was created when using an impact angle of 17.4 º, i.e. a stand-off distance equal to 2.5 mm and a LWZ equal to 8 mm, and a charging voltage of 17 kV. The results achieved in run 3 can mean that this parameter’s combination is one of the limits for the weldability window and that several intervals of parameter’s combinations (stand-off distance, LWZ and charging voltage) can result in successful welds.

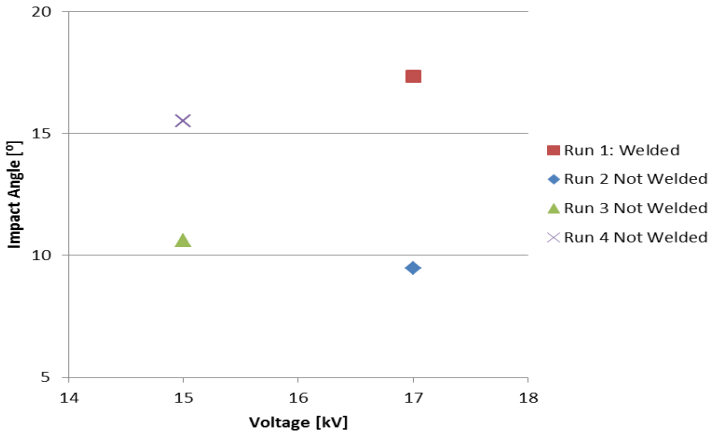

Figure 10: *Weldability window of the AW 6063-T5- St37 application.*

4 Conclusions

This paper focuses the study of the welding conditions for an aluminum-steel application by using the MPW process. For this application, an aluminum flyer tube with an internal diameter of 18 mm and a solid steel rod were considered. A series of experiments were performed taken into account the variation of controllable process and geometrical parameters in order to study the influence of such parameters in the achievement of a successful cold weld between the two parts. Compression tests and microscopic observations were accomplished in the joined samples and an effective joining of the two dissimilar materials was attained by using a combination of the 3 studied parameters.

Further investigation will focus the study and definition of the weldability window for this material combination. A new DoE will be performed, narrowing the limits of the considered levels for the controllable factors. Additionally, other inspection methods for assessing the weld quality will be considered, namely Scanning Electron Microscopy analysis.

5 Acknowledgments

Authors gratefully acknowledge funding of Project SAESCTN-PII&DT/1/2011 co-financed by Programa Operacional Regional do Norte (ON.2 – O Novo Norte), under Quadro de Referência Estratégico Nacional (QREN), through Fundo Europeu de Desenvolvimento Regional (FEDER).

References

[1] Eguia, I., P. Zhang, and G.S. Daehn, "Improved Crimp-Joining of Aluminum Tubes onto Mandrels with Undulating Surfaces". 1st International Conference on High Speed Forming, 2004.

[2] Weddeling, C., et al. "Development of design principles for form-fit joints in lightweight frame structures". in 4th International Conference on High Speed Forming. 2010.

[3] Psyk, V., et al., "Process Model and Design for Magnetic Pulse Welding by Tube Expansion". 5th International Conference on High Speed Forming, 2012.

[4] Watanabe, M. and S. Kumai, "High-Speed Deformation and Collision Behavior of Pure Aluminum Plates in Magnetic Pulse Welding". The Japan Institute of Light Metals-Materials Transactions, 2009. 50(8): p. 2035-2042.

[5] Berlin, A., et al., "Metallurgical analysis of magnetic pulse welds of AZ31 magnesium alloy". Science and Technology of Welding and Joining 2011. 16(8): p. 728-734.

[6] Verstraete, J., W.D. Waele, and K. Faes, "Magnetic Pulse Welding: Lessons To Be Learned From Explosive Welding". Sustainable Construction and Design, 2011.

[7] Loncke, K., "An exploratory study into the feasibility of magnetic pulse welding", in Department of Mechanical construction and production2009, Gent University.

[8] Sivarao, et al., "DOE Based Statistical Approaches in Modeling of Laser Processing – Review & Suggestion". International Journal of Engineering & Technology IJET-IJENS 2010. 10(4).

[9] Taguchi, G., "Introduction to Quality Engineering: Designing Quality into Products and Processes". 1986.

SESSION 4

MODELING AND SIMULATION (FORMING)

Modeling of Temperature Dependent Strain Rate Sensitivities of 5xxx Alloys

J.W. Yoon*

School of Engineering / Institute for Frontier Materials, Deakin University, Geelong Waurn Ponds, VIC 3220, Australia
* Corresponding author: E-mail address: j.yoon@deakin.edu.au; Tel.: +61 3 5227 3425

Abstract

Some 5XXX series alloys exhibit negative strain-rate sensitivity which is a softening of the flow stress with increasing strain rates. This effect is known as the PLC effect and can be manifested in a jagged stress-strain response. The solution technique in a constitutive model relies on a locally linear response in the solution space. The strain-rate sensitivity also varies with temperature. It is negative for temperatures, but positive for higher temperatures. For problems where the strain rates and defor-mation levels are relatively low, the variable sensitivity does not have much effect. This is because the stored energy density and corresponding adiabatic temperature increase are relatively small. However, in the example of a ballistic impact, strain rates as well as temperature increases are very large. The variable strain-rate sensitivity has a significant impact on the results. When measuring the strain-rate sensitivity of a material, the effect of temperature over the range of interest should be included. This paper describes the implementation of negative and variable strain-rate sensitivities into a constitutive model and gives a few examples demonstrating the effect. Also, this work addresses the importance of the strain-rate dependency on temperature when ballistic simulation has been conducted for 5XXX alloys.

Keywords

Failure, Aluminium, Impact

An experiment and simulation study of the rebound effect in electromagnetic forming process*

Xianlong Liu, Liang Huang, Jianjun Li

State Key Laboratory of Materials Processing and Die & Mould Technology, College of Materials Science and Engineering, Huazhong University of Science and Technology, Wuhan 430074, China

Abstract

Electromagnetic forming (EMF) has been proved to be a useful method to form the aluminium alloy sheet as it has so many advantages. As a high-speed forming process, it can suppress crack, reduce springback, and improve the formability of material at room temperature. But in the process of EMF, the rebound effect caused by high velocity impact has an important effect on the flatness of the formed part. Then a spring damper system has been added under the female stop block to eliminate this effect. The results of formed shape, thickness distribution and stress and strain state are investigated by comparing with free-forming process. On the other hand, the influence of spring stiffness and damping coefficient is analysed by using of ANSYS loose-coupled method. The results shows that it helps to improve the flatness of formed parts with a spring damper system used. Beside of the changing of formed shape, the difference of stress strain state results in difference of thickness distribution. And crack happened at the bottom is supressed, and this does favour for further processing. Furthermore, the results also shows that low spring stiffness and right damping coefficient are benefit for reducing the rebound effect.

Key words

Electromagnetic metal forming (EMF), Impact, Rebound effect, Spring damper

---

* This work was supported by the National Basic Research Program of China (No. 2011CB012802)

1 Introduction

Electromagnetic metal forming (EMF) has been proved to be a useful method to form the aluminium alloy sheet, it has many advantages such as unnecessity of lubricant, simple designed mold and high production rates in contrast to the conventional sheet metal forming, and it can also suppress crack, reduce springback, and improve the formability of material at room temperature[1].

As a high-speed forming process, the workpiece is accelerated up to 300m/s. The rebound effect caused by high velocity impact between the workpiece and dies has an important effect on the forming precision and quality of the formed part. So far, most attentions have been focused on changing the shape of bottom die to increase the fittability, but there is little research of controlling rebound effect when the die is flat-bottomed. J.Imbert Boyd[2,3] had done conical die experiments, its results showed that the workpiece fitted good with die. Oliveira[4] implemented a simulation for electromagnetic forming with a flat-bottomed die by 3D loose coupling method, the results shows that excessive rebound happens. And an experiment was also carried out, it shows that maximum fraction of cavity fill is less than 50%. D. Risch[5,6] proposed to locally increase the stiffness of the workpiece to handle the rebound effect. In EMF process, the speed of workpiece is high. When it contacts with dies, one part of the kinetic energy is transformed to plastic deformation work, the other part could not dissipate in a short time, and then the rebound effect happens.

The system with a spring damper is added under the female stop block in this paper, the resuls of formed shape, thickness distribution and the stress-strain sate are compared with free forming. The effect of spring stiffness and the damping coefficient on the rebound is also studied by simulation. The results provides a foundation for electromagnetic forming with a die.

2 Research Method

2.1 Experiment Method

The pulse generator for electromagnetic forming is shown in Figure 1 (a). The maximum stored energy is 96kJ with 213 μF capacitance at 30kV. The set up used in experiments is shown in Figure 1 (b).

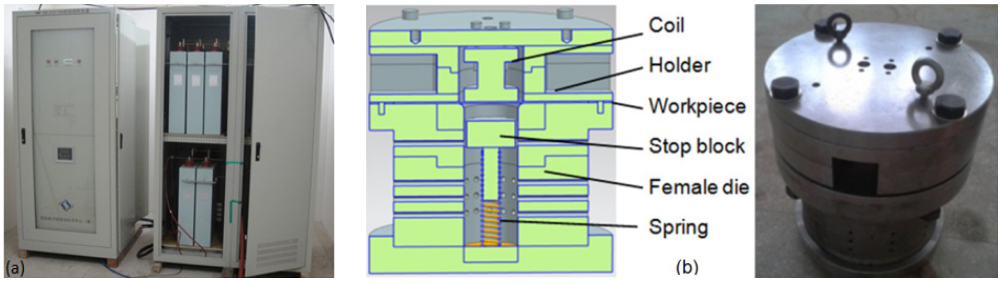

***Figure 1**: Forming equipment (a) electromagnetic pulse generator (b) set up used in the experiments*

The material used in this study is aluminium alloy 5A06 with the diameter 180mm and the thickness 1mm. The coil was made of six layers of copper wire and each layer has three turns, the section of each turn is 3mm wide and 6mm high. The bottom die chosen for this study is 100mm for the diameter, 290mm for the depth, 20mm for the radius. The spring parameters are as follows: shear modulus G is 200GPa; spring wire diameter d is 2.5 mm; spring pitch diameter D_2 is 32mm;number of active coils n is 20;

$$K = \frac{Gd^4}{8D_2^3 n} \tag{1}$$

So the spring stiffness K is 1656N/m which is computed by formula (1).

As shown in Figure 2(a), a spring damper system is added under the workpiece. The spring damper system consists of a nylon block to insulate from the aluminium sheet, a steel block with a guide bar to keep stability of the system and a spring. During the forming process, the workpiece always moves with the system. The schematic diagram of a time in the process is shown in Figure 2(b).

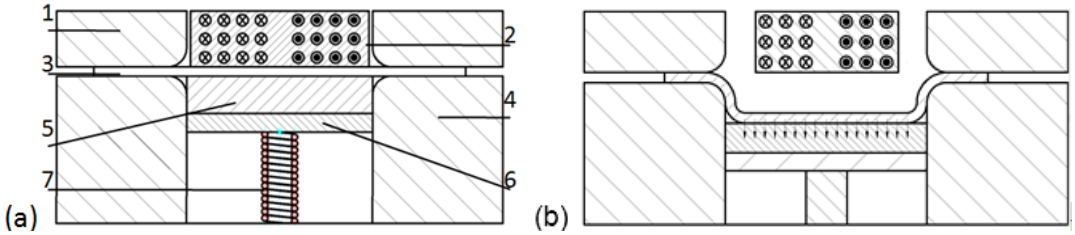

***Figure 2 :**The schematic diagram of experiment (a) before the forming (b) in the forming process. Where, 1-holder, 2-coil, 3-workpiece, 4- female die, 5-nylon block, 6-steel block, 7-spring.*

2.2 Finite Element Simulation

In this paper, a axisymmetric model is set up using two-dimensional loose-coupling method. The main thought is to calculate electromagnetic (EM) forces in ANSYS Emag and use it as load to compute structure deformation.

The propagation of the electromagnetic field is defined by quasi-stationary Maxwell

equations as follows:

$$\nabla \times H = j \tag{2}$$

$$\mu_a \frac{\partial H}{\partial t} = -\nabla \times E \tag{3}$$

$$j = \sigma(E + \mu_a v \times H) \tag{4}$$

where H is the magnetic field intensity, j is the current density, E is the electric field intensity, σ is the electric conductivity, v is the velocity, μ_a is the magnetic permeability of medium under consideration.

Based on these rules, a two-dimensional finite element model of electromagnetic field is established as shown in Figure 3(a). Magnetic flux parallel conditions is set at x=0, when x=300mm is made as far field by the use of infi110 to insure accuracy. The current curve used as load in the simulation of EM field is depicted as Figure 3(b). Only the first half of the curve is selected to do the computation because of two reasons: 1.the current itself is weakened; 2.with the forming carrying on, the distance between the workpiece and the coil increases, the effect of follow-up current is reduced.

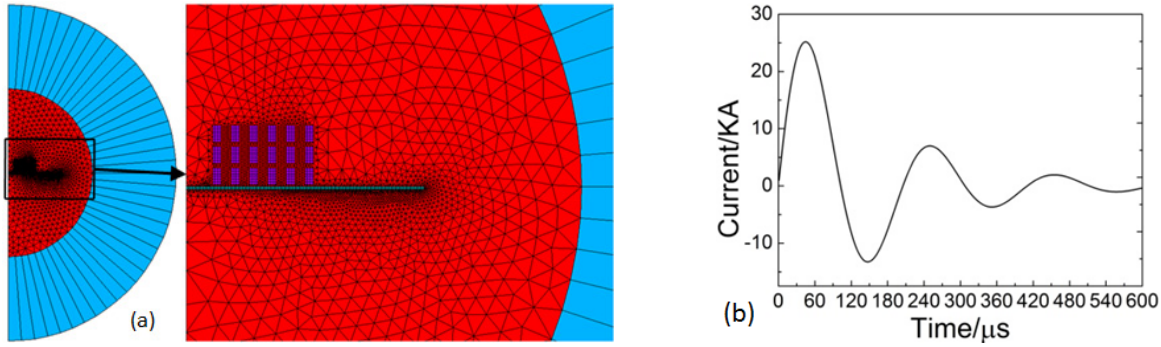

***Figure** 3 :Electromagnetic field analysis (a) electromagnetic fieldmodel (b) current curve used in the simulation*

Dynamic elastic-plastic deformation of solids can be defined by the following equations:

$$\rho \frac{d}{dt} \int_V v dV = \int_S \sigma \cdot ds + \int_V f dV \tag{5}$$

In this paper, an extra pressure is given by the spring damper system, so the formula changes as：

$$\rho \frac{d}{dt} \int_V v dV = \int_S \sigma \cdot ds + \int_V f dV + pds \tag{6}$$

where σ is the stress tensor, ρ is the density; f is electromagnetic force calculated from maxwell equations, p is the pressure provided by the spring damper system.

The finite element model of structural field is shown as Figure 4(a), the coil, blank holder and the female die are set as rigid body. Property of spring is simulated by setting spring stiffness and damping coefficient parameters of Combin14, and the friction factor is set as 0.1. The true stress-strain curve of 5A06 aluminium alloy as shown in Figure 4(b) is getted by quasi-static tensile tests. As to the high speed quality of EMF, Cowper-Symonds multiplier is introduced to considered the effect of strain rate. The constitutive equation is based on over stress strengthening model, as shown in formula (7):

$$\sigma = \sigma_0 (1 + (\frac{\dot{\varepsilon}}{C})^m) \tag{7}$$

where, to aluminium, C=6500 s-1,m=0.25, σ_0 is the flow stress of the quasi-static tensile curve.

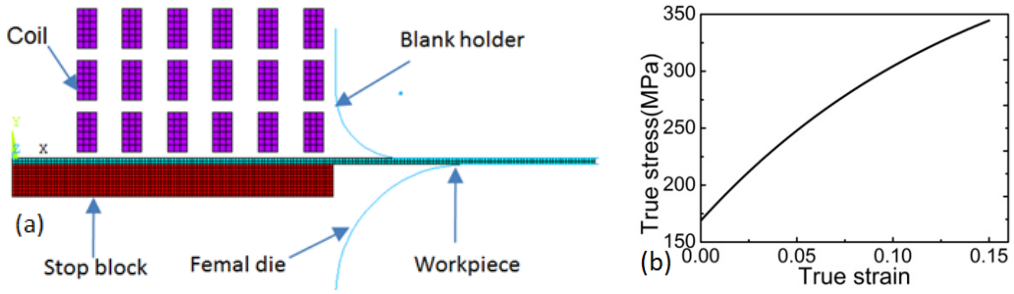

***Figure 4** : Structual field analysis (a) structual field model (b) true stress-strain curve of 5A06*

3 Results and Discussions

3.1 Comparison between free forming and forming with spring damper system

In the following, experiment and simulation are done with the spring damper system used as described in the before paragraph. Free-forming process is also fulfilled to make a contrast.

3.1.1 The difference of shape

It is the free-forming process when the cavity is empty. An experiment is implemented with the charging voltage set as 8kV. As is depicted in Figure 5, the simulation results on the right column are in agreement with experimental results on the left column. The deformed part is always conical without a die even when the discharged voltage is changed. As to this reason, when a second forming is needed to be accomplished, a complicated coil conformed with formed shape must to be made and the cost is increased.

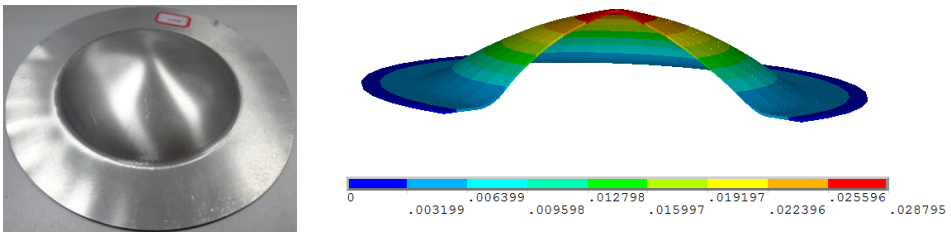

Figure 5 *:Experimental results and the simulation results for the free-forming process*

By using of spring damper system, with the same voltage as free forming process, an study is carried out. The experimental and simulation results are shown as Figure 6. A rather flat bottomed part is formed with the spring damper system applied, and this will do favor to moving down the coil. Multi steps forming would be introduced in the future paragraph based on getting flatted bottom at each step, and this is devoted to solving the difficult problem of forming deep drawing parts by EMF. However, there is a small pit in the center of deformed part which is not predicted by simulation. And there are two reasons caused this problem: firstly, the air resistance is not consider in the simulation; secondly, the EM forces provided by the coil is small in the middle places.

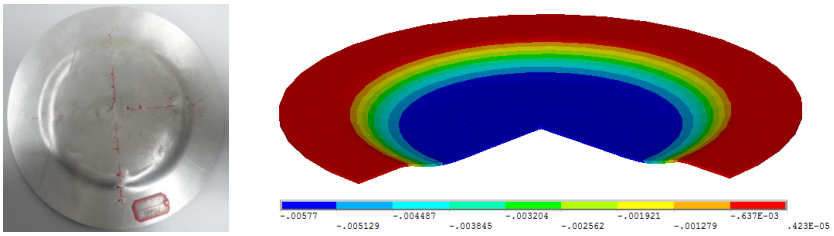

Figure 6 *:Experimental results and the simulation results for the forming with spring damper system*

3.1.2 The difference of thickness distribution

By use of sonic thickness sensor, the thickness of deformed parts are measured by choosing four symmetrical paths to get a mean value. The thickness distribution results of free forming and forming with spring damper system with the discharged voltage 8KV is shown in Figure 7(a),(b).

In the free forming, the distribution of thickness is inhomogeneous as shown in Figure 7(a). The thickness is lower close to the center of the part, and it is higher away from the center. The thinnest place is located at the centerline of the workpiece, where the thickness is 0.89mm. When discharged voltage, the crack damage will happen on the top as shown in Figure 8(a). Even though the deformed parts in deep drawing must not to be flat-bottomed, the sheet metal in free forming is main under stretching state locally. If a second voltage is applied, then thickness in local places is thicken again, and this is an obstacle for further processing.

When forming with the spring damper system, the thickness distribution as shown in

Figure 7(b) is more uniform than that without it. The thickness reduction at different points of the bottom is nearly the same, with flange area growing a little thicker. The thinnest area is the connection of stop block and the die radius, the reason will be discussed in the following segment.

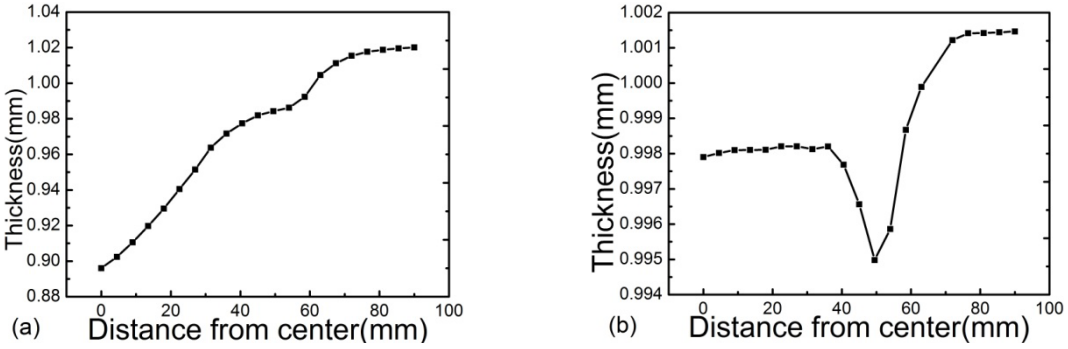

***Figure 7** :Distribution of thickness of discharged voltage 8KV (a) free forming (b) with spring damper system applied*

3.1.3 The difference of stress and strain state

As shown in top column of Figure 8(a), when the discharged voltage is increased to 10.5KV in free forming process, a bulging crack on the top of deformed part will be happen. The stress and strain state of workpiece is presented at the bottom column of Figure 8(a), it is bi-axial tensile strains state at the crack region. When a spring damper system is added under the workpiece, there will be a fiction provided by the stop block, and the stress and strain state has been changed as shown in Figure 8(b). Radial stress σ_1 and hoop stress σ_3 are tensile stress, σ_2 is stress through thickness is compressive stress. Based on volume conservation law, the condition of $\varepsilon_1+\varepsilon_2+\varepsilon_3=0$ is satisfied, and the strain through thickness is $\varepsilon_2=-(\varepsilon_1+\varepsilon_3)$. When the faction force is small, the radial strain and hoop strain are all tensile strain, so ε_1, ε_3 >0. In contrast with free forming, the tensile stress of σ_1 and σ_3 is reduced by the faction force provided by stop block, then tensile strain ε_1 and ε_3 are cut down. Because of this, the strain through thickness is reduced, that is to say the thinning of the workpiece is reduced. When the faction force is big enough, hoop strain ε_3 may low than zero, there will be fewer thinning after the forming.

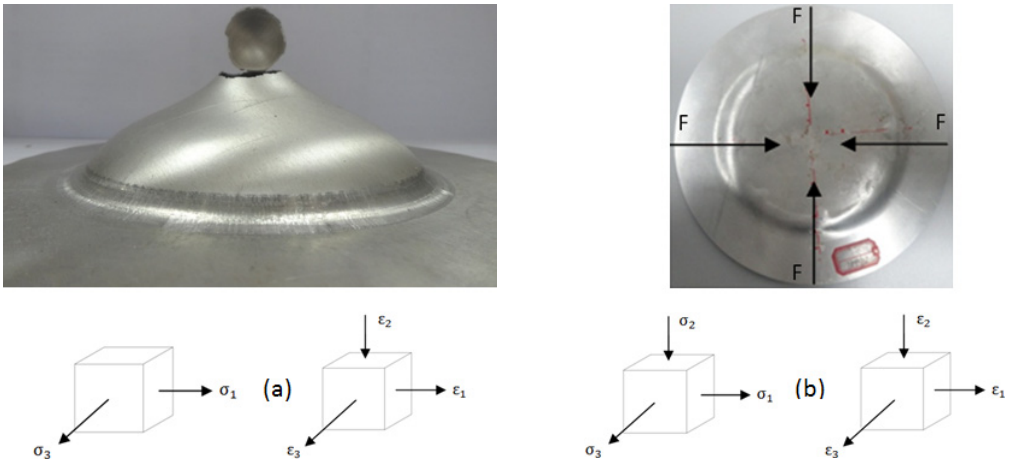

***Figure 8** : Formed part and its stress strain state (a) free forming (b) forming with spring damper system*

To make a better understanding of relation between strain and time, simulation of free forming and forming with spring system are implemented to make an comparison. With the discharged voltage set as 8KV in both conditions, the strain-time curve of middle point of the workpiece are shown as Figure 9 (a), (b). By contrast of the simulation results of two forming state, the stain history of free forming is a typical plane stress state. There are tensile strains in two directions, and compressive strain in one direction. But when the spring damper system is used, the strain state is changed. There are compressive strains in two directions, and tensile strain in one direction. As to the friction force provided by the stop block during the forming process, the hoop strain changes to compressive strains, this would be helpful to cutting down the thinning of the workpiece and good for subsequent process.

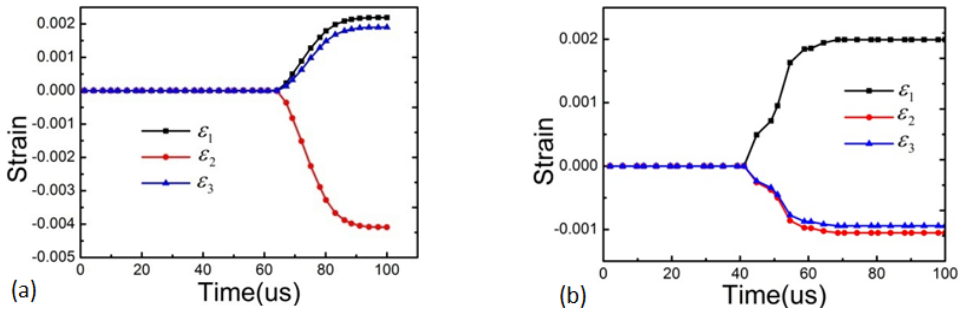

***Figure 9** : The strain-time curve of middle point (a) free forming (b) forming with spring damper system*

3.2 Effect of spring stiffness and damping coefficient on the rebound with spring damper system

The degree of deformation and forming efficiency is low when the discharged voltage is comparable low. When it is contacted with the die, one part of the kinetic energy is

transformed to plastic deformation work, the other part could not dissipate in a short time, then the rebound effect happens. The effect of spring stiffness and damping coefficient on the rebound with spring damper system adopted is studied by simulation. The parameters of the spring stiffness K have been varied starting from 1e3 N/m to 1e5 N/m, and damping coefficient c have been varied starting from 10 Ns/M to 10000 Ns/M. And the results is shown in figure10, figure12, figure13.

Figure 10(a)-(d), Figure 11(a)-(d), Figure 12(a)-(d) shows that the higher the damping coefficient the better the workpiece fittability when the spring stiffness are the same. But the forming depth is smaller at the same time. On the contrary, when the damping coefficient is lower, though the forming depth is deeper, but the fittability becomes worse. So there is an optimal damping coefficient that not only good for getting higher forming depth but also benefit for obtaining flat bottomed workpiece.

As shown in Figure 10(a)-12(a), Figure 10(b)-12(b), Figure 10(c)-12(c), Figure 10(d)-12(d), the rebound effect is worse and the fittability decreases as the spring stiffness increases. On the other hand, the forming depth is smaller when the spring stiffness is bigger. But, the workpiece could move down with the die easier with lower spring stiffness. With lower spring stiffness, the bottom flatness of formed parts is improved, and the forming depth is also .

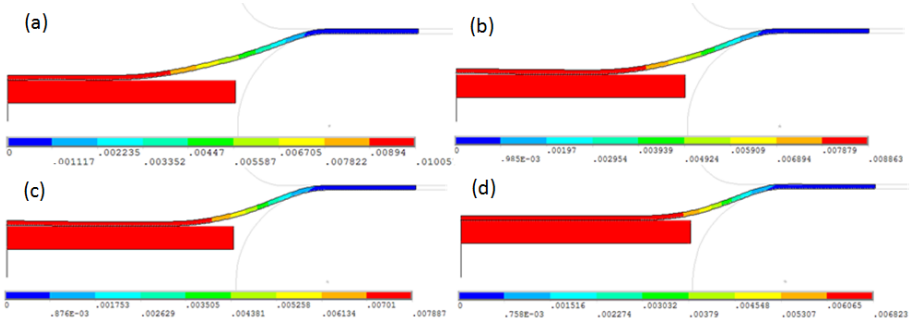

Figure 10 *:Displacement at different damping coefficient with the same spring stiffness 1e3 (a) 10Ns/M (b) 100Ns/M (c) 1000Ns/M (d) 10000Ns/M*

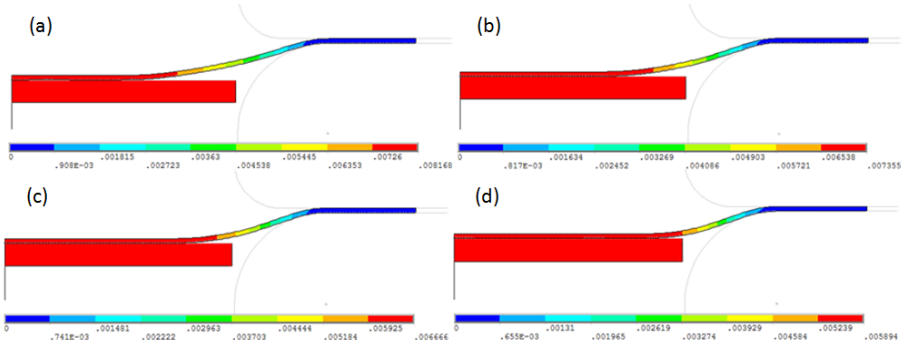

Figure 11 *:Displacement at different damping coefficient with the same spring stiffness 1e4 (a) 10Ns/M (b) 100Ns/M (c) 1000Ns/M (d) 10000Ns/M*

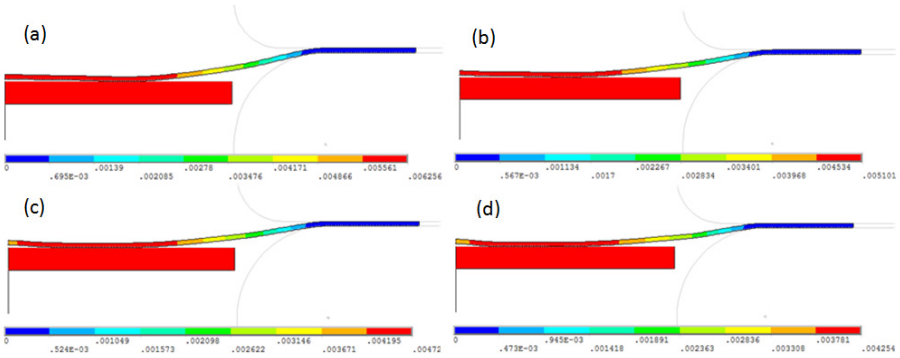

Figure 12 *:Displacement at different damping coefficient with the same spring stiffness 1e5 (a) 10Ns/M (b) 100Ns/M (c) 1000Ns/M (d) 10000Ns/M*

4 Conclusions

1. With a spring damper system added under the female stop block, the flatness of formed parts is improved.
2. Compared with free forming, difference of the stress strain-sate leads to the difference of thickness distribution, and the crack at the bottom is supressed.
3. The simulation results show that low spring stiffness and appropriate damping coefficient is beneficial to control the rebound effect when spring damper system is adopted.

References

[1] *Psyk, V.; Risch, D.; Kinsey, B. L.; et al.:* Electromagnetic forming—A review[J]. Journal of Materials Processing Technology, 2011, 211(5): 787-829.

[2] *Golovashchenko, S.; Imbert, J. M.; Worswick, M. J.:* Contributing Factors to the Increased Formability Observed in Electromagnetically Formed Aluminum Alloy Sheet[J]. 2006.

[3] *Boyd, J. M. S. I.:* Increased formability and the effects of the tool/sheet interaction in electromagnetic forming of aluminum alloy sheet[D]. University of Waterloo, 2005.

[4] *Oliveira, D. A.; Worswick, M. J.; Finn, M.; et al.:* Electromagnetic forming of aluminum alloy sheet: free-form and cavity fill experiments and model[J]. Journal of Materials Processing Technology, 2005, 170(1): 350-362.

[5] *Risch, D.; Brosius, A.; Kleiner, M.:* Influence of the workpiece stiffness on the electromagnetic sheet metal forming process into dies[J]. Journal of materials engineering and performance, 2007, 16(3): 327-330.

Numerical and Experimental Approach to Deform the Sheet with Middle Block Die by EMF*

Hak Gon Noh[1], Hong Kyo Kim[1], Beom Soo Kang[1], Jeong Kim[1*]

[1] Department of Aerospace Engineering, Pusan National University, Pusan, South Korea

Abstract

Electromagnetic forming process (EMF) is one high strain-rate forming process using Lorentz force. In this study, numerical simulations were conducted to reduce the bouncing effect in EMF process with middle rectangular block and were using the cushion plate. A 3D electromagnetic numerical model was considered using the spiral type forming coil. Current circuit, coupled with spiral coil, was made in the numerical simulation to determine the design parameters, such as the system input current and the electromagnetic force. The velocity of plastic deformation was considered to predict the bouncing effect on the surface. A cushion plate was used between the forming coil and deformed sheet to reduce the bouncing effect. In the numerical simulation, the sheet is well fitted with objective die using the cushion plate. The simulation result shows that the bouncing effect was drastically reduced because of the velocity direction of the cushion plate. The experiment was performed in 24kJ to deform the Al 3104 with thickness of 0.5mm. The deformed sheet was well formed to fit with objective die. In addition, Z-displacement of the final shape was measured by 3D scan to compare with the simulation result. The measured experimental result and the numerical final shape are in good agreement when it comes to deformation.

Keywords

Electromagnetic forming, Lorentz force, Bouncing effect, 3D FEM, High strain-rate forming.

This work was supported by the National Research Foundation of Korea (NRF) grant funded by the Korea government (MSIP) through the Engineering Research Center (No. 2012R1A5A1048294) and excellent scientists support program in regional university (NRF-2012R1A1A4A01015131)

1 Introduction

Electromagnetic forming (EMF) is a kind of high strain-rate forming technology based on the repulsive forces generated by opposite magnetic fields in adjacent conductors. Recently, interest in electromagnetic forming for sheet metal for automotive, appliance, aerospace and other fields has been growing due to its feasibility as a method of forming aluminium and other low formability materials [1]. Electromagnetic forming process could be applied to various fields. In this paper, electromagnetic forming with a rectangular block shape on the middle of the forming die was presented to see the possibility and the potential of application of EMF. In the electromagnetic forming process, bouncing effects occur during the forming process due to its extremely high speed. The sheet easily bounced off the die because there is no medium between the sheet and the die. Therefore, the sheet poses a problem since it does have a proper shape. In this study, a cushion sheet was positioned between the forming sheets and the coil to in order to minimize the bouncing effect. To predict the deformation behaviour, numerical simulation model was presented with spiral coil, forming die and blank. In the electromagnetic forming simulation, the current density and the magnetic flux density of coil were presented; and Lorentz force, calculated by electric field, was also presented. In addition, an electromagnetic forming experiment with cushion plate was conducted to verify the forming simulation results. When the experiment was conducted without cushion plate, a large bouncing effect occurred and onset large wrinkling on the surface. However, when we deform the sheet using a cushion plate could significantly reduce the bouncing effect and the sheet was well deformed along the forming die. Consequently, cushion plate should be used for electromagnetic forming process in order to get a high quality product.

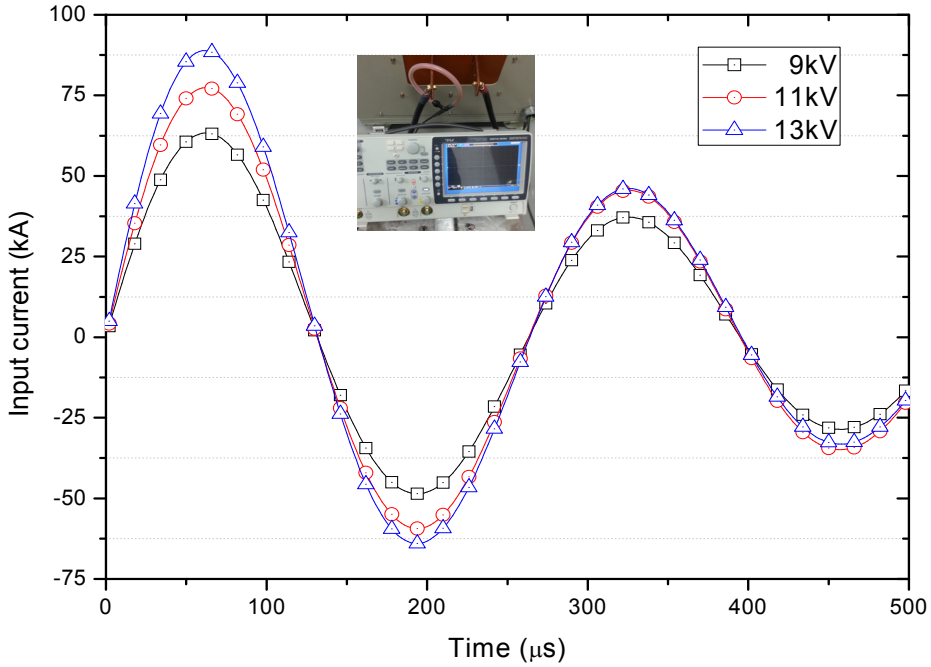

Figure 1: Input current measured by rogowski coil

2 Numerical simulation for EMF process

2.1 Numerical simulation model

As with any electromagnetic forming process, determining the value of the input current and the capacity is a primary parameter for determining the capacity of EMF machine. Furthermore, coil is a crucial component, as it is the means of delivering the force to deform the sheet. Therefore, prediction of the force and distribution of the coil become crucial since it is quite expensive and time consuming to fabricate all forming coils. For these reasons, numerical simulation is required to settle the EMF process since it enables the determining of the plastic deformation behavior with enough efficiency. To predict the deformation behavior and the proper forming coil shape in EMF process, an electromagnetic-structural coupling simulation was performed using the FEM and BEM. In the LS/DYNA EM module[2-3], 3-D finite element model was made by a spiral type coil. A finite element model of electromagnetic forming process was established as shown in Fig. 2. There are four parts: 6turns spiral type coil, forming plate and cushion plate with 0.5mm and rigid body die with a middle block. The size of the blank was 260mm by 260mm and the diameter of the forming coil was 140mm. The dead zone was 50mm in the center area with the forming depth of 15mm while the height of the middle block die was 5mm in the forming die. As shown in Fig. 1, a sign wave current flow was applied through the forming coil with 9V, 11V, 13kV, and the total simulation time was 500μs in the forming process.

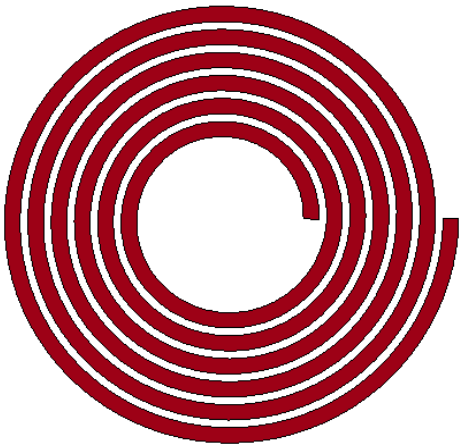

(a) Coil

(b) Die

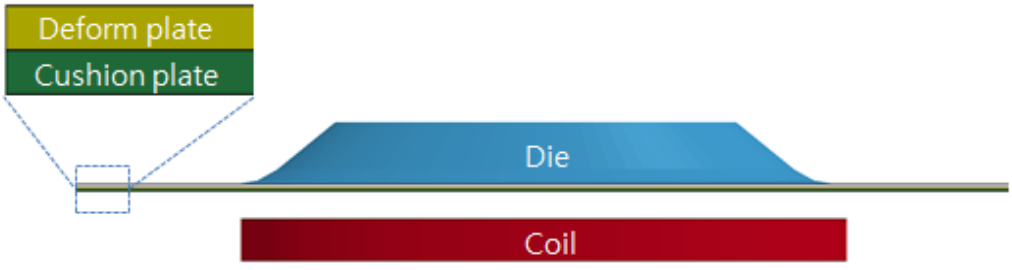

(c) Entire model

Figure 2: Numerical model for EMF process

2.1 Numerical simulation result

Figure. 3 shows the top view of the current density and magnetic flux density vectors of forming coil during the forming process. As offered in Fig. 3(a), the current density flow around the center area of coil is stronger than it is in other areas, and the current density vector moves in parallel along the coil. The maximum value of current was $7.15\times10^{9}\,A/m^{2}$ at 64μs, The vector direction of the current density was changed during the process. The vectors of the magnetic field in the coil are shown in Fig. 3(b). The maximum value of the magnetic field was 3.815 T(Wb/m^{2}) at 64μs and its direction was outside of coil form the center. Current density on the sheet generated from eddy current at 64μS was shown in Fig. 4(a) and the maximum value of the current density was $12.52\times10^{9}\,A/m^{2}$.

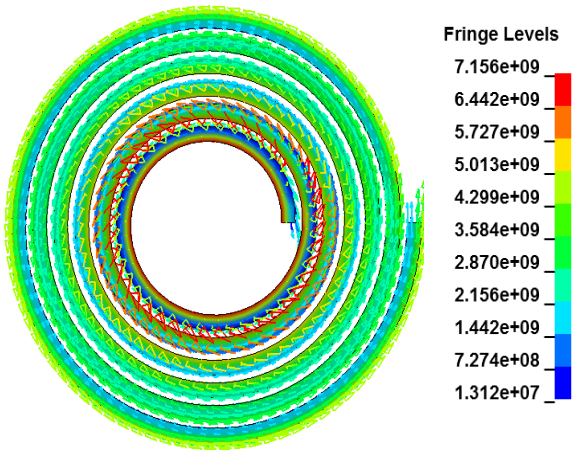

(a) Current density

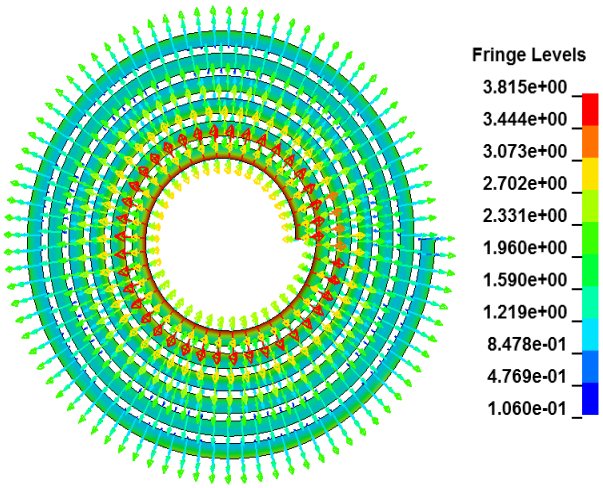

(b) Magnetic flux density

Figure 3: Numerical simulation result on the coil

Magnetic flux density on the sheet was also shown in Fig. 4(b) at 64μs. The maximum value of magnetic field was 5.73T at 64μs on the sheet. In addition, the direction of the current density on the sheet is in the opposite compared with the direction on the coil. Furthermore, given that the magnetic field vectors are perpendicular to the current density vectors, we can conclude that Lorentz's forces are occurred to deform the sheet by Faraday's law as shown in Fig. 4(c).

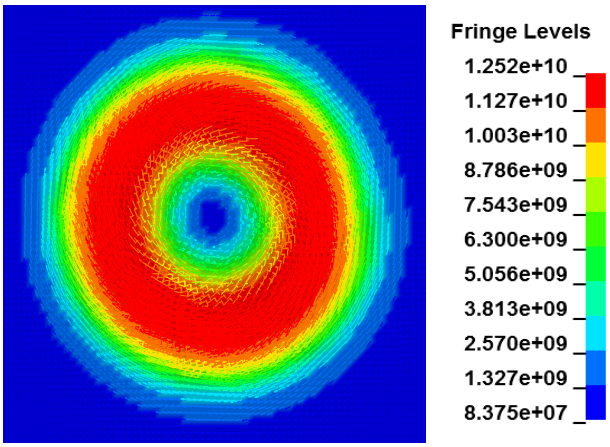

(a) Current density

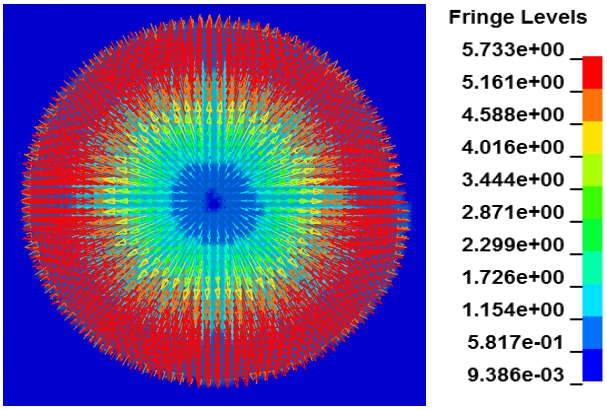

(b) Magnetic flux density

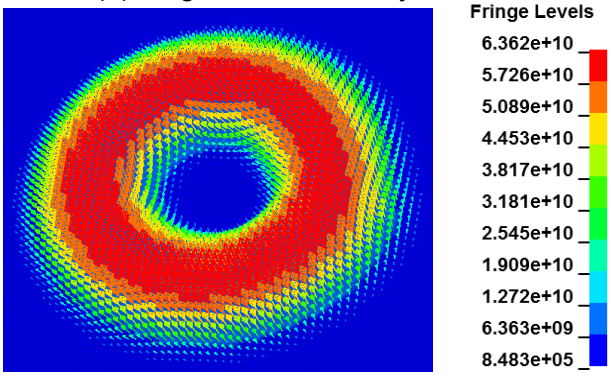

(c) Lorentz force

Figure 4: Numerical simulation result on the sheet

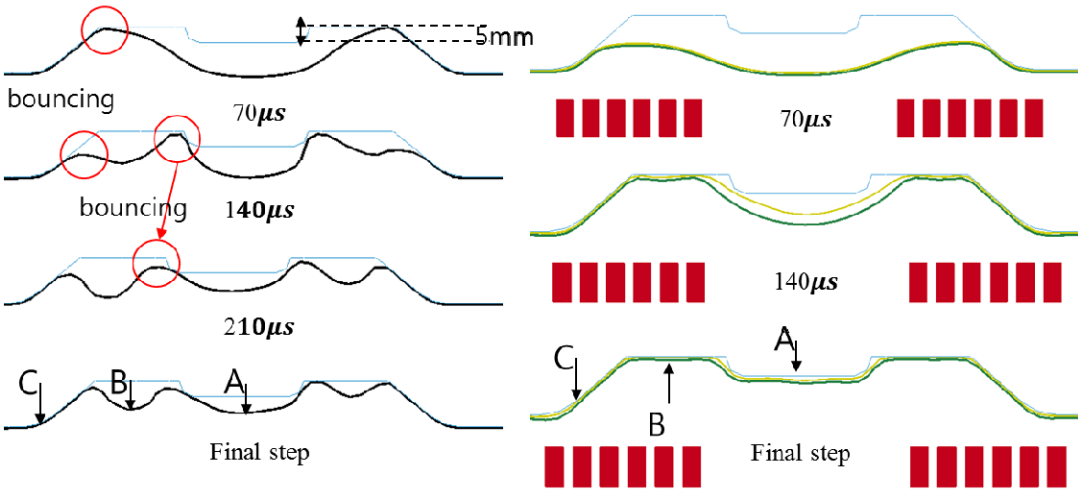

(a) Without cushion plate (b) With cushion plate

Figure 5: Plastic deformation during the forming process

The plastic deformation of the sheet with cushion plate and without cushion plate at 12kV is shown in Fig. 5. Figure. 5(a) shows 2-D schematic of the deformed sheet without cushion plate. The severe wrinkling was occurred after contact with die due to its high speed effect. However, the plastic deformation behaviour with cushion plate show in Fig. 5(b), the wrinkling was clearly reduced and the sheet was well contacted with the middle block die.

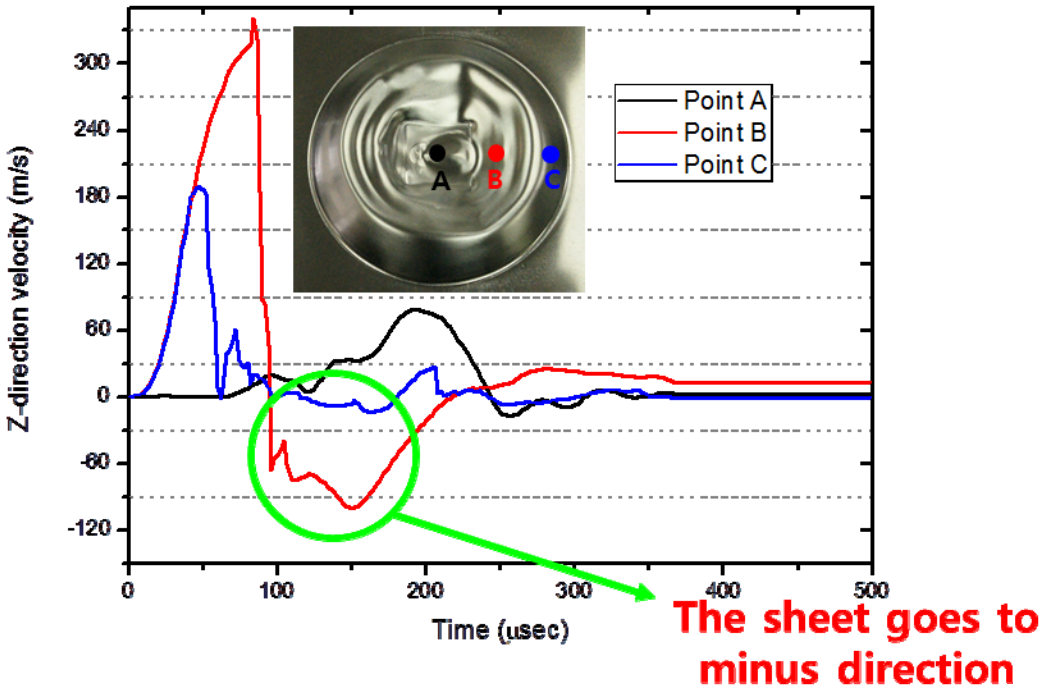

(a) Z-velocity at each points without cushion plate

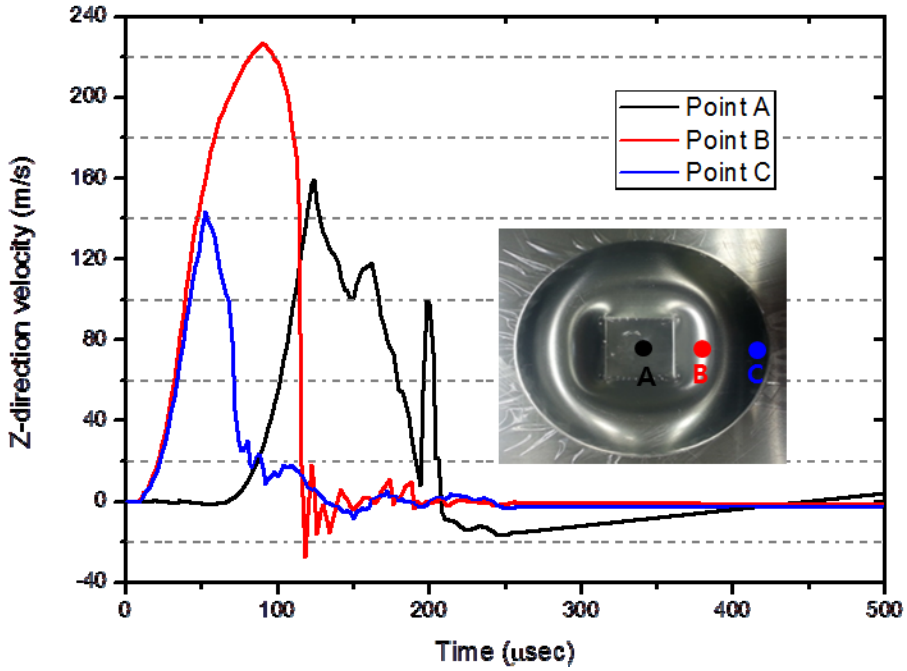

(b) Z-velocity at each points with cushion plate

Figure 6: Z-direction velocity in numerical simulation

Fig. 6(a) shows the Z-direction velocity at specified points A, B and C of the sheet. ; the maximum value was 330 m/s at point B. The sheet near the point B starts to bounce off at 82μS and the value of velocity was decreased until -100 m/s. The minus velocity was continued to 220μS, so the direction of the plastic deformation of the sheet was minus z direction between 82μS and 220μS. Consequently, the sheet dose not contact with the middle block dies because of the large bouncing effect around the point B. The cushion plate was inserted between the coil and the sheet. The cushion plate was also Al 3104 with 0.5T. The plastic deformation of the entire parts is shown in Fig. 5(b) at 70μs, 140μs and the final step. The sheet was close to each other at 70μs and the deformation behavior of the sheet was changed at 140μs. When the forming sheet was contacted with the die, its velocity was higher than the cushion plate and well deformed along the die at the final step. In the Fig 6(b), most of the velocity was in the upper zero points due to the cushion plate. So, a slight bouncing effect was occurred compared with previous result. In particular, at point B in the cushion plate, the peak velocity value was somewhat smaller than the deformed plate. The velocity at B point in both the deformed plate and the cushion plate shows that when the velocity at point B goes down to the minus direction, the large velocity of the cushion plate at point B still goes plus direction So, the bouncing effect on the deformed plate is drastically reduced due to the cushion plate because each sheet collided in the opposite direction. Based on this numerical simulation, we can see that the cushion plate should be used in EMF process to reduce the bouncing effect on the sheet.

3 Set up the EMF process

The capacitor, as one of the energy storage devices, accumulates the electrical charge in order to apply high value of current to the forming coil. They were connected using a flat busbar having a high electrical conductivity, as shown in Fig. 7. The storage energy can be controlled by a remote control with respect to the forming process. The energy could be obtained by Eq. (1). Here, the energy U is defined by the capacitance of capacitor C and the input voltage V.

$$(1)\ U = \frac{1}{2}CV^2$$

In the numerical simulation, electromagnetic forming equipment with 12 kV and 333μF must form the sheet with the cushion plate. The total energy was 24kJ to deform the sheet. Forming coil was designed as a spiral type having 50mm dead zone (Di=50) based on the simulation results. Schematic of coil and design parameters are shown in Fig. 7. A copper wire of 5mm(S=5) 10mm was used to form the patter shape die. The insulation films are attached between the forming coil, and its space was 2mm (W=2) each. The diameter and the number of turns were 140mm (Do=140) and 6(N=6), respectively.

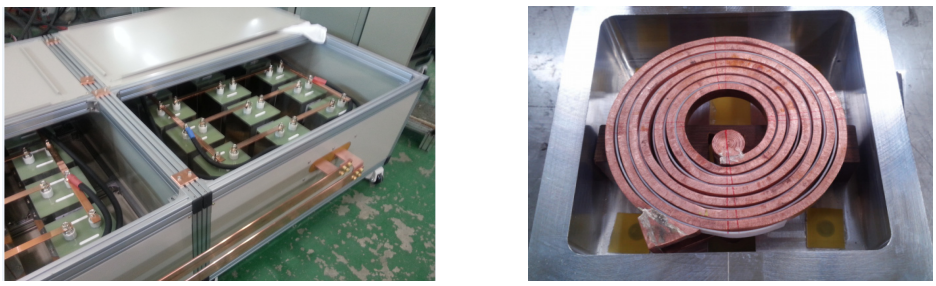

Figure 7: EMF machine and spiral coil

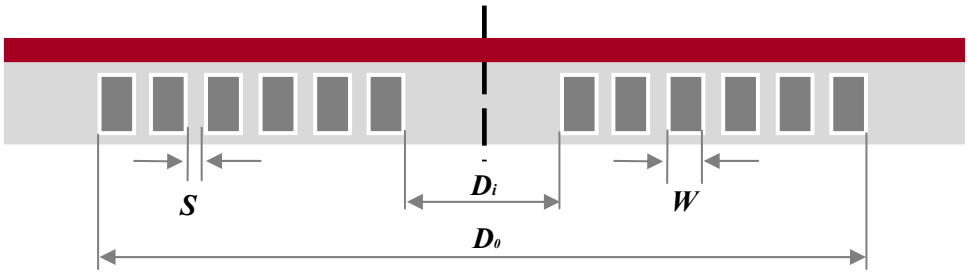

Figure 8: Spiral coil paramaters

3.1 EMF experiment using cushion plate

A forming test using the PNU-32 machine was conducted under the same condition. The EMF experiment was carried out using Al 3104, which is the initial thickness of 0.5mm. The forming coil clamped with the upper die with four ling bolts after placing the sheet on the coil as shown in Fig. 9. When the forming was conducted without the cushion

plate, a severe wrinkling was occurred due to the large bouncing effect. So, the shapes of sheet are not proper to use. As a result, the cushion plate was used to reduce the bouncing effect. The cushion plate was also Al 3104 with 0.5T, same as the deformed plate. Fig. 10 shows the experimental result of the deformed plate using the cushion plate at 12kV input voltage. The shape of the sheet, which is well deformed and wrinkling was significantly minimized on the surface compared with previous result. The numerical displacement date was compared with the experimental displacement data in X-direction view. The displacement of the experimental and the simulation results are compared in Fig. 11; the measured experimental profiles and the numerical final shape were in good agreement, although the height of the simulation part in some locations was slightly longer than the experimental data and the edge was sharper than in the experimental result. To sum up, it is obvious that using the cushion plate was better for EMF process with middle block die.

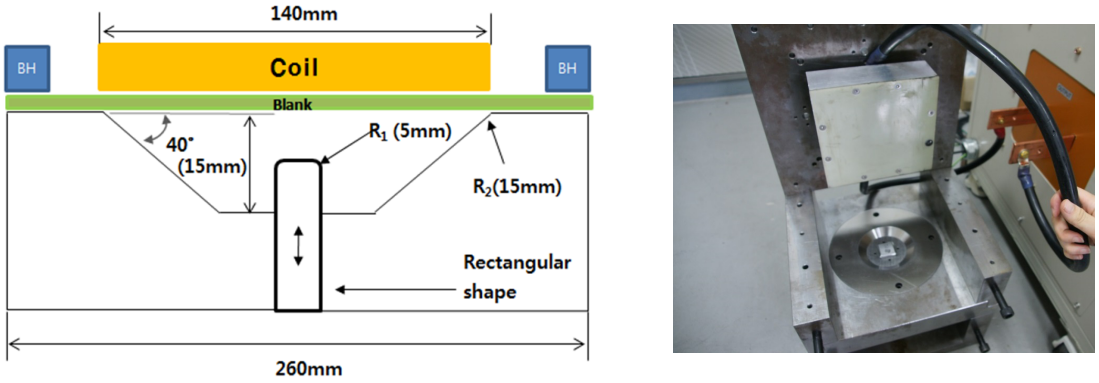

Figure 9: Forming set for EMF

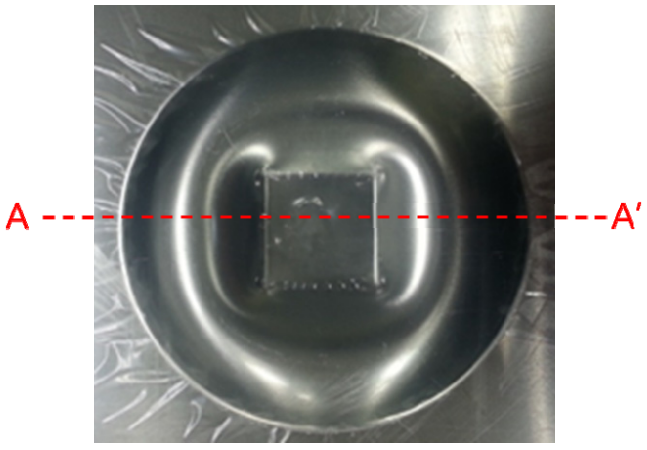

Figure 10: Experimental result with cushion plate

4. Conclusion

In this paper, an electromagnetic forming process with middle blocks was presented. 3D electromagnetic model combined with a current circuit was used in LS-Dyna EM module. First, a numerical simulation without cushion plate was conducted by LS-Dyna. The simulation result shows that the final deformation sheet does not fit well with die due to the bouncing effect between the sheet and the high strain rate. Therefore, a cushion plate was used to reduce the bouncing effect on the surface. The use of a cushion plate in EMF process drastically reduced the bouncing effect because of the velocity direction of the deformed plate and the cushion plate. The EMF machine was prepared based on the numerical simulation results to perform the forming test. The experimental results show that the sheet with cushion plate well formed with die in 12kV case. From this, we conclude that it is possible to set up EMF process by 3D numerical simulation and to reduce the bouncing effect on the surface to make a good product. In addition, we add that the bouncing effect should be reduced during the forming process in order to make well-formed sheet.

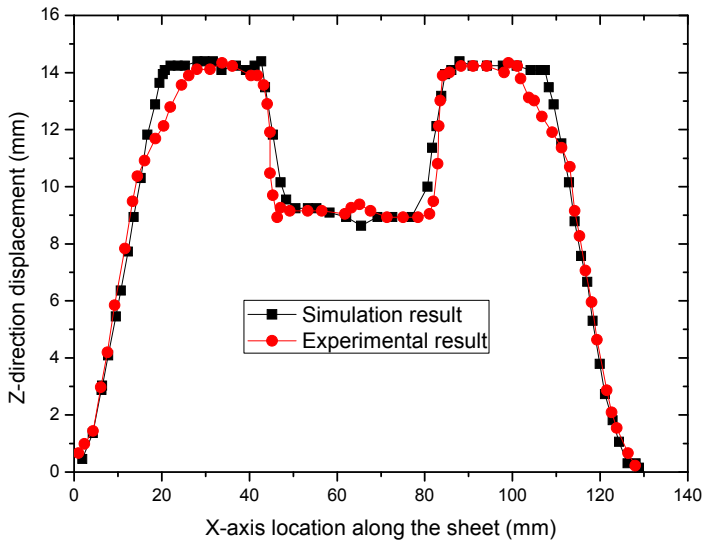

Figure 21: Z-displacement profile simulation and experiment result

References

[1] *Psyk, V.; Risch, D.; Kinsey, B.L; Tekkaya, A.E.; Kleiner, M.:* Electromagnetic forming-A review. J. Mater. Process. Tech., v.211, p.787-829.

[2] *L'Eplattenier, P.; Cook, G.; Ashcraft, C.:* Introduction of an electromagnetism module in LS-DYNA for coupled mechanical thermal electromagnetic simulations. 3rd international conference on High Speed Forming, 2008, p.85-96.

[3] *LSTC.: EM theory manual : Electromagnetism and linear algebra in LS-DYNA.*

A Numerical Investigation on Magnetic Pulse Cladding of Bi-Metal Tubes *

Zhisong Fan[1], Haiping Yu[1, 2], Chunfeng Li[1, 2]

[1] School of Materials Science and Engineering, Harbin Institute of Technology, Harbin, China
[2] National Key Laboratory for Precision Hot Processing of Metals, Harbin, China;

Abstract

Bimetal tubes are widely applicable in refrigerating industry, liquid conduit systems and other similar installations. Magnetic pulse cladding (MPC), based on a sequential joining/welding of lapping portions of long tubes, is a novel approach to fabricate bimetal tubes. This work presents an efficient numerical simulation of the MPC process to analyze the dynamic deformation and its effect on cladding result from a numerical view. A 2D axisymmetric model was established and a multi-steps cladding by forming was simulated based on the models similar to an actual MPC process. Between two subsequent steps, the stresses and strains were transferred from previous step to next one. The model predictions and experimental results were compared by the contour of the clad tube and showed an acceptable agreement. The advantages of a new field shaper with tile angle α1 of 3° and angle α2 of 13° were presented, and the magnitude of the magnetic pressure, the stress-strain field and velocity of collision were investigated. The numerical simulation benefits the process knowledge and assists the design of the field shaper.

Keywords

Numerical simulation, Magnetic pulse cladding, Bimetal tube, Field shaper

---

* *This work is based on the results of the National Basic Research Program of China (973 Program) [2011CB012805].*

1 Introduction

Bimetal tubes are widely applicable in refrigerating industry, liquid conduit systems and other similar installations. They have material properties that cannot be obtained from a single material. Enhanced mechanical properties, corrosion resistance, electrical conductivity, and wear resistance are the main industrial demands that can be met in this way [1-2].

Magnetic pulse cladding (MPC), based on a sequential joining/welding of lapping portions of long tubes, is a novel approach to fabricate bimetal tubes. Fig. 1 shows the general outline of MPC derived from the paper of Yu et al. [3].To investigate the dynamic deformation and determine its potential for a certain application, numerical simulation technique is an important part of the research process [4-5].

The general object of this study is to understand the complex phenomenon of deformation and investigate the effect of processing parameters on the quality of a bimetal tube during MPC. The MPC process was simulated by means of ANSYS/LS-DYNA code. The predicted results were validated with the profiles of a deformed tube in experiments.

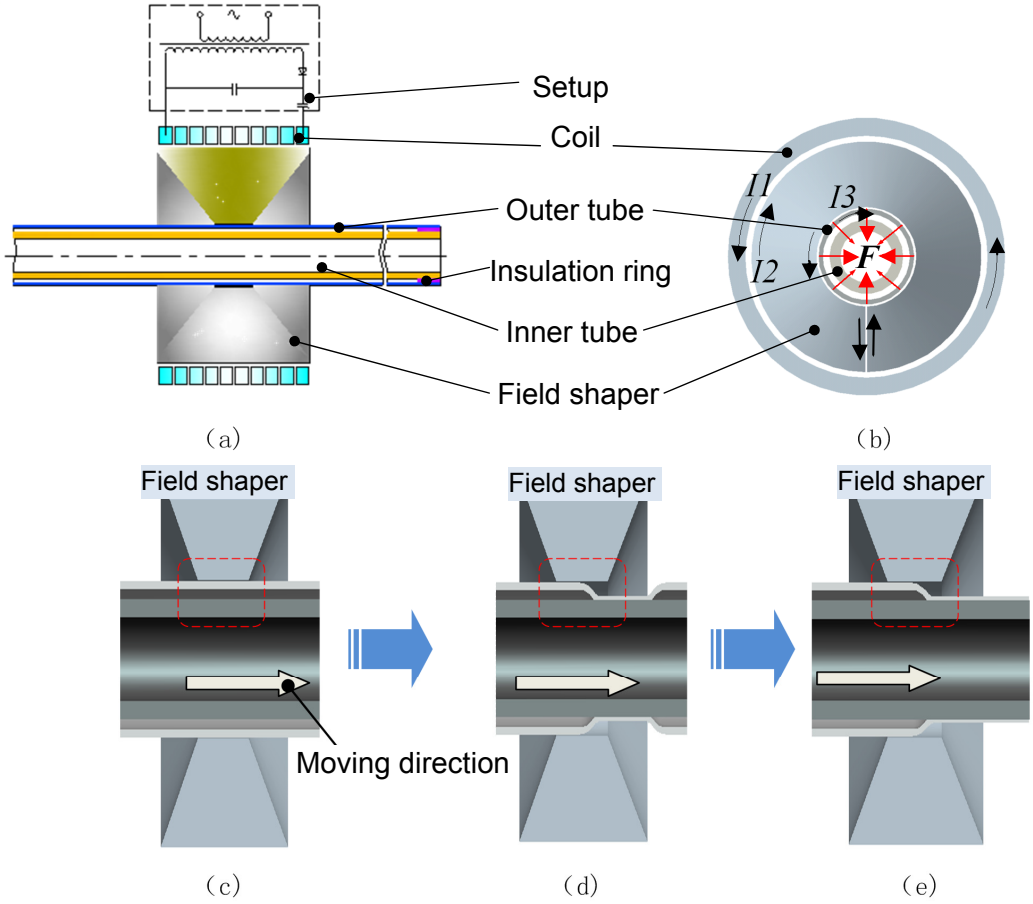

***Figure 1**: Schematic diagram of the MPC process from the published paper of Yu et al. [3]: (a) the setup assembly; (b) the magnetic force exerted on the outer tube; (c) co-axially aligned tubes for the 1st step of the MPC process; (d) the 2nd step of the MPC process with a defined feeding size; (e) the 3rd step of the MPC process with a defined feeding size.*

2 Methodology

2.1 Description of computational model

According to its deformation characteristics, the MPC process can be divided into a series of separate forming sub-steps, namely a “multi-steps” cladding process. Fig. 2 shows the numerical scheme for the proposed “multi-steps” cladding by forming on the basis of ANSYS EMAG/LS-DYNA software platform. In one step of MPC, EM model based on ANSYS/EMAG module was used to calculate the transient magnetic field. Then the resulted equivalent magnetic pressures were acted as the loading condition in mechanical model based on LS-DYNA module to predict the dynamic plastic deformation of the two tubes. When it comes to EM field simulation in the next step of MPC, the coil (including the field shaper) was moved to a new axial position controlled by the feeding size, and the deformed geometry of work piece was input by user-defined subroutines in APDL language. The modified EM model was used to predict the new body forces affected by the new configure of the work piece. For the second and subsequent steps in the mechanical model, the full restart method of the explicit code LS-DYNA was applied to link deformation (such as the stresses and strains) to exhibit a successive deformation sequence.

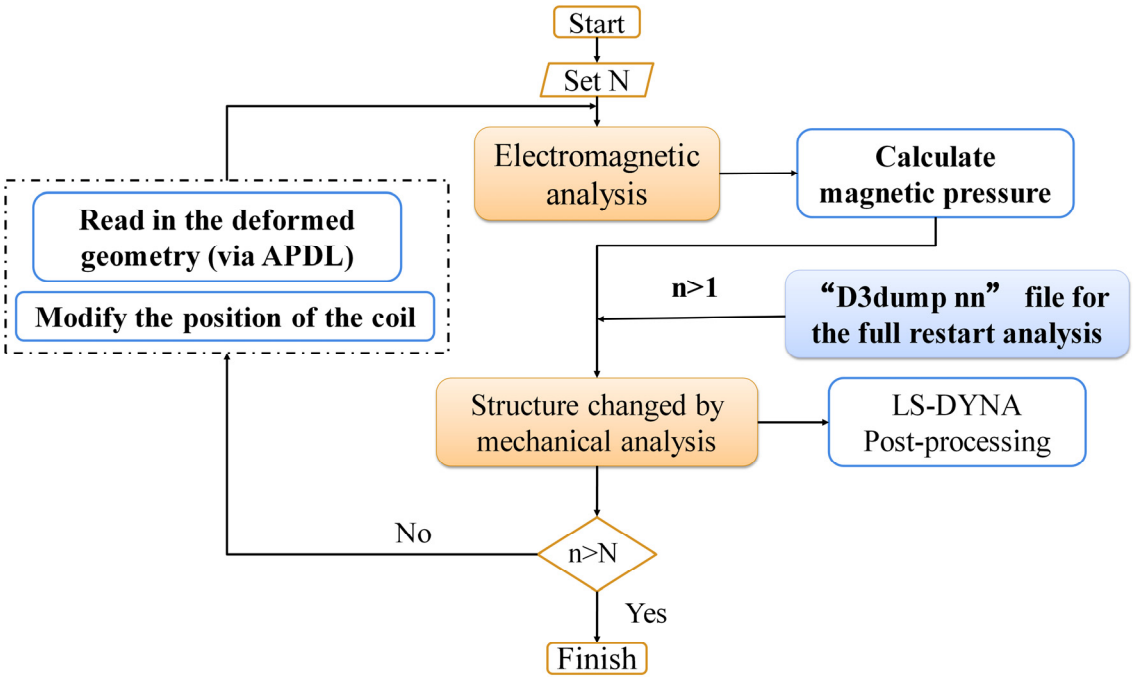

***Figure 2**: Flow chart of simulation procedure for the MPC process using ANSYS/LS-DYNA (N represents the feeding times, n is the ordinal number of N)*

2.2 The FE model and its features

A 2D axisymmetric model as shown in Fig. 3 (a) was established, which makes the most of the experimental geometric symmetry. The EM model of the 1st step of MPC was shown in Fig. 3 (b) and it corresponding mechanical model was shown in Fig. 3 (c).

In the EM simulation phase, the electromagnetic model was excited by a pulse of current through the coil, which is measured experimentally by a Rogowski coil. The typical discharge current is a damped sinusoidal function given as:

$$I = I_0 \exp(-\beta t)\sin(\omega t) \tag{1}$$

where I_0 is the nominal peak value of the discharge current; β is the damping exponent and ω is the angular frequency. The parameters in equation (1) were fitted from the experimentally measured data. The resulted equivalent magnetic pressures were used in this work [6]. The magnetic pressures applied as a loading condition were also via a user subroutine in APDL language.

In the mechanical simulation phase, the strain-rate hardening effect was considered by means of the Cowper-Symonds constitutive model:

$$\sigma = \sigma_y \left[1 + \left(\frac{\dot{\varepsilon}}{C}\right)^P\right] \tag{2}$$

where σ_y is the quasi-static flow stress; $\dot{\varepsilon}$ is the plastic strain rate (s^{-1}); C=6500 s^{-1} and p=0.25 are specific parameters for aluminium and C=40 s^{-1},p=0.2 for steel. The coil and the field shaper were attributed to rigid body. The detailed material parameters were given in Table 1.

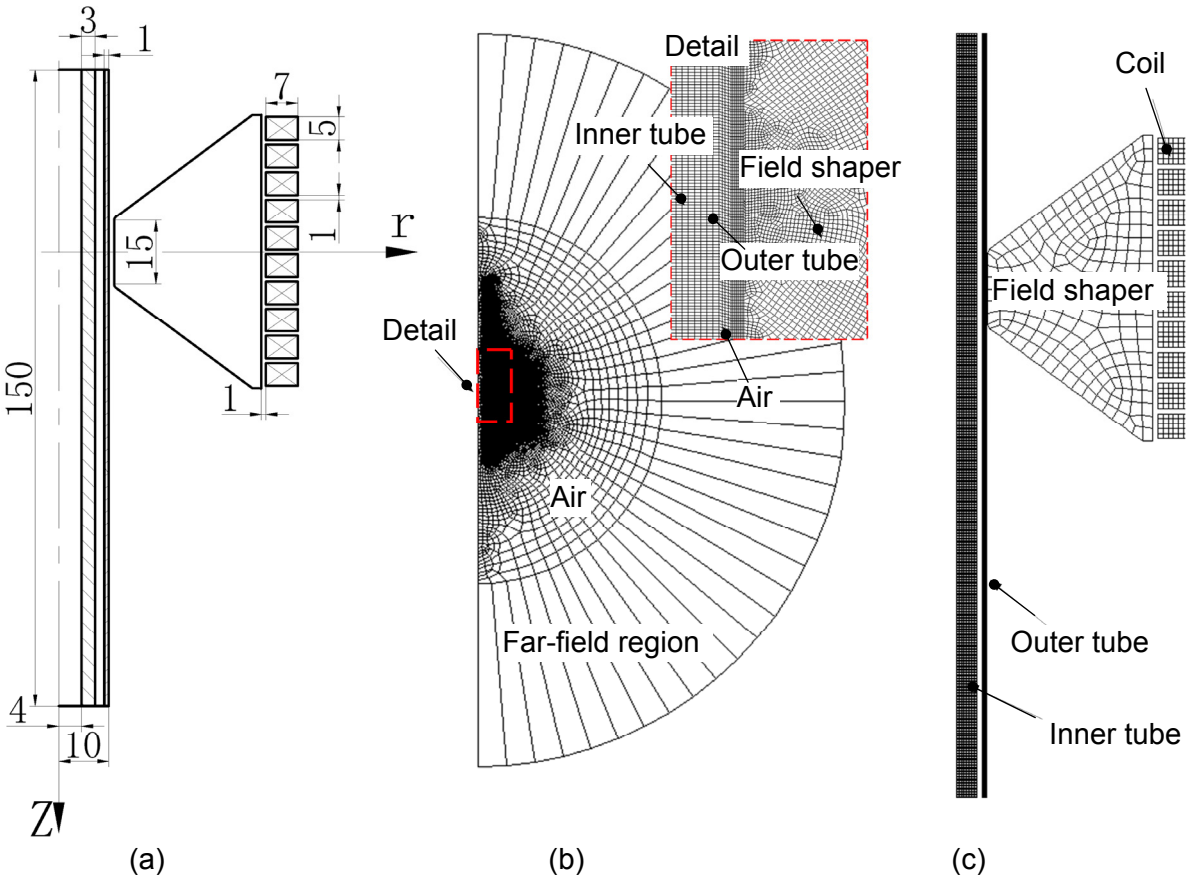

***Figure 3**: Geometry model and finite element region for magnetic pulse cladding system:(a) Geometry model; (b) Electromagnetic field for 1st stage of MPC and detail including tubes and field shaper; (c) Mechanical field of MPC*

Material	Resistivity (Ω•m)	Yield strength σ_s (MPa)	Young's modulus (GPa)
AA3003 (outer tube)	3.4e-8	162	68.6
Mild Steel 1020 (inner tube)	1.0e-7	310	207
Copper (coil and field shaper)	2.17e-8	--	--

Table 1: *Material parameters of the tubes*

2.3 Magnetic pulse cladding experiments

In order to verify simulation results, relevant experiments were carried out. The MPC process was studied experimentally and all basic data could be found in Refs. 3. The verification experiments were performed using 20 kJ EMF systems. The setup has a capacitor with 100 μF capacitance which may be charged to a maximum of 20 kV. The coil has 10-turns with a 5×7 mm cross-section. It was noted that two kinds of field shaper were modelled in this work for the reason that it could be of much value in designing its geometry. Geometry parameters of two kinds of field shapers were derived from Ref. 3, as shown in Fig. 4.

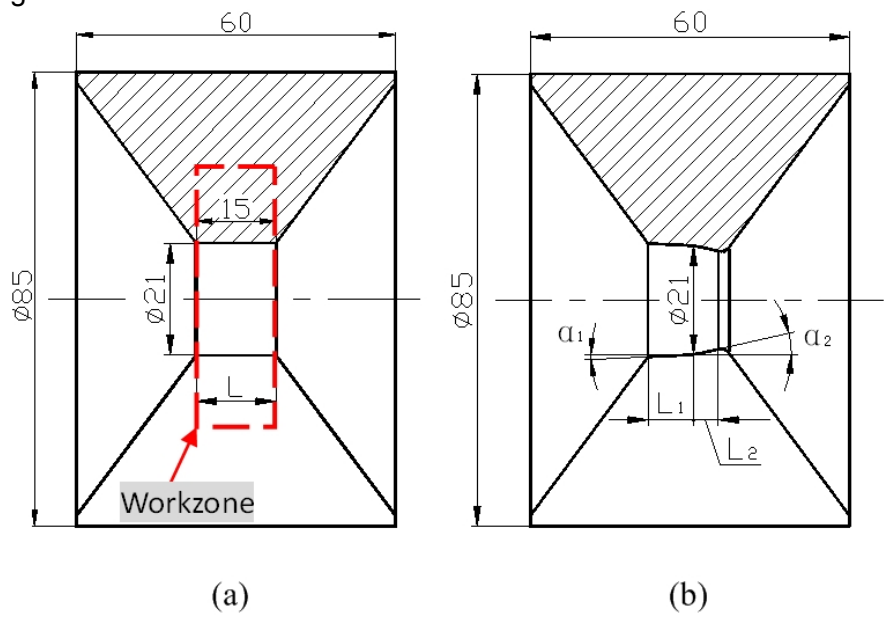

Figure 4*: The cross-section of two kinds of field shaper geometry: (a) the constant cross-section field shaper (C-field shaper) and (b) the profiled field shaper (P-field shaper)*

3 Results and discussion

3.1 Verification experiments

Fig. 5 (a) shows the final formed part with the predicted radial displacement. To extend the 2D model into a 3D format is to compare it with the experimental sample formed by MPC using the C-field shaper. The ripple defect could be observed in the outer surface of the clad tube in Fig. 5 (b). The height of the ripple was measured via the distribution of the final radial displacement, as illustrated in Fig. 6. Fig. 7 presented an optical micrograph image of the transition region including one ripple. The height of a hump (about 0.06 mm) is slightly smaller than the predicted height (0.09 mm).

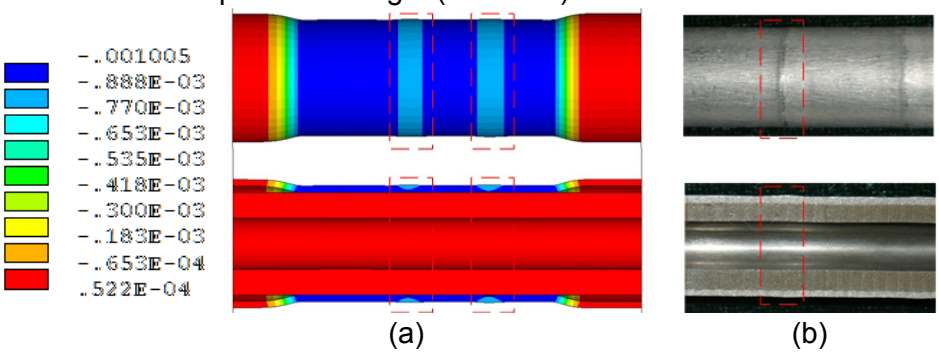

***Figure 5**: Predicted and experimental profiles deformed by MPC: (a) Predictions of final radial displacement contours and (b) the ripple in the surface of the formed part*

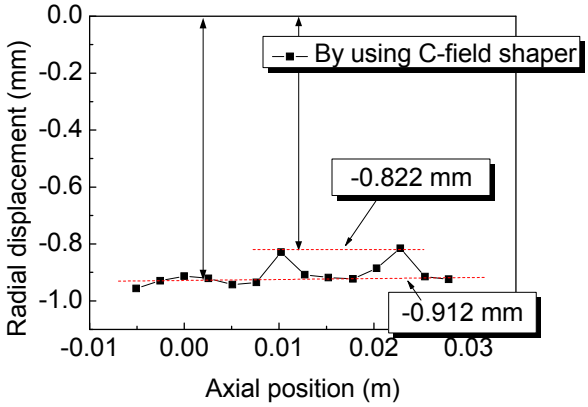

***Figure 6**:The distribution of the final radial displacement of the outer tube for three steps of MPC*

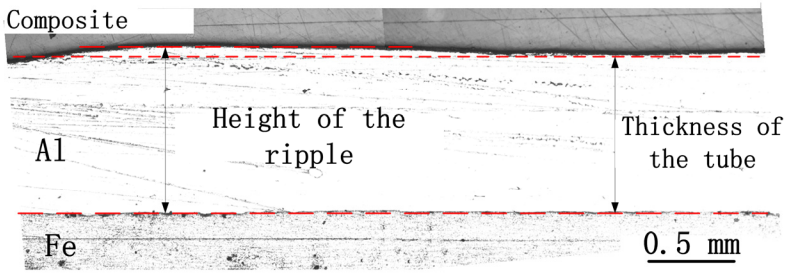

***Figure 7**: Cross-section for one ripple in the optical micrograph image*

3.2 Deformation behaviours in local transition region

3.2.1 The case of C-field shaper

As stated earlier, the magnetic pulse cladding process consists of a repeated unit. Fig. 8 showed the characteristics of the magnetic field in the second step by using C-field shaper. The magnetic lines diffuse through the transition zone. And the induced current in the transition zone is smaller than that flowing in its adjacent region. The resulting magnetic pressure was illustrated in Fig. 9. So the ripple defect generates in the transition zone.

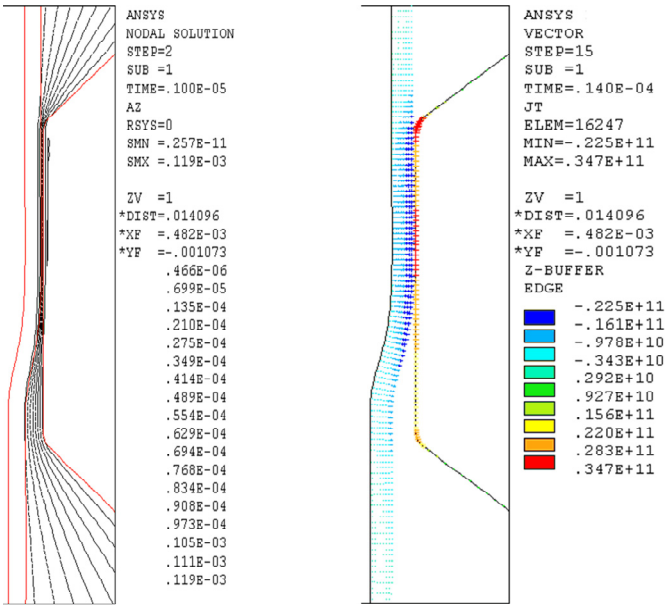

(a) (b)

***Figure 8**: Characteristics of the magnetic field in the early time of the 2nd step of MPC: (a) Distributions of magnetic flux line; (b) Contours of induced current on the workpiece and the C-field shaper*

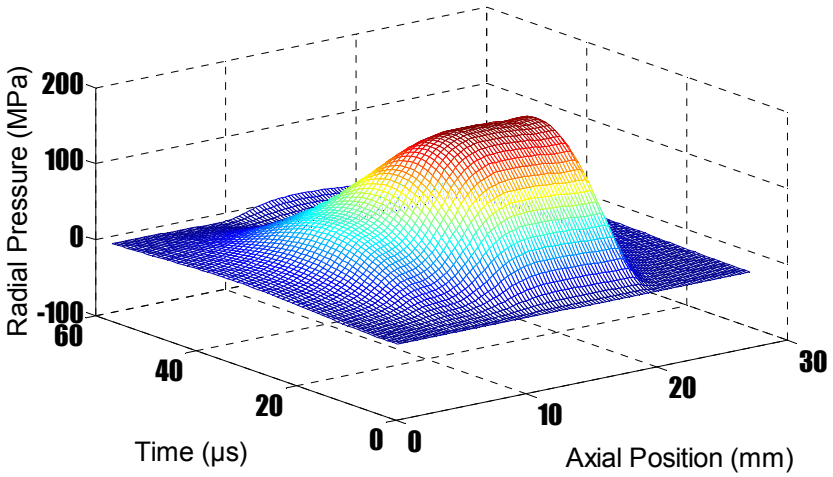

***Figure 9**: The distribution of magnetic pressure over time along the axial direction during the 2nd step of MPC in the case of C-field shaper*

3.2.2 Modelling of the P-field shaper

The transition geometry between two cladding steps depends on magnetic pressures distribution and the latter lies on the relative position between outer tube and working zone of field shaper. The smaller gap between them causes larger pressure acting on the outer tube. Therefore, to fit the profile of the transition geometry, the profile of working zone of field shaper was changed and a P-field shaper was proposed. The P-field shaper with a tile angle α1 of 3° and angle α2 of 13° was modelled. Fig. 10(a) shows the magnetic flux lines in the second step of MPC. In the early time, all the magnetic flux lines are restrained in the gap between the outer tube and the P-field shaper. Due to the tile angle of 13°, the density of the magnetic flux line in transition zone increases compared to that of the C-field shaper used. Fig. 10(b) and (c) presented the distribution of the induced current and Lorentz's force. Fig. 11 showed the resulting distribution of magnetic pressure. The peak locating in the transition zone is about 200 MPa, 2.5 times of that of the C-filed shaper in same region shown in Fig. 9. Away from the transition zone, the magnetic pressure decreases slightly due to the setting of title angle α1 of 3°. This kind of distribution characteristic of magnetic forces helps to deform the transition zone and obtain the oblique collision during the multi-step stage of MPC.

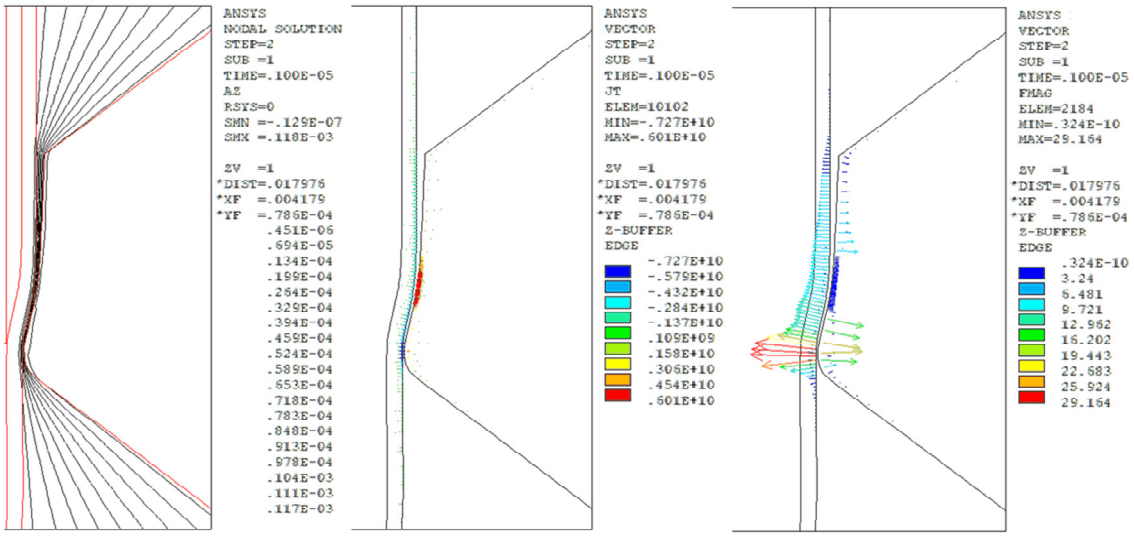

(a) (b) (c)

***Figure 10**: characteristics of the magnetic field in the early time of the 2nd step of MPC: (a) Distributions of magnetic flux line; (b) Contours of induced current on the work piece and the P-field shaper; (c) The distribution of the vector resultant of the Lorentz's forces developed in the work piece and the P-field shaper.*

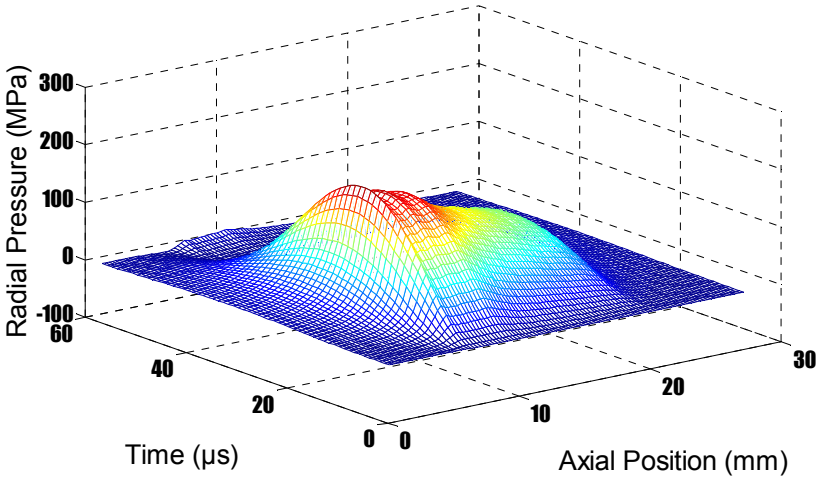

***Figure 11**: The distribution of magnetic pressure over time along the axial direction during the 2nd step of MPC.*

3.2.3 Comparison of two collision mode

Fig. 12 showed the comparison of clad tubes' geometry with the original and the improved field shaper. Fig. 13 presented the results of the bonding area, conducted by the peeling test. As can be seen, the bonding area concentrated in the first collision region and the bonding area was about 22% of the whole cladding area in the C-field case. By using the P-field shaper, the bonding area increased to 47%, as shown in Fig. 13. With improved field shaper, the clad tube deforms in a desired manner that it can dynamically impact the base one obliquely in a cladding step. The numerical simulation could assist the design of the field shaper.

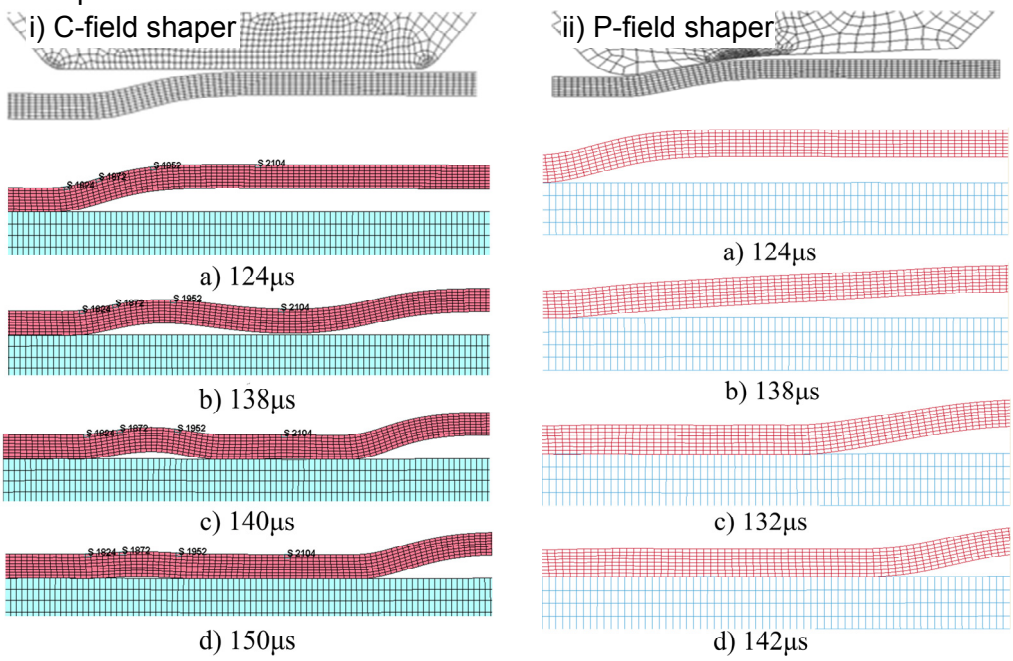

***Figure 12**: LS-DYNA prediction of the change of geometry of the clad tube during the second step of MPC: (i) in the case of C-field shaper and (ii) in the case of P-field shaper*

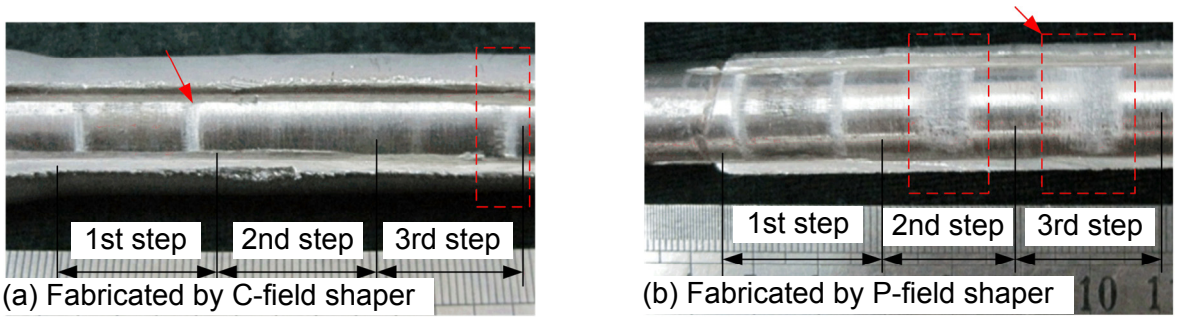

***Figure 13**: Comparison of the rate of the bonding area: (a) in the case of C-field shaper and (b) in the case of P-field shaper*

4 Conclusions

In the present paper, the basic aspects of the magnetic pulse cladding process were numerically simulated. The proposed numerical method was validated by the results of contour of the deformed tube in experiments. The following conclusions are drawn:

1) Based on the models similar to an actual MPC process, a numerical scheme for multi-steps cladding by forming was proposed. The scheme was successfully applied to simulate the MPC process that provides the basis for further investigating the deformation mechanism of MPC.

2) In the subsequent cladding phase, the inharmonious deformation results in the ripple defect in the surface of the clad tube. The profile of working zone of field shaper can be changed to fit the profile of the transition geometry to shape the distribution of the magnetic field.

3) The P-field shaper improves the distribution of the magnetic pressure during the multi-step stage of MPC. With improved field shaper, the outer tube deforms in a desired manner that it can dynamically impact the base one obliquely in a cladding step.

References

[1] Schulz, W.; Worringer, J.; Osborn, D.: Process for the manufacture of cladded metal pipes. United States Patent, No. 5940951, 1999.

[2] Mohebbi, M. S.; Akbarzadeh, A.: Fabrication of copper/aluminum composite tubes by spin-bonding process: experiments and modeling. The International Journal of Advanced Manufacturing Technology, 54(9-12), p. 1043-1055, 2011.

[3] Yu H. P.; Fan Z. S.; Li C. F,: Magnetic pulse cladding of aluminum alloy on mild steel tube [J]. Journal of Materials Processing Technology, 214(2): p. 141-150, 2014.

[4] Oliveira, D. A.; Worswick, M. J.; Finn, M.; Newman, D.: Electromagnetic forming of aluminum alloy sheet: free-form and cavity fill experiments and model. Journal of Materials Processing Technology, 170(1), p. 350-362, 2005.

[5] Fenton, G. K.; Daehn, G. S.: Modeling of electromagnetically formed sheet metal. Journal of Materials Processing Technology, *75*(1), p. 6-16, 1998.

[6] Psyk, V.; Risch, D.; Kinsey, B.L.; Tekkaya, A.E.; Kleiner, M.: Electromagnetic forming-A review. Journal of Materials Processing Technology 211, 787-829, 2011.

Analysis of Strain Nonuniformity Index (SNI) in electrohydraulically formed sheet metal component

S. K. Salunke[1)], **P. P. Date**[1)]

[1)] Department of Mechanical Engineering, Indian Institute of Technology, Bombay, India

Abstract

In sheet metal parts formed by Electrohydraulic (free forming) process, a spherically shaped reflector is predicted to result in a highly non-uniform thickness strain distribution. As expected, the thickness strain (and hence thinning) is maximum at the top of the formed dome. The probability of failure is therefore highest at this location. A finite element model is formulated in ABAQUS explicit to generate the strain distribution in sheet metal. The model considers a water filled chamber to transmit the pressure pulse. The effect of the electrical discharge between the electrodes is modeled as a pressure wave of a certain magnitude originating from the location of the electrodes. The constitutive relation for the sheet is described by the Johnson-Cook model and non-deformable/ stiff tools are used.

The extent of non-uniformity in thickness strain distribution has been expressed in terms of Strain Non-uniformity Index (SNI). It is the difference between the peak thickness strain (PTS) and the average thickness strain (ATS). For successful forming, the value of SNI should be as low as possible. This is enabled by an alternate design of the reflector which is compared with the spherical shape. The pros and cons of using either shape of reflector are examined in the paper.

Keywords

Electrohydraulic forming, Thickness strain, SNI analysis

1 INTRODUCTION

The conventional approach to sheet metal forming uses two-sided tooling (e.g., solid die and a solid punch) and involves metal-to-metal contact between the punch, die and the work piece to achieve forming. This introduces certain difficulties, given increasing strength (requiring greater forming force and better lubrication to overcome the higher force of friction) and hardness of the metals that are being formed. Also, conventional sheet metal forming

processes use significant amounts of energy to form the sheet metal. Despite all efforts, the strain distribution remains highly non-uniform on account of frictional effects inhibiting sheet deformation at regions in contact with the tools, thereby shifting deformation to the 'unsupported region'. This makes it difficult to form thin, high strength sheet material used to produce very thin automotive panels required to significantly decrease the weight of the automobiles. [2, 5]

Electrohydraulic forming (EHF) is a high-rate forming process based on the high-voltage discharge of capacitors between two electrodes positioned in a fluid-filled chamber. Since pressure is transmitted through a liquid medium, the distribution of pressure is expected to be more uniform than when conventional tools are used. One therefore expects a better uniformity of strain distribution over the deformed sheet compared to the conventional forming route. EHF process is extremely fast; uses lower-cost, single-sided tooling; and allows significantly increased formability for many sheet metal materials because it involves high strain rates [1]. Setup time, which presently is relatively high, can be reduced by automation. Advancements in the EHF process have the potential to reduce the thickness variation of sheet metal used in the construction of automobile panels and frames. The application of EHF by automotive manufacturers and their suppliers will significantly enhance the product quality, compared to the conventional stamping process.

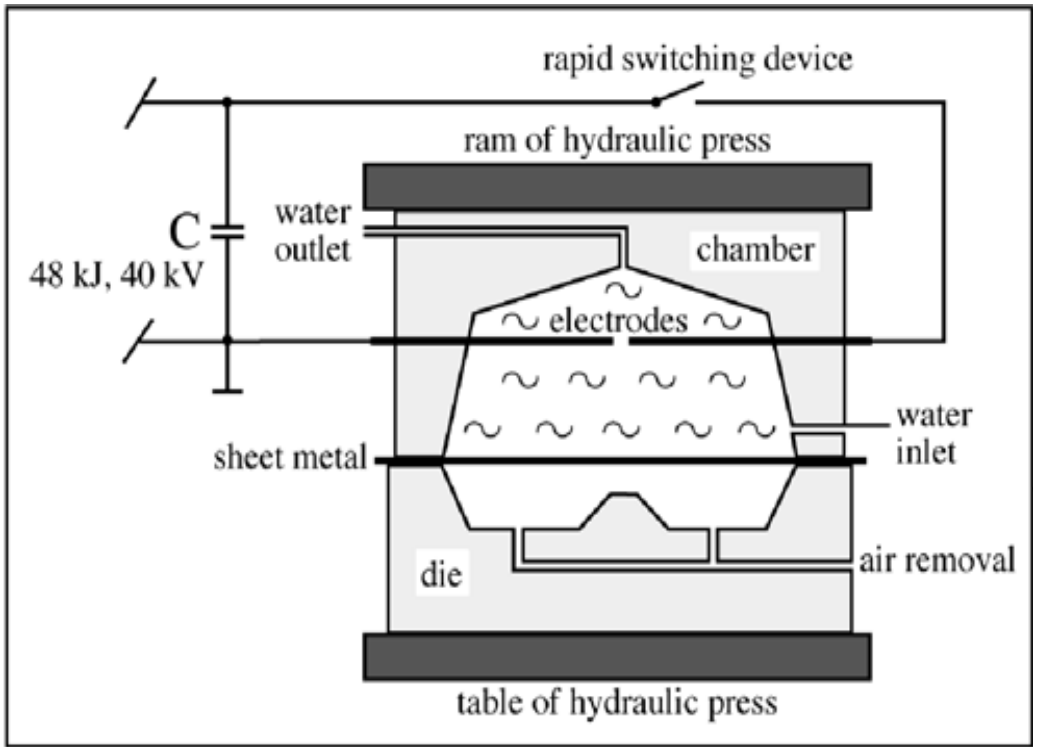

Figure 1: *Basic Principle of Electrohydraulic forming [1]*

Mathematical modeling of high-speed forming processes is widely used for various ends. In the present work, the effect of reflector geometry in electrohydraulic forming, on the resulting pressure and true thickness strain distribution is studied. A spherical reflector (representing a relatively simple geometry) is compared with that of the less simple geometry of a convex reflector with reference to pressure and thickness strain distributions.

2 FINITE ELEMENT SIMULATION

Electrohydraulic forming simulation is a considerable challenge because of the Multiphysics nature of the process. At first electrical energy must be converted into plasma. There is a boundary between the high pressure plasma and high pressure water vapor, and a boundary between the water vapor and the liquid. The liquid interfaces with the steel blank, and the steel blank accelerates and interacts with the die surface. Models must therefore be developed for: 1) the electrical nature of the discharge channel or plasma; 2) physical water vapor channel; 3) the liquid as a pressure transmitting medium; 4) blank deformation; 5) chamber (tool) deformation and 6) the blank in contact with the die [3].

Since, Electrohydraulic forming process is high strain rate process and completes within few microseconds, following simplifying assumptions are made here in simulations:

1. Heat transfer via heat conduction is neglected;
2. Phase conversion from water to vapor is neglected entirely;
3. All energy that is discharged into plasma is considered to contribute to the generation of blast waves only;
4. Plasma is treated as a gas with a constant mass that is surrounded by an acoustic medium (water), in which blast waves are generated;
5. Time lag between the direct and reflected incident waves is negligible owing to small size of the work piece investigated, and relatively high velocity of shock waves.

A dynamic explicit Finite Element analysis was carried out to simulate the Electrohydraulic Forming process. The program used for the simulation is ABAQUS Explicit. The water is the media which transmits the shock waves which in turn deform the blank. Water is shaped as the inside surface of the chamber that contains it. In the EHF experiment the pressure is build up by an electric discharge in the rear end of the water containing chamber, which in the simulation is represented by pressure wave generated at the point shown in Figure 2.

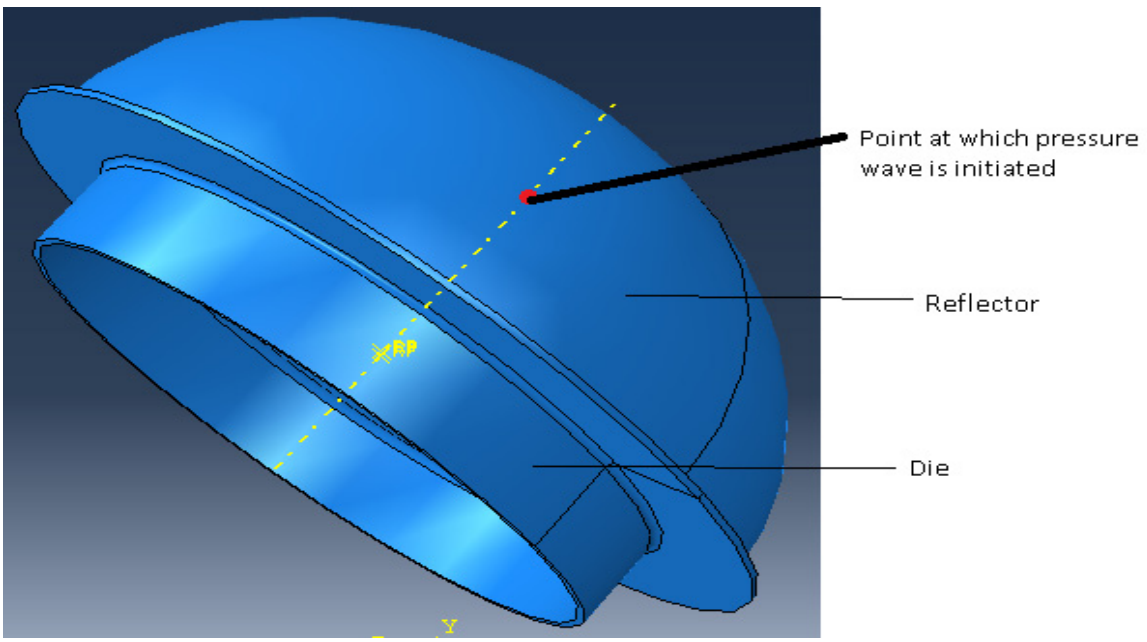

Figure 2: *Assembled model used in simulation*

2.1 Material Properties

Blank:

The JC model is a widely used and well recognized model for high strain rate material deformation analysis, [4]

$$\sigma = \left[a + b(\varepsilon)^n \right] \left[1 + C \ln\left(\frac{\dot{\varepsilon}}{\dot{\varepsilon}_0} \right) \right] \quad (1)$$

Table 1: *Material property for the simulated sheet material [2]*

Steel grade	IF 210
Johnson Cook A, [MPa]	300
Johnson Cook B, [MPa]	344
Johnson Cook, C	0.03
Johnson Cook, n	0.53
Strain rate, (1/s)	0.01
Density ϱ, (kg/m^3)	7800
Poisson's ratio, μ	0.3
Young's Modulus, E [GPa]	210

Water:

The property for the water was set to an acoustic medium with a density of 1000 [kg/m^3] and a bulk modulus of 2.3*10^9 [Pa].

- The bulk modulus

$$K = -V\left(\frac{\partial \rho}{\partial \upsilon} \right) \quad (2)$$

- The speed of sound,

$$c = \sqrt{\frac{K}{\rho}} \quad (3)$$

2.2 Interactions

The contact interaction between die and blank is set to a surface to surface condition, with contact property, tangential behavior and a friction coefficient of 0.1 in penalty contact. The incident wave interaction is used to specify magnitude of pressure at source point.

2.3 Load

The driving force in the EHF process is the electric discharge above the sheet. In the model it is represented by the pressure wave originating on the common axis of the chamber and the circular blank at distance of 50 mm from the top of the blank. The normalized pressure pulse variation with time is shown in Figure 3. It is seen that the pressure at the point of discharge (origin of the pressure pulse) dies down in about 100 microseconds.

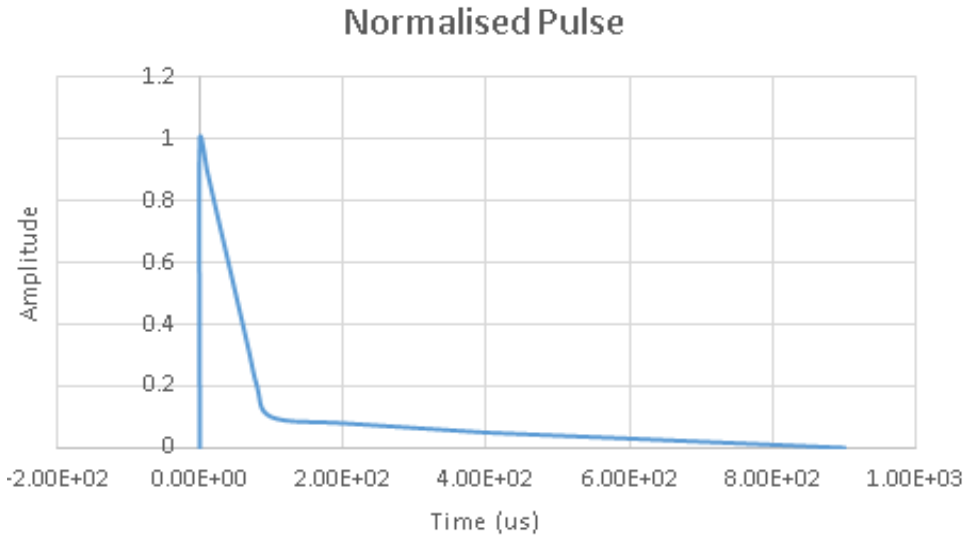

Figure 3: *Normalized Pulse used for the simulation in ABAQUS*

2.4 Reflector geometries

The geometries of the two reflectors used in the study are spherical and convex as shown in Figure 4. A spherically shaped reflector is predicted to result in a comparatively non-uniform thickness strain distribution than convex reflector.

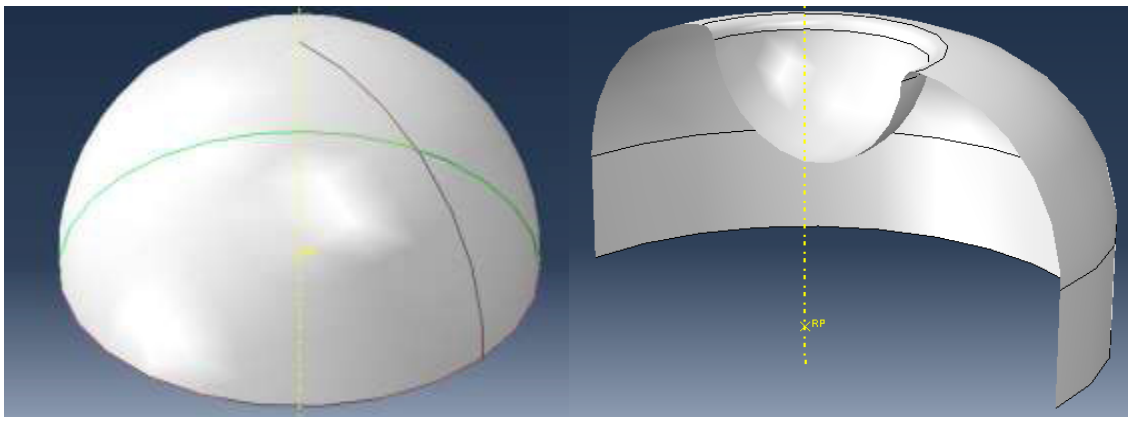

Figure 4: *Two shapes of reflectors used in simulations-1) Spherical, 2)* Convex

3 SIMULATION RESULTS

As expected, the thickness strain is maximum at the top of the formed dome. The probability of failure is therefore highest at this location. The extent of non-uniformity in thickness strain distribution has been expressed in terms of Strain Non-uniformity Index (SNI). It is the difference between the peak thickness strain (PTS) and the average thickness strain (ATS) [6].

$$SNI = PTS - ATS \tag{4}$$

From figure 5 it is clear that spherical reflector results in high thickness strain at the top of dome.

3.1 Strain distribution

The true thickness strain variation along the radius is shown in figures 5, 6 and 7 for the two reflectors. It may be noted that the minimum true thickness strain occurs radially outward (at a greater radius) in a convex reflector at low depths as compared to the spherical reflector. The reverse is true at higher depths. With increasing depth of forming, this point of minimum thickness strain is seen to move away from the center for both the reflector geometries. Table 2 shows the relative non-uniformity of thickness strain distribution in the form of the SNI. At low deformation, the SNI values do not differ very much. However, as the depth increases the difference in SNI also increases (figure 8). In all cases, the SNI for the spherical reflector is always higher than that of the convex reflector, indicating superior quality with a convex reflector.

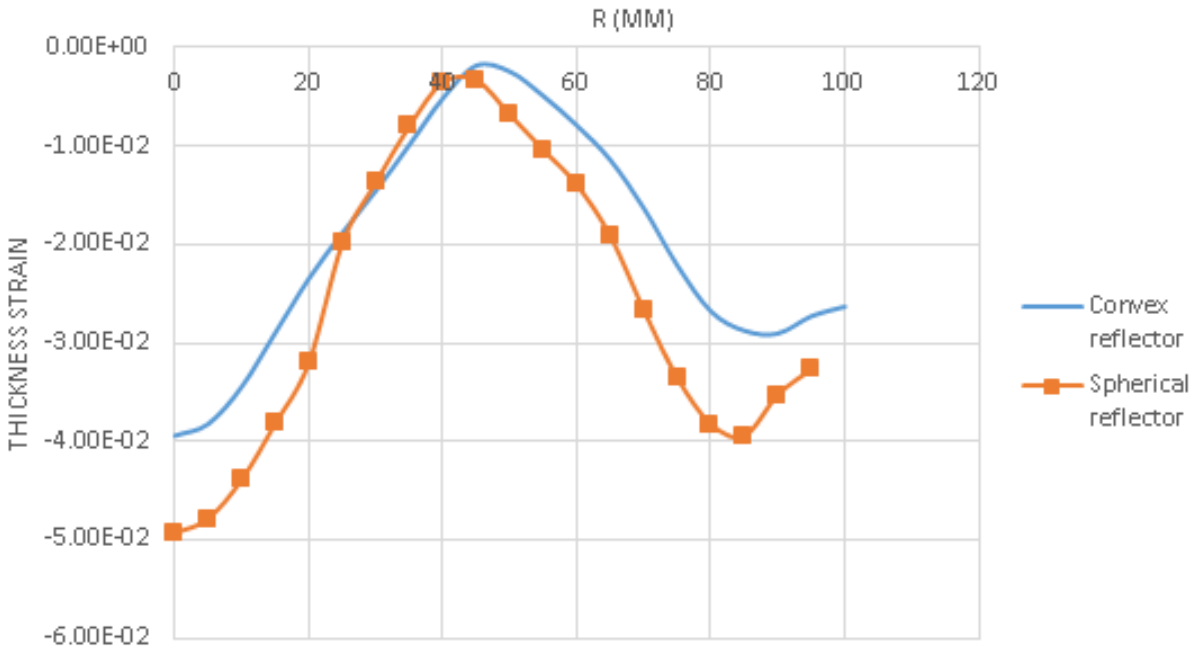

Figure 5: *Thickness strain variation for two reflectors (depth = 25mm)*

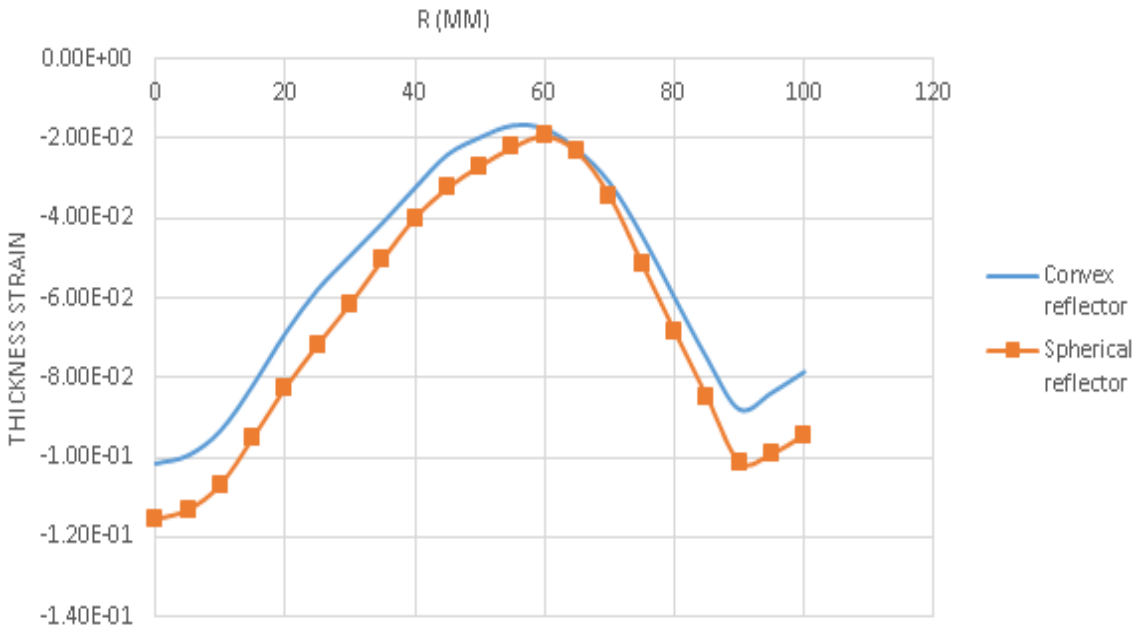

Figure 6: *Thickness strain variation for two reflectors (depth = 40mm)*

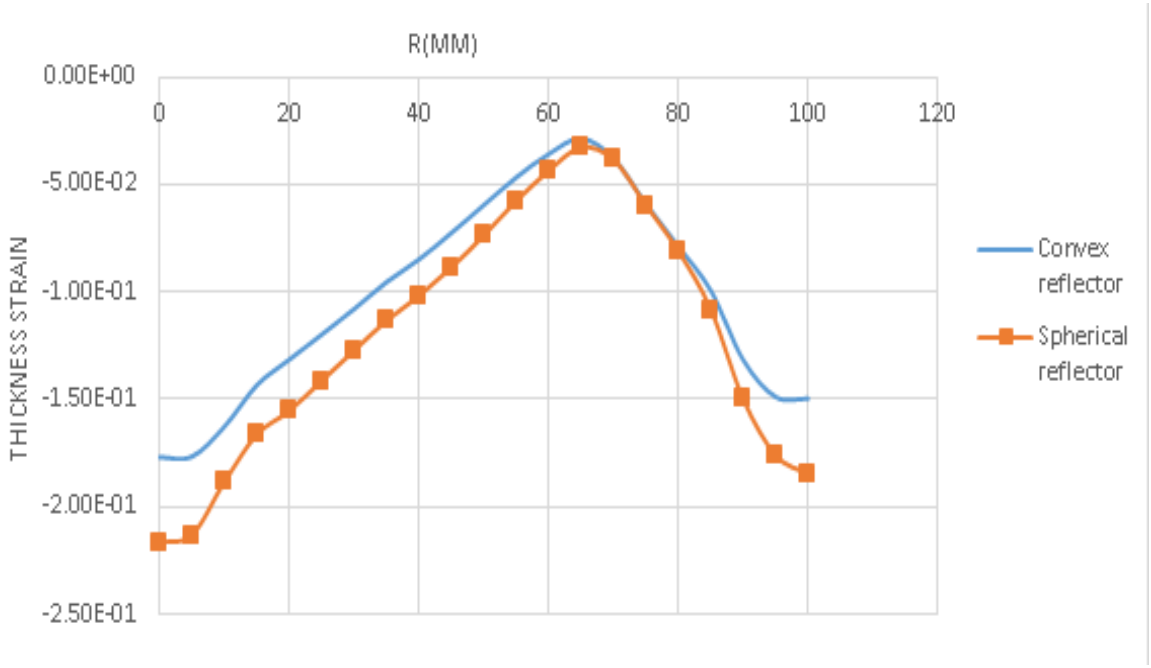

Figure 7: *Thickness strain variation for two reflectors (depth = 50mm)*

Table 2: *SNI values for different depth of cup and reflector shapes*

Depth of cup	Magnitude of pressure at source point (MPa)	Reflector type	Peak true thickness strain	Average true thickness strain	SNI
25mm	120MPa	Spherical	0.0494	0.0258	0.0236
		Convex	0.0394	0.0199	0.0195
40mm	240MPa	Spherical	0.1156	0.0664	0.0492
		Convex	0.1015	0.0565	0.045
50mm	300MPa	Spherical	0.2166	0.120	0.0966
		Convex	0.1766	0.102	0.0746

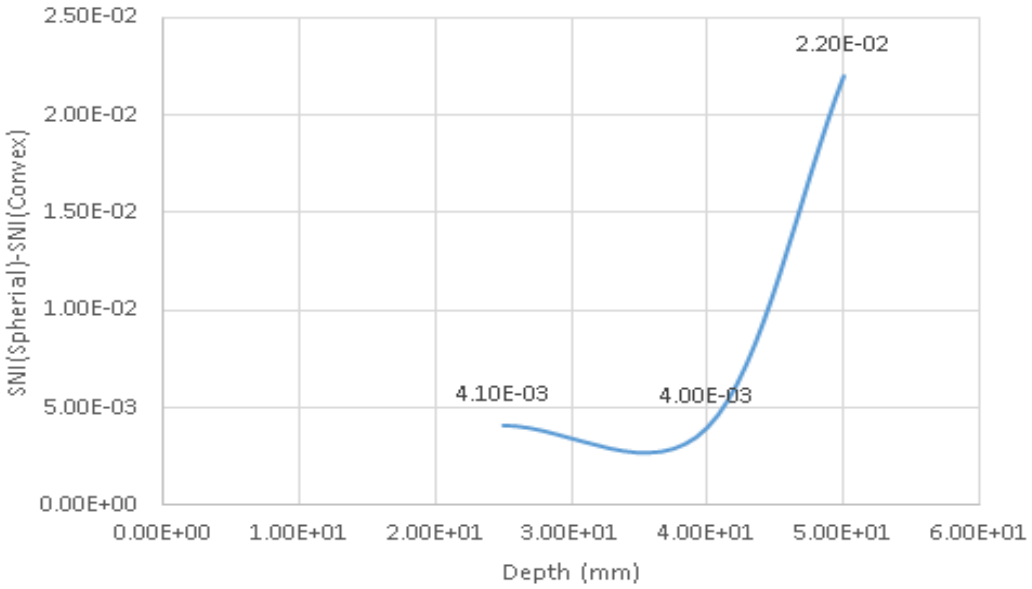

Figure 8: *Difference in SNI values for spherical and convex reflectors for various depth of drawing*

3.2 Pressure distribution

Pressure distribution at depths of 25mm and 50mm for the two reflectors is shown in Table 3. It may be inferred that the pressure distribution for both the reflectors for 25mm depth is very similar in trend and magnitude. The same is reflected in a minor difference between the SNI values for the two geometries. In contrast, the pressure distribution for the two reflectors between R = 0 and R = 100 is understandably different, though the shapes at a given time interval (100, 200 or 300 microseconds) are still somewhat similar. In particular, the pressure distribution is more similar at 100 microseconds and the similarity decreases with time. This also explains the increasing thickness strain variation (and hence the SNI) with increasing depth and time.

***Table 3**: Pressure distribution on the blank surface for two reflectors*

Depth	Spherical reflector	Convex reflector
25mm	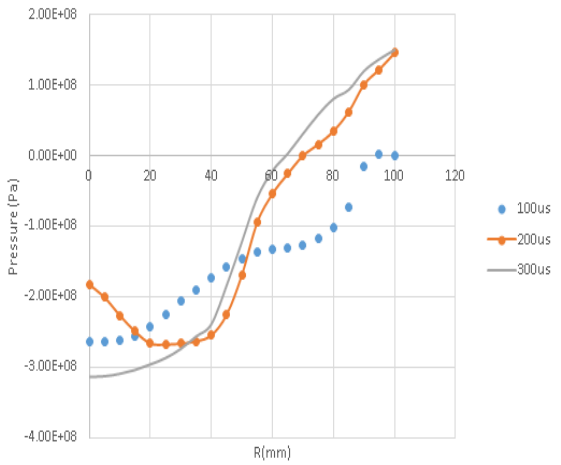	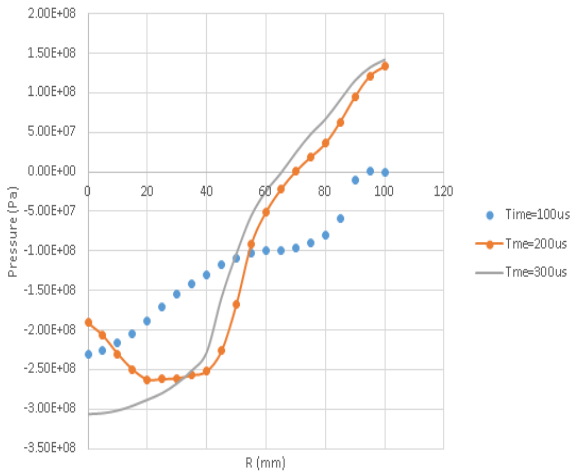
50mm	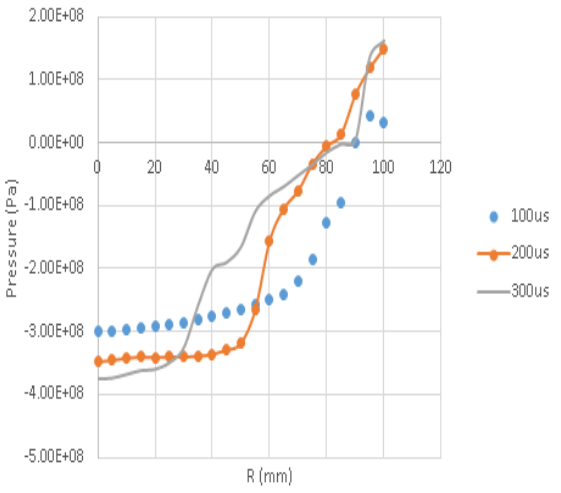	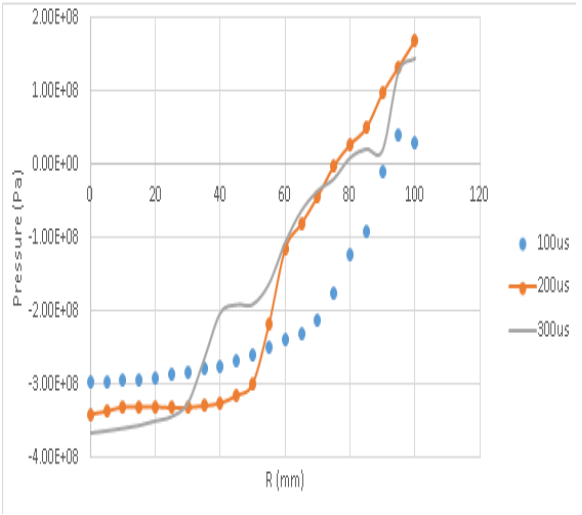

4 Conclusions:

From the foregoing, the following conclusions emerge:

1. The pressure distribution and hence the thickness strain distribution in a deforming sheet metal blank is sensitive to the shape of the reflector.
2. The convex reflector gives more uniform strain distribution (based on a lower value of SNI).

3. The trends observed in SNI variation with increasing depth (increasing forming energy) are well explained.
4. The similarity in pressure distribution at low depths and similar SNI are well understood. An increase in forming depth leads to an increase in difference between the SNI values and also dissimilarity between the two pressure distributions.
5. Further investigations are required into optimizing the shape of the reflector to obtain a uniform strain distribution even at large depths of deformation, i.e., a near zero value of SNI.

References

[1] *J. Varis, H. Martikka:* Prototyping of 3D sheet metal parts using electrohydraulic forming. ISSN 1392 - 1207, MECHANIKA, Nr.3 (53), p. 44-51, 2005.
[2] *A. Melander, A. Delic, A. Bjorkblad, P. Juntunen, L. Samek, L. Vadillo*: Modelling of electro hydraulic free and die forming of sheet steels. International Journal of Material Forming, Vol. 6, p. 223-231, 2013.
[3] *J. Bonnen, S. Golovashchenko, S. Dawson, A. Mamutov, A. Gillard:* Electrohydraulic Sheet Metal Forming of Aluminum Panels. Trends in Materials and Manufacturing Technologies TMS, p. 449-454, 2012.
[4] *H. Huh, J. H. Lim and S. H. Park:* High speed tensile test of steel sheets for the stress-strain curve at the intermediate strain rate. International Journal of Automotive Technology, Vol. 10, No. 2, p. 195−204, 2009.
[5] *W. Homberg, C. Beerwald, A. Pröbsting*: Investigation of the Electrohydraulic Forming Process with respect to the Design of Sharp Edged Contours. Proc. of the 4th International Conference on High Speed Forming, Columbus, Ohio, USA, 2010.
[6] *S.G. Desai, P.P. Date*: On the quantification of strain distribution in drawn sheet metal products. Journal of Materials Processing Technology Vol. 177, p. 439–444, 2006.

Finite Element Analysis of Electromagnetic Incremental Forming of Cylindrical Components*

X. Yao[1], H. Yang[1], H.W. Li[1], S.L. Yan[1]

[1] School of Materials Science and Engineering, State Key Laboratory of Solidification Processing, Northwestern Polytechnical University, Xi'an, P. R. China

Abstract

Traditional electromagnetic sheet forming method shows its weakness in forming large depth cylindrical component due to its character of transient. Therefore, an electromagnetic incremental forming method is introduced in the present work. During the forming process, one coil is used and two-steps discharges are applied. The coil moves towards the workpiece in drawing direction after the first discharge. This process was modelled by finite element method. Magnetic force distribution of the second discharge is analysed, which results in maximal deformation distributing around the side of coil. Conical degree of the deformed workpiece after the first discharge increases after the second discharge, and profile of the workpiece is closer to the desired cylindrical shape. The maximal stress and strain in the second discharge are smaller than the ones in the first discharge under the conditions of the same forming depth. It can be concluded that multi-steps discharges play a key role in increasing conical degree of post-deformed component and attaining cylindrical shape. In addition, forming characteristics and deformation rules are demonstrated, and major forming parameters are discussed. A winkle phenomenon is also analysed in this paper.

Keywords

Flexible manufacturing, Electromagnetic Incremental forming, Finite element method (FEM)

* *Supported by National Basic Research Program of China (No. 2012CB012802)*

1 Introduction

Large sheet metal components manufactured via deep drawing process are in urgent need in aeronautic and astronautic applications [1, 2]. However, problems arise such as over-complicated process procedures, large equipment tonnage, high cost and undesirable material properties for forming. In view of the advantages of agreeable flexibility, contact-free and formability improvement, electromagnetic forming (EMF) becomes a potential technique to solve the restrict problem of manufacturing large-scale deep-drawn components [3, 4].

Conventional electromagnetic sheet forming method shows its weakness in forming large depth cylindrical component due to its character of transient [5]. The forming force can't last long enough to achieve such depth. Shang and Daehn [6] obtained a large drawn depth by electromagnetically assisted sheet metal stamping (EMAS) technology. Cui and Mo [7] formed a large sheet by discharging a small coil in several positions, which proposes an electromagnetic incremental forming (EMIF) method. Therefore, EMIF is introduced in the present work to form a cylindrical component of aluminium alloy.

2 Principle of Electromagnetic Incremental Forming

Figure 1 shows the process of a two-steps discharges EMIF. The first discharge has no difference with conventional EMF. After the first discharge, the sheet deforms to the conical profile. In the second step, the coil moves towards the workpiece in drawing direction to reduce energy loss, and then the second discharge is performed. The second step increases forming depth and forms the profile closer to the desired cylindrical shape. Voltages of two discharges can be adjusted so as to obtain a suitable set of forming parameters aiming at the desired profile of the component.

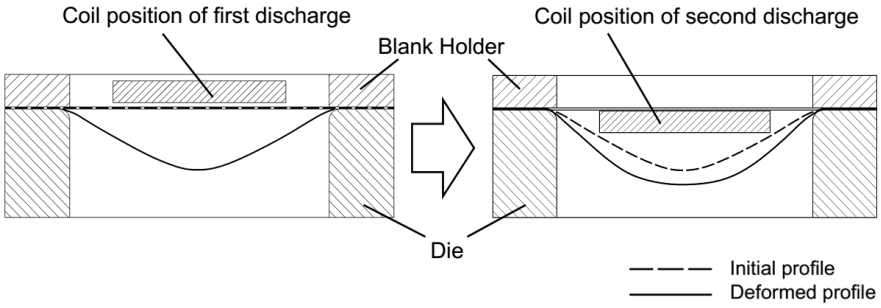

***Figure 1**: Process of a two-steps discharges EMIF*

Research contents of this study is based on contact-free forming process, in which the die does not contact the blank except for the flange, and the sheet is fully fixed in the flange area by the blank holder. Coil used in the discharge process is a flat spiral coil.

3 Research Method and Forming Parameters

3.1 Research Method

This study is based on the above-mentioned two-steps discharges EMIF using finite element method, and a numerical model containing two-steps discharges process is developed. The finite element model is a sequentially-coupled method containing discharge circuit, electromagnetic field and structure field.

In the first discharge process, the circuit model simulates a time-dependent current from discharge parameters and transfers the current data to the electromagnetic field simulation program. Magnetic force on the workpiece is then calculated and transferred to the structural field, which gives the deformation result after the first discharge.

In the second discharge process, the previous deformation data is transferred into the second discharge electromagnetic field model, according to which coil position and discharge current are updated and air is remeshed. Next, the second magnetic force is calculated and transferred to the geometry-updated structural field model, and final result of the two-steps discharges electromagnetic incremental forming is simulated.

This numerical model is checked by simulating the same forming process described by Zhang [8]. The maximum error on forming depth is 8.7%, which proves the accuracy of the finite element model.

3.2 Forming Parameters

Major forming parameters in the simulations are listed in Table 1. Material used in the study is 5A06 aluminium alloy, and the following Johnson-Cook material model is adopted.

$$\sigma = (176.7 + 832.6\varepsilon^{0.69})(1 + 10^{-4}\varepsilon^{0.65}\ln\varepsilon^{*}) \quad (1)$$

Forming parameters	
Total capacitance	2.13×10^{-4} F
Total inductance	2×10^{-6} H
Total Resistance	2.55×10^{-2} Ω
Voltage of the first discharge	4000-6000 V
Voltage of the second discharge	6000-8000 V
Sheet's thickness	1 mm
Die's internal diameter	120 mm
Coil's diameter	80 mm

***Table 1**: Major forming parameters*

4 Results

4.1 Distribution of Magnetic Force

Distribution of magnetic force in the first discharge has been fully analysed by Al-Hassani [9], hence this study focuses on force of the second discharge. Figure 2 (a) shows the distribution of magnetic force in the second discharge with voltage of 6000V, and voltage

of the first discharge is 4000V (marked as 4000 + 6000V). It can be found different discharge voltages lead to the same pattern of the force distribution. The direction of magnetic force is vertical to the deformed sheet's profile, since the magnetic line is vertical to sheet's upper surface. Maximal magnitude of force distributes in 3/5 of the internal radius of die from the center. This part of the workpiece has the closest distance to the coil, and is also in the maximal magnetic density area of flat spiral coil.

As voltage of the first discharge increases, conical degree of the formed component decreases. The deformed structure increases the distance between coil and the top of the workpiece for the second discharge. This lowers the magnetic force on the conical top, while increases the force near the middle of conical surface (Figure 2 (b), (c)). Thus a large voltage of the first discharge will reduce the forming depth of the second discharge.

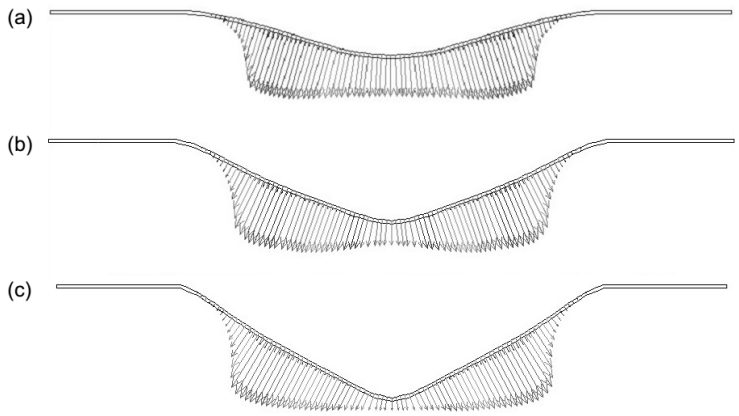

***Figure 2**: Vectorial distribution of the magnetic force in the second discharge with different voltages of the first discharge (a): 4000 + 6000V, (b): 4000 + 5000V, (c): 6000 + 6000V*

4.2 Deformation Rules

Deformation results of both discharges in a 4000 + 6000V EMIF process are shown in Figure 3. It shows that the second discharge not only raises forming depth, but also changes the deformed profile so as to be closer to the desired cylindrical shape. This can be explained by the distribution of the second magnetic force described above, which results in the maximal deformation distributing near the middle of conical surface.

It can be concluded that EMIF is more suitable in forming large cylindrical components than traditional electromagnetic forming. 1) The final profile of EMIF is closer to the desired cylindrical shape, and orthopedic could be the next process in some applications. 2) The approximate cylindrical profile is with a larger inner diameter compared to the conical shape under the condition of the same forming depth, so that the coil could be placed in a deeper position. Thus energy loss is reduced and forming depth increasing are achieved. 3) Maximal stress and strain in the two-steps discharges are both smaller than the ones containing only one discharge with identical forming depth, as listed in Table 2. Reductions of maximal equivalent stress and maximal equivalent strain are 15% and 10%, respectively.

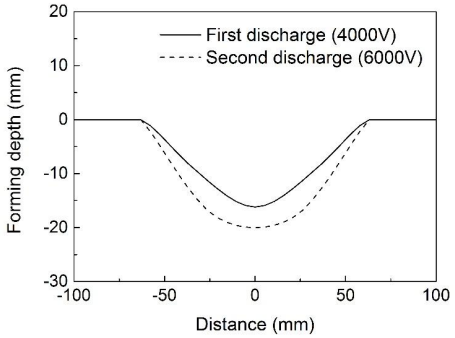

***Figure 3**: Deformed profile of two-steps discharges (4000 + 6000V)*

Discharge steps	Voltage of the first discharge	Voltage of the second discharge	Forming depth	Maximal equivalent stress	Maximal equivalent strain
One-step	5000 V	-	22.3 mm	445.7 MPa	0.0713
Two-steps	4000 V	7000 V	23.0 mm	378.9 MPa	0.0642

***Table 2**: Comparison of one-step and two-steps discharges with identical forming depth*

4.3 Influences of Discharge Parameters

Influences of voltage of the first discharge on EMIF process are demonstrated in Figure 4, which are studied with the same voltage of the second discharge (set as 6000V). Forming depth obtained in the second discharge decreases as voltage of the first discharge rising, seeing Figure 4 (a). Thus the distance between coil and center of the workpiece increases, and so magnetic force of the second discharge decreases, which results in reduction of forming depth in the second discharge. Figure 4 (b) shows the final profile of a large voltage of the first discharge (which is 6000V) process. There is an annular bulge on the side surface, which is exactly in the maximal magnetic force area. This is formed by the force near the middle of conical surface in Figure 2 (c). Thus, it is can be concluded that larger voltage of the first discharge will reduce energy efficiency of the second discharge, and even lead to an undesirable final profile.

Energy efficiency of the second discharge is less than the one of the first discharge, so it makes less contribution to the total forming depth. Voltage of the second discharge and final depth are linear correlated, as shown in Figure 5 (voltage of the first discharge is 4000V. Final profile still holds cylindrical shape as voltage of the second discharge increases.

4.4 Wrinkling in EMIF Process

It is discovered that blank holder should fully cover the flange area, otherwise sheet could wrinkle in forming and flange area, as shown in Figure 6. During the forming process, sheet on the flange area will impact the rigid mould with a high speed, and tend to rebound at the case when nothing resists it above. Meanwhile, sheet in the forming area still moves downward in high speed. These generate tensile stress in radial direction and

compressive stress along the circumferential direction near the filleted corner, resulting in wrinkling.

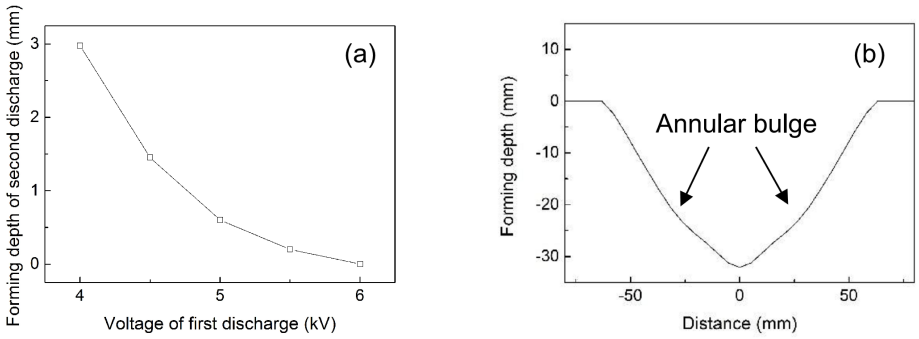

***Figure 4**: Influences of voltage of the first discharge on EMIF process (a): forming depth of the second discharge decreases as voltage of the first discharge increases (b): final profile after the 6000 + 6000V process*

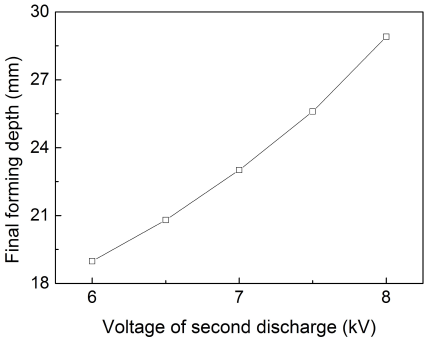

***Figure 5**: Relation of voltage of the second discharge and final forming depth*

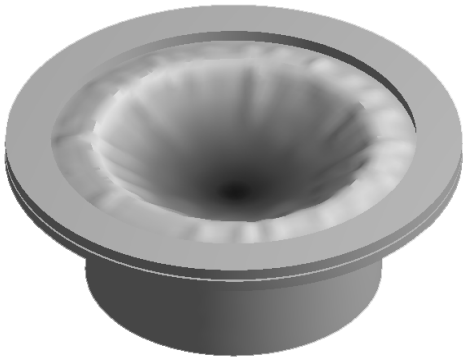

***Figure 6**: An example of wrinkling at flange and near filleted corner in EMIF*

5 Conclusions

(1) EMIF increases conical degree of traditional EMF, and the final profile of the workpiece is closer to the desired cylindrical shape. It also decreases maximal stress and strain level. Therefore, EMIF is a potential method in forming large-depth cylindrical component.

(2) Voltage of the first discharge in EMIF should be appropriate to increase second discharge's efficiency, while avoids shape distortion. Voltage of the second discharge and final depth are linear correlated.

(3) Blank holder should fully cover the flange area to avoid winkling.

References

[1] *Neugebauer R, Bouzakis K D, Denkena B, et al.:* Velocity effects in metal forming and machining processes. CIRP Annals-Manufacturing Technology, 2011, 60(2), p.627-650.

[2] *Kleiner M, Geiger M, Klaus A.:* Manufacturing of lightweight components by metal forming. CIRP Annals-Manufacturing Technology, 2003, 52(2), p.521-542.

[3] *Psyk V, Risch D, Kinsey B L, et al.:* Electromagnetic forming—A review. Journal of Materials Processing Technology, 2011, 211(5), p.787-829.

[4] *Oliveira D A, Worswick M J, Finn M, et al.:* Electromagnetic forming of aluminum alloy sheet: free-form and cavity fill experiments and model. Journal of Materials Processing Technology, 2005, 170(1), p.350-362.

[5] *Belyy I V, Fertik S M, Khimenko L T.:* Spravochnik Po Magnitno-impul'Snoy Obrabotke Metallov [Electromagnetic Metal Forming Handbook]. English translation by Altynova, MM, online available at http://www.mse.eng.ohio-state.edu/~Daehn/metalforminghb/index.html (shown on 04.11. 2010), 1977.

[6] *Shang J, Daehn G.:* Electromagnetically assisted sheet metal stamping. Journal of Materials Processing Technology, 2011, 211(5), p.868-874.

[7] Cui X H, Mo J H, Li J J, et al. Electromagnetic incremental forming (EMIF): A novel aluminum alloy sheet and tube forming technology. Journal of Materials Processing Technology, 2014, 214(2), p.409-427.

[8] *Zhang H T.:* Finite element simulation of magnesium alloy sheet based on uniform pressure coil. Wuhan, P. R. China, Wuhan University of Technology, 2010.

[9] *Al-Hassani S T S, Duncan J L, Johnson W.:* Techniques for designing electromagnetic forming coils. Proceedings of the Second International Conference of the Center for High Energy Forming, AA Ezra, ed., Denver, Colo.: University of Denver. 1969, 5: 1-5.1.

SESSION 5

PROCESS TECHNOLOGIES (WELDING & JOINING)

Collision Welding of Tungsten Alloy 17D and Copper Using Vaporizing Foil Actuator Welding

A. Vivek, B. C. Liu, G. S. Daehn

Dept. of Materials Science and Engineering, The Ohio State University, 2041, College Road, Columbus, OH, 43201, USA

Abstract

The objective of this study was to implement collision welding of tungsten alloy 17D (6.5% Ni, 3.3% Fe) and copper at a laboratory scale and subsequently investigate the relationship between interfacial structure and mechanical properties. Vaporizing Foil Actuator (VFA) has recently been demonstrated as a versatile tool for metalworking applications, such as impact welding of dissimilar materials. Its implementation for welding is termed as VFA welding or VFAW. With 8 kJ input energy into an aluminum foil actuator, a 0.5 mm thick Cu110 alloy sheet was launched toward a tungsten alloy target resulting in a collision at a velocity of 580 m/s. The two sheets were found to be welded in the region where the collision velocity and angle were optimal. This range, termed as the welding window was found to be narrow for this combination of target and flyer materials. Scanning electron microscopy of sectioned samples showed regions of wavy interface with significant plastic deformation on both sides. Microhardness tests revealed significant increase in hardness near the interface. Instrumented peel tests showed that the welds were quite strong with peel strength of 60 N/mm.

Keywords

Collision welding; VFAW; copper; tungsten alloy; photonic Doppler Velocimeter (PDV); wavy interface

1 Introduction

Tungsten has one of the highest melting points and strengths among metals. Due to this, it is a suitable material for applications which require high wear resistance and heat resistance. However, in many of these applications, the tungsten tool has to be joined to a different material which can provide mechanical toughness or can conduct away the heat. Copper, because of it high thermal conductivity is an ideal material to be used as a heat sink. Tungsten, due to its high melting point, is very difficult to weld to another material using traditional welding techniques. Therefore, there is a need for exploring other methods. Mitteau et al [1] used electron beam welding for successfully joining tungsten and copper. Manikandan et al. [2] demonstrated underwater explosive welding of tungsten foil and

copper, but there are inherent issues with use of explosives. In this work, collision welding of a copper flyer sheet to a tungsten alloy 17D target plate has been attempted using vaporizing foil actuator welding (VFAW). To induce some ductility, some elements such as nickel, iron, and copper are often mechanically alloyed in small quantities with tungsten and the resulted composite is termed as a tungsten alloy.

VFAW is a novel technique for collision welding at a laboratory scale and was developed by Vivek et al [3]. Vaporizing Foil Actuators (VFA) are based on the phenomenon of rapid vaporization of thin metallic foils and wires caused by passage of a capacitor bank-driven current, on the order of 100 kAmps [4]. The burst of the conductor is accompanied with a high-pressure pulse which, as in the case of VFA, can be used for working metal at high strain rates. VFA has been applied toward a variety of impulse-based metal working operations such as impact welding, embossing, shearing, dynamic powder consolidation, shape calibration, and closed-die forming [5]. This paper focuses on impact welding application of VFA. Copper-titanium, aluminum-copper, aluminum-magnesium, titanium-steel, copper-steel welds were created by Vivek et al. under the same set of input electrical parameters. Flyer sheet impact velocities up to 670 m/s were measured. The weld interfaces were found to have significantly different structures and strengths. Some of the welds, such as copper-titanium, had high peel strength of 30 N/mm and had typical wavy interface, free of intermetallics and voids. However, a few others like steel-titanium were found to be weak and riddled with interfacial defects. It was noted that the welding parameters were not optimized for each combination. It was also shown that some of the welds which were weak in peel, failed in a parent material when subjected to lap shear test commonly applied for lap welds created by MPW. Therefore, peel test was proven to be more discriminatory in terms of quality of a weld, and will be used in this study as well.

Impact welding has been traditionally practiced using explosive driven pulses or less commonly by electromagnetic launch of flyers. Critical diameter [6], increasingly stringent regulations, and inability to scale down the process are some issues due to which explosive welding (EXW) finds limited application in traditional industrial environments. The most significant drawback of magnetic pulse welding (MPW) is the limited magnetic pressure that the actuators can operate at without catastrophic failure [7]. Additionally, magnetic pulse technology works efficiently only for combinations where the flyer sheet is electrically conductive or is driven by an electrically conductive material such as copper [8]. VFAW can be used to create welds of the length scales similar to that of MPW, and can make flyers reach velocities similar to those during EXW. The issue of actuator longevity does not exist as the foil actuator, which is disposable, can be easily replaced after every experiment at a low cost.

A set up very similar to the one used by Vivek et al [3] was used here to weld a 6.25 mm thick tungsten alloy 17D plate with 0.5mm thick copper sheet. The welded samples were subjected to peel tests, optical microscopy, and microhardness tests.

2 Experimental Procedure

The energy source used in these experiments was a Maxwell Magneform capacitor bank with a total capacitance of 426μF, inductance of 100 nH, and short circuit current rise time of 12 μs. When charged to the maximum voltage of 8.6 kV, this capacitor bank can supply 16 kJ of electrical energy.

Tungsten alloy 17D (ASTM B 777 Class 1 Type 2) was used as the target material. As supplied, this alloy contained 6.75% nickel and 3.3% iron. The tensile strength was rated at 860 MPa and the strain to failure was 6.5%. This material will be referred to as W-alloy in this paper. The average hardness was measured to be 378 HV. Rectangular strips, 25 mm x

55 mm, were cut out from 3 mm thick W-alloy plates. Commercially pure copper (99.99% pure) was used as the flyer material. Square strips, 75 mm x 75 mm, were cut out of 0.5 mm thick copper sheet. The initial average hardness of the copper used in this study was measured to be 95 HV.

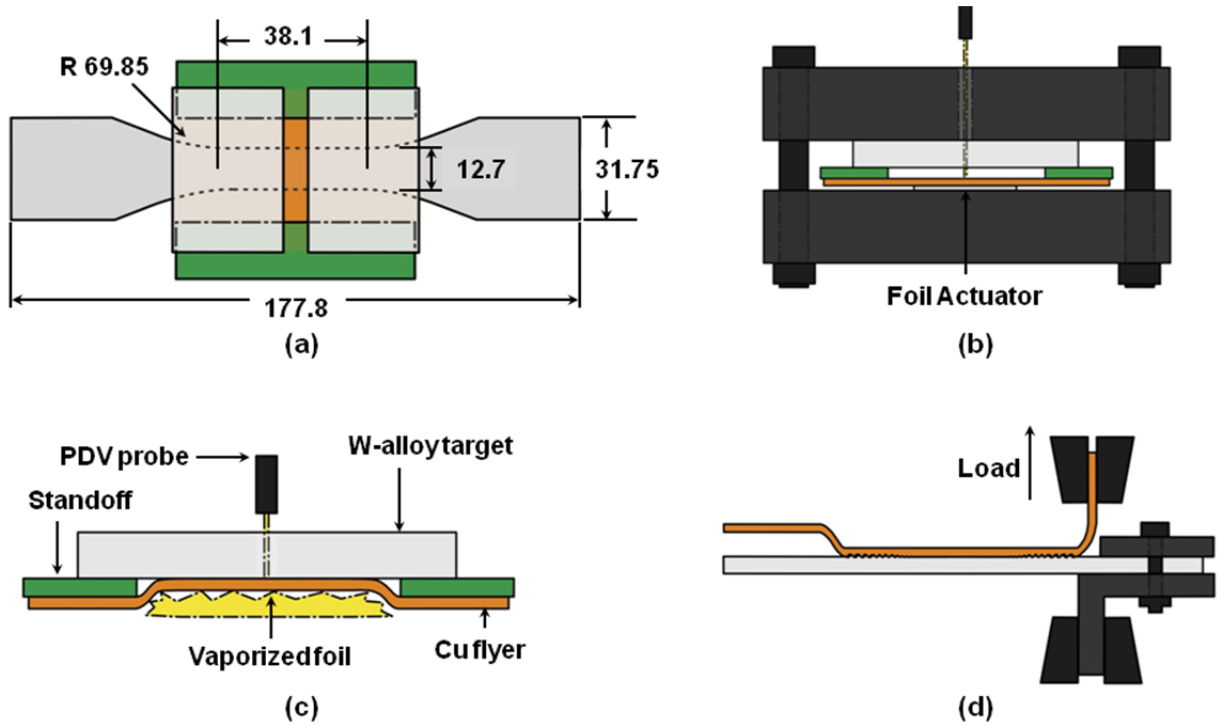

Figure 1: Vaporizing foil actuator welding (VFAW) set up for welding Cu110 with W-alloy. (a) top view of the foil actuator, flyer sheet, standoff, and target stack, (b) side view of the stack along with the positioning of the photonic Doppler velocimeter (PDV) probe, (c) formation of weld after foil actuator's vaporization, (d) peel testing set up.

A schematic of the VFAW set up is shown in Figure 1. Aluminum foil actuators of thickness 0.0762 mm and shape as shown in Figure 1a were placed underneath the flyer sheets which were stood off from the W-alloy target plates at a standoff distance of 1.6 mm. The horizontal gap between the standoffs was 30mm. The standoffs were inserted to provide sufficient distance for acceleration of the flyer plates. The capacitor bank was charged to an energy level of 8 kJ and discharged through the foil actuator. Passage of the capacitor bank-driven current, on the order of 100 kAmps, through the foil actuator caused its rapid vaporization, thereby leading to a high pressure pulse which was used for launching the flyer sheet at high speed toward the target. The thick steel backing block ensured that the expanding plasma, formed from foil actuator's burst, did most of the mechanical work on the flyer sheet. A hole drilled through the backing blocks and the gap between W-alloy target plates provided a line of sight for a focuser probe of the Photonic Doppler Velocimeter (PDV) [9].

Use of PDV as a diagnostic tool for impulse metal working applications has been discussed by Johnson et al. [10]. PDV utilizes the interference of original and reflected, Doppler-shifted laser to measure the velocity of the object from which the laser is reflected. Most of the transmission of light happens inside fiber-optics, with the laser going out into or collected back from free air via focusers, collimators or, in some cases, bare fibers. The PDV used here can measure velocities up to 1550 m/s with a temporal resolution of 1 ns for a

time duration of 2 ms. Discharge current was measured by a 100kA:1V Rogowski coil, and a 1000:1 voltage divider was used to measure voltage.

The welded sample was sectioned using a circular abrasive saw and either mounted for microscopy and hardness testing, or subjected to peel testing. Microhardness testing was done along two lines across the wavy interface. One line went across the crest of the wave and the other line traversed across the trough. A diamond indenter with 200 gm load was used for the W-alloy side while a 50 gram load was used for the copper side. For peel testing of the welded samples, the flyer sheets were bent to 90° with respect to the target plate and the samples was pulled apart using a MTS 831.10 load frame moving at a speed of 0.1mm/sec. The peel strength of the weld was normalized by dividing the sustained load by the width of the sample being peeled in line with the work of Kendall et al [11].

3. Results and Discussion

The temporal evolution of the flyer sheet's velocity is shown in Figure 2a. This figure also illustrates the variation of current and voltage with time, indicating that a maximum current of 127 kA was reached within 10μs of discharge and the foil burst occurred shortly after. Plotted in Figure 2b, the displacement was calculated by integrating the velocity data with respect to time and it was found that the flyer collided with the target at 550 m/s after travelling 1.6 mm.

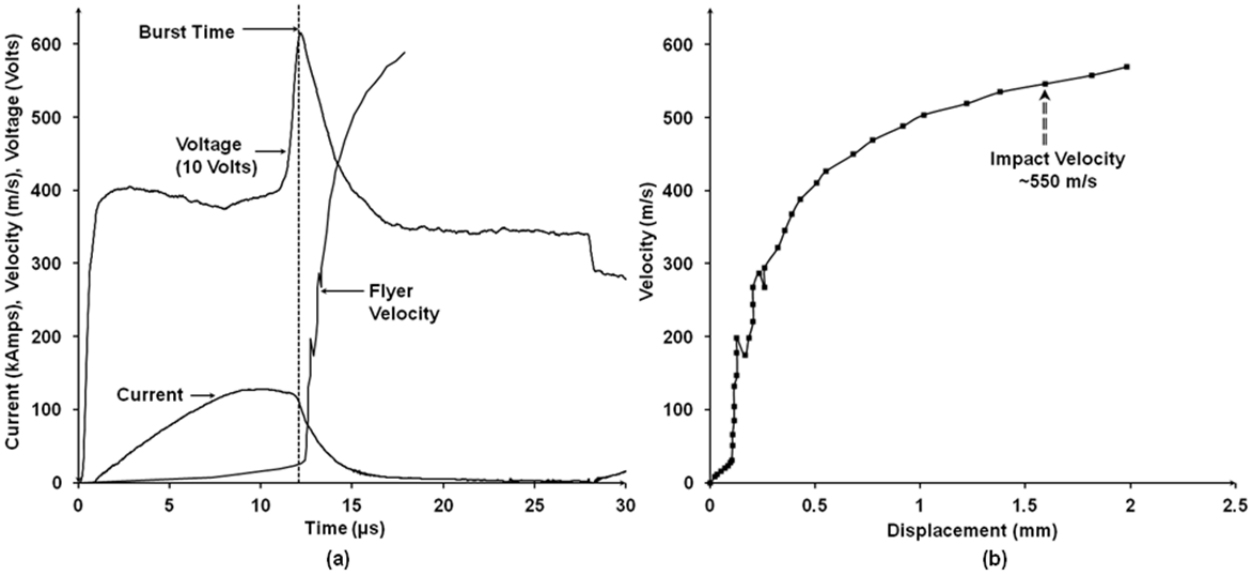

Figure 2: Results of the diagnostics run during the VFAW experiment. (a) Temporal evolution of current, voltage and velocity with 8 kJ input energy into a 0.0762 mm thick aluminum foil, (b) Velocity of the flyer plate plotted against distance travelled indicating impact with target plate at 550 m/s

The welded sample and micrograph of a wavy region of the welded interface is shown in Figure 3. Since the W-alloy was mechanically alloyed, distinct regions with higher iron and nickel content were distributed in the tungsten matrix. Elongation of these regions along the weld interface, as seen in the micrograph with highest magnification indicated severe plastic deformation. Similar effect would be seen on the copper side if it was etched. The weld was created outside the region of zero angle impact directly above the former area of the foil actuator. The cross section across the weld shows two distinct regions where welding occurred. The width of the wavy region or the "good weld region" was nearly 0.5 mm

which shows that the range of collision velocities and angles for which good welds are created for this pair of materials is rather limited.

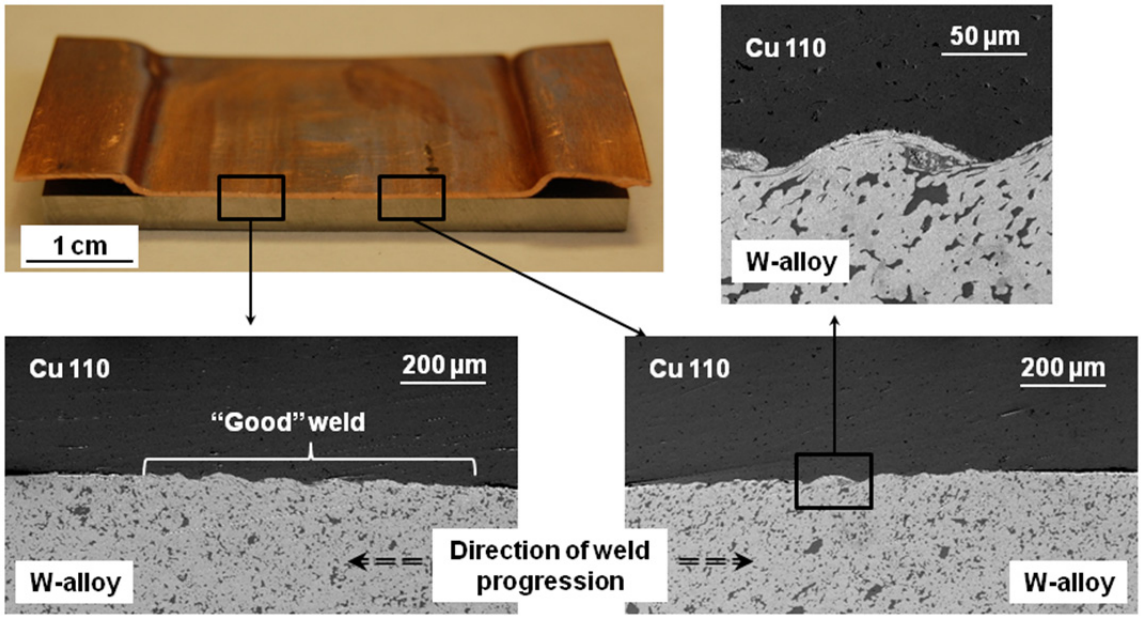

Figure 3: Images showing the welded Cu-W alloy sample and SEM images at various magnifications. The wavy region of the interface indicated as "good" weld.

Figure 4 represents the weld in progress in the configuration implemented here. The flyer material directly above the foil actuator is assumed to be launched flat and that whole section impacts at the measurement flyer plate velocity, V_P. In that region the impact angle, β, is zero due to which no welding is observed. However, rest of the flyer sheet trails behind and folds onto the target as the weld progresses to either side of initial impact region. The velocity of the flyer at a point located at a distance, x, from the foil actuator has a velocity of V_{Px}, which decreases with increasing x. It can be expected that there is a monotonically varying velocity gradient from region directly above foil actuator ($V_{P(x=0)}= V_P$) to the region below the standoffs ($V_{P(x=d)}=0$).
For low angles, V_w is related to flyer plate velocity and collision angle, β, as,

$$V_w = \frac{V_P}{\sin(\beta)} = V_F \qquad (1)$$

V_{Wx}, V_{Px}, and V_{Fx} would be related similarly. Therefore, it can be seen that V_{Fx} decreases as the weld progresses away from the initial impact region and as the impact angle increases.

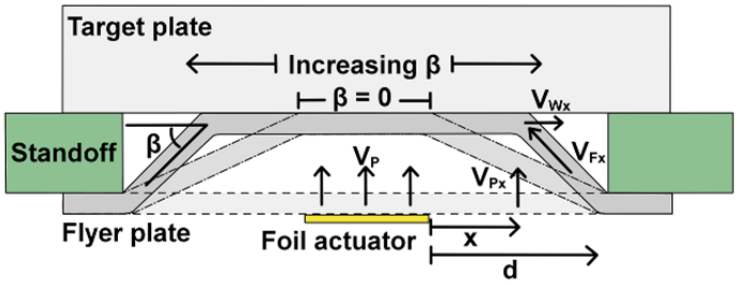

Figure 4: VFAW with the relevant configuration in progress

According to Eq. 2, due to Cowan et al. [12], for a constant Reynolds number, R_t, for a given pair, the welding velocity, V_w at which smooth-wavy transition happens is lower for a lower sum of hardness of the two materials. The lower bound or the smooth to wavy transition criteria is given by

$$R_{transition} = \frac{(\rho_{flyer}+\rho_{target})V_{F-transition}^2}{2(H_{flyer}+H_{target})} = K_{E-P} \quad (2)$$

Here ρ (kg/m^3) stands for density, V_F (m/s) for velocity of flow of the flyer material into the collision point, which approximately equals welding velocity, V_w for low collision angles. H represents Vicker's hardness (N/m^2). The smooth to wavy transition criteria depends on the hardness of two colliding members of the joint. If the sum of hardnesses is high, then the transition flow velocity, hence the transition welding velocity would also be high. Therefore smooth to wavy transition would happen at low values of β or x. Since the hardness of the target plate is quite high, it is not unexpected that the good weld region was very narrow.

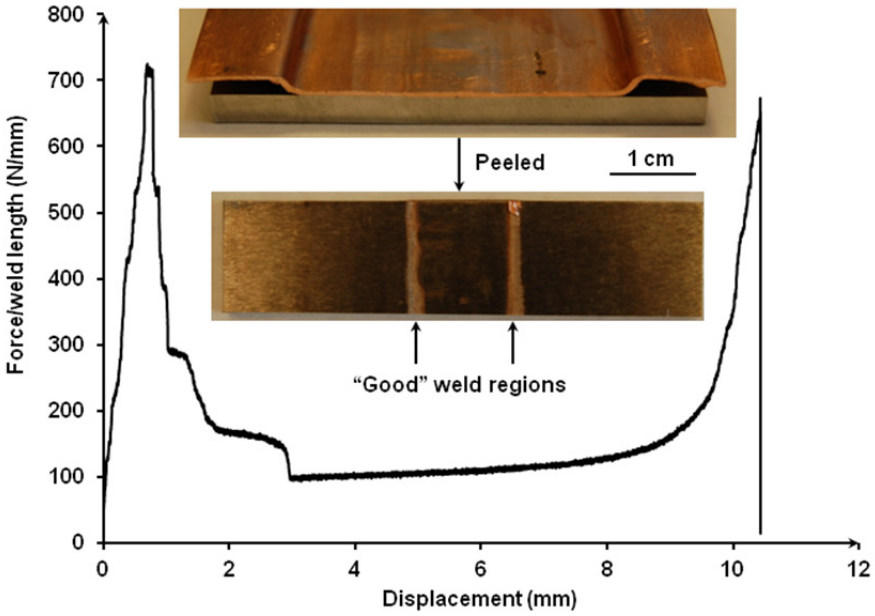

Figure 5: Peel test data showing two peaks corresponding to the two welded regions. The welded and subsequently peeled sample is shown inset in the figure.

The data from the peel test conducted on the welded sample is shown in Figure 5. The W-alloy side inset in the figure depicts, very clearly, the two bands along which optimal welding occurred. Accordingly there were two maxima in the force/weld length vs displacement plot. The peel strength was found to be nearly 60 N/mm.

The data obtained from the microhardness tests along the two lines across the interface is shown in Figure 6. The hardness of both Cu-110 and W-alloy were significantly higher than those of the original materials. Highest hardness for Cu side was found to be 129 HV while that on the W-alloy side was 483 HV. While the hardness generally increased monotonically as the interface was approached, it was found that along line A, the indent closest to the interface on the W-alloy side was larger and the hardness was measured as 382 HV. Further microstructural analysis is required to understand this anomaly.

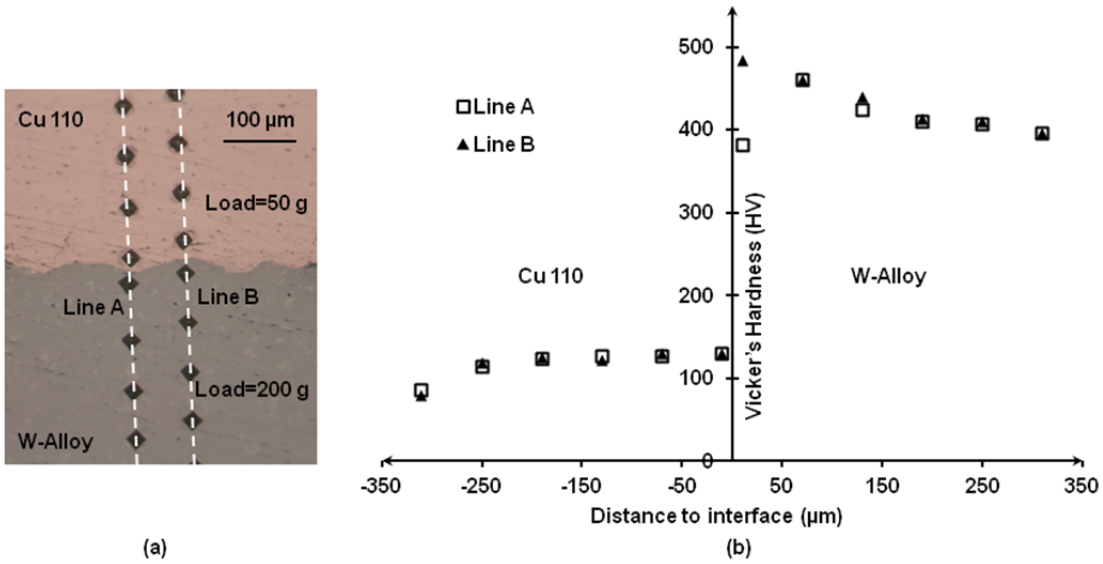

Figure 6: Microhardness tests. (a) post-test image of the Cu-110/W-alloy welded region showing the two lines along which tests were run, (b) A plot showing the variation of microhardness across the interface.

4. Conclusions

Based on this work, following conclusions can be drawn:

- It is possible to weld W-alloy 17D with copper using VFAW. The welded sample had significant peel strength of 58 N/mm.
- Since the aluminum foil is a consumable of each run, its longevity is not a concern while trying to increase the driving pressure. Impact velocity of nearly 550 m/s was attained within 1.6 mm of travel thereby indicating a very high driving pressure.
- It was found that the range of collision angle and velocity for which a good weld can be created between the copper and W-alloy is very narrow. This was verified against an analytical model, which indicated that the transition from a smooth to wavy interface occurs at higher welding velocities for combinations where either or both the materials in the welding couple are hard.
- Large amounts of plastic deformation on either side of the weld interface resulted in increased hardness as compared to parent materials. There was an anomaly on the W-alloy side where the hardness decreased near the trough of a wave.

Acknowledgements

The authors would like to thank the ALCOA foundation for supporting this work through the Advancing Sustainability Research Initiative.

References

[1] Mitteau, R., Missiaen, J. M., Brustolin, P., Ozer, O., Durocher, A., Ruset et al., 2007, Recent developments toward the use of tungsten as armour material in plasma facing components. Fusion Engineering and Design,82(15), 1700-1705.

[2] Manikandan, P., Lee, J. O., Mizumachi, K., Mori, A., Raghukandan, K., & Hokamoto, K., 2011, Underwater explosive welding of thin tungsten foils and copper. Journal of Nuclear Materials, 418(1), 281-285.

[3] Vivek, A., Hansen, S. R., Liu, B. C., & Daehn, G. S., 2013, Vaporizing Foil Actuator: A Tool for Collision Welding. Journal of Materials Processing Technology.

[4] Chace, W. G., & Moore, H. K. (Eds.)., 1959, Exploding wires (Vol. 4). Plenum Press.

[5] Vivek, A., 2013, Rapid Vaporization of Thin Conductors Used for Impulse Metalworking. The Ohio State University.

[6] Cooper, P., 1997, Real Effects in Explosives, Explosives Engineering. Wiley-VCH, New York, pp. 290–293

[7] Golovashchenko, S. F., 2007, Material formability and coil design in electromagnetic forming. Journal of Materials Engineering and Performance,16(3), 314-320.

[8] Psyk, V., Risch, D., Kinsey, B. L., Tekkaya, A. E., & Kleiner, M. (2011). Electromagnetic forming—A review. *Journal of Materials Processing Technology*, *211*(5), 787-829.

[9] Strand, O. T., Goosman, D. R., Martinez, C., Whitworth, T. L., & Kuhlow, W. W., 2006, Compact system for high-speed velocimetry using heterodyne techniques. Review of Scientific Instruments, 77(8), 083108-083108.

[10] Johnson, J.R., Taber, G., Vivek, A., Zhang, Y., Golowin, S., Banik, K., Fenton, G.K., Daehn, G.S., 2009, Coupling experiment and simulation in electromagnetic forming using photon Doppler velocimetry. Steel Research International 80 (5), 359–365.

[11] Kendall, K., 1973, Shrinkage and peel strength of adhesive joints. Journal of Physics D – Applied Physics 6 (15), 1782–1787.

[12] Cowan, G. R., Bergmann, O. R., & Holtzman, A. H. (1971). Mechanism of bond zone wave formation in explosion-clad metals. *Metallurgical and Materials Transactions B*, *2*(11), 3145-3155.

Influence of Axial Workpiece Positioning during Magnetic Pulse Welding of Aluminum-Steel Joints*

A. Lorenz[1], J. Lueg-Althoff[2], G. Göbel[3], C. Weddeling[2], E. Beyer[1,3], A. E. Tekkaya[2]

[1] Institute of Manufacturing Technology, TU Dresden, Germany
[2] Institute of Forming Technology and Lightweight Construction, TU Dortmund, Germany
[3] Fraunhofer Institute for Material and Beam Technology (IWS), Dresden, Germany

Abstract

Magnetic Pulse Welding (MPW) offers a method to economically join similar and dissimilar metals without the need for external physical or chemical binders, while avoiding the adverse heating effects seen in many welding techniques. MPW allows for the fabrication of joints via the harnessing of Lorentz forces, which result from discharging a current pulse through a coil. In the process an outer piece (flyer) is accelerated onto an inner piece (parent), and welding is achieved using propagating impact fronts. There are several geometrical factors to be considered including the flyer-coil distance, the parent-flyer distance, as well as the axial relationship between flyer and coil (working length). Various shapes of the front are possible and each configuration has its own advantages and drawbacks. The goal of this work is to show not only how the aforementioned parameters are related, but also ways to optimize front propagations, which are vital to the welding result. This is done primarily by determining the influence of the working length of tubular MPW specimens. It is shown that for steel-aluminum joints in the given arrangements, three different front regimes exist, which are related to geometrical factors. These results are especially useful to avoid seemingly favorable but nevertheless suboptimal conditions for flyer movement that would reduce weld quality and energy efficiency of the process.

Keywords

Joining by Forming

---

* *This work is based on the results of subproject A1 of the priority program 1640 ("joining by plastic deformation"); the authors would like to thank the German Research Foundation (DFG) for its financial support*

1 Introduction

Magnetic Pulse Welding (MPW) is an impact welding process that enables the joining of tubular or flat partners. Through the fast discharge of capacitor banks, a magnetic field is generated in a coil, which leads to eddy currents in the electrically conductive outer (flyer) piece. Both the coil and the work piece generate Lorentz forces, which act in opposing directions, causing the flyer to accelerate towards the inner (parent) work piece. Under adequate conditions, the flyer and parent pieces will form a weld. This process enables the creation of joints of dissimilar materials, such as steel/aluminum and copper/aluminum, which are not easily welded by standard techniques [1].
The properties of the welding front, influenced greatly by the evolution of the flyer deformation and collision, is ultimately the determining factor in welding success. Under the correct conditions a mass flux containing oxides and debris ('jet') is formed, which cleans the surfaces and allows for metallurgical bonding [2]. The two main factors typically considered in joint formation are the collision angle β and the collision velocity v_c. Figure 1 shows a schematic of the welding front, as well as a micrograph of a welding interface.

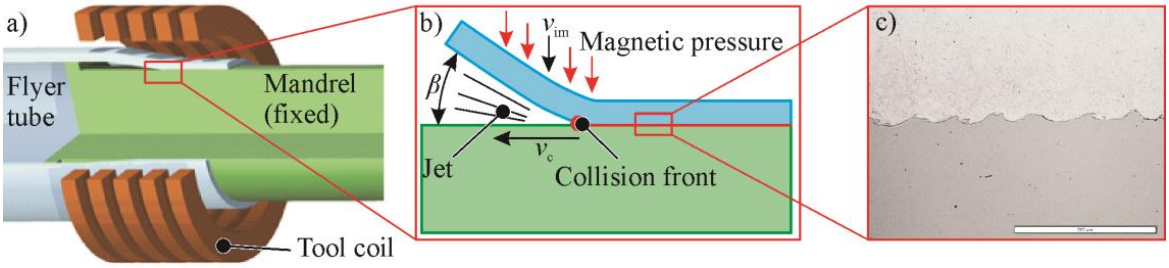

Figure 1: *Magnetic Pulse Welding of tubular work pieces. a) Setup, b) process principle, and c) image of the weld seam (according to [3]).*

The welding front contour is determined by many factors, including the radial relationships between coil/flyer and flyer/parent distance, as well as the axial arrangement of the coil and the flyer (the "working length", l_w). For example, by positioning the flyer edge to extend beyond the coil edge, a two-sided front process can be realized (see Figure 2).

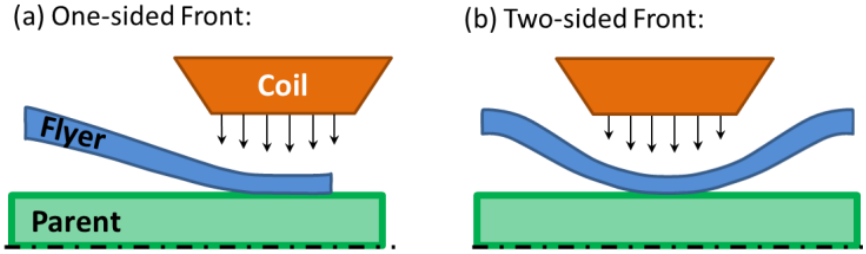

Figure 2: *a) One- and b) two- sided welding, adapted from [6].*

There are advantages to one- or two-front welding processes. As one can imagine, the heavy deformation of the flyer causes shearing forces in the part, which may lead to shearing and tearing of the flyer material above the formed weld. For this reason, a two front process may be advantageous as it creates symmetric forces with opposite directions, counteracting each other globally. However, the energy needed to deform a

part along two fronts is higher than a single front, potentially reducing process efficiency and the resulting weld lengths are generally smaller than in a single-front process.
Experiments based on two-front processes have been performed by Kojima et al. [4]. The purpose of this work was an evaluation of the tapering angle of the parent part on the length of resulting welds. Faes et al. [5] reported that the overlap of the field shaper edge and the outer work piece had a significant effect on (tube) welding conditions for copper/brass joints. Working distance of up to 5.5 mm were evaluated on a field shaper with a maximum working zone of 15 mm. No experiments were performed with two-sided fronts and phenomena beyond the occurrence of a weld were not evaluated.
It has been reported by sources such as Zhang [6] that the determination of a one- or two-sided welding process can be done by the axial positioning of the work piece in a coil of maximum working length l_{coil}. If $l_w < l_{coil}$, the process will occur along a single front in which the front edge of the flyer makes impact with the parent, and from there proceeds to collapse via a single front onto the parent. If $l_w > l_{coil}$, a two-front process occurs, in which the flyer impacts the parent in the center of the field shaper/working zone, and collapses outwardly along two fronts. A transition zone between one- and two-fronted processes may exist, for instance with working lengths close to but not exceeding the coil length; however, evaluation of this has not been found in literature. There is also a lack of publications discussing an experimental comparison of one- vs. two-front welding, and no works with in-depth analysis and comparison of the front regimes.
The purpose of this work is to evaluate the effect of the working distance on the features of MPW experiments. This is done by the axial positioning of the flyer piece over the edge of the coil, at the coil edge, and at several positions within the coil. At various positions, the discharge energy was also varied in order to observe if there is a noticeable effect. Simulations were used for comparison and to gain a more in-depth understanding of the process.

2 Experimental Design

2.1 Joining Materials and Tools

Flyer materials consisted of EN AW-6060 (AlMgSi0.5) tubes with an outer diameter of 40 mm and a thickness of 1 mm. The static yield stress of the material was 222 MPa, determined by tensile tests. The parent material was a cylinder of C45-grade steel with a diameter of 33 mm.
A single-turn coil made of a CuCrZr-alloy with a maximum working zone of 15 mm was used for forming. The coil was designed to be able to conduct PDV measurements of flyer deformation, an idea presented by Jäger and Tekkaya [7]. Experiments were conducted on a 32 kJ Bmax pulsed-power generator and workstation. This system has a maximum charging voltage of 20 kV, capacitance of 160 µF, and a discharge frequency of 25 kHz.

2.2 Experiment

Experiments were conducted under fixed flyer-coil and flyer-parent radial distances while varying the axial position of the flyer and the charging voltage. Working distances of 17 (flyer edge placed 2 mm beyond the coil edge), 15, 12, 11, 10, 9, 8, 7, and 4 mm were evaluated. For each working length, the initial charging energy was set at 11.5 kJ and was increased or decreased for select working lengths, depending on initial results. Figure 3a and b show a picture of the experimental set-up and a schematic of the welding set-up/working length distances, respectively. Current measurements were conducted for each trial using a Rogowski coil. After joining, flyers were cut and peeled from the parent in order to expose the interface.

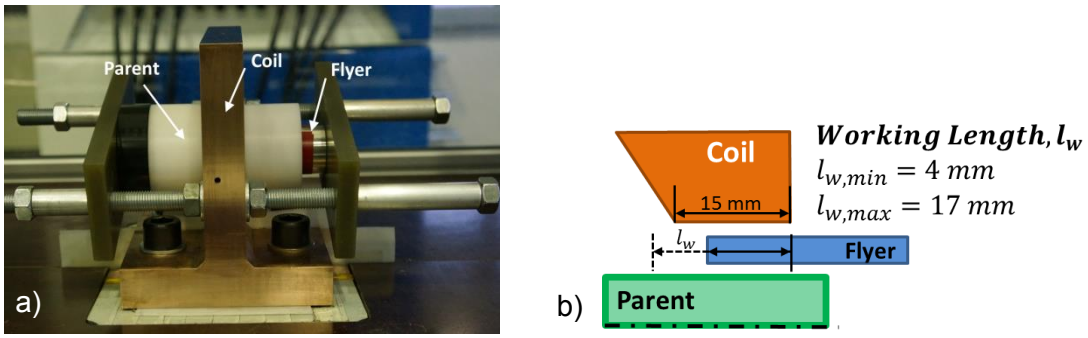

Figure 3: *a) Picture of the experimental setup and b) schematic showing working lengths.*

2.3 Simulation

Due to the high speed and restrictive conditions of MPW, the angles of the welding front are extremely difficult if not impossible to measure directly. For this, coupled mechanical-electromagnetic simulations mirroring the conditions of the experimental part have been conducted. LS-DYNA (Version R 7.0) was used; the electromagnetic fields are computed using a Finite Element Method (FEM), coupled with a Boundary Element Method (BEM) for the surrounding air and insulators (L'Eplattenier et. al [8]). Recorded current curves from the experiments served as input data. The simulations were calibrated based on Photon Doppler Velocimeter (PDV) data obtained by the authors during welding experiments at Bmax in Toulouse, France. The basics of this heterodyne method were described by Strand et al. [9]. This reference contains an in-depth description of the PDV measurement principle and the system properties. In order to adapt the impact velocities in the simulations to the measured data, the Cowper-Symonds constitutive equation (Eq. 1) was used. Here, σ_o' stands for the dynamic flow stress at a uniaxial plastic strain rate $\dot{\varepsilon}$, σ_o is the associated static flow stress and D and q are constants for a particular material [10]. D and q were chosen in a manner, so that the impact velocities of simulations and experiments were comparable.

$$\sigma_o'/\sigma_o = 1 + \left(\frac{\dot{\varepsilon}}{D}\right)^{1/q} \quad (1)$$

The collision angles β were calculated for selected nodes with the vectors of the velocities in axial and radial direction. For the simplified, time harmonic calculation of the magnetic field intensity between coil edge and flyer, the program FEMM 4.2 [11] was used.

3 Results and Discussion

3.1 Experimental Results - Varied Working Length

By pulse-forming flyer tubes onto parent parts at energies slightly lower than those required for welding or to points for which the weld is weaker than the base material, important details about the rolling process of the flyer can be extracted. By cutting and removing the flyer after pulsing, the surface was able to be observed. This has advantages over other analysis techniques. For example, a push or tension test of welded samples reveals the joint area, but can smear the part interface during removal, and metallographic images of the interfaces show only a very isolated area of the interface. The results of experiments are shown in Figure 4a and b. It can be seen here that for the initial charging voltage of 11.5 kJ, any existing welds broke before the flyer material.

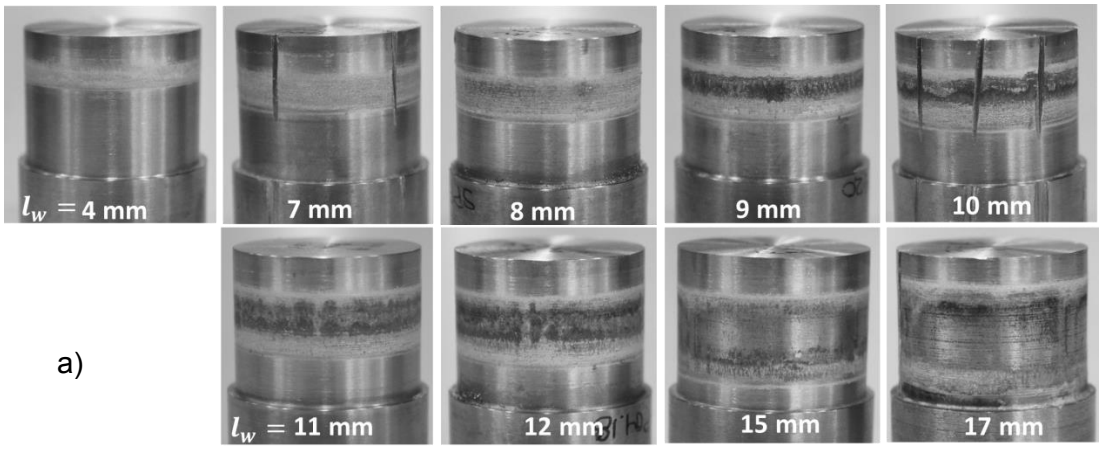

a)

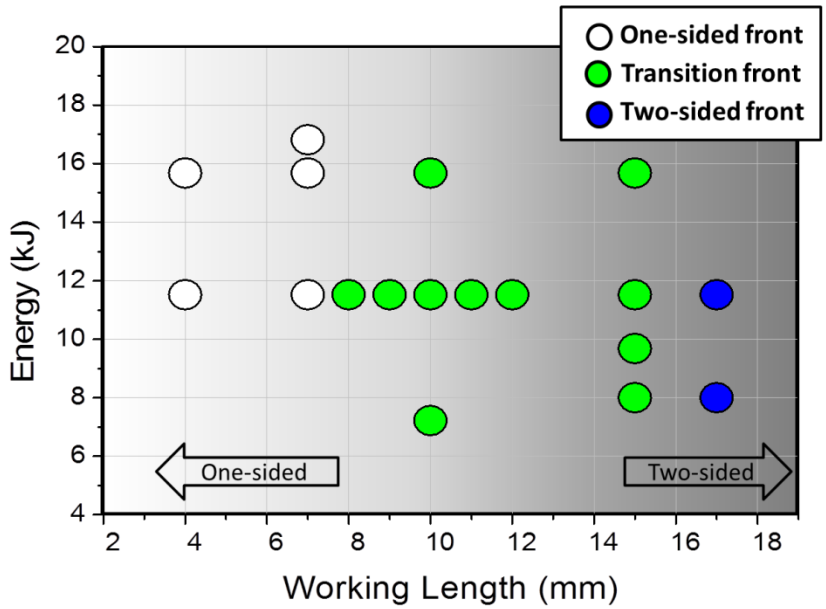

b)

Figure 4: *Overview of welding results: a) images of samples pulsed at constant energy for various working lengths, b) plotted results showing the front-type for each sample.*

As can be seen, in essence three different regimes exist:

A) A one sided front, starting at flyer edge and propagating away from it
B) A transition regime, where (as will by clarified by simulation) the flyer impacts the parent under the correct conditions to create damage or potentially weld at the front of the flyer and near the coil edge, but the area in between contains a grey residue.
C) A two-front process, in which a bowed impact at the center of the coil occurs and two fronts run in opposite directions from this region

Each of the presented regimes leads to distinct surface interface characteristics. Regime A (one front) leads to a short region at the flyer edge, which is clearly seen in Figure 4a for samples with working lengths of 4 and 7 mm.
The other easily recognizable regime is for the working length of 17 mm and corresponds to regime C (two fronts). Here, the parent area near the middle of the coil appears in a similar condition to the state before welding. This is because the initial impact occurred perpendicular to the surface, and the initial pressure of the running fronts was not sufficient to deformation the material interface. The sample surface indicates that the flyer only propagates with high enough pressures for parent deformation as it reached the ends of the coil.
Regime B is present for samples pulsed at working lengths from about 8 mm to about 12 mm. Samples with working lengths of 15 mm are also thought to be included here, as will be seen later. In this regime, grey matter appears between the beginning of the flyer deformation zone and near the opposite coil edge. This matter is due either to low angles, for which the surface is perturbed but no welding occurs, or to non-uniform flyer deformation. If the latter is the case, it is thought that concentration of the magnetic field at the coil edge may cause forces on the flyer exceeding the material strength, leading to early deformation at this point and hindering an existing jet from completely escaping the collision front area. Simulations were performed in order to gain better understanding of this regime.

3.2 Experimental Results – Varied Energy

In order to assure that results presented above could be applied to other charging energies, several working distances were selected for further analysis at higher and lower pulsing energies.
As the energy was changed for a given working length, the width of the distinct areas tended to increase or decrease in accordance with the charging voltage; however, the general interface characteristics remained constant (Figure 5). At higher energies of 15.7 kJ and 16.8 kJ, welding occurred for working lengths of 4 mm and 7 mm, respectively; Figure 6 shows metallurgical analyses of these samples. The increase in welding length in accordance with the working distance is apparent.

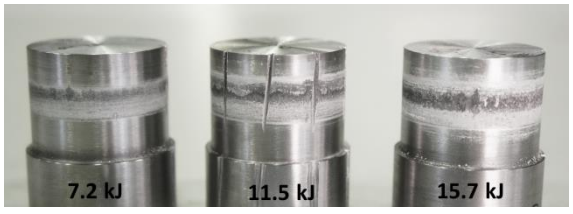

Figure 5: *Samples with 10 mm working length at various energies.*

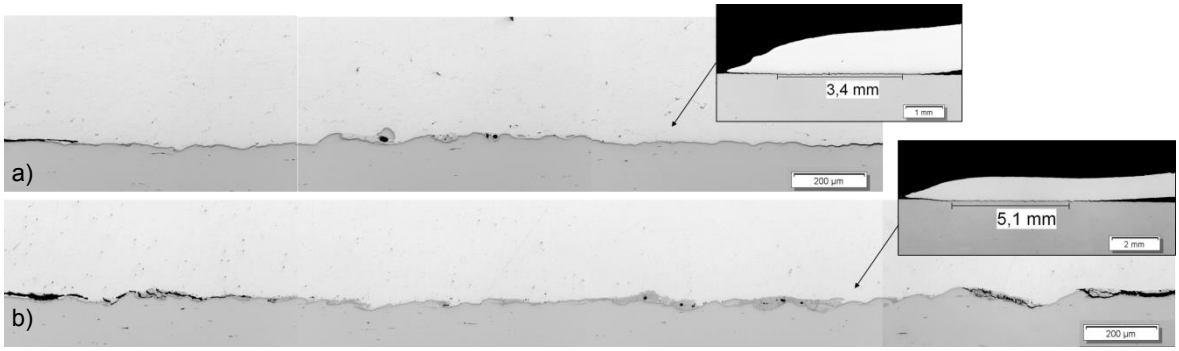

Figure 6: *Overview images and detailed images of samples with working lengths of a) 4 mm and b) 7mm.*

3.3 Simulation

Figure 7a-c shows simulated images of the aluminum tubes at the time of initial impact with the parent part for $l_w < l_{coil}$, $l_w = l_{coil}$ and $l_w < l_{coil}$, respectively. The area of first contact between the parent and flyer part are visible in the simulation. The area appears in the color of the flyer due to a slight immersion of the flyer part into the rigid parent part. The angles at the contact point for each image have also been calculated in order to aid analysis. An exemplary recorded current curve for a charging voltage of 9.7 kJ was used as input for the coupled electromagnetic-mechanic simulation.

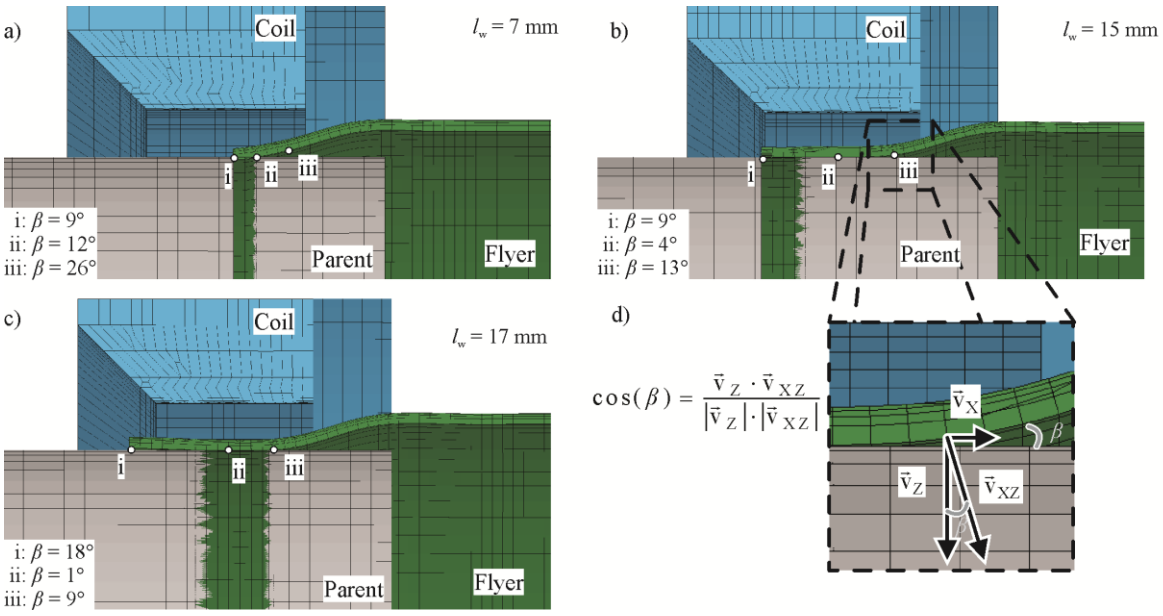

Figure 7: *LS-DYNA simulations of setup with a) $l_w < l_{coil}$, b) $l_w = l_{coil}$, c) $l_w > l_{coil}$, d) Determination of the collision angle β*

Figure 7a and c present clear indications of a one- or two-sided front, correlating with regimes A and C, respectively and match well with the experimental results presented above. At working distances under about 7 mm (half of the coil length), the front is one-sided. This is an indication that the relationship between magnetic pressure at the flyer interface and the material stability is such that the flyer deforms first at the edge, and then

continues along a single, continuous collision front. The simulation in Figure 7c show that deformation for samples placed over the coil working length ($l_w = 17\ mm$) occurs in a bowed manner. If the bow-shape of the flyer was too flat (in this case, a low value of about 1°), it may be that the correct conditions to cause visible damage to the parent were only reached at the edges, in agreement with Figure 4a.

The simulation results shown in Figure 7b are more complicated and may require additional in-depth analysis. As the angular measurements show, the tube near the rear coil edge is slightly bowed towards the parent; this may be an indication of non-uniform flyer deformation leading to jet entrapment, as mentioned earlier. This deformation regime is thought to be very unfavorable not only for potential jet entrapment, but also because of the generally flat characteristics of the front. Both of these would lead to insufficient impact pressures and unfavorable welding conditions.

Through simulations, as well as viewing the interfaces of samples joined under non-welding conditions, it can be seen that positioning the edge of the flyer piece inside the coil/field shaper width does not guarantee a continuous one-sided front process. In order to see if the increase in magnetic field density at the corners of the coil has an influence in the flyer deformation for these trials, an assessment of the magnetic field for various working lengths was performed. Figure 8 presents the simulated effect of the working distance on the magnetic field $H_{tangential}$ for an exemplary harmonic current amplitude of 500 kA at 20 kHz. This shows that the magnetic intensity on the workpiece is inversely related to the working distance and for a working distances $l_w \leq l_{coil}$, the field intensity has a peak at the end of the flyer. However, the process efficiency is not directly inversely proportional to the working distance. Also, it is shown that for this setup the radial position of the flyer piece is far enough away from the coil edge that the increase in magnetic field density at the coil edges does not affect the forces on the flyer.

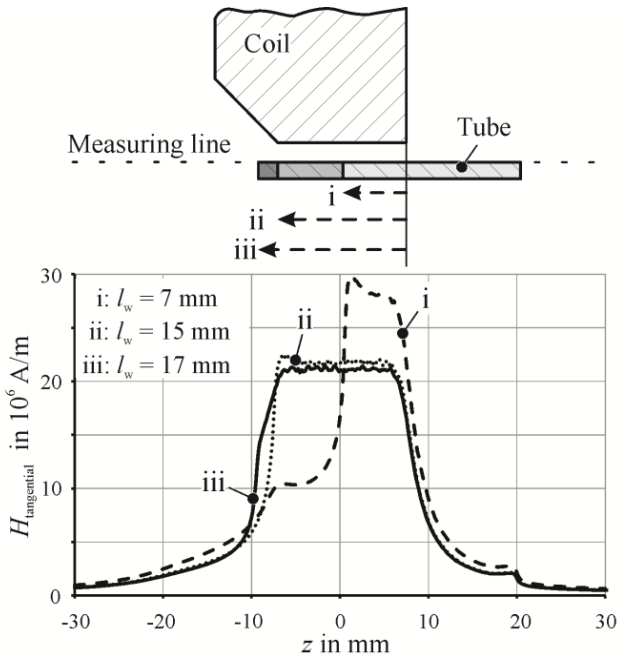

Figure 8: *Axis-symmetric FEMM simulation of the tangential magnetic field intensity* $\boldsymbol{H_{tangential}}$ *at the outer flyer surface for the given setup for different working lengths.*

The results seen above indicate that the magnetic field intensity is relatively even over the part surface, showing a slight increase at the flyer edge. This indicates that flyer acceleration should occur in a uniform manner, beginning with the flyer edge. For transition regime (B), the case is probably such, that the flyer end impacts the sample first, while the rest of the flyer follows in a chiefly flat manner, in slight contradiction with the simulation seen in Figure 7b. Entrapment of the jet is still possible in this case, as projectile particles may impact the flyer or parent surfaces before escaping the joining pair, becoming trapped between flyer and parent and hindering further jetting and welding processes. This, in addition to a flat impact (insufficient angles), is a likely reason for welding failure in regime B. The contradiction between expected flyer deformation based on the magnetic field intensity and the simulation of the flyer deformation requires more in-depth analysis.
Simulation results oppose notions that a longer working length is better in order to increase welding probability/efficiency by harnessing more of the magnetic field. More energy may be used in deformation; however, deformation may occur in a manner unfavorable to welding. Results presented here may be used as a basis for understanding the impact of the working length as well as determining conditions under which partners will weld in MPW. Here, parts with welding distance equal to less than half of the coil length exhibited welding with single-front flyer impact under the given conditions.

4 Conclusions

The presented research has shown three basic regimes for flyer deformation based on its axial position within a MPW coil. If the flyer is placed all the way through the coil, a two-front process ensues in which the flyer contacts the parent first at the coil center, then propagates outwardly. At working distances (in this case) smaller than half of the total coil length, impact between the flyer and parent occurs first at the flyer edge, and propagates along a single front. At working distances between 8 and 15 mm, a transition regime was seen in which the front propagated in either a flat or non-uniform manner. The transition regime is thought to provide sub-optimal conditions for MPW processes. The presented results as well as additional simulation can be used as a basis to establish a more generalized theory of the relations between relative working length and weld result.
In order for a more thorough assessment of the coil-flyer position and deformation relationship, future trials on a coil with a smaller maximum coil working length are planned. This will allow for the investigation of the relationship between the coil length and the working length on the deformation and welding front (for instance, if the features seen in samples joined with $l_w > l_{coil}$ and $l_w = l_{coil}$ are consistent with those investigated here). Additionally, experimental trials on coils with diameters smaller than ∅40 mm are planned in order to see the effect of the part size on the deformation and welding abilities.

References

[1] Mori, K.; Bay, N.; Fratini, L.; Micari, F.; Tekkaya, A.E.: Joining by plastic deformation, CIRP Annals – Manufacturing Technology, 2013, 62, pp. 673-694.

[2] Deribas, A.A., Simonov, V.A. Zakcharenko, I.D.*:* Surface effects with oblique collisions between metallic plates. Translated from Fisika Goreniya I Vzryva, Vol. 10, No. 3. 409-421 (1975).

[3] Göbel, G.; Beyer, E.; Kaspar, J.; Brenner, B.: Dissimilar metal joining: Macro- and microscopic effects of MPW, Proceedings of the 5th International Conference on High Speed Forming, 2012, pp. 179-188.

[4] Kojima, M., Tamaki, K. Furuta, T.: Effect of collision angle on the result of electromagnetic welding of aluminum. Transactions of the Japan Welding Society, Vol 20, No. 2, 1989, pp. 36-42.

[5] Faes, K., Baaten, T., De Waele, W., Debroux, N.: Joining of copper to brass using Magnetic Pulse Welding, Proceedings of the 4th International Conference on High Speed Forming, 2010, pp.84-95

[6] Zhang, P. Joining Enabled by High Velocity Deformation. Doctorate Dissertation, The Ohio State University, 2003.

[7] Jäger, A.; Tekkaya, A.E.: Online measurement of the radial workpiece displacement in electromagnetic forming subsequent to hot aluminum extrusion, Proceedings of the 5th International Conference on High-Speed Forming, 2012, pp. 13-22.

[8] L'Eplattenier, P.; Cook, G.; Ashcraft, C.: Introduction of an electromagnetism module in LS-DYNA for coupled mechanical thermal electromagnetics simulations, Proceedings of the 3rd International Conference on High Speed Forming, 2008, pp.85-96.

[9] Strand, O.T.; Goosman, D.R.; Martinez, C.; Whitworth, T.L.; Kuhlow, W.W.: Compact system for high-speed velocimetry using heterodyne techniques, Review of Scientific Instruments, 2006, 77 (083108).

[10] Jones, N.: Structural Impact, Cambridge University Press, 1989.

[11] Meeker, D.C.: Finite Element Method Magnetics, Version 4.2, http://www.femm.info.

Magnetic Pulse Welding: welding windows and high velocity impact simulations

J.-P. Cuq-Lelandais[1)*], S.Ferreira[1)], G. Avrillaud[1)], G. Mazars[1)], B. Rauffet[1)]

[1)] Bmax, 30 bd de Thibaud, ZI de Thibaud, 31100 Toulouse Cedex 9 – France
Website : www.bmax.com
* Corresponding author: E-mail address: jean-paul.C@bmax.com ; Tel.: +335 34 61 16 68

Abstract

Magnetic Pulse Welding (MPW) is a solid state welding process that can be used for couples of material difficult to weld using conventional methods or when high mechanical characteristic of the joint is required. The MPW process is a cousin of the EXplosive Welding (EXW). It consists in accelerating a part locally, few millimetres thick at maximum, using the magnetic pressure induced by a high pulsed current in a coil. High velocity impact with the parent part can generate welding if adequate ballistic conditions are reached.
In this work, simulation is used to better understand the mechanisms involved in this dynamic and multi-physical problem. Models were developed by using the explicit dynamic code LS-Dyna, which provides 2D/3D calculations with a strong coupling between mechanical, electromagnetic and thermal solvers. In this paper, a welding window for MPW and derived from EXW is proposed. Then, electromagnetic Lagrangian simulations of the process are performed to predict the ballistic path along the flyer during collision. The validity of these simulations has been checked thanks to comparison with results of experiments using a time resolved Photon Doppler Velocimeter (PDV) to measure the flyer velocity . Also, both numerical and tests results are superposed on the angle vs. impact velocity graph providing an experimental welding window for a given material couple.

Keywords

Magnetic Pulse Welding (MPW), Dynamic simulations, Welding Windows

1 Introduction

Welding 2 dissimilar materials or particular alloys can be hardly achievable using traditional melt based techniques. This generally comes from the difference in the melting

temperature between the present compounds. Such processes can generate thick layers of brittle and sometime cracked intermetallics that reduce the mechanical strength of the joint. Moreover, the resolidification process leads to internal stresses along the interface, possibly large grains size and creating a weak heat affected zone. When such a joint is not suitable, solid state bonding processes are a valid and superior alternative solution. EXplosive Welding (EXW) and Magnetic Pulse Welding (MPW) are two solid state processes based on high velocity oblique impacts. When the impact parameters are properly chosen for a given couple of material, a high performance joint can be achieved, and often stronger than the weakest base material strength. Because no melting appears during the process, no significant Heat Affected Zone is generated around the interface, leading often to a failure out of the welded zone during mechanical tests [1]. For obvious production rate reasons, only MPW is used in mass production. Moreover, this solution provides a more secured use (no explosive implied) and at a reduced cost due to minimal energy consumption.

The process is based on the High Pulsed Power technology consisting a flash discharge of electrical energy. This technology is also used in Bmax for Magnetic Pulse Forming applications as well as Magnetic Pulse Crimping or Electro-HydroForming applications.

The aim of this paper is to present the numerical investigations developed at Bmax to design MPW cases leading to the welding of a large variety of given material couples by using both analytical and numerical tools. Firstly, a brief description of the MPW principles and theory is given and compared to the EXW method. The MPW theory allows to predict the weldability window which gives the required ballistic conditions to obtain welding (collision angle and velocity). 2D multi-physical simulations with the dynamic explicit LS-DYNA code are shown as they provide the means to predict the ballistic path of the collision point and to plot it in the graph of the welding window. Such results can be compared to experimental MPW configurations, using the final welded length. In addition, a comparison of experimental and simulated velocities is made to prove the validity of such simulations.

2 MPW Principles and Analytical Aspects

To perform a Magnetic Pulse Welding between two pieces, a high current is discharged through a coil creating an induced eddy current in the conductive workpiece (tube or sheet). The magnetic field induced in the flyer creates Lorentz forces that accelerate it away from the coil at high speed, i.e. several hundreds of meters per second (See Figure 1). During this phase, the high magnetic pressure yields the metal into a viscoplastic state. Then, the flyer reaches the anvil with a collision angle and a velocity, similarly to the EXW process. If these two parameters are adapted to the couple to weld, jetting occurs at the collision point. This jet cleans all the oxides and contaminants on the surface of the two materials [2]. A high pressure field is generated near the collision point, able to provide an atomic bonding. Moreover, in some cases, instabilities can be generated resulting in a wavy interface. This pattern can add an additional hook to the weld. This also shows that the two metals have a hydrodynamic behaviour, i.e. they act as liquids during the impact, although they remain at the solid state.

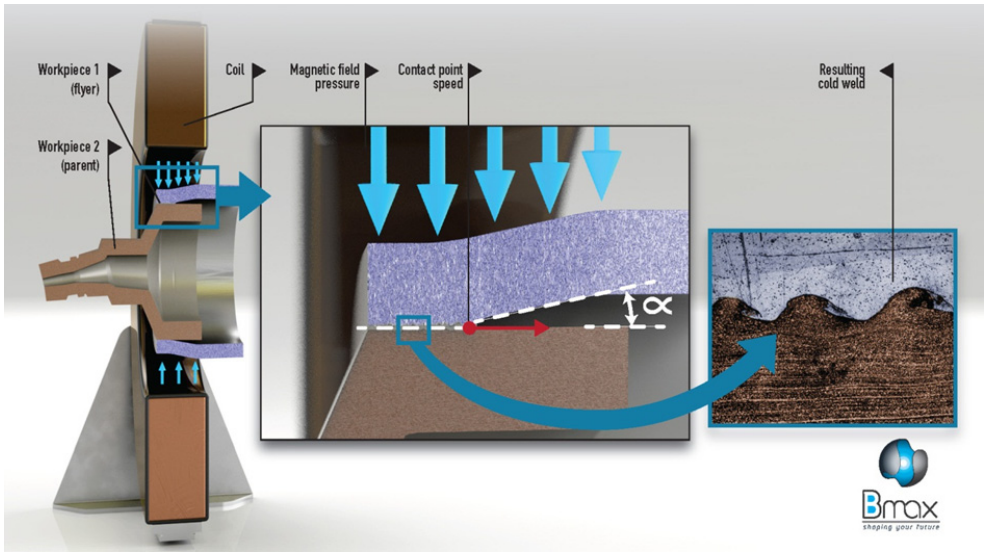

***Figure 1**: MPW general principle for two tubes*

The MPW process takes place in a few microseconds. Other advantages are that no heat, no filler materials, protecting gases or special degreasing are required, and moreover, very few smoke, sparks or radiations are generated during the process.

An important requisite in impact welding (EXW and MPW) is to determine the correct ballistic parameters to obtain jetting, a necessary condition to weld, and eventually to obtain a wavy pattern, this latter being optional depending on the material couple. To predict them, EXW experimental studies showed it is convenient to locate a weldability window as a function of the two main ballistic parameters [3], the collision point velocity V_c and the collision angle α.(See Figure 2)

The Welding Window can be analytically estimated by using the formulas developed initially for EXW. Impact welding process implies multi-physical and dynamic phenomena, including mechanical, thermal and thermodynamics fields. In the case of MPW, electromagnetics aspects also have to be taken into account. To obtain a strong welding, several necessary conditions have to be reached:

- **Jetting conditions:** the collision point has to be subsonic compared to the local materials speed of sound to generate a jet. A supersonic case leads to an oblique shock wave behind the collision point. In this case no jet is induced and in addition, the shocks reflections on the parts boundaries create tension states which may debond already welded zones nearby.
- **High Pressure regime:** the impact velocity has to be sufficient to obtain a hydrodynamic regime. If the velocity is too low, the parts are only crimped or formed (elastic-plastic regime)
- **No fusion during the collision:** The process has to remain “cold”. If the pressure is too high, the materials can locally melt and then re-solidify. This induces no weld or weaker ones generally with cracks due to the Heat Affected Zone or too thick intermetallics.
- **The smooth/wavy regime:** The unstable regime can be obtained if a given critical collision point velocity is exceeded. A wavy structure can appear but is not needed

to get a strong bond. Such a wavy interface is illustrated in the fig. 2 with a LS-Dyna simulation of an Al / Steel case.

***Figure 2**: Example of wavy interface with jetting on LS-Dyna, density contours - Al / Steel*

The main difference between MPW and EXW is that the angle and the velocity are almost constant during the EXW process (controlled by the geometry and the constant deflagration velocity) whereas they continuously vary for MPW. Thus, the main issue in MPW is to ensure that the collision parameters remain in the welding window over the zone to be bonded. To better control the parameters evolution during the MPW process, the welding window is plotted in the plane angle / radial impact velocity instead of collision point velocity traditionally used in EXW. In fact, the impact velocity is preferred because it can be linked more easily to the High Pulsed Power machine parameters as the acceleration from the Lorentz forces is mostly radial.

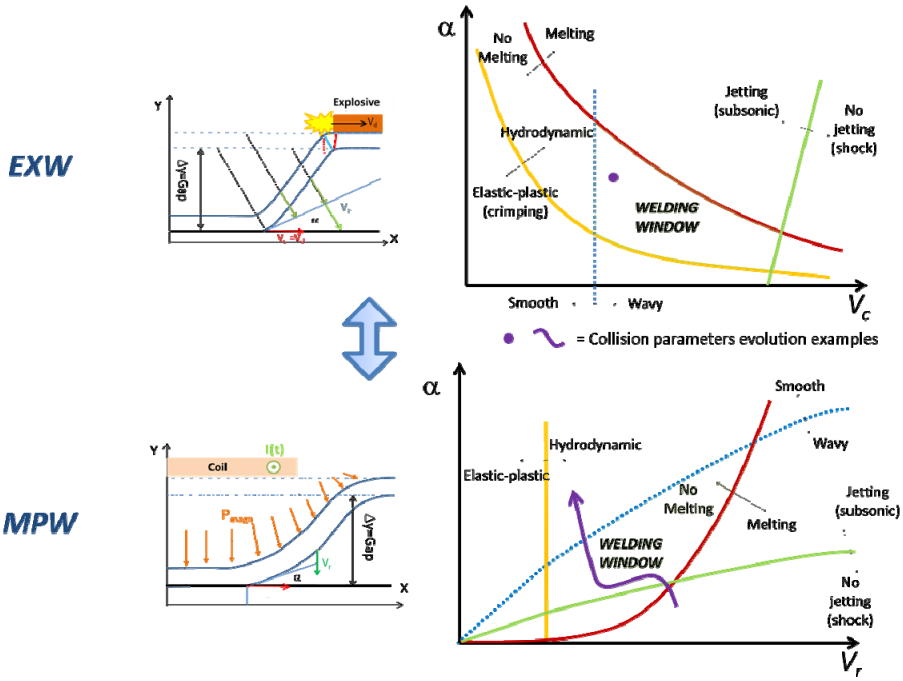

***Figure 3**: EXW/MPW principles and Welding Windows comparison*

3 MPW Electro-Mechanical 2D/3D Simulations

At Bmax, the main objective of simulations is to have the ability to answer customer needs faster and more accurately. Simulations help in evaluating project feasibility with limited physical testing and accelerate the development of successful new applications. Moreover, designing with simulations allows to reduce the number of experiments and the global cost of a project.

As a MPW process occurs in a timescale of microseconds, specific simulations are needed to analyse the main physical phenomena. For this, we are running 70 LS-DYNA licenses with a simulation team of 6 physicists and engineers. LS-DYNA is a parallel 3D Magneto-Hydro-Dynamic (MHD) multi physics code. It is the only actual code available on the market that strongly couples high speed mechanics (including impact), thermal effects (including Joule effects and the evolution of the electrical conductivity with temperature), electromagnetics and fluid/structure coupling [4] at the same time. The electromagnetic solver uses the eddy current approximation. Maxwell's equations are solved using a Finite Element Method (FEM) for the solid conductors. These latter are coupled with a Boundary Element Method (BEM) to consider the surrounding air or insulators without meshing them and thus save calculation time [5].

When the Analytical Welding Window of a given couple is defined, it is possible to tune in the simulation geometrical and electrical parameters so that the path of the collision point remains mostly in the welding window traced in the graph impact angle vs radial velocity.

An example of 2D and 3D MPW LS-DYNA analysis is shown in Figure 4 and 5. This case study is the MPW of an aluminium alloy outer tube on a stainless steel anvil. The coil surrounds the system and delivers the magnetic pulse necessary to accelerate the outer tube, as it can be seen on the 2D axisymmetric approach (Figure 5). This model provides a complete analysis of the collision. In this case, the deformed shape of the tube is not optimized and presents large variations in collision angle. This leads to a tube rebound in the middle of the zone where welding is desired.

***Figure 4**: 2D MPW axisymmetric simulation of Al6061-T4/SS304 tubes*

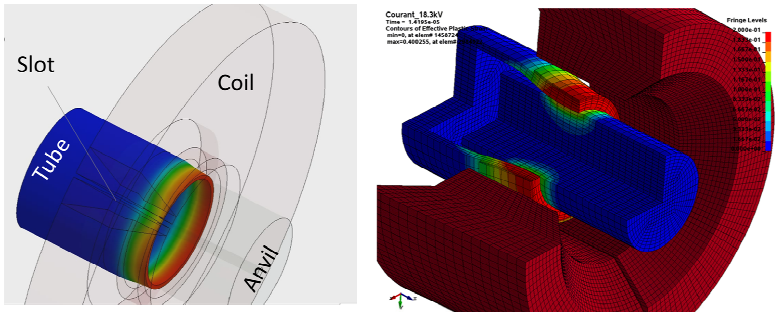

***Figure 5**: 3D MPW simulation including slot influence on the tube impact velocity (left) and plastic strain (right)*

Complementary to the 2D models, it is possible to run a 3D analysis for example to predict the influence on the collision parameters due to the coil slot or the setup geometry.

4 Experimental/Numerical Comparisons

In order to validate the numerical method predicting weldability, comparisons between numerical models and experiments have been performed on the Aluminium/Stainless Steel case study. Comparisons can be done by analysing the welded areas on the samples after shot.

4.1 Comparison of the welded length

Welded zones are checked using micrographs. Figure 6 shows them for the Aluminium Stainless Steel case study. It can be seen that two zones have been bonded, leaving a central region unwelded due to the bounce back described above.

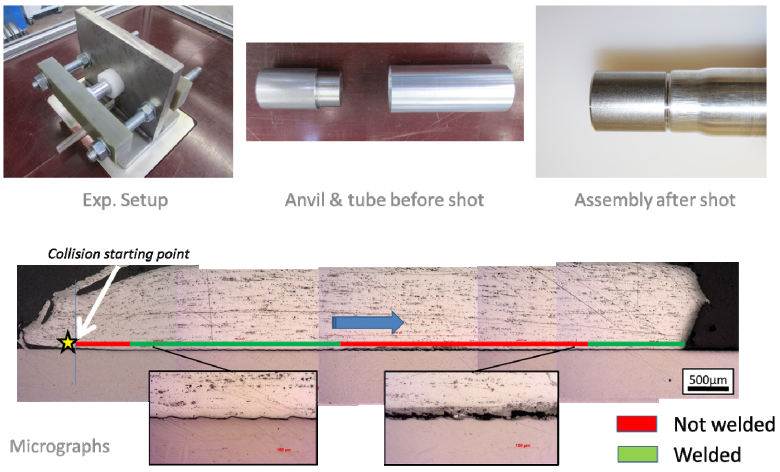

***Figure 6**: Aluminium on Stainless Steel MPW test and micrographs*

Thus, it is possible to locate the welded zones along the ballistic path and observed its location compared to the analytical welding window (see Figure 7). The curve associated to the previous micrograph is on the left. There is a high correlation between the calculated welding window and the experimental welded zones. Moreover, the ballistic path evolution allows to explain the causes of non-weldability. In the present case, the first non-welded length is at the collision starting point. It is due to the time lag needed to get the jet establishment. Then, welding occurs until the ballistic path crosses the jetting limit curves. Welding is stopped also after a time lag due to a pressure field change into a shockwave regime. This regime implies no more jet and a potential rebound as observed in the 2D axisymmetric model. The welding regime starts again, also delayed after the re-entry in the welding window. Welding is obtained until high angles and low velocities make the process stop.

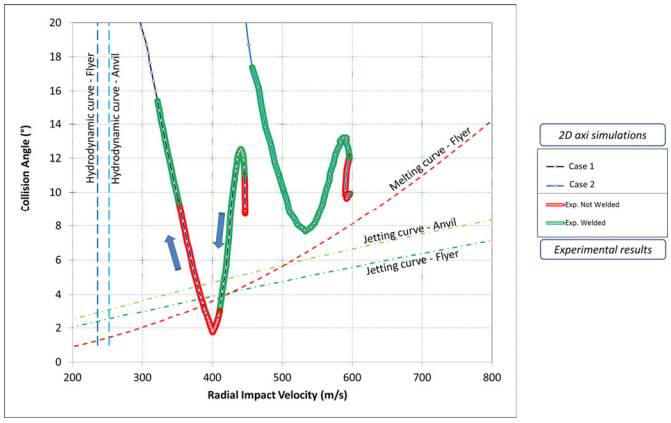

***Figure 7**: Experimental/Numerical comparison on the MPW ballistic Welding Window (Aluminium on Stainless Steel) – Intervals between two dots represent an advance of the collision point of 0.1mm.*

From this test, it is possible to adjust the experimental parameters to obtain a single welded area. In this case, as the gap and the peak current are increased, a second ballistic path is obtained (right curve) and remains within the welding window during the complete collision. This experimental test shows high correlation between the experimental results and the analytical welding window.

4.2 Time-Resolved Photon Doppler Velocimeter (PDV)

In order to validate the accuracy of the simulations, complementary time-resolved measurements have been performed in a MPW like configuration. For this, a 4 channels Photon Doppler Velocimeter has been developed at Bmax in collaboration with the Ohio State and Dortmund Universities.

This device allows to measure the velocity vs time at different axial positions, and different angular positions to identify the decrease of velocity at the coil slot location. Figure 8 shows a scheme of this setup, with three PDV probes located at different axial positions.

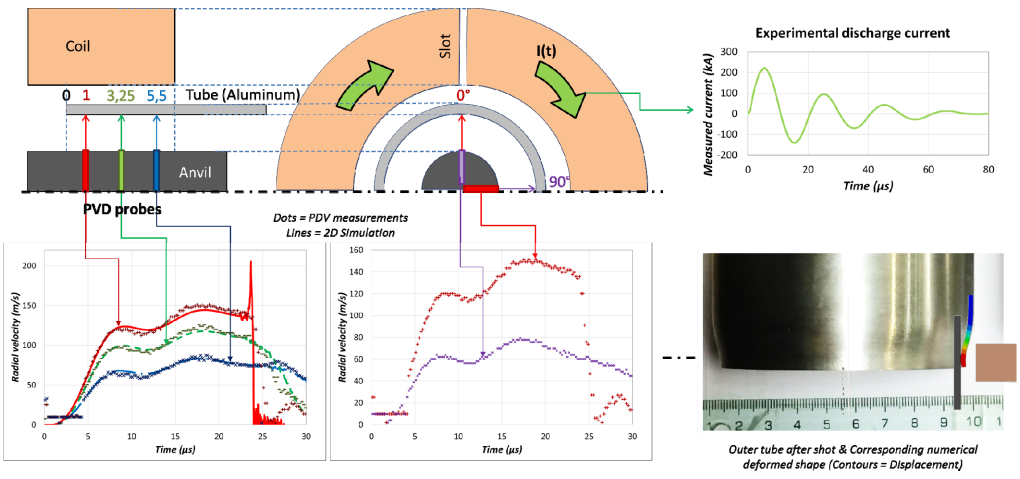

***Figure 8**: Experimental/Numerical comparison of radial velocity at different axial positions (1.5 mm thick and 80mm diameter aluminium tube)*

The experimental PDV signals present an acceleration until the first quarter period of the current is reached. Then, a deceleration is observed followed by a new acceleration coming from the second peak current. A fast velocity drop is then observed corresponding to the impact of the tube on the anvil. The velocities magnitudes depend on both the axial and angular positions. The axial influence has been reproduced numerically with a very good resemblance, showing that 2D MPW simulations reproduce the process with good accuracy. Moreover, the simulated global shape fits the experimental one.

5 Conclusion

An intensive work has been performed at Bmax to develop MPW design tools. The method is based on the impact conditions exploitation, including the construction of welding windows dedicated to the process. The process can be modelled thanks to the multi-physical LS-DYNA code providing a solution to represent with accuracy induced magnetic pressures leading to high velocity impacts. The resulting collision parameters, angle and velocity, can be plotted in the graph of the welding window in order to define precisely the welding parameters. This method has been validated by using several experimental results associated to micrographs. In addition, simulated velocities in a cylindrical MPW geometry have shown a good match with experimental results coming from a Photon Doppler Velocimeter, which gives additional confidence in the methodology. These tools provide Bmax the ability to define efficiently the welding parameters of new couples of materials. Moreover, it brought us a better and deeper understanding of the physical phenomena happening during a MPW process. Thanks to these developed tools and methods, Bmax has the ability today to answer customer's requirements and questions in matter of hours or days even when new material combinations are presented. This ability brings the technology closer to commercial use.

References

[1] Aizawa T. & al., Application of MPW for aluminum alloys abd SPCC steel sheet joints, Welding Journal, 86 (2007) pp. 119-124

[2] Göbel G. & al., Dissimilar metal joining: macro and microscopic effects of MPW, Proceedings ICHSF (2012) pp. 179-188

[3] F. Grignon, D. Benson, K.S. Vecchio and M.A. Meyers, Explosive welding of aluminum to aluminum : analysis, computations and experiments. Int J. Imp. Eng., (2003) 30 pp1333–1351.

[4] John O. Hallquist. LS-DYNA® Theory Manual, March 2012.

[5] L'Eplattenier P. & al., Introduction of an electromagnetic module in LS-DYNA for coupled mechanical – thermal – electromagnetic simulations, Steel Research Int., (2009) 80, 5.

Magnetic Pulse Welding of the “Tube – Plug” Pair of STS410 Steel*

V. Krutikov[1], S. Paranin[1], V. Ivanov[1], A. Spirin[1], D. Koleukh[1], J.-G. Lee[2], M.-K. Lee[2], C.-K. Rhee[2]

[1] Institute of Electrophysics of the Ural Branch of Russian Academy of Sciences (IEP), Russian Federation
[2] Korea Atomic Energy Research Institute (KAERI), Republic of Korea

Abstract

The research was focused on the magnetic pulse welding (MPW) of 12.5% Cr steel STS410. The experiments were performed in the tube-plug geometry (both details were made of the same steel). Magnetic pulse unit consisted of pulsed current generator (PCG) loaded to a single-turn coil. Magnetic field amplitude of 40 T was generated in the coil during experiments. The amplitude of pulsed current reached 750 kA.

The effects of energy storage capacity, charging voltage, and end plug shape were studied. The welded samples were investigated by optical microscopy. The optimal velocities of impact and contact front motion were evaluated as 300 m/s and 3-3.5 km/s, respectively.

The paper includes the leakage test results as well. To date, the joints with a helium leak rate of 10^{-9} mbar·l·s^{-1} have been produced.

Keywords

Welding, Steel, Magnetic Pulse Welding

* This work is based on the results of the Joint Research Project between KAERI in Korea and IEP in Russia (Agreement № 13/13) supported by KAERI R&D Program. This work is also supported by Russian Foundation for Basic Research (project № 13-08-00883-a) and Ural Branch of the Russian Academy of Sciences (project № 12-Y-2-1029).

1 Introduction

The widely used steel STS410 (identical in chemical composition to AISI 410) is employed for a variety of applications due to its high heat- and corrosion-resistance. However, the welding process is still an issue. The development of approaches, which facilitate the production of high quality joints, is very important.

A candidate method of making joints is magnetic pulse welding [1,2] (MPW) due to the following reasons:

- MPW has proven repeatability and high processing rate.
- The obtained joint has high mechanical strength and large area [3].
- The produced joint does not adversely affect the heat treatment and microstructure of the steels, so the procedure does not require preliminary and post-weld heat treatment.

The purpose of this study was to find a range of optimal parameters for MPW in geometry of tube - end plug in terms of the largest welding area and the best weld seam microstructure.

2 Experiment

The tubes and end plugs were machined from an extruded bar. The sample's surface was not treated after the manufacturing process. Table 1 presents the chemical composition of STS410.

C, %	Si, %	Mn, %	P, %	S, %	Cr, %	Fe, %
0.15	1.00	1.00	0.040	0.030	12.50	Bal.

Table 1: *Chemical composition of STS410*

The magnetic pulsed unit consisted of pulsed current generator (PCG) loaded to a single-turn coil (inductor). The generator was based on the capacitors battery that consisted of 36 capacitors connected in parallel. The battery was discharged to inductor by 12 triggered vacuum switches (1 switch per 3 capacitors module). The total PCG capacity, C, was 425 μF, the charging voltage, U_0, was up to 25 kV. A half of the battery was used in several experiments (in that case the capacity was 210 μF). The current oscillation period was 27 and 20 μs at capacities of 425 and 210 μF, respectively (Figure 1a). The single-turn inductor, made of hardened steel, had the working diameter of 8.8 mm and the length of 12 mm.

For the experiments reported here typical PCG parameters were the following: charging voltage was 8.5 kV; magnetic field amplitude in empty coil was 37 T and peak current was 700 kA.

The typical geometry of the welding parts was the same as in [3,4]. The thin-wall steel tube was welded to inner steel end plug. Figure 1b shows a schematic diagram of the experimental setup. Under magnetic pressure copper driver together with steel tube were accelerated radially inward and collapsed to the end plug. Copper was used as a driver material due to its high electric conductivity and low mechanical strength. Collapse velocity is one of the critical parameters in the welding process. The tapered shape of the end plug (Figure 2a) helps to achieve the impact front motion along the plug surface. The

contact front velocity is the second critical parameter of the welding process. Certain values of the impact and contact front velocities are required to make a good weld seam [2], and different materials or material's combinations have their own values.

The parameters of magnetic pulse, tube strength and initial acceleration gap between tube wall and end plug surface determined the impact velocity. In turn, the contact front velocity was determined by impact velocity and the end plug taper angle.

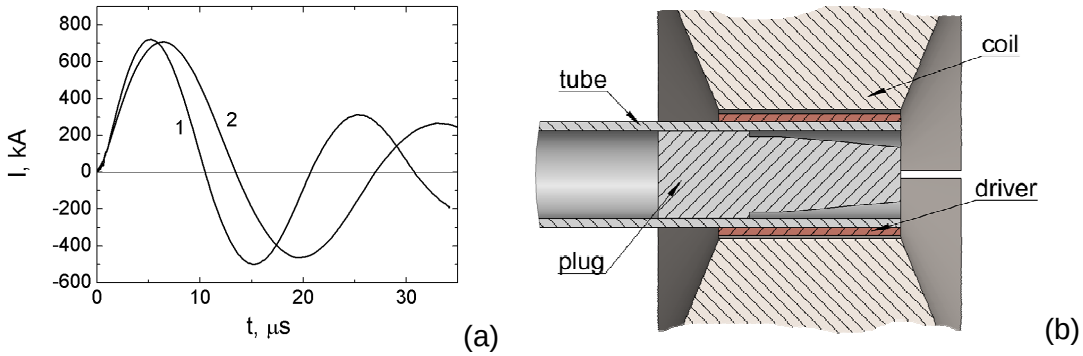

Figure 1: *a – typical current wave-forms at different circuit parameters (C[μF]/U$_0$[kV]): 1 – 210/13, 2 – 425/8.5; b – schematic diagram of MPW experiment*

The steel tubes of 7 mm in outer diameter and of 0.6 mm in thick were used. The copper driver of 8 mm in outer diameter and 0.5 mm in thick slipped over the end of the tube prior to welding without any inserted insulator between the driver and the tube.

The intensive plastic deformation of near-contact volumes during high velocity impact leads to the solid-state bonding of the tube to the plug [2,5].

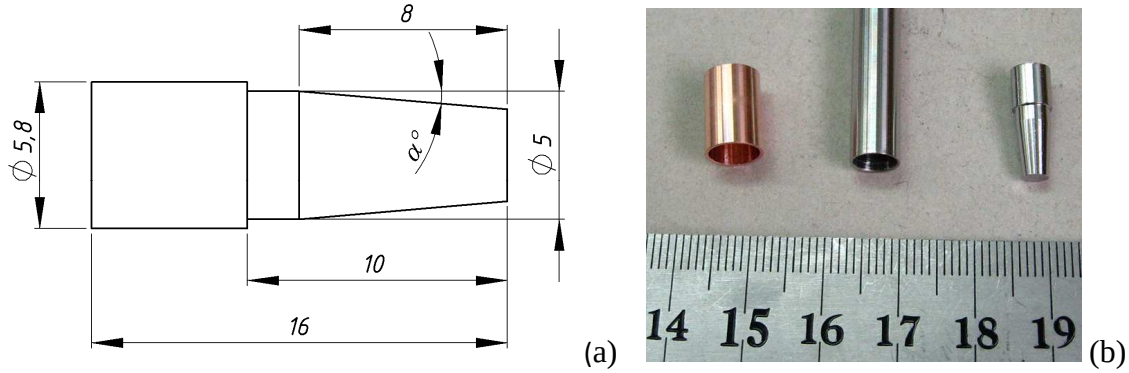

Figure 2*: a – end plug design; b – welding parts view*

The longitudinal sections of the welded samples were made in order to investigate weld seam properties. The samples were cut in the plane that coincides with the inductor slit. So, the photomicrography shows two weld segments: one of those close to the coil slit and the other one on the opposite side.

The obtained sections were investigated with optical metallographic microscope Olympus BX-41RF.

The leakage tests were carried out with helium leak tester.

For microstructure investigations the sample surfaces were chemical etched with hydrochloric acid and ethanol in proportion of 1:1 at room temperature [6].

3 Results and Discussion

3.1 Weldability Window

The PCG charging voltage, battery capacity and plug taper angle α (Figure 2a) were varied during the experiments.

The different sample's photomicrographs of longitudinal sections were superposed into bigger pictures (see Figure 3). The weld seam on these pictures looked like a confluence between tube and plug materials. The discernible boundary (black line) between the tube and end plug is an absence of joint. The lengths of the weld seams and diameters on the plug cone at weld starting point were measured on these pictures.

Typical experiment results are described in Table 2. The charging voltage, battery capacity, and end plug taper angle were varied. First, the charging voltage at which welding starts was defined. For the full PCG capacity of 425 μF it was 8 kV. For a half of the capacity (210 μF) it was about 12 kV. The comparison of the weld seam lengths (Table 2) demonstrated that for the full capacity the optimal parameters were: 8.5 kV charging voltage and 5° taper angle. For 9.5 kV charging voltage the narrow end of the plug was destructed (Figure 3c).

For a half of the generator capacity (Samples C25, C26) the current half-period T/2 decreased from 13.6 μs to 10.0 μs. In case of 13 kV charging voltage, the current amplitude was 720 kA. That current amplitude could be reached if the generator with the full capacity had charged to 8.7 kV.

#	α [°]	U_0, [kV]	C, [μF]	I_m, [kA]	T/2, [μs]	L_1, [mm]	L_2, [mm]	d_1, [mm]	d_2, [mm]
C18	5	7,0	425	592	13,5	no weld			
C21	5	8,0	425	670	13,4	6,69	2,92	4,74	4,47
C23	5	8,5	425	704	13,4	6,57	6,96	4,71	4,83
C24	5	8,5	425	704	13,4	7,12	5,20	4,58	4,61
C28	5	8,5	425	708	13,5	6,22	4,81	4,58	4,67
C27	3	8,5	425	704	13,6	2,56	6,11	4,32	4,69
C19	5	9,0	425	748	13,8	6,94	7,15	4,67	4,80
C22	5	9,5	425	808	13,4	3,92	5,15	4,67	4,80
C25	5	11,0	210	604	10,0	no weld			
C26	5	13,0	210	720	10,0	7,21	7,41	4,79	4,85

Table 2: *MPW experiments data*

Table notes: C – battery capacity; U_0 – charging voltage, I_m – current amplitude, T/2 – current half-period, L_1, L_2 – weld seam lengths, d_1, d_2 – diameters on the plug cone at weld starting point. Subscripts 1 and 2 correspond to the weld seams at the opposite side and close to the inductor slit.

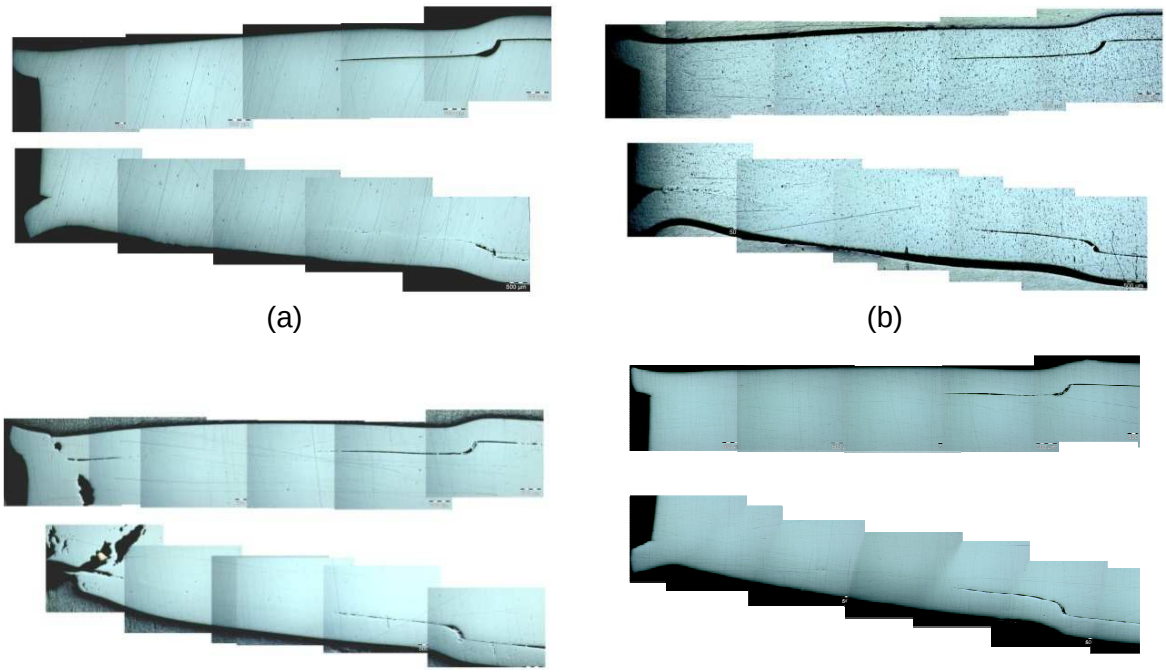

Figure 3: *Optical microscopy of the polished surfaces (longitudinal section) of the samples obtained at different MPW conditions (C[μF]/U_0[kV]): a – 425/8.5 (Sam. #C23), b – 425/9.0 (#C19), c – 425/9.5 (#C22), d – 210/13.0 (#C26)*

3.2 Welding conditions estimation: collapse velocity and contact front speed

For the inductor in the absence of the welding sample, the ratio of the generated magnetic field to the discharge current, B_m/I_m, was measured to be 0.053 T/kA. At MPW experiments the amplitude of magnetic field was estimated using this ratio. It should be noted that this estimation gives slightly lower value of B_m. Typical values of the estimated magnetic field amplitude were about 40 T.

Table 3 summarizes the calculated parameters of magnetic pulse welding process.

They are the velocities of impact V_i and the contact front motion V_{ki} at the time moments, t_i, when the welding started. The subscripts *1* and *2* refer to the parameters which were calculated for the certain joint segments position with respect to the inductor slit, namely, *1* – opposite position, *2* – close to the inductor slit. Generally, these parameters differed due to the magnetic field nonuniformity close to the inductor slit.

The time moment t_i, when the inner tube diameter became equal to d_i (see Table 2), and the velocity V_i at this moment were estimated by the solution of the equation describing radial motion in a compressing copper–steel tube. The velocity (V_{ki}) of contact point motion was determined as

$$V_{ki} = V_i / \sin \alpha \qquad (1).$$

The comparison of t_i values shows that, for C = 425 μF, welding starts prior to attaining a maximum value of magnetic field and approximately in maximum at C =

210 μF, U_0 = 13 kV. It should be emphasized that the last parameters gave the best quality of weld. Under optimal conditions, V_i values are about 300 m/s while V_{ki} values are about 3-3.5 km/s.

As shown in [2], a joint is usually failed if the joint speed V_k exceeds a sound speed in material. Therefore, the results, obtained for the samples with the angle of 3°, are well consistent with literature data. In this case, the joint speed of 6.9 km/s was higher than the sound speed in the steel (6.25 km/s for STS410).

#	α, [°]	I_m, [kA]	B_m, [T]	t_1, [μs]	V_1, [m/s]	V_{k1}, [km/s]	t_2, [μs]	V_2, [m/s]	V_{k2}, [km/s]
C19	5	748	40	5.9	300	3.4	5.7	270	3.1
C21	5	670	36	6.3	260	3.0	6.6	300	3.5
C22	5	808	43	5.7	310	3.7	5.5	290	3.4
C23	5	704	37	6.0	270	3.2	5.8	250	3.0
C24	5	704	37	6.2	295	3.6	6.1	290	3.5
C28	5	708	38	6.2	300	3.5	6.1	280	3.3
C27	3	704	37	6.6	340	6.9	6.1	280	5.7
C26	5	720	38	5.0	290	3.4	4.9	280	3.3

Table 3: *The calculated parameters of MPW process*

Table notes: B_m – magnetic field amplitude; t_1, t_2 – time when welding starts; V_1, V_2 – tube wall impact velocities at welding start.

3.3 Leakage testing

The samples, successfully welded at the C[μF]/U_0[kV]: (1) 425/8.5 and (2) 210/13, were tested on the helium leakage. For the first sample group the leak rate was less than 2.0×10^{-9} mbar·l·s^{-1}. For the next sample group the leak rate as low as 1.0×10^{-9} mbar·l·s^{-1} was achieved. Obtained results confirm high quality of welding, according to the results reported in [3,4].

3.4 Weld seam and bulk microstructure

Figure 4 shows the etched surface micrographs of the specimens joined at different conditions of magnetic pulse welding. In all cases, we observed smaller size material grains in the vicinity of the weld seam: the effect became more pronounced with increasing U_0. The best results were obtained at U_0 = 8.5 kV. The seam exhibited a characteristic wavy structure and the area of complete interpenetration. The joint thickness did not exceed 2 μm.

Thus, the comparison of the samples weld zone microstructure showed that the best weld was achieved at 8.5 kV among the samples welded at 425 μF. In this mode, the amplitude of the discharge current was 700 kA, and the corresponding amplitude of the magnetic field was at a level of 37-40 T.

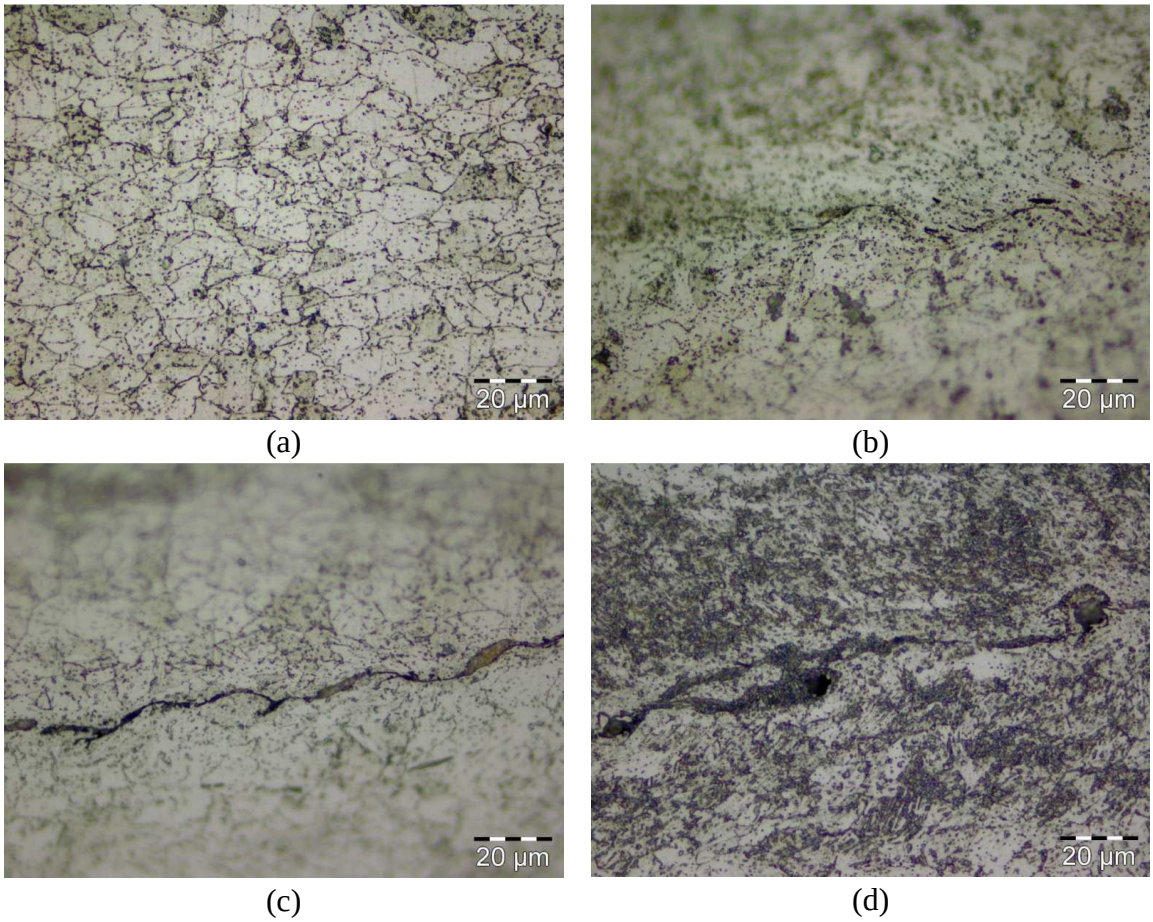

(a) (b)

(c) (d)

Figure 4: *Optical microscopy of the polished and etched surfaces (longitudinal section): bulk region – a; weld seam at U_0=8.5 kV – b, U_0=8.0 kV – c, U_0=9.5 kV – d (capacity – 425 µF)*

4 Conclusions

The magnetic pulse welding of the steel STS410 has been investigated. The experiments were performed in the geometry of “tube – plug”. The optimum welding conditions were found. The most appropriate impact velocity was about 300 m/s at the contact point velocity of 3-3.5 km/s. For achieving the required magnetic field amplitude (40 T at the period length of 20-27 µs), the current amplitude of 700-750 kA was employed at the inductor with the working length of 12 mm.

The leakage test showed a good helium tightness at the level of 1×10^{-9} mbar·l·s^{-1}.

The weld microstructure in comparison of different samples confirmed that the optimum value of current amplitude was 700 kA. The weld was wavy and with several areas where both metals were completely fused. The grain refinement was observed near the weld as well.

References

[1] US Patent № 3126937, Forming method and apparatus therefor. D.F. Brower et. al., 1964

[2] A.A. Dudin. Magnitno-impulsnaya svarka metallov (Magnetic Pulsed Welding of Metals). Moscow: Metallurgiya, 1979, 128 s. – in Russian.

[3] W.F. Brown, J. Bandas, N.T. Olson. Pulsed magnetic welding of breeder reactor fuel pin end closures. Welding Journal, June 1978, p. 22-26.

[4] John McGinley. Electromagnetic pulsed technology as a means of joining generation IV cladding materials. Proceedings of the 17th International Conference on Nuclear Engineering (ICONE17) July 12-16, 2009, Brussels, Belgium

[5] E.S. Karakozov. Soyedinenie metallov v tvyordoj faze (Joining of metals in solid phase). Moscow: Metallurgiya, 1976. – 264 s – in Russian.

[6] M. Bekkert, H. Klemm. Spravochnik po metallographicheskomu travlenijy. (Metallographic etching hand-book). Moscow: Metallurgiya, 1979. – 336 s. – in Russian.

SESSION 6

PROCESS TECHNOLOGIES (FORMING)

Process reliability and reproducibility of pneumo-mechanical and electrohydraulic forming processes

W. Homberg[1], E. Djakow[1], O. Damerow[1]

[1] Chair of Manufacturing and Forming Technology (LUF), Paderborn University, Paderborn Germany

Abstract

A sufficiently high process reliability and reproducibility is mandatory if a high-speed forming process is to be used in industrial production. A great deal of basic research work into pneumo-mechanical and electrohydraulic forming has been successfully performed in different institutions in the past. There, the focus has been more on process related correlations, such as the influence and interaction of different parameters on the course and result of those processes. The aspects of reliability and reproducibility have not been examined to a sufficient extent. Hence, in the case of pneumo-mechanical forming, insufficient investigations have been conducted into the effect that key parameters like the kinetic energy level, the filling height of the working media or the conditions inside the acceleration tube have on the reproducibility and course of the process. For electrohydraulic forming, the repeatability has worsened on occasions up to now. To improve the forming results and, in particular, the reputability of the process, it is necessary to examine the tool parameters associated with the electrodes and the working media. That is why research of this type is currently ongoing at the LUF. One important issue here is examining the options that exist for visualising the way the spark takes hold in the discharge chamber.

Keywords

High Speed Forming, Pneumo-mechanical Forming, Electrohydraulic Forming

1 Introduction

The global trend towards the sustainable use of rare resources and the increasing demands of consumers for security items for products, for example, are leading to more complex components that are subject to high quality requirements. Due to the current processing limits, classical stamping processes like deep drawing or conventional hydroforming frequently fail to provide usable production results. Hence, there is a need to develop innovative production processes for industrial use which can meet up to these

requirements. In this context, pneumo-mechanical (PMF) and electrohydraulic (EHF) high speed forming processes have a high potential [2][5][6], since they can increase the formability of large numbers of materials and, through that, produce more complex geometrical shapes. At the same time, high-speed forming (HSF) processes are particularly energy efficient compared to conventional forming processes. The technology of high-speed forming processes has been known since the 20th century already, when intensive research work was performed in the United States, Germany and the Soviet Union in particular [1], focusing on the correlation between the different process parameters and their influence on the forming result. Several working principles, including the use of explosives and electrohydraulic or pneumo-mechanical pressurization, are used in both research work and industrial practice.

MAZUKIN J.G. first introduced the principal of pneumo-mechanical high speed forming in 1961, using compressed air inside a pipe to accelerate a plunger diving into the working media filled pressure chamber. An initial investigation showed that pressures up to 1200 MPa and energies of 60 kJ in the working media were possible [2][3]. Typical process times were only a few milliseconds. The first known prototype machine based on the pneumo-mechanical principle was developed by TOMIGANA and TAKAMATSU and was presented in 1964 [3]. KOSING and SKEWS presented a further development of this principle by dividing the tube into different sections using membranes to transfer the energy from one section to the next [4]. FROLOV used this method not only for forming operations like stretch drawing but also for cutting operations, where the plunger was used as a stamp, with no working media in the chamber. The cutting result depends on the attainable energies as well as on the properties of the blank, including the blank thickness [5]. So far, the pneumo-mechanical method has only been used for the production of small tube and sheet metal parts. In the Soviet Union and the United States, more than 35 machines for stamping, cutting and metal forming were developed up until the 1990s. At present, a number of research projects using similar pneumo-mechanical high speed forming setups are focused on the further investigation of the process and material parameters in order to achieve an in-depth understanding of process phenomena and improve on the simulation models for high speed forming processes [2][6]. Furthermore, certain research institutes in the Ukraine and Russia are attempting to create new and more efficient tool systems and develop new pneumo-mechanical forming machines with innovative, efficient energy sources, such as the use of environmental fuels, electricity or explosives for the acceleration of the plunger and its impact on the forming result [7].

The electrohydraulic effect was first introduced by SVEDBERG in 1905, who used it for rock fragmentation [9]. The further development of this effect in the 1960s led to its implementation in different industrial sectors like the forming (EHF) of tubes and blanks, rock fragmentation and medical applications such as lithotripsy [8]. In the 1960s, in particular, a large number of scientists from many different countries attempted to understand the processes phenomena and developed working tools for forming tubes and blanks [11], but only a minority of them tried to set different process parameters to achieve specific forming results, such as HAMMANN et al. [9] and HÄUSLER et al. [10]. Both investigated the effect of different process parameters, such as the wire diameter and material and the conductivity of the working medium on the forming result with tubes. KNYAZYEV was the first to investigate the pressure distribution on the blank in conjunction with different numbers of electrodes, employing a phenomenological approach for calculating the pressure level [12][18]. So far, the EHF technology has been successfully used for deep drawing, calibration, expansion and joining processes, for example [1][13].

Current research work in the above-mentioned countries and also at the LUF is focused on the development of pneumo-mechanical and electrohydraulic processes for industrial use.[13][14][17][18] It is thus essential to investigate the reproducibility and reliability of these processes and the influence of different process parameters.

This paper presents recent research results for PMF and EHF with regard to the influence of different process parameters on the forming result, and especially on the reliability and reproducibility of each of the processes. Using these results, it will be possible to boost the reputation of these high speed forming processes and put them to industrial use in future.

2 Experimental setups and measurement techniques

To investigate the reproducibility and reliability of PMF and EHF, different tests were performed with the aim of analysing the influence of different process parameters such as the venting level of the acceleration tube and the working media on the course and result of these processes. Important information about the reproducibility and the reliability of these processes is provided by an analysis of the formed parts on a coordinate measuring machine (CMM). Here, a phenomenological approach [5,6] was adopted, where sheet metal blanks were formed into a die with multiple cylindrical recesses, producing dents in the blank, which are located on specified radii on the blank. This method is also known as the multi-point-membrane method and is successfully used in other research institutions for determining the cavity pressure and pressure distribution during HSF [9][18]. The CMM is able to measure the overall geometry of the formed blank, recording the highest point of each dent for further analysis (Figure 1). This analysis shows the forming height as a function of these radii. With this information, it is possible to draw conclusions on the reproducibility and the pressure distribution acting on the blank [4].

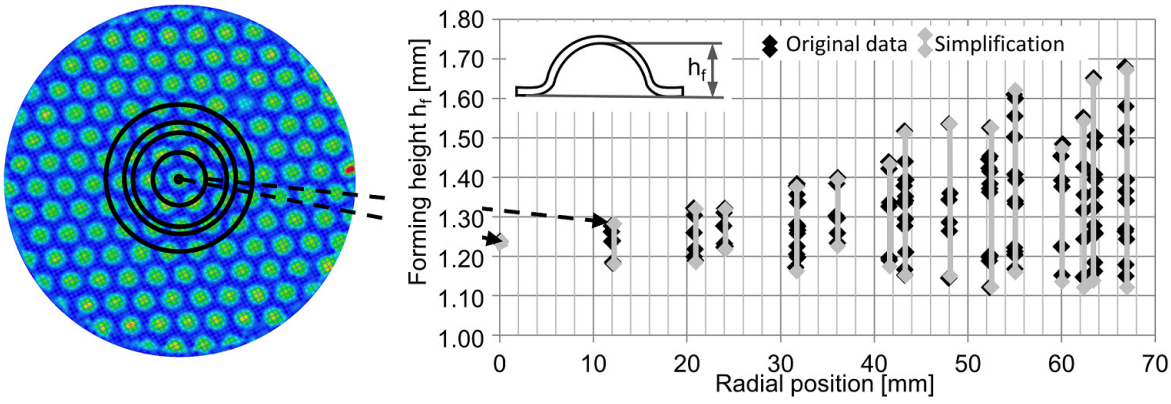

Figure 1: *Measurement and illustration of the results using the CMM*

An optical 3D forming (GOM, Argus) analysis system was used to investigate the forming limits attained and to visualize these.

2.1 Setup for pneumo-mechanical forming (PMF)

The pneumo-mechanical setup consists of a pressure generation unit, a vertically arranged acceleration tube and a working tool used to form sheet metal blanks into a die (Figure 2). Inside the tube, a plunger is accelerated by stored, compressed air and dives

into the water-filled chamber, thereby generating very short pressure pulses of up to 100 MPa for forming sheet metal blanks in a die. The maximum acceleration pressure p_a is 1.5 MPa, the length of the acceleration tube is 5.1 m, and the tube diameter employed is 38 mm. At the lower end of the acceleration tube, there are several vent holes for releasing the air in front of the plunger. Depending on the size, number and position of the venting holes, the set acceleration pressure and the filling level in the pressure chamber, it is possible to vary the number of plunger impacts and hence the number of pressure pulses during a forming process. Above the vent holes, at a distance of 300 mm from the forming tool, there is a device for measuring the plunger speed (two light barriers) in order to determine the plunger energy. A high-frequency ICP pressure sensor (109C11) from PCB performs pressure measurements inside the chamber.

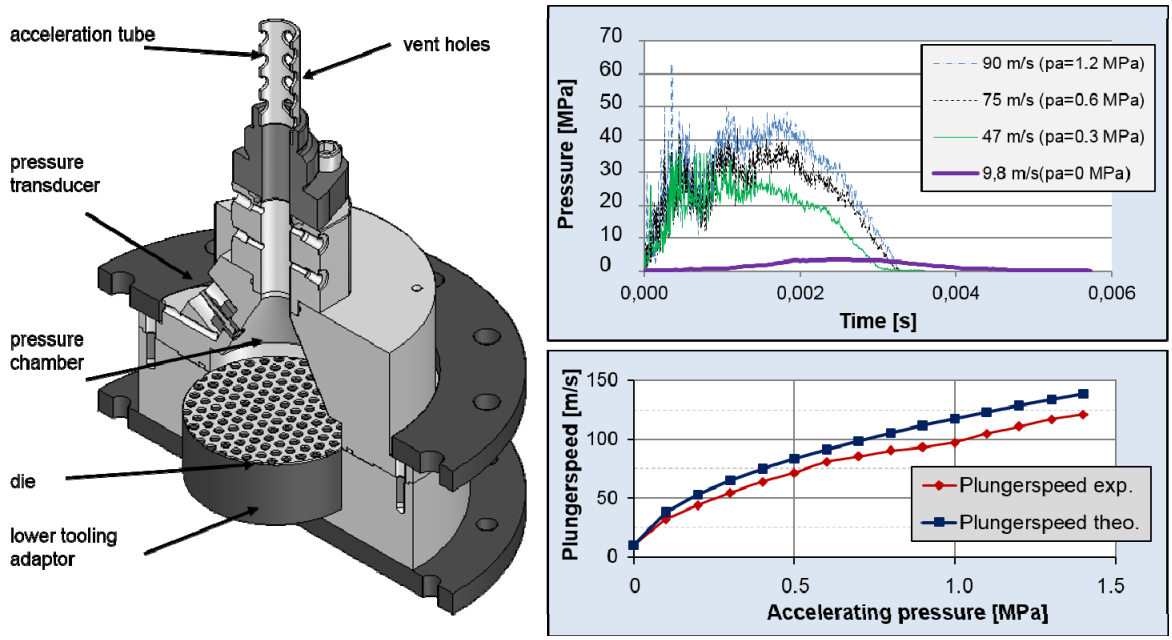

Figure 2: *Cut-away of the current PMF-tool for forming sheet metal blanks and process characteristic of PMF (dynamics of wave pressure at the top of the workpiece and impact velocity of the plunger in correlation to the accelerating pressure)*

2.2 Electrohydraulic setup

The electrohydraulic setup consists of a pulse power generator containing two capacitors from Poynting GmbH, Germany, which is connected via a coax-cable to the EHF-tool used for sheet metal forming (Figure 3). With a capacity of 15 µF (per capacitor) and a maximum charging voltage of 20 kV it is possible to obtain a maximum charging energy of 6 kJ. When using two capacitors a maximum current of 160 kA can be achieved. Overload tests with 9 kJ and 25 kV are also possible. The present working tool contains two electrodes, which are installed opposite each other and connected by a constantan wire (CuNi44). The blank to be formed is located on a perforated blank as the die, which provides the desired geometry. The discharge chamber has to be filled with a working medium, which is often water. When running the process, a Rogowski-coil measures the discharge current and an oscilloscope records it.

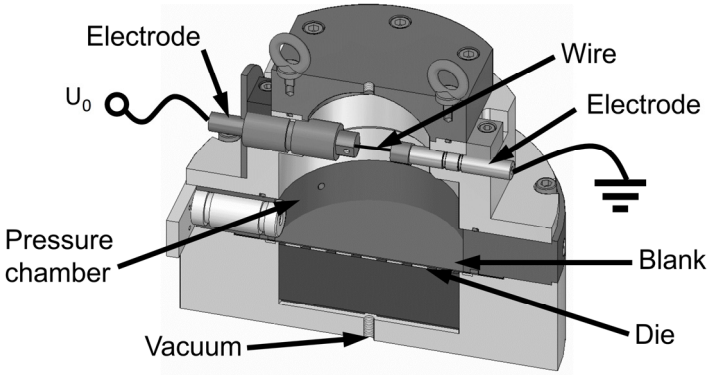

Figure 3: *Cut-away of the current EHF-tool for forming blank materials*

3 Results and Discussion

The focus of this work is on analysing the influence of different process parameters on the forming result, and especially on the reproducibility and reliability of each process, with the aim of making pneumo-mechanical and electrohydraulic forming suitable for industrial use.

3.1 Influence of the venting level on the forming result using pneumo-mechanical forming (PMF)

Previous work on pneumo-mechanical forming has shown that the resulting pressure pulse has a major influence on the reliability and reproducibility of the forming result, which is determined primarily by the working media and the kinetic energy, see [5-9] for detailed information. The kinetic energy depends on the acceleration distance, the mass of the plunger, the level of the acceleration pressure and the venting of the acceleration tube. One important aim of the current research work is to analyse the influence and interactions of the kinetic energy and the venting of the acceleration tube on the forming result with PMF. These results will make it possible to draw conclusions regarding the reproducibility and reliability of the process.
Due to the fact that the plunger displaces the air in front of it inside the tube as it moves, it is obvious that this resistance has a major influence on the attainable kinetic energy of the plunger and hence on the course and result of PMF. Previous work has shown that, at high acceleration pressures in particular, a lot of the kinetic energy is wasted due to the air resistance by comparison to simple theoretical calculations. Hence, a higher energy is necessary to achieve the same forming levels as those worked out theoretically.
To analyse how the venting of the tube influences the forming result as a function of different pressure conditions, several tests were performed varying the size of the venting holes from 0 mm² to 2,500 mm² (Figure 4).
Experiments without venting holes showed hardly any forming of the blank, due to the above-mentioned air resistance in the tube at all acceleration pressures. An increase in the venting area normally leads to more pronounced forming of the blank, attaining a maximum at 1,300 mm² when applying a 3-bar acceleration pressure. A further increase in the size of the venting area reveals a reduction in the forming level for the blank plus an increase in the deviation of the measured forming heights of up to 0.4 mm, thus leading to poorer reproducibility and reliability of the process. If the venting area is increased still further, the plunger speed or kinetic energy is so high that the plunger collides with the

blank, leaving dents or holes in the blank (Figure 4). These phenomena occurred with all the other accelerating pressures tested too, but at a much earlier point in time depending on the level of the accelerating pressure selected (see the collision line of the plunger in Figure 4), which meant that the maximum forming height, as shown at 3 bar, could not be attained. It can be assumed that, in this case, a lot of working media splashes through the venting holes during the plunger's first diving phase, so that the filling level is not sufficient to prevent the plunger from colliding with the blank during the first or subsequent immersion phases.

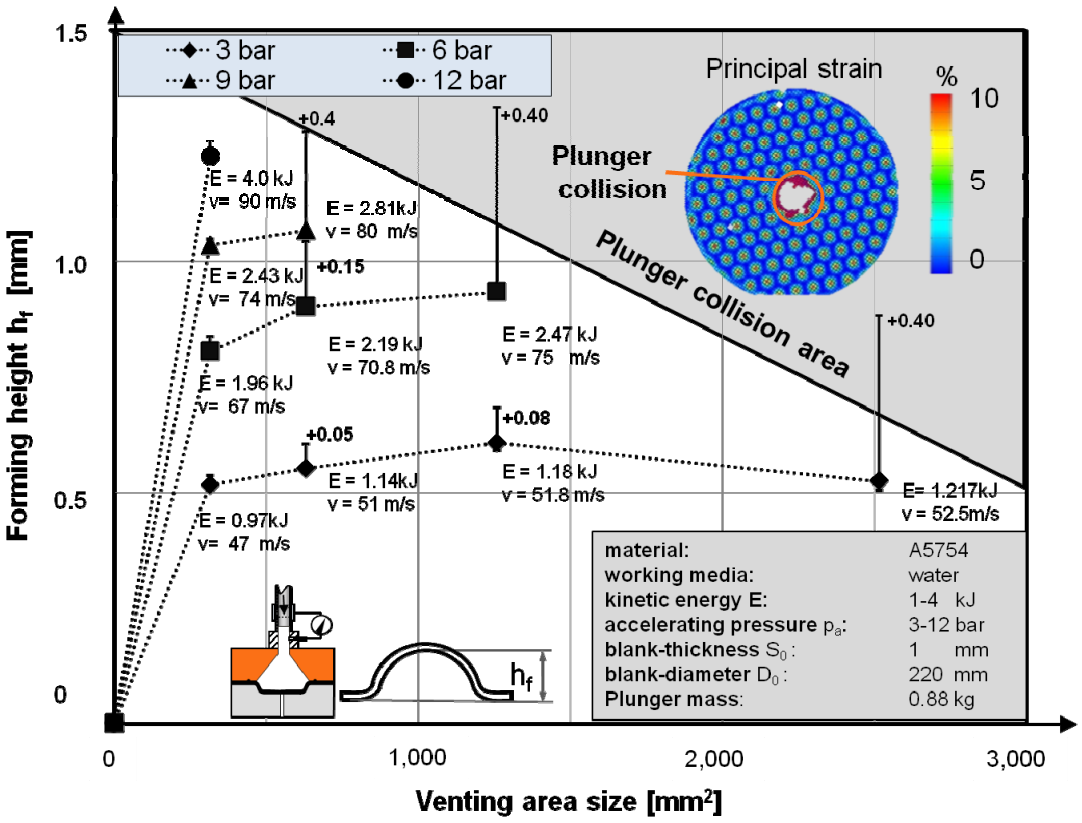

Figure 4: *Reproducibility of the forming results with different venting area sizes*

These findings led on to the question as to how the number of plunger impacts in the working media is influenced by the size of the venting area. Corresponding tests were performed with an accelerating pressure of 3 bar using an audio measurement system to record the punches of the plunger in the water. Figure *5* shows that without venting holes in the acceleration tube almost no forming of the blank occurs, with only one impact of the plunger on the water. The resulting pressures were identical to the pressure at acceleration pressure of 0 MPa, see Fig 2. By increasing the size of the venting area, the number of impacts increases to as many as 10. Here, a maximum number of impacts as well as the maximum forming height can be observed at approximately 800 mm². In the same way as for the curves in Figure 4, the forming height curves, the number of impacts decrease with higher venting areas but the scatter of the forming heights and also the plunger speed/ impact velocity(v) increases again, resulting in a worse reproducibility of the forming results.

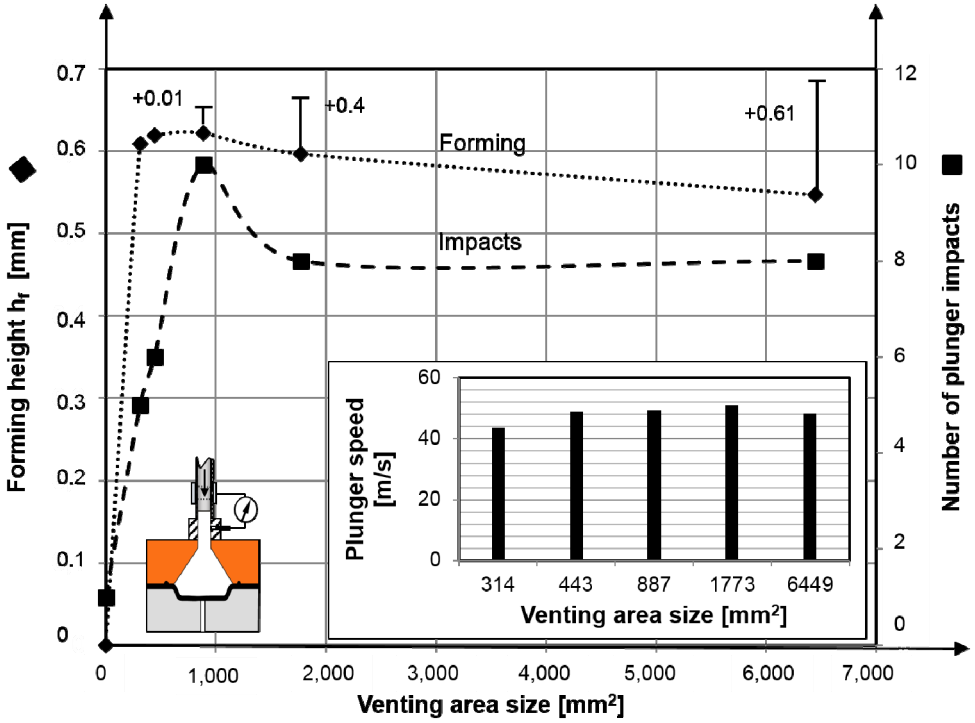

Figure 5: *Influence of venting level on sheet forming, plunger impacts and plunger speed*

Optical 3D forming analyses showed non-uniform forming heights of the dents in both tests, leading to the assumption that the pressure distribution that acted was not uniform either. This occurred especially with venting area sizes which exceeded the optimal area size, leading to reduced forming heights and plunger speeds. Here, the deviations of the forming heights were up to 0.61 mm in the radial direction of the part, leading to poorer reproducibility of the forming results. The maximum forming heights or pressures were obviously achieved in the center and also in the outer region of the workpiece.
Summarizing, it can be said that an increase in the size of the venting area leads to greater forming of the part and to a higher plunger speed, as well as to an increase in the number of plunger impacts with the water. Once these parameters have attained a given maximum, a reduction occurs in all of them in conjunction with an increase in the deviation of the forming heights. Increasing the size of the venting area further leads to the plunger colliding with the blanks. A boundary line was identified showing which parameter results in a plunger collision with the blank for the conditions examined.
The phases of the process during which the plunger collides with the blank, configuring the filling level of the working media to prevent a collision and establishing a means of influencing this finding in a positive way are all tasks to be solved in the future, aiming for better reproducibility and reliability of PMF.

3.2 Results of electrohydraulic forming (EHF)

To study the reproducibility of the forming height and the pressure distribution on the blank use was made of a die with a large number of recesses. By varying parameters like the load energy, the working medium and also the electrode material, it proved possible to analyse the influence of these parameters on the reproducibility of the process as well as to draw conclusions on the pressure distribution acting on the blank.

3.2.1 Influence of the working media type

Using water as a working medium is not always convenient due to handling difficulties and the corrosion problems with some blanks, such as the mild steel 1.0338 that was used. It is thus very interesting to try out different working media and see their influence on the results of the electrohydraulic forming process. By changing the working medium, it is possible to vary different parameters of the working medium employed, with the aim of achieving better forming results, i.e. pressure distribution and reproducibility. The first tests were carried out using the three different working media of borax slime[1], starch-water[2] and ethylene glycol. These media differ in their density, viscosity and conductivity as well as in their fluid-mechanical behaviour, since slime and starch-water are non-Newtonian and ethylene glycol is a Newtonian fluid. Slime and starch-water were chosen because of the good results achieved by HOMBERG for pneumo-mechanical forming [15] and ethylene glycol was chosen because of the good results obtained by HARTMANN, but using a different setup [19]. Representative results of each working medium for a load energy of 2 kJ by comparison to results using water at 1.75 kJ are shown in Figure 6.

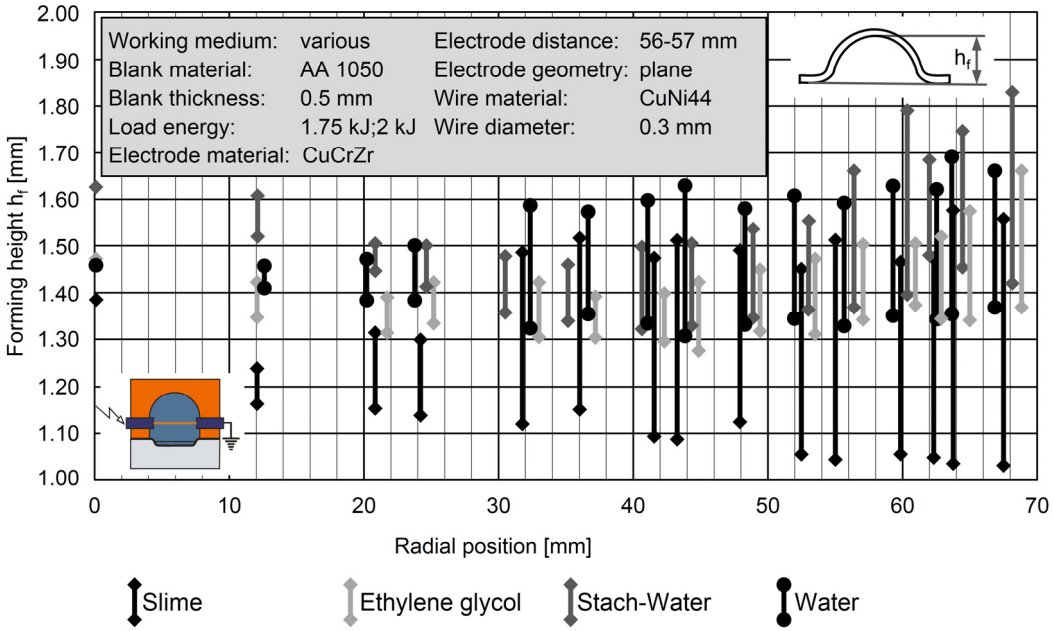

Figure 6: *Representative forming results with different working media using EHF*

With the exception of ethylene glycol, all the other working media generated a non-uniform pressure distribution on the blank. The forming height range extends up to 0.43 mm when using starch-water, for example, which is very high by comparison to ethylene glycol. Here, the forming height range is much lower in the middle of the part, but quite high in the outer radii. This is due to the reflections of the working media waves on the tool surface. While the forming heights of the dents with ethylene glycol, starch-water and water are comparable to each other, slime shows a much lower forming height level in some cases.

[1] Slime: mixture of borax ($Na_2B_4O_7$) with polyvinyl alcohol ($-C_2H_4O)_n$ and distilled water
[2] Starch-water: mixing ratio of 1.5 starch/1 water

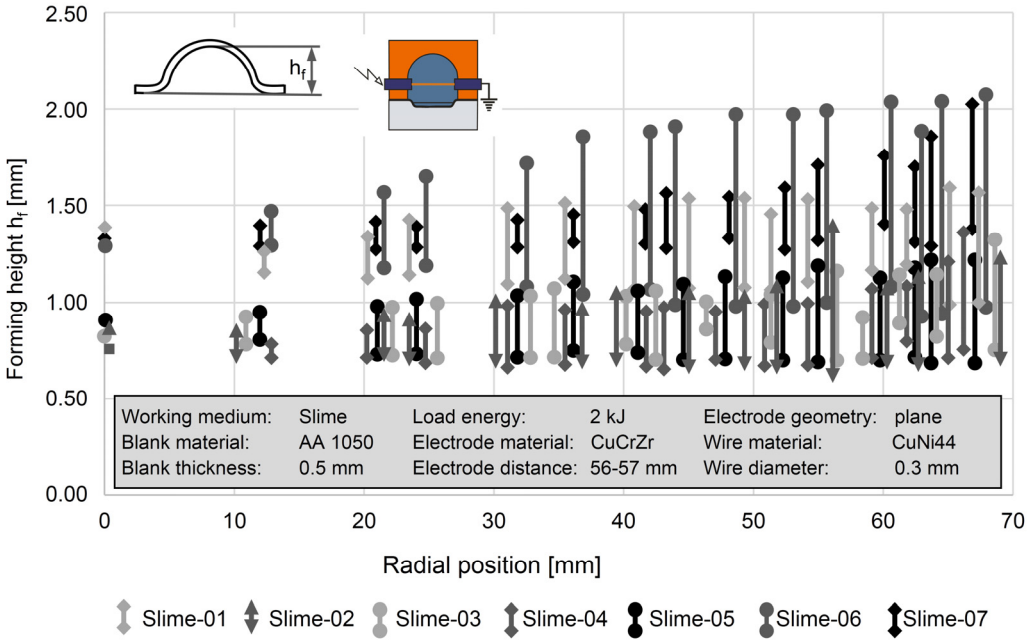

Figure 7: *Reproducibility of the forming results and discharge process of slime at 2 kJ*

While all the other working media showed quite good reproducibility of the forming results, of about Δ < 0.1 mm in most cases when keeping all the process parameters constant, slime had the worst reproducibility and displayed different discharge currents and forming heights (Figure 7). Very different forming heights and a very high scatter of the forming heights is evident on each radius. This high scatter in the forming height, and especially in the outer radii, results in the assumption that the spark did not follow the path to the mass-electrode but took a shorter and more convenient route to discharge on the inside of the working tool. Hence the pressure wave was not formed in parallel to the blank, but at an angle to it, and proceeded up to the corner of the discharge chamber. This can constitute an explanation for the one-sided pressure distribution, which is confirmed by the pictures taken by an optical measuring system (Figure 8).

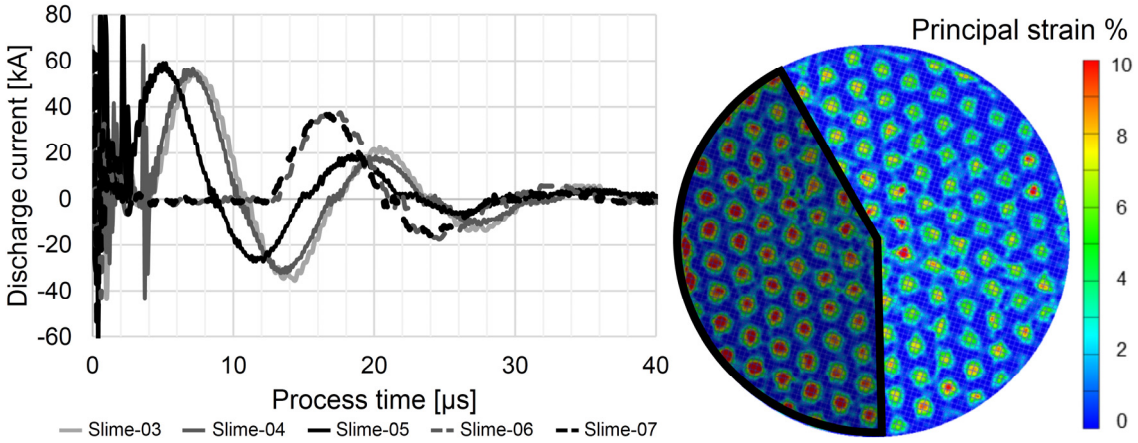

Figure 8: *Discharge current and optical measurements of the forming load*

The discharge-current measurements reveal two different types of curve. The first is the expected discharge current (Figure 8) showing a so-called dark phase and, after that, an oscillated discharge of the capacitor bank. On the other curve, the dark phase is missing completely, which confirms the assumption of a different discharge route being taken.

These results show that the working medium has a major impact on the reproducibility of the forming results. Using different working media has the advantage of making it possible to visualize the way the discharge took place in the working media by removing it in layers. Hence, the factors that influence the discharge route can be analyzed and, with this information, it will be possible to stabilize the discharge process, which will lead to better reproducibility of the forming results and to more uniform pressure distribution. Figure 3-5 shows examples of burning marks in slime and starch-water.

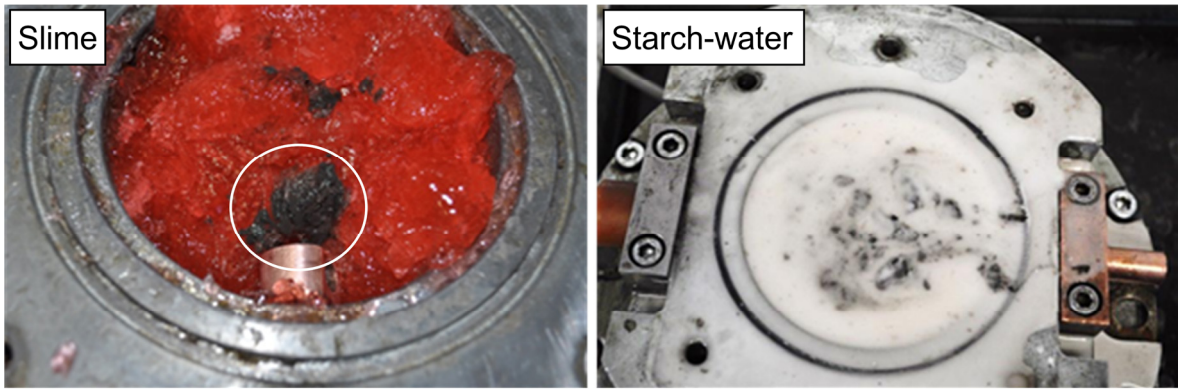

Figure 9: *Burning marks in slime and starch-water produced after one discharge*

3.2.2 Influence of the electrode material

Further experiments were conducted using different electrode materials with the aim of analyzing the influence of the electrode material on the reproducibility of the forming results (Figure 10).

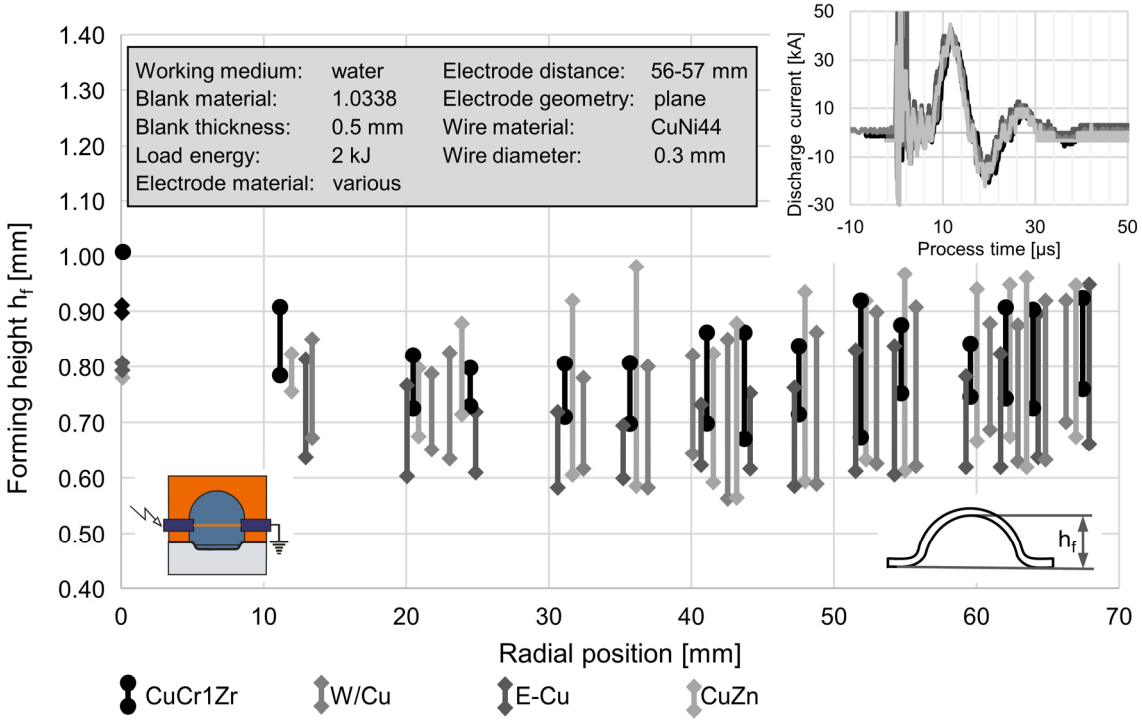

Figure 10: *Forming results using different electrode materials*

These results show that reproducibility of the forming results is achieved when the same parameters are used. If different electrode materials are compared, however, it can be seen that the range of forming heights within a single radius extends from Δ=0.22 mm

with CuCr1Zr-electrodes to 0.43 mm with E-Cu (Figure 9). It also can be seen that, when using CuCr1Zr-electrodes, the pressure distribution is more uniform than for all the other materials tested. The comparison of the discharge currents shows mostly the same behaviour of all materials. Here, E-Cu and CuZn show a rise in the current of 5 kA compared to the other materials. Hence, it is obvious that the choice of electrode material can influence both the reproducibility and the pressure distribution on the blank but doesn't influence the discharge current significantly. In our tests, CuCr1Zr-electrodes showed both the best reproducibility and pressure distributions.

4 Conclusion

The subject of this paper was to identify the influence of significant process parameters on the reliability and reproducibility of the pneumo-mechanical and electrohydraulic forming processes. In the case of pneumo-mechanical forming, it was shown that a minimum venting level is absolutely essential for the homogeneous and efficient forming of sheet metal parts. A certain increase in the optimal venting level leads to a reduction in the forming heights and yet also to an increase in the geometrical deviation within an individual blank. The reproducibility and reliability are thus given within a particular frame but ought to be improved by analysing the effects leading to the results presented.
In the case of electrohydraulic forming it was shown that process parameters like the working media type and the electrode material can influence the forming result and the course of the process. For future work, it will be essential to better visualize the way the discharge takes place in the discharge chamber so as to be able to stabilize the discharge process. This will result in better reproducibility and reliability of electrohydraulic forming.

References

[1] *Wilson, F.*: High Velocity Forming of Metals. Prentice-Hall International, London, 1964

[2] *Bragin A.P.*: Hydrodynamical forming on pneomomechanical high speed forming machines. Journal of aerospace technique and technology, 2007, P. 296, Ukraine

[3] *Tominga*, *H.*; *Takamatsu*, *M.*: Hydropunch, a pneumatic-hydraulic-forming machine.2. International Conference of the Center for High Energy Forming, Estes Park, USA,1969

[4] *Kosing, O.E.*, *Skews*, *B. W.*: The use of liquid shock waves for metal forming; 21st International Symposium on Shock Waves, Great Keppel Island, Australia, 1997

[5] *Frolov, E-A*: Technologiceskie vozmoznosti processa impulsnoj stampovki elasticnoj sredoi. Kuznecno-stampovocnoe proizvodstvo, obrabotka materialov davleniem. Band 36, Heft 9, Moskau 1994

[6] *Vovk, A.:* Verfahrensentwicklung zur Fertigung qualitätsgerechter Bauteile mit dem Hydro-Impuls-Umformen von Blechen, Dissertation, Magdeburg, 2008

[7] *Bragin A.P.*; Zaizew W.E.; Melnishuk A.P.; Poltarushnikow S.A.: Grounds and background of research activities in the field of pneomomechanical forming. Journal of aerospace technique and technology, 2007, P. 42, Ukraine

[8] *Steiger E.*: Extracorporal Laser Induced shock wave Lithotripsy (ESWL). Laser in medicine and surgery: journal for application and exploration of laserbeam, Laser Assoc. of Neurolog. Surgeons of Europe; 1987

[9] *Hammann, J.-F.*; *März*, *H*. et al.: Untersuchung zur Stoßwellenerzeugung, Werkstoffbelastung und Technologie beim Hydrospark-Verfahren; BMFT-FB T 76-78; 1974

[10] *Haeusler*, *J.; März, G.*: Optimierung von Drahtexplosionen zum Aufweiten zylindrischer Rohre nach dem Hydrospark-Verfahren; 1968

[11] *Bruno E.J.:* High-velocity forming of metals. American society of tool and manufacturing engineers, Dearborn, Michigan, 1968

[12] *Eguia, I.; Jose, J. S.; Knyazyev, M.; Zhovnovatyuk, Y.*; Pressure Field Stabilisation in High-Voltage Underwater Pulsed Metal Forming Using Wire-Initiadet Discharges. Key Engineering Materials Vol. 473, Sheet Metall, 2011

[13] *Golovashchenko, S.F., Bessonov, N.M., Ilinich, A.M.:* Two-step method of forming complex shapes from sheet metal, Journal of Materials Processing Technology, Volume 211, Issue 5, 1 May 2011, P 875-885

[14] *Homberg*, *W.; Beerwald, C.; Pröbsting, A.:* Investigation of the Electrohydraulic Forming Process with respect to the Design of Sharp Edged Contours. Proceedings ICHSF 2010, Ohio USA

[15] *Homberg, W.; Djakow E. Akst O.:* Some aspects regarding the use of *a* pneumo-mechanical high speed forming process, Proceedings ICHSF 2012, Dortmund, Germany, 25 April 2012

[16] *Homberg, W.; Djakow E.:* The investigation of a pneumo-mechanical high speed forming process; 13th International scientific and technical conference “The Progressive Engineering & Technique" Journal of mechanical engineering (Vesnik) 64, 2012, S. 172-177, Sevastopol, Ukraine

[17] *Homberg, W.; Djakow E.; Akst, O.:* Investigation of a pneumo-mechanical high speed forming process with respect to the forming of complex sheet and tube components; 14th International scientific and technical conference “The Progressive Engineering & Technique". Journal of mechanical engineering (Vesnik) 67, 2013, S. 180-188, Sevastopol, Ukraine

[18] *Knyazyev, M.; Perez, I.; San José, J.; Zhovnovatyuk, Y.*: Pressure Fields Repeatability at Electrohydraulic Pulse Loading in Discharge Chamber with Single Electrode Pair. Proceedings ICHSF 2012, Dortmund, Germany, 25 April 2012

[19] *W. Hartmann, A. Member, J. Kieser, K. Rohde:* The Thermohydraulic Generator – A Pulse Power Source of Intense Pressure Pulses, Erlangen, 2000

[20] *Thewes, R.:* Hydro-Pulseforming-eine vorteilhafte Alternative zum Umformen von Blechplatinen. Hydroumformung von Blechen, Rohren und Profilen. Band 6, Fellbach 2010

Investigation of Tailored Pressure Distributions by Vaporizing Tailored Foils

S. Cai[1]*, C. Weddeling[1], A. E. Tekkaya[1]

[1] Institute of Forming Technology and Lightweight Construction, TU Dortmund, Germany

Abstract

The rapid vaporization of thin metallic conductors can be used for innovative high speed forming processes. Metal wires or foils are vaporized when a high current is applied. The generated metal gas or plasma expands very rapidly with high pressure and impacts on an intermediate polyurethane plate near the wires or foils. A shock wave is induced into the polyurethane plate and provides the pressure pulse to the sheet metal, leading to a deformation of the sheet. This process requires no expensive tool coils and no electrical conductivity of the workpiece, which makes it attractive to multiple fields of application such as forming and impact welding. In this study, the basic process parameters that influence the shock pressure were experimentally identified including the charging energy of capacitor bank, foil geometry (thickness and width) and thickness of polyurethane plate. Based on the experiments of the parameter investigations, different new foil designs were investigated in order to acquire a tailored pressure distribution. The results show that the shock pressures can be located at different positions in a discontinuous way. Besides, the pressure amplitudes and areas at different positions can also be varied, which depends on the vaporized foil geometries at those positions.

Keywords

Impact forming, Vaporizing foil actuator forming, Sheet metal forming

1 Introduction

Electromagnetic forming is currently the most common high speed forming method that can improve the forming limit and reduce the spring back as V.Psyk et al. detailly reviewed [1]. The basic principle of electromagnetic forming is to utilize the induced Lorenz force on the workpiece in a changed magnetic field produced by a tool coil when the discharged current by a capacitor bank passes through it. Therefore, it is required that the formed workpiece in electromagnetic forming should have high electrical conductivity. The Joule heating effect of current on the tool coil and strong mechanical loads can

greatly reduce the lifetime of the coil. In addition, it is also difficult for electromagnetic forming to produce the forming part with graded heights because of the rebound effect. However, vaporizing thin conductors like metal wires or foils could be an alternative to solve the challenging problems in electromagnetic forming process. This process requires no electrical conductivity of forming workpiece and expensive tool coil.

2 State of the Art

Vaporizing thin conductors has been originally used to research the physical process of plasma such as the electrical resistivity and conductivity of plasma and other physical problems [2]. An intensive research about this topic is concentrated between 1959 and 1962 which is concluded as the conference proceedings [3]. The basic principle of this process is to utilize the Joule heating effect of current to heat the thin conductor in the circuit until it is vaporized. The electrical circuit basically consists of the electric pulse generator and the thin conductor which is connected with the electric pulse generator to form a whole electrical circuit. The pulse generator can be described as an oscillating circuit characterized by its capacity C, the inductance L and the resistance R. The vaporizing process is initiated by triggering the high current switch of the pulse generator leading to a sudden discharge of the energy stored in the capacitor C. The discharge results in a damped sinusoidal current I(t) (see Figure 1b) running through the thin conductor which is then heated by the deposited electrical energy into it. The thin conductor is firstly melted and finally vaporized. The burst time of current which denotes the termination of the energy deposition into the thin conductor has been demonstrated to be the moment when the voltage begins to collapse (see Figure 1b).

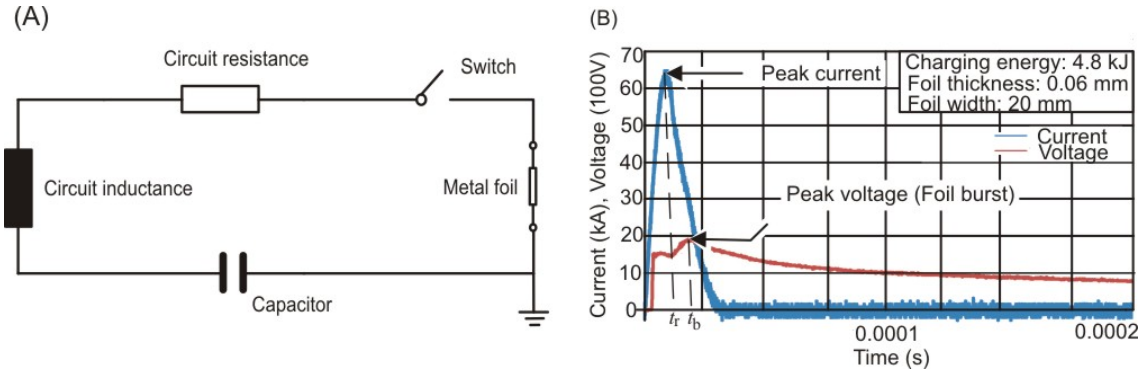

Fig. 1 (A) Schematic drawing of vaporizing foil circuit. This circuit is not necessarily the same as the one used in this study. (B) Current and voltage curves during vaporizing foils

The rapid vaporization of thin metallic conductors can be used for innovative high speed forming processes. Metal wires or foils are vaporized when a high current is applied. The generated metal gas or plasma expands very rapidly with high pressure and impacts on an intermediate polyurethane plate near the wires or foils. A shock wave is induced into the polyurethane plate and provides the pressure pulse to the workpiece, leading to a deformation of it. In consideration of the specific form of shock wave, vaporizing wires is normally used for tube forming and vaporizing foils is applied to sheet metal forming. Vivek et al. investigated several metal forming processes by vaporizing thin conductors such as tube expanding [4] and perforated sheet forming [5]. For tube

expanding, aluminum and copper wires with diameter 1.524mm were chosen as the vaporizing material which was surrounded by a urethane rod with hardness 80 A. It was found that aluminum wires are better than copper wires for this process. The perforated sheet forming process was conducted with changed charging energies as well as foils with different thicknesses. By qualitatively analyzing the trends regarding the pressure magnitudes and distributions, the effect of foil thickness on efficiency of energy conversion was acquired, which showed that thicker foils kept generating higher pressures with increasing energy than thinner foils. It can also be seen that the pressure magnitudes and distributions were different with changing the thickness of foils, which implies that the foil thickness has an influence on the induced shock pressure. However, the process parameters that can influence the shock pressure including the foil geometry and the thickness of polyurethane plate have not been investigated yet. Besides, in consideration of reducing rebound effect which is a common problem in electromagnetic forming, the possibility to realize tailored pressure distribution by vaporizing tailored foils should be also explored.

3 Experimental Procedure

3.1 Parameter Investigations

3.1.1 Effect of the Thickness of the polyurethane Plate

With the aim of identifying the effects of the process parameters on the forming results the free bulging height was chosen as the scale variable to indicate the amplitude of the shock pressure. Three different polyurethane plates with a thickness of 3 mm, 5 mm and 10 mm respectively were used as the intermediate plate to transmit shock waves. For each polyurethane plate, three charging energies were investigated: 3.2 kJ, 4 kJ and 4.8 kJ. The minimum charging energy was required to vaporize the whole active part of the foil. For example, the foil area with a thickness of 0.06 mm, a width of 20 mm and a length of 40 mm can be vaporized by applying a charging energy of 3.2 kJ. Based on this minimum value the charging energy was increased by 25% and 50%. Each parameter set was repeated three times. The free bulging height of the final part was measured by GOM Atos optical system, which can be seen in Fig. 3. For each thickness of polyurethane plate, the points show a linear distribution with respect to changing charging energies. As shown in Fig. 4, the final bulging height increases with increasing the charging energy. It is also clearly shown that, for each individual charging energy, the final parts formed with 3 mm polyurethane plate always exhibit highest bulging height while the parts formed with 10 mm polyurethane plate have the smallest bulging height.

The electrical energy deposition into the foil before the voltage collapses determines the final shock wave pressure on the sheet metal. With an increase in charging energy, the current through the foil gets bigger as well as the voltage drop across the foil. As a result, the deposited electrical energy into the foil which can be expressed as the integration of the current and voltage is also increased. As the thickness of the polyurethane plate gets bigger, the dissipation of the shock amplitude is increased because the shock wave must travel a longer distance until it reaches the interface of the polyurethane plate and the sheet metal. The increased number of internal interfaces

enhances the scattering effect on the shock wave, which results in an attenuation of pressure amplitude.

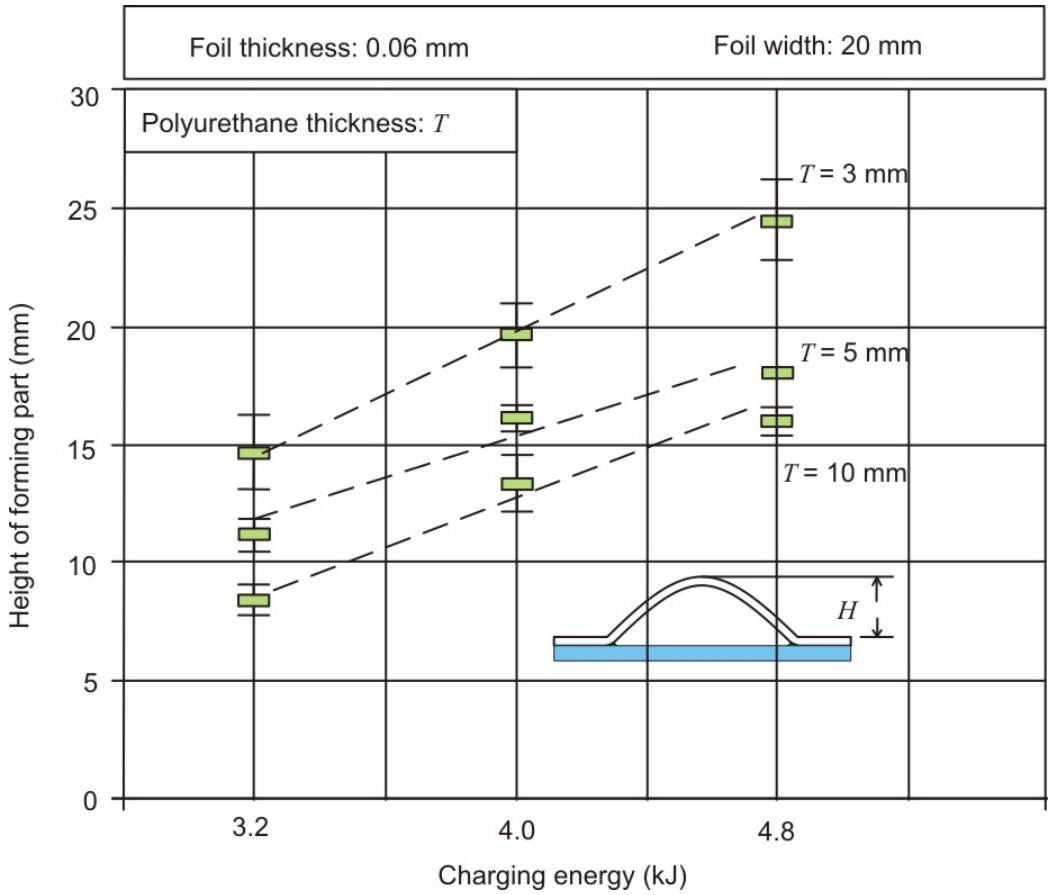

Fig. 4 Bulging heights with respect to charging energy and different thicknesses of polyurethane plates

3.1.2 Effect of the Geometry of the Foil

The influence of the geometry of the foil on the shock wave pressure was investigated by varying the thickness and width of the foil respectively under the constant charging energy 4.8 kJ and the same polyurethane plate thickness 3 mm. This resulted in two sets of specimens: 0.03 mm, 0.06 mm, 0.08 mm and 0.1 mm in thickness; 6 mm, 12 mm, 16 mm and 20 mm in width. For each set of specimens, the point distributions again show a linear relationship between the thickness or width and the bulging height. As shown in Fig. 5, the final bulging height decreases with increasing the thickness or width of the foil. In the case of the foil with thickness 0.03 mm, the formed part was cracked, which means the shock wave pressure was much bigger than in the cases with the other thicknesses.

The influence of the foil thickness or width on the shock wave pressure could be attributed to the fact that the current density across the foil section is increased when the thickness or width of the foil decreases. This results in a more intensive deposition of electrical energy into the foil. As the induced plasma reaches a higher temperature and has greater ion and electron densities, the internal energy of these particles is improved to

a higher degree and thereby triggers a more intensive shock wave into the polyurethane plate.

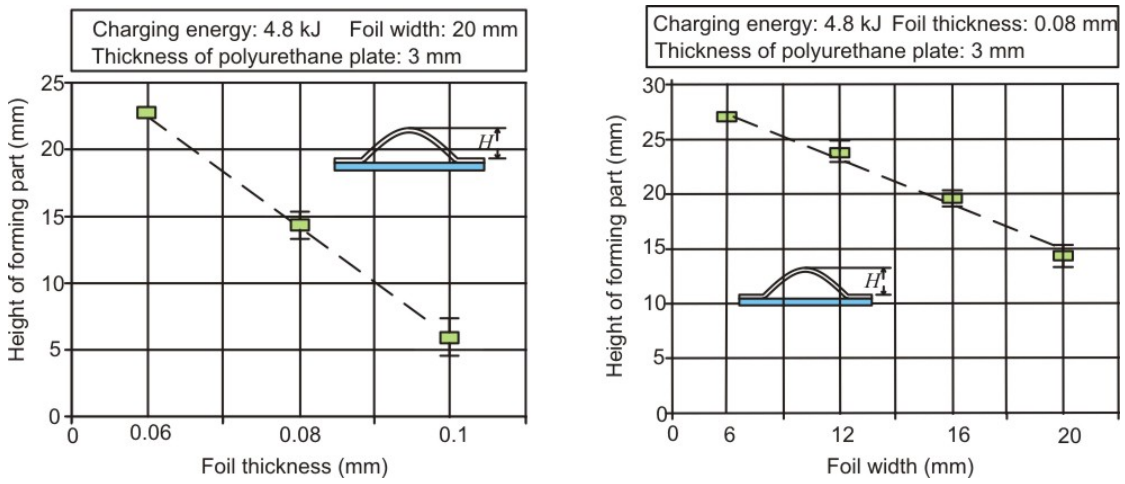

Fig. 5 Bulging heights with respect to thickness and width of foils

3.2 Perforating Sheet Forming under Tailored Pressure Distribution

Based on the results of the parameter investigations, the shock pressure induced by vaporizing foils is affected by the charging energy and geometry of the foils. In this section, the foils were cut in tailored shapes in order to acquire pressures at different positions in a discontinuous way. Therefore, there are mainly two aspects to be noted. One is if the two thin areas at different positions of the foil can be completely vaporized. The other is how the pressure amplitudes and pressure areas at these two positions change with different charging energies and geometries of the vaporized areas. Hence, three sets of foil specimens were prepared as shown in Table 1.

	Length at position 1 (mm)	Length at position 2 (mm)	Charging energy (kJ)
Set 1	30	30	4, 5, 6
Set 2	30	30	5
	60	60	5
	90	90	5
Set 3	30	90	5
	50	90	5
	70	30	5

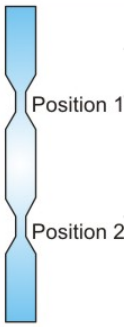

Table 1 Sets of specimens for vaporizing tailored foils

3.2.1 Tailored Pressure Distribution under Different Charging Energies

In this section, the geometry of the foils (see Set 1) was kept the same for all specimens with length 30 mm at two vaporized positions. The charging energies were chosen as 4 kJ, 5 kJ and 6 kJ respectively to examine its effect on the pressure distribution. The pressure area was indicated by the bulged points on the sheet after the perforating forming process.

The results in Fig. 6 show that the length of the pressure areas is close to the length of the vaporized parts of the foil. With increasing the charging energies of capacitor bank, the width of the pressure areas is enlarged. Meanwhile, the pressure amplitude is also improved under more charging energies, which can be seen from the bigger bulging heights of points or sheared holes. However, the pressure is not uniform over the whole pressure distributed area. It can be seen that the pressure within the original vaporized dimension of the foil is bigger than the surrounding areas.

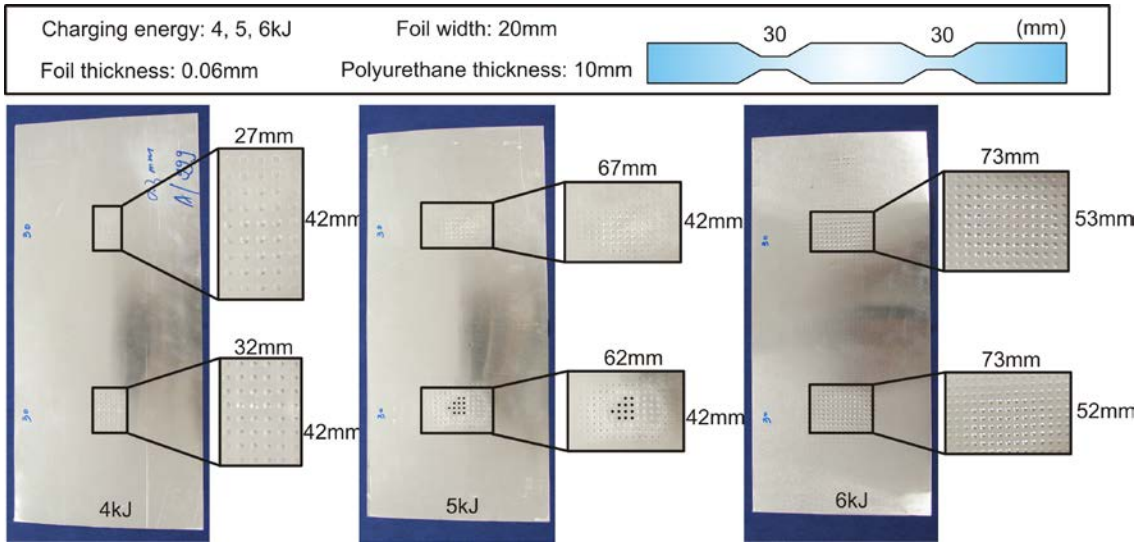

Fig. 6 Perforating formed sheets with respect to different charging energies

3.2.2 Tailored Pressure Distribution under Different Foil Geometries

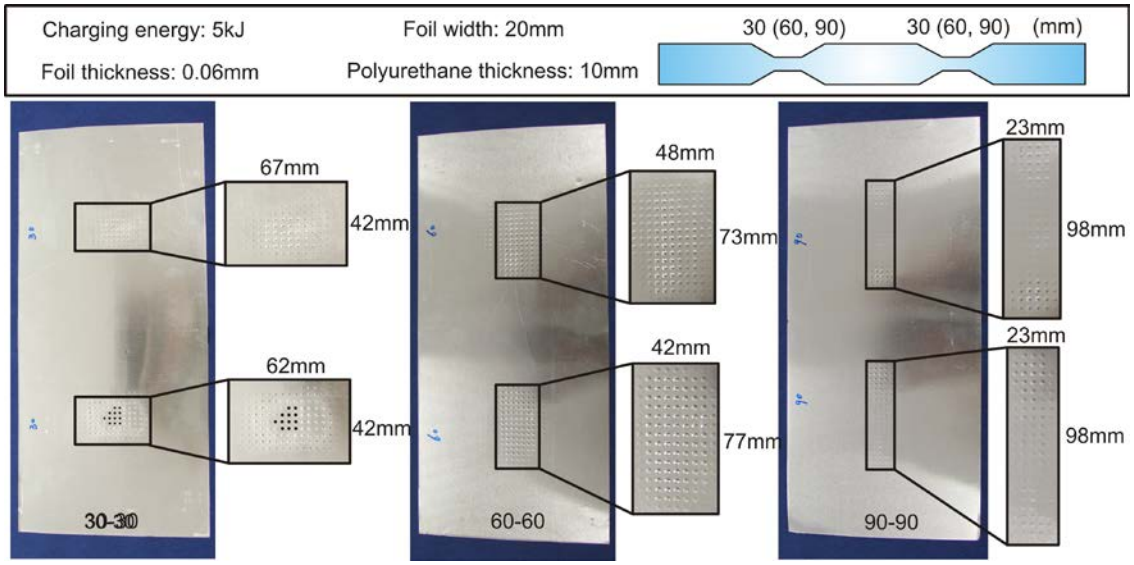

Fig. 7 Perforating formed sheets with respect to different vaporized lengths at tailored positions

Firstly the lengths of the vaporized areas at two positions (see Set 2) were varied which were 30 mm, 60 mm and 90 mm respectively. At the same time, the lengths of two

vaporized parts of a specimen are kept the same with each other all the time. The charging energy of capacitor bank was chosen 5kJ for all the specimens. The vaporized results are shown in Fig. 7. It can be seen that all the tailored foils were successfully vaporized even when the length of the vaporized part was increased to 90 mm (180 mm vaporized in total). The pressure area on the perforating formed sheet in the case of tailored length 90 mm is almost the same with the dimension of the vaporized part of the foil. With regard to the tailored length 30 mm, the pressure area on the perforating formed sheet is extended in the transverse direction. Meanwhile, the pressure amplitude induced by short foil is also enlarged compared to that induced by long foil.

Secondly the lengths of the vaporized areas (see Set 3) were only changed at one vaporized position while the lengths of the vaporized areas at the other position were kept constant. The changed lengths at one position were chosen as 30 mm, 50 mm and 70 mm respectively and the constant length at the other position was chosen as 90 mm. The initial charging energy of capacitor bank was used as 5 kJ.

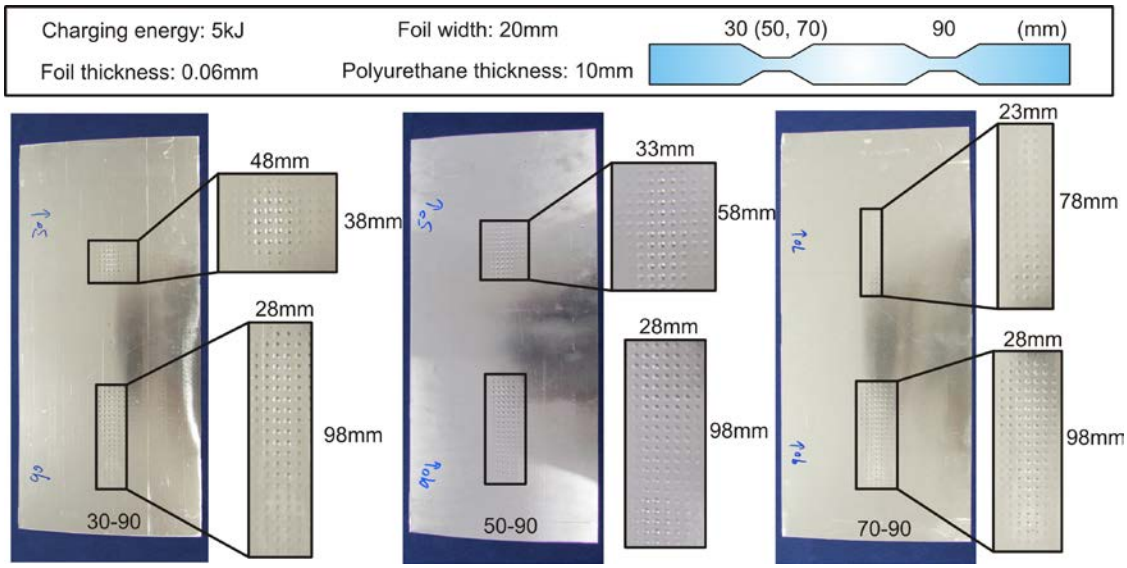

Fig. 8 Perforating formed sheets with respect to different lengths at two vaporized positions in a specimen

As Fig. 8 shows all the tailored parts of the foils were totally vaporized. The lengths of the pressure area are determined by the separated vaporized parts of the foils. The pressure amplitudes are decreased when the lengths of the vaporized parts are increased. Because the dimensions of the two tailored parts in a specimen are different, the pressure areas and amplitudes at two vaporized positions are different.

Based on the results above, the charging energies of capacitor bank and the dimensions of the tailored parts of the foils determine the final pressure areas and pressure amplitudes at two vaporized positions. Under the same charging energy short tailored parts tend to produce a pressure area in a stubby form which means the pressure area is extended to the transverse side while long tailored parts tend to generate a pressure area in a strip form due to the limited electrical energies for the large vaporized dimensions of foils. Therefore, it is important to choose a proper charging energy for a specific tailored geometry of foil in order to acquire an ideal pressure areas and pressure amplitudes.

4. Conclusion

The process parameters that can influence the shock pressure were experimentally identified through the free bulging tests by vaporizing foils. The charging energy, thickness of polyurethane plate and geometry of foils can greatly affect the final shock pressure on the sheet metal. Based on the parameter investigation results, the foils were cut in tailored shape which causes the foils vaporized at different positions. By varying the charging energies of capacitor bank, the pressure amplitudes at two vaporized positions were changed. In addition, the pressure areas and amplitudes were also dependent on the tailored part dimensions at two vaporized positions in a specimen. Therefore, by means of an appropriate combination of charging energy and tailored foil geometry, a tailored pressure distribution including the pressure amplitudes and areas can be realized at different positions in a discontinuous way.

Acknowledgements

The German Academic Exchange Service (DAAD) provides financial support for this paper, which is gratefully acknowledged here.

References

[1] *V. Psyk, D. Risch, B. L. Kinsey, A. E. Tekkaya, M. Kleiner,* Electromagnetic forming-A review, Journal of Materials Processing Technology, Volume 211, no. 5, pp. 787-829, 2011

[2] *A. W. DeSilva, J. D. Katsouros,* Electrical conductivity of dense copper and aluminum plasmas, Physical Review, Volume 57, Number 5, 5945-5951, 1998

[3] *Chace, William G*., Exploding wires 1, Plenum Press, New York, 1959

[4] *Vivek, A., Taber, G.A., Johnson, J.R., Woodward, S.T., Gaehn, G.S*., Electrically driven plasma via vaporization of metallic conductors: A tool for impulse metal working, Journal of Materials Processing Technology 213, 1311-1326, 2013

[5] *Vivek, A*., Rapid vaporization of thin conductors used for impulse metalworking, Ph.D thesis, Ohio state university, 2012

[6] *Saveway Isolierstoffe GmbH*, www.saveway-isolierstoffe.de

Experimental Study on Electromagnetic Forming of High Strength Steel Sheets with Different Dimensions of Aluminum Driver Plate*

Hyeon Il Park[1], Daeyong Kim[1+], Jinwoo Lee[1], Ji Hoon Kim[1], Myoung-Gyu Lee[2], Youngseon Lee[1], Jung Han Song[3]

[1] Materials Deformation Department, Korea Institute of Materials Science, Changwondaero 797, Changwon, Gyeongnam 642-831, Republic of Korea
[2] Graduate Institute of Ferrous Technology, POSTECH, Cheongamro 77, Pohang, Gyeongbuk 790-784, Republic of Korea
[3] Metal Forming Technology R&D Group, Incheon Regional Division, Korea Institute of Industrial Technology, Gaetbul-ro 156, Incheon Metropolitan City 406-840, Republic of Korea

Abstract

Recently, the potential of the electromagnetic forming process has been introduced to form the shallow longitudinal reinforcement ribs in the lateral walls of roll formed parts, made of high strength steel sheets of 340MPa tensile stress grade [1]. However, it seems that the application may not be easy for high strength steel sheet because of its high tensile strength and low electric conductivity. In order to overcome this difficulty, aluminum driver plate could be considered to enhance the formability of high strength steel sheets in the electromagnetic forming process. In this paper, in order to investigate the effect of aluminum driver plate on forming height of high strength steel sheet in electromagnetic forming process, DP780 workpiece sheets were formed into a hemi elliptical protrusion shape with Al1050 driver plate of various thicknesses and sizes. Experiments were performed with a flat spiral coil actuator connected to an electromagnetic forming system. The results, the aluminum driver plate helps to increase the forming height of high strength steel sheets. In addition, the forming height of high strength steel sheet increases as the thickness and size of a driver plate increases.

Keywords

Electromagnetic forming, Flat spiral coil, High strength steel sheet, Aluminum driver plate, Reinforcement rib

---

* *This study was financially supported by Fundamental Research Program of the Korea Institute of Materials Science and R&D programs on Fusion Core Technology for Industry (No. 10040078) funded by Ministry of Science, ICT and Future Planning, Republic of Korea.*

1 Introduction

There is a global trend nowadays of increasing the usage of high strength steel sheets in the automotive industry, aimed at producing lighter and safer cars. More specifically, high tensile steel sheets have been applied in the production of the impact energy absorbing member. Furthermore, to enhance their strength and rigidity more, the reinforcement ribs were often formed at the wall side of the members. Recently, Eguia et al. [1] showed the potential of the electromagnetic forming process to form the shallow longitudinal reinforcement ribs in the lateral walls of roll formed parts, made of high strength steels in a continuous manner.

Electromagnetic forming is a type of high speed forming where the electric current is induced on a specifically shaped coil to generate Eddy current, making a corresponding electric current on a conductive material and making an electromagnetic field on the coil, which generates the Lorentz force used to form the material [2]. It is widely renowned for its potential of formability improvement and springback reduction [3-5]. This technique can be easily used to form materials with a high electric conductivity, but has the disadvantage of requiring a driver plate to form materials with a low electric conductivity [6].

Although Eguia et al. successfully formed the reinforcement ribs with high strength steels sheets of 340 MPa tensile stress grade, it is not easy for high strength steel sheet of higher grade because of increasing tensile strength and decreasing electric conductivity. Therefore, aluminum driver plate might be used to enhance to formability of high strength steel sheets.

In this paper, It is experimentally demonstrated how the thickness and size of the aluminum used for driver plate affects the forming height of the high strength steel sheets. The high strength dual phase steel sheets, DP780 were utilized as a workpiece while aluminum alloy 1050-H16 sheet was used as a driver plate. Experiments were performed with a flat spiral coil connected to an electromagnetic forming system (EmFS) with the energy capacity of 119kJ. In order to consider forming the reinforcement rib, the hemi elliptical protrusions were formed by the open cavity die.

2 Experiments

2.1 Materials

Dual phase steel DP780 sheets with thickness of 1.4mm were utilized as workpiece sheet. The sizes of DP780 workpiece sheets were 200 x 200 mm^2. Aluminum Al1050-H16 sheets were chosen as driver plate because it has low tensile strength and high conductivity. The chemical compositions of DP780 workpiece sheet and Al1050 driver plate are listed in Table 1. The mechanical and electromagnetic material properties are summarized in Table 2.

Material							
Steel	**C**	**Mn**	**P**	**S**	**Si**	**-**	**Fe.**
DP780	0.070	2.26	0.012	0.0030	1.06	-	Bal.
Aluminum	**Si**	**Fe**	**Cu**	**Mn**	**Mg**	**Zn**	**Al.**
A1050	0.25	0.40	0.05	0.05	0.05	0.05	Bal.

***Table 1**: Chemical composition of DP780 workpiece sheet and Al1050 driver plate.*

Material	Young's modulus (GPa)	Yield stress (MPa)	Tensile stress (MPa)	Total strain (%)	Electric conductivity (S/m)	Magnetic permeability (H/m)
DP780	210	546.9	832.4	23.89	7.04×10^6	8.75×10^{-4}
Al1050	71	90.78	108.1	8.07	3.55×10^7	1.26×10^{-6}

***Table 2**: The mechanical and electromagnetic properties of DP780 workpiece sheet and Al1050 driver plate*

In order to investigate the effect of thickness of aluminum driver plate on forming height of high strength steel sheet, the DP780 workpiece sheets were formed into hemi elliptical protrusion shape in electromagnetic forming process without and with aluminum driver plate having thickness of 0.4, 0.6, 0.8 and 1.0mm. In this case, the size of Al1050 driver plate was fixed as 200 x 200 mm^2. On the other hand, the aluminum driver plate having sizes of 100x200, 150x200 and 200x200 mm^2 are adapted to investigate the effect of size of aluminum driver plate. In this case, the thickness of Al1050 driver plate was fixed as 1.0mm.

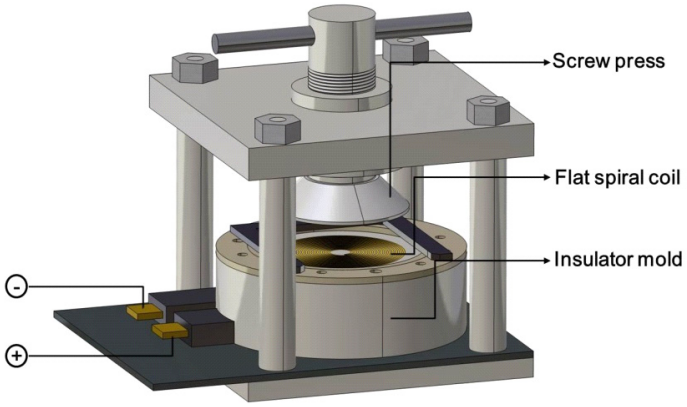

***Figure 1:** Configuration of the flat spiral coil actuator*

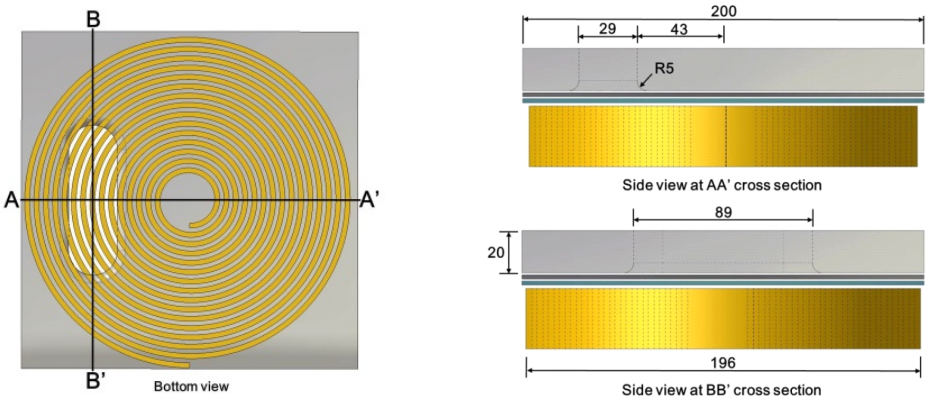

(a) (b)

***Figure 2:** (a) Bottom view and (b) side view of the flat spiral coil and the open cavity die (unit: mm).*

2.2 Electromagnetic forming

In order to form a hemi elliptical protrusion shape on the workpiece sheet with open cavity die, the flat spiral coil actuator was used as shown in Figure 1. The copper strip with cross

sectional area 30 x 3 mm^2 was wound into spiral coil with fifteen turns. The gap between coil turns was 2.5mm. The flat spiral coil was insulated and fixed by epoxy resin inside of the insulator mold. The hole of open cavity die was machined at mean radius of the flat spiral coil to avoid the dead zone that occurs at the center of the winding [7-8] as shown in Figure 2 (a). Detailed dimension of the open cavity die is shown Figure 2 (b). The flat spiral coil actuator was connected to the electromagnetic forming system having a maximum stored energy of 119kJ for maximum working voltage of 17kV.

In this paper, all experiments were performed with charge voltage of 7.3kV. The representative current profile measured by an oscilloscope and a Rogowski flexible coil is shown in Figure 3.

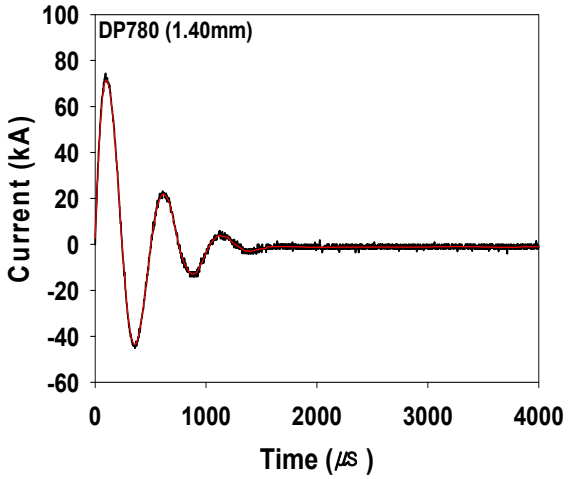

Figure 3: *Primary current profile measured for charge voltage of 7.3kV*

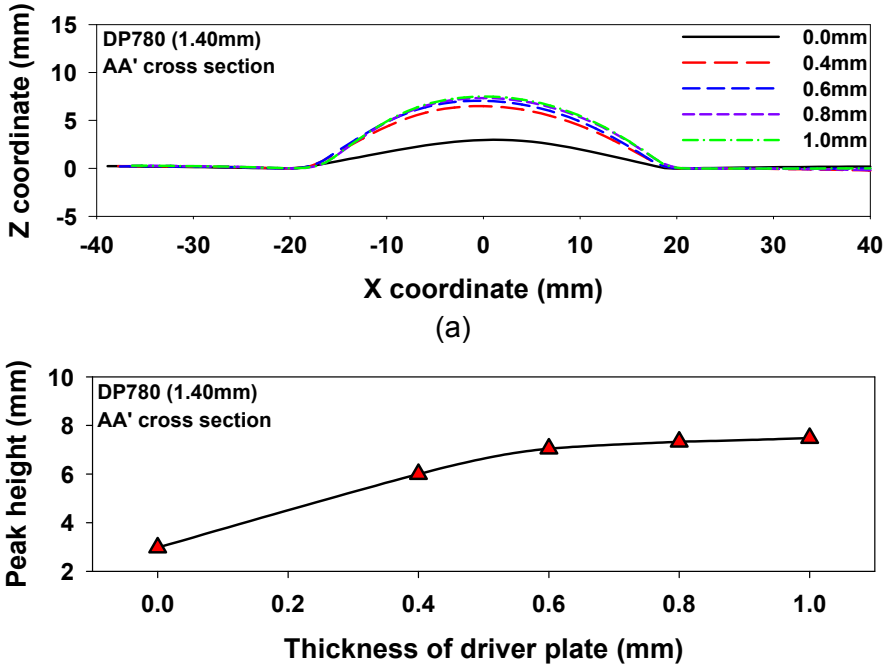

Figure 4: *(a) Forming shape in AA' cross section, (b) peak height of DP780 workpiece sheet with different thicknesses of Al1050 driver plate at charge voltage of 7.3kV.*

3 Results

3.1 Effect of thickness

Forming shape in AA' cross section and peak height of DP780 workpiece sheet after electromagnetic forming with different thicknesses of Al1050 driver plate are shown in Figure 4 (a) and (b), respectively. In these experiments, the size of driver plate was fixed as 200 x 200 mm^2. The peak height of DP780 workpiece sheet was remarkably increased when Al1050 driver plate was used as expected. In addition, the peak heights of DP780 workpiece sheet increase as the thickness of Al1050 driver plate increase and are gradually saturated while the thickness of Al1050 driver plate is approaching to 1.0mm.

3.2 Effect of size

Figure 5 shows the deformed shapes of the DP780 workpiece sheet and Al1050 driver plate after electromagnetic forming with the different sizes of Al1050 driver plate.

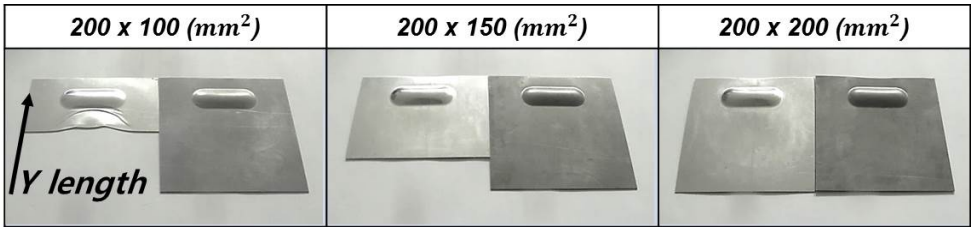

Figure 5: *Deformed shape of DP780 workpiece sheets after electromagnetic forming with the different sizes of Al1050 driver plate.*

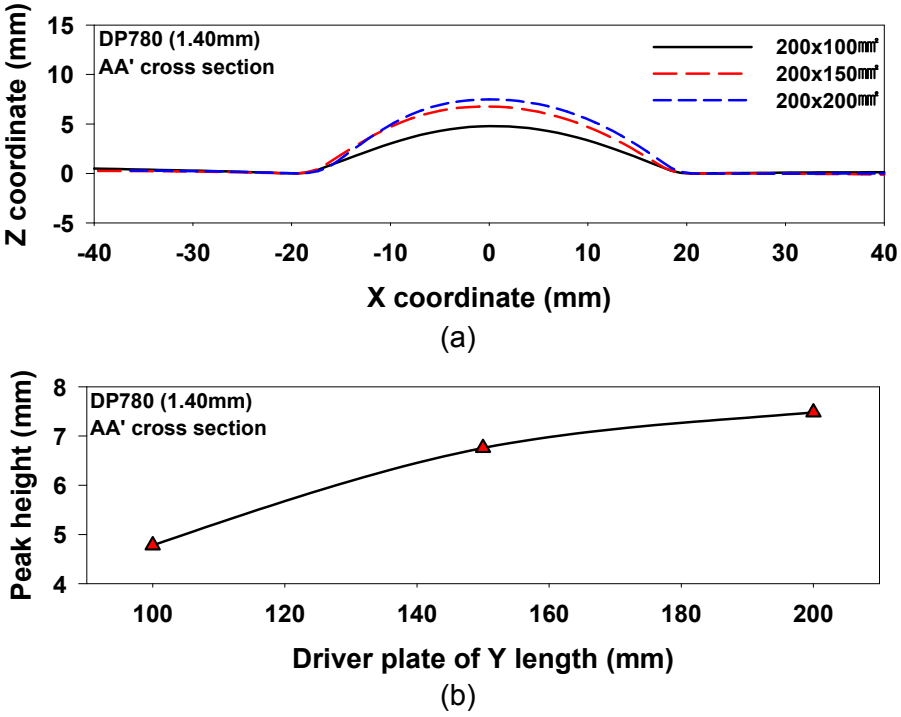

Figure 6: *(a) Forming shape in AA' cross section and (b) peak height of DP780 workpiece sheet with different sizes of Al1050 driver plate at charge voltage of 7.3kV.*

Forming shape in AA' cross section and peak height of DP780 workpiece sheet after electromagnetic forming with different sizes of Al1050 driver plate are shown in Figure 6 (a) and (b), respectively. In these experiments, the thickness of driver plate was fixed as 1.0mm. The peak heights of DP780 workpiece sheet decrease as the size of Al1050 driver plate decrease.

4 Summary

The effect of an aluminum driver plate has been investigated on electromagnetic forming of high strength steel sheet DP780 workpiece sheets were formed into hemi elliptical protrusion shape with Al1050 driver plate of various thicknesses and sizes in electromagnetic forming process. As results, the aluminum driver plate helps to increase the forming height of high strength steel sheet. In addition, the forming height of high strength steel sheet increases as the thickness and size of driver plate increases. The aluminum driver plate might be indispensable for electromagnetic forming of high strength steel sheets because of their low conductivity. It is expected that these results can be utilized to select proper dimensions of an aluminum driver plate.

Reference

[1] *Eguia, I.; Mangas, A.; Iturbe, R.; Gutierrez, M.A.:* Electromagnetic forming of longitudinal strengthening ribs in roll formed automotive profiles. Proceedings of 4th International Conference on High Speed Forming, 2010, pp.198-207.

[2] *Psyk, V.; Risch, D.; Kinsey, B.L.; Tekkaya, A.E.; Kleiner, M.:* Electromagnetic forming – A review. Journal of Material Process Technology 211, 2011, pp. 787-829.

[3] *Mamalis, A.G.; Manolakos, D.E.; Kladas, A.G.; Koumoutsos, A.K.:* Electromagneitc forming and powder processing: trends and developments. Applied Mechanics Reviews 57(4), 2004, pp.299-324.

[4] *Correia, J.P.M.; Siddiqui, M.A.; Ahzi, S.; Belouettar, S.; Davies, R.:* A simple model to simulate electromagnetic sheet free bulging process. International Journal of Mechanical Sciences 50(10-11), 2008, pp.1466-1475.

[5] *Haiping, Yu.; Chunfeng, L.; Hongwei, J.; Zhiheng, Z.; Jianghua, D.; Zulun, L.; Xiaofeng, Z.:* Reaearch on magnetic pulse sizing of aluminum tube. International Journal of Advanced Manufacturing Technology 38(11-12), 2008, pp.1165-1171.

[6] *Harvey, G.W.; Brower, D.F.:* Metal forming device and method. US Patent Nr.2976907, 1958.

[7] *Al-Hassani, S.T.S.:* Magnetic pressure distributions in sheet metal forming. Electrical Methods of Machining, Forming and Coating. Institute of Electrical Engineers Conference Publications 133, 1975.

[8] *Imbert, J.M.; Winkler, S.L.; Worswick, M.J.; Oliveira, D.A.; Golovashchenko, S.:* The effect of tool-sheet interaction on damage evolution in electromagnetic forming of aluminum alloy sheet. Journal of Engineering Materials and Technology 127(1), 2005, pp.369-379.

Ball Pad Mold Electromagnetic Forming Process for Aluminium Alloy Sheet*

Wen-Ping Wang[1], Xiang-Dong Wu[1], Min Wan[1], Xiao-Wei Chen[1], Wei-Ren Xiong[1]

[1] School of Mechanical Engineering and Automation, BeiHang University, 37 xueyuan road, Beijing, 100191, China

ABSTRACT

In order to meet requirements of lightweight technology in the field of aerospace, the new forming technology for aluminium alloy skin parts and integral panel are brought to more attention. Based on the principle of electromagnetic forming (EMF) and energy distribution, a new electromagnetic forming process using ball as pad mold for aluminium alloy sheet forming was suggested and test apparatus was designed. The new method was verified by the finite element simulation and experimental technology, and all studies were carried out on 2024-T3 aluminium alloy sheet. The results show that the new process of ball pad mold electromagnetic forming is feasible to aluminium alloy sheet parts forming. Rubber cushion thickness and electromagnetic pulse voltage are significant contributors to the curvature radius of the test sample. Based on these observations, application advantages and prospects of this new process were pointed out, and the subsequent research was put forward.

Key words:

Aluminium alloy, Sheet metal, Electromagnetic forming, Ball pad mold

---

*This work was supported by the National Key Basic Research and Development Program of China (973 Program) (No. 2011CB012804); the authors would like to thank the 973 Program for its financial support.
Corresponding author: Xiang-Dong Wu; xdwu@buaa.edu.cn; Tel.:+86 010-82338613

1 Introduction

In order to meet requirements of lightweight technology in the field of aerospace, large-scale aluminium alloy skin panel is used to lightweight structure parts [1]. The strength, the stealth effect, and other performances of large-scale aluminium alloy skin panel are better than that of the mosaic structure with small skin panels. But forming large-scale skin panel is limited by the size and capacity of manufacturing machine. In the field of aerospace manufacturing, there is perennial interest in seeking adaptive methods for forming large aluminium alloy skin panels.

Electromagnetic forming (EMF) is an impulse or high energy rate forming technology, which uses high-voltage pulse current through an electromagnetic coil or actuator to generate a strong transient magnetic field that induces eddy currents in the nearby conductive workpiece. These eddy currents in turn produce an associated secondary magnetic field around workpiece. This causes the coil and workpiece to repel each other by the electromagnetic force (Lorentz effect) and this force accelerates the workpiece away from the coil. In an EMF process, the material can achieve velocities in the order of 100m/s in less than 0.1 ms [2]. Meanwhile, single side tooling or no tooling can be used because of non-contact loading. In comparison to conventional quasi-static forming processes, the electromagnetic forming process has prominent advantages such as significantly improved formability, slight springback and reduction in residual stresses [3-6]. In addition, the electromagnetic force can be adjusted steplessly according to the technical requirements, that to satisfy the flow characteristics of metal parts. At present, the EMF technology is mainly used in aviation, aerospace, weapon and automobile manufacturing. The researches and applications focus on lightweight structure sheet and tube forming, difficult machining parts forming and hybrid forming [2-9].

However, it has rarely reported about the electromagnetic forming of aircraft skin panel. Only in 1999, Newman et al [10] did some researches about electromagnetic forming of aircraft skin panel, which was supported by Navy SBIR Program IAP Research. They presented a new process named MagneStretch process, in which the EMF process was introduced into stretch forming. The formability trials were performed directly on 7075 aluminum alloy sheet from T6 heat treatment condition. The results show that the MagneStretch process can (1) allow stretch forming of 7075 from T6 condition with little or no springback, (2) eliminate costly pre and post forming heat treating steps in conventional stretch forming process, (3) not alter the microstructure. Compared with the traditional process, the new process method is flexible, short production cycle and greatly reduce costs.

In this paper a new electromagnetic forming process with ball pad mold for aluminum alloy sheet forming is suggested that bases on the principle of electromagnetic forming and energy distribution. In order to determine the feasibility of this ball pad mold electromagnetic forming process, forming process is analyzed firstly by the finite element method, and then experiment apparatus is designed and aluminium sheet forming tests is carried out.

2 The principle of ball pad mold EMF

In the process of electromagnetic forming, the plastic indentation can be produced on the surface of workpiece as shot peening if the electromagnetic pressure is great enough. In the literatures [11,12], James S. Shaw and James. R. Dydo et al applied for two patents about Balanced Electromagnetic Peening and Electromagnetic Pulse Surface Treatment base on the characteristic of electromagnetic. However, it is difficult to treat the workpiece surface only by the electromagnetic pulse force. EMF is a kind of high speed and high strain rate forming process. According to impact dynamics, the certain plastic indentation and compressive residual stress layer with certain thickness can be produced on the workpiece surface, only when the impulse pressure acts on the workpiece surface achieve and exceed the dynamic yield strength of the material. Because the dynamic yield strength is greater than the static yield strength, Electromagnetic Peening or electromagnetic Pulse Surface Treatment requirement for EMF equipment is extremely high and it is difficult for present equipment to meet it, the energy efficiency is only 10-20 percent, the highest energy efficiency is not over 40 percent [3,13]. Therefore, in order to implement the effect as above patents show, the electromagnetic pulse force per unit area need to be increased. There are two approaches to achieve this goal: firstly, the energy and energy efficiency of electromagnetic forming equipment should be improved, at the same time, the contact area between coil and workpiece also should be reduced; secondly, according to the principle of energy distribution, force area on the sheet metal should be decreased by altering the tooling structure.

Based on the existing 20kJ electromagnetic forming equipment, considering tooling structure, a new method of ball pad mold electromagnetic forming process is put forward. The basic idea is described as follows: First, a certain amount of balls are mounted and arranged as a die cushion, so a series of micro mold cavity can be formed in the gap of adjacent spheres. Then a sheet metal specimen is placed on the ball pad mold. When the transient pulse magnetic force applies the specimen, the force per unit area of the specimen is greatly increased because of application of ball pad mold. So, both upper and lower sheet surface will produce plastic deformation indentations in the interaction of the magnetic pressure and the ball support force, and hardening and forming of the specimen will be realized

On the basis of the above proposed idea, the forming experimental system was set up. Fig.1 shows a schematic diagram of test apparatus for aluminium sheet specimen. The apparatus is composed of four parts that includes a control system, an electromagnetic pulse power source, a ball pad mold and a working coil. During the experiment, the specimen is fixed on the ball pad mold. The discharge voltage of capacitor bank is adjusted through the control system of electromagnetic pulse power. The high-speed switch is triggered to deliver a high-frequency current pulse to the working coil. The conductive sheet metal is exposed to an intense transient magnetic field. The resulting Lorentz force pushes the sheet metal away from the coil. At the same time, the sheet metal withstands the supporting force of the ball pad mold. Different degree of surface plastic indentation occurs under the two force fields in the top and bottom sheet. After unloading , specimen will show certain plastic deformation.

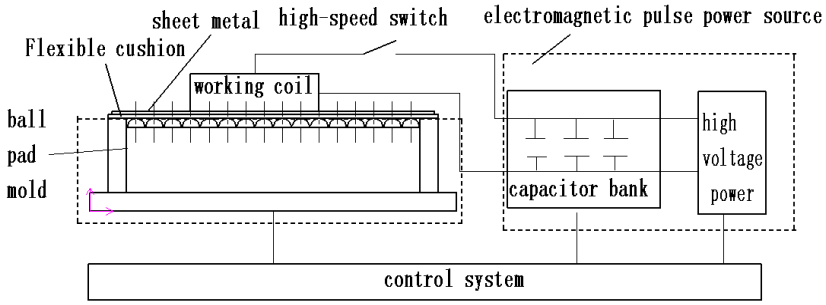

Figure 1 *schematic diagram of test apparatus*

3 Finite element analysis

Numerical modeling of the ball pad mold electromagnetic forming process requires the analysis of the discharge circuit, electromagnetic field and structural field (mechanical problem). The laws of current density distribution of the working coil can be got in the discharge current analysis. In the process of electromagnetic field analysis, the current density is loaded as the magnetic field excitation conditions that can be obtained by the above analysis, then the laws of induced eddy currents and magnetic pulse force distribution of the specimen can be obtained. Finally, the specimen deformation behavior can be gained in the structural field analysis. In the whole process of numerical analysis, the analysis of discharge circuit and electromagnetic field are carried out by finite element software ANSYS/EMAG. The mechanical problem is developed with the commercial finite element code ABAQUS/Explicit.

According to reference [14], the discharge loop and electromagnetic field of the ball pad mold electromagnetic forming was analyzed. Based on above analysis results, the finite element model of the structural field were established by ABAQUS/Explicit code as Fig.2 shows. In the model, the aluminium sheet and rubber pad are modeled as deformable parts, while the ball pad die and coil clamp are considered to be planar rigid. The ball diameter is 30 mm. The material tested is 2024-T3 aluminium alloy sheet. The sheet size is 480 × 120 × 1.8 mm. Ball pad mold and coil clamp are fixed during the forming process. Electromagnetic pulse force area under the coil clamp is 225 × 120 mm^2. Fig. 3 shows electromagnetic pulse amplitude curve, the peak pressure is 50MPa.

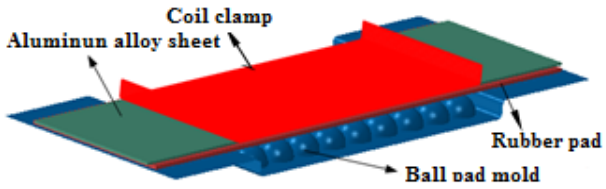

Figure 2 *Finite element model of structural analysis of ball pad mold EMF*

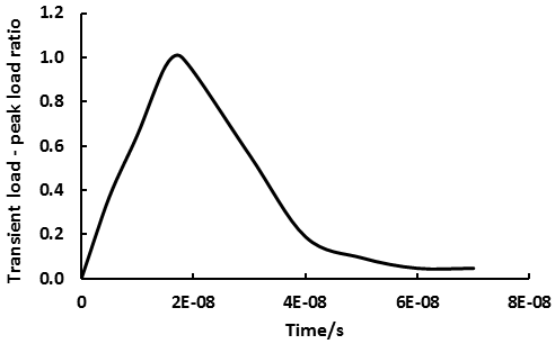

Figure 3 *Electromagnetic pulse force amplitude curve*

When the rubber cushion is not used between sheet metal and ball pad mold in the process of electromagnetic forming, the simulation results of sheet deformation is shown in Fig. 4. This is because the sheet metal comes into contact with the ball pad mold directly and the diameter of the ball is large, then the sheet pressed into the gap of the adjacent balls under the action of electromagnetic pulse force, finally the wave-shaped specimen is easily observed from the graph.

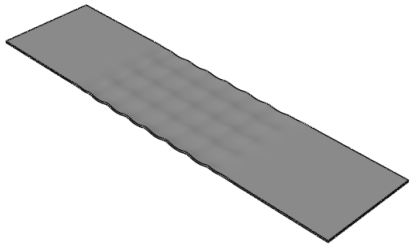

Figure 4 *the morphology without rubber cushion*

In order to improve the surface condition of the forming specimen, a rubber cushion is placed between the sheet metal and ball pad mold. When the strong transient electromagnetic pulse force acts on the blank, the indentations and wave-shape will be avoided due to the rubber cushion buffer action. Fig. 5 shows the finite element analysis result of sheet deformation. It is seen that the sheet has been formed to a certain curvature part, and there are no obvious indentations on the sheet surface.

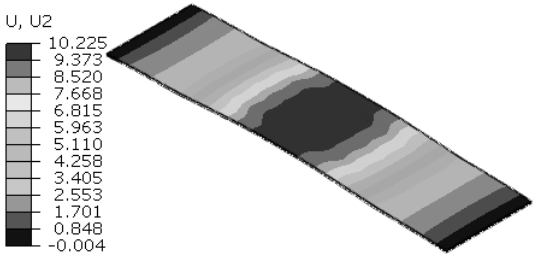

Figure 5 *the morphology with rubber cushion*

4 Ball pad mold EMF experiment

From the above finite element analysis, it can be seen that the new process of the ball pad mold EMF is feasible for forming a certain curvature part of the 2024-T3 aluminum alloy sheet. Consequently, test fixture of the ball pad mold EMF is designed and manufactured. The structure of the ball pad mold is depicted as Fig. 6(a). The cross-section area of a ball is 30 × 30 mm^2, and the balls array is 6 × 8 mm. A flat circular spiral coil (Fig. 6(b)) is adopted as electromagnetic coil. The specification for the coil is presented in Table 1. The maximum energy storage of the EMF equipment in the experiment is 20kJ. The specimens are the 2024-T3 aluminium alloy with the thickness of 1.8 mm and the plane size of 482 × 120 mm. The discharge voltage levels used range from 1800 V to 2800 V. The capacitance is set to 2400 μF.

Figure 6 *Ball pad mold (a) and Electromagnetic coil (b)*

Table.1 Electromagnetic coil specifications(*mm*)

Number of windings	Internal radius	External radius	Thickness	The effective internal radius	The effective external radius	Copper wire section
23	20	140	40	30	125	1.7×6.3

5 Results and Analysis

Firstly, the discharge voltage is set to 1800 V and 2000 V, and a sample is placed on the ball pad mold directly in the EMF test. The results show that there are obvious dents in the sample and a significant wave-shaped morphology specimen without certain curvature shape is obtained as shown in Fig. 7, which is agree with the result of the finite element analysis in Fig. 4.

Secondly, the thickness of 1.5 mm or 3 mm flexible rubble cushion is placed between the specimen and ball pan mold. Considering the existing electromagnetic forming equipment capacity, ensure adequate electromagnetic pulse force to act on the whole blank, the specimen is struck sequentially 8 times at the same discharge voltage. Each action position is transformed by adjusting relative positions between the electromagnetic coil and the sample. Fig. 8 shows the relative positions between the edge of electromagnetic coil and the sheet. An interval of 25 mm is allowed between the adjacent position. The effect of deformed samples is shown in Fig. 9.

Figure 7 *Specimen after forming*

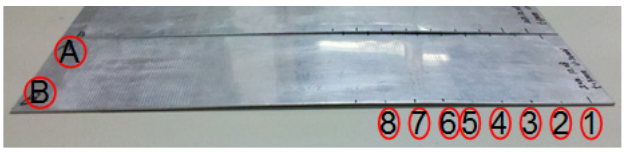

Figure 8 *Relative positions in order*

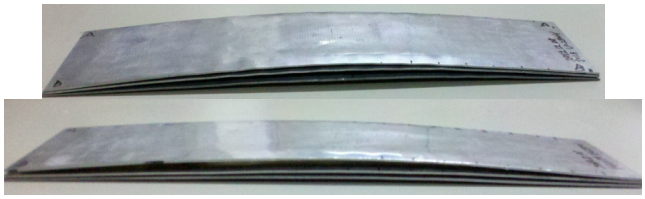

(a) 1.5 mm thickness of the rubber pad (b) 3 mm thickness of the rubber pad

Figure 9 *Specimens after the ball pad mold EMF*

The specimen deformation deflection of A and B sides (Fig. 8) is measured, and both sides of deflection is almost the same, the maximum difference is no more than 0.5 mm. The result shows that the sample has good deformation uniformity in the ball pad mold electromagnetic pulse forming process. The measured deflection curve is presented for 1.5 mm and 3 mm thickness of the rubber pad in Fig. 10. It can be seen from the chart that forming deflection increased with the discharge voltage increasing, whereas reduced with the thickness of rubber pad increasing.

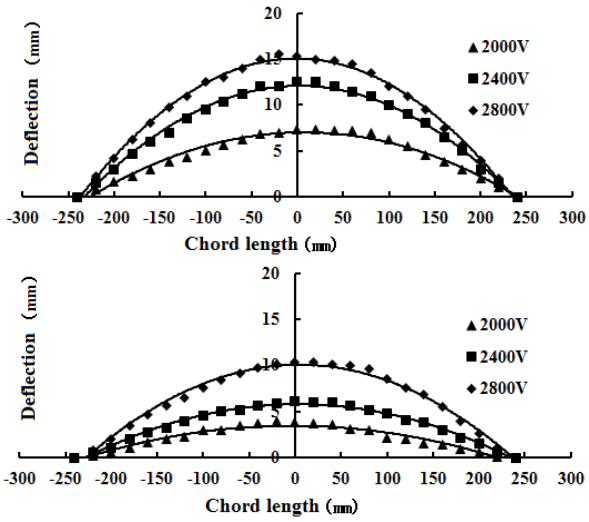

(a) 1.5 mm thickness of the rubber pad (b) 3.0 mm thickness of the rubber pad

Figure 10 *Deflection curve under the different thickness of rubber pad*

Curvature is the ratio of the change in the angle of a tangent that moves over a given arc to the length of the arc. While radius of the curvature is the absolute value of the reciprocal of the curvature of a curve at a given point and it can be used to describe the bending degree somewhere in the curve. The formula of the radius of the curvature is

$$\rho = \frac{\sqrt{(1+y'^2)^3}}{y''} \tag{1}$$

In the formula, y' is the first order derivative of x of the curve on y, y'' is the second order derivative of x on y. In this paper, y is the specimen bending deflection and x is the specimen chord length.

The functional relation between the specimen deflection (y) and the specimen chord length (x) is created by curve fitting. Then the radius of specimen curvature is calculated by the above formula. The radius versus chord length is depicted in Fig. 11.

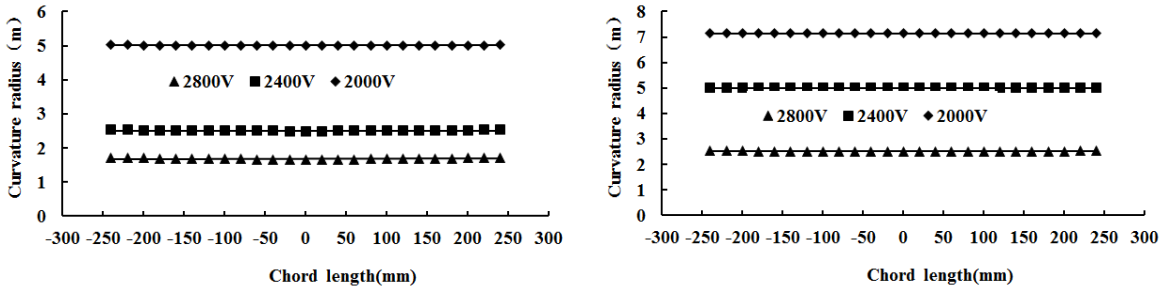

(a) 1.5 mm thickness of the rubber pad (b) 3.0 mm thickness of the rubber pad

Figure 11 *Curvature radius under the different thickness of rubber pad*

As we can see from the Fig. 11, the radius of curvature of the specimen surface is relatively uniform. Also, the relation curve between the curvature radius and the discharge voltage is obtained by averaging the radius of curvature at each point under different discharge voltages as Fig.12 shows. Obviously, radius curvature decreases with the increase of discharge voltage and increases with the increase of the rubber pad thickness. The rubber cushion thickness and discharge voltage are both important factors that influence the curvature radius of specimen. Meanwhile, the curvature is small in the range of 10^{-3} mm^{-1} to 10^{-4} mm^{-1}. So, the ball pad mold EMF process has potential to form the large integral aluminium alloy skin panels with small curvature and large length-to-width ratio.

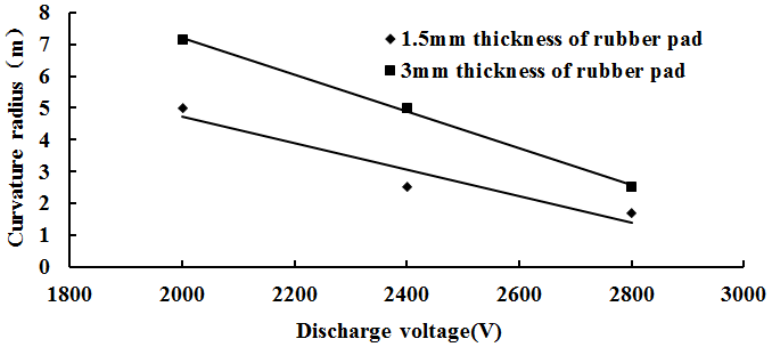

Figure 12 *Relationship between curvature radius and discharge voltage*

It can be observed from the experiment deformation results that the specimen deformation is maximum at the 2800 V discharge voltage, and the maximum thickness variation is only 0.004 mm for 1.5 mm rubber cushion and 0.002 mm for 3mm rubber cushion separately. Hence, the thickness variation of the specimen is negligible when a certain curvature sheet metal was formed using the ball pad mold EMF.

In follow-up studies, the forming mechanism of the ball pad mold EMF will be deeply analyzed. The sheet metal dynamic deformation behavior and inertial stress variation rules under the action of strong transient electromagnetic force will be revealed by the comprehensive application of plastic dynamics, electromagnetics theory, experiments and multi-physics coupling finite element analysis. Multi-step forming path of the single curvature and complicated curvature integral skin panels will be designed by optimization method and will be carried out by the ball pad mold EMF experiments. These researches will lay a solid foundation for the future application of the ball pad mold EMF process in the integral aluminum skin panels forming.

6 Conclusions

The method of the ball pad mold EMF process is presented. For certain diameter balls, the rubber cushion thickness and discharge voltage are the important factors that influence the workpiece curvature.

Because large repulsive electromagnetic forces can accelerate the workpiece to high velocities and make the workpiece have high inertia forces, the new ball pad mold EMF process allows forming directly from the T condition aluminium alloy eliminating the need of conventional process for the pre and post heat treating steps .

Because of using the simple structure, strong versatility ball pad mold device, ball pad mold EMF process requires smaller energy EMF equipment than the general EMF process. Therefore, ball pad mold EMF process can reduce costs, save energy, as well as improve the life of electromagnetic coil.

References

[1] *Han Zhiren, Dai Lingjing, Zhang Ling.* Current status of large aircraft skin and panel manufacturing technologies[J]. Aeronautical Manufacturing Technology, 2009, 4: 64-66(in Chinese)

[2] *Anter El-Azab, Mark Garnich,* Ashish Kapoor. Modeling of the electromagnetic forming of sheet metals: state-of-the-art and future needs[J]. Journal of Materials Processing Technology 142 (2003): 744–754

[3] *V. Psyk, D. Risch, B.L. Kinsey, etc.* Electromagnetic forming—A review[J]. Journal of Materials Processing Technology, 2011 (211): 787–829

[4] *J. Imbert, M. Worswick.* Reduction of a pre-formed radius in aluminum sheet using electromagnetic and conventional forming[J]. Journal of Materials Processing Technology, 2012 (212) : 1963–1972.

[5] *YU Hai-ping, LI Chun-feng, LIU Da-hai, et al.* Tendency of homogeneous radial deformation during electromagnetic compression of aluminium tube[J]. Transaction of Nonferrous Metals Society of China, 2010, 20: 7-13.

[6] *Xu Junrui, Yu Haiping, Li Chunfeng.* Effects of process on electromagnetic forming of AZ31 magnesium alloy sheets at room temperature[J]. International Journal of Advanced Manufacturing Technology, 2013, 66:1591-1602.

[7] *Pradip K. Saha.* Electromagnetic forming of various aircraft components[J]. SAE transactions, 2005,114(1): 999-1009.

[8] *S. Golovashchenko. Electromagnetic* Forming and Joining for Automotive Applications[C]. 2nd International Conference on High Speed Forming , 2006: 201-206.

[9] *G. Zittel.* A historical review of high speed metal forming[C]. 4th International Conference on High Speed Forming, 2010: 2-15.

[10] *D. C. Newman, and D. P. Bauer.* MagneStretch Process Reduces Stretch Forming Manufacturing Costs: Magnetic Forming Technology Enables Forming of Al7075 Directly from T6 Condition[R]. IAP Research Magnepress, 1999,4.

[11] *James S. Shaw, Neil N. Johnson.* Balanced electromagnetic Peening: US, 5813265[P], 1998-09-29.

[12] *James. R. Dydo, Sergei P. Yushanov.* System and method for electromagnetic pulse surface treatment: US, 7378622B2[P], 2008-05- 27.

[13] *Zi Bingtao, Ba Qixian, Cui Jianzhong.* A survey of electromagnetic forming equipment at home and abroad[J]. Metalforming Machinery, 1998, 3: 8-10, 50 (in Chinese).

[14] *Chen Xiaowei, Wang Wenping, Wan min, etc.* Study of Magnetic Force Distribution in Electromagnetic Sheet Forming[J]. Journal of Netshape Forming Engineering, 2013, 5(2): 20-24 (in Chinese).

Pulsed Electromagnetic Attraction Processes for Sheet Metal Components *

Yuri V.Batygin[1], Sergey F.Golovashchenko[2], Andrey V.Gnatov[1], Evgeniy A.Chaplygin[1]

[1] Kharkov National Automobile and Highway University, Kharkov, Ukraine
[2] Ford Research and Advanced Engineering, Ford Motor Company, Dearborn, USA

Abstract

The work is dedicated to EMF attraction processes which can deform both ferromagnetic and non-ferromagnetic sheet metal materials (low carbon steels, stainless steels and aluminum alloys) using low frequency discharges. The analytical models of both tooling configurations are based upon the solution of Maxwell equations in axially symmetrical formulation. For ferromagnetic materials, the attraction effect is based upon magnetic forces prevailing over the Lorentz forces for low frequency discharges. For non-ferromagnetic materials, the attraction forces are created by employing the auxiliary screen which attracts the sheet metal blank. The concept of attraction in this inductor system is based upon inducing currents flowing in the same directions in the screen and in the sheet metal blank. In addition to the analytical models, the described concepts are illustrated by the experimental results on attraction of sheet metal blanks employing a single turn inductor.

Keywords

Electroforming, metal forming, tool

1 Introduction

Electromagnetic forming, crimping, welding and cutting are well known in industry since 1960s. A comprehensive review of these technologies was published by Psyk et al. (2011). All these processes are based upon repelling Lorentz forces between the EMF coil and the conductive blank. In such a configuration, the coil and the tool (the forming die or the mandrel to which the blank is welded or crimped, or the shearing die with sharp cutting edges) are positioned from the opposite sides of the blank. In addition to such repelling processes, another configuration of EMF processes is possible where the blank is attracted to the coil. The objective of this paper is to introduce a new manufacturing process of the thin-walled metal sheets attraction using low frequency discharges.

2 EMF attraction process for ferromagnetic materials

The objective of this part is to describe the concept, provide a simplified mathematical model predicting attracting electromagnetic forces for ferromagnetic materials and illustrate this concept with experimental results supporting the major conclusions of the analytical study.

2.1 Analytical model of the process and numerical examples

The initial experiments described in details in Batygin (2013) illustrated that the effect of attraction is possible only for the low frequencies, when

$$\omega << \frac{1}{\mu \cdot \gamma \cdot d^2} \tag{1}$$

where $\omega = 2\pi \cdot f$, $f -$ is the working frequency, $\mu -$ is the permeability of metal, $\gamma -$ is the electric conductivity of sheet metal, and $d -$ is the sheet metal thickness.

The interaction between a single turn inductor and a ferromagnetic sheet metal blank is being analyzed. The schematic of the process is shown in Figure 1.

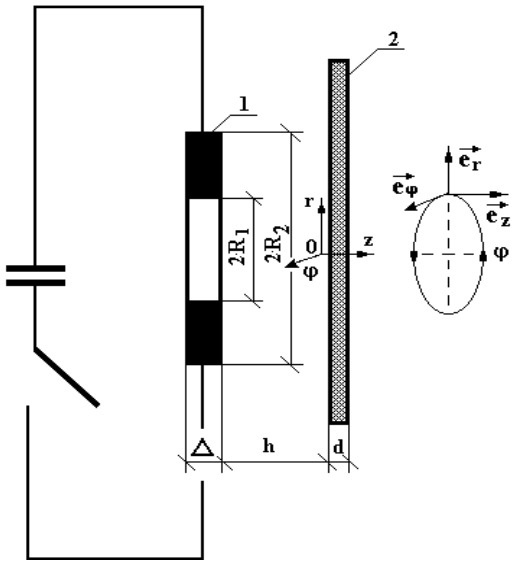

Figure 1: *The schematic of the single turn inductor (1) interacting with ferromagnetic sheet metal blank (2) where* $\vec{e}_r, \vec{e}_\varphi, \vec{e}_z -$ *are the unit vectors in the cylindrical coordinate system*

The following assumptions were made in order to simplify the mathematical model of the process:

1) the single turn inductor is sufficiently thin (its thickness $\to 0$) and "transparent" for the acting fields, so its metal has no effect on considered electromagnetic processes;

2) the process is considered quasi stationary according to the criterion $\omega/c \cdot \ell << 1$, where ω – is the cyclic frequency of the process, c – is the light velocity for vacuum, ℓ – is the greatest typical dimension of the system under consideration;

3) the system has an axial symmetry, so $\partial/\partial\varphi = 0$ (φ – is the polar angle);

4) the sheet metal blank is sufficiently thin, and its radial dimension is sufficiently large, so $d/R_{1,2} << 1$ and $\omega \cdot \tau << 1$ ($\tau = \mu_1 \cdot \gamma \cdot d^2$, γ, d – are conductivity and thickness of the sheet metal blank, $R_{1,2}$ – are the internal and external radii of the inductor);

5) the permeability of the sheet billet metal is constant and is equal to μ_1, $\mu_1 = \mu_0 \mu_r$, μ_0 and μ_r – are the vacuum permeability and the relative permeability of metal accordingly;

6) reproduction of the mutual inductance of tool coil and work piece is neglected;

7) the sheet metal's motion is not taken into account;

8) nonlinear behavior of ferromagnetic saturation is neglected considering an average value of magnetic permeability;

9) variability of conductivity as a consequence of temperature rise due to Joule heating as well as due to magnetization is neglected;

10) reversion of magnetization is not taken into account.

The Maxwell equations were solved with usage of the Laplace and Fourier-Bessel integral transforms with zero initial conditions for the non-trivial components of the electromagnetic field vector $(E_\varphi \neq 0, H_{r,z} \neq 0)$ in limits of the formulated assumptions.

The detailed discussion of the mathematical procedures was provided by Batygin et al (2013). The resulting parameter is an integrated average force applied to the circular area of the sheet metal blank. It was calculated through integration of pressure through the radial coordinate and time and then averaging its value through the time period of the acting field. This averaged force is analyzed as a function of the discharge frequency to provide the recommendations for the pulse generator.

The numerical calculations were performed for the single turn coil – $R_1 = 0.025\,\text{m}$, $R_2 = 0.03\,\text{m}$; insulating gap – $h = 0.0005\,\text{m}$. The sheet metal blank: $\gamma = 0.4 \cdot 10^7$ 1/(Ohm·m), $\mu_r \approx 2.5$, $d = 0.00075\,\text{m}$. The amplitude of the discharge current was $I_m = 50\,\text{kA}$, and the frequency was $f = 2 \div 8\,\text{kHz}$. The results of calculations are presented in Figure 2.

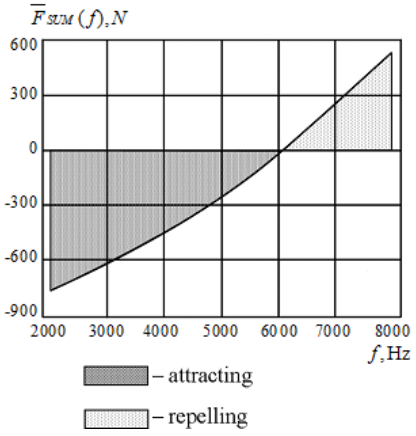

Figure 2: *An average integral force acting on the thin-walled ferromagnetic sheet as a function of the frequency of acting field*

According to Figure 2, reducing the discharge frequency below the some critical value of ~ 6 kHz leads to change of the direction of the integrated force: below the marked critical frequency ~ 6 kHz thin-walled sheet ferromagnetic metal is being attracted to the inductor: above the frequency of ~ 6 kHz, the sheet metal blank is being repelled.

For the frequency range $f \in [2,8]\,\mathrm{kHz}$ the applied electromagnetic force acting on the sheet ferromagnetic metal was changing its direction: for $f > 6\,\mathrm{kHz}$ repelling took place, but for $f < 6\,\mathrm{kHz}$ attraction was displayed.

2.2 Experimental validation

Experimental validation of the proposed concept was done with the intent of practical application of the proposed process to dent removal from automotive exterior panels manufactured from steel. The experimental setup is shown in Figure 3.

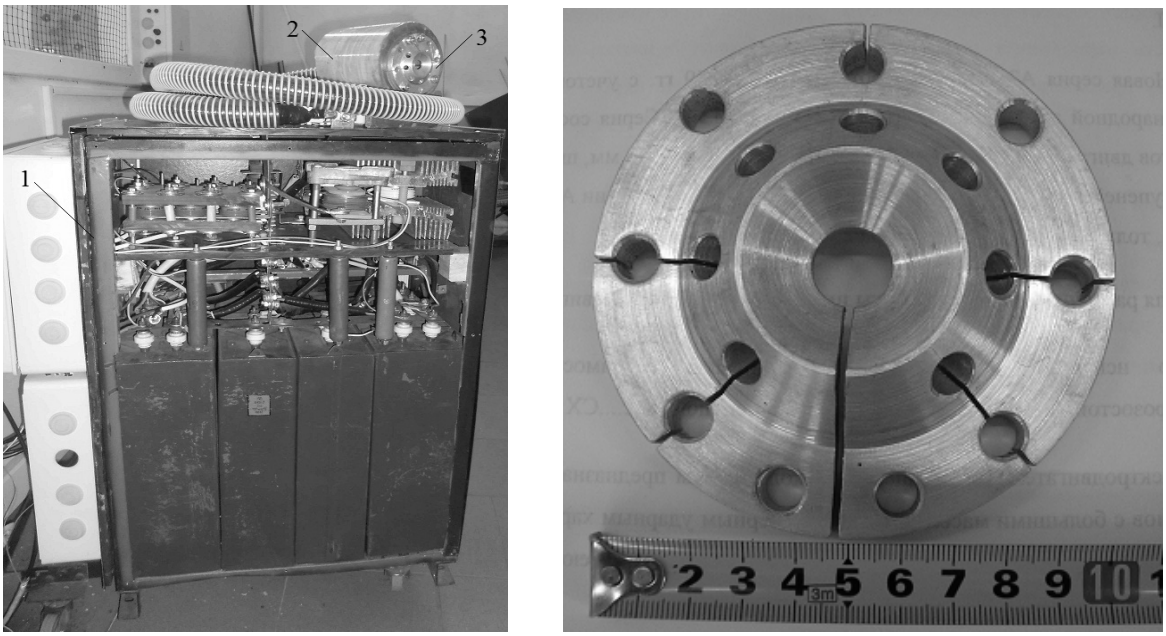

a) b)

Figure 3: *The experimental setup:*
a) the laboratory equipment for EMF attraction processes with maximum charging voltage of 2kV and accumulated energy of 2kJ: 1 – pulse generator; 2 – pulsed current transformer;
3 – single turn inductor;
b) the single turn massive inductor.

The single turn massive inductor with the working zone diameter of 40 mm was connected to the pulse generator via current pulse transformer with the coefficient of transformation of five. The discharge frequency was measured as 1.9 kHz. The amplitude of electric current flowing through the coil was 38 kA. The DDQ (Deep Drawing Quality) flat sheet steel samples 0.8 mm thick (the steel DDQ yield strength is equaled to 180 MPa, stainless steel – 350…300 MPa) were positioned next to the single turn coil. The sample

was insulated from the coil with ~1 mm layer of insulation. Initially flat samples were bulged by attraction inside the working zone of the single turn coil. The bulge was axisymmetric and had the maximum height of 1.5 mm at the axis of symmetry of the coil.

After the initial bulge was produced on a flat blank using the described process of electromagnetic attraction, it was flipped over, and dent removal process was physically simulated by pulling the bulge back with the electromagnetic attraction process. The experimental sample is shown on Figure 4. The dent was successfully removed which confirmed the suggested concept.

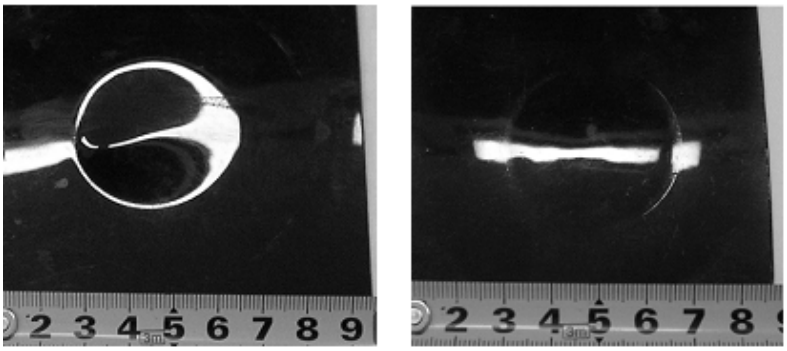

Figure 4: *The experimental DDQ steel sample:*
a – after producing the dent; b – after removing the dent.

3 EMF attraction process for non-magnetic materials

The objective of this part is to describe the concept and provide a simplified mathematical model of pulsed electromagnetic attraction of non-magnetic materials in the «Inductor System with an Attracting Screen» as well as to illustrate the experimental results supporting the suggested concept and the major conclusions of the analytical study.

3.1 Theoretical analysis, numerical calculations

The schematic of the proposed process of sheet metal attraction is employing an Inductor System with Attracting Screen (ISAS) shown in Figure 5.

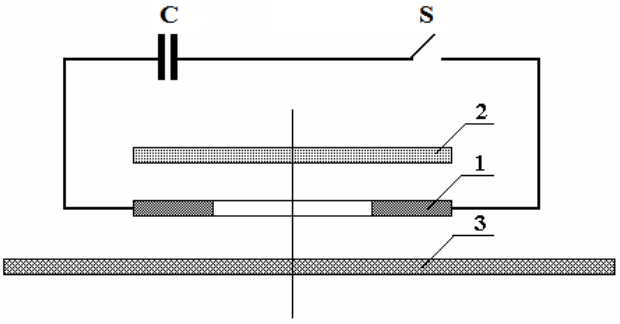

Figure 5: *Schematic of ISAS: 1 – is the single-turn inductor, 2 – is the auxilary attracting screen, 3 – is the sheet metal blank,* C *– is the bank of capacitors,* S *– is the switch of the discharge circuit.*

When the switch (S) gets into a closed position by a special ignition circuit not shown in Figure 5, the preliminary charged capacity storage (C) starts discharging through the single-turn inductor (1) with the internal radius R_1, the external radius R_2 and rather small thickness. The discharge current is inducing the unidirectional eddy currents in the attractive screen (2) and sheet metal blank (3) both made of similar non-ferromagnetic sheet material. If the screen (2) is rigidly mounted on an insulated plate of the tool, it remains stationary during the discharge process while the sheet metal blank (3) will be attracted to the working surface of the inductor (1) in accordance to Ampere law. The suggested system is working in the low frequency range specified by inequality (1).

The analytical solution of this problem is described by Batygin et al. (2014).

The numerical calculations were performed for an experimental inductor system where single-turn inductors with different internal and external diameters. The screen and the sheet metal blank are identical thin-walled sheets with the thickness $d = 0.001$ m from the non-magnetic metal with the specific conductivity $\gamma = 0.4 \cdot 10^7$ (1/Ohm·m). They are located symmetrically relatively to the plane of the single-turn inductor at a distance h=1.5 mm from each other. In the conducted experiments, the electric current amplitude in the inductor was $I_m = 40\,\text{kA}$, and the frequency of the pulse was $f = 2\,\text{kHz}$. The relative damping coefficient was calculated as the damping coefficient divided by the cyclic frequency and was equal to $\delta_0 = 0.3$. The predicted distribution of the attracting specific forces is illustrated in Figure 6. The integrated attracting force is illustrated in Figure 7 as a function of the radius of the circular window of the coil.

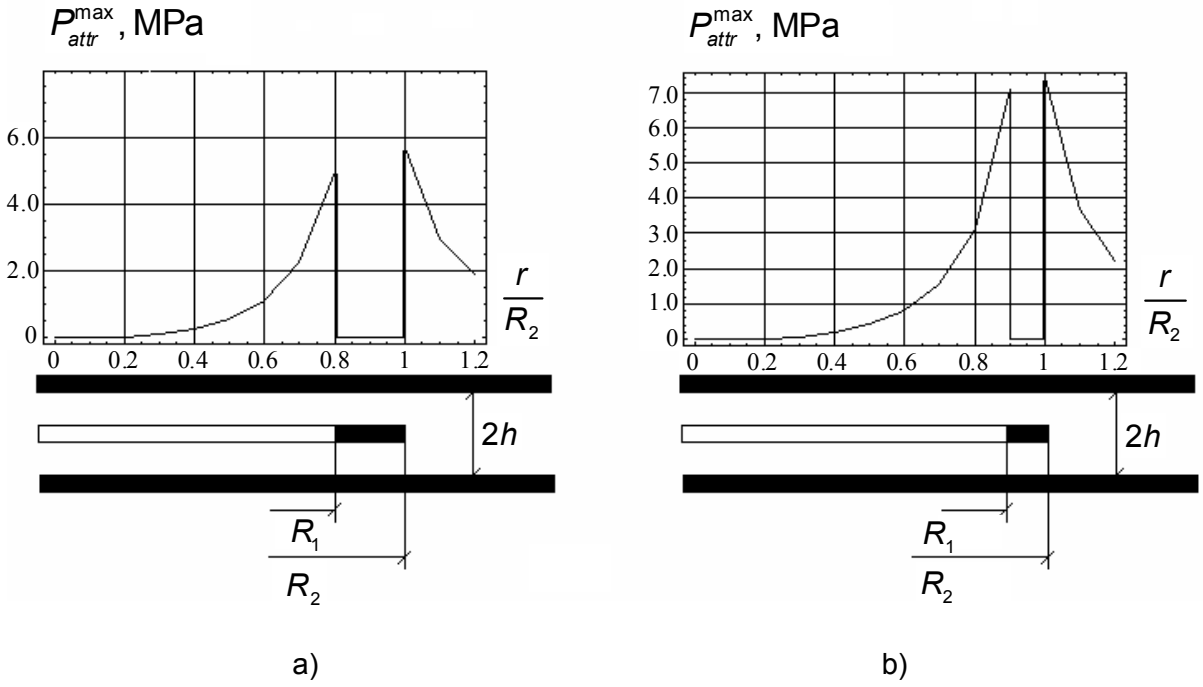

Figure 6: *The distribution of the density of attraction forces at the time moment when they have their maximum values for the following combinations of the dimensions of the inductor:*

a) $R_1 = 0.035\,\text{m}$, $R_2 = 1/0.8 \cdot R_1$; ***b)*** $R_1 = 0.035\,\text{m}$, $R_2 = 1/0.9 \cdot R_1$.

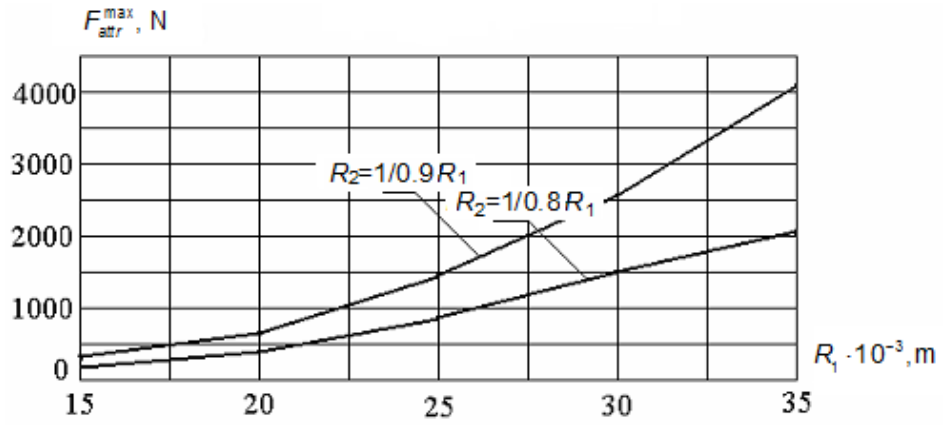

Figure 7: *The effect of the inner radius of the inductor on the attracting force between the screen and the blank*

The main results of this analysis can be formulated the following way: in the suggested ISAS, substantial amplitudes of the attraction forces are achievable: their densities can reach ~ 7.0.....8.0 MPa (Figure 6) and their integral values can reach ~ 4000 N (Figure 7) for the coil with 35 mm radius of the inner window.

3.2 Experimental validation

The laboratory version of the ISAS is shown in Figure 8a.

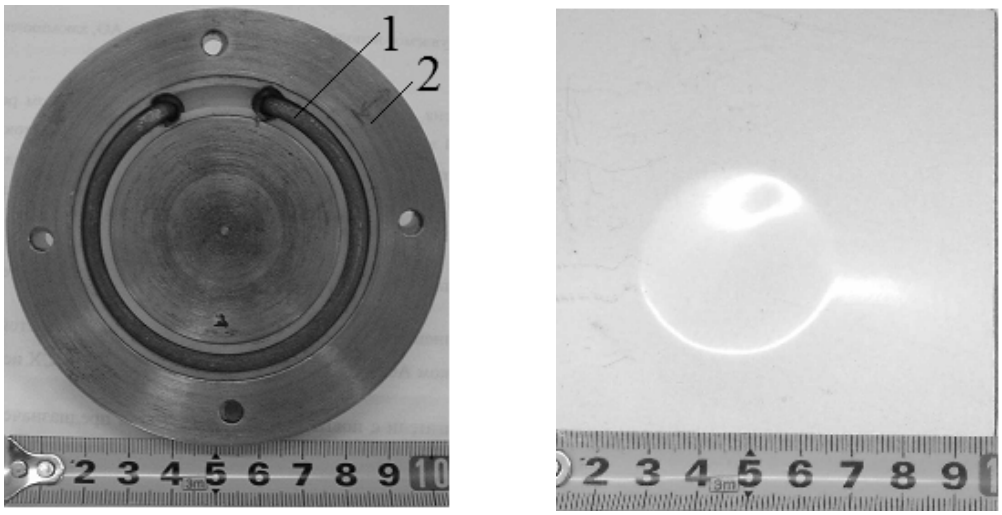

a) b)

Figure 8: The laboratory version of the ISAS (a, 1 – is the inductor, 2 – is the screen) and result of the EMF attraction of the part of the stainless steel sheet (b)

Structurally, the thin flat screen is fulfilled from 1mm sheet of stainless steel.

The material had the following properties: yield stress was 310 MPa; specific conductivity was $0.4 \cdot 10^7$ 1/Ohm·m. The sheet metal screen was rigidly mounted on a surface of a massive dielectric plate preventing deformation of the screen. A single-turn inductor with the inner diameter of 60mm was mounted on top of the screen and was covered by an insulating plate 1 mm thick. The blank was made from the same 1mm stainless steel sheet. The working zone of the investigated inductor system is the round opening with diameter 45 mm in the insulating plate on the inductor. The part of the sheet metal blank positioned against the opening in the insulating plate was expected to be deformed by the EMF attraction forces. The amplitude of the electric current running through the coil was J_m = 39.2 kA, and the frequency of the discharge was $f = 2\ kHz$. The relative damping coefficient was $\delta_0 = 0.3$. After eight discharges, the sheet metal blank was attracted into the inner opening of the working zone: the dent had a diameter of 40 mm and a the depth of 1mm formed on the surface of sheet metal blank (Figure 8b).

4 Conclusions

The conducted theoretical analysis and experiments confirmed the proposed concepts of the inductor systems for ferromagnetic and non-ferromagnetic blank materials. The tools for both versions of the EMF attraction require the low frequency discharge when repulsion caused by the Lorentz forces is negligible compared to the attraction forces.

References

[1] Psyk*, V.; Risch, D.; Kinsey, B.L.; Tekkayaa, A.E.; Kleiner, M.:* Electromagnetic forming – A review. Journal of Materials Processing Technology 211, 2011, p.787-829*.*

[2] *Batygin Y. V.; Golovashchenko S.F.; Gnatov A.V.*: Pulsed Electromagnetic Attraction of Sheet Metals – Fundamentals and Perspective Applications. Journal of Materials Processing Technologies. 213, 2013, p. 444-452.

[3] *Batygin Y. V.; Golovashchenko S.F.; Gnatov A.V.*: Pulsed Electromagnetic Attraction of non-magnetic Sheet Metals. Applications. Journal of Materials Processing Technologies. 214, 2014, p. 390-401.

SESSION 7

MODELING AND SIMULATION (FORMING)

Electrohydraulic Pressure Characterisation and Use in Fluid/Structure Coupled Simulations for Electro-Hydroforming Applications

J. Deroy[1], G. Avrillaud[1], J.P. Cuq-Lelandais[1], J.Fuzeau[1], G. Mazars[1]

[1] Bmax, 30 bd de Thibaud, 31104 Toulouse, France

Abstract

Electrical discharges in water have been produced with a modular electrohydraulic generator. The characterisation of the resulting pressure wave is of prime importance as it is to be applied on a blank during an electrohydraulic forming process. To improve the forming, the maximum generated pressure needs to be higher than the yield strength of the blank material to plastically shape it on a die. The momentum which will be used to put the blank in motion depends on these two quantities and also on the temporal shape of the pressure wave. The latter relates to its fall time only, in the case of shock wave, but also on its rise time in some cases where the pressure wave is not a shock. Those relevant quantities were simultaneously measured with multiple pressure sensors based on various physical principles and designs. We obtained the maximum pressure with the study of shockwave propagation via Schlieren imaging.

A comparison with an Electro-hydroforming case was performed to assess the validity of our measurements. This method involves the velocity measurement during the forming of a sheet. A LS-DYNA® simulation was performed with the incident pressure wave being the one measured by each pressure sensor.

We used the pressure signal of the chosen sensor as an input to simulate a 3D forming which was also compared with experiment. This characterisation provides a reliable determination of the pressure generated by an electrohydraulic forming system.

Keywords

Process, Hydro forming, Methodology

1 Introduction

Electro-hydroforming is based on the ultra-high-speed deformation of metal, up to 10^5 s^{-1} on impact with the die, using shockwaves in water. Optimisation of this process is rather difficult as it requires accurate dynamic pressure measurements among other things. In this study, we investigated the characteristics of shockwave generated in an Electro-hydroforming system. We used some techniques including the visualization of pressure wave propagation and the pressure measurement sensors to improve the design of discharge chambers using numerical simulations. These simulations are multiphysics as they couple electromagnetism with plasma physics, hydrodynamics, fluid structure interaction and thermal analysis.

2 Principles

This process has many industrial applications [1]. As water exhibits a very small compressibility, the rapidly expanding gaseous volume created, generates strong pressure waves. In liquid water, these pressure waves quickly evolve into shockwaves while propagating due to the inherent property of sound speed increase with pressure. The aforementioned gaseous volume is created by a dielectric breakdown of liquid water. This breakdown occurs when the water is submitted to a high electric field for a time which can typically be on the order of the hundred of nanoseconds [2] for supersonic breakdown with very strong electric field, on the order of several MV/cm, to hundred of microseconds in the case of subsonic breakdown [3] where a lower electric field is applied. As a result, a conductive plasma channel is formed and a quick release of electrical energy stored in a capacitive high pulsed power generator occurs. This induces the fast expansion of the plasma column which also vaporises the liquid water and form a gaseous bubble in the later stages of the expansion when all the electrical energy has been released. The different stages of the process are depicted in the following figure where one can see some images extracted from several movies recorded at Bmax during a previous investigation, in partnership with Institut P' - ENSMA.

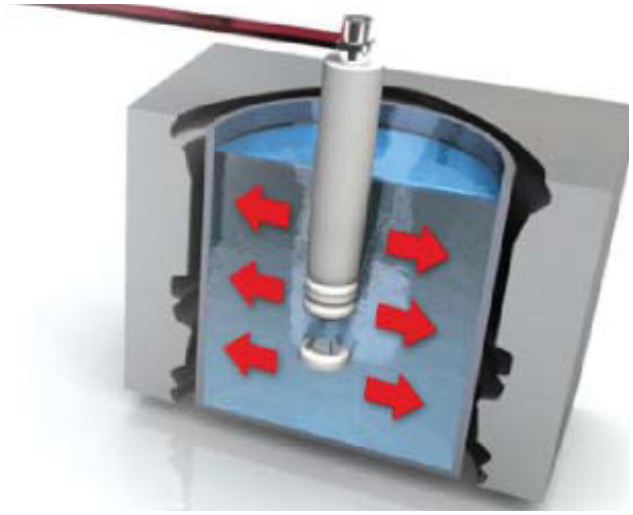

***Figure 1**: Electrohydraulic forming of a tube*

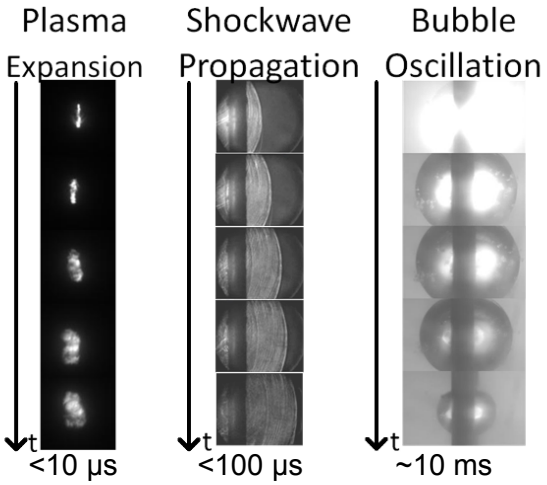

***Figure 2**: Visualisation of different stages of an electrohydraulic discharge*

3 Characterisation of the Pressure in a Electrohydraulic Forming System

3.1 On the importance of a Suitable Pressure Measurement Sensor

One of the main concerns for a thorough understanding of the electrohydraulic forming process is the ability to measure the pressure wave generated by a system. The actual waveform is to be used during two critical steps in the design of a full electrohydraulic system comprising a high pulsed power generator and a discharge chamber. On the one hand, for engineering purposes, the relation between a given high pulsed power generator configuration and the generated shockwave is to be known. On the other hand, for simulation purposes, the incident pressure wave is used as an input for the design of discharge chambers adapted to customer needs, such as the material of the blank or the level of details, e.g. dimensions and depth, on the final part. It is easily understood that requirement in electrical energy and pressure will differ when it comes to forming of a 40cm large oil-deflector for a helicopter [4] or a small casing for a USB memory stick, a case study which will be presented in section 3 of this paper.

3.2 Visualisation of Pressure Wave Propagation

The pressure wave generated by the electrical discharge in water modifies the density of water during its propagation, therefore changing its optical index as stated by the Gladstone-Dale law. Those changes in optical index were observed thanks to the Schlieren [5] technique. Depending on the measured propagation speed D, the maximum pressure can be obtained using an approximation of the Rankine-Hugoniot relationships, giving equation 1, where c_0 is the sound speed of water at rest and s is the shock Hugoniot slope and $D=c_0+su$, where u is the material speed.

$$P \approx \rho_0 \frac{D(D-c_0)}{s} \quad (1)$$

An example of pictures obtained in Schlieren configuration, see figure 3, is shown in figure 4.

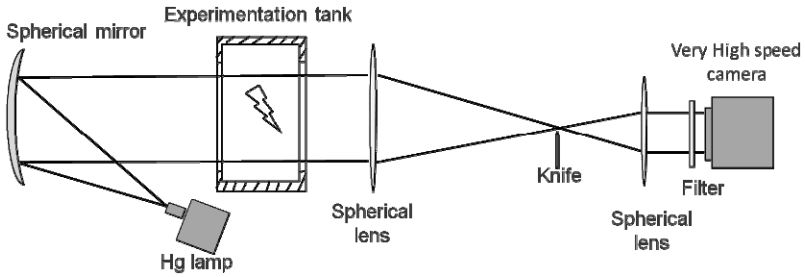

Figure 3: Optical arrangement of a Schlieren visualisation.

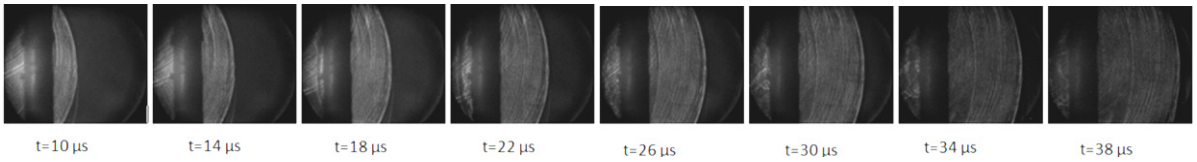

Figure 4: Pressure wave propagation with Schlieren configuration from figure 1.

This method allowed us to estimate pressure comprised between 228 bars and 1898 bars depending on the energy stored in the generator, at a distance of 8 to 15 cm. The main drawback of this method was the uncertainty, mostly due to the limited “spatial resolution/acquisition frequency” trade-off. Nevertheless, these pictures helped us to understand how the pressure wave interacted with surrounding objects, such as the structure of the pressure sensors we used, which was useful during the pressure sensors signals post processing.

3.3 Comparison of Available Pressure Sensors

The optical measurements are only able to provide us with a rough estimate of the maximum pressure but no quantitative information regarding the actual pressure waveform. Therefore, we used several pressure sensors placed at the same distance of the discharge to determine how they actually respond to a dynamic pressure wave. We compared a high frequency piezoelectric crystal sensor, coupled to a charge amplifier and an in-house pressure sensor (UDPS for Underwater Discharge Pressure Sensor).

As can be seen in figure 5, our UDPS exhibits a very short response time, showing a bandwidth of at least 5 megahertz and possess only a small overshoot at the maximum pressure. This maximum is approximately 150 bars. The piezoelectric sensor exhibits a completely different waveform. The rise time is longer, several microseconds and the overestimation in maximum pressure make this sensor unpractical for such measurements. This was expected as the manufacturer gives a resonant frequency of 400 kilohertz only for its sensor, which is well below what is needed to properly measure a shockwave. For this reason, it is of prime importance to ensure that each sensor possess a sufficient bandwidth if one is willing to use it to characterise a shockwave propagating in water. In some cases, the maximum pressure, the measured rise and fall time significantly

differs from reality and can lead to critical error, up to 100% in the peak pressure and 300% in energy [6]. Those errors in the prediction of shockwave characteristics could lead to design flaws for the electrical generator needed in the forming industry, which would be unacceptable. According to our experiments, a typical minimum acceptable bandwidth would be at least 5 MHz.

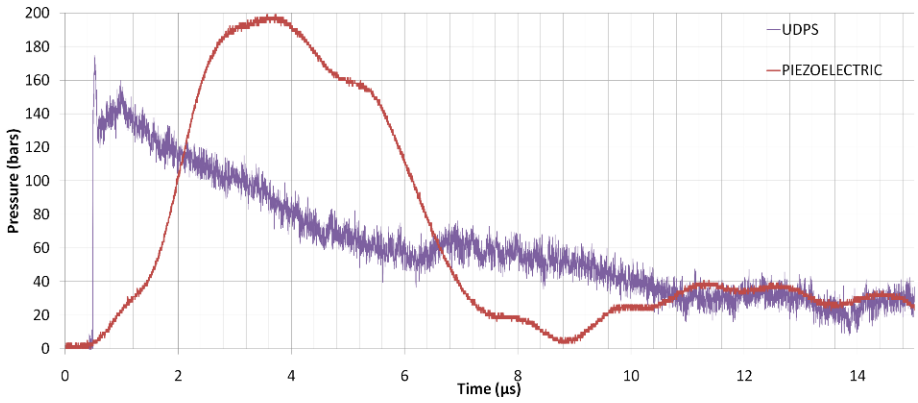

Figure 5: Comparison between the available pressure sensors

The two signals displayed in figure 5 were successively measured during a thin sheet forming test case. In addition, the velocity of the formed sheet was measured with a Photon Doppler Velocimetry (PDV) system to ensure reproducibility between shots. Using the measured velocity as a comparison, we performed a numerical simulation of this forming case with LS-DYNA using the two measured pressure as input. When using the piezoelectric pressure measurement, the predicted speed differed too much from the measured velocity in terms of rise time and maximum speed. In contrary, the velocity gotten using the UDPS pressure input was perfectly matching the experimental one. However, this was expected, since the pressure recording should have the form of a shockwave and display a sharp, sub-microsecond rise time and not a multi-microsecond one, as it is the case for the recorded piezoelectric signal. With this comparison between simulation and experiment, we demonstrated our capability to render the actual incident shockwave, in terms of rise time, maximum pressure and fall time, the three parameters of a shockwave that one needs to characterise the pressure generated in an Electro-Hydroforming system.

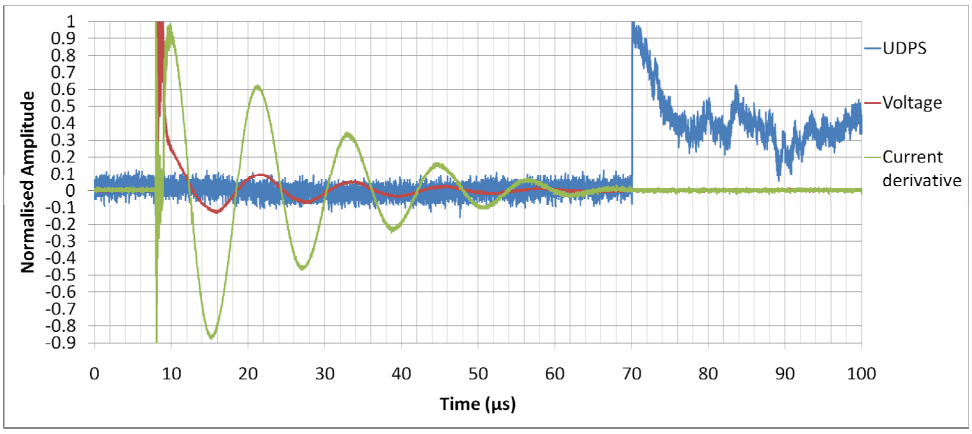

Figure 6: Fully instrumented electrohydraulic discharge recording

Figure 6 displays the current derivative, voltage and pressure measurement with our UDPS during an electrohydraulic discharge. This sensor shows no sensitivity to the electromagnetic field generated by the discharge, even at close distance from the discharge or when the discharge is not over, which would not be possible with a classic piezoelectric sensor.

With the capability to precisely measure the incident shockwave generated by an electrohydraulic system, we were able to assess the capability of a numerical model we developed to adequately describe the relation between the deposited electrical energy and the pressure generated in the water. We have implemented this model for internal use in 2D/3D electrohydraulic simulations. The model takes into account electrical and geometrical parameters, such as inductance, capacitance, charging voltage inter-electrode gap and ambient pressure.

4 Case Study: Electro-hydroforming of a USB Memory Stick

The objective of this case study, is to give an example showing how fluid / structure coupled simulations can predict the electro-hydroforming of a part and then can be helpful as well for the design of such parts as for the design of the tooling.

A pressure pulse is entering a cylindrical blank, generated by the discharge in water of the energy initially stored in a high voltage capacitor bank.

It is important to quantify how much the front wave and the reflected waves contribute in the forming of the part. We computed in figure 7 the momentum of the pressure entering the forming zone, obtained from the simulation of the setup.

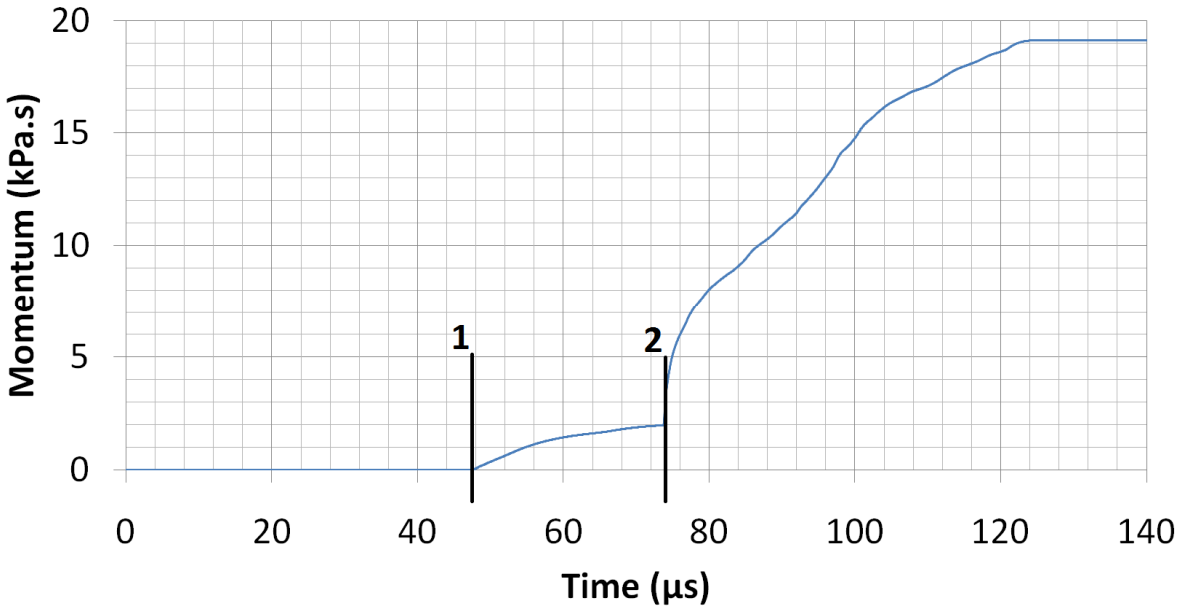

Figure 7: Momentum of the simulated pressure entering the forming zone. 1: time of arrival of incident pressure, 2: time of arrival of reflected waves

The simulated power deposition follows the measured one within 15%. It was observed that the simulated momentum of the incident pressure accounts for only 10% of the total momentum, the remaining being due to reflected waves. This clearly shows how important a proper design of the discharge chamber is in electro-hydroforming.

In those simulations, we modelled the forming of a previously deep-drawn blank made of 5657 and 1050 Aluminium (lighter gray shade separated by two lines in figure 8A and B). The first series of simulation used a blank with a round bottom. Given the desired shape of the formed part, our simulations predicted a tearing at the bottom due to a 48% thinning of the aluminium (see figure 8A.4, in the upper-left part of the corner). We then decided to use a blank with a flatter bottom and simulation showed improvement in the forming results as the part was formed with a reduced thinning of 38%, as can be seen in figure 8B.4 and 9, due to additional material coming radially while the caps end deforms.

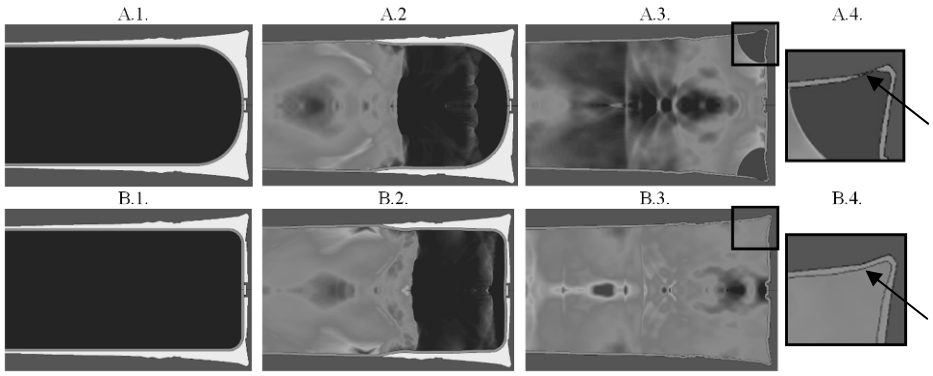

Figure 8: 2D-axisymmetric simulations of electrohydraulic forming for an initially round bottom (serie A) and an initially flat bottom (serie B)

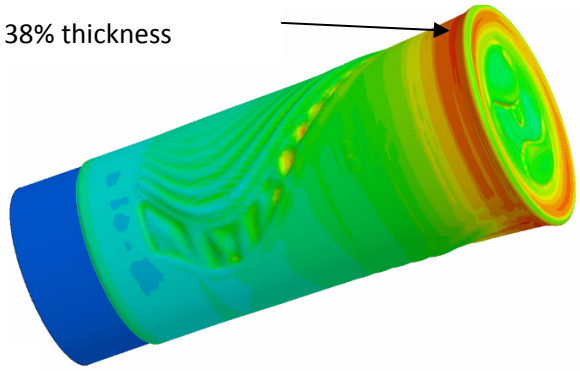

Figure 9: 3D simulation with the initially flat workpiece - contours of thickness reduction.

Independent tube expansions made in Bmax on Al5657 and Al1050 have shown that the formability at forming speed of interest on Al1050 (40%) was higher than Al5657 (35%). For information, the formability in static conditions for the Al1050 and Al5657 were respectively 25% and 20%. The constitutive parameters of both materials have been

determined and used in the simulations. The arising results show that Al5657 was predicted to tear apart in the necking region, in contrary to Al1050.

Experimental electrohydraulic forming tests have been carried out with both alloys. Al5657 has failed (figure 10-A), and this failure corresponds to the most critical region in the simulations. The forming of Al1050 was successful (figure 10-B), as this alloy could achieve higher strain levels. These results contribute to validate the multiphysical simulations, as well as the material characterization in terms of constitutive behavior and formability.

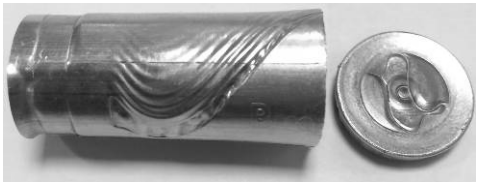

Figure 10-A*:* Experimental failure with the initially flat bottom – Al5657

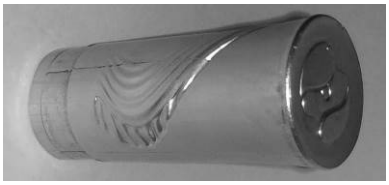

Figure 10-B*:* Experimental forming with the initially flat bottom – Al1050

5 Conclusion

We proposed an innovative method of ensuring the capability of various pressure sensors to adequately measure the characteristics of a shockwave generated by an electrohydraulic forming system using numerically simulated experimental results. The knowledge gained with those both actual and simulated experiments were then successfully applied to numerical simulations which accurately predicted the feasibility of a USB memory stick casing. These results showed that careful design and characterisation of pressure waves and material via simulation of an electrohydraulic system can lead to numerous interesting applications in the forming industry.

Acknowledgments

The authors would like to thank Institut P' for helping us by providing the cameras used to study our systems.

References

[1] « Electro-Hydraulic Forming | Bmax ». http://www.bmax.com/technology/electro-hydraulic-forming/
[2] L. K. Warne, R. E. Jorgenson, and J. M. Lehr, Resistance of a Water Spark. Citeseer, 2005.
[3] G. Touya, T. Reess, L. Pécastaing, A. Gibert, and P. Domens, « Development of subsonic electrical discharges in water and measurements of the associated pressure waves », J. Phys. Appl. Phys., vol. 39, no 24, p. 5236, déc. 2006.
[4] « EUROCOPTER Oil Deflector: when new technology maintains one's competitive advantage | Bmax ». http://www.bmax.com/case-studies/case-study-1/

[5] J-P Prenel and P Smigielski , « Techniques de l'ingenieur CND: methodes surfaciques », Editions T.I. af3332, 1999

[6] A. Grinenko, V. T. Gurovich, Y. E. Krasik, A. Sayapin, S. Efimov, and J. Felsteiner, « Analysis of shock wave measurements in water by a piezoelectric pressure probe », Rev. Sci. Instrum., vol. 75, no 1, p. 240‑244, déc. 2003.

FEM Study on Electromagnetic Formability of AZ31B Magnesium alloy

J. K. Doley*, S. D. Kore

[1)] Indian Institute of Technology, Guwahati, Assam, India.

* Corresponding author: E-mail address: j.doleyk@iitg.ac.in

Abstract

The formability of Mg alloy at room temperature is hindered by its microstructure and basal texture; because of it Mg alloy has to form at elevated temperature and at higher strain rate. As electromagnetic forming (EMF) is a high strain rate forming process in which a transient high frequency current is applied on a high electric conductive workpiece to obtain the required force to form the workpiece into a desired shape. In this paper FEM study is done to analyze the formability of AZ31B magnesium alloy at high strain rate and at elevated temperature. However as Mg alloy has poor electrical conductivity compared to aluminium alloy which is the desired metal for EMF process moreover electrical conductivity of a metal decreases with increasing temperature, hence aluminium driver will be used for better process efficiency. FEM simulation results is validated with the published experimental results and further warm forming simulation is done to study the effect of temperature at high strain rate forming process of AZ31B magnesium alloy by free dome height test.

Keywords

High speed forming, Electromagnetic forming, Warm forming

1 Introduction

Magnesium alloy is an excellent candidate for automotive white body construction because of its light weight characteristics and high strength to weight ratio [1], but due to its hexagonal close-packed structure and necessity of additional slip systems for normal homogenous deformation, magnesium alloys exhibit very low ductility room temperature [2, 3]. Which demerits its applicability, However, it shows excellent ductility and formability at elevated temperatures [1]. In fact AZ31B alloy sheet shows increased total elongation at temperature range between 200 to 400^0C on uni-axial tensile test [4].

The formability of AZ31B magnesium alloy at different strain rate from .001 to 1 S^{-1} at elevated temperatures has been test by (C. Bruni et. al.)[5] And found that the strain rate sensitivity coefficient increases with temperature rise meanwhile the strain hardening exponent increases with rising strain rate and reverse with increasing temperature. In addition to the increase in both ductility and flow stress at high strain rates [6, 7].

In this paper study will be done on the combined effect of high strain rate and high temperature on the forming process of AZ31B magnesium alloy simultaneously. The high strain rate condition will

be meet by the Electromagnetic forming technique which is a high velocity forming process and utilizes magnetic pulse forces to deform the workpiece. This pulse magnetic force is generated by an intense transient magnetic field between a current carrying copper coil tool and a conductive workpiece.

2 FEM Simulation

Commercial FEM software LS-DYNA EM module beta version has been used simulate the processes. The module develop an interface between a magnetic solver with mechanical solver and, helps in connecting a source electrical current into solid conductors and computes the corresponding magnetic field, electric field and induced current by solving the Maxwell equations in the eddy-current approximation [8]. For solid conductors the Maxwell equations are solved by using a Finite Element Method (FEM) and for the surrounding air Boundary Element Method (BEM) is used. At each node of the model the Lorentz force F is evaluated and added to the mechanical solver, once after computing electromagnetic fields by electromagnetic solver.

The temperature distribution in the workpiece during the electromagnetic forming process depends upon the heat exchange between the forming coil and the workpiece, the plastic deformation work, and Joule heating due to eddy currents induced in the workpiece. So, the major contribution to the temperature rise in the sheets is expected to come from impact pressure and heat dissipation due to eddy currents [9]. In our model, thermal properties considered are the thermal conductivity (k), the specific heat capacity (c_p), and the coefficient of thermal expansion (α) of the material. Now, in order to model the constitutive response of the material for a wide range of strain rates, the flow stress of the materials can be determined as a function of effective plastic strain, strain rate and temperature using the constitutive equation of Johnson-Cook. The John-Cook equation is:

$$\sigma = (A + B(\bar{\varepsilon})^n)\left(1 + C\, ln\dot{\varepsilon}_p\right)\left(1 - \left(\frac{T - T_{room}}{T_{melt} - T_{room}}\right)^m\right) \quad (1)$$

Where, $\bar{\varepsilon}$ =equivalent plastic strain,

$\dot{\varepsilon}_p$= plastic strain-rate for $\dot{\varepsilon}_0$= 1.0/s and,

The expression in the first set of brackets gives the stress as a function of strain for $\dot{\varepsilon}_p$ = 1.0 and T^*=0. The expressions in the second and third set of brackets represent the effects of strain rate and temperature, respectively. The equivalent flow stress σ is the product of three factors representing strain hardening, strain rate and temperature. Thus to describe the material behaviour the values of the constants A, B, C, n and m were required.

The formability of AZ31B magnesium alloy with and without an Aluminium driver sheet in a Electromagnetic pulse forming process was investigated experimentally by Jun Rui Xu *et al.* [10], so first simulated results will be validated with the experimental results of the mentioned paper. Meshed assembly of the coil, worksheets, driver sheet and die for simulation corresponding to the data given by Jun Rui Xu *et al.* [10] has been show in fig 1. As magnesium alloy has poor electrical conductivity, so, to maintain the energy efficiency of the EMF process, Aluminium driver disk is used for better limit dome height [10].

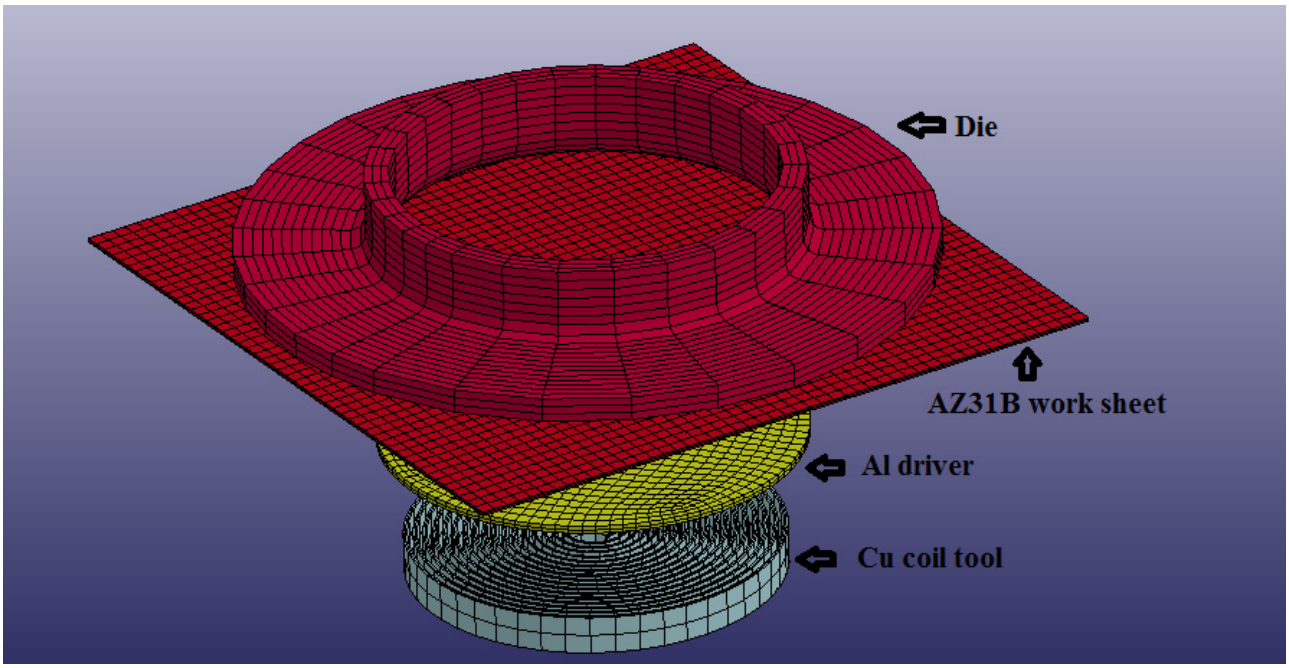

Figure 1: Exploded view of the meshed assembly.

The total numbers of elements after meshing is 9458 including the no. of shell elements taken for the die to save computational time. The material properties of Aluminium driver and Magnesium alloy worksheet used for experiment are summarised in table no.1and no. 2 respectively.

Material	**Diameter (mm)**	**Thickness (mm)**	**Yield strength (MPa)**	**Ultimate tensile strength(MPa)**	**Resistivity (Ω m)**	**Density (Kg/m^3)**
Al 5052	94	2	90	199	2.17×10^{-8}	2.7×10^3

Table 1: *Material properties of Al Driver [10].*

Materials	**Yield strength (MPa)**	**Ultimate tensile strength (MPa)**	**Elasticity modulus (GPa)**
AZ31B	172	244	34

Table 2: *Material properties of Magnesium work piece [10].*

Materials	A	B	n	C	T_m	m
Al 5052	167 MPa	596 MPa	.551	.001	620^0C	1.34
AZ31B	224 MPa	380 MPa	.761	.012	466^0C	1.554

Table 3: *Values of Johnson-Cook material parameters.*

3 The results

By varying the discharge energy with the help of changing input voltage while keeping the capacitance constant at 1152 μF, [10], different dome height is obtained for the workpiece. The result of the free-bulged forming with an aluminium driver sheet at C = 1152 μF is shown in fig 2, which shows significant increase in the dome heights with the increase in the energy. Due to the inertia effect of the aluminium sheet which experience much higher magnetic pressure against the coil then with the magnesium alloy, the magnesium alloy sheet receive a high velocity impact causing it deform at high strain rate. So, greater the energy, greater will be the magnetic force, in turn more impact force on the magnesium sheet.

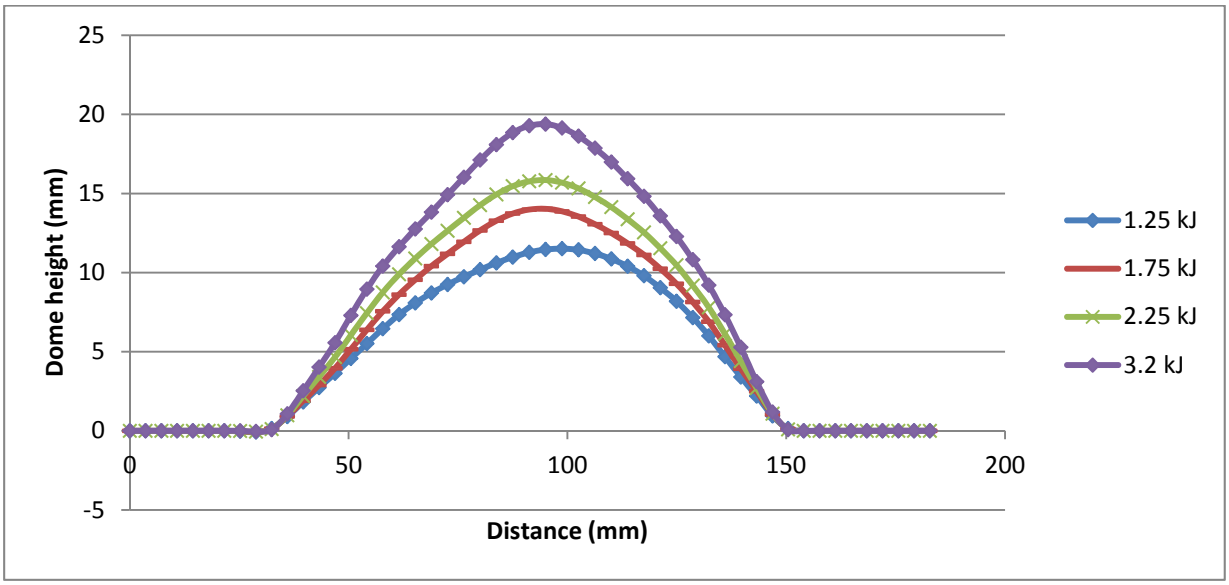

Figure 2: Dome heights at different energies with C=1152 μF.

The value obtained from the simulation results (figure 3) shows slightly above the experimental results given by Rui Xu *et al.* [10]. But at higher energy range the deviation of the simulation result from the experiment got minimized as at these range of energies the effect of voltage is more significant than other factors like resistance and inductance.

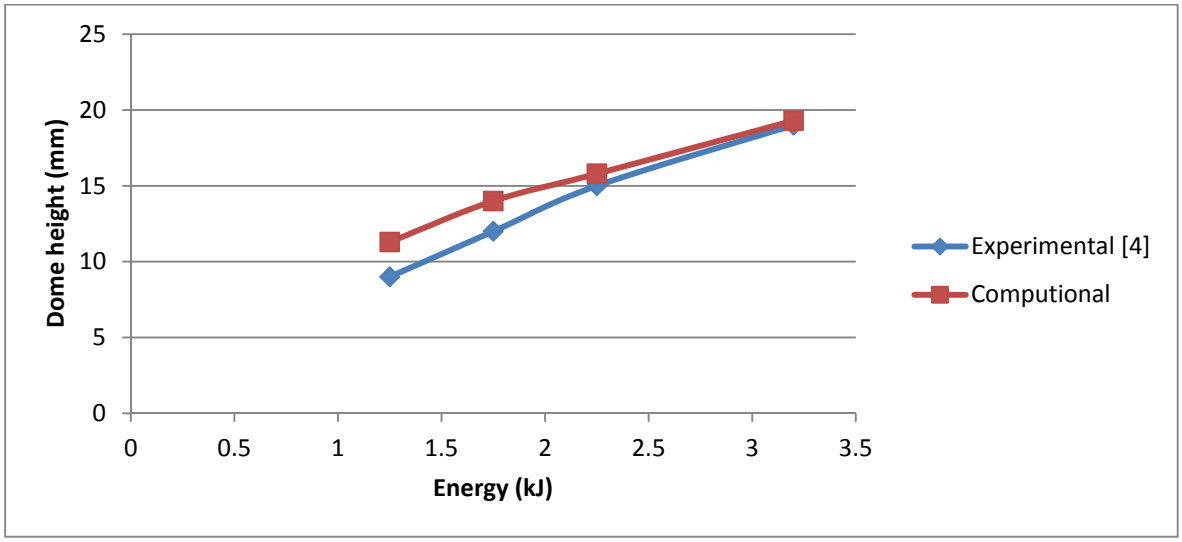

Figure 3: Comparison of experimental and simulation results.

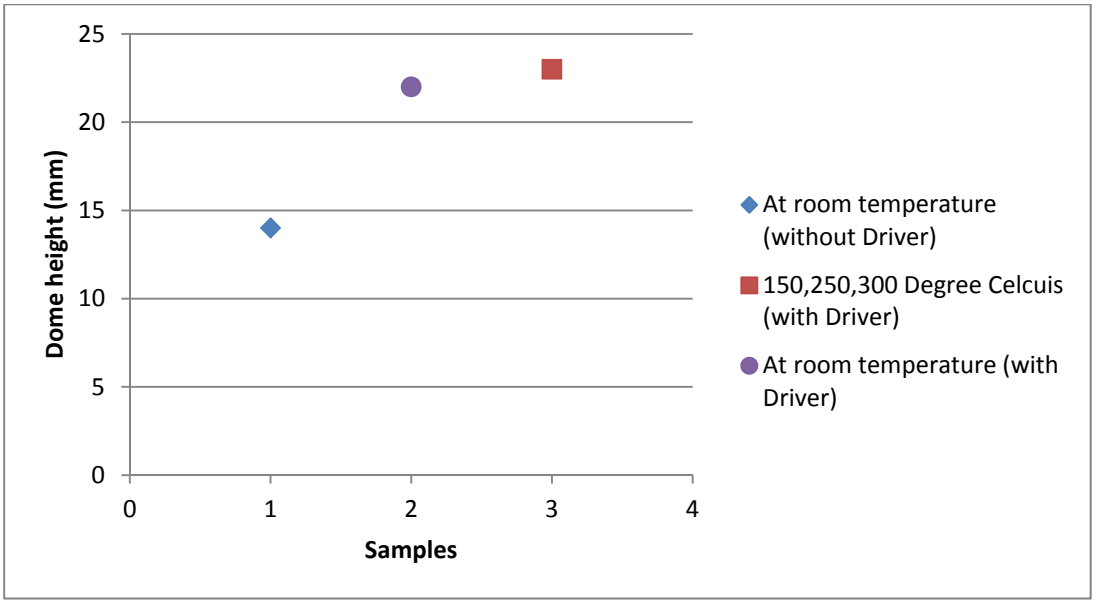

Figure 4: Dome heights at different temperature and at driver usage conditions at energy equal to 4.3 kJ.

Experimentally at room temperature the bulging height of magnesium alloy is 14 mm without the use of aluminium alloy driver sheet Rui Xu *et al.* [10], while the simulation results obtained for magnesium alloy with the use of aluminium alloy driver sheet at room and at high temperature of 250^0C are 23 mm and 30 mm respectively. The combined effect of high strain rate and high temperature shown by (figure 4) i.e. with the use of Aluminium driver at high temperature shows little effect in the final deformation. It has been experimentally found by Rui Xu *et al.* [10] from limit dome heights (LDH) test that formability of magnesium alloy increases with the use of aluminium alloy driver sheet. Because the intensity of magnetic flux density between aluminium driver sheet and the coil is larger than that between magnesium alloy sheet and the coil. The dome height at room temperature and at elevated temperature both with the application of Al drivers shows similar

results which agree well with the findings obtained by Hasenpouth [11], which state that the temperature influence on the high strain rate deformation of AZ31B magnesium alloy sheets is insignificant.

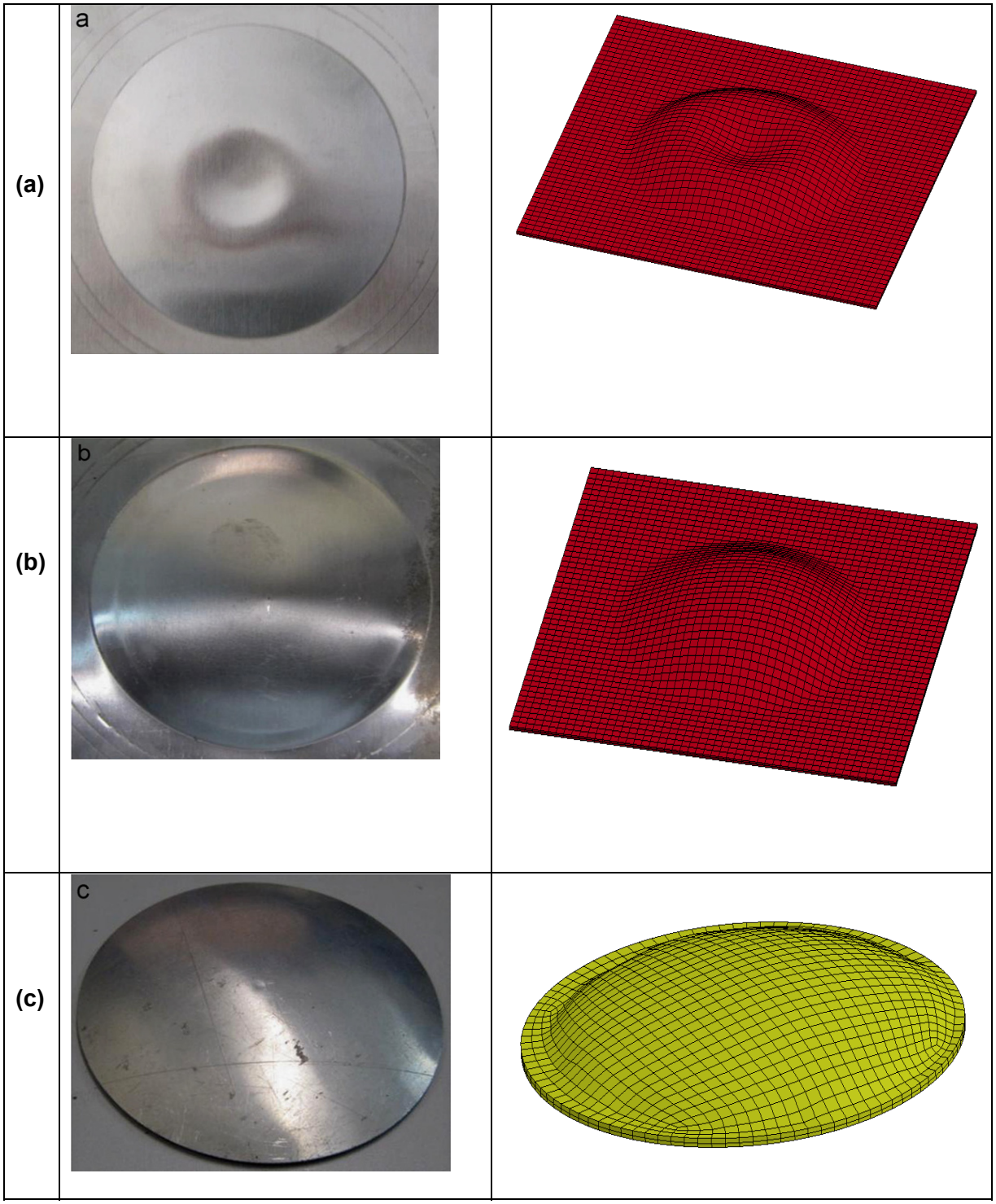

Figure 5: Experimental [10] and simulation parts with and without driver sheet at C=1152μF/V=1.5kV: (a) Without driver sheet (b) With Al driver (c) Formed driver sheet.

Without the application of Al driver sheet, a valley is created at the centre of the formed part (Figure 5(a)) which is then bulge out into a dome shape with the help of the Al driver sheet (Figure 5 (b)). The final formed driver sheet is shown in Figure 5 (c).

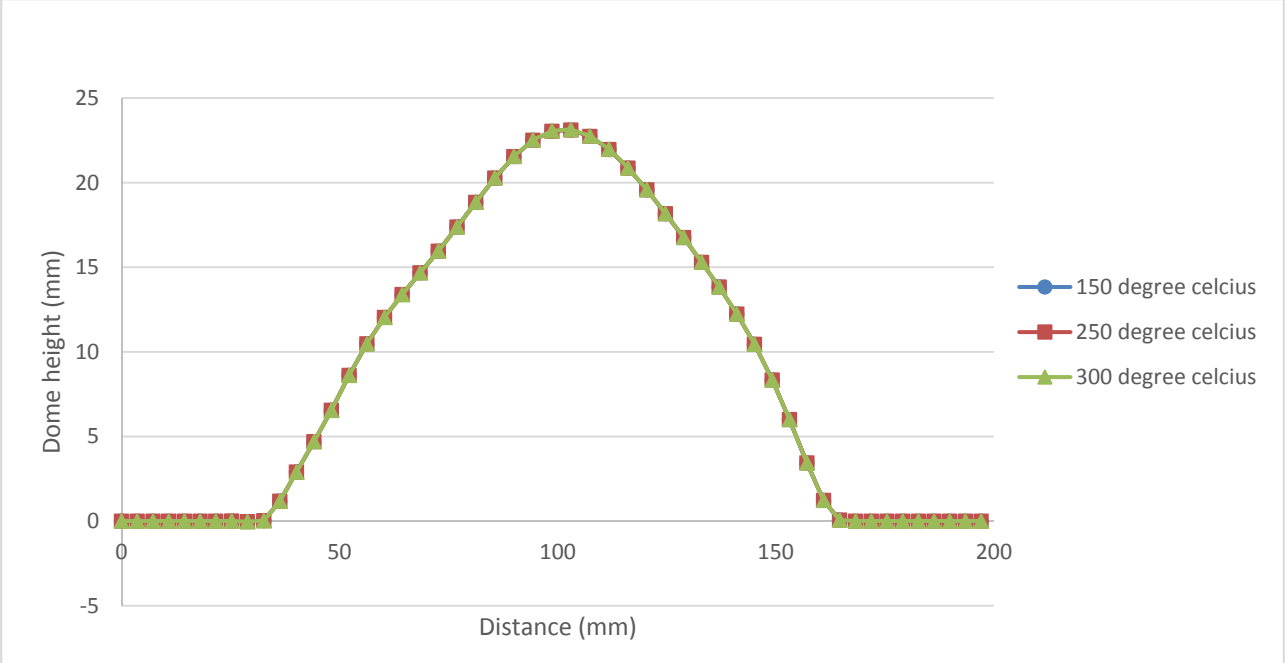

Figure 6: Dome height at different elevated temperature (V=2.8kJ).

At elevated temperature with the application of Al driver sheet the magnesium alloy shows similar dome height behaviour (Figure 6) as conductivity of the magnesium alloy material is overcame by the inertia effect of the driver.

4 conclusions

Simulations has been done for high strain rate electromagnetic forming process using magnesium alloys as work sheets and round aluminium sheet as driver. The simulation results agree with results of the published literature [10]. And further simulation has been done at high temperature using aluminium driver to study the effect of inertia at high temperature on the deformation of the workpiece. Results indicate that there is minimal influence of temperature on the high strain rate deformation of AZ31B magnesium alloy sheets as stated by Hasenpouth [11] and shown by warm forming of AZ31B Mg alloy at 150^0C, 250^0C and 300^0C by using Al driver.

References

[1]. Kleiner, M., Geiger, M., Klaus, A., 2003. Manufacturing of Lightweight Components by Metal Forming. In: CIRP Annals 2003, vol. 52, no. 2, Montreal, Canada, pp. 521–542.

[2]. Doege, E., Dr¨ oder, K., 2001. Sheet Metal Forming of Magnesiumwrought Alloys-Formability and Process Technology. J. Mater.Process. Technol. 115, 14–19.
[3]. Takuda, H., Morishita, T., Kinoshita, T., Shirakawa, N., 2005. Modelling of Formula for Flow Stress of a Magnesium Alloy AZ31 Sheet at Elevated Temperatures. Journal of Materials Processing Technology. 164–165, 1258–1262.
[4]. *Y.S. Lee, Y.N. Kwon, S.H. Kang, S.W. Kim, J.H. Lee,* Forming Limit of AZ31 Alloy Sheet and Strain Rate on Warm Sheet Metal Forming, Journal of Materials Processing Technology 2 0 1 (2 0 0 8) 431–435.
[5]. C. Bruni, A. Forcellese, F. Gabrielli, M. Simoncini, Effect of Temperature, Strain Rate and Fibre Orientation on the Plastic Flow Behaviour and Formability of AZ31 Magnesium Alloy, Journal of Materials Processing Technology 210 (2010) 1354–1363
[6]. I. Ulacia, J. Imbert, C.P. Salisbury, A. Arroyo, I. Hurtado1, M.J. Worswick, Electromagnetic Forming of AZ31B Magnesium Alloy Sheet: Experimental Work and Numerical Simulation, 3rd International Conference on High Speed Forming – 2008
[7]. I. Ulaciaa, C.P. Salisburyb, I. Hurtadoa, M.J. Worswickb, Tensile Characterization and Constitutive Modeling of AZ31B Magnesium Alloy Sheet over Wide Range of Strain Rates and Temperatures, Journal of Materials Processing Technology 211 (2011) 830–839.
[8]. L'Eplattenier, P.; Cook, G.; Ashcraft, C.; Burger, M.; Shapiro, A.; Daehn, G. S.; and. Seth M.: "Introduction of an Electromagnetism Module in LS-DYNA for Coupled Mechanical-Thermal Electromagnetic Simulations, 9th LS-DYNA Users Conference, Dearborn, Michigan, June 2005.
[9]. Johnson, G., Cook, W., 1983. A Constitutive Model and Data for Metals Subjected to Large Strains, High Strain Rates and High Temperatures. In: Proc. 7th International Symposium On Ballistics, pp. 541–547.
[10]. Jun Rui Xu, Hai Ping Yu, Jun Jia Cui, Chun Feng Li, Formability of AZ31 Magnesium Alloy Sheets During Magnetic Pulse Bulging, Materials Science and Engineering, A 569 (2013),pp. 150–158.
[11]. D. Hasenpouth, Ph.D. Dissertation, University of Waterloo, Ontario, Waterloo, 2010.
[12]. S.D. Kore, P. Dhanesh, S.V. Kulkarni, P.P Date, 2010. Numerical Modelling of Electromagnetic Welding. International Journal of Applied Electromagnetics and Mechanics 32, 1–19, doi:10.3233/JAE-2010-1062.
[13]. J.K Doley, S.D Kore, Fully Coupled Numerical Simulation of Electromagnetic Forming, ESAFORM 2012, *Key Engineering Materials Vols. 504-506 (2012) pp 1201-1206.*

Optimization of Combined Deep Drawing and Electromagnetic Corner Fill Process of DP980 Steel Sheet [*]

M. K. Choi [1], H. Huh [1], N. Park [1], C. G. Jung [2], J. Nam [2]

[1] School of Mechanical, Aerospace and Systems Engineering, KAIST, Daejeon, Korea
[2] Metal Forming Research Group, POSCO, Incheon, Korea

Abstract

DP980 steel sheet is one of advanced high strength steel sheets (AHSS) introduced in order to achieve both enhanced crashworthiness and lightweight design of auto-body. Due to its comparatively poor formability, the application of DP980 steel sheet to auto-body is limited with conventional deep drawing processes. One of remedies is a combined deep drawing and electromagnetic sheet metal forming process, which is one of the innovative forming methods to improve the formability. The process chosen in this paper consists of square cup drawing of DP980 1.2t steel sheet with punch radius of 30 mm firstly and electromagnetic corner fill process to reduce the radius to 10 mm.
This paper proposes an approach for numerical optimization of combined deep drawing and electromagnetic corner fill process of DP980 steel sheet. The numerical optimization was conducted by following procedures of optimization of electromagnetic forming force and coil design. Conventional square cup drawing analysis was conducted first and the target function and constraint function were established to minimize the deviation from an ideal shape without violating forming limits for optimization of the EMF force. Then, coil design was carried out for small loss of electrical power transmission. Numerical results and conclusions are demonstrated for the applicability of this combined forming process.

Keywords

Deep drawing, Electromagnetic, Numerical optimization

---

[*] *This work is based on the results of the POSCO research project; the authors would like to thank POSCO for its financial support.*

1 Introduction

Auto industries recently make efforts to develop lightweight vehicles with improvement of crashworthiness of auto-body. Advanced high strength steels (AHSS) have been introduced in order to achieve both enhanced crashworthiness and lightweight design of auto-body. DP980 steel, one of AHSS materials, is a high strength steel with a micro-structure of a soft ferrite matrix containing islands of martensite as the secondary phase. Due to its comparatively poor formability, the application of DP980 steel sheet to auto-body is limited with conventional deep drawing processes.

Electromagnetic forming (EMF) is one of the innovative forming methods to improve the formability. EMF is a high-speed forming process that uses pulsed magnetic fields to apply induced forces by a transient high frequency current. EMF can be combined with conventional deep drawing to make a sharp corner radius of a workpiece that cannot be obtained by conventional deep drawing. Regarding the combined deep drawing and electromagnetic corner fill process, many researchers carried out experimental and numerical study over the last years. Psyk et al. [1] studied integration of electromagnetic calibration into the deep drawing process to sharpen edge corner and Imbert and Worswick [2] showed that hybrid conventional/EM forming process using a specially designed coil could be successful in forming features in aluminium alloy sheet parts. Taebi et al. [3] developed a method for the computer aided design of process chains consisting of quasi-static and EMF in order to increase the classical quasi-static forming limits.

However, most of research works about the process are only limited to the application of aluminium alloys. Generally, electromagnetic forming is suitable for materials with a high electrical conductivity and low flow stress in order to achieve small loss of electrical power transmission. The application of DP980 steel sheet to electromagnetic forming is more difficult than other high conductive materials since DP980 steel has low electrical conductivity and very high flow stress. Therefore, it is necessary to optimize the combined deep drawing and electromagnetic corner fill process for the application of DP980 steel sheet.

The objective of this paper is to propose the optimization of EM forming force and coil design in the process without violating forming limits and with small loss of electrical power transmission. This approach requires adequate process parameters so that a desired shape is formed as close as possible. Numerical simulations were conducted to optimize the process with a commercial code LS-dyna and related experiments were carried out for the mechanical properties and FLD of the material. Conventional square cup drawing analysis was carried out first, and then the optimization procedures were conducted to set up the target function and constraint function to minimize the deviation from an ideal shape without violating forming limits for optimization of the EMF force. Based on the required EMF force obtained from the previous optimization, coil design was conducted for small loss of electrical power transmission as a noble proposal. Numerical results with optimization demonstrate the possibility of application this combined forming process to practical forming of DP980 for auto-body members.

2 Procedures for numerical optimization of the process

Numerical simulation of the process is regarded as multistep analysis which consists of pre-forming analysis and EMF coupled analysis using the deformed sheet in the pre-forming analysis. Since there are many process parameters of EMF system, optimization of process parameters of the EMF system directly is rather time-consuming. Hence, numerical optimization carried out in this paper follows the systematic procedures explained in Figure 1 (a). According to the flow chart, a conventional pre-forming analysis is followed by optimization for EM corner fill forming force, and then the EM tool coil is designed.

2.1 Optimization for EM corner fill forming force

Process parameters of the EMF force were optimized since the amount of sharpening of corner radius can be different with applied forming force. To solve the optimization problem, an objective function is setup to minimize the deviation from an ideal shape without violating forming limits. The process parameters should be carefully chosen and a design of experiment (DOE) method is used to reduce the number of simulations. Optimization of the resultant forming force to sharpen the corner radius is conducted using response surface method (RSM) with selected process parameters. The objective function was approximated by a regression equation to seek for optimum process parameters. Figure 1 (b) shows schematic diagram of the optimization procedures of the forming force.

2.2 Design of the EM tooling

To realize the optimized forming force with small loss of energy transition, EM tool coil was designed. Coil design is one of the most important problems in EM forming since tool coil delivers the energy to the corner filling area to be formed. Tool coil is integrated in the punch of the square cup drawing. This design process is carried out with dimensional analysis.

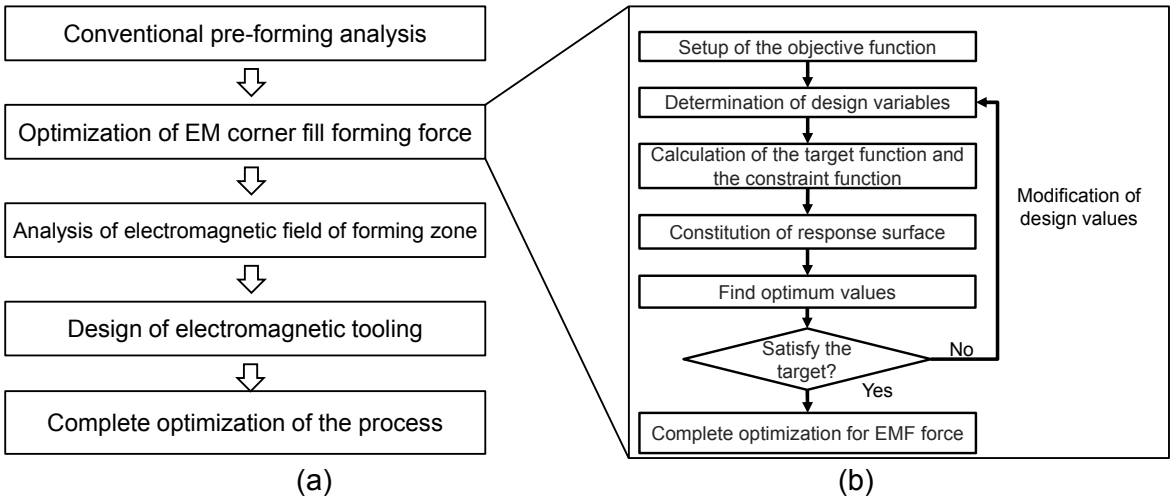

Figure 1: *(a) Optimization procedures of the process; (b) schematic diagram of the optimization procedures of the forming force*

3 Conventional square cup drawing analysis

FE analysis of conventional square cup drawing using a commercial code LS-Dyna is conducted as pre-forming analysis. Attempts are made to form the sheet with punch radius of 10 mm and 30 mm to check whether pre-forming is successful. The mechanical properties of DP980 1.2t steel sheet are obtained experimentally and strain paths of the material during pre-forming process are compared to predict the onset of fracture.

3.1 Mechanical properties of DP980 1.2t steel sheet

During combined deep drawing and electromagnetic corner fill process, a workpiece material exhibits high strain rates in the range of 10000 s^{-1} [4]. Therefore, strain rate effect on tensile properties of DP980 steel sheet is required to characterize the material behaviour. Uniaxial tensile tests were conducted at strain rates ranging from 0.001 s^{-1} to 100 s^{-1}. All conducted tensile tests were followed test procedures proposed by Huh et al. [5] to measure stress and strain with low uncertainties. For input data of numerical simulation of electromagnetic corner fill process, stress-strain relations with high strain rates in the range of 10000 s^{-1} could be obtained by extrapolating a strain rate dependent constitutive equation proposed by Huh et al. [6]. Lim−Huh model is a novel dynamic hardening model which is newly proposed to accurately express the change in the strain hardening with the change in the strain rate. The equation for Lim−Huh model is expressed as below:

$$\sigma(\varepsilon,\dot{\varepsilon}) = \sigma_r(\varepsilon)\cdot\frac{1+q(\varepsilon)\cdot\dot{\varepsilon}^{\,m}}{1+q(\varepsilon)\cdot\dot{\varepsilon}_r^{\,m}} \quad \text{where} \quad \sigma_r(\varepsilon) = K(\varepsilon+\varepsilon_0)^n, \quad q(\varepsilon) = \frac{q_1}{(\varepsilon+q_2)^{q_3}}$$

where $\dot{\varepsilon}_0 = 0.001\,s^{-1}$ is the reference strain rate. The material parameters K, ε_0, n are determined by the flow stress at the reference strain rate and the parameter q and m show strain rate sensitivity as functions of strain. Figure 2 (a) shows uniaxial tensile test results and Figure 2 (b) shows deviations of flow stress of Lim−Huh model from the measured data. Extrapolated data from Lim−Huh model could be used as input data of numerical simulations.

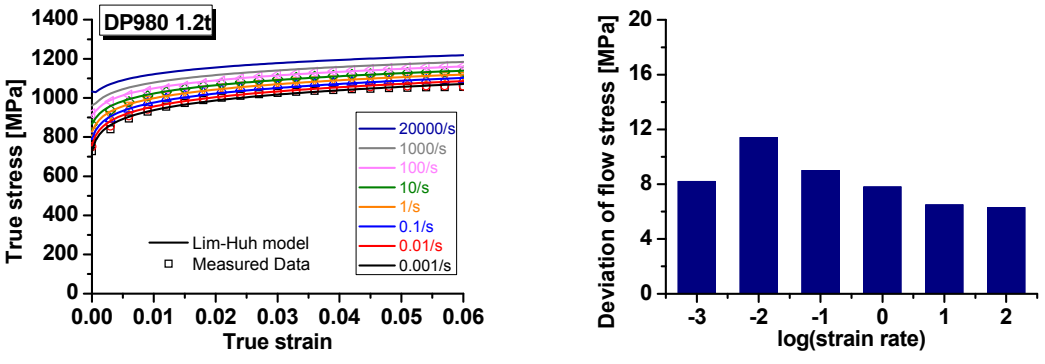

Figure 2: *Tensile test results of DP980 steel sheet (a) true stress-true strain measured data and Lim−Huh model fitted curve (b) deviation of flow stress of Lim−Huh model*

Consideration of fracture forming limits of the sheet is necessary to predict whether onset of fracture is observed during the process in the numerical optimization. Recently, Park et al. [7] have constructed a fracture forming limit diagram of DP980 steel sheet with fracture strains experimentally obtained at various loading paths. However, the fracture forming limit diagram is not able to account for the change of loading path during the process and the fracture forming limit diagram is not suitable to predict the onset of fracture during the process. Stoughton et al. [8] proposed a new strain-based forming limit criterion based on a polar diagram of the effective plastic strain with the direction defined by the arctangent of the ratio of the current plastic strain rates. This diagram is referred as the PEPS diagram in reference to its polar nature and its radial variable defined by the effective plastic strain, and has advantages that there is no dependence on the change of loading path and the stress-strain relation. Strain paths in major and minor strain space can be transformed to fracture based PEPS diagram by calculating the strain path as a function of θ and its corresponding equivalent plastic strain using the equation given below.

$$\bar{\varepsilon}_{pn} = \frac{1+r}{\sqrt{1+2r}} \sum_{i=1}^{n} \sqrt{\left(\Delta\varepsilon_{1i}\right)^2 + \left(\Delta\varepsilon_{2i}\right)^2 + \frac{2r}{1+r}\left(\Delta\varepsilon_{1i}\right)\left(\Delta\varepsilon_{2i}\right)}$$

$$\theta_n = \tan^{-1}\left(\frac{\Delta\varepsilon_{2n}}{\Delta\varepsilon_{1n}}\right) \Rightarrow \left(x_n, y_n\right) = \left(\bar{\varepsilon}_{pn}\sin\left(\theta_n\right), \bar{\varepsilon}_{pn}\cos\left(\theta_n\right)\right)$$

In this paper, a fracture based PEPS diagram is used as a fracture criterion to predict the onset of fracture during the process in the numerical simulation.

3.2 Finite element model and analysis condition

The stamping tool used for the pre-forming consists of a punch, die and blank holder. Figure 3 (a) shows an assembly of finite element models and figure 3 (b) shows dimensions of each part. The punch, die and holder are modelled with shell elements and treated as rigid surface.

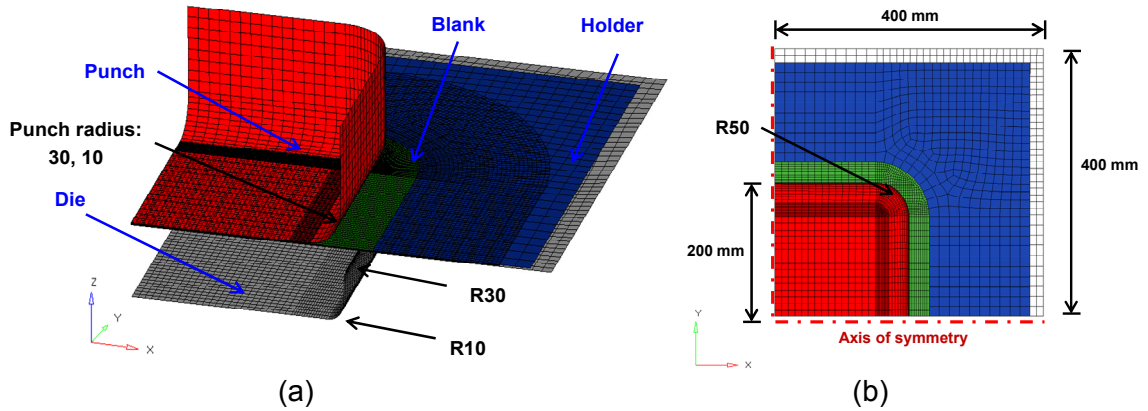

Figure 3. *Finite element model for pre-forming analysis: (a) assembly of finite element models; (b) dimension of each part*

The blank is modelled with 73325 8-node reduced integration solid elements with five elements along the through thickness direction since a solid element is required for EM coupled analysis. The stroke is set to 60 mm due to low formability of the material and the blank holding force given to the blank is 400 kN. The punch moves with 100 mm/s and friction coefficient of each contact surface is set to 0.1.

3.3 Analysis results

Strain paths of the material after the square cup drawing analysis with a punch radius of 30 and 10 mm are compared to predict the onset of fracture. Figures 4 (a), (b) show strain paths of 3 points at the punch corner, sidewall and die corner during the pre-forming in a fracture based polar EPS diagram. In this paper, it is determined that the onset of fracture is observed when any strain paths of a material exceed the fracture based polar EPS diagram of the material.

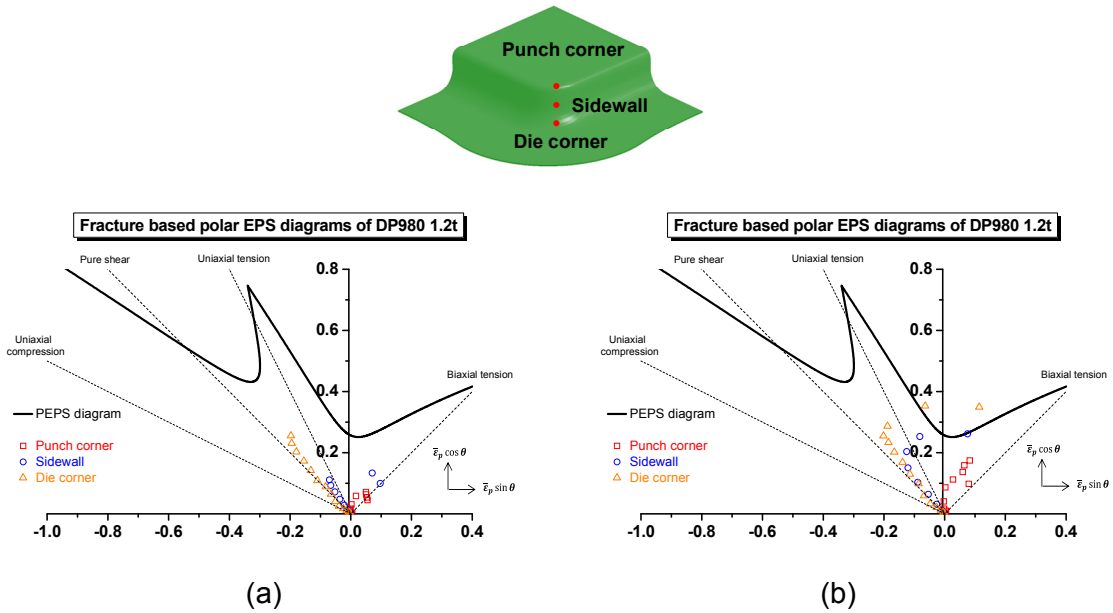

(a) (b)

Figure 4. *Strain paths during the square cup drawing analysis in fracture based PEPS diagram of: (a) punch radius 30 mm; (b) punch radius 10 mm*

The simulation results show that all strain paths are under the PEPS diagram of the material in the case of a punch radius of 30 mm, which leads a conclusion that square cup drawing with punch radius of 30 mm is safe. On the other hand, the simulation results show that strain paths of the die corner and sidewall exceed the PEPS diagram of the material, which leads a conclusion that the onset of fracture is observed in the case of a punch radius of 10 mm. According to this analysis results, it is noted that the radius of 10 mm cannot be obtained with the conventional forming and an electromagnetic corner fill process is necessary to obtain the sharp radius of 10 mm in square cup forming by enhancing formability of the material.

4 Numerical optimization of the EM corner fill forming force

4.1 Determination of design variables

Numerical optimization of the EM corner fill forming force is carried out using numerical simulation of corner fill process by imposing forming force to a workpiece directly. Calibration zone where EM corner fill forming force is applied is indicated in figure 5 (a) and a forming force is imposed on the force imposed plane directly. To represent an imposed forming force as the Lorentz force electromagnetically induced as closely as possible, the damping factor and frequency are considered to assume that it is similar to the system current. Distribution of the imposed forming force on the force imposed plane is assumed to be non-uniform, but the force profile is a convex shape as well.
Process parameters to be optimized are selected as the total forming force, the angle of distributed area (θ_a) and the position of the force imposed plane (θ_p) which are defined in Figure 5 (b). The total forming force determines how much corner filling is achieved. Due to different stress state of the pre-formed workpiece at the calibration zone, the angle of distributed area (θ_a) and the position of the force imposed plane (θ_p) have influence on the final deformed shape and the formability of the material. Initial ranges of design values for each process parameter are shown below and 3 levels of process parameters are considered. Design values are updated during iterations of the optimization process.

Initial ranges of design values

- total forming force F: 1.8 MN < F < 2.2 MN
- angle of distributed area θ_a: 20 ° < θ_a < 40 °
- position of force imposed plane θ_p: 30 °< θ_p < 60 °

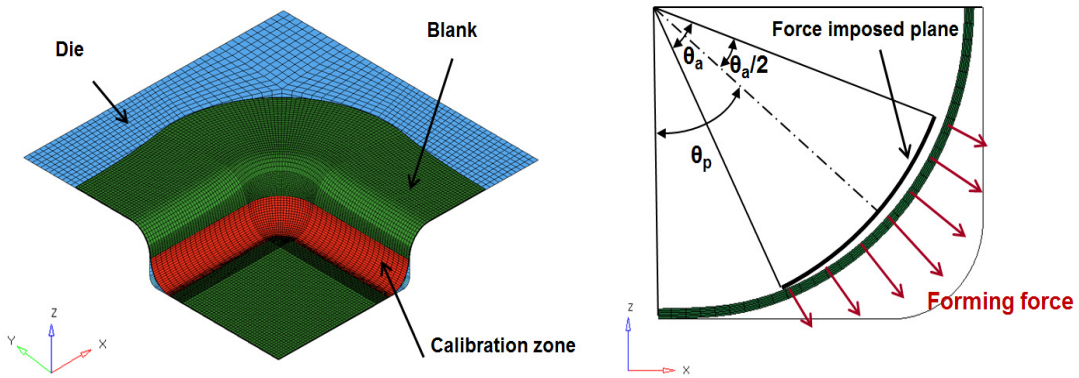

Figure 5: *(a) Calibration zone EM corner fill forming force applied; (b) definition of the process parameters to be optimized*

4.2 Objective function

Iteration of optimization procedure in Figure 1 (b) as mentioned in the previous chapter leads to the solution of the minimization problem which was introduced by Taebi et al. [3] as shown below:

$$\begin{aligned}&\text{minimize} \quad f(\lambda_1,\cdots,\lambda_n),\\&\text{subject to} \quad c(\lambda_1,\cdots,\lambda_n,t)\geq 0\end{aligned}$$

where f is the target function depending on n process parameters λ_k and it means the mean deviation of the shape of the deformed workpiece after a corner fill process from optimal geometry.

$$\begin{aligned}f(\lambda_1,\cdots,\lambda_n)&=\left(\frac{1}{S_{zone}}\int_S\left|s(x,y,\lambda_1,\cdots,\lambda_n)-s_{opt}(x,y)\right|^2 dxdy\right)^{\frac{1}{2}}\\&=\left(\frac{1}{N}\sum_{k=1}^{N}\left|s(x_k,y_k,\lambda_1,\cdots,\lambda_n)-s_{opt}(x_k,y_k)\right|^2\right)^{\frac{1}{2}}\end{aligned}$$

where S_{zone} is the area of the calibration zone, $s(x,y,\lambda_1,\cdots,\lambda_n)$ is the shape of the deformed blank, $s_{opt}(x,y)$ is the shape of optimal geometry which has a corner radius reduced to 10 mm and N is the number of nodes in the calibration zone. Integration is carried out over the whole surface of the calibration zone for the target function, but it can be considered as the mean deviation from nodes in the calibration zone.
The constraint function c is the minimum distance to the forming limits in the PEPS strain space at time t. The equation of the constraint function is shown below

$$c(\lambda_1,\cdots,\lambda_n,t)=\min\left[(-1)^m\cdot\mathrm{dist}((\bar{\varepsilon}_p\cos\theta(\lambda_1,\cdots,\lambda_n,t),\bar{\varepsilon}_p\sin\theta(\lambda_1,\cdots,\lambda_n,t)),F)\right]$$

$$\text{where } m=\begin{cases}0, & \text{when forming limits are not violated}\\1, & \text{when forming limits are violated}\end{cases}$$

where $(\bar{\varepsilon}_p\cos\theta,\ \bar{\varepsilon}_p\sin\theta)$ is a point of strain path in the PEPS strain space and F is a fracture based PEPS diagram of the material. The constraint function c has negative value when forming limits are violated and thus the constraint function has to be positive for all time t.

4.3 Optimization result

The target function and the constraint function were calculated and approximated by response surface method to seek for optimum values of process parameters. Numerical simulations are carried out according to the Taguchi's L^9 orthogonal table since the analysis takes account of only the main effect of three process parameters. After the simulations, the response surfaces of the target function and the constraint function are approximated by the regression equation for optimum searching as follows:

$$\begin{aligned}f(x_1,x_2,x_3)&=\beta_o+\beta_1x_1+\beta_2x_2+\beta_3x_3+\beta_4{x_1}^2+\beta_5{x_2}^2+\beta_6{x_3}^2\\c(x_1,x_2,x_3)&=\beta_o+\beta_1x_1+\beta_2x_2+\beta_3x_3+\beta_4{x_1}^2+\beta_5{x_2}^2+\beta_6{x_3}^2+\beta_7{x_1}^3+\beta_8{x_2}^3+\beta_9{x_3}^3\end{aligned}$$

where x_i and β_i are design values of each process parameter and the coefficients of the regression equation, respectively. Each regression equation is chosen to enhance the

approximation ability by adding the higher order terms in each regression equation. After response surfaces are constructed, optimum searching is conducted by solving the minimization problem in section 4.2. During the optimization process, the next iteration starts based on the design values of process parameters obtained from previous iteration until the converged values are acquired.
This optimization process converged after 4 iterations. A convergence criterion is the variation percentage of 1% for each process parameter. Figure 6 shows the optimum values of each process parameter and variation of the target function during the optimization process.

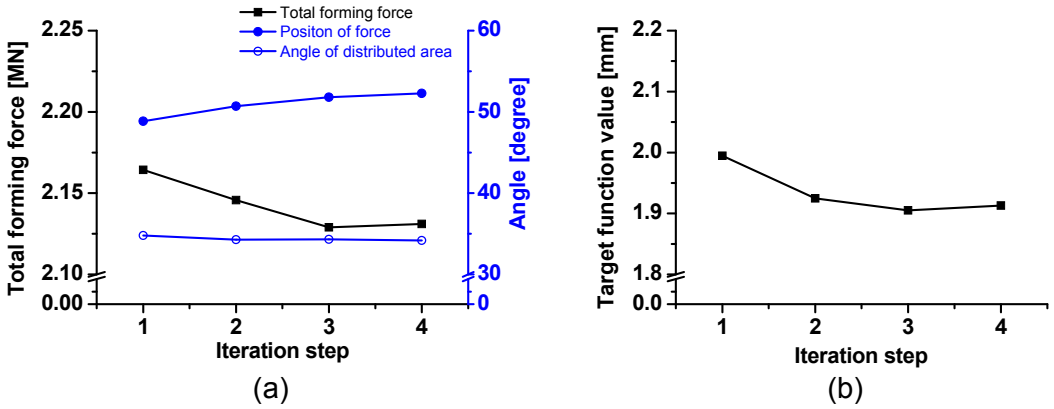

Figure 6: *(a) Optimum values of each process parameter and (b) variation of the target function during the optimization process*

5 Design of electromagnetic tool coil

After numerical optimization of the forming force, tool coil is designed, which is an important part delivering electromagnetic energy to the workpiece. The objective of this coil design is to realize the optimized forming force with small loss of energy transition.

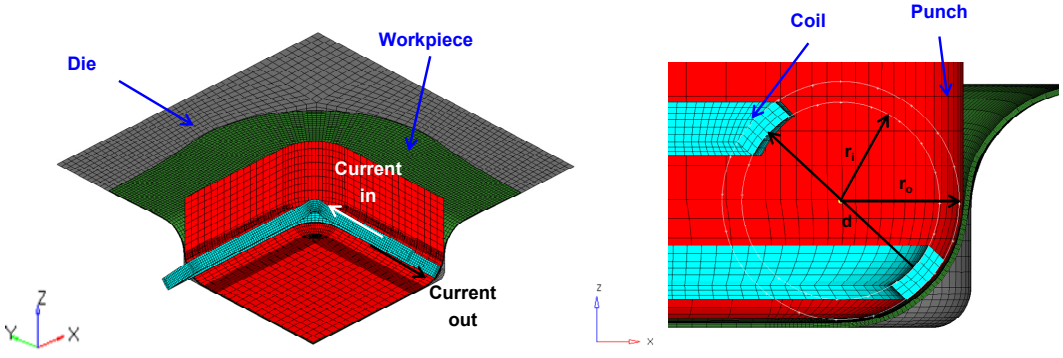

Figure 7: *(a) Shape and location of the coil and (b) definition of the dimension of the tool coil*

The type of an electro-magnetic tool coil for a successful corner fill process was studied by Imbert and Worswick [2] and the authors proposed U shape coil with the narrowed

section closest to a workpiece. In this paper, tool coil is designed with reference to the U shape with dimensional analysis. The shape and location of the coil are shown in Figure 7 (a). Coil dimensions for the angle of the force distributed area and the position of the tool coil located in the punch are determined from optimization results of EMF force. The gap between the punch and the coil is set to 1 mm.
Dimensional analysis is conducted numerically with various dimensions of the coil shown in Figure 7 (b) to compare the loss of energy transition. The effects of the coil thickness (r_o-r_i) and the distance between the upper and lower part of the coil (d) are also investigated. Numerical simulations are conducted using the LS-dyna EM module recently developed. The analysis time is 200 μs and input parameters representing EMF machine are the same for all analyses. The reference values of the dimension are selected as r_o-r_i = 5 mm and d = 50 mm. The normalized forming force exerted by the coil is compared with various dimensions in Figure 8.

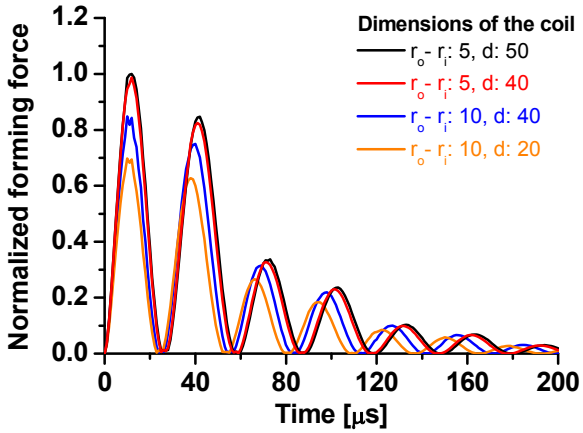

Figure 8: *Normalized forming force with various dimensions of the tool coil*

The forming force increases as the coil thickness decreases and the distance between the upper and lower part of the coil increases. Therefore, the coil designed with reference dimension has the smallest loss of energy transition among proposed designed coils. Using this coil, the required specifications of EMF machine regarded as an equivalent RLC circuit for the total forming force optimized can be calculated. The system resistance, the inductance and the capacity are supposed to be 6 mΩ, 230 nH and 380 μF respectively, the calculated charging voltage is 25 kV.

6 Conclusion

This paper proposes a systematic approach for numerical optimization of the combined square cup drawing and electromagnetic corner fill process, which is conducted to obtain process parameters for forming desired shape without violating forming limits. The strain rate dependent tensile properties and the strain path independent fracture forming limits are introduced for numerical simulation of the process. The optimization of the process is followed by an optimum design of the tool coil and required specifications of EMF system. It is noted that the combined deep drawing and electromagnetic corner fill process with DP980 steel sheet is possible for sharp corner edges with existing EMF machine to enhance the formability of the material. However, the required initial voltage for this process is larger than generally used values of EM forming for low strength materials and the feasibility of this process has to be proved by experiment. Moreover, the efficiency of the electromagnetic energy delivery would have to be enhanced to accommodate industrial settings.

References

[1] *Psyk, V.;* Beerwald, C.; Henselek, A.; Homberg, W.; Brosius, A.; Kleiner, M.*:* Integration of Electromagnetic Calibration in to the Deep Drawing Process of an Industrial Demonstrator Part, Key Engineering Materials, Vol. 344, p. 435-442, 2007.

[2] *Imbert, J.; Worswick, M.:* Electromagnetic reduction of a pre-formed radius on AA5754 sheet, Journal of Materials Processing Technology, 211, p.896-908, 2011.

[3] *Taebi, F.; Demir, O.K.; Stiemer, M.; Psyk, V.; Kwiatkowski, L.; Brosius, A.; Blum, H.; Tekkaya, A.E.:* Dynamic forming limits and numerical optimization of combined quasi-static and impulse metal forming, Computational Materials Science, 54, p.293-302, 2012.

[4] *Psyk, V.;* Risch, D.; Kinsey, B.L.; Tekkaya, A.E.; Kleiner, M.*:* Electromagnetic forming – A review, Journal of Materials Processing Technology, 211, p.896-908, 2011.

[5] *Huh, H.; Jeong S.; Bahng G.W.; Chae K.S.; Kim C.G.:* Standard Uncertainty Evaluation for Dynamic Tensile Properties of Auto-Body Steel-Sheets, Experimental Mechanics, DOI 10.1007/s11340-014-9847-5

[6] *Huh, H.; Ahn K.; Lim J. H.; Kim H. W.; Park L. J.:* Evaluation of dynamic hardening models for BCC, FCC, and HCP metals at a wide range of strain rates, Journal of Materials Processing Technology, 214, p.1326-1340, 2014.

[7] *Park, N.; Ahn, K.; Lim, S. J.; Huh, H.:* Anisotropy Effect on the Fracture Model of DP980 Sheets Considering the Change of Loading Path. Proceedings of the TUBEHYDRO 2013, Jeju, Korea, August 26-28, 2013.

[8] *Stoughton, T. B.; Yoon, J. H.:* Path independent forming limits in strain and stress spaces, International Journal of Solids and Structures, 49, p.3616-3625, 2012.

Research on homogeneous deformation of electromagnetic incremental tube bulging*

Xiaohui Cui, Jianhua Mo, Jianjun Li

State Key Laboratory of Material Processing and Die & Mould Technology, Huazhong University of Science and Technology, Wuhan 430074, PR China

Abstract:

The electromagnetic incremental forming (EMIF) method is used for tube forming process. Suitable 2D FE models are designed to predict the forming process with a moving coil. In comparison with experimental values, simulation method can obtain accurate results. Then, effect factors named overlapping ration of adjacent discharge positions, discharge voltage, forming sequence and die dimension on tube homogeneous deformation are discussed. The result demonstrates that it is feasible to produce long-straight wall tubes using a small coil by electromagnetic incremental tube bulging.

Keywords

Electromagnetic incremental forming, Tube bulging, Process parameters, Numerical simulation

1. Introduction

Electromagnetic forming (EMF) is a kind of high-velocity forming technology based on the repulsive forces generated by opposing magnetic fields in adjacent conductors. In comparison with conventional forming processes, EMF has many advantages, including no lubricants, contact-free, high repeatability, improved strain distribution and reduction in wrinkling [1]. At present, the EMF method is mainly used in tube bulging, tube compression and tube connection, which could meet industry requirements to some extent [2, 3].

However, only some simple and small parts can be produced by EMF. This is because larger parts require more energy if using EMF to form the whole metal parts alone. But the electromagnetic forces cannot be arbitrarily enlarged to form large parts due to the limitation of strength of the working tool and the capacity of the capacitor bank. Yu et al. [4] analyze the effect of coil length on energy efficiency of tube forming. It is found that the longer of coil

* *The work was supported by the National Natural Science Foundation of China (No.50875093) and the Major State Basic Research Development Program of China (973 Program) (No.2011CB012802)*

length corresponds to lower energy efficiency under the condition of the same discharge energy, which causes a higher equipment energy required under the same tube deformation.

Recently, Cui et al. [5] proposed a new method named electromagnetic incremental forming (EMIF). It is demonstrated that the EMIF technology is feasible to produce a large metal sheet part with small working coil and small discharge energy. In this paper,the EMIF method is used to produce a long tube with a small coil and small discharge energy.

2. Principle of electromagnetic incremental tube forming

Figure 1 describes the principle of electromagnetic incremental tube bulging. The small coil causes workpiece local deformation at a high speed. Finally, all local deformations accumulate into large parts. There are two kinds of forming process: (1) the coil sequential discharge from a tube end to another end (Figure 1(a)); (2) the coil discharging make the tube ends deformation firstly, then the tube center deforms (Figure 1(b)). In order to produce long-straight wall tubes, it introduces two important concepts, as showed in Eq(1) and Eq(2): δ is overlapping ratio of adjacent two discharge regions; η is used to evaluate the tube deformation uniformity.

$$d = \frac{L}{L_{coil}} \tag{1}$$

$$h = \frac{D_2 - D_1}{D_2} \tag{2}$$

Where, L is the overlapping region of the coil discharge in two adjacent positions. L_{coil} is the length of coil. In this paper, L_{coil} is equivalent to 56mm. D_1 is the smallest radial displacement at the valley region of the tube. D_2 is the maximum radial displacement.

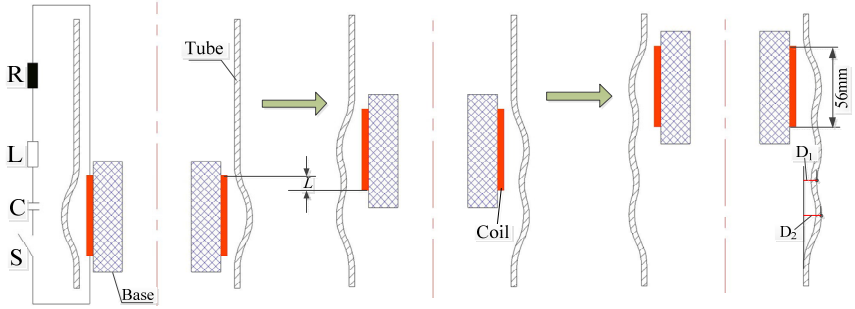

(a) the coil sequential discharge from a tube end to another end

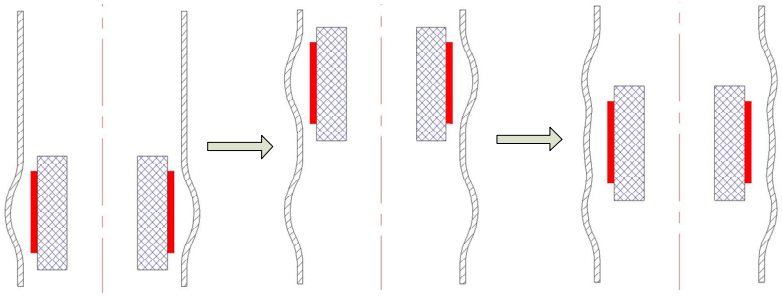

(b) the tube ends deform firstly and then the tube center deforms

Figure 1 The principle of electromagnetic incremental tube bulging

3. Numerical simulation of electromagnetic incremental tube forming

3.1 Finite element models

EMF equipment was made by Huazhong Univeristy of Science and Technology (Figure 2). The main parameters in the current experiments were: capacitance-900μF, rated voltage-10KV. A thirteen solenoid coil in conjunction with capacitor banks was used to make the tube deforms by magnetic force. The section area of the coil is 1×4mm^2. The inner radius of the coil is 38mm. The coil length is 56mm. The distance between coil and tube is 3mm. The discharge current, I(t), flowing in the coil is approximately described by the following equation:

$$I(t) = U\sqrt{\frac{C}{L}}e^{-bt}\sin wt \tag{3}$$

Where, U is the initial voltage, C =900μF is the capacitance, L=14.6μH is the inductance, β =616.44s^{-1}is the current damping factor and ω=8723.7 rad/s is the current angular frequency.

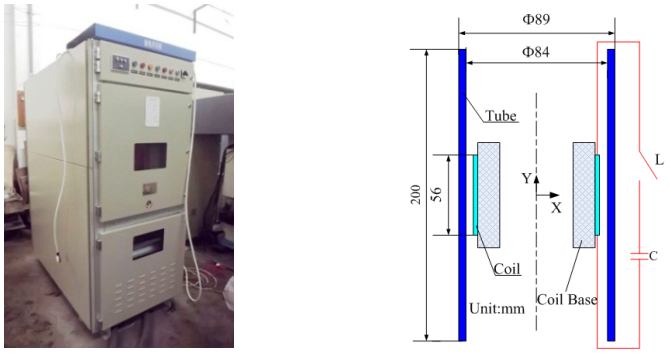

(a) (b)

Figure 2 Equipment condition for electromagnetic tube bulging (unit: mm): (a) Capacitor bank and vacuum switch; (b) Tube and solenoid coil

To predict the electromagnetic incremental tube forming by FEM, a method like "birth-death element" was proposed. Many coil models was required to be established and the coil does not move in the simulation process. The magnetic forces are calculated on the basis of stationary coil condition in the ANSYS/EMAG model.

Because of axial symmetrical placement of coil and tube in Figure 1 (b), only the half of forming system is taken into account in 2D FE model. Figure 3 shows meshes and boundary conditions for the EM model. The ANSYS/EMAG is used to calculate the magnetic force on the sheet. The EM model consists of far field air, air, coil and sheet. Regions of sheet, coil and far field air are all meshed into four-node quadrangular elements. The region of air is meshed into three-node triangular elements. The element types of sheet, coil and air are axisymmetric with plane 13. The element types of far field air is axisymmetric with infin110. As showed in Figure 3, the simulation process can be simply described as follows:

(1) The models of coil 1 and coil 2 are both built-in FEM. Both of the element types for coil 1 and coil 2 are plane 13.

(2) The current density in only loaded into the model of coil 1 to make the tube deform. The material property of air is assigned to the model of coil 2. This means the coil stays in the same position with coil 1 at present. And the model of coil 2 is the air region.
(3) Then, the current density is only loaded into the model of coil 2 to make the tube deform. The material property of air is assigned to the model of coil 1. This means the coil moves from the position of coil 1 to the position of coil 2. And the coil1 is the air region.

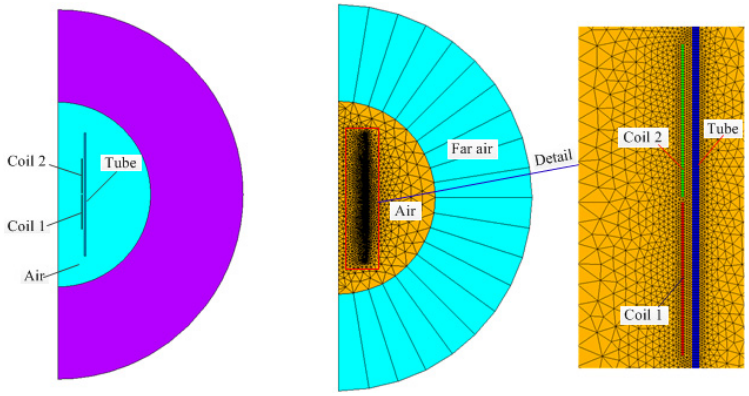

(a) Geometric model (b) Finite element model

Figure 3 Electroomagnetic field model

3.2 Material properties

The material used in this experiment is the aluminum alloy 3003 tube with 2.5mm in thickness. The annealing technology is: annealing temperature is 450℃, holding time is 3h. The yield strength of the material is 74Mpa. Properties of materials is measured by tensile tests at room temperature, in which 2.5mm thickness standard specimens were used. The true stress-strain curve of the aluminum alloy 3003 tube under quasi-static condition is shows Eq. (4):

$$s_y = 472(e + 0.0017)^{0.293} \tag{4}$$

Where, σ_y is the quasi-static constitutive behavior of the sheet, e is the plastic strain.

In order to consider the effect of high strain rate on the forming process, some scholars used the viscoplastic material behavior with rate-dependence law (Cowper-Symonds constitutive model) in the ANSYS software to analyze the EMF process. Liu et al. [6] established an experimental scheme according to the conventional stamping of cylindrical parts to analyze the formability of 5052 aluminum alloy sheet. The experimental results show that the EMAS technology can successfully produce an aluminum cup with smaller bottom corner radius than the one by conventional deep drawing process. Moreover, a “multi-step, loose coupling” numerical scheme was proposed to simulate the deformation behaviors of EMAS. The predicted and experimental profiles of cylindrical parts are in good agreement. Yu et al. [4] investigated the tendency of homogeneous radial deformation during electromagnetic compression. It is defined the R is length ratio of the tube to coil. There exists a critical value, 0.93≥R≥0.92, corresponding to the uniform radial deformation. A good agreement between the predicted and the experimental data is obtained. Thus, the Cowper-Symonds constitutive model (Eq.5) is also used to predict high speed forming process in this paper:

$$s = s_y(1+(\frac{\dot{e}}{P})^m) \quad (5)$$

Where, σ is the dynamic flow stress, σ_y is the quasi-static constitutive behavior of the sheet, $\dot{e}$ is the strain rate. P=6500 s-1 and m=0.25 are the special parameters for aluminum alloy.

3.3 Numerical simulation and experimental results

Figure 4 shows the magnetic force acting on the tube at the different time if there was no overlap region for the coil discharge in different position. The total time for forming process is N×400μs. N stands for the number of discharge regions. The simulation time for the coil discharge in a fixed position is 400μs.

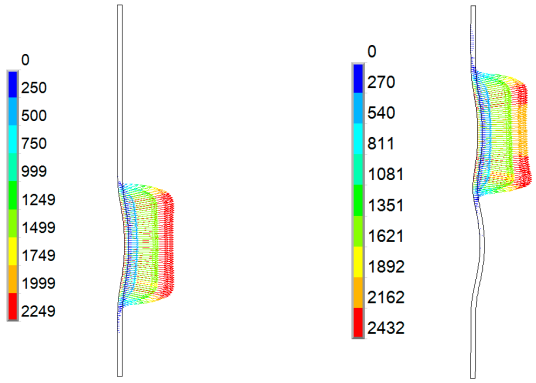

(a) t=200μs (b) t=600μs

Figure 4 Magnetic force on the tube at different time

Figure 5 shows the experimental results with different discharge parameters: (1) the coil discharge in one position and the discharge voltage is 5000V; (2) the discharge voltages are 5000V in two positions and there is no overlap region for the two discharge regions; (3) the coil sequential discharge from a tube end to another end. The discharge voltages are 5000V in three positions and the overlap ratio is 50% of the adjacent two discharge regions. Figure 6 shows the comparison between the experimental and simulation results. These show the simulation method has a high accuracy to analyze the electromagnetic incremental tube forming process.

(a) One-step forming (b) two-step forming (δ=0) (c) three-step forming (δ=50%)

Figure 5 Experimental results

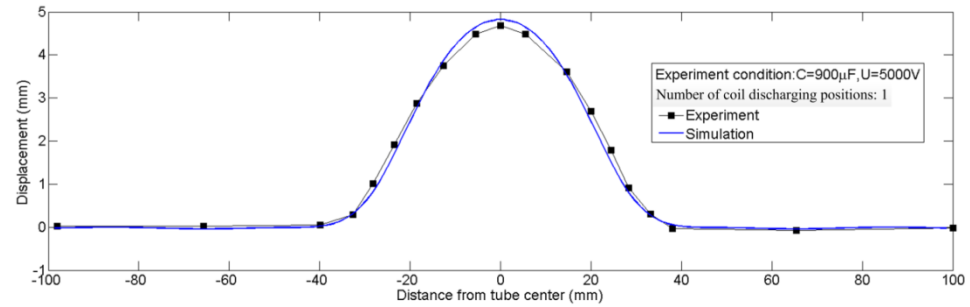

(a) One-step forming

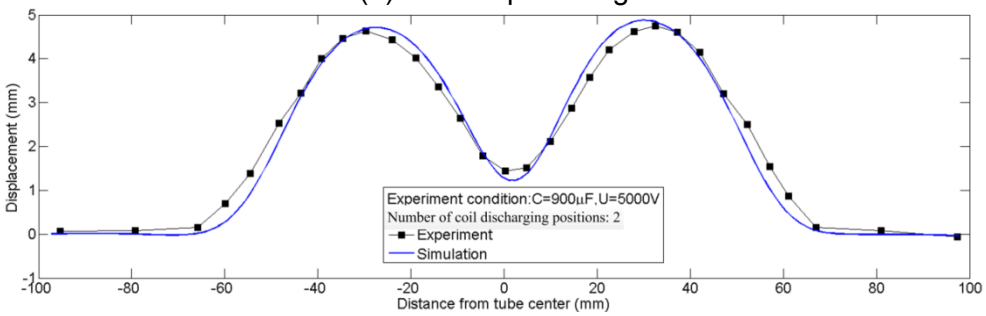

(b) two-step forming (δ=0)

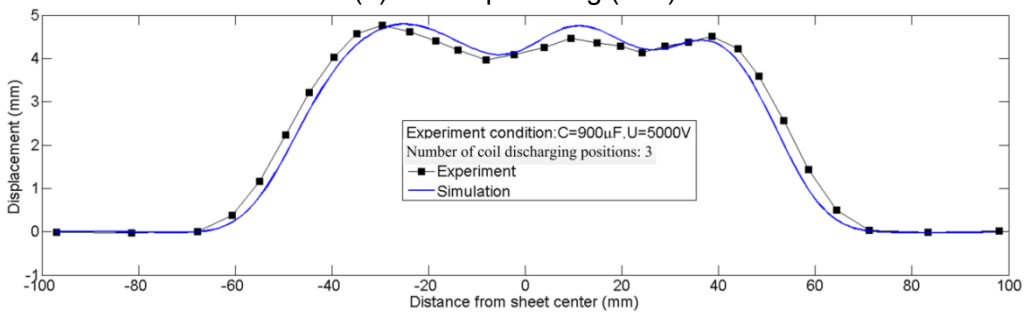

(c) three-step forming (δ=50%)

Figure 6 Experimental and simulation data of electromagnetic incremental tube bulging

4. Effect factors on tube homogeneous deformation

According to the results of the coil discharge in two or three different positions in Figure 6, it shows there exist the peak and valley on the deformed tube. Therefore, the sequency coupling method is used to analyze the effect named overlapping ratio of adjacent two discharge regions, discharge voltage, forming sequence and die structure on tube deformation uniformity.

4.1 Forming sequence and overlapping ratio

Figure 7 shows the effect of overlapping ratio on tube homogeneous deformation if the coil discharging in two different positions with the discharge voltage is 5000V. With the increase of the overlap ratio, the displacement at the position of 28mm away from the tube center slight increase due to the second discharge make the deformed region deform again. Higher of overlap ratio δ, the tube homogeneous deformation η is improved. However, there exists only one peak if the overlap ratio is higher than 70%.

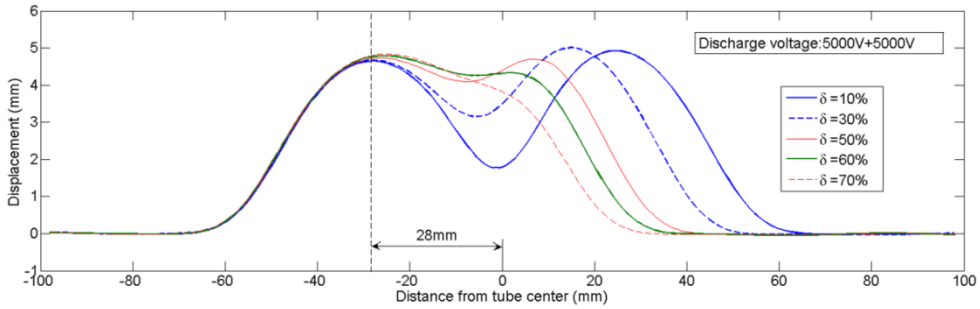

Figure 7 Deformed tube profiles vs δ if the coil discharging in two positions

Figure 8 shows the effect of overlapping ratio and forming process on tube homogeneous deformation if the coil discharging in three different positions with the discharge voltage is 5000V. It can be found there exist obvious peak and valley values on tube no matter what kinds of forming process or overlapping ratio of adjacent two discharge regions, which caused the tube has a low deformation uniformity.

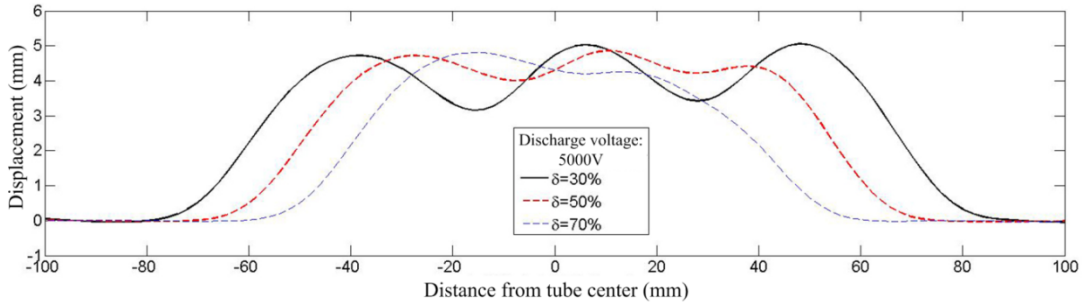

(a) the coil sequential discharge from tube end to another

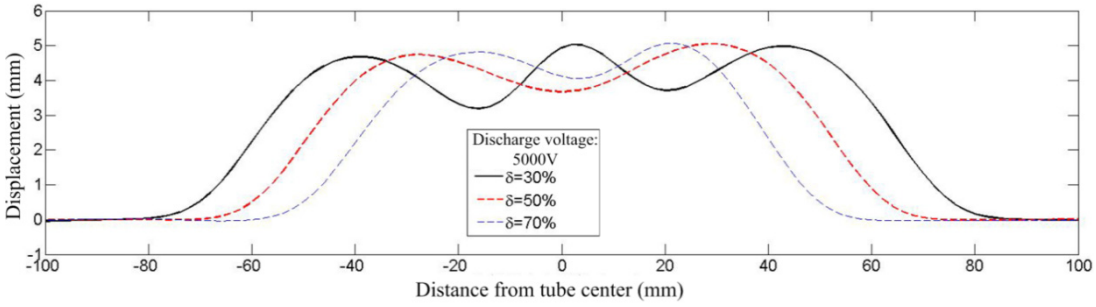

(b) the tube ends deform firstly and then the tube center deforms

Figure 8 Deformed tube profiles vs δ with different forming process (three-step forming)

4.2 Discharge voltage

As showed in Figure 7, there exist obvious peak and valley values on tube if $\delta \leq 50\%$ and the coil discharge in two different positions. Figure 9 shows the effect of the discharge voltage in the second position on deformed tube profiles. With the discharge voltage increased, the value of the tube deformation uniformity is increased firstly and then decreased. The great value of tube deformation uniformity η=3.3% if the discharge voltages are 5000V and 5125V in two different positions with theδ is equal to 60%.

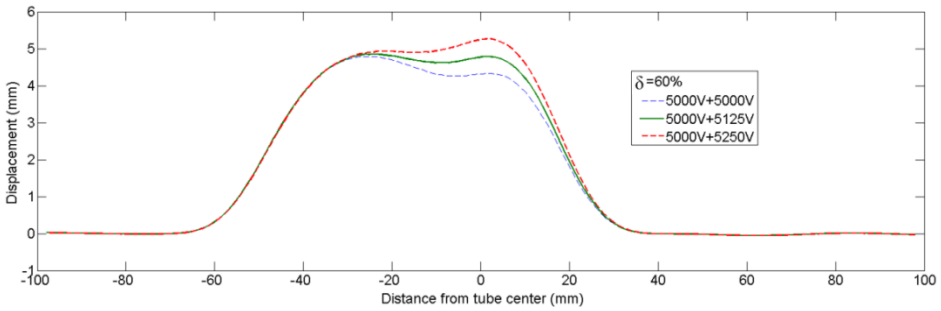

Figure 9 Deformed tube profiles vs discharge voltage (two-step forming)

In Figure 8, the displacement at the tube center is lower than its adjacent regions with δ =50% if the tube ends deform firstly then the tube center deforms. In order to improve the tube deformation uniformity, the higher discharge voltage is needed to increase the displacement at the tube center. As showed in Figure 10, with the discharge voltage increased, the displacement at the tube center is increased, while value of the tube deformation uniformity is increased firstly and then decreased. The value of tube deformation uniformity η=8.7% if the discharge voltages are 5000V, 5000V and 5250V in three different position and δ =50%.

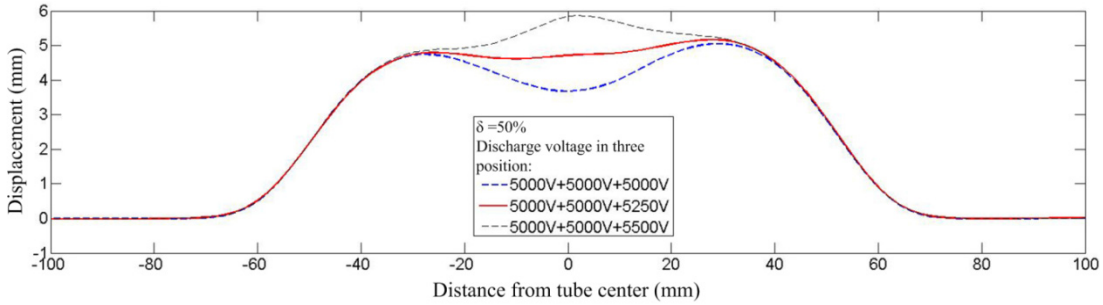

Figure 10 Deformed tube profiles vs discharge voltage (three-step forming)

4.3 Die dimension

In order to control the deformed tube shape, a die structure with reasonable inner radius is needed. Figure 11 shows the effect of die dimensions on deformed tube profiles. Under the condition of same discharge voltage, the value of the tube deformation uniformity under the condition of the die radius is 49.5 is lower than the one if the die radius is 49.2. In addition, the optimum value of the tube deformation uniformity η =1.3%if the discharge voltages are 5000V, 5000V and 5500V in three different position, die radius is equal to 49.2mm and δ =50%.

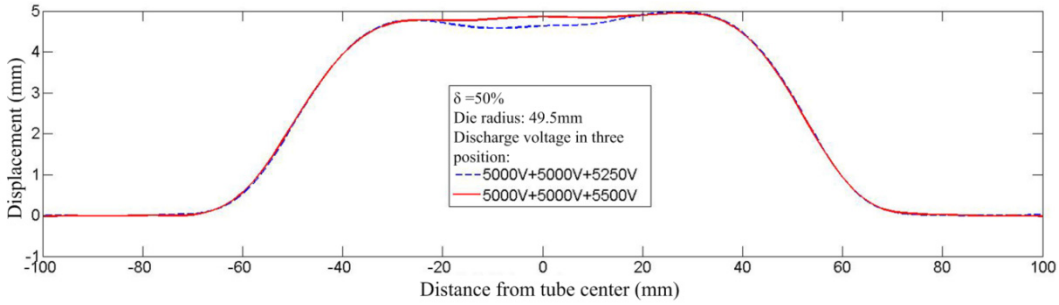

(a) the distance between the tube and die is 5mm in the initial state

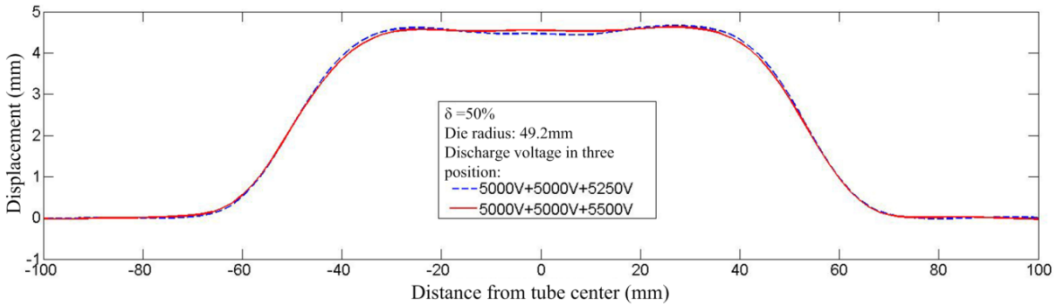

(a) the distance between the tube and die is 4.7mm in the initial state

Figure 11 Effect of die dimension on deformed tube profiles (three-step forming)

5. Conclusion

In this paper, the EMIF method is used in this paper to produce a long tube with a small coil and small discharge energy. A method like "birth-death element" is used in 2D FE model to predict the forming process with a moving coil. In comparison with experimental values, simulation methods can obtain accurate results. Then, it is found that the overlapping ratio of coil discharge positions, discharge voltage, forming sequence and die dimension has great influence on tube deformation uniformity. Finally, the value of the long tube deformation uniformity η is equal to1.3%if the discharge voltages are 5000V, 5000V and 5500V in three different positions, die radius is equal to 49.2mm and δ =50%.

References

[1] *Psyk, V., Risch, D., Kinsey, B L., Tekkaya, A E., Kleiner, M.: Electromagnetic forming- A review. Journal of Materials Processing Technology. 2011, 211: 787-829.*

[2] *Weddeling, C., Woodward, S., Nellesen, J., Psyk, V., Marré, M., Brosius, A., Tekkaya, A E., Daehn, G S., Tillmann, W.: Development of design principles for form-fit joints in lightweight frame structures. 4th International Conference on High Forming. 2010, 137-148.*

[3] *Jäger, A., Risch, D., Tekkaya, A E.: Thermo-mechanical processing of aluminum profiles by integrated electromagnetic compression subsequent to hot extrusion. Journal of Materials Processing Technology. 2011, 211: 936-943.*

[4] *Yu, H P., Li. C F.: Effects of coil length on tube compression in electromagnetic forming. Trans. Nonferrous Met. Soc. China. 2007, 17: 1270-1275.*

[5] *Cui, X H., Mo, J H., Li, J J., Zhao, J., Zhu, Y., Huang, L., Li, Z W., Zhong, K.: Electromagnetic incremental forming (EMIF): A novel aluminum alloy sheet and tube forming technology. 2014, 214: 409-427.*

[6] *Liu, D.H., Li, C.F., Yu, H.P.: Numerical modeling and deformation analysis for electromagnetically assisted deep drawing of AA5052 sheet. Trans. Nonferrous Met. Soc. China. 2009, 19: 1294-1302.*

Strain-rate effect on the dynamic behaviours of a rectangular conducting plate*

Y. Gao[1], H. Huh[2]

[1] Key laboratory of mechanics on western disaster and environment, Lanzhou University, Lanzhou 730000, P.R. CHINA
[2] School of Mechanical, Aerospace and Systems Engineering, KAIST, Science Town, Daejeon 307-701, KOREA

Abstract

This paper is concerned with thermo-elasto-plastic dynamic response of a conductive plate in a magnetic pulse field. The influence of the strain rate effect and the temperature effect are taken into account for the electromagnetic elasto-plastic dynamic transient response and deformation of the conductive plate which made of strain-rate sensitive materials. The Johnson-Cook model is employed to study the strain rate effect and the temperature effect on the deformation of the plate. Basic governing equations are derived for electro-magnetic field considering the eddy current. The analysis includes the elasto-plastic transient dynamic response and the heat transfer of a conductive rectangular plate, and then an appropriate numerical code based on the finite element method to quantitatively simulate the electro-magneto-elasto-plastic mechanical behaviors of the conductive rectangular plate. The numerical results indicate that the strain rate effect has to be considered for the conductive plates, especially for those with high strain rate sensitivity. Comparison of the influence of the temperature effect on the deformation of the plate with that of the strain rate effect shows that the influence of the temperature effect on the deformation of a plate is not significant.

Keywords

Multi-field coupling; Elasto-plastic dynamic response; Strain rate effect

---

* *This work is supported by the Natural Science Fund of China (11372120, 11121202), YG gratefully acknowledge their supports.*

1 Introduction

An electromagnetic forming (EMF) process is a dynamic, high-energy rate forming process, which utilizes the electromagnetic force to fabricate the work-pieces. Since it has many advantages of rapid forming, slight springback, high forming limit, high forming precision compared to the conventional forming process, the EMF process has potentially wide applications to industrial practice as a complementary approach of the conventional forming process [1].

As one of the basic problems of EMF processes, the research on the electro-magneto-elastic-plastic dynamic behaviours of conductive structures under the magnetic pulse is very important and useful for the design of the EMF process. However, because of the complicated multi-field coupling and nonlinear characteristics of these problems, the researches have been conducted are mainly restricted to two dimensions or axisymmetric geometries[2,3], and most of researches conducted on the dynamic behaviours of conductive structures are always focused on the elastic deformation. There are a few research works conducted on the electromagnetic elasto-plastic behaviours on the conductive structures. On the other hand, although some calculational frame for EMF processes have already been presented [1,4,5], most of them regard the electromagnetic force as a magnetic pressure [4], and never reveal the distribution characteristics of the eddy current and the electromagnetic force in detail and without consideration of the coupling between the deformation of a workpiece and the applied magnetic field. In addition, although the conductive sheets in the EMF process has very high strain rate, which is always higher than 10^3/s, even up to 10^4/s [5,6], there are a few research works which have been conducted to study the influence of the strain rate effect on the deformation of a conductive sheet. There are also a few reports for the influence of the temperature effect on the dynamic response or the deformation of the conductive sheet, which is due to the plastic work and the loss of the eddy current. Thus, it is necessary to investigate the influence of the strain rate effect and the temperature effect on the deformation of the conductive plate.

In this paper, we investigate the elasto-plastic dynamic response of a rectangular plate with consideration of the coupling effect between the deformation of plate, the thermal field and the magnetic field to reveal the distribution characteristics of the applied magnetic field, eddy current and the electromagnetic force in a conductive plate. This study investigates the influence of the strain rate effect and temperature effect, which is due to the plastic work and the loss of the eddy current, on the deformation of the conductive plate under a magnetic pulse.

2 Governing Equation

2.1 Electromagnetic force

Consider a thin conductive rectangular plate with the length of a, the width of b, and the thickness of h, which located in an applied magnetic pulse field $\mathbf{B_0} = B_{0x}\mathbf{i} + B_{0y}\mathbf{j} + B_{0z}\mathbf{k}$ as shown in Figure 1. Here $\mathbf{i}$, $\mathbf{j}$, $\mathbf{k}$ are the unit vectors in the Cartersian coordinates (x, y, z). $\mathbf{k}$ is normal to the mid-plane of a plate, and the x- and y-axes are coincident with the length and width directions of a plate, respectively.

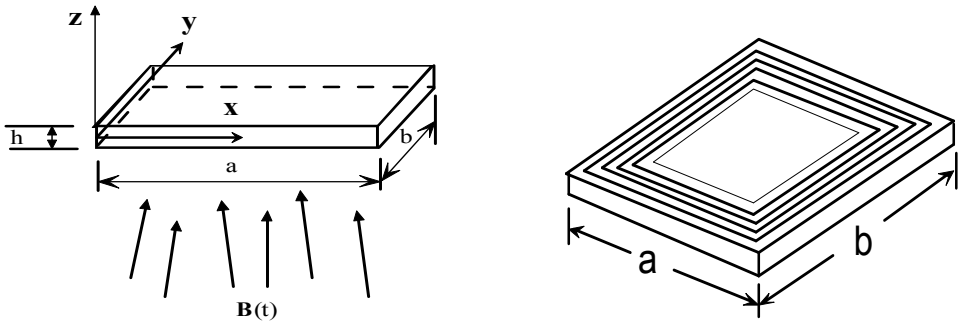

(a) (b)

Figure 1. Schematic of the conductive plate in an applied magnetic field: (a) the conducting plate; (b) the rectangular coils

Based on the Maxwell equations and T-method for calculation of eddy current [7,8], a governing equation for the eddy current vector potential T is expressed as

$$\nabla^2 T - \eta\mu_0 \frac{\partial T}{\partial t} - \frac{\eta\mu_0}{4\pi}\int_s \frac{\partial T_n^{'}}{\partial t}\frac{\partial}{\partial z}(\frac{1}{R})ds' = \eta[\frac{\partial B_{0z}(t)}{\partial t} - (B_{0x}\frac{\partial^2 w}{\partial x \partial t} + B_{0y}\frac{\partial^2 w}{\partial y \partial t})] \tag{1}$$

The boundary conditions and the initial conditions are respectively described as

$$\frac{\partial T}{\partial s} = 0 \qquad \text{at } x = 0, a \text{, and } y = o, b \tag{2}$$

$$T(x, y, 0) = 0 \qquad at \quad t = 0 \tag{3}$$

Without consideration of the magnetism and polarization, as well as assuming that the eddy current is uniform along the thickness of a plate, the electromagnetic force $\mathbf{F}$ of the conductive plate, given by the Lorentz force formula, becomes

$$\mathbf{F} = F_x\mathbf{i} + F_y\mathbf{j} + F_z\mathbf{k} = \int_{-\frac{h}{2}}^{\frac{h}{2}} (\mathbf{J}_e \times \mathbf{B})\, dz = h(\mathbf{J}_e \times \mathbf{B}) \tag{4}$$

where $\mathbf{J_e} = \nabla \times \mathbf{T}$ and $\mathbf{T} = T(x, y, t)\mathbf{k}$.

2.2 Dynamic governing equations of a rectangular conductive plate

According to the theory of vibration of a thin plate, the dynamic governing equations of the conductive plate can be expressed as

$$\frac{\partial N_x}{\partial x} + \frac{\partial N_y}{\partial y} + F_x(x, y, t) = \rho h \frac{\partial^2 u}{\partial t^2} \tag{5}$$

$$\frac{\partial N_y}{\partial y}+\frac{\partial N_{xy}}{\partial x}+F_y(x,y,t)=\rho h\frac{\partial^2 v}{\partial t^2} \tag{6}$$

$$\frac{\partial^2 M_x}{\partial x^2}+\frac{\partial^2 M_{xy}}{\partial x\partial y}+\frac{\partial^2 M_y}{\partial y^2}+(N_x\frac{\partial^2 w}{\partial x^2}+2N_{xy}\frac{\partial^2 w}{\partial x\partial y}+N_y\frac{\partial^2 w}{\partial y^2})+ (\frac{\partial N_x}{\partial x}+\frac{\partial N_{xy}}{\partial y})\frac{\partial w}{\partial x}+(\frac{\partial N_{xy}}{\partial x}+\frac{\partial N_y}{\partial y})\frac{\partial w}{\partial y}+F_z(x,y,t)=\rho h\frac{\partial^2 w}{\partial t^2} \tag{7}$$

where ρ is the mass density, M_x and M_y are the bending moments, M_{xy} is the twisting moment.

We assume that the boundary is clamped; the boundary and initial conditions can be described as

$$w(x,y,t)=0,\quad \frac{\partial w(x,y,t)}{\partial x}=0,\qquad on\qquad x=0,a \tag{8}$$

$$w(x,y,t)=0,\quad \frac{\partial w(x,y,t)}{\partial y}=0\qquad on\qquad y=0,b \tag{9}$$

$$\frac{\partial w(x,y,0)}{\partial t}=0,\quad w(x,y,0)=0 \tag{10}$$

2.3 Johnson-Cook model and the Von-Mises Yield criterion

In order to investigate the influence of strain rate on the deformation of metal sheet, the Johnson-Cook material model is employed as below: [9]

$$\sigma=(A+B\varepsilon^n)(1+C\ln\dot{\varepsilon})(1-T^{*m}),\quad T^*=\frac{T-T_{room}}{T_{melt}-T_{room}} \tag{11}$$

where T^* is the homologous temperature T is the temperature of work pieces, and T_{melt} is the melting temperature of a workpiece. The Johnson-Cook model contains five material constants, A,B,n,C,m which need to be determined. The first bracket in the equation is the strain hardening term, the second is the strain rate hardening term, and the third is the thermal softening term.

The Von Mises yield function is employed to for the plastic strain produced in the plate. In the case of a thin plate [9], it is expressed as

$$f=\frac{1}{\sqrt{2}}[(\sigma_x-\sigma_y)^2+\sigma_y{}^2+\sigma_x{}^2+6\tau_{xy}^2]^{1/2}-\sigma_Y(\varepsilon^p,\dot{\varepsilon}^p,T) \tag{12}$$

2.4 Heat transfer equations

Due to the loss of the eddy current and the plastic work, the temperature of a plate increases quickly in the strong applied magnetic field, hence the temperature effect on the deformation is considered in this paper.

The governing equation of heat conduction with heat generation can be described as follows:

$$\rho C\frac{\partial T^t}{\partial t}=\lambda\nabla^2 T^t+W\ ,\quad W(x,y,t)=|J_e(x,y,t)|^2/\eta+\beta\bar{\sigma}^{eff}\dot{\varepsilon}_p \tag{13}$$

where T^t is transient temperature, ρ , λ , C denote the mass density, thermal conductivity and specific heat respectively , W is the heat flux due to the eddy current loss and plastic work, $J_e(x,y,t)$ is the magnitude of the vector of the eddy current, $\bar{\sigma}^{eff}$ is the effective stress of a point in the plate, $\dot{\varepsilon}^p$ is the plastic strain rate. β is a coefficient usually in the range of 0.85~0.95

The initial value of temperature and the insulating thermal boundary can be expressed as

$$T^t(x,y,z)=T^0(x,y,z)\ ,\quad \frac{\partial T^t(M,t)}{\partial n}|_{M\in\Gamma}=0 \tag{14}$$

where M is a point in the boundary Γ , n is the normal direction of the thermal boundary.

3 Numerical Approach

3.1 The eddy current and magnetic field

With the aid of the Garlerkin finite element method, the Eqs.(1 - 2) of the eddy current of the plate, can be stated in a discrete form as [8,10]

$$\mathbf{K}^{ec}\mathbf{T}+\mathbf{P}\frac{\partial\mathbf{T}}{\partial t}=F^{ec}(\mathbf{B}_0(t),\dot{\mathbf{w}}) \tag{15}$$

in which, $\mathbf{K}^{ec}$ is the total magnetic stiffness matrix; $\mathbf{P}$ is the stiffness matrix related to magnetic flux induced by the eddy current, $\mathbf{F}^{ec}(\mathbf{B}_0,\mathbf{w})$ is the column matrix of the force related to the applied magnetic field.

In order to deal with Eq. (15), the Crank-Nicolson's method [8] is employed here for the time integration to reform the finite element formulation of Eq. (15) as

$$(\frac{\mathbf{P}}{\Delta t}+(1-\theta)\mathbf{K}^{ec})\mathbf{T}_{n+1}=(\frac{\mathbf{P}}{\Delta t}-\theta\mathbf{K}^{ec})\mathbf{T}_n+\theta\mathbf{F}^{ec}(\mathbf{B}_{0z},\mathbf{w})_n+(1-\theta)\mathbf{F}^{ec}(\mathbf{B}_{0z},\mathbf{w})_{n+1} \tag{16}$$

in which θ is a relax factor satisfied with $0 < \theta < 1$.

After calculation of the eddy current vector potential component $\mathbf{T}$ for all discrete points, the magnetic force F_x, F_y, F_z can be calculated by Eq. (4) in sequence.

3.2 Transient dynamic response of elastic-plastic plate

From the principle of virtue work, one can easily get the finite element formulation of the dynamic equation of the plates as

$$\mathbf{M}\ddot{\mathbf{u}} + \mathbf{C}\dot{\mathbf{u}} + \mathbf{P}^{\text{int}} = \mathbf{F}(\mathbf{T}) \tag{17}$$

where $\mathbf{u} = \{u, v, w\}$ is the displacement vector, $\mathbf{C}$ is the damping matrix. $\mathbf{P}^{\text{int}}$, $\mathbf{F}$ are the matrices of internal force and external force, respectively.

A central difference method, which is the most popular of the explicit methods in computational mechanics and physics, is employed here to obtain the solution of the dynamic equation of Eq. (17).

3.3 Backward-Euler algorithm for returning mapping to the yield surface

In order to effectively achieve integrating of the flow equation of plastic deformation, a backward-Euler scheme [9] is adopted to update the stresses, the stress changes are related to the strain changes with

$$\dot{\boldsymbol{\sigma}} = \mathbf{Y}(\dot{\varepsilon} - \dot{\varepsilon}_p) \tag{18}$$

where $\mathbf{Y}$ is the elastic constant matrix. The increment of the strain and stresses at the respective iteration are described as [9]

$$d\varepsilon_{i+1}^{pl} = \frac{f_i - \mathbf{a}^T\mathbf{Q}^{-1}\mathbf{r}_i}{\mathbf{a}^T\mathbf{Q}^{-1}\mathbf{Y}\mathbf{a} + H'} \qquad d\boldsymbol{\sigma}_{i+1} = -\mathbf{Q}^{-1}\mathbf{r}_i - d\varepsilon_{i+1}^{pl}\mathbf{Q}^{-1}\mathbf{Y}\mathbf{a} \tag{19}$$

where $\mathbf{a} = \dfrac{\partial f}{\partial \boldsymbol{\sigma}}$, H' is the hardening parameter, $\mathbf{r}_i$ is residual vector, $\mathbf{Q} = (\mathbf{I} + \Delta\varepsilon_i^{pl}\mathbf{Y}\dfrac{\partial \mathbf{a}}{\partial \boldsymbol{\sigma}})$.

3.4 Finite element formulation of the heat transfer

Similar to the approach for the eddy current, we can easily derive the finite element formulation for a thermal conductive problem as

$$\mathbf{C}^{et}\frac{\partial \mathbf{T}^{temp}}{\partial t} + \mathbf{K}^{et}\mathbf{T}^{temp} = \mathbf{R}^{et} \tag{20}$$

in which $\mathbf{C}^{et}$ is the thermal specific matrix, $\mathbf{K}^{et}$ is the stiffness matrices related with the thermal conduction and $\mathbf{R}^{et}$ is the heat flux matrix related to the heat flux

As mentioned previously in the analysis on the eddy current, the Crank-Nilcoson's method can be used to deal with the heat transfer problem

4 Results and discussions

In the follow simulations, the length, the width and thickness of plate are assigned as $a = b = 0.15m$, $h = 0.003m$. The mass density, the specific heat density, the electric conductivity, the thermal conductivity are set as
$\rho = 7800kg/m^3$, $\eta = 4.532 \times 10^6$ S/m, $\rho C = 1.2 \times 10^6\ (J/m^3K)$, $\lambda = 404.0\ (W/mK)$.

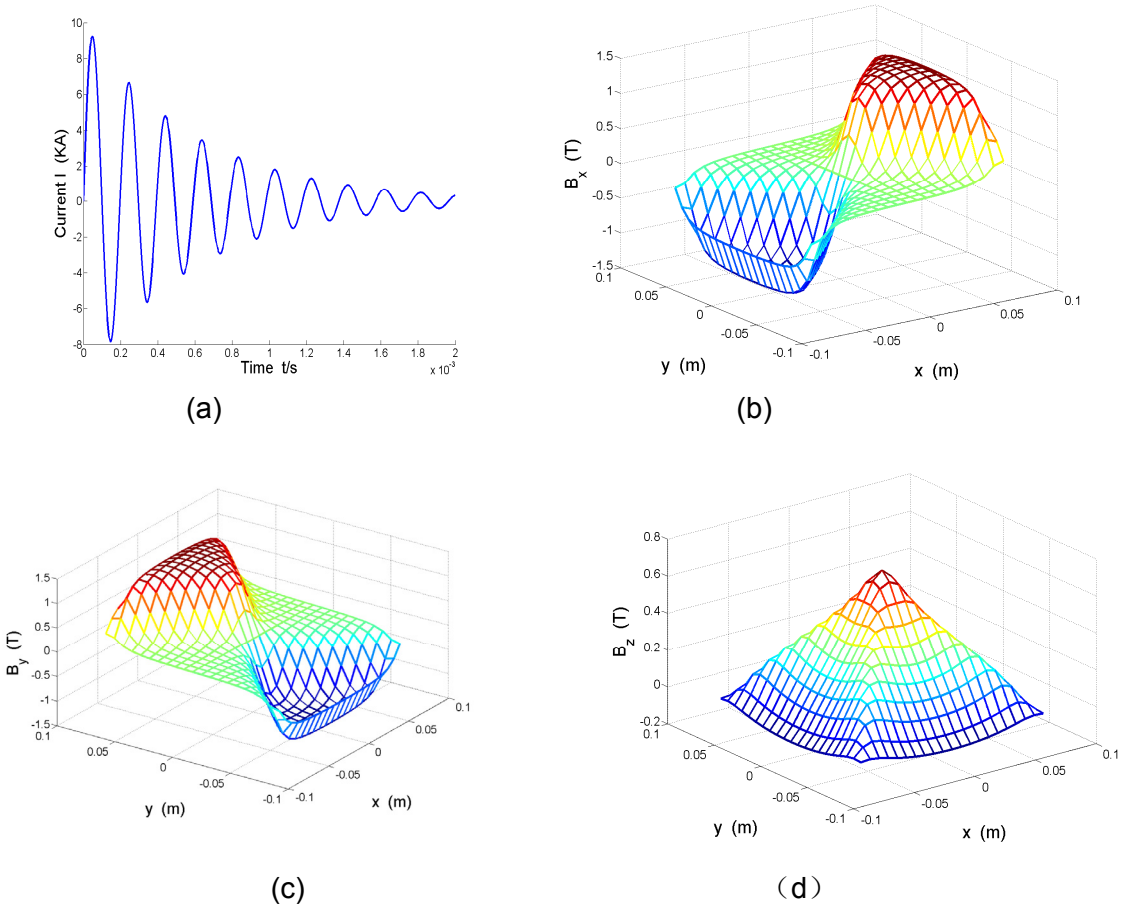

Figure 2. The magnetic field of coils with electric current: (a) the applied current in coils; (b) the x-directional component of the magnetic field; (c) the y-directional component of the magnetic field; (d) the z-directional component of the magnetic field

Now we assume that the applied magnetic field is generated by the rectangular coils with carrying electric current, and approximate theoretical formulae of the magnetic fields of coils with electric current as given in [11]. Figure 2 shows the characteristics of the

applied current and the magnetic field produced by the rectangular coils with electric current, respectively. The distance between the plane of the coils and the plane that we investigated is $z = 0.01m$. The applied current in the coils varies with time as shown in Figure 2(a) expressed as a decaying periodic function $I = I_0 \exp(-t/\tau)\sin(\omega t)$. In the simulation, we set $I_0 = 10kA$, $\tau = 6\times10^{-4}$, $\omega = 3.0\times10^{4}$, turns of coil $N = 10$, The distribution characteristics of the x-, y-, z-direction of the magnetic field B_{0x}, B_{0y} and B_{0z} are plotted in Figures 2(b), (c), (d) respectively. It can be found that B_{0x}, B_{0y} are skew-symmetric to the $x = 0$ and $y = 0$, respectively, while B_{0z} is symmetric to $x = y$ and $x = -y$.

Figure 3 displays the influence of the strain rate on the deformation at the location (a/2, b/2) of the conductive plate which is made up of SGACD, SPCC and TRIP60. The material parameters of SGACD, SPCC and TRIP60 are given in [12, 13]. It can be found for those conductive plates, whose materials are sensitive to strain rate such as SGACD, SPCC that the influence of the strain rate on the deformation of plates is significant and thus the strain rate effect should be considered in the quantitatively simulation or experiments in the EMF process. However, for those plates whose material is less sensitive to the strain rate such as TRIP60, the influence is small and can be neglected in the forming process. On the other hand, the deformation of plates under consideration of the strain rate effect is smaller than that without considering the strain rate effect.

Figure 4 displays the influence of the different magnetic pulse parameter on the deformation of a plate, τ which is a parameter that governs the attenuation of the applied current in coils and the magnetic field. It is found that with the parameter τ increasing, the deformation of the plate increases remarkably.

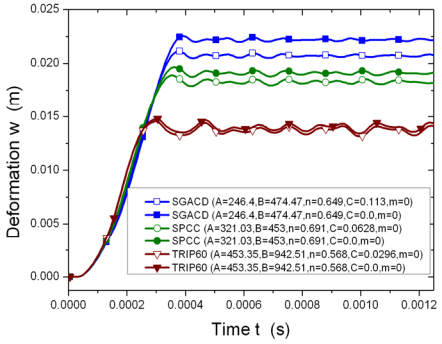

Figure 3. The influence of the strain rate on the deformation of plates

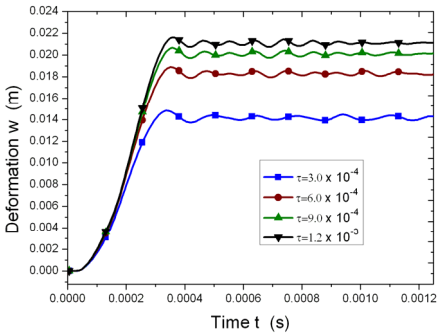

Figure 4. The deformation of a conductive plate of with different pulse parameters

Figure 5 displays the plastic strain at the point (a/2, b/2, h/3) of plate varying with the time for the three different materials SGACD, SPCC and TRIP60 with consideration of the strain rate. It can be found that at the beginning the plastic strain is zero, which means the plate only generate the elastic deformation. Then, with the increase of time, the plastic strain increases sharply and quickly reaches a constant value for the conductive plates. In addition, it can be found that under the same applied magnetic field, the plastic strain produced in the plate of SGACD is larger than those of the other two materials.

Figure 6 explains the transverse electromagnetic force varying with time. Due to the transverse magnetic force at the middle of plate (a/2, b/2) is almost zero, thus the

transverse magnetic force at the location (3a/32, b/2) is shown in this figure. It is interesting to note that the frequency of electromagnetic force is twice of that for the applied current and the value of electromagnetic force is almost positive.

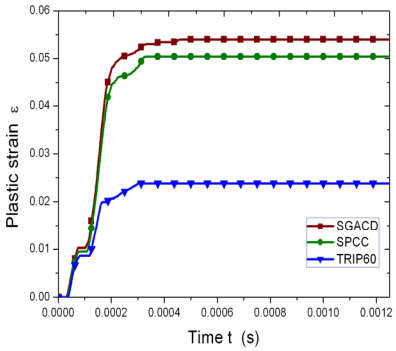

Figure 5. The strain at (a/2, b/2,-h/3) *of plate varying with time*

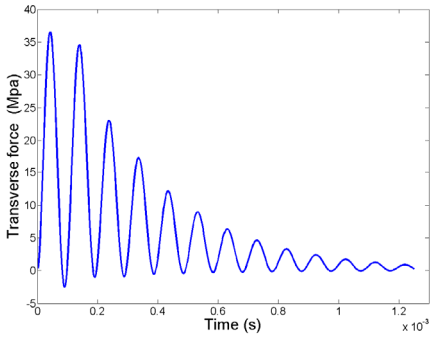

Figure 6. the electromagnetic force with respect to time

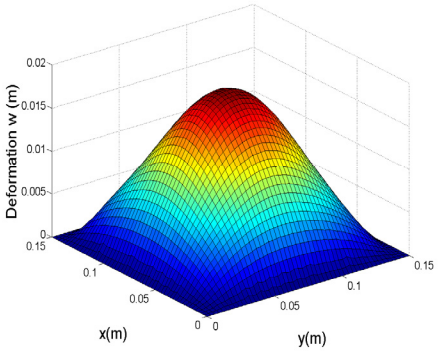

Figure 7. Configuration of conductive plate

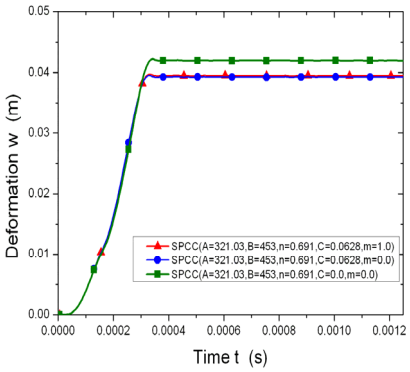

Figure8. The effect of the strain rate and temperature on the deformation

Figure 7 displays the configuration of the conductive plate under the magnetic pulse ($t = 1.25 \times 10^{-3}$ s), which shows rather smooth deformation.

Figure 8 displays the effect of the temperature and the strain rate on the deformation at (a/2, b/2) of the plate, respectively. It can be found that the effect of the strain rate on the deformation is larger than that of the temperature effect. The deformation of the conductive plate with consideration temperature effect is almost the same as that of the plate without consideration of the temperature effect in our case study.

5. Conclusions

The electro-magnetic thermo-elasto-plastic dynamic response of a rectangular conductive plate has been studied with consideration of the coupling between the mechanical behaviours, thermal field and electro-magnetic field. The study investigated the effect of the plastic strain rate and the temperature on the transient dynamic response or the deformation of conductive plates under a magnetic field produced by the coils with electric current. Numerical simulations of the conductive plates in this paper provide the

characteristics of applied magnetic field produced by the coils, the dynamic response curves, the configuration, the distribution of eddy current and the temperature varying with the time. The numerical results demonstrate that the strain rate effect should be considered in the electro-magnetic forming process and the temperature effect on the deformation is smaller than that of the strain rate and could be neglected in EMF processes.

References:

[1] *Unger, J., Stiemer, M., Svendsen, B., Blum, H.*: Multifield modeling of electromagnetic metal forming processes. J. Mater. Process. Technol. **177**, 2006, p.270–273.

[2] *Fenton, G.K., Daehn, G.S.*: Modeling of electromagnetically formed sheet metal. J. Mater. Process. Technol. **75**, 1998, p.6–16.

[3] *Song, F.M., Zhang, X., Wang, Z.R., Yu, L.Z.*: A study of tube electromagnetic forming. J. Mater. Process. Technol. **151**, 372–375 (2004)

[4] Bahmani, M.A., Niayesh, K., Karimi, A.: 3D Simulation of magnetic field distribution in electromagnetic forming systems with field-shaper. J. Mater. Process. Technol. **209**, 2009, p.2295–2301.

[5] *Thomas, J.D., Seth, M., Daehn, G.S., Bradley, J.R., Triantafyllidis, N.*: Forming limits for electromagnetically expanded aluminum alloy tubes: Theory and experiment. Acta Mater. **55**,2007, p.2863–2873

[6] *Unger, J., Stiemer, M., Schwarze, M., Svendsen, B., Blum, H., Reese, S.*: Strategies for 3D simulation of electromagnetic forming processes. J. Mater. Process. Technol. **199**, 2008, p.341–362

[7] *Zhou, Y.H., Zheng, X.J.*: The electromagnetic solid structural mechanics. Science Press, Beijing (in Chinese),1999

[8] *Takagi, T., Hashimoto, M., Arita., S., Norimatsu, S., Sugiura, T., Miya, K.*: Experimental verification of 3D eddy current analysis code using T-method. IEEE T. Magn. **26**, 1990. p.474–477

[9] *Crisfield, M.A.*: Non-linear finite element analysis of solids and structures. John wiley & Sons, Chichester,1991

[10] *Hashizume, H., Kurusu, T., Toda, S.*: Numerical simulation of current distribution in type-II superconductors based on T-method. Int. J. Appl. Electrom. Mater. **3**, 1993, p.205–213

[11] *Tsopelas, N., Siakavellas, N.J.*: Performance of circular and square coils in electromagnetic–thermal non-destructive inspection. NDT & E Int. **40**, 2007,p.12–28

[12] *Huh, H., Kim, S.B., Song, J.H., Lim, J.H.*: Dynamic tensile characteristics of Trip-type and DP-type steel sheets for an auto-body. Int. J. Mech. Sci. **50**, 2008,p.918–931

[13] *Huh, H., Kang, W.J., Han, S.S.*: A tension split hopkinson bar for investigating the dynamic behavior of sheet metals. Exp. Mech. **42**,2002, p.8–17

SESSION 8

PROCESS TECHNOLOGIES (FORMING)

Experimental Investigations on the Optimum Driver Configuration for Electromagnetic Sheet Metal Forming*

S. Gies[1], C. Weddeling[1], A. E. Tekkaya[1]

[1] Institute of Forming Technology and Lightweight Construction, TU Dortmund University, Baroper Str. 301, 44227 Dortmund, Germany

Abstract

Electromagnetic forming is a high speed forming process especially suitable for materials with high electrical conductivity such as copper or aluminum. In case of materials with comparatively low electrical conductivity (e.g. stainless steel or titanium) the use of so-called driver sheets is a common approach. Various publications proved that this way materials with low electrical conductivity and even non-conductive materials can be formed. Although the use of driver sheets is common practice, there are no or only contradicting recommendations regarding the optimum driver sheet configuration.
Based on experimental investigations of the electromagnetic sheet metal forming process, this paper investigates the optimum material and thickness of the driver sheet. The results prove that aluminum should be favored over copper as driver material. The optimum driver thickness was found to be dependent on thickness and electrical conductivity of the workpiece. Even in case of a workpiece made of aluminum the use of a driver sheet could enhance the efficiency of the process.

Keywords

Electromagnetic forming, sheet metal forming, driver materials

---

* *This work is based on the results of the transfer project TE508/34-1 within the research group PAK343 which is kindly supported by the German Research Foundation (DFG). Thanks also to the industry partners TRUMPF Werkzeugmaschinen GmbH + Co. KG, TRUMPF Hüttinger GmbH + Co. KG, and Outokumpu Nirosta GmbH for their participation and intensive support within the transfer project.*

1 Introduction

Electromagnetic forming is a high speed forming process using pulsed alternating magnetic fields for a contact-free application of forces to the workpiece. Referring to WINKLER [1], the repelling force between workpiece and coil decreases with decreasing electrical conductivity of the workpiece. This hinders or completely prevents electromagnetic forming of materials with low electrical conductivity such as stainless steels or titanium.
The dependency of the magnetic forces on the electrical conductivity can be attributed to the smaller amount of eddy currents induced into the workpiece. This, in turn, weakens the shielding of the primary magnetic field so that the field penetrating through the workpiece increases. An indicator for the shielding is the ratio of workpiece thickness t_W to skin depth σ_S. Taking into account the discharge frequency f as well as electrical conductivity κ and permeability μ, the skin depth is defined as follows:

$$\sigma_s = \sqrt{\frac{1}{\pi \cdot f \cdot \kappa \cdot \mu}} \tag{1}$$

To ensure that the amount of the penetrating field is sufficiently small, the ratio t_W/σ_S should be at least 1.5 [2]. Assuming a given workpiece geometry and material and taking into account the definition of the skin depth σ_S according to Eq. (1), this ratio can only be affected by increasing the discharge frequency f. BELYY ET AL. [3] recommend frequencies between 60 and 100 kHz to form low conductive materials. But, as the discharge frequency is an inherent characteristic of pulse generator and tool coil, this value is not adjustable by the user.
An alternative concept to form materials with low electrical conductivity and even non-conductive materials was introduced by WEIMAR [4]. By placing an additional sheet with high electrical conductivity between workpiece and tool coil (see Figure 1a), hereinafter referred to as driver sheet, a good shielding of the primary magnetic field is attained. Consequently, a large amount of magnetic force is acting on the driver sheet. Due to the contact between driver sheet and workpiece this force is mechanically transferred to the workpiece. If the equivalent stresses in driver sheet and workpiece arising from the magnetic force exceed their yield stress, both parts are formed simultaneously.

2 Driver Sheets in Electromagnetic Forming

When it comes to process design for driver-assisted electromagnetic forming operations three questions arise:

1. Is a driver sheet necessary?
2. Which is the best driver material?
3. Which is the optimum driver thickness $t_{D,opt}$?

Regarding the first point, WEIMAR [4] recommends the use of driver sheets if the electrical conductivity of the workpiece κ_W is below 20 % to 10 % than the one of copper. This equates to a value between 11.2 and 5.6 MS/m. Assuming a discharge frequency f in the

range of 10 – 20 kHz, BELYY ET AL. [3] define a threshold value of about 14 MS/m. Neither of them gives an explanation for their recommendation. However, these values correspond to the publications on driver-assisted electromagnetic sheet metal forming summarized in Table 1. Here, the electrical conductivity of the workpiece material is in the range of 10 MS/m (DC04) to 1 MS/m (Titanium).

#	Workpiece		Driver		t_D/σ_S	Ref.
	Material	**Thickness t_W**	**Material**	**Thickness t_D**		
1	DC04	0.80 mm	Copper	0.65 mm	1.0	[5]
2	Titanium	0.50 mm	Copper	0.65 mm	1.0	[5]
3	DP600	0.70 mm	Copper	0.60 mm	0.90	[6]
4	Ti-6AL-4V	0.50 mm	CU-DHP	0.50 mm	0.82	[7]
5	X5-CrNi18-10	0.15 mm	EN AW-1050	0.30 mm	0.73	[8]
6	X5Cr-Ni-Mo17-12-2	0.25 mm	Copper	0.10 mm	0.22	[6]
7	X12CrMn-NiN17-7-5	0.08 mm	Copper	0.15 mm	n/a	[9]
8	Titanium	0.08 mm	Copper	0.15 mm	n/a	[9]
9	Carbon steels	0.15 – 0.3 mm	EN AW-6111	1.0 mm	n/a	[10]
10	AZ31B-O (Mg)	0.55 mm	Aluminum	n/a	n/a	[11]
11	Titanium CP-1	0.50 mm	Aluminum	n/a	n/a	[11]

Table 1: *Publications focussing on driver-assisted electromagnetic sheet metal forming*

The material most suitable for the driver sheet has to meet two requirements at once: A high electrical conductivity and a low yield stress. The high electrical conductivity is necessary to ensure a good shielding of the magnetic field. The low yield stress should minimize the forming energy consumed by the driver so that the energy ratio available for the workpiece is increased. Based on this theoretical consideration, aluminum and copper seem to be proper materials. Since copper has a higher electrical conductivity but also a higher yield stress compared to a low alloyed aluminum, an ordinal comparison of copper and aluminum is not possible without further theoretical or experimental investigations. While BELYY ET AL. [3] recommend annealed copper as driver material, DENGLER AND GLOMSKI [12] claim that aluminum should be favored. None of these two contradicting recommendations is based on investigations and the authors do not explain their suggestion. Only DESAI ET AL. [13] gave a comparison of aluminum and copper drivers based on a numerical simulation. The results prove that in case of a workpiece made of stainless steel (κ_W = 1.1 MS/m) the copper driver causes the highest Lorentz forces whereas the aluminum driver leads to the highest collision velocity. As the investigations of DESAI ET AL. focus on the magnetic pulse welding process they conclude that aluminum drivers should be favored. However, this does not necessarily mean that aluminum is also the best choice for electromagnetic forming processes which are rather energy-based than based on the collision velocity. Also the publications listed in Table 1 do not show a clear dominance regarding the driver material used.

A proper thickness of the driver sheet t_D is likewise important for the efficiency of driver-assisted forming processes as the driver material. According to SANO ET AL. [14], there is an optimum value for the driver thickness t_D. In case of a too thin driver sheet the induced eddy currents and, consequently, the resulting Lorentz force acting in the driver are comparatively small. If the driver thickness exceeds the optimum value, only a slight

increase of the Lorentz forces can be observed. As this slight increase cannot compensate the increase of energy required for the deformation of the driver, the remaining forming energy for the workpiece decreases.
Recommendations regarding the optimum driver thickness are contradictory. TILLMAN ET AL. [5] as well as SANO ET AL. [14] recommend a driver thickness t_D equal to the skin depth σ_S. BELYY ET AL. [3] claim that the optimum driver thickness equates to half of the skin depth σ_S. None of these recommendations is proved by experimental investigations. As the authors do not even give an explanation justifying their suggestions, their recommendations must be treated as hypothesis. Only the recommendations given by DESAI ET AL. [13] are based on numerical results. According to their simulation the optimum thickness of an aluminum driver is $0.83 \cdot \sigma_S$ whereas a driver made of copper should have a thickness equal to the skin depth σ_S. For several reasons the validity of these results is doubtful and needs further verification. On one hand the recommendations are based on the observation, that the absolute optimum thickness for copper and for aluminum drivers is identical and equates to $t_D = 0.5$ mm. This result is questionable as the higher electrical conductivity as well as the higher yield strength of copper must cause a smaller optimum thickness compared to the one of aluminum. The failure might be caused as only three driver thicknesses (0.25, 0.5, and 1 mm) have been simulated. This very coarse step size makes it nearly impossible to identify differences in the optimum thickness of copper and aluminum, leading to the wrong assumption that the optimum values are identical. On the other hand, experimental verification of the numerical results was realized by comparison of the joint quality in magnetic pulse welding experiments. Even if an ordinal comparison of the collision velocity based on the joint quality is possible, it does not give an exact value of the deviation between numerical and experimental collision velocity. Also the publications listed in Table 1 prove that there is insufficient knowledge about the proper driver thickness. The wide range of values between $0.22 \cdot \sigma_s$ and σ_s cannot just be attributed to different workpiece properties and thicknesses. The workpiece material in line #5 and #6, for example, is quite similar, but the chosen drive thickness varies by a factor of more than 3.
The investigations discussed so far prove that there is no clear recommendation regarding material and thickness of driver sheets verified by experimental results. Both parameters are crucial for the efficiency of driver-assisted forming operations.
In this paper copper and aluminum drivers are compared by experimental investigations on the electromagnetic sheet metal forming process. The optimum thickness is determined for both driver materials. The effect of variations in charging energy, workpiece material, and workpiece thickness on the optimum driver thickness is investigated.

3 Experimental Setup and Procedure

The setup used for the experimental investigations is depicted in Figure 1a. Instead of a closed die only a drawing ring was used to facilitate free forming of the workpiece and the driver (Figure 1b). A flat forming coil with n = 7 turns and an outer diameter of d_o = 65 mm was used. The coil was connected to a Maxwell Magneform pulse generator. Two capacitor banks with a total capacitance of C = 629 µF and a maximum charging voltage of U = 8 kV were selected. Inner inductance and inner resistance of the chosen pulse

generator configuration equate to L_i = 60 nH and R_i = 4.2 mΩ respectively, leading to a short circuit frequency of f = 25 kHz.

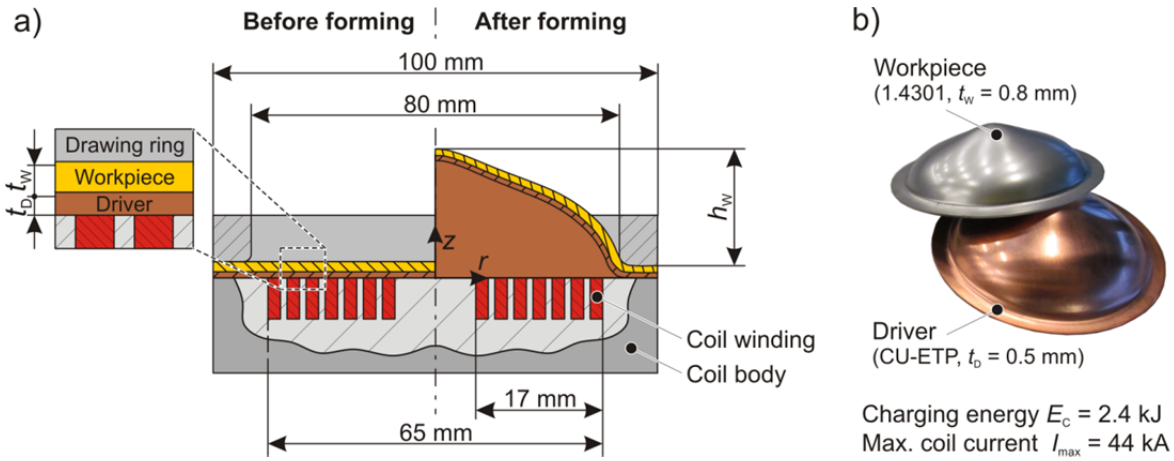

Figure 1: *a) Experimental setup for free forming experiments b) Workpiece and driver sheet after electromagnetic forming process*

Two stainless steels and one cold-rolled low carbon steel were used as low conductive workpiece materials. Additionally, the wrought aluminum alloy EN AW-5083 was used to analyze the effect of the electrical workpiece conductivity κ_W on the optimum driver thickness. With the exception of EN AW-5083 the workpiece thickness was varied from 0.5 to 1.0 mm. The wrought aluminum alloy EN AW-1050A and the copper alloy CU-ETP (CW004A) were used as driver materials. For the experiments with low conductive workpiece materials the driver thickness was varied in the range of 0.3 mm to 2.0 mm (see Table 2). To identify the comparatively small optimum thickness when using the aluminum alloy EN AW-5083, additional drivers with a thickness of 0.05, 0.1, 0.15, 0.2, and 0.25 mm were used. Within all experiments workpiece and driver sheet had a constant outer diameter of d = 100 mm. Mechanical and electrical properties of the workpiece and driver materials are summarized in Table 2.

Material	Elec. conductivity κ in MS/m	Yield stress k_f in MPa	Density ρ in kg/dm³	Thickness t in mm
1.4301 (X5CrNi18-10)	1.4	290	7.90	0.5, 0.8, 1.0
1.4509 (X2CrTiNb-18)	1.5	315	7.70	
1.0338 (DC04)	8.2	199	7.85	
EN AW-5083 (AlMg4.5Mn)	16	162	2.66	1.0
EN AW-1050A (AL 99.5)	34	107	2.70	0.3, 0.5, 0.7
CW004A (CU-ETP)	56	229	8.93	0.8, 1.0, 2.0

Table 2: *Electrical, mechanical, and geometrical properties of workpiece and driver materials*

After the electromagnetic forming operation the bulge height h_W of the workpiece is measured (see Figure 1a). This parameter is used to evaluate the quality of a driver configuration. To eliminate the effect of a varying discharge frequency *f,* the driver thickness t_D is divided by the corresponding skin depth σ_S. The dimensionless value obtained this way is used in the following presentation and discussion of the results.

4 Results and Discussion

4.1 Effect of driver material and charging energy

In Figure 2a the bulge height h_W for the stainless steel 1.4301 is plotted against the specific driver thickness t_D/σ_S. Due to nearly identical curves the relevant parameters $t_{D,opt}/\sigma_S$ and $h_W(t_{D,opt})$ for the ferritic stainless steel 1.4509 are summarized in Figure 2b.

a)

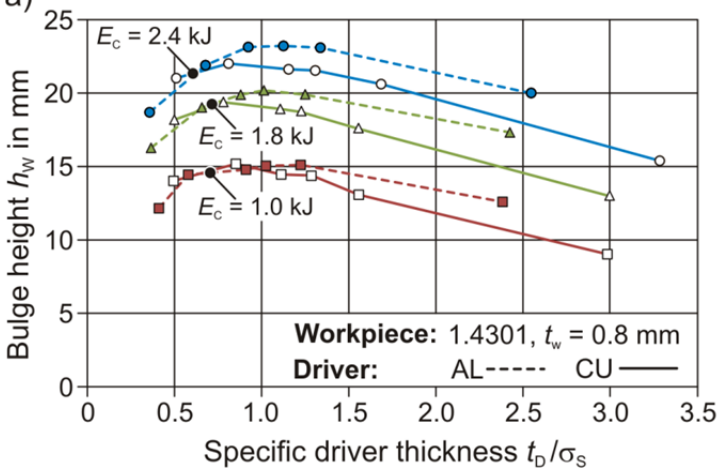

b)

Workpiece:		1.4509, t_w = 0.8 mm			
		$\frac{t_{D,opt}}{\sigma_s}$		$h_W(t_{D,opt})$ in mm	
Driver:		AL	CU	AL	CU
Charging energy E_c	1.0 kJ	1.06	0.81	14.03	13.68
	1.8 kJ	1.05	0.80	19.01	17.76
	2.4 kJ	1.24	0.83	22.00	20.78

Figure 2: *Bulge height h_W for the stainless steels a) 1.4301 (austenitic) and b) 1.4509 (ferritic) (workpiece thickness t_W = 0.8 mm, charging energy E_C = varied)*

The curves shown in Figure 2a prove the existence of an optimum value for the driver thickness as stated by SANO ET AL. [14]. This general course of the curves was observed for all investigated combinations of charging energy, driver material, workpiece material, and workpiece thickness.

Summarizing the results of the two stainless steels (see Figure 2), the optimum specific thickness for aluminum drivers ranges between 1.01 and 1.13 with an average value of 1.06. In case of the copper driver the values are in the range of 0.78 to 0.85 with an average value of 0.81. The effect of differences in the electrical conductivity of the driver materials is eliminated in the definition of the specific driver thickness by consideration of the skin depth σ_S. The fact that there is still a difference in the optimum specific thickness for aluminum and copper can consequently be attributed to the differences in the mechanical properties of the two driver materials (see Table 2). A rough definition of the maximization problem which can be used to explain this correlation is given in Eq. (2). This approach takes the magnetic pressure acting on driver $p_{m,D}$ and the pressure required for plastic deformation of the driver sheet $p_{p,D}$ into account. Additionally the magnetic pressure acting on the workpiece $p_{m,W}$ is considered.

$$\max_{t_D} \frac{p_{m,D} + p_{m,W}}{p_{p,D}} \tag{2}$$

In case of the results given in Table 2 the parameter $p_{m,W}$ can be neglected as the electrical conductivity of the workpiece material is sufficiently small. Thus the optimum driver thickness is defined by the following condition:

$$\left|\frac{\partial p_{m,D}}{\partial t_D}\right| = \left|\frac{\partial p_{p,D}}{\partial t_D}\right| \tag{3}$$

According to the eddy current distribution obtained by WERDELMANN [15] given in Eq. (4), the current density $J(z)$ is decreasing monotonically along the driver thickness. This means that the current is concentrating in the surface-near region of the driver sheet.

$$J(z)/J(z=0) = cosh\left[(1+i)\frac{z-t_D}{\sigma_s}\right] \Big/ cosh\left[(1+i)\frac{t_D}{\sigma_s}\right] \tag{4}$$

Consequently, an asymptotic course as shown in Figure 3a can be assumed for the magnetic pressure $p_{m,D}(t_D)$. This, in turn, means that the function $f(t_D) = \partial p_{m,D}/\partial t_D$ is decreasing monotonically (see Figure 3b).
Referring to JONES [16], the yield pressure for the circular driver plate $p_{p,D}$ is proportional to its yield stress $k_{f,D}$ and to the square of its thickness t_D. Regardless of the detailed definition of $p_{p,D}$ the derivate of this function with respect to the driver thickness is consequently a straight line, as shown in Figure 3b. Assuming a modification of the driver yield stress $k_{f,D}$, a shift of the intersection point as shown in Figure 3b occurs. Consequently, a higher yield stress causes a decreasing optimum driver thickness and vice versa.

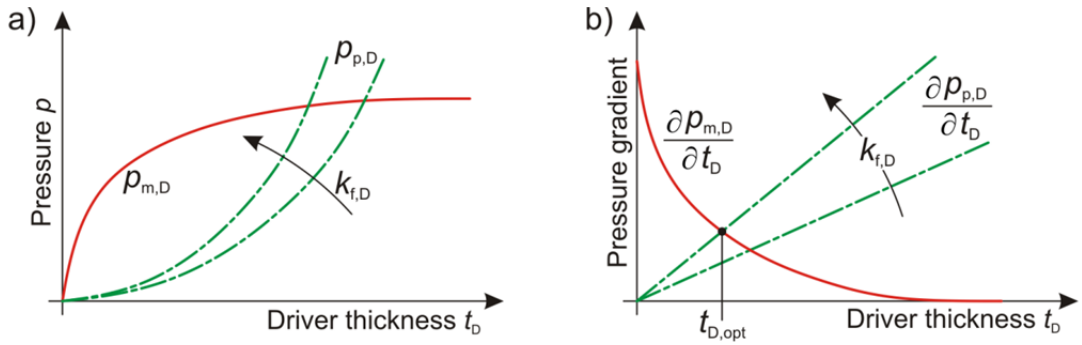

Figure 3: *Effect of driver material yield stress $k_{f,D}$ on the optimum driver thickness $t_{D,opt}$*

These results prove that recommendations for the optimum thickness always need to refer to a specific driver material. General recommendations as given by TILLMAN ET AL. [Til08], SANO ET AL. [San86], and BELYY ET AL. [Bel77] can only be a rough rule of thumb.
The results in Figure 2 show that the optimum driver thickness is not affected by the charging energy E_C, but that it is a crucial parameter when it comes to the choice of the driver material. In case of the smallest charging energy E_C = 1 kJ copper and aluminum drivers reach nearly identical maximum workpiece heights. In case of increased charging energies (E_C = 1.8 kJ and 2.4 kJ) the driver made of aluminum gives higher maximum values. This effect can be attributed to the increasing effective strain $\bar{\varphi}$ in workpiece and driver caused by the higher charging energy. This higher strain, in turn, entails an increase of the forming energy consumed by the driver sheet. Owing to the higher yield stress (see Table 2) the additional energy consumed by the driver sheet is higher in case of copper compared to aluminum. Accordingly, aluminum should be favored as driver material for forming operations with high effective strains. In case of calibration or coining

processes copper should be preferred instead as the negative effect of the higher yield stress is not that pronounced because of the small effective strains. In case both driver materials give identical forming heights (here: E_C = 1 kJ) the decision about the driver material should be based on economic considerations. In this case aluminum should be preferred as the costs for a copper driver are on average by factor 7 higher.

4.2 Effect of workpiece thickness and workpiece material

A variation of the workpiece thickness t_W was conducted for the three low conductive workpiece materials 1.4301, 1.4509, and DC04. To reach similar bulge heights h_W, the charging energy E_C was increased when increasing the workpiece thickness and vice versa. The results are summarized in Figure 4a.

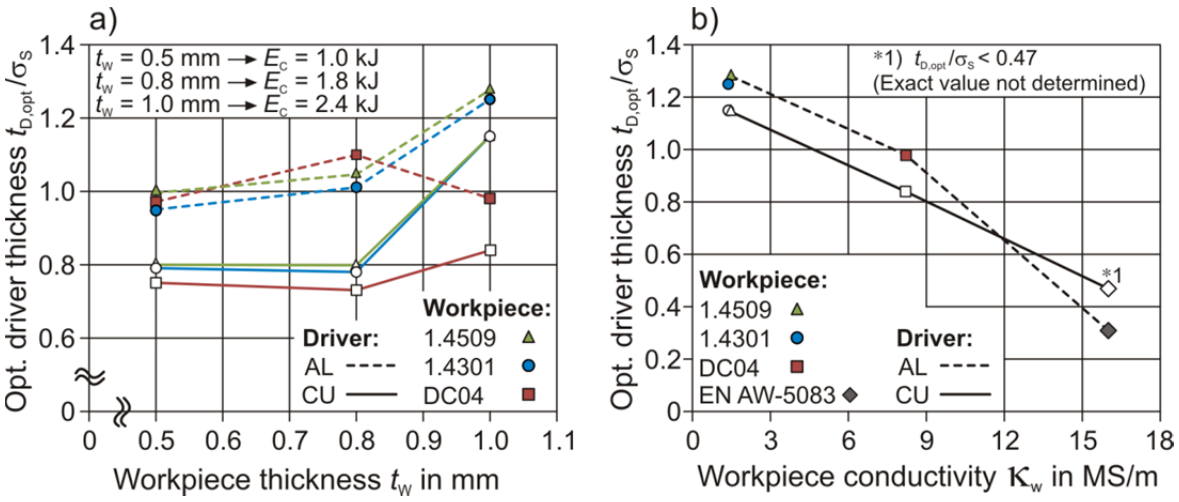

Figure 4: *Effect of a) workpiece thickness t_W and b) electrical workpiece conductivity $\boldsymbol{\kappa_W}$ on optimum specific driver thickness $t_{D,opt}/\boldsymbol{\sigma_S}$*

The results in Figure 4a reveal that the optimum driver thickness $t_{D,opt}$ tends to increase with increasing workpiece thickness t_W. An exception to that is the optimum thickness for DC04 using aluminum drivers. Consequently, no general recommendation for the adoption of the driver thickness in case of a varying workpiece thickness can be derived.
The results of the workpiece material variation are summarized in Figure 4b and show a clear correlation between workpiece material and optimum driver thickness. The optimum driver thickness $t_{D,opt}$ decreases with increasing electrical conductivity of the workpiece, regardless of the driver material. Consequently, the optimum driver thickness for the highly conductive aluminum alloy EN AW-5083 is significantly smaller than the optimum value for the low conductive stainless steels. The optimum thickness for EN AW-5083 using a copper driver is even smaller than the upper bound shown in Figure 4b. The exact value could not be determined due to a minimum copper sheet thickness of 0.3 mm which was not thin enough to reach the optimum. The correlation between optimum driver thickness and electrical workpiece conductivity can be explained considering the maximization problem defined in Eq. (2) by the following line of arguments: If the electrical conductivity of the workpiece is increased the shielding of the magnetic field penetrating through the driver is enhanced. This means that the pressure $p_{m,W}$ increases if all other

parameters remain equal (see Figure 5a). Consequently, the curve describing the sum of the magnetic pressure acting on driver $p_{m,D}$ and workpiece $p_{m,W}$ is shifted, as shown in Figure 5a. Due to this shift the derivate of this function with respect to the driver thickness decreases (see: Figure 5b). As the function $g(t_D) = \partial p_{p,D}/\partial t_D$ is not affected by a change of the workpiece conductivity the intersection point and, thus, the optimum driver thickness is shifted to a smaller value.

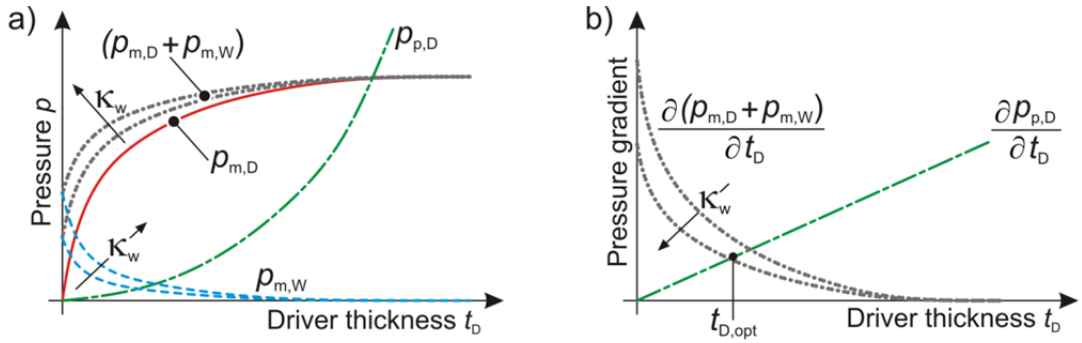

Figure 5: *Effect of electrical workpiece conductivity κ_W on the optimum driver thickness $t_{D,opt}$*

Beside this negative correlation of workpiece conductivity and optimum driver thickness the driver-assisted forming using a workpiece made of EN AW-5083 revealed that a proper driver sheet configuration can even enhance the forming of a workpiece material with high electrical conductivity. Without a driver sheet the bulge height of the aluminum workpiece was measured to be h_W = 27.15 mm in contrast to a maximum value of h_W = 28.18 mm in case of a driver-assisted process.

5 Conlusions

- The optimum specific driver thickness t_D/σ_S depends on the workpiece conductivity κ_W and on the yield stress $k_{f,D}$ of the driver material. Both parameters show a negative correlation.
- In case of forming operations with high effective strains aluminum should be preferred as driver material. In case of low effective strains (e.g. calibration or coining processes) copper drivers should be favored.
- Charging energy E_C and the amount of effective strain $\bar{\varphi}$ do not affect the optimum specific driver thickness.
- Even in case of workpiece materials with sufficiently high electrical conductivity for electromagnetic forming the use of a driver can enhance the forming process.

References

[1] *Winkler, R.:* Hochgeschwindigkeitsbearbeitung – Grundlagen und technische Anwendung elektrisch erzeugter Schockwellen und Impulsmagnetfelder. VEB-Verlag Technik, Berlin, 1973.

[2] *T Dietz, H.; Lippman, H. J.; Schenk, H.:* Theorie des Magneform-Verfahrens: Erreichbarer Druck. Elektronische Zeitschrift, Ausgabe A, Volume 88 (1967), Issue 9, pp. 217–222.

[3] *Belyy, I. V.; Fertik, S. M.; Khimenko, L. T.:* Spravochnik Po Magnitno-impul' Snoy Obrabotke Metallov (engl.: Electromagnetic Metal Forming Handbook), 1977. English translation by M. M. Altynova. Available at: http://www.matsceng.ohio-state.edu/~daehn/metalforminghb (shown on 04.02.2014).

[4] *Weimar, G.*: Hochgeschwindigkeitsbearbeitung III – Umformung von Blechen und Rohren durch magnetische Kräfte. Werkstatt und Betrieb, 96 (1963), pp. 893-899.

[5] *Tillmann, W.; Vogli, E.; Nebel, J.; Giemsa, T.:* Funktionsangepasste Schichten für die elektromagnetische Blechumformung. Werkstatttechnik online, Volumen 98 (2008), Issue1/2, pp. 102-108.

[6] *Andersson, R.; Syk, M.:* Electromagnetic Pulse Forming of Carbon Steel Sheet Metal. In: Proceedings of the 3rd International Conference on High Speed Forming – ICHSF 2008, Dortmund, pp. 233-244. Available at: http://hdl.handle.net/2003/27086

[7] *Li, F.; Mo, J.; Zhou, H.; Fang, Y.:* 3D Numerical Simulation Method of Electromagnetic Forming for low conductive metals with a driver. International Journal of Advanced Manufacturing Technology, Volume 64 (2013), Issue 9-12, pp. 1575-1585. doi:10.1007/s00170-012-4124-1

[8] *Ishibashi, M.; Okagawa, K.; Aizawa, T.:* Electromagnetic Bulging of Stainless Steel Sheet by using Flat One-Turn Coil. Materials Science Forum, Volume 673 (2011), pp. 101-106. doi:10.4028/www.scientific.net/MSF.673.101

[9] *Srinivasan, S.; Wang, H.; Taber, G. A.; Daehn, G. S.:* Dimensional Control and Formability in Impact Forming. Proceedings of the 4th International Conference on High Speed Forming – ICHSF 2010 – Columbus, Ohio, USA, pp. 239-249. Available at: http://hdl.handle.net/2003/27180

[10] *Seth, M.; Vohnout, V. J.; Daehn, G. S.:* Formability of steel sheet in high velocity impact. Journal of Materials Processing Technology, Volume 168 (2005), pp. 390-400. doi: 10.1016/j.jmatprotec.2004.08.032.

[11] *Revuelta, A.; Larkiola, J.; Korhonen, A. S.; Kanervo, K.:* High velocity Forming of Magnesium and Titanium Sheets. In: Proceedings of the 10th ESAFORM Conference on Material Forming, pp.157-162.

[12] *Dengler, K.; Glomski, G.:* Die Hochleistungsimpuls-Technik – eine zukunftsträchtige Hochgeschwindigkeits-Umformtechnologie. Bleche Rohre Profile, Volume 38 (1991), Issue 4, pp. 285-286.

[13] *Desai, S. V.; Kumar, S.; Satyamurthy, P.; Chakravartty, J. K.; Chakravarthy, D. P.:* Improvement of performance of Electromagnetic welding process by use of driver materials. International Journal of Applied Electromagnetics and Mechanics, Volume 35 (2011), Issue 2, pp.113-121. doi: 10.3233/JAE-2011-1325.

[14] *Sano, T.; Takahashi, M.; Murakoshi, Y.; Matsuno, K.*: Electromagnetic Forming Method by Use of a Driver. United States Patent, Patent Number: 4,619,127, 1986.

[15] *Werdelmann, P.*: Zielgerichteter Entwurf von Werkzeugsystem und Energiespeicher für die elektromagnetische Blechumformung. Dr.-Ing Thesis, Technische Universität Dortmund, 2009.

[16] *Jones, N.*: Structural Impact. Cambridge University Press, digital version, 2003. ISBN 0 521 62890 3

Control of Velocity, Driving Pressure, and Planarity During Flyer Launch with Vaporizing Foil Actuator*

S.R. Hansen[1], A. Vivek[1], G. S. Daehn[1]

[1] Department of Materials Science and Engineering, The Ohio State University, USA

Abstract

Electrically-driven rapid vaporization of thin conductors produces a high-pressure pulse which can be used to accelerate thin metal sheets to high velocities. Recently, vaporizing foil actuators (VFA) have been applied toward a variety of impulse-based metalworking operations such as collision welding, closed-die forming, embossing, and shearing. To better apply VFA to different purposes, it is necessary to develop an understanding of how variations on the characteristics of the foil actuator affect its mechanical impulse generation. In this work, actuators made out of 0.0508, 0.0762, and 0.127 mm thick full hard temper AA1145 foil were used to launch 0.508 mm thick AA2024-T3 sheets toward a photonic Doppler velocimeter (PDV) probe. Launch velocities ranging between 300 and 1000 m/s were observed over a distance of less than 3 mm, and repeated trials demonstrated repeatable results. Velocity, current and voltage traces were used to examine the effect of deposited energy on average pressure and resulting velocity for foil actuators of various thicknesses. The planarity of the flyer sheets' launch and flight was demonstrated with 0.0762 mm foil actuators by experiments that employed multiple PDV probes simultaneously recording the velocity evolution at different locations across the surface of the flyer.

Keywords

Impulse metalworking, Collision welding, Vaporizing foil actuator (VFA)

---

* *This work was done with the support of the U.S. Department of Energy Award Number DE-PI0000012 and the ALCOA Foundation's Advancing Sustainability Research Initiative.*

1 Introduction

Rapid discharge of a high voltage through a thin metal conductor results in the rapid vaporization of the conductor, creating a high-pressure pulse around it as the gases expand. Typically, the source of the electrical discharge is a capacitor bank, and the conductor is a thin foil or wire, referred to in this work as a vaporizing foil actuator (VFA). The impulse produced can be used to accelerate metal workpieces to velocities on the order of 1 km/s, within a distance of only a few millimeters.

Vivek et al [1], [2], [3] have applied this phenomenon as a tool for collision welding of dissimilar materials, as well as other impulse metalworking applications such as closed-die forming, embossing, coining, tube expansion, high-speed shearing, and springback calibration. Some of the results of this work are shown in Figure 1. Since the quality of these processes depends largely on control of the velocity of the workpiece, it is necessary to gain a better understanding of the development of the pressure pulse and how it can be optimized for different applications by changing the input parameters of the VFA technique.

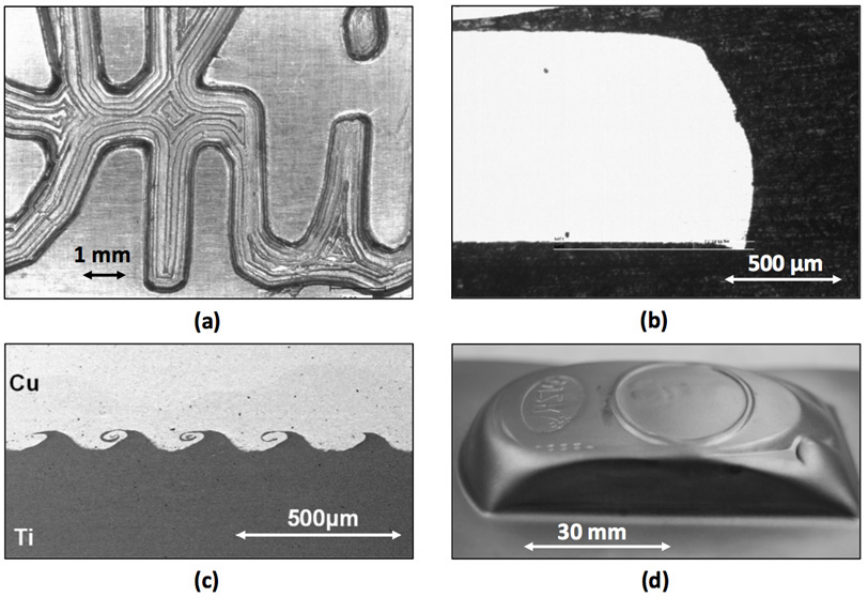

Figure 1: *(a) Embossing/coining, (b) burr-free shearing of high-strength steel, (c) VFA weld interface, (d) closed-die forming.*

Though the use of vaporizing conductors for impulse metalworking is a recent development, the phenomenon (often referred to as exploding conductors) has been known for some time. In 1962, Keller and Penning [4] used vaporizing foils to drive thin dielectric flyers into targets at more than 4 km/s, reaching impact pressures of up to 10 GPa. In 1980, Chau et al. [5] reached flyer velocities of 20 km/s and pressures of over 500 GPa, by adding a metal layer to the dielectric flyer; the increased shock impedance of the metal resulted in much higher impact pressures. That system has been used to study high-pressure impacts, including the shock initiation of explosives. Vaporizing wires have also found limited use in industry with electrohydraulic forming; however, as noted by Daehn [6], their use has proven difficult to commercialize.

This work was specifically performed under the parameters of VFA-driven collision welding (referred to as VFAW), in which the pressure pulse accelerates one metal sheet (the flyer) across a short standoff distance, as illustrated in Figure 2(a). The ideal impact velocity and impact angle (which is a function of standoff distance in the current welding setup) vary among different metal pairings to be joined; therefore, it is desirable to be able to predict the evolution of flyer velocity. This work investigates how, across a range of input energies, variations in foil thickness affect the evolution of velocity of the flyer sheet. It goes on to relate the current density at the time of vaporization to the velocity of the flyer.

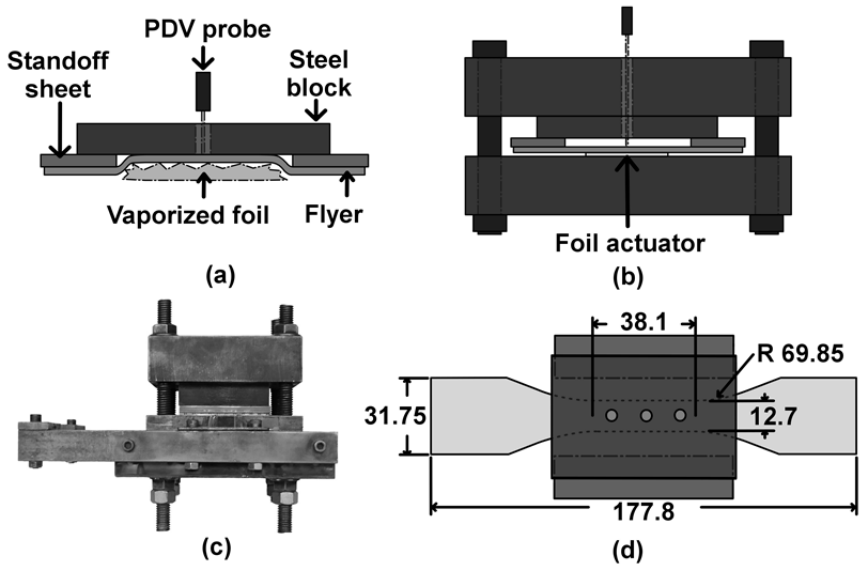

Figure 2: *(a) Side view during flyer launch, (b) side view of experimental setup, (c) actual experimental fixture, (d) top view of foil actuator setup, dimensions in mm.*

The work of Grigoriev and Pavlenko [7] demonstrated that the magnitude of the pressure pulse produced by a vaporizing foil is proportional to the energy deposited in the foil at the time of vaporization. This energy E_d can be calculated as the integral with respect to time of the product of current I and voltage U, to the vaporization time t_v:

$$E_d = \int_0^{t_b} I(t)U(t)\,dt \tag{1}$$

The average pressure pulse P_{av} can be calculated by the following equation, where ρ_f is flyer density, h_f is flyer thickness, V_2 and V_1 are impact and initial flyer velocities, and t is the time from vaporization to flyer impact against the target:

$$P_{av} = \rho_f h_f \frac{V_2 - V_1}{t} \tag{2}$$

Chau et al. [5], who used the electrical Gurney model proposed by Tucker and Stanton [8], showed that the final velocity V_f of a flyer plate launched by a vaporizing foil can be related to the square root of the vaporization current density J_B, where K and b are empirically derived, and M/C is the ratio of foil mass to flyer sheet mass:

$$V_f = \left(KJ_B^b\right)^{0.5}\left(\frac{M}{C} + {}^1/_3\right)^{-0.5} \quad (3)$$

Cho et al. [9] concluded that more energy is deposited into a vaporizing wire when the current rise time – the time by which the current reaches its peak value – is shorter, resulting in a greater amount of the conductor being vaporized.

Previous experiments with copper and aluminum vaporizing wires by Vivek et al. [2] indicated that the conversion from electrical to kinetic energy upon vaporization is much more efficient in aluminum. Contributing to the greater pressure produced by vaporizing aluminum is the exothermic reaction forming alumina, which is on the same time scale as the flyer launch. Aluminum is therefore considered to be the preferable material with which to construct vaporizing foils.

2 Experimental Parameters

The experimental setup is pictured in Figure 2(b) and (c). The foil actuator was electrically insulated on each side with polyimide tape, except for the ends, which were fixed to copper terminals leading to a capacitor bank. The faces of the flyer sheet and the steel base that touched the foil were also insulated with polyimide tape to prevent current flow through the fixture or the flyer plate. The flyer was centered over the narrow section of the foil. Standoff sheets were placed on the edges of the flyer, parallel to the length of the foil, to separate the flyer at a distance from the steel backing blocks.

All flyer sheets were 76.2 mm square, cut from 0.508 mm thick T3 temper AA2024. The standoff distance between the flyer and the backing block was 2.5 mm in all cases.

The design of the foil actuators is pictured in Figure 2(d). Since the vaporization is initiated where the current density is highest, the foils are designed with a narrow section under the workpiece, to ensure that the pressure pulse occurs there. These were cut from 0.0508, 0.0762, and 0.127 mm thick full hard temper AA1145. The foils of each thickness were cut from their parent rolls along the same direction. Each foil thickness was tested at 2, 4, 6, and 8 kJ input energies from the 8-capacitor bank, the parameters of which are listed in Table 1. Each of these trials was performed twice.

C	L	R	Max. charging voltage	Max. charging energy	Short-circuit current rise time
426 µF	100 nH	10 mΩ	8.66 kV	16 kJ	12 µs

Table 1: *Electronic parameters of the capacitor bank.*

The evolution of flyer velocity over time was recorded through a hole in the center of the top of the fixture, using a photonic Doppler velocimetry (PDV) system capable of measuring velocities up to 2 km/s. PDV is a technique for measuring high velocities, developed by Strand et al [10]. In 2009, Johnson et al [11] demonstrated the use of PDV as a diagnostic for impulse metalworking operations. In this technique, light from a laser probe is directed perpendicularly onto the surface of the workpiece in motion; the probe collects the light reflected back from the surface, which is Doppler-shifted. This is mixed with non-Doppler-shifted light, creating a measurable beat frequency that is directly proportional to velocity. An oscilloscope simultaneously recorded the velocity, current and

voltage at a sampling rate of 5 GHz. Current was measured using a 100 kA:1 V Rogowski coil, and voltage was measured using a 1000:1 voltage divider.

To investigate the planarity of the flyer sheet launch, three trials were performed using 0.0762 mm thick foils at input energies of 4, 6, and 8 kJ. In each of these tests, three PDV traces were recorded simultaneously, using the voltage spike as the trigger for the oscilloscope. The three PDV probes were positioned 15 mm apart from each other, for a total spread of 30 mm along the length of the narrow section of the foil (referred to as the active area), as illustrated in Figure 2(d).

3 Results and Discussion

Figure 3(a) combines velocity, current, and voltage traces for a trial using a 0.0762 mm thick foil at 6 kJ input energy. A notable feature is the region of acceleration to low velocity, marked *A* in the figure. This was the result of the countercurrent induced in the workpiece by the current in the foil: the opposing electromagnetic fields repelled the flyer from the (immobile) foil. At its end is the voltage spike, which signifies the point at which the foil vaporized. Webb et al. [12] explain this: as the foil vaporize, its resistance increases abruptly, causing the voltage spike. As the vapor expands and cools, it begins to conduct again, discharging the remaining energy in the system, which produces the wide peak in the current trace starting at the time marked *B*.

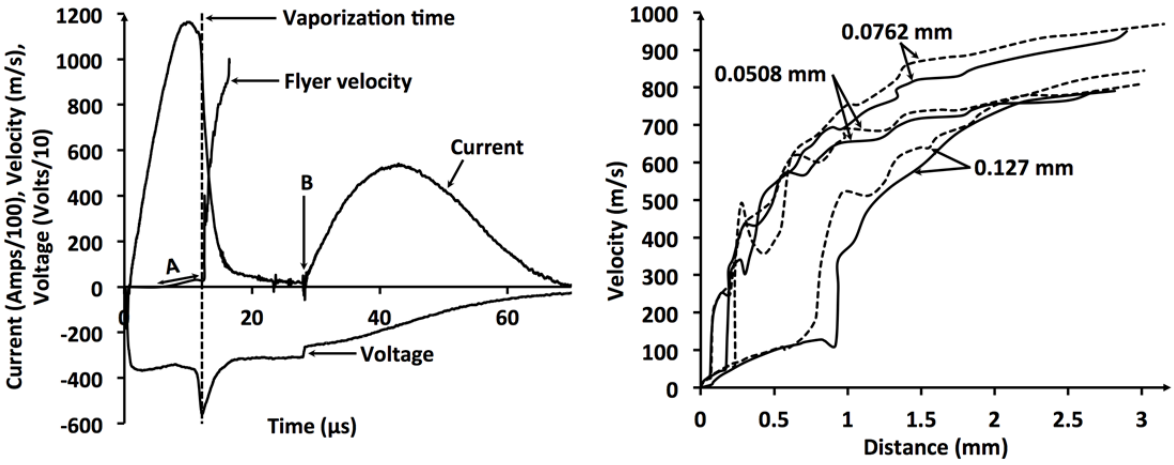

(a) (b)

Figure 3: *(a) Current, velocity, and voltage vs. time for 0.0762 mm foil at 6 kJ input energy, (b) velocity vs. distance traveled from foils at 6 kJ input energy.*

To obtain the velocity at many different possible welding standoff distances, the velocity vs. time data from the PDV was integrated in order to plot velocity vs. distance traveled. Figure 3(b) compares the traces for the three foil thicknesses at 6 kJ input energy. Traces produced by repeated trials overlapped with one another fairly well, indicating the repeatability of the launch process – though additional sets of trials will be necessary to demonstrate this with confidence.

It can be noted in Figure 3(b) that the measured distance traveled was greater than the standoff distance of 2.5 mm. This was because a circular plug of the flyer was sheared off through the hole in the backing block through which the PDV probe measured flyer

velocity. The velocity of this plug continued to be recorded until it rotated enough to no longer reflect laser light back to the probe.

In Figure 3(b), it can be also seen that the region of electromagnetically driven low acceleration was much larger for the 0.127 mm foils than for the other two foil thicknesses. The flyers driven by the 0.127 mm foil traveled nearly 1 mm away from the foil before the vaporization occurs, while the others moved less than 0.25 mm. This occurred largely because the thicker foil – having approximately twice the mass of the other two – required a longer time before the current density increased enough to vaporize the metal. In fact, at lower input energies, the thicker foils melted rather than vaporized, since there was not enough energy to exceed their enthalpy of vaporization. This occurrence is important to consider in application to impulse metalworking because the large movement of the flyer sheet away from the foil lessened the confinement of the pressure pulse, reducing the potential driving force behind the flyer launch. Additionally, for metalworking requiring acceleration distances on the order of 1 mm, this behavior would not be suitable, since the flyer would reach its target before significant acceleration occurred.

Figure 4(a) shows the average distances traveled by the flyer before vaporization for all foil thicknesses and input energies. (Note: there is no data point for 0.127 mm foil at 2 kJ because the deposited energy was not enough to vaporize it.) It can be seen that the pre-vaporization distance decreases somewhat with increasing input energy. This is because the rise time of the capacitor bank remained approximately 12 μs even as its charging energy was increased. Therefore, the rate of energy deposition increased and the energy density necessary to vaporize the foil was reached more quickly, leaving less time for the electromagnetic repulsion to affect the workpiece.

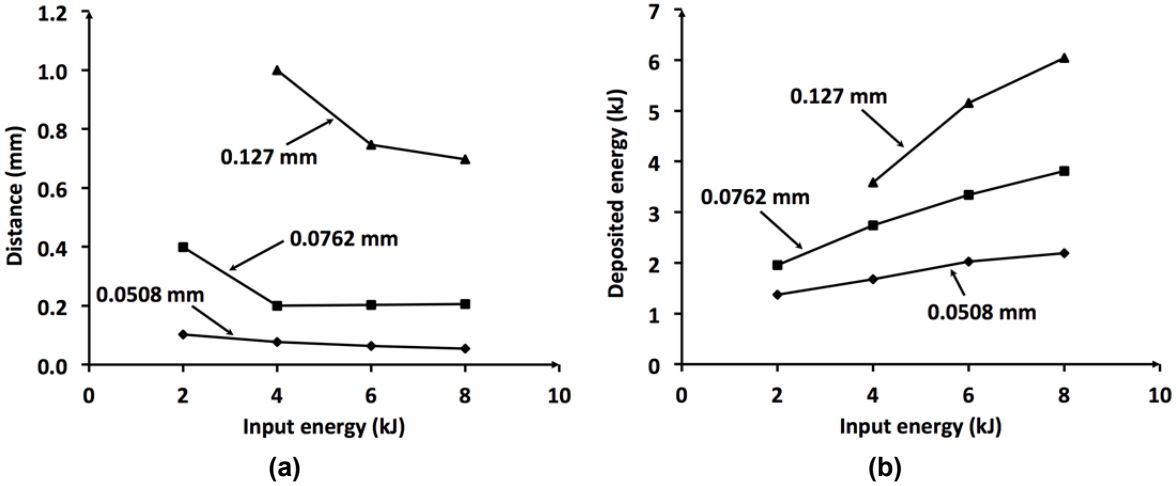

Figure 4: *(a) Distance traveled before vaporization vs. input energy, (b) energy deposited before vaporization vs. input energy.*

Figure 4(b) shows how the average energy E_d deposited in the foil actuator before the vaporization – integrated from the current and voltage vs. time traces, as according to Eq. (1) – varied with input energy for each foil thickness. The energy deposited in the conductors increased with increasing input energy from the capacitor bank; however, the increase was not linearly proportional. This indicates that, while faster energy deposition

improves the energy density in the foil at vaporization, there is a limit to how much energy can be deposited in a foil of a given mass. Foils of greater mass display the potential for greater energy deposition, as may be expected.

Figure 5(a) shows the average flyer velocity at a distance of 1.6 mm, which was a standoff distance used in preliminary vaporizing foil collision welding experiments. Average flyer velocity showed a similar trend toward non-linear increase with increasing input energy. In spite of the greater deposited energy in the 0.127 mm thick foils, these produced the lowest flyer velocities.

The lower velocity can be partially attributed to the reduction in confinement pressure due to the observed significant electromagnetic push. Also contributing to the lower velocity was the much greater mass of aluminum – more than double that of the other foils – being vaporized. Although the deposited energy was greater for the thicker foils, the vaporization current density was lower than for the thinner foils. It appears, however, that, if the input energy were increased further, or the energy deposition rate were increased through faster capacitors, the thicker foils have the potential to produce greater flyer velocities.

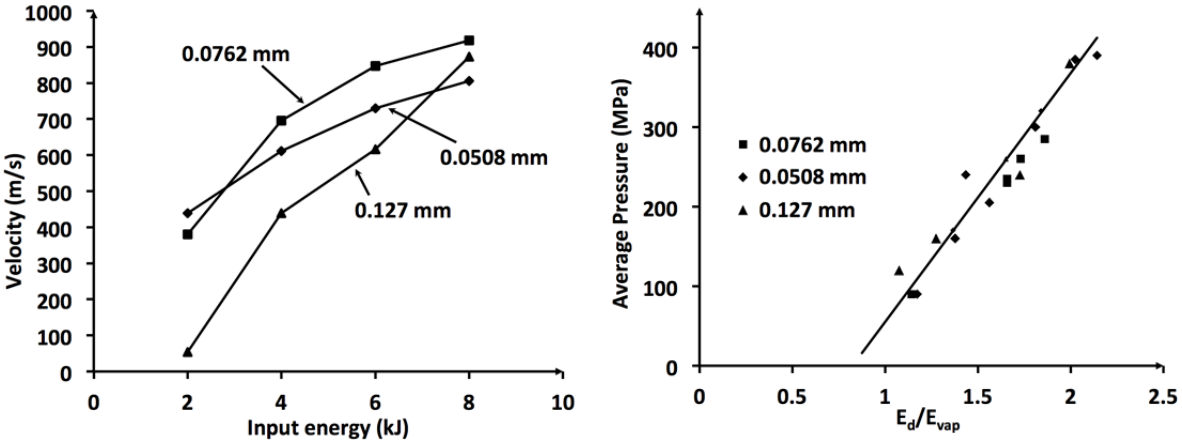

Figure 5: *(a) Flyer velocity at 1.6 mm vs. input energy, (b) average driving pressure vs. the ratio of deposited energy to energy of vaporization for a given foil.*

In order to completely vaporize the aluminum foil, heat has to be supplied to raise the temperature to melting point, to melt the given mass, to raise the temperature of melted mass to boiling point, to vaporize the liquid, and to raise the temperature of the gas to 2793 K (boiling point of aluminum). According to Osher et al [13], the total heat needed for this is 356 kJ/mol. Taking the active area of the foil to be the relevant portion of the mass being vaporized, the energy E_{vap} necessary to vaporize this section is calculated to be 1.478, 2.191, and 3.643 kJ, respectively, for the 0.0508, 0.0762, and 0.127 mm thick foils. Figure 5(b) plots the average pressure P_{av}, as calculated by Eq. (2), against the ratio E_d/E_{vap}. The velocities V_1 and V_2 were found from the velocity vs. distance curves, such as Figs. 4 and 5. V_1 was the velocity when the vaporization occurred, and V_2 was the velocity at 2.5 mm. A linear trend is observed, enabling the following empirical relationship to be obtained for this specific system (P_{av} in MPa):

$$P_{av} = 345.79\left(\frac{E_d}{E_{vap}}\right) - 223.75, \textit{ correlation} = 0.9385 \quad (4)$$

An attempt was made to relate terminal flyer velocity to vaporization current density, as in Eq. (3). However, due to the non-uniform shape of the foil actuators, which are designed specifically to induce current crowding in the narrow region, it proved difficult to accurately calculate the vaporization current density. An estimate was attempted, assuming the current density to be constant throughout, but a plot of terminal velocity against the estimated current density displayed no apparent trends.

Figure 6 depicts the flyer displacement over time, integrated from velocity vs. time, for the three launch planarity experiments. The three probes are identified by their location above the foil's active area, relative to the RLC circuit: one on the end closest to the negatively charged terminal of the capacitor bank, one in the center of the active area, and one closest to the ground side of the bank.

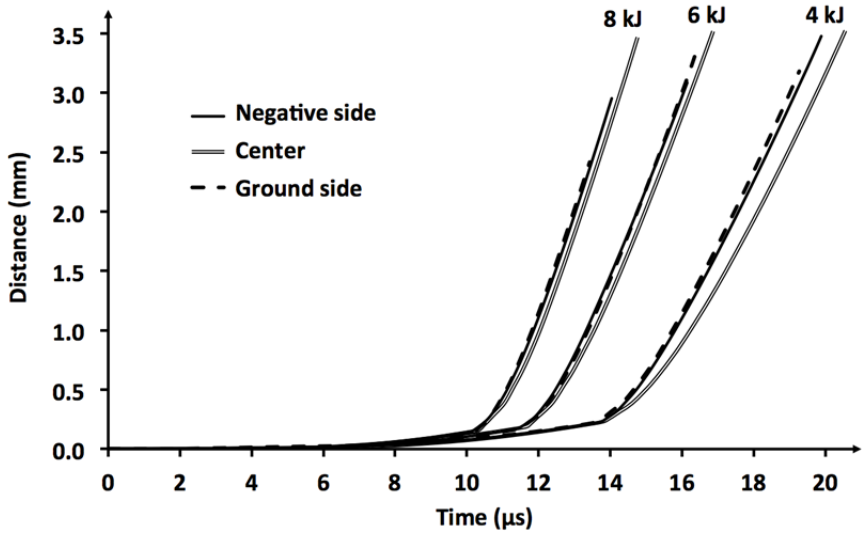

Figure 6: *Flyer displacement vs. time for 0.0762 mm thick foils.*

The time delay before launch decreased with increasing input energy due to the effect described above; that is, the rate of energy deposition into the circuit increases with increasing charging energy on the capacitors. It can be seen that the flyer launch was very nearly simultaneous across the active area at higher input energies, where E_d/E_{vap} is larger. The distance traces for the ends of the active area are nearly indistinguishable from one another, while the center lags behind by about 0.2 µs, or about 0.5 µs for the 4 kJ trial. This is due to a phenomenon termed "end effect." The vaporization is most likely to initiate where the change in current density is the highest, which for these foil actuators is the ends of the straight section. This effect can be reduced or eliminated by refining the shape of the foil actuators.

Additional trials using flyer sheets of materials of different densities, alloys, and tempers would be required to decidedly verify that, irrespective of flyer material, the relationship between average driving pressure and the energy ratio is linear.

4 Results and Discussion

- Vaporizing foil actuators can be used to consistently launch AA2024 sheet metal flyers on the order of 0.5 mm thick to velocities between 300 and 1000 m/s within distances from 0.25 to 3 mm. The velocity reached at a certain distance can be reliably controlled by jointly or separately varying the VFA thickness and the input energy.
- The fundamentals of the VFA method are not expected to change when parameters are varied. Though a faster current source and resultant greater pre-vaporization energy deposition, E_d, may be preferable, the proportionality of the relationship between the ratio E_d/E_{vap} and the vaporization pressure remains linear. This relationship holds true regardless of foil thickness.
- The ideal foil thickness and shape is dependent on the intended application. Thicker foils require more input energy to vaporize, better pressure confinement in the setup, and a greater acceleration distance, but appear to have the potential for greater final flyer velocities given greater current density. The temporal development of pressure from thinner foils was more suitable for the VFA welding setup used in these experiments, in which a shorter acceleration distance is preferable and greater workpiece velocity is not necessary.
- The flyer sheet launch and flight are fairly planar across the active area of the foil, with a < 0.5 μs delay in the center as compared to the edges. The delay is reduced when E_d/E_{vap} is increased. The lag in the center can be compensated for by redesigning the foil actuator to eliminate the end effect.

References

[1] Vivek, A., Hansen, S.R., Liu, B.C., and Daehn, G.S.: “Vaporizing Foil Actuator: A Tool for Collision Welding,” *Journal of Materials Processing Technology*, **213**(12), 2013, pp. 2304-2311.

[2] Vivek, A., Taber, G.A., Johnson, J.R., Woodward, S.T., and Daehn, G.S.: “Electrically Driven Plasma via Vaporization of Metallic Conductors: A Tool for Impulse Metal Working,” *Journal of Materials Processing Technology*, **213**(8), 2013, pp. 1311-1326.

[3] Vivek, A., Brune, R.C., Hansen, S.R., and Daehn, G.S.: “Vaporizing Foil Actuator Used for Impulse Forming and Embossing of Titanium and Aluminum Alloys,” *Journal of Materials Processing Technology*, **214**, 2014, pp. 865-875.

[4] Keller, D.V. and Penning, R.J.: “Exploding foils – The Production of Plane Shock Waves and the Acceleration of Thin Plates,” *Exploding Wires*, W. Chase and H. Moore, eds., Plenum Press, **2**, 1962, pp. 263-277.

[5] Chau, H.H., Dittbener, G., Hofer, W.W., Honodel, C.A., Steinberg, D.J., Stroud, J.R., Weingart, R.C., Lee, R.S.: “Electric Gun: A Versatile Tool for High-Pressure Shock Wave Research,” Review of Scientific Instruments, **51**(12), 1980.

[6] Daehn, G.S.: “High Velocity Metal Forming,” *ASM Handbook*, **14B**, ASM International, 2006, pp. 405-418.

[7] Gregoriev, A.N., and Pavlenko, A.V.: “Pressure Generated by the Electric Explosion of Metal Foils,” *Technical Physics Letters,* **25**(9), 2009, pp. 865-868.

[8] Tucker, T.J. and Stanton, P.L.: “Electrical Gurney Energy: A New Concept of Modeling Energy Transference from Electrically Exploded Conductors,” SAND-74-0244, Sandia National Laboratory, Albuquerque, NM, 1975.

[9] Cho, C., Murai, K., Suzuki, T., Suematsu, H., Jiang, W., and Yatsui, K.: “Enhancement of Energy Deposition in Pulsed Wire Discharge for Synthesis of Nanosized Powders,” *IEEE Transactions on Plasma Science,* **32**(5), 2004, pp. 2062-2067.

[10] Strand, O.F., Goosman, D.R., Martinez, C., Whitworth, T.L., and Kuhlow, W.W.: “Compact System for High-Speed Velocimetry Using Heterodyne Techniques,” *Review of Scientific Instruments*, **77**(8), 2006.

[11] Johnson, J.R., Taber, G., Vivek, A., Zhang, Y., Golowin, S., Banik, K., Fenton, G.K., and Daehn, G.S.: “Coupling Experiment and Simulation in Electromagnetic Forming Using Photon Doppler Velocimetry,” *Steel Res. Int.*, **80**(5), 2009, pp. 359–365.

[12] Webb, F.H., Chase, N., Ernstene, M., Tollestrup, A.V.: “Submicrosecond Wire Explosion Studies at Electro-Optical Systems, Inc.,” *Exploding Wires,* **1**, 1959, p. 33.

[13] Osher, J.E., Barnes, G., Chau, H.H., Lee, C., Speer, R., Weingart, R.C.: "Operating Characteristics and Modeling of the LLNL 100-kV Electric Gun," *IEEE Transactions on Plasma Science,* 17(3), 1989, pp. 392-402

Effect of the Duration of Electromagnetic Pulse Force on the Rebound Suppression in V-Bending Experiment *

WeiRen Xiong[1], WenPing Wang[1], Min Wan[1],Long Pan[1]

[1] School of Mechanical Engineering & Automation, BeiHang University, 37 xueyuan road, Beijing, 100191, China

Abstract

Electromagnetic Forming (EMF) is one of the high speed forming technologies. The spatial distribution and temporal evolution of electromagnetic body force and the constraint imposed by the die on the sheet metal, are key factors which influence the dynamic deformation behaviour of sheet metal. The great force induced by the collision at high speed of the sheet and the die causes the rebound of the sheet off the die. The rebound has a significant influence on the final shape of the part. On the basis of the comparison of time relationship between the displacement of the sheet metal and the amplitude of electromagnetic force, the study about the rebound phenomenon in an electromagnetic V-bending experiment and its numerical simulation model is carried out in this paper. Collision promotes deformation process, resulting in a drastic change of sheet geometry in which a new distribution of electromagnetic force helps the part to fit the die. The attenuation of force caused by distance increase is comparatively weak when forming into a shallow die, so that the electromagnetic force maintains enough intensity which can effectively suppress the rebound and help to calibrate the V-Shape of the part. Increasing the duration of coil current pulse helps to suppress rebound effect of sheet metal when forming into a shallow die.

---

* *This work is based on the experiments of Long Pan; the authors would like to thank the National Key Basic Research and Development Program of China (973 Program) (No. 2011CB012804) for its financial support.*
Corresponding author: Wen-Ping Wang; wwp_2003@163.com; Tel.:+86 010-82338613

Keywords

Electromagnetic forming, Aluminium alloy, V-bend, Rebound, Duration

1 Introduction

The application of aluminium alloys is under the restriction of low formability at room temperature, though the advantages of high strength-to-weight ratio, corrosion resistance and weldability [1]. Electromagnetic forming (EMF) is one of the high speed forming technologies, and can improve the formability without the costly expense and time period of thermal treatment. Electromagnetic forming (EMF) has been applied in the aerospace and automotive industries [2].

The finite element method is an important approach to study the instantaneous process of dynamic deformation behaviour of the sheet metal. The sequential coupling strategy and loose coupling strategy are two major strategies used in numerical model of EMF. Comparing the sequential coupling strategy with the loose coupling strategy, the latter does not consider the influence of structure deformation on the electromagnetic calculation. G. Bartels indicates that the deviations between the two strategies increase with time and also draws the conclusion that the loose coupling strategy can only be used as a good approximation for relatively fast deformation processes and small displacement through the numerical simulation of tube forming [3]. With the advantages of lower calculation cost and faster speed, the loose coupling strategy is wildly adopted in the research despite losing some accuracy.

In the loose coupling strategy, the nodal electromagnetic force which has been calculated without the deformation of a work-piece in the electromagnetic field is directly transferred into the work-piece in structure field as input load [2].

The spatial distribution and temporal evolution of electromagnetic body force and the constraint imposed by the die on the sheet metal, are major factors which influence the dynamic deformation behaviour of sheet metal.

The electromagnetic force decays with increasing distance between the coil and sheet during deformation, so the electromagnetic force in loose coupling is usually overestimated, resulting in a more violent collision. The undesirable violent impact often causes the rebound phenomenon preventing us from gaining the target shape of the parts. For this reason, J.Imbert takes a quarter circle of the sinusoid coil current to calculate the electromagnetic force [4]. D.A.Oliveira takes the time period between a quarter and a half of the sinusoid coil current pulse [5]. X.-h.Cui takes half of the sinusoid coil current pulse for his calculation. By neglecting a portion of the time for electromagnetic (EM) calculation, the overestimated force is compensated in structure field [6]. X.Cui investigates the influence of the number of pulse on deformation in a flat sheet free-bulging by comparing the loose coupling with the sequential coupling strategy [7].

J.Imbert reports that the predicted rebound is higher than the experimental result, and attributes the reasons to the energy excessively transmitted, the lower flow stress than actual material, and the extra pulses [4]. D.Risch adopts a spring-dashpot system representing the die's physical behaviour to draw the conclusion that the optimum

combination of stiffness and damping coefficient exists [8] and also introduces the geometrical stiffness of the desired work-piece geometry to investigate the rebound effect [9].

In this paper, we conducted a V-bending experiment and established the corresponding numerical model with the loose coupling strategy. The rebound phenomenon observed in V-bending numerical model is obviously higher than that in experimental result. Through studying the time relationship of the displacement of sheet and the amplitude of electromagnetic force in sheet, the effect of the pulse duration on rebound suppression can still be revealed. In addition, the effect of the update of distribution of force on the part's final shape was also analyzed. A better understanding of these factors will help to gain a desirable shape of the part.

The experimental procedure and the numerical simulation are introduced in section 2 and section 3 respectively, then the rebound suppression effect is analyzed in section 4, and the conclusion is given in section 5.

2 Experiment

Bend is one of the typical deformation modes in sheet metal forming. In order to gain insights into the local bend deformation behaviour of aluminium sheet metal in electromagnetic forming process, an electromagnetic V-bend experiment is conducted.

2.1 Sample

Sample of 2024-T3 aluminium alloy of 1.8 mm thick is considered in this experiment with the plane dimension of 100 mm × 40 mm. Basic mechanical properties and physical properties of 2024-T3 are shown in table 1.

Table 1: *The mechanical and physical properties of 2024-T3*

Parameter	Value	Parameter	Value	Parameter	Value
Density ($kg \cdot m^{-3}$)	2.68×10^{3}	Tensile Strength (MPa)	483	Resistivity ($\Omega \cdot m$)	5.82×10^{-8}
Elasticity Modulus (GPa)	73.1	Yield Strength (MPa)	345	Heat Conductivity (W/(m·K))	121
Poisson's Ratio	0.33	Elongation (%)	18%	specific heat (J/(g·K))	0.875

2.2 Tool and Die

It is well known that flat spiral coil is commonly used in study. Here an enhanced four-layer flat spiral coil, which provides greater forming force than the single-layer coil, is used in experiment. The geometric and electrical parameters are shown in table 2.

The die used in experiment is shown in Figure 1, and the experimental set-up of the experiment is shown in Figure 2.

Table 2: *Geometric and electrical parameters of the coil*

Parameter	Value	Parameter	Value
Resistance (Ω)	0.001	Number of Turns	16
Inductance (H)	2×10^{-6}	Gap between Turns (mm)	0.8
Cross-sectional Area (mm^2)	2×4	Gap between Layers(mm)	0.4
Number of Layers	4		

Figure 1*: The die*

2.3 Experiment Set-up and Method

The coil is placed at the bottom, and the sheet is pressed by the die with its cavity facing the upper surface of the coil. The set-up of experiment is shown in top view in figure 2 (a) and side view in figure 2 (b). The charging voltage of capacitor is set at 18 kV. And the formed part is shown in figure 3.

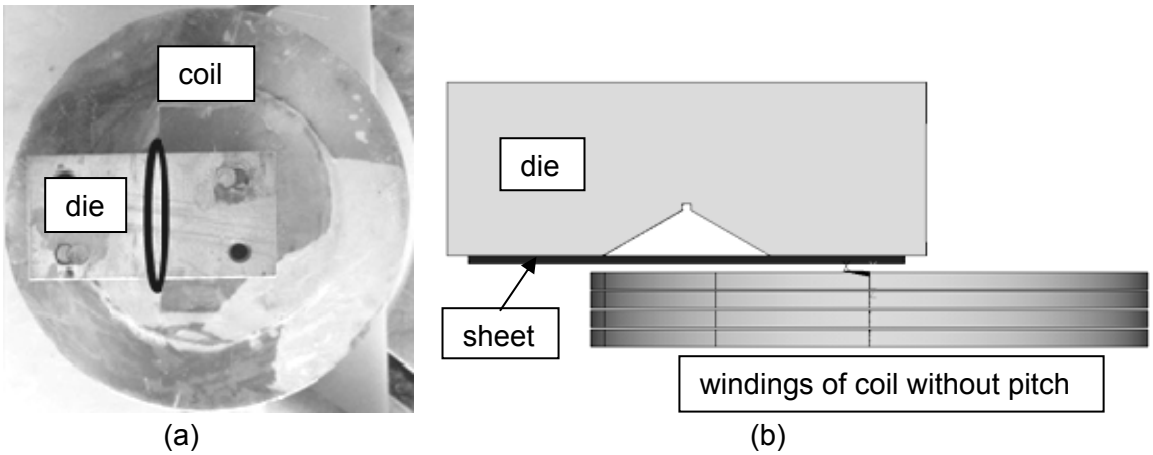

Figure 2*: The experiment set-up. (a) The top view, (b) The side view.*

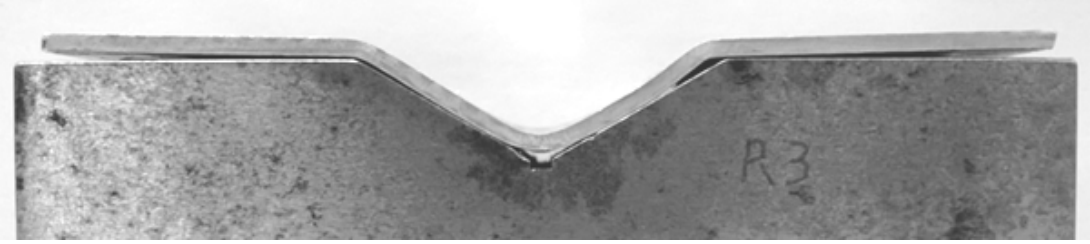

***Figure 3**: Forming result of part after EMF*

3 Numerical Analysis

3.1 Simulation Method

In this paper, the loose coupling strategy is chosen as a numerical simulation approach to perform the analysis. An electromagnetic field simulation is firstly conducted with the actually measured pulse current as excitation source to solve the nodal electromagnetic force in the sheet in electromagnetic field, and then the electromagnetic force is directly input into the structure field as driving load that form the sheet. The measured coil current used for simulation is presented in figure 4, and the coupling approach is illustrated in figure 5. Only the first pulse of coil current is applied in the simulation.

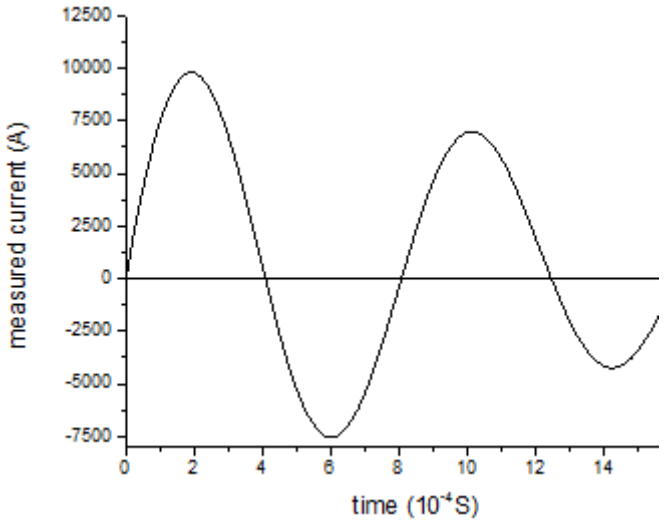

***Figure 4**: Measured coil current*

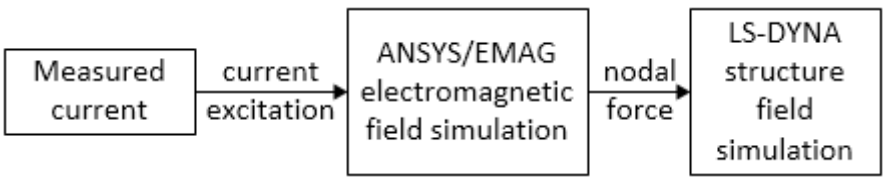

***Figure 5**: Flowchart of the loose coupling strategy*

3.2 Material Model

Equation (1) expresses the rate-dependent constructive model, Cowper-Symonds model, which is applied with the rate-dependent parameters C=6500 s^{-1} and P=4 [10]. σ_y is the dynamic flow stress at plastic strain rate $\dot{\varepsilon}$, σ_{ys} is the quasi-static flow stress. For the value of σ_{ys}, refer to [11].

$$\sigma_y = \left[1+\left(\frac{\dot{\varepsilon}}{C}\right)^{\frac{1}{p}}\right]\sigma_{ys} \tag{1}$$

4 Rebound Effect Suppression

Without considering the decay of electromagnetic force with increasing distance between the coil and the sheet in deformation stage, the electromagnetic force in the sheet is always overestimated. In order to compensate the over-input energy, the electromagnetic force is removed at 1.3×10^{-4} second when the sheet has not reached its deepest position in the die cavity, then the sheet continue to move into the inner die cavity in initial state with velocity field at this moment. Then, the sheet decelerate, rebound and stop at the position in figure 6. The kinematic energy stored in the sheet at this moment is high enough to push the sheet off the die, though part of the energy has been dissipated in collision.

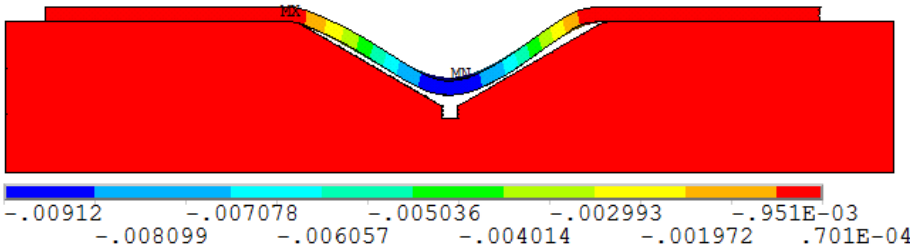

***Figure 6**: The final shape of the part at the condition of relasiing electromagnetic force at 1.3×10^{-4} second*

However, the fact that the sheet in experiment keeps contact with the die reveals that the intensity of the electromagnetic force is strong enough to efficiently suppress the rebound. In reality, after the time of 1.3×10^{-4} second, the sheet still undergoes the electromagnetic force. Figure 7 shows the final shape of the part under a whole current pulse excitation. The gaps between the part and die at both left side wall and right side wall of the part are obviously more significant than those in figure 3 and in figure 6. The gap at left side is caused by rebound. The compartive bigger gap at the right die radius is mainly caused by asymmetric electromagnetic force towards left at the right side of the sheet. The duration of force in figrure 7 is apparently longer than that in figure 6.

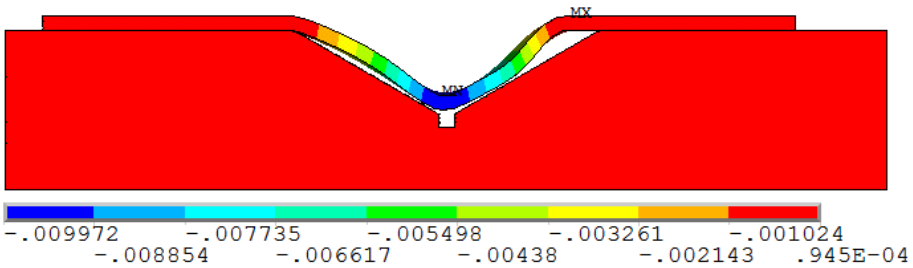

***Figure 7**: Final shape of the part under a whole current pulse excitation*

Figure 8 shows the time relationship between several different normalized physics quantities. *J* is the current in the coil, *Uz* is the displacement of the sheet towards –Z direction, *Fz1* and *Fz2* is the nodal electromagnetic force corresponding to the elements in position "1" and "2" as shown in figure 9. We are primarily concerned with the temporal evolution of absolute value. For ease of comparison, the maximum value of *J* is normalized to 3, the maximum value of *Uz* is normalized to 2, the maximum value of *Fz1* and *Fz2* is normalized to 2. The sheet reaches its deepest position in its deformation history at the time of 1.5×10^{-4} second when the displacement tracking process is stopped. It can be observed from the graph that the width of force pulse is narrower than that of current pulse.

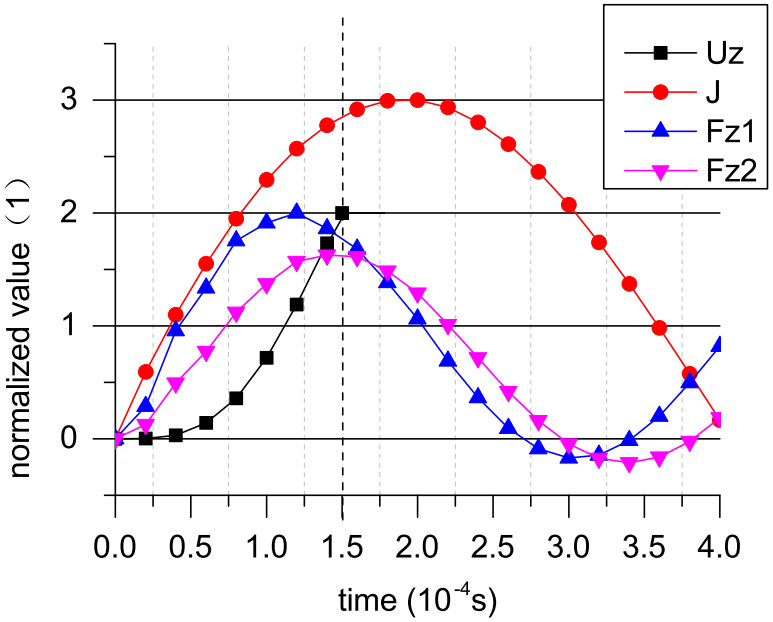

***Figure 8**: The graph of displacement, current and the electromagnetic force versus time*

In flat sheet free-bulging process, due to unlimited motion of the sheet and longer period of time for deformation, the increased distance between sheet and die causes a significant attenuation rate of force. However, in this article, the distance of the sheet from the coil is limited by the shallow die, wherein the attenuation of force is relatively weaker. Meanwhile, as shown in figure 8, the electromagnetic forces, *Fz1* and *Fz2*, reach their peaks ahead of coil current. When the sheet reaches the deepest position, the forces maintain enough intensity nearby their own peaks.

The distance dependent decaying curve of electromagnetic force versus time has already been analysed by [7]. Figure 10 shows the schematic curve of sequential coupling electromagnetic force. Its amplitude is relatively lower compared to the electromagnetic force in a loose coupling simulation. The abscissa is time and the ordinate axis is the amplitude of normalized force. The sheet reaches its maximum depth at the time *t1*, then rebounds away from the die until time *t2* when the sheet fit the die for a second time.

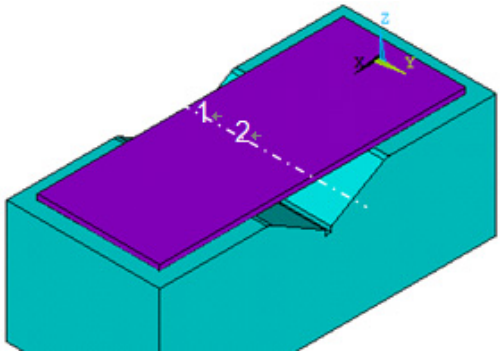

Figure 9. Positions of *Fz1* and *Fz2*

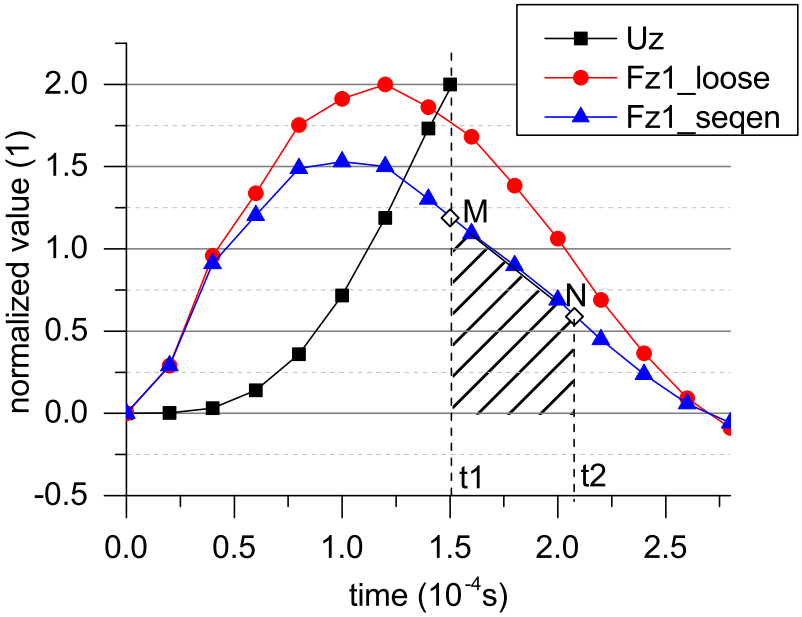

Figure 10: *The electromagnetic force in loose coupling strategy and the schematic one in sequential coupling strategy*

Assuming that the rest of kinematic energy has been dissipated in the second collision, the force from *t1* to *t2* plays the role of preventing the sheet from bouncing back away from the inner surface of the die. The area of the shaded portion in figure 10 is the impulse applied to the sheet by force within the time period between *t1* and *t2*.

The distribution of electromagnetic force also influences the forming result. X. Cui investigated the effect of the second current pulse on deformation in free bulging experiment and concluded that the width of current pulse plays a role on the accuracy of

the predication by comparing a loose coupling strategy with a sequential coupling strategy [7]. And, the fact that the electromagnetic force is mainly perpendicular to the curved surface of the sheet geometry is presented in [12, 13]. The following equation defines the electromagnetic force.

$$\boldsymbol{F}=\boldsymbol{J}\times\boldsymbol{B} \tag{2}$$

Where, ***F*** is electromagnetic force, ***J*** is current, ***B*** is flux intensity.

The geometric meaning of the equation (2) expresses that ***F*** is normal to the plane of ***J*** and ***B***. Since that the induced eddy current can only flow in the sheet geometrical surface, there is always a component of the force normal to the surface of the sheet. Figure 11 shows the contour graph of components of electromagnetic force in the deformation region in another numerical model where the sheet has gotten the V-shape. These two components all push the sheet to the die. The circles show the region with maximum amplitude of force along X and Z direction in figure 11 (a) and figure 11 (b) respectively. And the force in the circles help to reduce the gaps at right die radius as shown in figure 7 and figure 3 by preventing the right part of sheet from moving toward the cavity of die. That is, the new direction of electromagnetic force after deformation helps to press the sheet toward the sidewall of the V-shape die. So, this is a calibration-like process. However, the accuracy of prediction of the loose coupling strategy is limited in the prediction of forming process with die for its insufficient in updating the distribution of force.

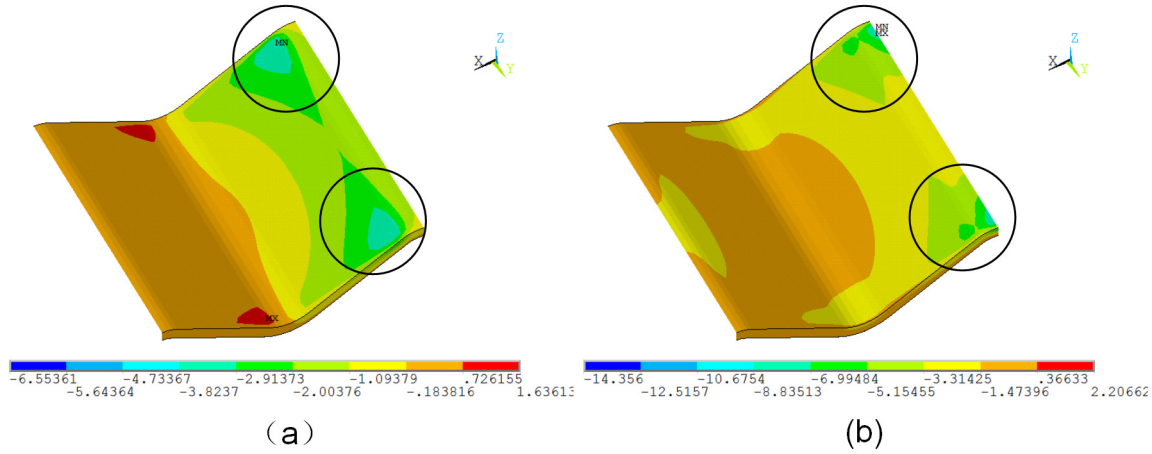

***Figure 11**: (a) X component of electromagnetic force and (b) Z component of electromagnetic force*

5 Conclusion

Our analysis shows that, the bigger electromagnetic force pulse width extends the time period of acting force. So, a more accurate part can be manufactured through supressing the rebound effect by means of widening the width of electromagnetic pulse when forming into a shallow die wherein a weaker attenuation of electromagnetic force exists as a result

of the small distance between the sheet and the coil. The new distribution of force helps to push the sheet to the die, therefore helps to maintain the V-shape of the part. In addition, the sequential coupling strategy that can update the amplitude and distribution of force is needed to conduct a more accurate prediction.

References

[1] *J.Y.Shim., B.Y.Kang., D.H.Park., Y.Ghoi., I.S.Kim.,* A Study on Contour on Workpiece According to the Shape of Forming Coil in EMF Process, in: Proceedings of ICHSF2012, Dortmund, 2012, pp. 135-142.

[2] *A.G. Mamalis, D.E. Manolakos, A.G. Kladas, A.K. Koumoutsos,* Electromagnetic Forming Tools and Processing Conditions: Numerical Simulation, Materials and Manufacturing Processes, 21 (2006) 411-423.

[3] *G. Bartels, W. Schätzing, H.P. Scheibe, M. Leone,* Comparison of two different simulation algorithms for the electromagnetic tube compression, International Journal of Material Forming, 2 (2009) 693-696.

[4] *J. Imbert, M. Worswick,* Electromagnetic reduction of a pre-formed radius on AA 5754 sheet, Journal of Materials Processing Technology, 211 (2011) 896-908.

[5] *D.A. Oliveira, M.J. Worswick, M. Finn, D. Newman,* Electromagnetic forming of aluminum alloy sheet: Free-form and cavity fill experiments and model, Journal of Materials Processing Technology, 170 (2005) 350-362.

[6] *X.-h. Cui, J.-h. Mo, S.-j. Xiao, E.-h. Du,* Magnetic force distribution and deformation law of sheet using uniform pressure electromagnetic actuator, Transactions of Nonferrous Metals Society of China, 21 (2011) 2484-2489.

[7] *X. Cui, J. Mo, J. Li, L. Huang, Y. Zhu, Z.W. Li, K. Zhong,* Effect of second current pulse and different algorithms on simulation accuracy for electromagnetic sheet forming, The International Journal of Advanced Manufacturing Technology, 68 (2013) 1137-1146.

[8] *D. Risch., C. Beerwald., A. Brosius., M. Kleiner.,* On the Significance of the Die Design for Electromagnetic Sheet Metal Forming, in: Proceedings of ICHSF2004, Dortmund, 2004, pp. 191-200.

[9] *D. Risch., E. Vogli., I. Baumann., A. Brosius., C. Beerwald., W. Tillmann., M. Kleiner.,* Aspects of Die Design for the Electromagnetic Sheet Metal Forming Process, in: Proceedings of ICHSF2006, Dortmund, 2006, pp. 189-200.

[10] *G.S.Sohoni., M.V.Walame.,* Dynamic Behavior Characterization of Lead at High Strain Rates Using High Speed Photography for Finite Element Simulation, in: Proceedings of IMECE2005, Orlando, 2005, pp. 1-6.

[11] *X. Gao, J. Kim,* Modeling of ductile fracture: Significance of void coalescence, International Journal of Solids and Structures, 43 (2006) 6277-6293.

[12] *D.-h. Liu, C.-f. Li, H.-p. Yu,* Numerical modeling and deformation analysis for electromagnetically assisted deep drawing of AA5052 sheet, Transactions of Nonferrous Metals Society of China, 19 (2009) 1294-1302.

[13] *X. Cui, J. Mo, S. Xiao, E. Du, J. Zhao,* Numerical simulation of electromagnetic sheet bulging based on FEM, The International Journal of Advanced Manufacturing Technology, 57 (2011) 127-134.

High Speed Forming Press Using Electromagnetic Pulse Force

C. G. Park, Y. Choi, J. Y. Shim, B. Y. Kang

Convergence Components & Agricultural Machinery Application Center, Kitech, Jeonju, Jeonbuk, Korea

Abstract

In this paper, the finite element analysis for the design of a high speed forming press using electromagnetic pulse force has been performed. The punch of the press has been fixed on a aluminium plate, which is driven by the electromagnetic pulse force. The force is the repulsive force between aluminium plate and the coil. The coil has been supplied with a high voltage AC current impulse from the capacitors and then the magnetized aluminium plate has been forced to move upward with high speed. For the analysis of the pressing, the coupled analysis of electromagnetic field and rigid-body dynamic of the aluminium plate has been performed with a commercial FE-software, ANSYS and the rigid-body dynamics theory.

Keywords

High Speed Forming, Electromagnetic Force, Press, FE-analysis

1 Introduction

To overcome the lower formability of high strength material, high speed forming is widely investigated [1]. The papers related to electromagnetic forming(EMF) and magnetic pulse welding(MPW) are 79% in the field of high speed forming, ICHSF2012. In general, the punch is not required in EMF process because the electromagnetic forming force is applied to the workpiece directly. However, some high speed forming technology have been developed for the forming processes with need of the punch, such as high speed blanking and stamping with a small radius [2~4].

In this paper, the finite element analysis for the design of a high speed forming press using electromagnetic pulse force has been performed. The punch of the press has been fixed on a aluminium plate, which is driven by the electromagnetic pulse force. The force is the repulsive force between aluminium plate and the coil. The coil has been supplied with a high voltage AC current impulse from the capacitors and then the magnetized

aluminium plate has been forced to move upward with high speed. The forming press is an energy limit machine. The forming is limit to the kinematic energy of the aluminium plate. The kinematic energy is determined with the mass and velocity of the plate.
To evaluate the velocity of the plate, the analysis of the pressing, the coupled analysis of electromagnetic field and rigid-body dynamic of the aluminium plate has been performed with a commercial FE-software, ANSYS [5] and the rigid-body dynamics theory [6].

2 High Speed Press using Electromagnetic Pulse Force

2.1 Press system

As shown in Figure 1, the high speed press system which consists of an aluminium plate with the punch, a steel fixture, a spacer, an upper die and a coil. When charged electrical energy was discharged from magnetic pulse power source to the coil, electromagnetic force is generated between the aluminum plate and the coil. The aluminum plate has been moved high speed by this electromagnetic pulse force.
The coil shape is one of important factor for achieving successful forming because electromagnetic force value and distributions on the aluminium plate is changed according to the shape of the coil. The bar-type coil was employed for getting high electromagnetic force during forming process as shown Figure 2 in this study. The bar-type coil has high speed current flow than others shape, and generates the high electromagnetic field the between the coil and the aluminium plate instantaneously.

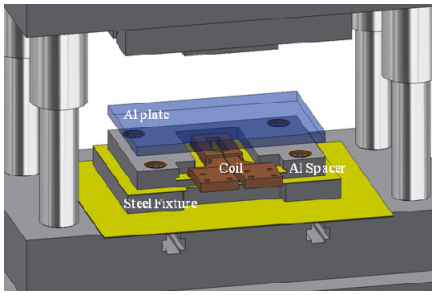

***Figure 1**: Schematic diagram*

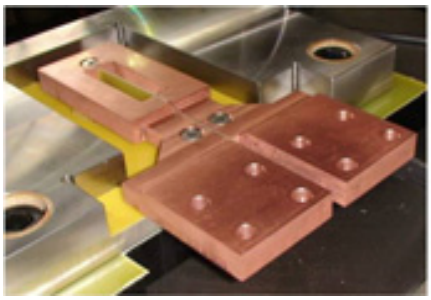

***Figure 2**: Bar-type coil*

2.2 Electromagnetic pulse power source

As shown in Figure 3, electromagnetic pulse forming system which manufactured by Welmate Co.,Ltd. for this study includes a magnetic pulse power source which consists of a capacitor bank with a maximum charging energy of 42kJ as shown Table 1. Additionally, in order to observe a discharge waveform and peak current, Rogowski coil was installed around the magnetic pulse power source and the coil.

Parameters	Specification
System capacitance	840uF
Charge voltages	1kV – 10kV
Inductance	0.4uH
Energy levels	0.4kJ – 42kJ

***Table 1**: Specification of magnetic pulse forming system*

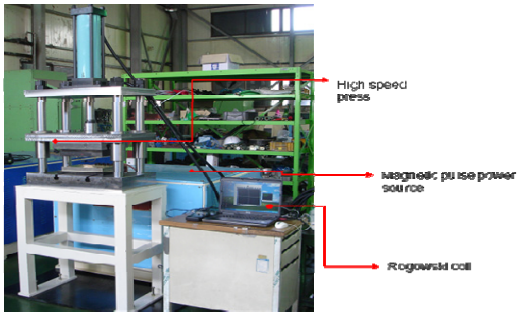

***Figure 3**: Electromagnetic forming system*

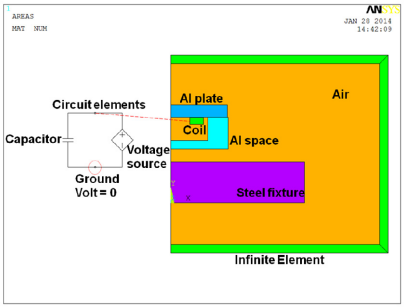

***Figure 4**: FE-model for the electromagnetic analysis*

3 Coupled Analysis

3.1 Electromagnetic field analysis

Using ANSYS [5], the electromagnetic force has been performed. For simplification of modeling, the coil and the aluminium plate have been assumed to be axisymmetric. Figure 4 shows the FE-model for the analysis. Firstly, the electric circuit has been evaluated. FE-model was constructed using the element PLANE53. nodes and elements of each area have been shown in table 2.

Part	Number of node	Number of element
Coil(Copper)	371	98
Al plate	2,153	741
Steel fixture	16,873	5,494
Air	24,706	8,303
Infinite Air	1,202	360

***Table 2**: Finite element model*

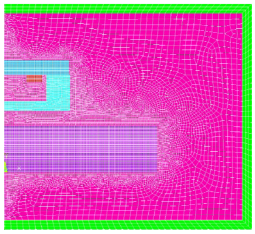

***Figure 5**: Finite element meshed*

In the model, the capacitance is 840uF. The charged energy is 10.5kJ and 15.12kJ with the initial capacitor voltage is 5kV and 6kV, respectively. The magnetic fields have been analysed with the obtained circuit on the coil. Table 2 shows the material properties and the dimensions of coil and plate.

Part	Electric resistivity (Ω·m)	Relative Permeability	Model dimension (mm)	Real dimension (mm)
Coil(Copper)	1.70e-8	1	ID : 90, OD : 156, T : 15	140X105X15 Hole : 90X22
Al plate	2.82e-8	1.000021	OD : 270, T : 30	195X295X30
Steel fixture	2.18e-8	200		
Air		1		
Infinite Air		1		

***Table 3**: Material properties and the dimensions of the FE-model*

3.2 Rigid-body dynamic analysis

The motion of the aluminium plate assumed to be a particle with the plate weight can be evaluated with rigid-body dynamics.

$$a = \frac{m_{al}}{F} \tag{1}$$

where, the force, F, is the z-directional total force obtained from the electromagnetic analysis. Adams-Bashforth two step method [6] is applied to solve the equation (1). The z-directional displacement of the aluminium plate can be calculated with the velocity.

$$v_1 = v_0 + \frac{\Delta t}{2}(3a_1 - a_0) \tag{2}$$

3.3 Coupled analysis

To solve the coupled fields, the electromagnetic force is obtained with electromagnetic analysis. The force is applied to the aluminium plate and the displacement of the plate can be calculated with the dynamics. The FE-model of the plate is changed with new position and the electromagnetic analysis has been repeated. Figure 5 shows the coupled analysis method.

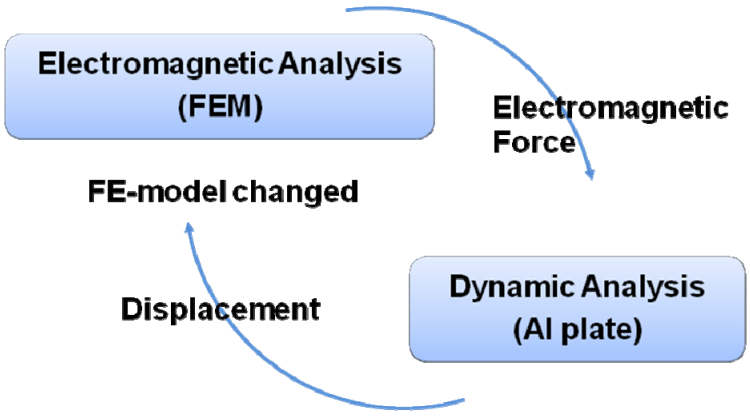

***Figure 6**: The coupled analysis method*

4 Results and Discussion

4.1 Electromagnetic force

Figure 6 shows the electromagnetic force applied to the aluminium plate. The force varied with the discharged electrical current. First peak force increased with the high initial

capacitor voltage, 6kV and the lighter plate. Because the displacement of the plate increased with the same conditions. Figure 7 shows the distribution of the electromagnetic force at the first peak with 6kV and 2.0kg. The force has been generated at the small region closed the coil.

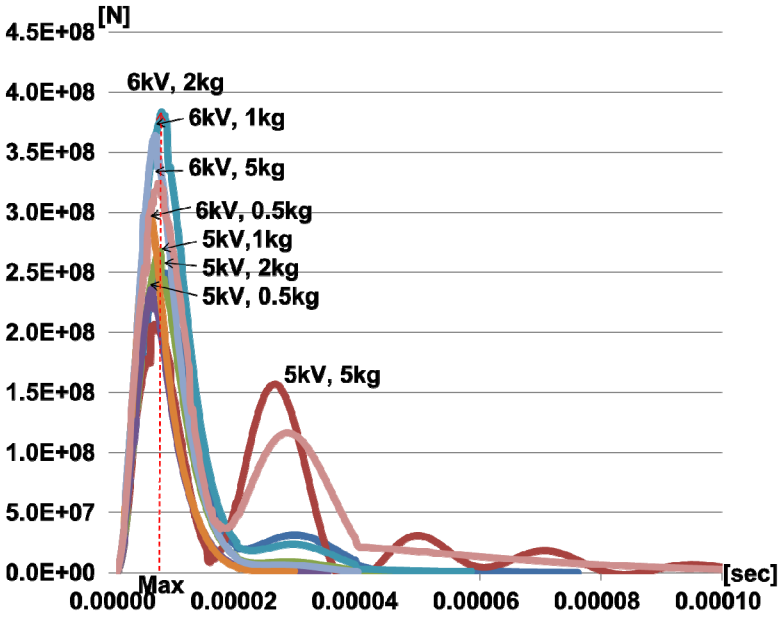

***Figure 7**: The electromagnetic force with various conditions*

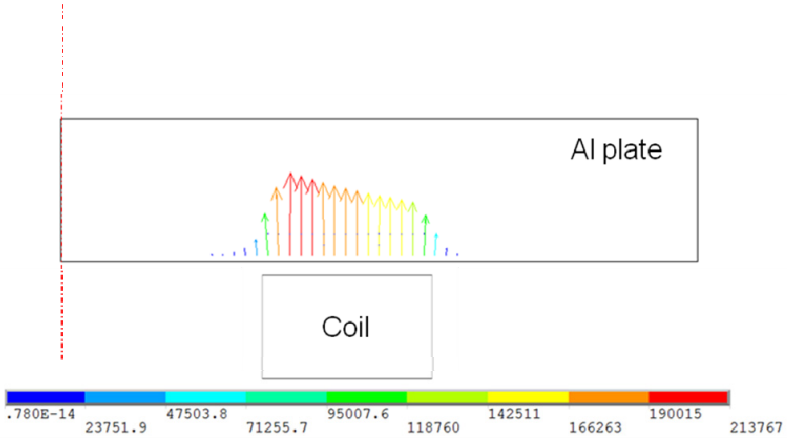

***Figure 8**: The electromagnetic force distribution on the plate*

4.2 Forming speed

Because the punch is fixed on the aluminium plate, forming speed is same as the velocity of the aluminium plate. Figure 8 shows the forming speed. With 6kV and 0.5kg plate, 4.3m/s can be obtained. On the design of the press, the mass of the aluminium plate must

be considered to obtain the certain velocity. The capacity of the magnetic pulse power source is important for the forming speed. The kinematic energy of the aluminium plate is shown in Table 3.

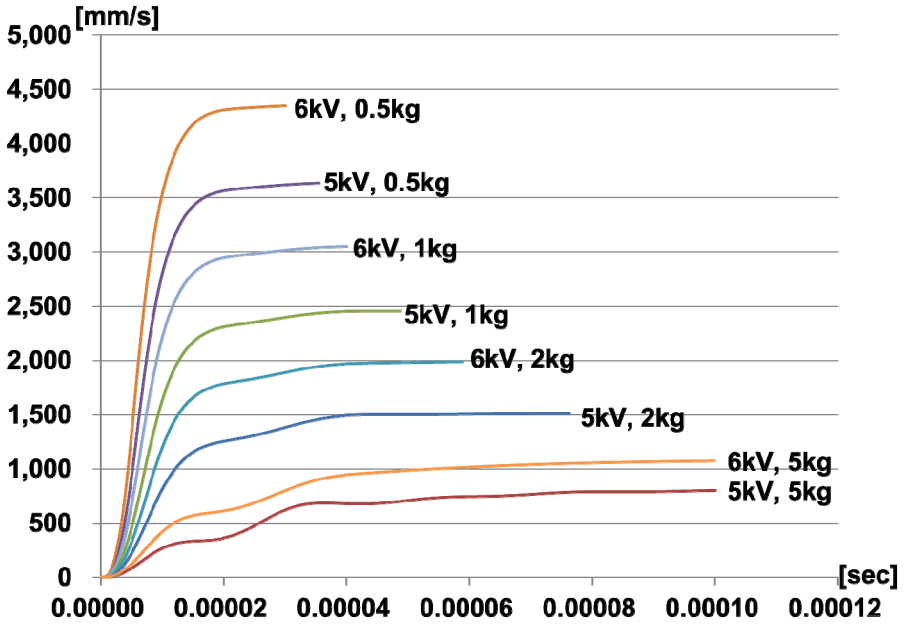

***Figure 9**: Forming speed of the press*

The initial capacitor voltage (kV)	Mass of the Al plate (kg)	Forming Speed (m/s)	The kinematic energy (J)
5	0.5	3.635	3.303
	1.0	2.456	3.016
	2.0	1.508	2.274
	5.0	0.801	1.604
6	0.5	4.348	4.726
	1.0	3.051	4.654
	2.0	1.987	3.948
	5.0	1.073	2.878

***Table 4**: Forming speed and kinematic energy of the moving aluminium plate*

5 Conclusion

In this paper, the coupled analysis of the high speed forming press has been performed using the electromagnetic pulse force. Some conclusions have been obtained. The obtained electromagnetic force are distributed very closed region with the coil. The forming speed depends on the mass of the aluminium plate and the capacity of the magnetic pulse power source(the initial capacitor voltage).

References

[1] *Tekkaya, A. E.; Daehn, G. S.; Kleiner, M.:* Proceedings of the 5th International Conference "High Speed Forming 2012", Dortmund, 2012.

[2] *Vohnout, V. J.:* A Hybrid Quasi-Static/Dynamic Process for Forming Large Sheet Metal Parts from Aluminium Alloys. Ph.D. Thesis, Ohio State University, 1998.

[3] *Martin G.; Jochen, B.; Altan, T.:* Influence of High Cutting Speed on the Quality of Blanked Parts "Report No. ERC/NSM-S-96-19", Columbus, Ohio, OSU, 1996.

[4] *Shim, J. Y.; Choi, Y.; Kang, B. Y.:* Development of Electromagnetic-Mechanical Coupled FE-Model for Thin Aluminium Plate Forming Using Electromagnetic Force. Key Engineering Materials Vols. 535-536, pp.267-270, 12013

[5] *ANSYS Low-Frequency Electromagnetic Analysis Guide, ANSYS Release 9.0, 2004.*

[6] *Richard, L. B. : Numerical Analysis, PWS-KENT, pp. 262, 1988.*

Development of Space-Time-Controlled Multi-Stage Pulsed Magnetic Field Forming and Manufacturing Technology at the WHMFC*

Liang Li[1,2], Xiaotao Han[1,2], Quanliang Cao[1,2], Qi Chen[1,2], Zhipeng Lai[1,2], Zhongyu Zhou[1,2], Qi Xiong[1,2], Xiao Zhang[1,2], Xin Li[1,2], Jiekai Fu[1,2] and Yuanhang Liu[1,2]

[1] Wuhan National High Magnetic Field Center, Huazhong University of Science and Technology, Wuhan, China
[2] State Key Laboratory of Advanced Electromagnetic Engineering and Technology, Huazhong University of Science and Technology, Wuhan, China

Abstract

In November 2011, the Project of Basic Research of Forming by Space-Time-Controlled Multi-Stage Pulsed Magnetic Field (Stic-Must-PMF) was supported by the National Basic Research Program of China (973 Project, 2011.11-2016.08). It is aimed at achieving breakthroughs in manufacturing technology to solve current problems in forming large-scale and complex sheet and tube parts and components, imposed by the limitations of existing equipment and materials forming properties. The objective of our research group focuses on the design principles and structural layout optimization of Stic-Must-PMF facility. And this paper will report the development of Stic-Must-PMF forming and manufacturing technology at the Wuhan National High Magnetic Field Center (WHMFC) including numerical modeling, experimental setup and experimental studies.

Keywords

Electromagnetic forming, Space-time-controlled, Finite element method

1 Introduction

Electromagnetic forming (EMF) is a high-speed forming technique that reshapes metal workpieces by means of pulsed electromagnetic force. Compared with conventional

* *The authors would like to thank National Basic Research Program of China (973 Program): 2011CB012800 (2011CB012801) for its financial support*

quasistatic forming processes, the EMF technology has been proved that it can efficiently improve the forming limits of metal workpieces and reduce wrinkling and springback [1]. And the technology has been investigated with various numerical and experimental studies for a long time. However, two problems have restricted its extensive applications in forming large-scale and complex sheet: 1) how to generate strong pulsed electromagnetic force (i.e., the design of high-field drive coils; 2) how to generate a space-time-controlled electromagnetic force acting on the workpiece in the EMF process.

To solve the current bottleneck problems of the EMF technology, a Space-Time-Controlled Multi-Stage Pulsed Magnetic Field (Stic-Must-PMF) forming and manufacturing technology has been proposed in our previous work [2]. And in the past two years, our work has focused on the three research aspects for developing the technology: (1) Numerical modeling for the full coupling of EMF process with a large-scale deformation, which can consider the effects of the sheet geometry and velocity on the circuit parameters and the electromagnetic force distribution on the workpiece as well as the effect of sheet-die. This research is a prerequisite for accurately predicting the dynamic behavior of the workpiece under the action of the multi-stage and multi-direction pulsed high magnetic field. (2) Building the key components of an experimental setup for Stic-Must-PMF forming system, including pulsed power supplies, forming magnets and control and measurement system. (3) Carrying out preliminary experiments by the use of the high pulsed magnetic field. And more details of these developments of the technology at the Wuhan National High Magnetic Field Center (WHMFC) will be reported in this paper.

2 Numerical modeling and simulation

To better understand the dynamic deformation behavior of the workpiece for designing the EMF system well, numerous numerical methods have been performed by using developed codes or commercial finite element method (FEM) [3]-[7]. Due to the fact that the numerical simulation based on FEM is much easier to implement, more researchers have used the finite element method to investigate the EMF process, mainly including the loose coupling method and sequential coupling method. Compared with the former, the sequential coupling method is more accurate since it can consider the effect of workpiece deformation on the electromagnetic force distribution. However, the effect of the change in system inductance, caused by the deformation of the workpiece, on the coil current was not considered in the method as well as the effect of the workpiece velocity. To consider the point, an efficient FEM using multi-physics software COMSOL has been developed [8], which can consider the effects of the sheet geometry and velocity on the circuit parameters and the electromagnetic force distribution on the workpiece. Unfortunately, it cannot consider the effect of sheet-die. Meanwhile, remeshing the airgap region situated between the coil and the workpiece in the method to eliminate the distortion introduces additional complication and inconvenience, and its convergence is getting worse as the deformation increases. And these are also the drawback of the sequential coupling method.

To overcome these problems for a fully coupled analysis, a numerical method based on a combination of Matlab and FEM models has been developed by our group, as shown in Figure 1. The mechanical model in the method is an ordinary structures problem involved large deformation, high strain rate and contact, which can be solved using the

finite element method. This part is similar with other numerical simulation methods. A distinguishing feature of this method is that the whole electromagnetic part of EMF is regarded as an accurate equivalent circuit network problem. Then only the coils and workpieces are considered in the model without considering the air meshes, and thus there are no convergence problems in the deformation process in our method. In the calculation, the solid conductors of the system are divided into a large number of current filaments, in which uniform distribution of current is assumed. Because the magnetic field generated by these current filaments can be calculated in the 2D model using the semi-analytical or semi-analytical formulas, the problem of electromagnetic force distribution in the workpiece can be effectively solved in Matlab. It should be noted that the displacement and velocity values of the calculation nodes in the deformed workpiece are updated at each simulation step to reflect their effects on the current and the magnetic force distribution in the forming process.

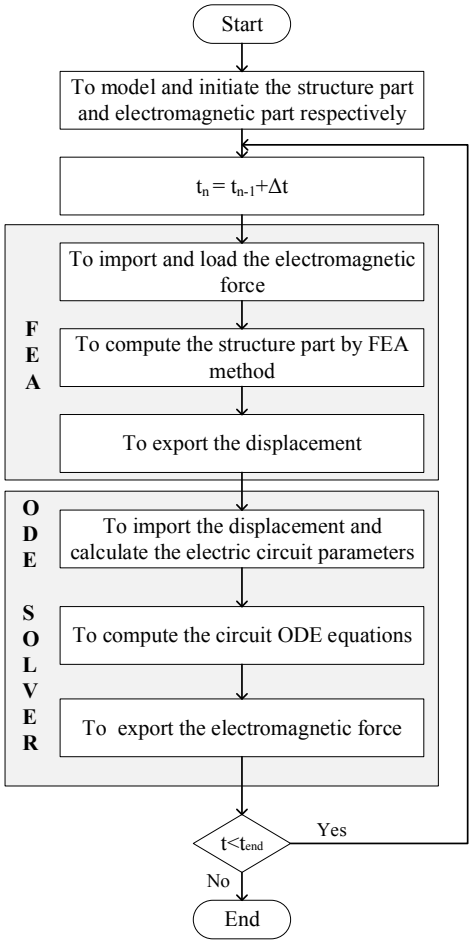

***Figure 1**: Flowchart of the implemented algorithm for the EMF model.*

Figure 2 shows the prediction profiles of the deformed workpiece in an EMF model for the three cases: (a) the workpiece end is assumed to be fixed and it can be calculated by use of ANSYS based on a sequential coupling method; (b) the workpiece end is free and the simulation is based on our numerical method; (c) the workpiece end is free and the simulation is based on a loose coupling method. Contact conditions are considered between the die and the sheet as well as the sheet and holder in the simulations. It can be seen a radial indent will exist when the workpiece end is assumed to be free in the simulation and that should be highly problematic for air meshing and the calculation of electromagnetic field in the sequential coupling method. This problem can be sovled well by our method and the loose coupling method. However, the accuracy of the calculation result is low in the loose coupling method due to the effect of the workpiece deformation on the magnetic analysis is neglected. And it can be seen from Figure 2 that the simulation deformation of the workpiece is much larger than that in the other methods. More detailed results about the axial displacement at the sheet center for the three cases are shown in Figure 3. In summary, our numerical method can avoid the problem of the air mesh processing and study the impact contact behavior between the workpiece and die with considering the effects of the workpiece deformation on the circuit parameters and the electromagnetic force distribution on the workpiece.

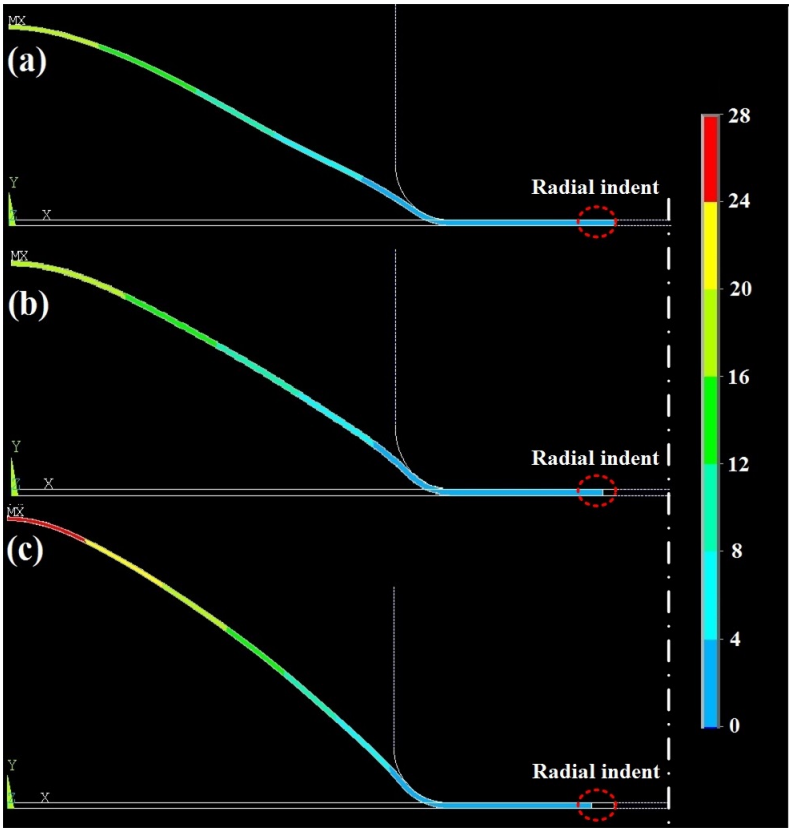

***Figure 2**: Numerical prediction profiles of the deformed workpiece for the three cases: (a) the workpiece end is assumed to be fixed and the simulation is based on a sequential coupling method; (b) the workpiece end is free and the simulation is based on our numerical method; (c) the workpiece end is free and the simulation is based on a loose coupling method.*

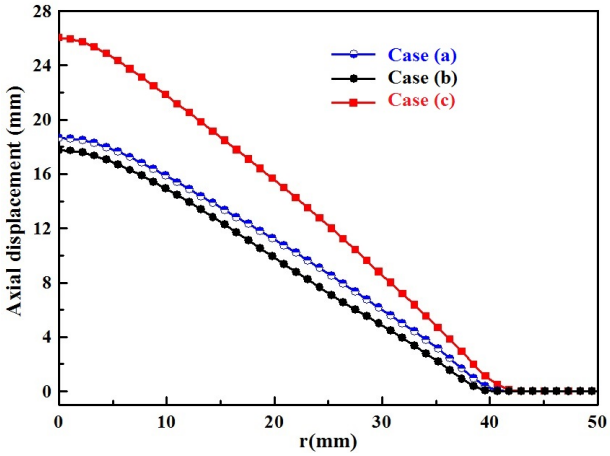

***Figure 3**: Axial displacements of the workpiece at the center for the three cases: (a) the workpiece end is assumed to be fixed and the simulation is based on a sequential coupling method; (b) the workpiece end is free and the simulation is based on our numerical method; (c) the workpiece end is free and the simulation is based on a loose coupling method.*

3 Experimental setup and studies

3.1 Pulsed Power Supply

Three types of pulsed power supply, capacitor banks of 1 MJ/25 kV/3.2 mF, 200 kJ/25 kV/640 μF and 14.4 kJ/30 kV/32 μF, have been developed and built for the Stic-Must-PMF forming system at the WHMFC in China, as shown in Figure 4. These three types of pulsed power supplies can be used singly or in combination to generate short and long pulsed magnetic fields with different tool coils.

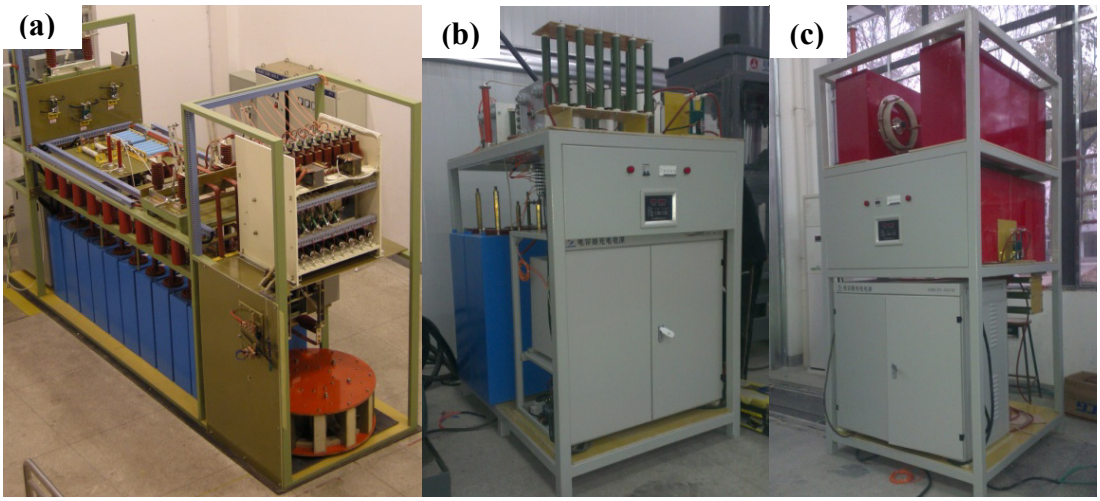

***Figure 4**: Three types of capacitor bank power supply system: (a) 1 MJ/25 kV/3.2 mF, (b) 200 kJ/25 kV/640 μF, (c) 14.4 kJ/30 kV/32 μF.*

3.2 Tool Coil

Several tool coils have been designed and fabricated by introducing the nondestructive pulsed high field magnet technology to suit the requirements of high strength and long life performances, as shown in Figure 5. These coils have been used for different experimental studies of EMF system, such as electromagnetic ring expansion, electromagnetic flanging, electromagnetic sheet bulging and electromagnetic hardening.

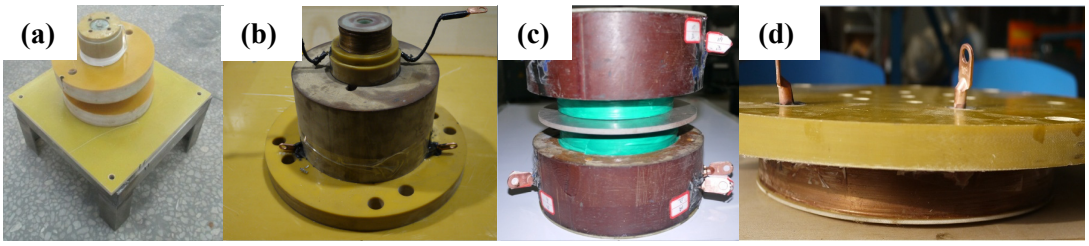

***Figure 5**: Tool coils for different electromagnetic applications: (a)* ring expansion, *(b) two-stage sheet bulging, (c) hardening, (d) flanging.*

3.3 Multi-stage Timing Control System

A three-stage timing control system has been designed and implemented in Figure 6 for controlling the on-and-off of the tool coils to adjust the magnetic field distribution, which is an important part of the Stic-Must-PMF forming technology. The system has following properties: (i) it can be controlled independently or in combination; (ii) it has a high stability due to electrical-optical isolation between the control room and the local control units. (iii) it can provide a triggering time at microsecond level and multi-channel high-speed data acquisition (sample rate > 1 MS/s) for the requirements of high precision control.

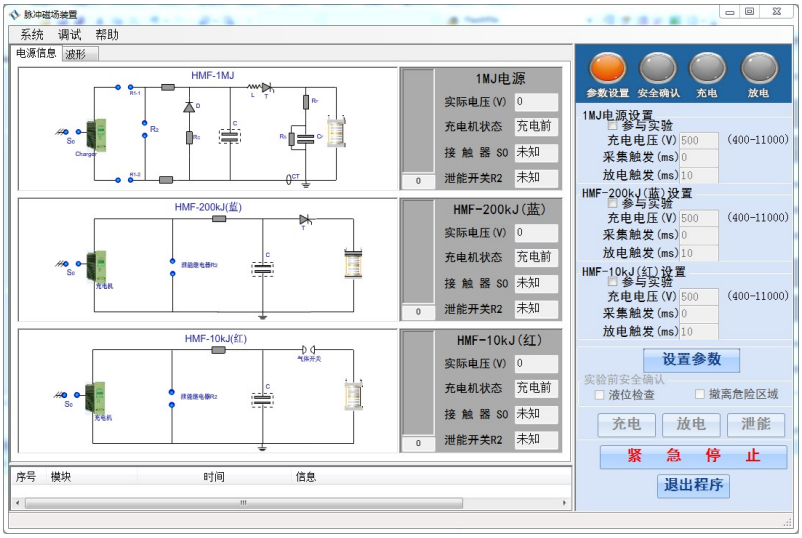

***Figure 6**: Interface of the three-stage timing control system.*

3.4 Experimental Study of a Large-Scale Sheet Forming

The experimental studies mainly focused on the tube EMF system, few of which touch upon the application of metal sheet [1], especially for the large-scale sheet workpiece. An important reason resulting in such phenomena is a strong pulsed electromagnetic force cannot be arbitrarily enlarged to form large parts due to the limitation of the strength of the coil [2]. Recently, the electromagnetic flanging of a large-scale aluminum alloy sheet (AA5083-O), whose outer diameter, bore diameter, sheet thickness are 640 mm, 180 mm and 5 mm, respectively, was investigated at the WHMFC. The quasi-static stress-strain curve of the material is shown in Figure 7. The Hollomon's hardening equation $\sigma = K\varepsilon^n$ (K and the n are 0.5352 GPa and 0.27316, respectively) was adopted to fit the stress-strain relationship of AA5083-O and used to calculate the deformation behavior of the sheet, which didn't consider the high strain-rate effect on the mechanical properties of the workpiece.

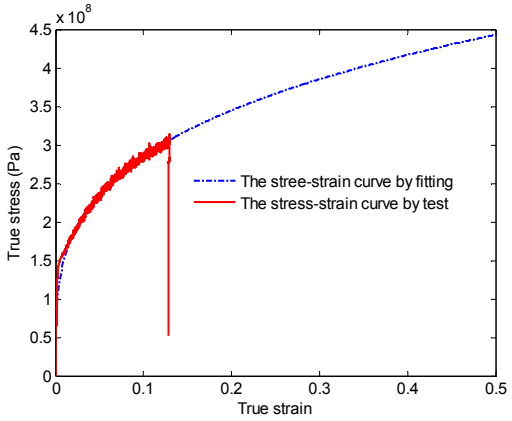

Figure 7: *The quasi-static stress-strain curve of AA5083-O.*

To generate enough electromagnetic force, the discharging energy should be large enough. Thus a bank of capacitor with the maximum energy of 200 kJ was equipped. To make sure the coil's lifetime, the non-destructive pulsed high field magnet technology, where internal reinforcement is inserted between the conductor layers, was used to fabricate the coil. The structural strength of the coil was assessed by numerical calculation of the stress distribution of the coil by FEA. To assess the forming capacity of the EMF system, both the simulation and experimental study of the electromagnetic flange of a large-scale aluminium alloy sheet in the case of 155 kJ have been done.

3.4.1 Coil Design

The design of the coil firstly is the electromagnetic design and secondly is the structural strength design. According to the electromagnetic design, the inner diameter (100 mm), the outer diameter (132 mm), the height (25 mm) and the turns (10 layers in radial direction, each layer has 5 turns in axial direction) of the coil were determined. And for the structural strength design, the reinforcement mode was determined: the conductor was copper wire (4 mm X 2 mm) and each layer was reinforced by Zylon fiber. To assess the structural strength, the stress distribution in the mid-plane of the coil at the coil current's peak value time was calculated by FEM. As shown in Figure 8, the maximum von Mises

stress is about 0.8 GPa in the Zylon, which is only one fifth of the ultimate tensile strength of Zylon and confirms that the coil is able to bear the huge Lorentz force.

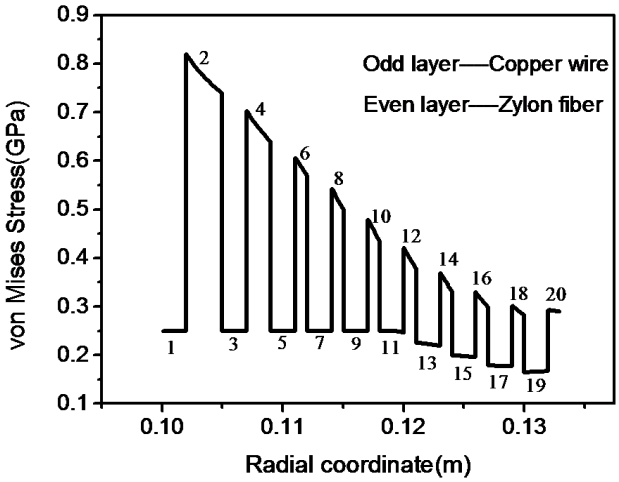

***Figure 8**: The von Mises stress of the mid-plane of the coil [8].*

3.4.2 Simulation and Experimental Results

Both the simulation and experimental study of the electromagnetic flange of a large-scale aluminium alloy sheet in the case of 155 kJ were done. Figure 9 shows the main dimensions of the experimental equipment. And Figure 10 shows the setup of the experiment. Figure 11 shows the displacements of the inner bore. The maximum axial and radial displacements are 87 mm and 27 mm, respectively, while the axial displacement by experiment was 90 mm, the relative error was 3%. It can be seen that the agreement between the simulation and experiment results is satisfactory and the EMF system has the capacity to form the large-scale workpiece.

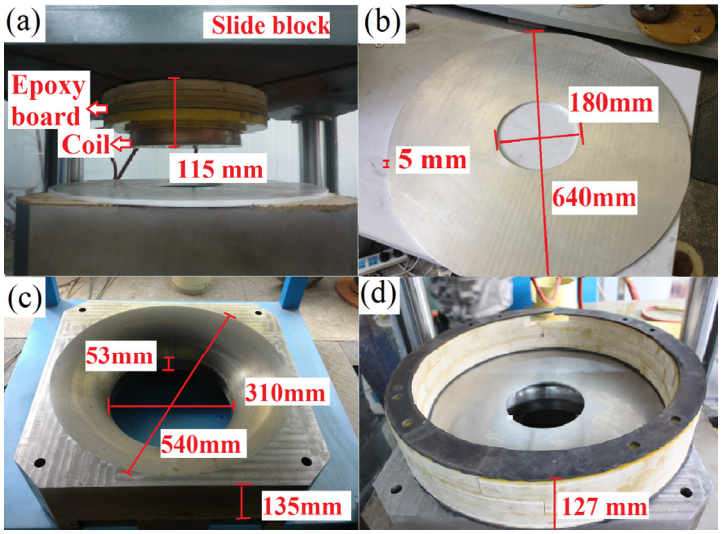

***Figure 9**: (a) The coil and several epoxy boards were fixed on the slide block; (b) the workpiece; (c) the die; (d) the blank holder [8].*

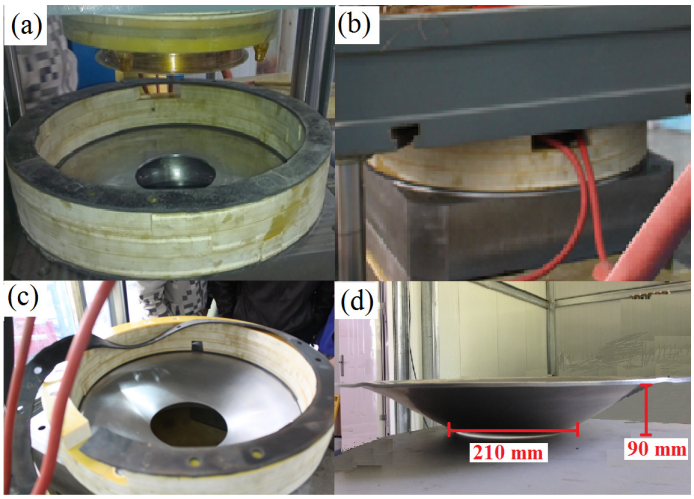

***Figure 10**: The experiment setup: (a) before the slide block was moved down; (b) the slide block was moved down; (c) after the discharge; (d) the formed workpiece [8].*

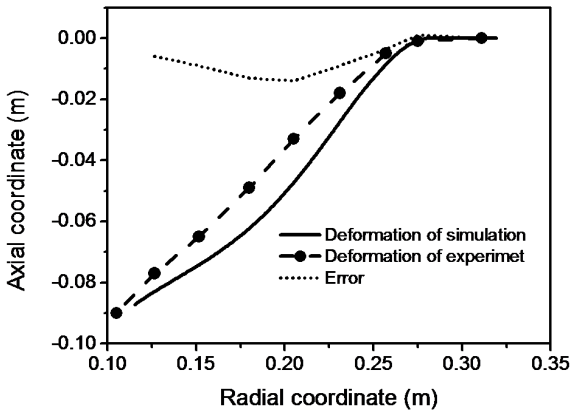

***Figure 11:** The comparison of the simulation and the experiment deformation profiles [8].*

4 Conclusion

A strong and well-designed space-time distribution of electromagnetic force could lead to the forming and manufacturing of sheet and tube parts and components with controlled materials properties. However, there are great challenges in developing such new forming and manufacturing technology. In the project, we need to solve a key scientific problem: the rules of space-time distribution of the strong space-time-controlled multi-stage pulsed magnetic field and control of the force field in forming. For this, an effective numerical simulation method has been developed, which can be used to predict the dynamic behavior of the workpiece in a single coil system or multi-stage coil system (although the numerical studies presented in the paper is just for a single coil system). Meanwhile, three types of pulsed power supply, tool coils and three-stage timing control system have been designed and implemented for the future researches of the Stic-Must-PMF forming system.

In particular, a two-stage forming coil system has been developed for axisymmetric deep drawing in our lab recently. More numerical and experimental results are still on going and will be reported later.

References

[1] *Psyk V.; Risch D.; Kinsey B.L.; Tekkaya A.E.; Kleiner M.:* Electromagnetic forming-A review. J. Mater. Process. Tech., 2011, vol. 211, p. 787-829.

[2] *Li L.; Han X.; Peng T.; Ding H.; Ding T.; Qiu L.; Zhou Z.; Xiong Q.:* Space-time-controlled multi-stage pulsed magnetic field forming and manufacturing technology. Proc. Int. Conf. High Speed Forming, Dortmund, Germany, 2012, p. 53-58.

[3] *Takatsu N.; Kato M.; Sato K.; Tobe T.:* High-speed forming of metal sheets by electromagnetic force. Jpn. Soc. Mech. Eng. Int. J., 1988, vol. 31, no. 1, p. 142-148.

[4] *Fenton G.K.; Daehn G.S.:* Modeling of electromagnetically formed sheet metal. J. Mater. Process. Technol., 1998, vol. 75, no. 1–3, p. 6-16.

[5] *Oliveira D.A.; Worswick M.J.; Finn M.; Newman D.:* Electromagnetic forming of aluminum alloy sheet: free-form and cavity fill experiments and model. J. Mater. Process. Tech., 2005, vol. 170, p. 350-362.

[6] *Correia J.P.M.; Siddiqui M.A.; Ahzi S.; Belouettar S.; Davies R.:* A simple model to simulate electromagnetic sheet free bulging process. Int. J. Mech. Sci., 2008, vol. 50, p. 1466-1475.

[7] *Yu H.P.; Li C.F.; Deng J.H.:* Sequential coupling simulation for electromagnetic mechanical tube compression by finite element analysis. J. Mater. Process. Tech., 2009, vol. 209, p. 707-713.

[8] *Lai Z.P.; Han X.T.; Cao Q.L.; Qiu L.; Zhou Z.Y.; Li L.:* The Electromagnetic Flanging of a Large-Scale Sheet Workpiece. IEEE Trans. Appl. Supercond., 2014, vol. 24, no. 3, 0500805.